UNIVERSITÄT ZU KÖLN – I. PHYSIKALISCHES INSTITUT
MATHEMATISCH – NATURWISSENSCHAFT FAKULTÄT
&
OBSERVATOIRE DE PARIS – LERMA
ECOLE DOCTORALE D'ASTRONOMIE ET D'ASTROPHYSIQUE
D'ÎLE-DE-FRANCE

PhD Thesis
To obtain the degree of Doctor

Author:
STÉPHAN Gwendoline

Modeling chemistry in massive star forming regions with internal PDRs

Supervisors:
Prof. Dr. SCHILKE Peter / Prof. Dr. LE BOURLOT Jacques

Defense: 4th November, 2016

Members of the jury

Prof. Dr.	WOLF Sebastian	(Referee)
Dr.	DESPOIS Didier	(Referee)
Prof. Dr.	SAUR Joachim	(President)
Prof. Dr.	SCHILKE Peter	(Supervisor)
Prof. Dr.	LE BOURLOT Jacques	(Supervisor)
Prof. Dr.	BOCKELÉE MORVAN Dominique	(Member)
Prof. Dr.	PINEAU DES FORÊTS Guillaume	(Member)
Dr.	SÁNCHEZ-MONGE Álvaro	(Member)

Modeling chemistry in massive star forming regions with internal PDRs

INAUGURAL – DISSERTATION

zur
Erlangung des Doktorgrades
der Mathematisch – Naturwissenschaftlichen Fakultät
der Universität zu Köln

vorgelegt von

Gwendoline Stéphan
aus Pont l'Abbé

Köln 2016

Berichterstatter: Prof. Dr. SCHILKE Peter
                    Prof. Dr. WOLF Sebastian
                    Prof. Dr. DESPOIS Didier

Tag der mündlichen Prüfung: 4th November, 2016

THÈSE DE DOCTORAT

de l'Université de recherche Paris Sciences et Lettres
PSL Research University

Préparée dans le cadre d'une cotutelle entre
Observatoire de Paris – LERMA
Universität zu Köln – I. Physikalisches Institut

Modeling chemistry in massive star forming regions with internal PDRs

Modélisation de la chimie dans les régions de formation d'étoiles massives avec PDRs internes

École Doctorale n° 127
École Doctorale d'Astronomie et d'Astrophysique d'Île-de-France
Spécialité: Astronomie et Astrophysique

soutenue par Gwendoline STÉPHAN
le 4 novembre 2016

dirigée par
Prof. Dr. Peter SCHILKE & Prof. Dr. Jacques LE BOURLOT

À ma famille
et à son tout nouveau membre, Éléanore

"When walking through the 'valley of shadows',
remember,
a shadow is cast by a Light"

Austin O'Malley

Acknowledgements

For this work, I used the Lapack and Blas Fortran libraries as well as several Python packages: numpy, astropy, matplotlib, pp and scipy. For the parallel jobs I also used the free software GNU parallel and some plots were generated with the command-line tool gnuplot. Furthermore, I made use of the following visualization softwares: ds9, kvis and Paraview. For the debugging and optimization of *Saptarsy* I used the application performance analyzer and visualizer Instruments integrated in environment Xcode.

Now, I would like to thank personally all the people who helped me to carry out this work and supported me during these four years.

First, I thank my supervisors Peter Schilke and Jacques Le Bourlot for their advice, for pushing me to be more accurate in my thinking and widening my view. Your assistance and the discussions we had were not just helpful but also necessary for me to improve the results and move forward. Despite your busy schedule and the distance, you always have been available to sit/skype with me when needed. I am very grateful you introduced me to the astrochemistry field and gave me the opportunity to pursue this very interesting research. I would also like to thank both of you for accepting this co-tutelle which was not easy to set up and had a few hick-ups on the way but end up to be very useful for me.

Second, I would like to thank my colleagues and collaborators: Rumpa Choudhury and Benjamin Godard (astrochemistry and *Saptarsy*), and Anika Schmiedeke (*Pandora* and *RADMC-3D*). This work would not have been possible without you developing the tools I used and helping me improving/optimizing them. Rumpa, you spent a lot of time at the beginning of my thesis explaining astrochemistry and how *Saptarsy* works. Benjamin, you were always there to answer the questions I had when I was in Paris and your help and advice on the optimization of *Saptarsy* was significant. Anika, thank you for spending so much time with me explaining *Pandora*, for helping me to implement new parts necessary for my work, for meeting with me or answering all my e-mails when I had questions, even silly ones or the ones I had already asked months before, and for giving me a lot of useful tips.

Abstract

Title   Modeling chemistry in massive star forming regions
with internal PDRs

Keywords Astrochemistry: Chemical evolution
Massive star formation: HC/UCHII regions – Hot molecular cores –
Photodissociation regions

Over the past decades star formation has been a very attractive field because knowledge of star formation leads to a better understanding of the formation of planets and thus of our solar system but also of the evolution of galaxies. Conditions leading to the formation of high-mass stars are still under investigation but an evolutionary scenario has been proposed: As a cold pre-stellar core collapses under gravitational force, the medium warms up until it reaches a temperature of 100 K and enters the hot molecular core (HMC) phase. The forming central proto-star accretes materials, increasing its mass and luminosity and eventually it becomes sufficiently evolved to emit UV photons which irradiate the surrounding environment forming a hyper compact (HC) and then a ultracompact (UC) HII region. At this stage, a very dense and very thin internal photon-dominated region (PDR) forms between the HII region and the molecular core.

Information on the chemistry allows to trace the physical processes occurring in these different phases of star formation. Formation and destruction routes of molecules are influenced by the environment as reaction rates depend on the temperature and radiation field. Therefore, chemistry also allows the determination of the evolutionary stage of astrophysical objects through the use of chemical models including the time evolution of the temperature and radiation field.

Because HMCs host a very rich chemistry with high abundances of complex organic molecules (COMs), several astrochemical models have been developed to study the gas phase chemistry as well as grain chemistry in these regions. In addition to HMCs models, models of PDRs have also been developed to study in particular photo-chemistry. So far, few studies have investigated internal PDRs and only in the presence of outflows cavities. Thus, these unique regions around HC/UCHII regions remain to be examined thoroughly.

My PhD thesis focuses on the spatio-temporal chemical evolution in HC/UC HII regions with internal PDRs as well as in HMCs. The purpose of this study is first to understand the impact and effects of the radiation field, usually very strong in these regions, on the chemistry. Secondly, the goal is to study the emission of various tracers of HC/UCHII regions and compare it with HMCs models, where the UV radiation field does not impact the region as it is immediately attenuated by the medium. Ultimately we want to determine the age of a given region using chemistry in combination with radiative transfer.

To investigate these transient phases of massive star formation, we use the astrochemical code *Saptarsy*, optimized and improved during this PhD thesis. *Saptarsy* is a gas-grain code computing the spatio-temporal evolution of relative abundances. It is based on the rate equation approach and uses an updated Ohio State University (OSU) chemical network. Moreover, *Saptarsy* works along with the radiative transfer code *RADMC-3D* via a Python based program named *Pandora*. This is done in order to obtain synthetic spectra directly comparable to observations using the detailed spatio-temporal evolution of species abundances.

To summarize the *Pandora* framework: We use *RADMC-3D* to self-consistently compute the spatio-temporal evolution of the dust temperature and mean intensity of the radiation field adopting first, a model of accreting high mass proto-star which gives the time evolution of the stellar luminosity and second, a Plummer-like function as the density radial profile. Based on these parameters and initial conditions obtained with *Saptarsy* for a pre-stellar core model, *Saptarsy* computes the evolution of relative abundances which are next used by *RADMC-3D* to produce time-dependent synthetic spectra assuming Local Thermodynamic Equilibrium (LTE). These spectra can then be post-processed, i.e. convolved to the beam of the observations we want to compare them with.

In addition to comparing a HC/UCHII region to a HMC model, we analyze models with different sizes of HII regions, with various densities at the ionization front as well as with two different density profiles. We investigate the critical dependance of the abundances on the initial conditions and we also explore the importance of the emission coming from the envelope for various species. We find that among the dozen of molecules and atoms we have studied only four of them trace the UC/HCHII region phase or the HMC phase. They are C^+ and O for the first and CH_3OH and $H_2^{18}O$ for the second phase. However, more species could be studied to probe and identify these phases. For instance, CO^+ seems a good candidate to trace PDRs but it is not abundant enough in our model. It appears that models including an outflow cavity produce more of this molecule. Thus, we could modify the geometry of our source structure by adding an outflow, and later even more complex geometries. More improvements could also be made such as simple computation of the gas temperature in *Saptarsy* which might strongly affect the chemistry inside the PDR.

Zusammenfassung

Titel	Chemische Modellierung in massereichen Sternentstehungsgebieten durch interne PDRs
Schlüsselwörter	Astrochemie: Chemische Evolution massereiche Sternentstehung: HC/UCHII Regionen – Heiße molekulare Kerne – Photodissoziationsregionen

Während der letzten Jahrzehnte hat die Bedeutung des Forschungsgebiets der Sternentstehung stark zugenommen. Das Wissen darüber liefert ein besseres Verständnis über die Entstehung von Planeten, des Sonnensystems und der Entwicklung von Galaxien. Obwohl die genauen Bedingungen für die Entstehung von massereichen Sternen noch untersucht werden müssen, kann trotzdem ein grundsätzliches Szenario angenommen werden: Unter dem Einfluss der Gravitation kollabiert der kalte Vorgänger eines Sterns. Dabei erwärmt sich dieser bis auf Temperaturen von ungefähr 100 K und geht in die "heiße molekulare Phase" (HMC) über. Der entstehende Protostern akkretiert Material, wächst somit in Masse. Ist der Stern hinreichend entwickelt beginnt er UV Strahlung zu emittieren. In der beschienene Umgebung bildet sich eine hyperkompakte (HC) und dann ultrakompakte (UHC) HII Region aus. Zwischen der HII Region und dem molekularen Kern bildet sich eine dichte, dünne interne photonen-dominierte Region (PDR) aus.

Die chemische Information kann Aufschluss geben über die physikalischen Prozesse der verschiedenen Phasen der Sternentstehung, da Reaktionsraten durch die Temperatur und das Strahlungsfeld des Umfeld bestimmt werden. Die Chemie und deren zeitliche Modellierung erlaubt dadurch eine Bestimmung des Entwicklungsstandes von astrophysikalischen Objekten.

HMCs weisen eine komplizierte chemische Zusammensetzung auf mit einem hohen Anteil an komplexen organischen Molekülen (COM). Um die Gasphasen- und Staub-Chemie in den angesprochenen Gebieten zu untersuchen wurden mehrere astrochemische Modelle entwickelt. Hinzu kommen spezielle Modelle, die sich mit der Photochemie in PDRs beschäftigen. Nur wenige Arbeiten zielen auf interne PDRs ab und das meist nur in Gebieten mit geringer Dichte, welche durch die Gegenwart von Ausflüssen entstanden sind. Die einzigartigen HC/UCHII Regionen müssen noch gründlicher erforscht werden.

Meine Doktorarbeit beschäftigt sich mit der chemischen Entwicklung in HC/UCHII Regionen durch interne PDRs und HMCs. Ein Ziel dieser Arbeit ist das grundsätzliche Verständnis wie das Strahlungsfeld auf die Chemie Einfluss nimmt. Es soll die Emission unterschiedlicher Tracer in HC/UCHII Regionen erklärt und mit dem HMC Model, in denen das UV Strahlungsfeld sofort abgeschwächt wird, verglichen werden. Letztendlich möchte ich das Alter einer gegeben Region mit Hilfe von Chemie und Strahlungstransfer-Simulationen bestimmen.

Zur Untersuchung dieser kurzen Phase in der Sternentstehung benutze ich den astro-chemischen Code *Saptarsy*, welcher während der Dissertation verbessert und optimiert wurde. *Saptarsy* ist ein Gas-Staub Programm, welches die zeitliche und räumliche Entwicklung der relativen Häufigkeiten chemischer Spezies berechnet. Es basiert auf einen Ratengleichungsansatz und nutzt dazu ein -von der Ohio State University (OSU)- überarbeitetes chemischen Netzwerk. Zusätzlich arbeitet *Saptarsy* mit dem Strahlungstransfer Code *RADMC-3D* über eine *Python* basierende Schnittstelle, *Pandora* genannt, zusammen. Schlussendlich ist es damit möglich, die erhaltenen synthetischen Spektren mit Beobachtungen zu vergleichen.

Eine kurze Zusammenfassung von *Pandora*: *RADMC-3D* berechnet selbst-konsistent die räumliche und zeitliche Entwicklung der Staubtemperatur und die mittlere Intensität des Strahlungsfeldes. Angenommen wird dazu ein Modell eines massereichen Proto-Sterns und desses Leuchtkraft sowie ein Plummer-Dichte-Profil. Mit diesen Parametern und den Anfangsbedingungen aus *Saptarsy* wird die Entwicklung der relativen Häufigkeiten berechnet. *RADMC-3D* erzeugt daraus zeitabhängige synthetische Spektren unter der Annahme eines lokalen thermodynamischen Gleichgewichts. Diese Spektren können nun mit dem zu beobachtenden Strahl gefaltet werden und sind somit mit Beobachtungen vergleichbar.

Zusätzlich werden Größen von HII Regionen bei unterschiedlicher Dichte der Ionisationsfront und bei zwei weiteren Dichteprofilen bestimmt. Es wird gezeigt, dass die Anfangsbedingungen entscheidend sind für die chemische Häufigkeit von chemischen Spezies und dass die Emission der Einhüllenden eine entscheidende Rolle spielt. Unter Dutzenden von Molekülen und Atomen, die die Phase in HC/UCHII oder der HMC beschreiben, betrachten wir vier näher. Für die erste genannte sind dies C^+ und O sowie CH_3OH und $H_2^{18}O$ für die zweite. Weitere Spezies wären möglich. Als Beispiel hierfür sei CO^+ genannt. Jedoch weist diese Spezies in unserer Beschreibung eine zu geringe Häufigkeit auf verglichen mit Modellen die auch Gebiete niedriger Dichte in Betracht ziehen. Zukünftig sollte deswegen die ursprüngliche Geometrie angepasst werden. Eine weitere Verbesserungen ergebe sich durch die direkte Berechnung der Gastemperatur in *Saptarsy*. Dadurch könnte sich die Chemie in PDRs deutlich verändert werden.

Résumé

Titre   Modélisation de la chimie dans les régions de formation
               d'étoiles massives avec PDRs internes

Mots clés Astrochimie: Evolution chimique
               Formation d'étoile massive: Régions HII hypercompactes et ultracompactes –
               Cœurs chauds moléculaires – Régions de photodissociation

Au cours des dernières décennies, la formation des étoiles a été un sujet très attractif.
La connaissance de la formation des étoiles conduit à une meilleure compréhension de
la formation des planètes, donc de notre système solaire mais également de l'évolution
des galaxies. Les conditions menant à la formation des étoiles massives sont toujours
étudiées mais un scénario de leur évolution a été avancé: lors de l'effondrement d'un cœur
froid pré-stellaire sous l'effet de la gravité, le milieu se réchauffe jusqu'à atteindre une
température de 100 K. Il entre ainsi dans la phase de cœur chaud moléculaire (CCM).
La proto-étoile centrale en formation accrète de la matière, augmentant sa masse et sa
luminosité. Finalement elle devient suffisamment évoluée pour émettre des photons UV.
Ceux-ci irradient l'entourage de l'étoile formant ainsi une région HII hypercompacte (HC),
puis une région HII ultracompacte (UC). À ce stade, une région de photo-dissociation
(PDR) se forme entre la région HII et le cœur moléculaire.

La composition chimique du milieu nous permet de connaître les processus physiques
ayant lieu pendant les différentes phases de la formation des étoiles. Les chemins de
formation et de destruction des molécules sont influencés par l'environnement parce que
les taux de réaction dépendent de la température et du champ de rayonnement. De
plus, la chimie nous permet également de déterminer le stade de l'évolution d'un objet
astrophysique par l'utilisation de codes chimiques incluant l'évolution temporelle de la
température et du champ de rayonnement.

Plusieurs codes ont été développés afin d'étudier la chimie en phase gazeuse ainsi
que la chimie de surface dans les cœurs chauds moléculaires. Ces régions abritent une
chimie extrêmement riche avec de très fortes abondances pour les molécules organiques
complexes. En plus des modèles de cœurs chauds, des modèles de PDRs ont été développés
pour étudier notamment la photochimie. Jusqu'à présent, très peu d'études ont examiné
les PDRs internes et cela a été fait uniquement en présence d'une cavité formée par un
écoulement de matière depuis les pôles de la proto-étoile vers le milieu environnant (appelé
ici outflow). La connaissance de ces régions uniques autour des régions HII hypercompact
et ultracompact restent donc à approfondir.

Ma thèse de doctorat se concentre sur l'évolution spatio-temporelle de la chimie dans
les régions HII hypercompact et ultracompact avec des PDRs internes ainsi que la chimie
dans les cœurs chauds moléculaires. Premièrement, l'objectif de ce travail est de compren-

dre l'impact et les effets sur la chimie du champ de rayonnement, en général très fort dans ces régions. Deuxièmement, le but est d'étudier l'émission de diverses espèces spécifiques aux régions HII HC/UC et de comparer cette émission à celle des CCMs, régions où le champ de rayonnement UV n'a pas d'influence vu qu'il est immédiatement atténué par le milieu. En fin de compte, nous voulons déterminer l'âge d'une région donnée en utilisant la chimie associée au transfert radiatif.

Pour étudier ces stades transitoires de la formation des étoiles massives, nous utilisons le code astrochimique *Saptarsy* optimisé et amélioré pendant cette thèse de doctorat. *Saptarsy* est un code gaz-grain calculant l'évolution spatio-temporelle d'abondances relatives. Il est basé sur l'approche des équations des taux de réactions et il utilise le réseau chimique OSU (Université de l'État de l'Ohio) mis à jour. De plus, *Saptarsy* est couplé au code de transfert radiatif *RADMC-3D* via un programme, basé sur le langage Python, nommé *Pandora*, en vue d'obtenir des spectres synthétiques directement comparables avec des observations en utilisant l'évolution spatio-temporelle détaillée des abondances chimiques.

Pour résumer le fonctionnement de *Pandora*: nous utilisons *RADMC-3D* pour calculer de manière auto-cohérente l'évolution spatio-temporelle de la température des grains et de l'intensité du champ de rayonnement. Tout d'abord, nous adoptons un modèle de proto-étoile massive qui fournit l'évolution temporelle de la luminosité de l'étoile. Dans un deuxième temps, nous utilisons une fonction de Plummer pour définir le profil radial de la densité. Avec ces paramètres et des conditions initiales obtenues avec *Saptarsy* pour un modèle de cœur pré-stellaire, *Saptarsy* calcule l'évolution des abondances relatives. Elles sont ensuite utilisées par *RADMC-3D* pour produire, dans l'approximation ETL (Équilibre Thermodynamique Local), des spectres synthétiques dépendant du temps. Ces spectres peuvent finalement être convolués afin qu'ils aient la même résolution que les observations avec lesquelles nous voulons les comparer.

En plus de la comparaison entre un modèle de région HII HC/UC et un modèle de CCM, nous comparons des modèles avec des tailles différentes de régions HII, avec plusieurs densités au front d'ionisation, ainsi qu'avec deux profils de densité différents. Nous étudions les abondances qui dépendent de manière critique des conditions initiales et nous explorons aussi l'importance de l'émission venant de l'enveloppe pour diverses espèces chimiques. Nous constatons, parmi la douzaine d'espèces étudiées, que seulement quatre d'entre elles sont spécifiques à la phase de région HII ou à la phase de cœur chaud. Ces espèces sont C^+ et O pour la première phase et CH_3OH et $H_2^{18}O$ pour la deuxième phase. Cependant, un plus grand nombre d'espèces pourrait être utilisées pour étudier et identifier ces phases. Par exemple, CO^+ semble un bon candidat pour tracer des PDRs mais il n'est pas assez abondant dans notre modèle. Il semble que des modèles incluant une cavité produite par un «outflow» accroissent la production de cette molécule. Nous pourrions donc modifier la géométrie de la structure de la source en ajoutant un «outflow» et ultérieurement, une géométrie bien plus complexe. D'autres améliorations pourraient être apportées, tel un calcul simple de la température du gaz dans *Saptarsy* ce qui pourrait fortement affecter la chimie à l'intérieur de la PDR.

Contents

List of Figures

List of Tables

List of Abbreviations

AMR	Adaptive Mesh Refinement
CNM	Cold Neutral Medium
COM	Complex organic molecules
CR	Cosmic-Rays
DVODPK	Differential Variable-coefficient Ordinary Differential equation solver with the Preconditioned Krylov method
FIR	Far Infrared
FUV	Far Ultraviolet
GMRES	Generalized minimal residual method
HII	Ionized hydrogen
HCHII	Hypercompact HII (region)
HHMC	Hollow Hot Molecular Core
HMC	Hot molecular core
HSL	Harwell mathematical Software Library
IR	Infrared
IGM	Intergalactic medium
ISM	Interstellar medium
KH	Kelvin-Helmholtz
KIDA	KInetic Database for Astrochemistry
LTE	Local thermodynamic Equilibrium
MIR	Mid-Infrared
MHD	Magneto-hydrodynamical
NIR	Near Infrared
OSU	Ohio State University
PAH	Polycyclic Aromatic Hydrocarbon
PDR	Photon-dominated region / Photo-dissociation region
TDR	Turbulence Dissipation Region
UCHII	Ultracompact HII (region)
UV	Ultraviolet
WIM	Warm Ionized Medium
WNM	Warm Neutral Medium

1

Introduction

Contents

Our galaxy, the Milky Way, is a spiral galaxy, of a total mass of 8×10^{10} M$_\odot$ (Peñarrubia et al. 2014), composed principally of stars (M$_* \sim 7 \times 10^{10}$ M$_\odot$; Li & White 2009, McMillan 2011) and gas. Like other galaxies the Milky Way is a gravitationally bound astrophysical object in the shape of a disk and of a size of $\sim$ 20 kpc in length and $\sim$ 250 pc in height (Sparke & Gallagher 2000). Its different components interact with each other. One of its major components is the interstellar medium (ISM) containing gas that is slowly converted into stars as the Galaxy evolves. Gas can be ejected into the intergalactic medium (IGM)

through galactic winds and can infall from the IGM as well. Most of the gas in the Galaxy is situated within a thin disk (≤ 500 pc; Dickey & Lockman 1990, Savage & Wakker 2009) where the majority of the stars populating the Galaxy are formed.

1.1 Interstellar medium

The medium between stars, the so called interstellar medium, is composed of a mixture of gas and dust and is a major component of galaxies. It represents only $10 - 15\%$ of the mass of the Milky Way's disk but the different processes taking place there such as motions, heating, cooling, etc. affect the matter as well as its physical and chemical state. Furthermore, the ISM is an environment with a great variety of scales in size, temperature and also density despite it remains one of the less dense media of galaxies.

1.1.1 Interstellar medium cycle

The matter in the ISM is constantly renewed and enriched with heavy elements due to the cycle of star formation. This cycle can be described as follows (see also Fig. 1.1): A diffuse cloud begins to collapse under the effect of gravity, fragments and form denser cores. Proto-stars form in these cold and dense cores through the accretion of the envelope. Then, the proto-star rotation fastens and its surrounding cloud flatten up into an accretion disk. Proto-stars also eject material through bipolar outflows which show that the proto-star still accretes materials through the disk. Accretion stops once radiative pressure is strong enough to blow away the internal part of the disk. The remains are called a proto-planetary disk. Inside this disk the ice and dust accrete and aggregate to form planetesimals which then become planets or smaller objects like satellites. During their lifetime, stars modify their environment via photodissociation, ionization and heating. Finally, the stars either shed their outer layers if they have a low mass and most of this mass is transferred back into the ISM or explode as supernovae at the end of their lifetime, i.e. when they have exhausted all their materials and are not able to hold fusion processes anymore. They eject newly formed heavy elements and heat the surrounding medium. Then, this medium cools and disperses the material which is thus injected back into the ISM.

1.1.2 Gas

The gas is the main component of the ISM as it represents 99% of its mass (Hildebrand 1983). The interstellar gas is composed of hydrogen (90.8%) and helium (9.1%). The remaining percentage is heavier elements formed within the previous generations of stars. In mass these percentages become: 70.4% of H, 28.1% of He and heavier elements 1.5%. The gas can be atomic, molecular or ionized depending on the environment and the physical processes happening there. It is structured in different phases in constant interactions
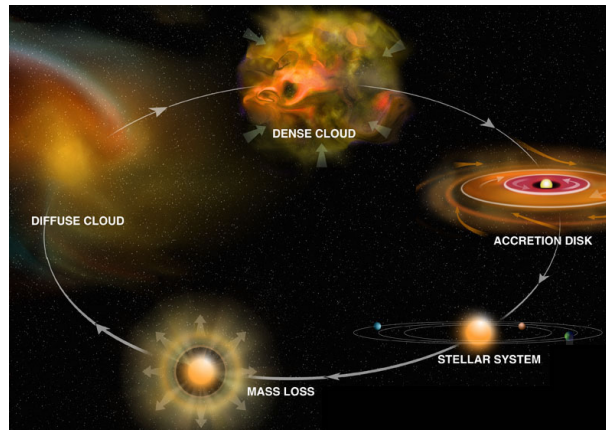
Figure 1.1: Interstellar medium cycle. Image credit: Bill Saxton, NRAO/AUI/NSF

one with another.

Most of the gas is found in the atomic form, observable in the visible and UV range, and it can be divided into two phases. The first one, the Cold Neutral Medium (CNM), is a low density, neutral and cold medium (see Tab. 1.1). The second medium, the Warm Neutral Medium (WNM), has higher temperature and the same density as the CNM. These two atomic phases can exist in a stable pressure equilibrium due to the cooling and heating mechanisms. The Warm Ionized Medium (WIM) has the same temperature as the WNM but a lower density and the hydrogen is ionized. This phase occupies a large volume given a volume filling factor of 0.25 (McKee & Ostriker 1977), although it is not the most voluminous. Other kinds of ionized gas regions exist such as hot interclouds and HII (ionized hydrogen) regions. Hot interclouds fill the largest volume and are extremely hot, $T \sim 10^6$ K. As for HII regions they have a typical temperature of 10^4 K (Peimbert 1967; Wilson et al. 2015) and a density n_H ($= n(H) + 2n(H_2)$) spreading from 1 to 10^5 cm^{-3}. They undergo expansion as they are not confined by their own gravity or by the gravity of the stars they contained and external pressure is insufficient to confine them. This is not the case of molecular clouds which are self-gravitating objects occupying only a small fraction of the ISM volume. Molecular clouds are mainly composed of molecular hydrogen. Molecular clouds have a temperature inferior to 100 K and a density superior to 5×10^2 cm^{-3}. It is within molecular clouds that star formation happens.

Dividing the gas phase into these phases is a conventional, but probably too simple, vision of the ISM. HI observations suggest that a significant amount of the atomic gas has a temperature between the CNM and WNM phases and thus is in the thermally unstable regime ($500 \leq T_k \leq 5000$ K – T_k is the kinetic temperature; Heiles & Troland 2003; Roy et al. 2013). The thermal instability of the gas is a major physical process inducing turbulence in the ISM along with supernovae feedback, stellar winds or bipolar outflows. The interaction between magneto-hydrodynamical (MHD) turbulence and thermal instability might drive the formation of dense structures in molecular clouds. For example, Miville-Deschênes et al. (2016) suggests that dense structures in the Draco Nebula originate from the collision of diffuse gas which triggers the transition from WNM to CNM via the HI thermal instability because of the compression and increase in density of the WNM. This scenario was also proposed by several numerical simulations, e.g. Saury et al. (2014). Same properties of dense structures are found in other molecular clouds. MHD simulations show also than turbulence acts to mix the different phases of the ISM

Table 1.1: Characteristics of the different phases of the ISM in the Milky Way. The given number are approximations (Tielens 2005; Draine 2011).

Phase	Temperature (K)	Density n_{H} (cm^{-3})	Total mass (M$_\odot$)
CNM	100	5×10^1	1.5×10^9
WNM	8000	5×10^{-1}	1.5×10^9
WIM	8000	10^{-1}	10^9
HII regions	10^4	$1-10^5$	5×10^7
Hot interclouds	10^6	0.005	10^8
Molecular clouds	<100	>500	1.5×10^9

(Seifried et al. 2011).

1.1.3 Dust

Despite the fact that dust grains represent a very low percentage in mass of the ISM they are a very important component of it. Indeed, they play an essential role in the spectral energy distribution in the Galaxy. They are the main shield against low energy non ionizing photons with energies ranging in the visible and near/mid-infrared (NIR/MIR) spectrum. Dust grains scatter starlight efficiently, even more when they are fluffy and porous despite the low abundances of this kind of grains (Boulanger et al. 1996; Smith & Dwek 1998). They also absorb almost half of the photons in the ultraviolet (UV) and visible spectra of the Galaxy, and then reradiate them in IR and sub-millimetric (sub-mm) range. It seems that $\sim 30\%$ of the emitted starlight is reradiated by dust in the infrared (Bernstein et al. 2002).

Dust grains, precursors of solar system solids, possess different morphologies and composition which can be deduced from absorption and emission (Draine 2003; Draine & Li 2007). Their size spans from ~ 1 nm to ~ 1 μm (Mathis et al. 1977; Mathis 1990; Draine 2003). A widely used size distribution of dust grains is derived from the MRN (from Mathis, Rumpl and Nordsieck, authors of Mathis et al. 1977) model where the size distribution follows a power law with an exponent of -3.5. As for their composition, thanks to spectroscopic observations grains' bulk is thought to be mainly carbonaceous, e.g., graphite, amorphous carbon, polycyclic aromatic hydrocarbons (PAHs) or silicates, principally amorphous ones. Depending on the environment, the grains' bulk can be covered with an ice mantle of various composition, mainly water and carbon monoxyde. For instance, this is the case in molecular clouds, regions where star formation takes place.

A new dust model has been suggested by Jones et al. (2013) where they use two dust materials (amorphous carbon, either hydrogenated or not, and amorphous silicates) and three dust populations (amorphous carbon grains, silicates grains with amorphous carbon mantle and silicate grains with coagulated amorphous carbon mantle). They show that their model using the code *DustEM* and the optEC$_s$(a) optical property data (Jones 2012) explain many FUV and mm dust observables and their inter-correlations. They also present a schematic view of the dust life circle as shown in Fig. 1.3. The dust grains travel from the dust shell around AGB stars where they are formed to the diffuse ISM
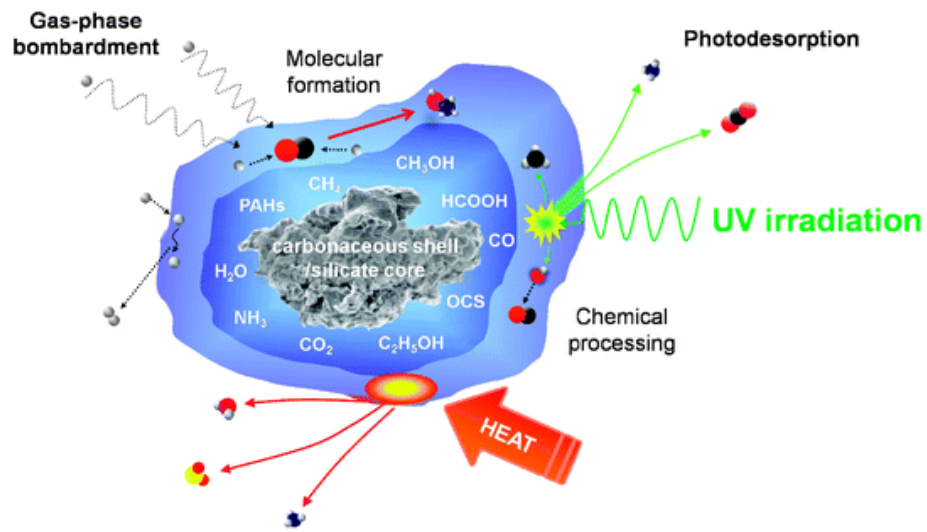
Figure 1.2: Schematic showing the composition of a dust grain and different processes taking place on its surface or within its ice mantle. Image credits: Burke & Brown (2010).
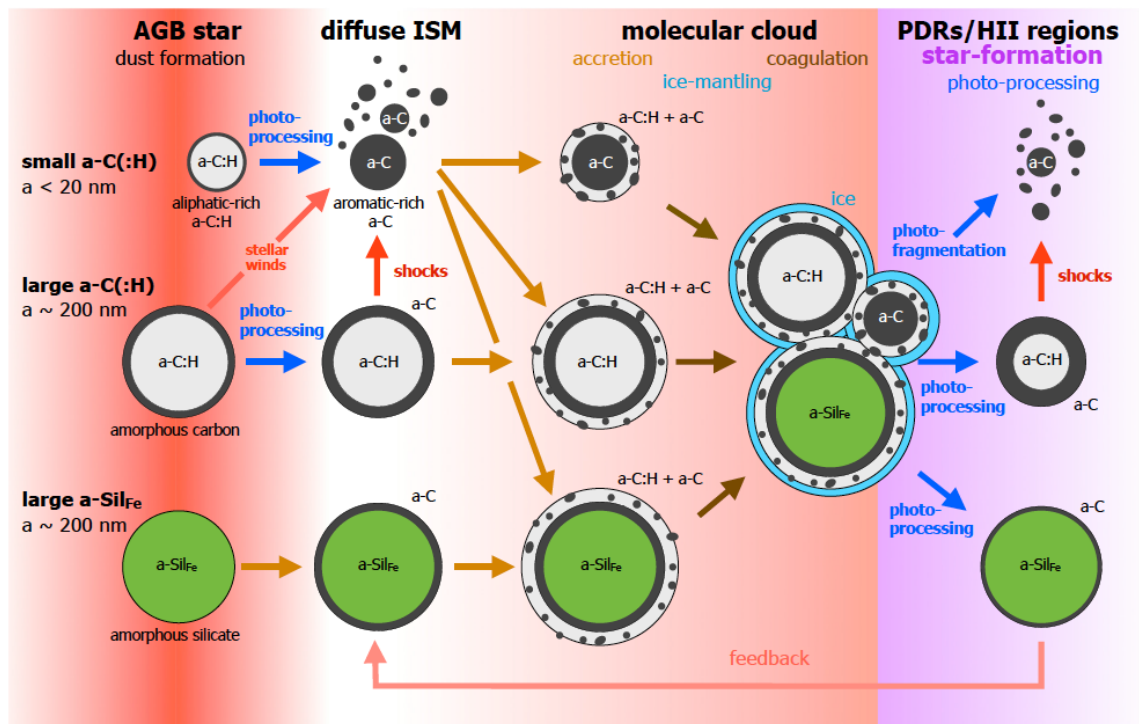
Figure 1.3: Schematic view of the life cycle of interstellar dust. Image credit: Jones et al. (2013).

Table 1.2: Different regions and their properties.

Regions	Diameter (pc)	Mean density (cm^{-3})
Protostar	0.01	$10^6 - 10^7$
Dense core	0.1	$10^5 - 10^6$
Clump	1	$10^4 - 10^5$
Molecular cloud	10	$10^2 - 10^4$
Giant molecular cloud	$10 - 30$	$10^3 - 10^4$

and then due to the core collapse to the dense cores where they accrete, coagulate or re-form. As they transit through the ISM, they are highly altered even destroyed in regions such as HII regions and photon-dominated regions (PDRs) where UV photo-processing is important.

1.2   Star formation

Dense cores, hosts of star formation, result from the condensation and fragmentation of self-gravitating objects referred to as clumps. The clumps are fragmented regions of (giant) molecular clouds too. Cores are not distributed randomly but they are thought to be organized along filamentary structures. They form for instance at the intersection of these gas filaments where matter accumulates through colliding flows (Csengeri et al. 2011). The characteristics of the different objects are found in Tab. 1.2.

Dense cores collapse when they become unstable due to gravitational perturbation such as the passage of Galactic shock wave or supernovae shock wave and once their mass reaches a critical mass, the Jeans mass $M_{\rm J}$ (defined in Eq. 1.1), due to accumulation of material. In the assumption of a homogeneous and spherical cloud, a free-fall collapse happens when the Jeans criteria is fulfilled (see Eq. 1.2, Jeans 1955) i.e., when gravity overcomes the internal pressures (thermal, magnetic) of the cloud. Indeed, at this stage the gas remains cold due to radiative cooling in molecular lines, the gas pressure is thus insignificant.

$$M_{\rm J} = \frac{1}{8} \left(\frac{\pi k_B T}{G \mu m_{\rm H}} \right)^{3/2} \frac{1}{\rho^{1/2}}, \qquad (1.1)$$

where k_B is the Boltzmann constant, T is the temperature of the medium, G is the gravitational constant ($G = 6.674 \times 10^{-11}$ m^3 kg^{-1} s^{-2}), μ is the mean mass per particle and ρ the density.

$$E_{\rm Th} = \frac{3}{2} \frac{M}{m_H} k_B T \leq E_{\rm grav} = \frac{GM^2}{R}, \qquad (1.2)$$

where $E_{\rm Th}$ is the thermal energy, M the mass of the cloud, m_H the hydrogen mass, T the temperature, $E_{\rm grav}$ the gravitational potential energy and R the cloud radius.

Collapse does not occur that often as most molecular clouds seem to be gravitationally stable. These stable clouds are also called sub-critical clouds in opposition to super-critical clouds which collapse (Shu 1977). This implies that only a small fraction of them form
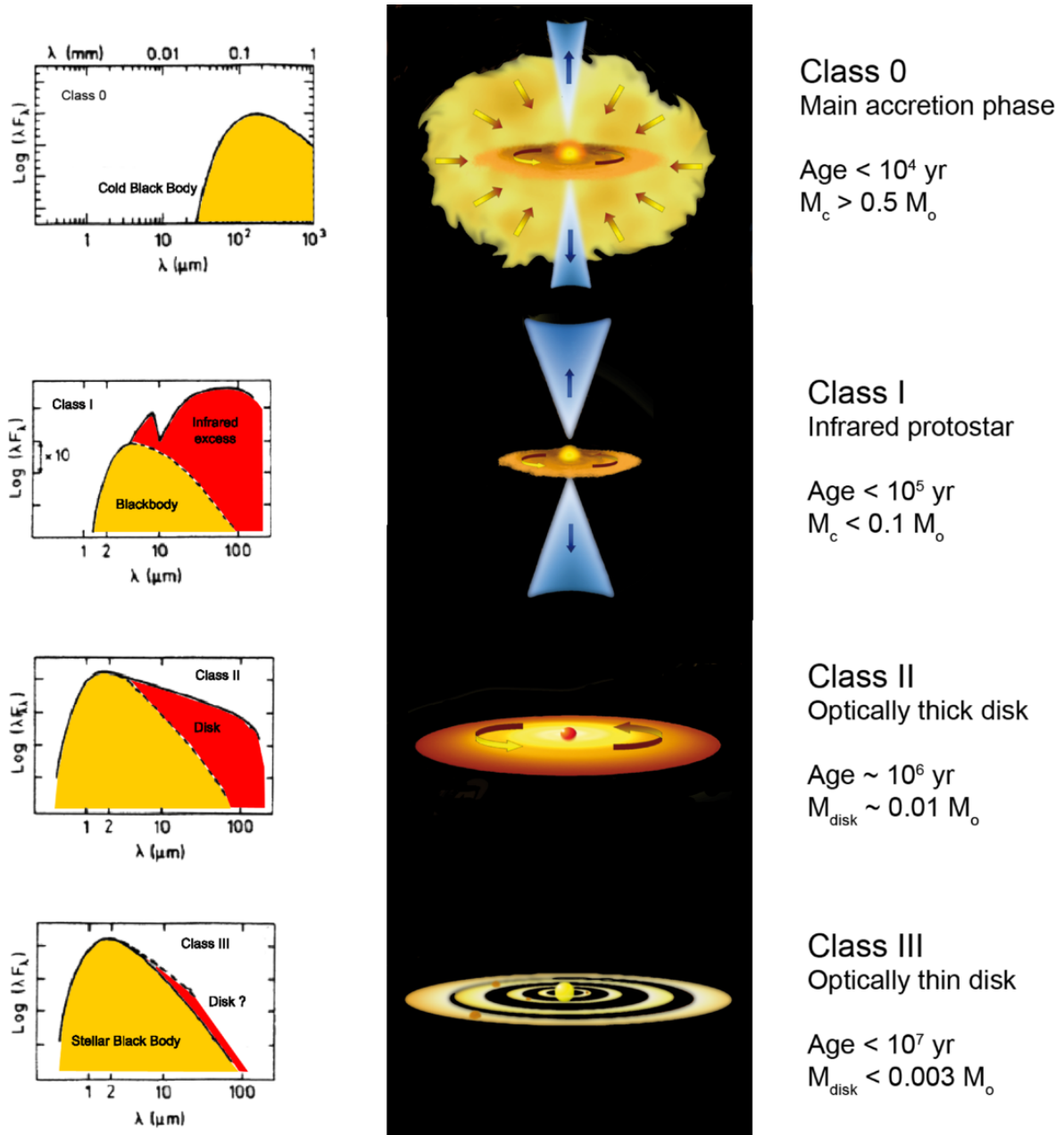
Figure 1.4: Schematic of low mass star formation. Image credit: Luca Carbonaro.

stars. But when it happens, two processes of star formation can be distinguished: low mass star formation ($0.1 \leq M_* < 8\ \mathrm{M_\odot}$) and high mass star formation ($8 \leq \mathrm{M_*} \leq 150\ \mathrm{M_\odot}$).

1.2.1   Theoretical star formation scenario(s)

Low mass star formation

Low mass stars are the main contributors to the total stellar mass of the Galaxy and they are much more numerous than high mass stars. The low mass star formation scenario is presented in Fig. 1.4. We briefly summarize it: During the first phase, the pre-stellar

phase, the core is cold, molecular and does not host a proto-star yet. Then the core enters a contraction phase once gravity becomes stronger than thermal and magnetic pressure. A stellar embryo or proto-star forms at the center of the core and the core becomes optically thick. It concludes the pre-stellar phase and the core enters the proto-stellar phase. The proto-star starts to rotate and an accretion disk appears as the cloud flattens due to gravitational instabilities. The proto-star then evolves through accretion of the envelope material onto the disk and from the disk to the star. This class 0 object is still cold and so it emits in the sub-mm range until it evolves to a class I object and emits in the IR. During these two stages, class 0 and class I, the proto-star also ejects material without loosing too much mass via bipolar outflows in order to conserve the angular momentum. Accretion stops once the star reaches its final mass, lower than 8 $M_\odot$, when the radiation pressure is able to overcome gravity. At this point, the proto-star enters the class II phase of the pre-main sequence and is classified as a T-Tauri star. The star emits in the visible/near-IR range while its disk, now called proto-planetary disk is still optically thick and emits in mid and far-IR (FIR). Finally, as the star reaches the class III stage the disk is made of debris and proto-planets.

Massive star formation

Mechanisms to form high mass stars are slightly different as other processes have to occur to counteract the effect of radiation pressure like having a higher accretion rate and a non spherical accretion. Furthermore the low mass star formation scenario does not take into account the fact that massive stars reach the main sequence before accretion is over and it does not explain why massive stars are often found to form in clusters containing low mass and high mass stars. Two main theoretical points of view try to describe high mass star formation: the competitive accretion scenario, e.g. Bonnell, Bate, Clarke, & Pringle (1997), and the monolithic collapse scenario, e.g. McKee & Tan (2003), also called turbulent core accretion scenario. The first scenario implies that a core gives birth to a star cluster containing a distribution of stars from low to high mass. High mass stars form at the center of this cluster due to the gravitational potential and thus accrete at higher rates. In the same manner binary systems contributes to this differential accretion as they accrete faster due to their potential. Bonnell, Bate, & Zinnecker (1998) also suggest that massive stars could form via collision and merging of lower mass stars assuming a very large stellar density within the cluster. The turbulent core scenario is an extension of low mass star formation scenario and it suggests that the mass of the cores determines the mass of the stars. Thus, massive stars form in massive dense cores unable to fragment contrary to the molecular cloud containing them. The physical processes leading to star formation are self-gravity combined with turbulent motions and magnetic field. In the assumption of an isothermal collapse, high accretion rates as modeled and observed in several regions are difficult to explain. This is not the case for non-thermal pressure support which can induce higher accretion rates needed to form massive stars (McKee & Tan 2003). The major differences between the competitive accretion scenario and the monolithic collapse scenario are the initial conditions and the physical mechanisms used to produce massive stars. More recently, another scenario stating that the most massive stars form from the global collapse of the molecular cloud has been proposed (Peretto et al. 2007, 2013). This process seems to be in competition with the fragmentation process, also called the local collapse scenario. In this scenario, two phenomena induce the formation of the massive star: the first one is the high rate of infalling matter to the center of the
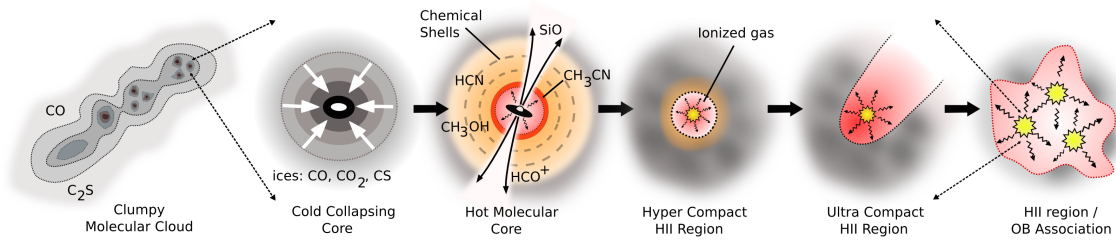
Figure 1.5: Schematic of high mass star formation scenario. Image credit: Cormac Purcell.

cloud ($\dot{M}_\odot > 10^{-3}$ M$_\odot$ yr^{-1}; Wolfire & Cassinelli 1987, Peretto et al. 2013), the second one is the fragmentation of the cloud into dense cores which migrate to the potential well where they can merge to give even more massive cores.

1.2.2 Massive star formation: From an observational point of view

From an observational point of view, these aforementioned theoretical models of high mass star formation cannot be differentiated easily. Fig. 1.5 presents the evolutionary scenario of massive stars as explained by observers. Within a clumpy (giant) molecular clouds, we find fragments, the cores. At the beginning of their lifetime these cores are cold (T $\sim$ 10 K) and diffuse ($n_{\rm H} \sim 10^3$ – 10^4 cm^{-3}) until they undergo gravitational collapse. The medium warms up and the density increases. The core reaches the hot molecular core (HMC) phase. The matter is slowly heated up by the proto-star to a temperature of 100 K and above. As the proto-star accretes material from the surrounding envelope, it starts to emit enough UV photons to ionize the neighboring gas and then form an hypercompact (HC) HII region. The ionization front propagates and the HCHII region develops into an ultracompact (UC) HII region and later into a classical HII region and further. Using the adaptive mesh refinement code $FLASH$[1], Peters et al. (2010a) show that HC/UCHII regions do not systematically expand to reach their next evolutionary phase but they can flicker due to variations in the accretion flow. It seems that a rapid increase in the high accretion flow leads to a shrinkage of the HII regions before they expand again. We describe in more detail the HMC and HC/UCHII region phases as well as the PDRs, frontiers between the HII region and the core, in the following subsections.

Hot molecular cores

Once the pre-stellar phase finishes and the warm-up phase occurs, the core enters the HMC phase. HMCs are compact objects ($\leq$ 0.1 pc) which are optically thick with high extinction ($A_{\rm V} > 100$ mag) and really dense ($n_{\rm H} \geq 10^6$ cm^{-3}). The embedded proto-star forming at the center of the core heat them up to high temperatures, $T \geq 100$ K (Kurtz et al. 2000). HMCs are also transient objects. Their lifetime are around 10^4 – 10^5 years (Herbst & van Dishoeck 2009) during which they exhibit a very rich chemistry. Numerous species, from simple ones to complex organic molecules (COMs), have been

---

[1] http://flash.uchicago.edu/site/

Table 1.3: Types of HII region and their properties (Kurtz 2005; Hoare et al. 2007).

Regions	Size (pc)	Density (cm^{-3})
Hypercompact	≤ 0.01	$\geq 10^6$
Ultracompact	≤ 0.1	$\geq 10^4$
Compact	≤ 0.5	$\geq 5 \times 10^3$
Classical	~ 10	~ 100
Giant	~ 100	~ 30
Super giant	≥ 100	~ 10

detected (Schilke et al. 2001; Calcutt et al. 2014), principally in the sub-mm regime due to the rotational transitions of COMs. Some well know hot core regions include: OMC–1 (Blake et al. 1987), Orion–KL (Wright et al. 1996), Sgr B2 (N) (Wilson et al. 1996) as well as G29.96–0.02 (Cesaroni et al. 1994, 1998). Many models have been developed to study their rich chemistry (this will be detailed in Sec. 1.3.3). Furthermore, HMCs are, in contrast to UCHII regions, almost undetectable in the cm-regime as their free-free emission is too weak to be detectable (Hoare et al. 2007). Otherwise, they show a similar spectral energy distribution in the IR/sub-mm frequency range.

Hypercompact/Ultracompact HII regions

HC/UCHII regions trace later stages of massive star formation. HCHII regions might actually coexist with the HMC phase (Beuther et al. 2007). HCHII regions eventually evolve into UCHII regions (Wood & Churchwell 1989; Kurtz 2000; Hoare et al. 2007) but for a period of time the development can be quenched (Walmsley 1995) because of the large mass accretion rates. They can as well fluctuate in sizes and thus going back and forth form a stage to another considering the variations in the accretion flow (Peters et al. 2010a,b). Furthermore, combined with other mechanisms such as outflows the variation of accretion can induce different HII region morphologies.

HCHII regions are approximately ten times smaller than UCHII regions (see Tab. 1.3) and a hundred times denser (Kurtz 2005). Their ionized mass is smaller by one order of magnitude (Ionized mass for HCHII regions $\sim 10^{-3}$ M$_\odot$; Kurtz 2000) and they are a thousand times brighter. Furthermore, the temperature is extremely high, $T_e \geq 10^4$ K. Thus, they have MIR emission originating from the hot dust. In HC/UCHII regions, the central proto-stars are sufficiently evolved to emit UV photons which ionize the surrounding medium. Photons with energies higher than 13.6 eV are used to ionize molecular hydrogen, thereby, creating an HII region. Photons with lower energies can penetrate the cloud and form an internal PDR ionizing other elements like C-bearing and O-bearing species.

Photon-dominated regions

Photon-dominated regions (PDRs), or photo-dissociation regions, are ubiquitous components of the ISM. They are produced by the far ultraviolet (FUV) radiation (5.16 eV < $h\nu$ < 13.6 eV or in wavelength 912 Å < λ < 2400 Å) coming from the ISM environment or in the case of internal PDRs by the central protostars of the cores. Even if most of the FUV photons are absorbed by the dust in PDRs, some of them remain and heat up the
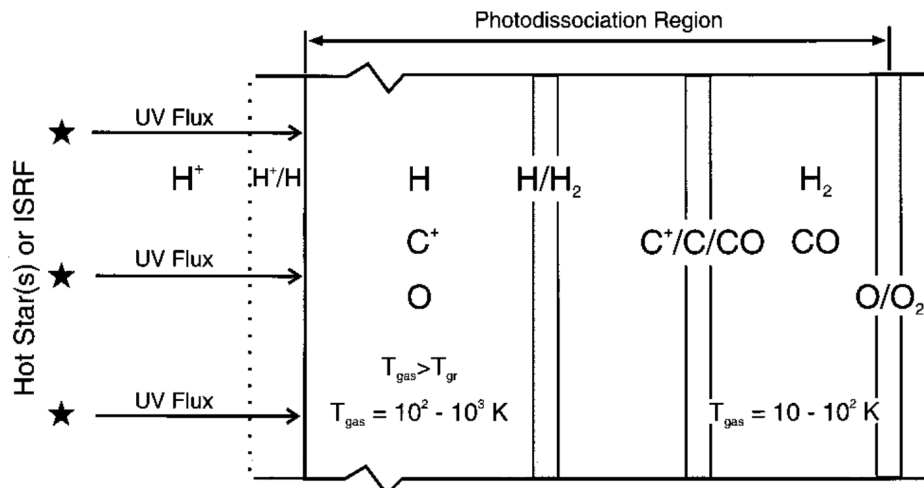
Figure 1.6: Schematic representation of a photon-dominated region presenting the different element layers ($H^+/H/H_2$, $C^+/C/CO$ and O/O_2). Image credit: Tielens (2005)

gas. While the photons with energies higher than 13.6 eV dissociate H_2 and then ionize hydrogen producing the HII region, lower energy photons go through the molecular core and dissociate and ionize other species on their way. The region of the PDR near the ionization front is composed of ions or atoms and deeper zones are composed of atoms and molecules. For instance, as shown in Fig. 1.6, carbon monoxide CO is dissociated to produce C (ionization potential of 11.1 eV) and the carbon is ionized ($h\nu = 11.26$ eV) producing C^+ (also noted CII, the II meaning singly ionized). Oxygen is also ionized into O^+ (OII) by photons of energy 13.6 eV.

Internal PDRs are really dense and so very thin because the radiation field cannot penetrate deep into the core (Bruderer et al. 2009a,b; Lee et al. 2015). They are about 200 AU in size, corresponding to a visual extinction A_V of 1.6 mag if the density is 10^6cm^{-3} using the standard Milky-Way values: R_v, the ratio of total to selective extinction equal to 3.1 and $N_H/E(B–V) = 5.8 \times 10^{21}$ cm^{-2} with N_H the total column density and E(B–V) the color excess between blue (B) and visual (V) wavelengths.

1.3 Chemistry in the ISM

COMs like methanol (CH_3OH), ethanol (C_2H_5OH) or methyl formate ($HCOOCH_3$) appear to be really abundant in HMCs as mentioned in Sec. 1.2.2. After experimental works showed that formation of COMs is inefficient in the gas phase (e.g., Horn et al. (2004) in the case of methyl formate), an alternative scenario has been proposed as follows: In a cold medium, e.g. during the pre-stellar phase where the temperature is around 10 K, molecules are frozen on the dust grain surface in the densest part of the core ($n_H \geq 10^4$ cm^{-3}). The dust grains formed originally of carbonaceous or silicates compounds build up a mantle mainly made of water and carbon monoxyde. As the medium warms up due to the heating of the proto-star, diffusion of molecules and mostly radicals on the surface can occur around 40 K to form COMs as suggested in Garrod & Herbst (2006). When the temperature reaches 80 K more COMs are evaporated and released into the

Table 1.4: Series of gas phase reactions leading to the formation of methyl formate and dimethyl ether (see also Tab. 1 of Balucani et al. (2015)).

OH + CH$_3$OH	$\rightarrow$	CH$_3$O + H$_2$O
CH$_3$O + CH$_3$	$\rightarrow$	CH$_3$OCH$_3$ + $h\nu$
O + CH$_3$OCH$_2$	$\rightarrow$	HCOOCH$_3$ + H
F + CH$_3$OCH$_3$	$\rightarrow$	CH$_3$OCH$_2$ + HF
Cl + CH$_3$OCH$_3$	$\rightarrow$	CH$_3$OCH$_2$ + HCl
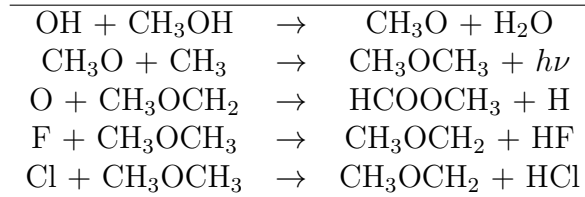
gas phase and, thus, observable in the hot core phase.

However, this formation scenario of COMs formation is revised as COMs were found in cold dense cores where the temperature is lower than 30 K like in L1689B (Bacmann et al. 2012). A new paradigm has emerged favoring a combined gas-grain chemistry to explain formation of COMs. Balucani et al. (2015) presents new formation routes for methoxy (CH$_3$O), methyl formate and dimethyl ether (CH$_3$OCH$_3$) based on experimental and theoretical works. The conclusions of this paper are presented in Tab. 1.4. They also found this series of gas phase reactions happens after the non-thermal desorption of methanol.

As for chemistry in HII regions, it seems to be mainly influenced by the UV radiation coming from the newly formed massive stars. Most complex molecules are destroyed by the high energy photons at least in the PDRs and their close environment where ionized and neutral atomic species dominate the composition of gas. Deeper in the core where radiation are attenuated by dust more complex molecules are preserved. Chemistry in the ISM depends a lot on the physical conditions and on the quantity of molecules present in the medium. The different chemical processes (see Fig. 1.7) taking place in HMCs, HII regions and PDRs as well as the astrochemical models developed to study them are explained in subsections 1.3.1 and 1.3.2.

1.3.1   Gas phase chemistry

Gas phase chemistry is dominated by two-body reactions, dissociation and ionization reactions. A list of gas phase reactions is given in Tab. 1.5. Several kind of two-body reactions are possible which form chemical bonds, destroy them or re-arrange them. In bimolecular reactions, reaction re-arranging the bonds, if A and B are the reactant molecules they react to form an activated complex AB*. This complex decomposes rapidly into two different products C and D: A + B $\rightarrow$ AB* $\rightarrow$ C + D. In order for the reaction to start, it requires a certain amount of energy from the local environment, the activation energy, and only collisions with kinetic energy higher than the activation energy lead to a reaction. These reactions can be exothermic or endothermic. A reaction is endothermic if it receives energy from the environment, i.e. if the energy necessary to break the reactants bonds is higher the energy released during the formation of the products. On the contrary, if the reaction releases energy it is exothermic.

In addition to two-body reactions, there are dissociation and ionization reactions triggered by photons or cosmic-rays. Photo-dissociation/ionization reactions are important
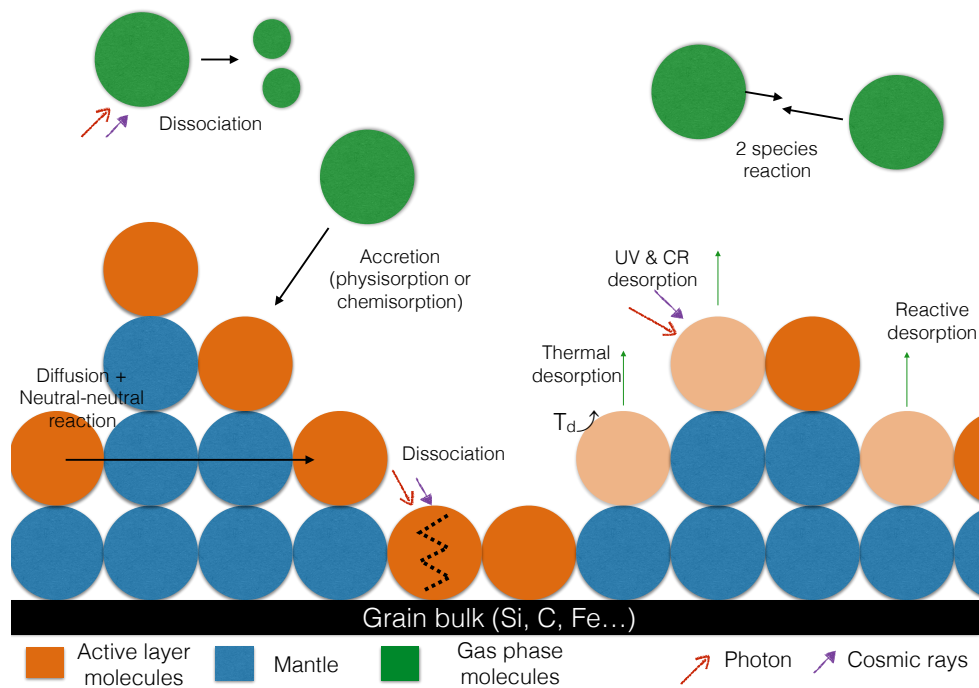
Figure 1.7: Scheme presenting the different reactions occurring in the ISM in the gas phase and on the grain surface.

in PDRs where irradiation by UV photons is high compared to other environments. If the energy of the interacting photon is sufficient the chemical bonds of the molecule are affected and can be broken. However the most abundant molecules, H_2 and CO, can protect deeper embedded H_2 and CO from photo-dissociation because the UV radiation is prevented from penetrating the PDR layer by H_2 or CO which absorb the radiation. This process is called self-shielding. Cosmic ray (CR) dissociation/ionization reactions depend on the CR ionization rate and can be direct or indirect. The indirect process occurs when a CR crossing the medium rips off some electrons to the gas components, i.e to H_2. These electrons have a very high energy, ~ 30 eV, and by collision they excite the gas. About 10% of the molecular hydrogen is dissociated (Stecher & Williams 1967). The remaining 90% go back the fundamental state by de-excitation through the emission of FUV photons (Black & Dalgarno 1976).

1.3.2 Surface chemistry

The gas phase components can also interact with the core or the mantle of the grains. At low temperature, $T \sim 10$ K, molecules from the gas phase are accreted onto the grain surface (see a summary of the grain surface reactions in Tab. 1.6). Two adsorption process are then possible: physisorption and chemisorption. In the first process caused by van der Waals force, with energies of 0.01 eV, the electronic structure of the atom or molecule is barely affected by the adsorption. Chemisorption involves the formation of new chemical bonds, with energies of a few eV, between the molecule and the surface. Chemisorption occurs only on the bare grain. Once the core is covered by a layer of ice

Table 1.5: The gas phase reactions.

	Reaction	Rate (from Tielens 2005)
Neutral – neutral	$A + B \rightarrow C + D$	$4{\times}10^{-11}\ \mathrm{cm^3\,s^{-1}}$
	$A + B \rightarrow C^+ + e$	
Ion – neutral	$A^+ + B \rightarrow C^+ + D$	$2{\times}10^{-9}\ \mathrm{cm^3\,s^{-1}}$
	$A^- + B \rightarrow C^- + D$	
Charge exchange	$A^+ + B \rightarrow A + B^+$	$10^{-9}\ \mathrm{cm^3\,s^{-1}}$
Cation – Anion recombination	$A^+ + B^- \rightarrow A + B$	
Radiative recombination	$A^+ + e \rightarrow A + h\nu$	
Electron attachment	$A + e \rightarrow A^- + h\nu$	
Radiative association	$A + B \rightarrow AB + h\nu$	
	$A^+ + B \rightarrow AB^+ + h\nu$	
Associative detachment	$A^- + B \rightarrow AB + e$	$10^{-9}\ \mathrm{cm^3\,s^{-1}}$
Dissociative recombination	$A^+ + e \rightarrow C + D$	$10^{-7}\ \mathrm{cm^3\,s^{-1}}$
Collisional dissociation	$AB + C \rightarrow A + B + C$	
Photo-ionization	$A + h\nu \rightarrow A^+ + e$	
Photo-dissociation	$AB + h\nu \rightarrow A + B$	$10^{-9}\ \mathrm{s^{-1}}$
Cosmic-Ray ionization	$A + CR \rightarrow A^+ + e$	
Cosmic-Ray dissociation	$AB + CR \rightarrow A + B$	

the adsorption only occurs via physisorption (Cazaux & Tielens 2004). Furthermore, all species do not have the same bond with the grain surface as it depends on the binding energy of each species, also called the desorption energy. Lighter species like atoms usually have lower binding energies and can then diffuse more easily. Furthermore, depending if the adsorption happens on bare grains or on ice, the binding energy varies (see some examples in Tab. 1.7 taken from Minissale et al. 2016). The binding energies also depend on the composition of the ice mantle.

Bimolecular reactions can occur once the molecules are depleted on grains. Two different mechanism are then possible: Langmuir-Hinshelwood or Eley-Rideal (see Fig. 1.8). The Langmuir-Hinshelwood mechanism, suggested by Irving Langmuir in 1921 and further developed by Cyril Hinshelwood in 1926, consists of two molecules adsorbed on neighboring sites. They diffuse, react when they are in the same potential well and finally the products desorb. At least one of the reactant has to be physisorbed so that migration of the species can happen. Two migration processes can be involved: quantum tunneling and thermal diffusion. All species undergo diffusion via thermal hopping from one site to the next one. Molecules and atoms can also undergo non thermal diffusion when they cross through a potential barrier by quantum tunneling. The lighter they are the faster the diffusion is. In the Eley-Rideal mechanism, proposed in 1938 by D. D. Eley and E. K. Rideal, only one reactant is adsorbed, usually chemisorbed, and react when a species of the gas phase directly hits it. The reaction is barrierless and exothermic and as the energy is not transferred to the surface the product, which desorbs immediately, is really energetic.

As in the gas phase, photons and CRs can trigger dissociations of molecules at the

Table 1.6: The grain surface reactions. We differentiate the surface species from the gas phase species by using the notation "s-" for the surface species. The bare grains are represented by the letter "G".

Gas-grain interaction	$A + G^- \rightarrow A^- + G$
Electron-grain recombination	$A^- + G \rightarrow A + G^-$
Surface accretion	$A \rightarrow$ s-A
Grain-surface chemical reactions	s-A + s-B $\rightarrow$ s-AB
Photodissociation by cosmic rays	s-AB $\rightarrow$ s-A + s-B
Photodissociation by background photons	s-AB $\rightarrow$ s-A + s-B
Cosmic Ray induced general desorption	s-A $\rightarrow$ A
Photo-desorption	s-A + $h\nu \rightarrow$ A
Thermal evaporation/desorption	s-A $\rightarrow$ A
Reactive desorption	s-A + s-B $\rightarrow$ AB
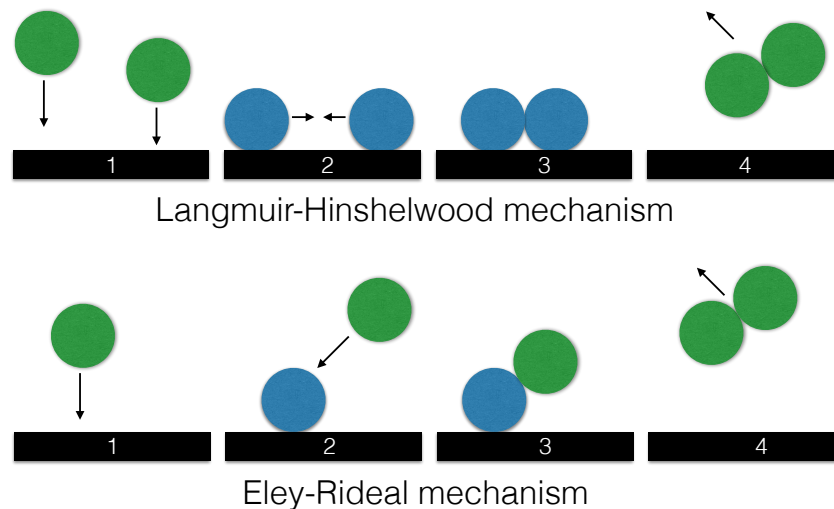
Figure 1.8: Scheme presenting the Langmuir-Hinshelwood mechanism (top) and the Eley-Rideal mechanism (bottom).

surface. In addition they can induce desorption. Direct and indirect CR desorption is possible. During the desorption process, the species detach from the surface and are released into the gas phase. In the warm-up phase of HMCs desorption is mainly thermal. When the dust temperature is higher than the binding energy evaporation can occur. For instance, at a temperature between 20 – 30 K, carbon monoxide can desorb whereas methanol only desorbs for a dust temperature superior to 100 K. During an exothermic reaction between two species it exists a certain probability that the product desorbs, this is called reactive desorption. Garrod et al. (2007) discuss the probability for reactive desorption which spans from 0.01 to 0.1. They are not able to constrain the probability while comparing with dark cloud observations and they show that reactive desorption does not considerably change the results even if it tends to improve the agreement with observations.

Table 1.7: Example of binding energies on bare grains and ice surface for several molecules from Minissale et al. (2016).

Species	E_{bare}	E_{ice}
H	550	650
H_2	300	500
N	720	720
N_2	790	1140
H_2O	4800	4800

1.3.3   Chemical models

Chemical modeling has a long history starting in the 1950's with the first chemical study from Bates & Spitzer (1951) following the detection of CH, CN and CH^+. Since then, many astrochemical models have emerged in order to study the gas phase chemistry as well as grain chemistry, for example in dense clouds (Hasegawa et al. 1992) or in HMCs (Garrod & Herbst 2006). Some models are restricted to gas phase chemistry (Wakelam & Herbst 2008) but an increasing effort has been made on developing the grain chemistry as it appears as a major component of COMs formation. Among such models, we can find for example the Hasegawa & Herbst (1993b) and Taquet et al. (2012b) models which are based on the rate equation approach[2], using numerical solvers to integrate the ordinary differential equations. But it has appeared that a more detailed modeling is necessary to study diffusive chemistry or the probability of adsorption on the surface. Thus, microscopic stochastic methods, i.e. methods based on the theory of probability to describe the interaction of microscopic particles, like Monte-Carlo techniques[3] (Charnley 2001; Vasyunin & Herbst 2013; Garrod 2013b) and Master equation approach[4] (Green et al. 2001) have flourished. These techniques also allows a better treatment of inhomogeneities, e.g. the number of adsorbed atoms is different from one grain to another and this aspect is not treated in the rate equation approach. However, because it is not simple to merge stochastic treatments of the surface with deterministic treatments of the gas phase chemistry several models continue to use the rate equation approach. In addition to chemical models, PDR models have also been developed (e.g. Hollenbach & Tielens 1997; Le Petit et al. 2006; Röllig et al. 2006) and they usually only include a steady-state chemistry. Furthermore, hydrodynamical and MHD models also study the evolution of chemistry as in the MHD shock models from Flower et al. (1985) or very recently in the 3D-MHD from Seifried & Walch (2016).

---

[2]The rate equation approach solves the differential equations using the rate of the reactions. They are derived from the Arrhenius law. More detail are given in Sec. 2.1.1.

[3]Monte Carlo methods are probabilistic techniques to compute an approached result via a repeated random sampling of possible inputs. In the astrochemistry field, the first Monte Carlo models were used by Charnley 1998 based on the stochastic simulation algorithm developed by Gillespie 1976.

[4]The master equation approach solves a set of first-order differential equations which describe the time evolution of the probability for a system to be in a set of states; in the case of gas-grain chemistry it describes the probabilities for a discrete number of molecules and atoms to be adsorbed on the grain surface.

1.4 About this work

1.4.1 Goal of the thesis

High mass star forming regions exhibit an extremely rich chemistry evolving from one transient phase to another. Dense clouds and HMCs have been the subject of various studies and models, whereas the next evolutionary stage, UCHII regions and their internal PDRs, did not receive the same attention. Only few models study internal PDRs and not around HC/UCHII regions but around outflow cavities (Bruderer et al. 2009b; Lee et al. 2015). The goal of this thesis is to characterize and model the chemistry taking place in HC/UCHII regions and their internal PDRs. We also want to compare it to the chemistry in HMCs to discover how the presence of an internal PDR impacts the lines emission. The UCHII regions studied with their surrounding PDRs appear to be already old. In addition, we want to identify chemical species/tracers, specific to the HMC and HII region phases. Understanding the influence of the radiation field on the chemistry and how this physical parameter affects the different species lines emission is a major point of this work.

1.4.2 Approach and strategy

As mentioned above, we want to study the line emission of various species using a detailed modeling of their abundances and ultimately compare them to observations. Thus, the first step of this work is to obtain synthetic spectra, which are directly comparable with observations, for relevant species. Consequently, we connect the astrochemical code *Saptarsy* to the radiative transfer code *RADMC-3D*. This is done through the framework *Pandora*. This also allows to obtain a self-consistent computation of the dust temperature and radiation field used by *Saptarsy*.

The next step is to modify *Saptarsy* in order to model HC/UCHII regions, i.e. we need to implement additional photo-reactions as well as self-shielding which is an important process in PDRs. Furthermore we have to set up the structure for the models, an HII region and a HMC model so that they are comparable to each other. Therefore, a proper grid is necessary. The first idea was to use an AMR (Adaptive Mesh Refinement) grid but for a single spherical symmetric core a spherical grid is more adapted. This also decreases the number of cells within the grid and so the computation time. The AMR grid is still functional and might be more convenient in the future to implement multiple cores in the structure more easily. In addition, so that the models are comparable, the HMC and HII region have to have the same structure, same dust temperature and same column density. Thus, an extension of the HMC model is required and we develop the hollow HMC model.

The final step is to identify the relevant species whose emission comes mostly from the inner part of the core, where the PDR is located, and molecules whose abundances appear to be different for the HMC and the HII region models.

1.4.3   Organization of the thesis

This thesis is composed of two parts: the first presents the different codes used in this work and the second part presents the different models and the results obtained for them.

1st *part*: In Chapter 2 we introduce the astrochemical code *Saptarsy* and the different improvements and modifications implemented in order to model UCHII regions. In Chapter 3 we explain how *Saptarsy* is coupled to *RADMC-3D* through the framework *Pandora*. It includes in particular a description of the models structure. In Chapter 4 we present the semi-analytical chemical code developed to study the dissociation front properties.

2nd *part*: In Chapter 5 we explain how we obtained the initial abundances for our models and then we describe the different models obtained for different sizes of HII region, different densities at the ionization front, etc. In Chapter 6 we compare the chemical abundances and the species line emission for the different models and we analyze the results.

Finally, in the conclusion we summarize the thesis and gives an outlook of this work.

List of publications:

1. Choudhury, R.; Schilke, P.; **Stéphan, G.**; Bergin, E.; Möller, T.; Schmiedeke, A.; Zernickel, A., *Evolution of complex organic molecules in hot molecular cores. Synthetic spectra at (sub-)mm wavebands*, 2015, A&A, 575, A68

2. Martin, P. G.; Blagrave, K. P. M.; Lockman, Felix J.; Pinheiro Gonçalves, D.; Boothroyd, A. I.; Joncas, G.; Miville-Deschênes, M.-A.; **Stéphan, G.**, *GHIGLS: HI Mapping at Intermediate Galactic Latitude Using the Green Bank Telescope*, 2015, ApJ, 809, 153

3. Louvet, F.; Motte, F.; Hennebelle, P.; Maury, A.; Bonnell, I.; Bontemps, S.; Gusdorf, A.; Hill, T.; Gueth, F.; Peretto, N.; Duarte-Cabral, A.; **Stéphan, G.**; Schilke, P.; Csengeri, T.; Nguyen Luong, Q.; Lis, D. C., *The W43-MM1 mini-starburst ridge, a test for star formation efficiency models*, 2015, A&A, 570, A15

In preparation:

4. **Stéphan, G.**; Schilke, P.; Le Bourlot, J.; et al. *Chemical modeling of UCH*II *regions and their internal PDR.*

5. **Stéphan, G.**; Bergin, E.; Schilke, P.; et al. *Dust spectral index determination in Sgr B2 (N).*

Part I:

Codes

2

The chemical code: *Saptarsy*

Contents

In this chapter we present the chemical code *Saptarsy* in Sec. 2.1 and explain the reactions used and the network employed for this work. We also describe the numerical solver *DVODPK*. In Sec. 2.2 we give details on some of the improvements made in *Saptarsy* and in Sec. 2.3 we compare *Saptarsy* with other codes like *NAUTILUS*, *ALCHEMIC* and the TDR code from Meudon.

2.1   What is Saptarsy?

Choudhury et al. 2015 developed the chemical code *Saptarsy* to study the spatio-temporal evolution of abundances in hot molecular cores. To study the chemistry in HII regions we have extended its functionalities (Stéphan et al. 2016 in prep). *Saptarsy* is a code based on the rate equation approach. It is a 1D+1 code as its solves both the spatial and the temporal evolution of abundances species in the gas phase and on grain surface. It uses the Netlib library solver *DVODPK* (Differential Variable-coefficient Ordinary Differential equation solver with the Preconditioned Krylov method GMRES (General Minimal RESidual) for the solution of linear systems) to solve the ordinary differential equations and *MA28* the solver of sparse system of linear equations from Harwell mathematical Software Library (HSL).

The particularity of *Saptarsy* is that it includes the spatio-temporal evolution of the temperature and the radiation field intensity, both obtained thanks to *RADMC-3D*. These parameters are given in separate inputs along with other inputs including the chemical network, the grain species and reactions properties and the initial abundances. Thus, it is also possible to use *Saptarsy* without *RADMC-3D*. *Saptarsy* starts by reading the inputs which provide the number of radii and time steps required by the user. Then, *Saptarsy* computes for each radius, one after the other, the time evolution of the abundances, one time step after the other. Increasing the number of radius increases the computing time but increasing the number of time steps does not lead to an increased computing time because the solver *DVODPK* uses internal time steps. One time step is divided into several ones, as many as necessary for the code to converge to a result. Thus, increasing the number of time steps required by the user can allow the solver to decrease the number of internal time steps. Furthermore *Saptarsy* can be used in two modes: the linear or the logarithm mode. The latter has been implemented for this work as we encountered stability issues and unphysical results with the linear mode.

2.1.1   Reactions and networks

In the simple case of a single bimolecular reaction like A + B → C + D the reaction rate depends on the quantity of reactants A and B, noted [A] and [B], and on a rate constant k. The speed of the reaction for this example is given as follows:

$$\frac{d[A]}{dt} = \frac{d[B]}{dt} = -\frac{d[C]}{dt} = -\frac{d[D]}{dt} = -k[A][B] \tag{2.1}$$

The role of *Saptarsy* is to determine the reaction rates for every species which are more complex than the one in the example. The chemical network is composed of hundred of species and thousands of reactions. The reactions involve one or two reactants and produce from one to four products. The rate constant depends on the reaction type. The reaction rates are linear equations and form a stiff system of differential equations. The different rates and the chemical network are presented in more detail in the following sub-sections.

Reactions and rates constant

Saptarsy is based on the rate equation approach derived from the Arrhenius law. This law describes the temperature dependence on the rate constant k:

$$k(T_\mathrm{g}) = A \exp\left(-\frac{E_\mathrm{A}}{RT_\mathrm{g}}\right), \tag{2.2}$$

where T_g is the gas temperature, A is the frequency - or collision factor (i.e., number of molecules per second), E_A is the activation energy of the reaction (in Kelvin) and R is the ideal gas constant. The term A is specific to each species and takes into account both the frequency of collisions, leading or not to a reaction, as well as the collisions' orientation. The exponential factor represents the probability for a collision to result into a reaction. This equation can also be written as in the following form:

$$k(T_\mathrm{g}) = \alpha \left(\frac{T_\mathrm{g}}{300K}\right)^{\beta} \exp\left(\frac{\gamma}{T_\mathrm{g}}\right), \tag{2.3}$$

where α, β and γ are experimentally determined parameters. α is the reaction rate value at a room temperature of 300 K, β defines the temperature dependence of the rate and is normalized to the room temperature and γ is the activation energy.

It is important to note that Eq. 2.3 is used only for two bodies reactions in the gas phase. For other reactions the rates are described later one by one and the values of the different parameters can be found in Tab. 2.1. All the rates are taken from Semenov et al. (2010) except for photo-desorption and secondary photon processes. The photo-desorption rate equation (Eq. 2.21) is the same as defined for H_2 in Le Bourlot et al. (2012). As for secondary photon processes we adopt the definition given in Le Petit et al. (2006). This is a list of the other reactions included in *Saptarsy* with their reactions rates:

- Gas-grain interaction or electron-grain recombination:

$$k = \alpha T_\mathrm{g}^{\beta} r_\mathrm{g/d}, \tag{2.4}$$

  where $r_\mathrm{g/d}$ is the gas-to-dust ratio that is defined as:

$$r_\mathrm{g/d} = \frac{4\pi \rho_\mathrm{d} r_\mathrm{d}^3}{3 G_d m_\mathrm{u}}, \tag{2.5}$$

  where ρ_d is the grain mass density, r_d is the grain radius, G_d is the dust to gas mass ratio and m_u is the atomic mass unit.

- Cosmic ray dissociation in the gas phase and on grain surface:

$$k = \alpha \zeta, \tag{2.6}$$

  where ζ is the cosmic rays ionization rate.

- Photo-dissociation in the gas phase and on grain surface:

$$k = \alpha \exp\left(-\gamma A_\mathrm{V}\right)\chi_0, \tag{2.7}$$

where A_V is the visual extinction in magnitude and χ_0 the radiation field strength in Draine unit. In the gas phase, H_2 is abundant enough to shield other, deeper embedded, H_2 molecules against the UV radiation. The same process happens for CO even if the shielding is not as strong because CO is less abundant. This phenomenon is called self-shielding and it decreases the reaction rates by a certain factor. For these two molecules the shielding factors are taken from Lee et al. (1996), Draine & Bertoldi (1996), Panoglou et al. (2012) and Sternberg et al. (2014). Fig. 2.1 shows the H_2 self-shielding as a function of column density and the factors are defined in equations 2.8 for H_2 and 2.11 for CO. In the case of a HMC model the radii are not coupled one to another in *Saptarsy* but for a HII region model the chemical abundances computation at a certain radius requires knowledge of chemistry at the previous radius as we need to know the column density of H_2 and CO to determine the self-shielding factor.

$$f_s(H_2) = \frac{0.965}{1 + \left(\frac{N(H_2)}{N_0 b_5}\right)^2} + \frac{0.035}{\sqrt{1 + \frac{N(H_2)}{N_0}}} \exp\left(-8.5 \times 10^{-4} \sqrt{1 + \frac{N(H_2)}{N_0}}\right), \quad (2.8)$$

where $N(H_2)$ is the H_2 column density, N_0 is the reference H_2 column density, b_5 is the normalized Doppler parameter, often chosen to be equal to 2, which is given by:

$$b_5 = \frac{\sqrt{v_{th}(H_2)^2 + v_{turb}^2}}{10^5 \text{ cm.s}^{-1}}, \quad (2.9)$$

where v_{th} is the turbulent velocity and v_{th} is the thermal velocity of a species and is defined as follows:

$$v_{th}(X) = \sqrt{\frac{8k_B T_g}{\pi m_u m_X}}, \quad (2.10)$$

where k_B is the Boltzmann constant and m_X the mass of the considered species X.

$$f_s(CO) = f_{CO}\, f_{H_2}\, f_{A_V}, \quad (2.11)$$

$$f_{CO} = \min\left(1, \left(\frac{N(CO)}{10^{15}}\right)^{-0.75}\right), \quad (2.12)$$

$$f_{H_2} = 0.8 \exp\left(-\frac{N(H_2)}{1.7 \times 10^{21}}\right), \quad (2.13)$$

$$f_{A_V} = \max\left(0.5 \exp\left(-3.5 A_V\right),\ 0.1 \exp\left(-3 A_V\right)\right), \quad (2.14)$$

where $N(CO)$ is the CO column density.

- Neutral-neutral reaction on grain surface:

$$k = \alpha x_f \exp\left(-\frac{E_A}{T_d}\right) \left(R_{diff}(X_1) + R_{diff}(X_2)\right) \frac{r_{g/d}}{n_H}, \quad (2.15)$$

where T_d is the dust temperature, n_H the total hydrogen density, $R_{diff}(X_i)$ is the thermal diffusion rate of the reactant species X_i, x_f is the branching ration of the reaction. No diffusion via tunneling is used in *Saptarsy*. About the branching
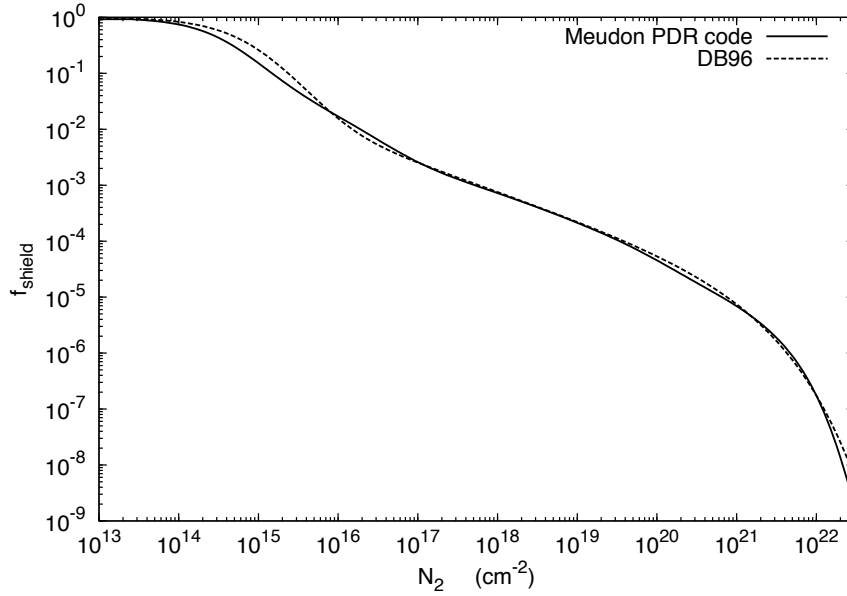
Figure 2.1: H_2 self-shielding factor as a function of the H_2 column density, noted N_2 here, calculated by the analytical formula from Draine & Bertoldi (1996) (dashed line) and by the Meudon PDR code (solid line).

ratios in *Saptarsy*, all neutral-neutral reactions involving the same reactants are assumed to have the same probability to happen. The diffusion rates R_{diff} for the two reactants are defined as follows:

$$R_{\mathrm{diff}} = \frac{\nu_0}{n_s} \exp\left(-\frac{E_{\mathrm{b}}}{T_{\mathrm{d}}}\right), \qquad (2.16)$$

where ν_0 is the characteristic vibrational frequency of the considered species, n_s is the number of adsorption sites on one grain and E_{b} is the activation energy of diffusion for the considered species. It is worth noting that for a large majority of species the diffusion energy is not well constrained. Thus, in our models we adopt the diffusion to desorption ratio $E_{\mathrm{b}}/E_{\mathrm{D}} = 0.50$ (Garrod & Herbst 2006), where E_{D} is the desorption energy. This ratio is an average value of the adopted ones among other models. Ruffle & Herbst (2000) and Semenov et al. (2010) assume for example a ratio of 0.77 and some other models assume a ratio of 0.30 (Tielens & Allamandola 1987). Tielens & Allamandola 1987 also estimate the vibrational frequency which is defined as:

$$\nu_0 = \sqrt{\frac{2S_d k_{\mathrm{B}} E_{\mathrm{D}}}{\pi^2 m m_{\mathrm{p}}}}, \qquad (2.17)$$

where m_{p} is the proton's mass and S_d is the surface density of sites on a grain. However there are still a lot of uncertainties about the surface processes but many experiments and theoretical works are in progress in order to better understand them. Therefore, we expect advances in the future that could be included into our model.

- Thermal Desorption:

$$k = \alpha R_{\mathrm{eva}}, \qquad (2.18)$$

where the evaporation rate R_{eva} is a function of E_{D} and is defined as:

$$R_{\mathrm{eva}} = \nu_0 \exp\left(-\frac{E_{\mathrm{D}}}{T_{\mathrm{d}}}\right) \tag{2.19}$$

- Cosmic ray desorption:

$$k = \alpha\nu_0 \; 3 \times 10^{-19} \exp\left(-\frac{E_{\mathrm{D}}}{T_{\mathrm{CR}}}\right) \tag{2.20}$$

where T_{CR} represents the dust temperature when a cosmic ray hits the grain assuming the particle deposits an energy of 0.4 MeV into the grain (Hasegawa & Herbst 1993a). The constant 3×10^{-19} represents the ratio of the grain cooling timescale via desorption ($\sim 10^{-5}$ s) to the timescale between successive heating events ($\sim 3\times10^{13}$ s from iron cosmic rays flux from Leger et al. (1985) and a grain size of 0.1 μm), i.e., time spent by grains at a temperature around T_{CR}.

- Photodesorption (including secondary photons created by cosmic rays):

$$k = \alpha\left(F + F_{\mathrm{sec}}\frac{2n(\mathrm{H_2})}{n(\mathrm{H}) + 2n(\mathrm{H_2})}\right)\frac{\pi r_{\mathrm{d}}^2}{n_s}, \tag{2.21}$$

where F is the photon flux coming directly from the heating source, while F_{sec} is the secondary photon flux. Cosmic rays tear way electrons to the gas. These electrons are very energetic and excite H_2 until the gas is thermalized. H_2 reemit photons during de-excitation hence the secondary photons.

Desorption is a particularly fast in HC/UCHII regions. Thus, the chemistry might be dominated by the initial conditions and not by the grain mantle evolution.

- Accretion on grain surfaces:

We assume that species are only able to accrete on grain via physisorption. Chemisorption is not taken into account.

$$k = \alpha s_{\mathrm{T}}\pi r_{\mathrm{d}}^2 v_{\mathrm{th}}\frac{n_{\mathrm{H}}}{r_{\mathrm{g/d}}}, \tag{2.22}$$

where s_{T} is the sticking coefficient. We assume a sticking probability of 100% for neutral species. Thus s_{T} is equal to 1, but it is assumed to be zero for ions.

- Secondary photon dissociation (in the gas phase):

$$k = \alpha\zeta\frac{2\,n(\mathrm{H_2})}{n(\mathrm{H}) + 2\,n(\mathrm{H_2})}\left(\frac{T_{\mathrm{g}}}{300\ \mathrm{K}}\right)^{\beta} \tag{2.23}$$

To summarize the different reactions included in *Saptarsy*: we have in the gas phase bimolecular reactions and dissociations (by CRs, photons and secondary photons). At the surface, we have accretion, desorption (thermal, chemical/reactive or by CRs and photons), dissociation (by CRs and photons) and neutral-neutral reaction. In addition a bare grain can react with electrons for neutral bare grains or ions for negatively charged bare grains.

Table 2.1: Values of the different parameters used in *Saptarsy*.

Parameter	Value	Unit
R	8.314	$\mathrm{Pa\,m^3\,K^{-1}\,mol^{-1}}$
ρ_d	3	$\mathrm{g\,cm^{-3}}$
G_d	0.01	
r_d	0.1	$\mu\mathrm{m}$
m_u	1.66054×10^{-24}	g
m_p	1.66054×10^{-24}	g
N_0	5×10^{14}	$\mathrm{cm^{-2}}$
n_s	1.885×10^6	
S_d	1.5×10^{15}	$\mathrm{sites\,cm^{-2}}$
ζ	1.3×10^{-17}	$\mathrm{s^{-1}}$
T_CR	70	K

Photo-desorption and secondary photon processes were not included in the first version of *Saptarsy*. Secondary photon processes were previously treated the same way as direct dissociation by cosmic-rays. We modify the rates as expressed above and add desorption via exothermic surface reactions, also called reactive desorption (Garrod et al. 2007). This occurs if a single product is formed. In the case when more than one product is formed, we assume than the energy is lost because of lateral translation on the surface. In all the models presented in this thesis we used an efficiency of 1% for these reactions. Further models could be made with different reactive desorption efficiency.

The grain species are only neutral species but the grains themselves can be neutral or ionized. No positively charged bare grain is yet included in the network. All grains have the same structure because they all are spherical, they have the same size of 0.1 μm and only a monolayer of ice species can be build at the surface. The composition of the bulk has no importance in *Saptarsy* as we only need to know is the total surface but the desorption energies are taken from experiments of desorption from carbonaceous or silicates surfaces but also some are from water ice surfaces.

Chemical network

We use two reduced Ohio State University (OSU) networks (Garrod 2008), one with 183 species and another with 334 species, to which we add new reactions for HCN and HNC (Graninger et al. 2014; Loison et al. 2014). We reduce the network to first considerably speed up the computation time. For a network of approximately 180 species and for a number of radii around 100 it takes $\sim$ 24 hours to run *Saptarsy* when the evolution of the temperature and radiation field are included. Second, most species are not necessary in this work such as Cl, P, Na and Mg-bearing molecules. Anions and carbon chains with more than four carbon atoms are not included as well. Plus, for Si and Fe only the neutral, ionized and grain surface atomic form are included in the network. We also have updated the desorption energies E_D of some species (see Tab. 2.2). In general we increase the energies, consequently decreasing the mobility of these species on the grain surface. Reactions forming more complex molecules such as methanol are much slower and we obtain less complex species compared to the old network because of this.

Table 2.2: Desorption energies used in *Saptarsy* which have been updated for this work. The first column shows the energies used in this work. The second column shows the energies used in Choudhury et al. (2015) and, thus, are referred to as "old".

Species	E_D (K)	Old E_D (K)
H_2	430[e]	23
O	1660[a]	800
O_2	930[b]	1000
O_3	1833[b]	1800
SO	1745[c]	2600
NO	2460[c]	1600
HNO	2910[c]	2050
H_2CO	3300[d]	2050
O_2H*	4510[c]	3650
OCN*	3260[c]	2400
HNCO*	3710[c]	2850
N_2O*	3260[c]	2400
NO_2*	4120[c]	2400
SiO_2*	6020[c]	4300
NHNO*	3710[c]	2850
NH_2NO*	4160[c]	3300
CH_3OCH_3*	4010[c]	3150
C_2H_5OH*	6260[e]	6580
$HCOOCH_3*$	5200[e]	6295
CH_2NH_2*	4680[e]	5006

[a] He et al. (2015)
[b] Jing et al. (2012)
[c] Derived from $E_D(O)$
[d] Noble et al. (2012)
[e] Garrod (2013a)
* Only for a network including COMs

2.1.2 Numerical solvers: *DVODPK* and *MA28*

DVODPK (Brown et al. 1989; Brown & Hindmarsh 1989) is the double precision version of the code *VODPK* which uses the Preconditioned Krylov subspace iterative method GMRES for the linear systems that arise in the case of stiff systems. A description of the code can be found at the beginning of the source file[1]. *DVODPK* solves the initial value problem for stiff, or non stiff systems, of first order ODEs (Ordinary Differential Equations) $\frac{dy}{dt} = f(t, y)$. In component form it gives $\frac{dy(i)}{dt} = f(i, t, y(1), y(2), ..., y(N))(i = 1, ..., N)$. The linear systems to be solved have the form: $Ax = b$, where $A = I - C\frac{df}{dy}$ is a $N \times N$ matrix. C is a scalar, I is the identity matrix, and $\frac{df}{dy}$ is the Jacobian matrix (an $N \times N$ matrix). In *Saptarsy*, y corresponds to the species abundances n_i. Thus, the time

---

[1] http://netlib.sandia.gov/ode/vodpk.f

derivative $\frac{dy}{dt}$ is actually written as:

$$\frac{dn_i}{dt} = f(t,y) = \sum_{m,l} k_{for} n_m n_l - \sum_{j(j \neq i)} k_{des} n_i n_j,$$

where k_{for} corresponds to the formation rates of the species i and k_{des} to the destruction rates. m and l are the reactants forming the species i, and j is the species reacting with i and thus leading to its destruction. In the case of some reactions as the density of one of the reactant is already taken into account into the rates k, like in the accretion or desorption reactions, the density n_j or n_m are equal to 1. The Jacobian matrix is defined as follows:

$$\frac{df}{dy} = J(i,j) = \frac{\partial \dot{n}_i}{\partial n_j} = \frac{\partial}{\partial n_j} \left(\frac{dn_i}{dt} \right)$$

Some statements about stiffness have been proposed by different authors and are as follows: (1) A linear constant coefficient system is stiff if all of its eigenvalues have negative real part and the stiffness ratio (the ratio of the magnitudes of the real parts of the largest and smallest eigenvalues) is large. (2) Stiffness occurs when stability requirements, rather than those of accuracy, constrain the step length. (3) Stiffness occurs when some components of the solution decay much more rapidly than others. And indeed, solving astrochemical kinetics equations is a stiff problem due to the wide range of chemical characteristics' timescales and fast-decaying processes in time compared to the wide time range. And because the problem is stiff we have to provide *DVODPK* with two routines to deal with the preconditioning of the matrix A: "JAC" which stands for Jacobian and "PSOL" which stands for preconditioners solution. We are using the HSL routine *MA28*[2] to perform the LU decomposition[3] and then solve the equations $Ax = b$ using the decomposition factors, also called preconditioners, of A without iterative refinement. The decomposition is done within the routine "JAC" where we first compute the Jacobian matrix. Solving the system is done in the routine "PSOL". A third routine "ODE", which stands for ordinary differential equation, is given to the solver and it computes the time derivative of the abundances $\frac{dn_i}{dt}$.

In the first version of *Saptarsy*, the rates' computation was performed before the call of *DVODPK*. In the second version, we implement the rates computation within the ODE routine so that for each internal time step of the solver the rates are updated with the new abundances. The difference in the final results is minimal and it increases the computing time but we reach a better accuracy.

2.2 Improvements to model a H$_{II}$ region

2.2.1 Radiation field evolution

In this work, we extend the use of *Saptarsy* to study HC/UCHII regions and the associated internal PDR. So, we include the spatio-temporal evolution of the radiation field strength

---

[2]http://www.hsl.rl.ac.uk/archive/specs/ma28.pdf

[3]LU decomposition: decomposition of a matrix as the product of a lower triangular matrix and an upper triangular matrix

χ_0 in addition to the evolution of the temperatures. χ_0 is obtained using the mean intensity of the radiation field J_ν computed by *RADMC-3D*. The calculation of the mean intensity is performed in the following way: if given an effective temperature and a stellar radius *RADMC-3D* assumes a simple blackbody model for the star represented by the Planck function defined as:

$$B_\nu = \frac{2h\nu^3}{c^2} \frac{1}{e^{\frac{h\nu}{k_B T_{\text{eff}}}} - 1}, \tag{2.24}$$

where h is the Planck constant, ν is the frequency and c is the speed of light. The effective temperature T_{eff} of the star is computed as:

$$T_{\text{eff}} = \left(\frac{L_{\text{tot}}}{4\pi R_*^2 \sigma}\right)^{1/4}, \tag{2.25}$$

where $L_{\text{tot}} = L_* + L_{\text{acc}}$ is the total luminosity, L_{acc} is the accretion luminosity and L_* is the interior luminosity. R_* is the stellar radius and σ the Stefan-Boltzmann constant. L_{tot} and R_* are provided by the accreting massive proto-star model of Hosokawa & Omukai (2009) described in more detail in Sec. 3.1.1.

The mean intensity of the radiation field J_ν as a function of the distance to the star r is computed as:

$$J_\nu(r) \quad = \quad \frac{F}{4\pi} \tag{2.26}$$

$$= \quad \frac{L_{\text{tot}}}{4\pi r^2} \frac{1}{4\pi} \tag{2.27}$$

$$= \quad \frac{R_*^2 B_\nu}{4r^2}. \tag{2.28}$$

where F is the flux. Now we convert J_ν into J_λ using the following relationship:

$$J_\lambda = \frac{\nu^2}{c} J_\nu.$$

The radiative scaling factor G_0 in the void is:

$$G_0 \text{ (Habing unit)} = \frac{1}{5.6 \times 10^{-14}} \int_{912\text{\AA}}^{2400\text{\AA}} \frac{4\pi}{c} J_\lambda(r_0) d\lambda \tag{2.29}$$

The factor 5.6×10^{-14} is in erg cm^{-3}. G_0 is determined in Habing unit defined in Habing (1968) giving reference values for the radiation density $u_\lambda = \frac{4\pi}{c} J_\lambda$ in the ISM. It is also possible to do this computation in Draine unit with 1 Draine unit ≈ 1.7 Habing unit (Draine 1978). G_0 is then noted χ_0 and the factor to apply is 1.08×10^{-13} erg cm^{-3}.

The medium is actually not void but filled with dust. The dust attenuates the radiation field and this attenuation is represented by the optical depth parameter $\tau_\nu(r)$ which is a function of the radius and defined as:

$$\tau_\nu(r) = (\kappa_{\nu_{\text{abs}}} + \kappa_{\nu_{\text{scat}}}) \int_{r_0}^{r} n_H(r) dr, \tag{2.30}$$

where $\kappa_{\nu_{abs}}$ is the absorption coefficient or opacity and $\kappa_{\nu_{scat}}$ is the scattering coefficient. In a hot molecular core, r_0 is equal to zero and represents the position of the proto-star. Otherwise it corresponds to the radius of the HII region. Furthermore, when $r = r_0$ the
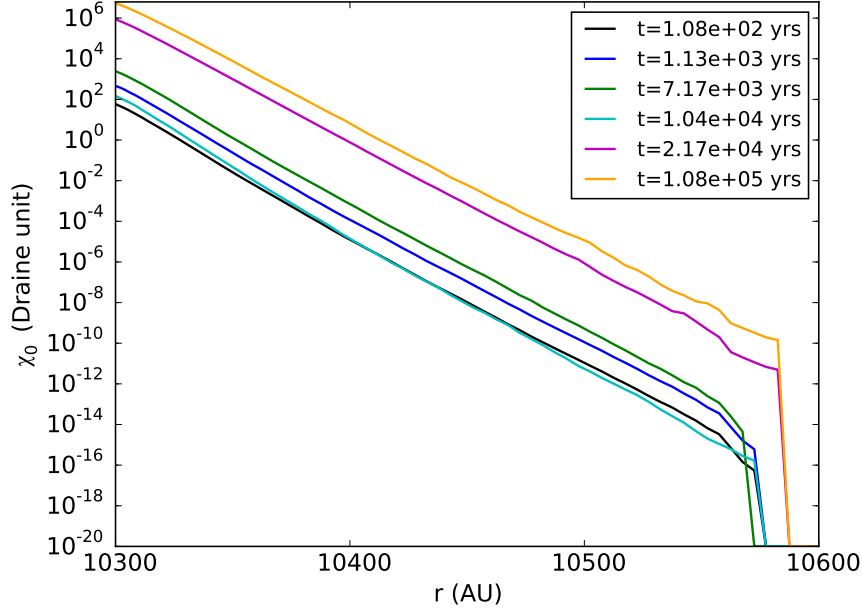
Figure 2.2: Evolution of the radiation field as a function of radius for a UCHII region model with a size of the ionized cavity $R_c = 0.05$ pc (1.03×10^4 AU) and and a density at the ionization front n_c = 10^7 cm^{-3}. It is shown for several times from 10^2 to 10^5 years.

optical depth is zero. Thus we can get the radiation field intensity $\chi(r)$ as a function of the radius:

$$\chi(r) = \frac{1}{5.6 \times 10^{-14}} \int_{912\text{Å}}^{2400\text{Å}} \frac{4\pi}{c} J_\lambda(r_0) e^{-\tau_\lambda(r)} d\lambda \qquad (2.31)$$

From the position of the star to r_0 the intensity of the radiation field decreases as r^{-2}, see Eq. 2.28, because there is no attenuation by dust in this region. As the intensity computed by *RADMC-3D* is attenuated by the dust, what we obtain is actually $J_\lambda(r_0)e^{-\tau_\lambda(r)}$. An example of the radiation field evolution as a function of radius from one of our model is shown in Fig. 2.2. Several, but typical, times are represented with different colors.

As *Saptarsy* now uses the spatio-temporal evolution of χ_0 and as this parameter already takes into account the attenuation by dust, the visual extinction A_V is assumed to be zero in Eq. 2.7. This assumption is done only when the evolution of the radiation field is used. This particularity is only used in the code for HII region models. For HMC models we do not include the radiation field. In this case, the visual extinction is computed using values from Bohlin et al. (1978).

$$A_V = \frac{3.1}{5.8 \times 10^{21}} N_H \qquad (2.32)$$

$$= \frac{3.1}{5.8 \times 10^{21}} \int_{r_0}^{r} n_H(r) dr. \qquad (2.33)$$

2.2.2 Logarithmic version

In the first version of *Saptarsy* we were in linear mode and so we were solving the linear equations using the abundances. The time derivative was defined as $\dot{X} = F(X)$ and the Jacobian matrix as $J_F = \frac{\partial F}{\partial X}$ with $X = n_x$, $\dot{X} = \frac{dn_i}{dt}$ and $J_F = \frac{\partial \dot{n}_i}{\partial n_j}$.

In the new version we use instead the logarithm of the abundances since it makes the code more stable and prevents unphysical results like negative abundances. The latter happened mostly for minor species bearing heavier elements like Cl or P. The variables are now defined as $Y = ln(X) = ln(n_x)$ and we obtain for the time derivatives $\dot{Y}$:

$$\dot{Y} = G(Y) = \frac{dln(X)}{dt} = \frac{\dot{X}}{X} = e^{-Y} F(e^Y) = \frac{1}{n}\frac{dn}{dt}$$

Thus the Jacobian matrix becomes:

$$\begin{aligned} J_G &= \frac{\partial G}{\partial Y} = \frac{\partial}{\partial Y}\left(e^{-Y}F(e^Y)\right) \\ &= -e^{-Y}F(e^Y) + e^{-Y}\frac{\partial F}{\partial X}e^Y \\ &= J_F - G(Y). \end{aligned}$$

We can also write the above equations with indices. This is straightforward for the time derivatives: $\dot{Y} = \frac{dln(n_i)}{dt} = \frac{1}{n_i}\frac{dn_i}{dt}$. For the Jacobian we do not get the same results for diagonal elements of the matrix and the others.

$$\begin{aligned} J_G(i,i) &= \frac{\partial ln(\dot{n}_i)}{\partial ln(n_i)} = \frac{\partial}{\partial ln(n_i)}\left(e^{-ln(n_i)}\frac{de^{ln(n_i)}}{dt}\right) \\ &= -e^{-ln(n_i)}\frac{de^{ln(n_i)}}{dt} + e^{-ln(n_i)}e^{ln(n_i)}\frac{\partial}{\partial e^{ln(n_i)}}\left(\frac{de^{ln(n_i)}}{dt}\right) \\ &= \frac{\partial \dot{n}_i}{\partial n_i} - \frac{1}{n_i}\frac{dn_i}{dt} \\ &= J_F(i,i) - G(i) \end{aligned}$$

$$\begin{aligned} J_G(i,j) &= \frac{\partial ln(\dot{n}_i)}{\partial ln(n_j)} = \frac{\partial}{\partial ln(n_j)}\left(e^{-ln(n_i)}\frac{de^{ln(n_i)}}{dt}\right) \\ &= e^{-ln(n_i)}\frac{\partial}{\partial ln(n_j)}\left(\frac{de^{ln(n_i)}}{dt}\right) \\ &= e^{-ln(n_i)}e^{ln(n_j)}\frac{\partial}{\partial e^{ln(n_j)}}\left(\frac{de^{ln(n_i)}}{dt}\right) \\ &= \frac{n_j}{n_i}\frac{\partial}{\partial n_j}\left(\frac{dn_i}{dt}\right) = \frac{n_j}{n_i}J_F(i,j) \end{aligned}$$

2.2.3 Interpolation: Temperatures and radiation field as variables

We now have the possibility to include more time steps in *Saptarsy* than the ones used in *RADMC-3D* to compute T_d and J_ν. This is done to save some computing time. Thus we can compute T_d and χ_0 with *RADMC-3D* for a hundred time steps for instance and increase this number for *Saptarsy* for example to three hundred or more, as a hundred steps are not enough to get a smooth evolution of abundances. However computing T_d and χ_0 for three hundred time steps would extremely time consuming (a hundred points already takes a couple of days). In addition we can extend the time range for the abundances computation. Computing T_d and χ_0 for times out of the range given by Hosokawa & Omukai parameters, approximately from 100 to 10^5 years, is not necessary (see Sec. 3.1.1 for details) but is useful for the computation of chemical abundances to understand their temporal evolution.

To obtain T_d, T_g and χ_0 at a certain time which is not included in the inputs we perform in *Saptarsy* a spline interpolation. These parameters can be written as polynomials with a degree defined in the source code. For a third order polynomial, one of these parameters, noted T, is expressed as follows:

$$T(t) = a_0 + a_1 t + a_2 t^2 + a_3 t^3$$

In the logarithmic form we have:

$$T(t) = 10^{a_0 + a_1 \log t + a_2 (\log t)^2 + a_3 (\log t)^3}$$

To compute the four unknown parameters we need to know four points t_i (with $T_i(t_i)$ known and defined in the temperature input) the closest to the time t we want to do the interpolation. And then solve the system:

$$\begin{cases} T_1(t_1) & = & 10^{a_0 + a_1 \log t_1 + a_2 (\log t_1)^2 + a_3 (\log t_1)^3} \\ T_2(t_2) & = & 10^{a_0 + a_1 \log t_2 + a_2 (\log t_2)^2 + a_3 (\log t_2)^3} \\ T_3(t_3) & = & 10^{a_0 + a_1 \log t_3 + a_2 (\log t_3)^2 + a_3 (\log t_3)^3} \\ T_4(t_4) & = & 10^{a_0 + a_1 \log t_4 + a_2 (\log t_4)^2 + a_3 (\log t_4)^3} \end{cases}$$

The system can be written in the matrix form $A\,x = V$ with:

$$A = \begin{pmatrix} 1 & t_1 & t_1^2 & t_1^3 \\ 1 & t_2 & t_2^2 & t_2^3 \\ 1 & t_3 & t_3^2 & t_3^3 \\ 1 & t_4 & t_4^2 & t_4^3 \end{pmatrix} ; \quad V = \begin{pmatrix} T_1 \\ T_2 \\ T_3 \\ T_4 \end{pmatrix} ; \quad x = \begin{pmatrix} a_0 \\ a_1 \\ a_2 \\ a_3 \end{pmatrix} .$$

The solution are:

$$a_0 = \frac{det(A_1)}{det(A)} ; \quad a_1 = \frac{det(A_2)}{det(A)} ; \quad a_2 = \frac{det(A_3)}{det(A)} ; \quad a_3 = \frac{det(A_4)}{det(A)}$$

where A_i is the A matrix whose i-th column has been replaced by the vector V.

As T_d, T_g and χ_0, depend on the time, we can derivate the expression and compute T_d, T_g and χ_0, using *DVODPK*.

$$\dot{T} = \frac{dT(t)}{dt} = \frac{T}{t} \left(a_1 + 2a_2 \log t + 3a_3 (\log t)^2 \right) .$$

As the variables are given in logarithm to the solver we actually have:

$$\dot{T}_{ln} = \frac{d \ln T(t)}{dt} = \frac{1}{T} \frac{dT}{dt} = \frac{1}{t} \left(a_1 + 2a_2 \log t + 3a_3 (\log t)^2 \right).$$

The Jacobian terms are

$$\frac{\partial \dot{T}_{ln}(t)}{\partial X_i} = 0,$$

where the X_i parameters are either the density of the species or T_d, T_g or χ_0.

2.3 Benchmarking

To demonstrate that *Saptarsy* results are reliable we benchmark *Saptarsy* against the results obtained by Semenov et al. (2010) where a benchmarking of the models *NAUTILUS* and *ALCHEMIC* is presented and also against the Turbulence Dissipation Region (TDR) model developed in Paris (Godard et al. 2014). For the comparisons we do not use the network defined earlier but networks closer to the ones used in the model we compare with.

2.3.1 Semenov code

For the comparison with models from Semenov et al. (2010), *Saptarsy*'s network is the same network as the one used in Semenov et al. (2010), i.e. we use the OSU network containing 655 species and 6065 reactions. It does not include photo-desorption and reactive desorption reactions. Secondary photon processes are treated the same way as direct CR dissociation reactions. In addition the desorption-diffusion ratio is set to 0.77 in this model instead of 0.50. Furthermore in these models, no time evolution of the dust temperature and radiation field intensity is included.

Fig. 2.3 and Fig. 2.4 present the abundances obtained with *Saptarsy* (solid lines) and the *NAUTILUS* code (point markers) presented in Semenov et al. (2010) where we can see that the *NAUTILUS* results fit perfectly the *ALCHEMIC* results. The first figure corresponds to a dark cloud model fitting the source TMC–1 (Taurus Molecular Cloud 1) which these properties: $T_\mathrm{d} = 10$ K, $n_\mathrm{H} = 2 \times 10^4$ cm^{-3}, $A_\mathrm{V} = 10$ mag and $\chi_0 = 1$ Draine unit. The second figure corresponds to a hot core model with these properties: $T_\mathrm{d} = 10$ K, $n_\mathrm{H} = 2 \times 10^4$ cm^{-3}, $A_\mathrm{V} = 10$ mag and $\chi_0 = 1$ Draine unit. We can see that our results fit nicely the *ALCHEMIC* and *NAUTILUS* results.

But it appears that at late times in the TMC–1 model the abundance of the negatively charged bare grain starts to drop with *Saptarsy* after 10^8 years whereas it does not with *ALCHEMIC* or *NAUTILUS*. This result is less apparent when using the linear version of Saptarsy. However, the logarithmic version reveals the instabilities present in the code: because some species, e.g. ClO, NH$_2$OH, C$_5$H$_3$, etc, seem to be only destroyed, their abundances drop until the numerical accuracy limit in the code is reached (this behavior is also happening for the hot core model). It denotes a problem coming from the network itself and not from the code. If species are only destroyed in the network the code continues

to run when using the linear version but the abundances become negative, even if a lower limit for the abundances as been set. But with the logarithmic version the code slows down and finally does not converge to a result.

2.3.2 TDR

The model comparison, *Saptarsy* in solid lines and the TDR model in dashed, shown in Fig. 2.5 has the following properties: $A_V = 10^{-1}$ mag, $n_H = 10^3$ cm^{-3}, $\zeta = 10^{-16}$ s^{-1} and $\chi_0 = 10^1$ Draine unit. Only the self-shielding for H_2 is included in *Saptarsy* and the chemical network, containing 138 species and 2662 reactions, is taken from the Meudon PDR code (Le Petit et al. 2006). Because this network does not have surface species except for H no formation of H_2 can occur on the grains, hence we add the standard formation reaction of H_2 whose rate is described in Jura (1974) and Le Bourlot et al. (2012). Thus, the network diverges from the TDR model and some differences might still show up. Furthermore, we use the same time evolution of the temperature and the same initial conditions. The properties of the model presented in Fig. 2.6 are: $A_V = 1$ mag, $n_H = 10^2$ cm^{-3}, $\zeta = 10^{-16}$ s^{-1} and $\chi_0 = 1$ Draine unit. For both models the codes give similar results despite some small differences in particular for H^+.

In conclusion, the astrochemical code *Saptarsy* including gas-grain chemistry and the spatio-temporal evolution of the temperature was developed to investigate the chemistry in HMCs. For this work in order to study HC/UCHII region as well, we have improved *Saptarsy* by including, in particular, photo-reactions as well as the spatio-temporal evolution of the radiation field. We have also optimized the code by implementing the interpolation of T_g, T_d and χ_0 and, more important, the logarithmic version to stabilize the code and prevent unrealistic results. Additionally, we have developed a tool to, given a species, recompute from its abundance the reactions rates involved in its formation and destruction. Then this tool allows us to analyze the formation and destruction reactions as it plots the rates as a function of time or radius. *Saptarsy* can reproduce the results from two others codes. We can then use this code to obtain the detail modeling of the relative abundances to be used with *RADMC-3D*.
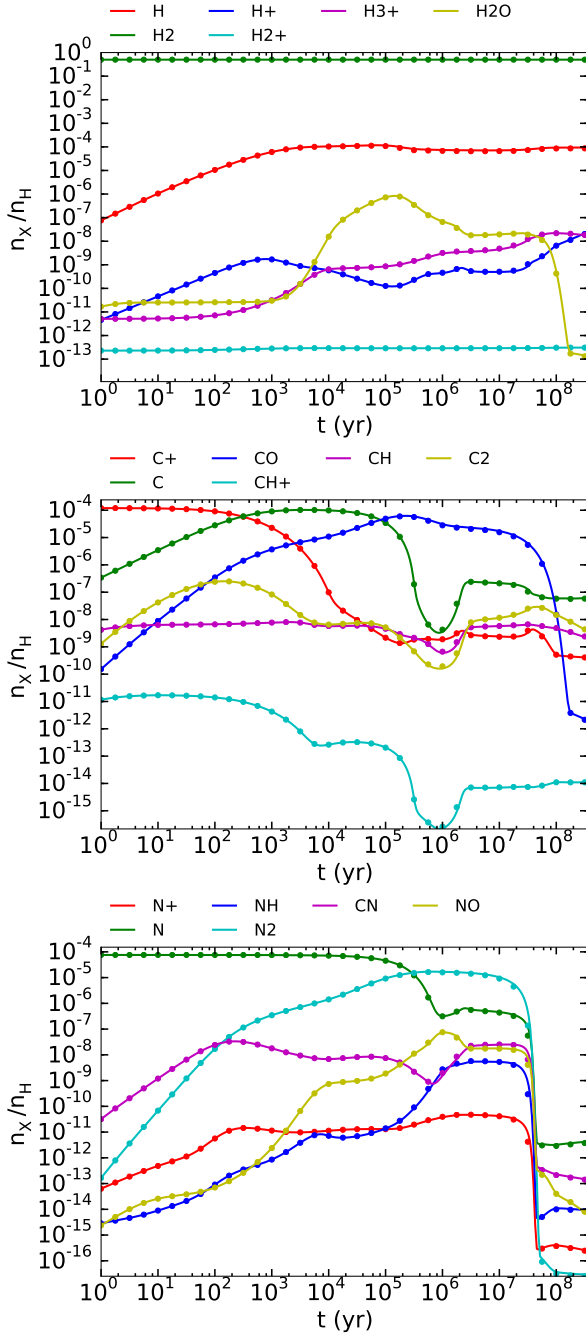
Figure 2.3: Abundances for the TMC-1 model obtained with *Saptarsy* (solid lines) and from Semenov et al. (2010) (point markers).
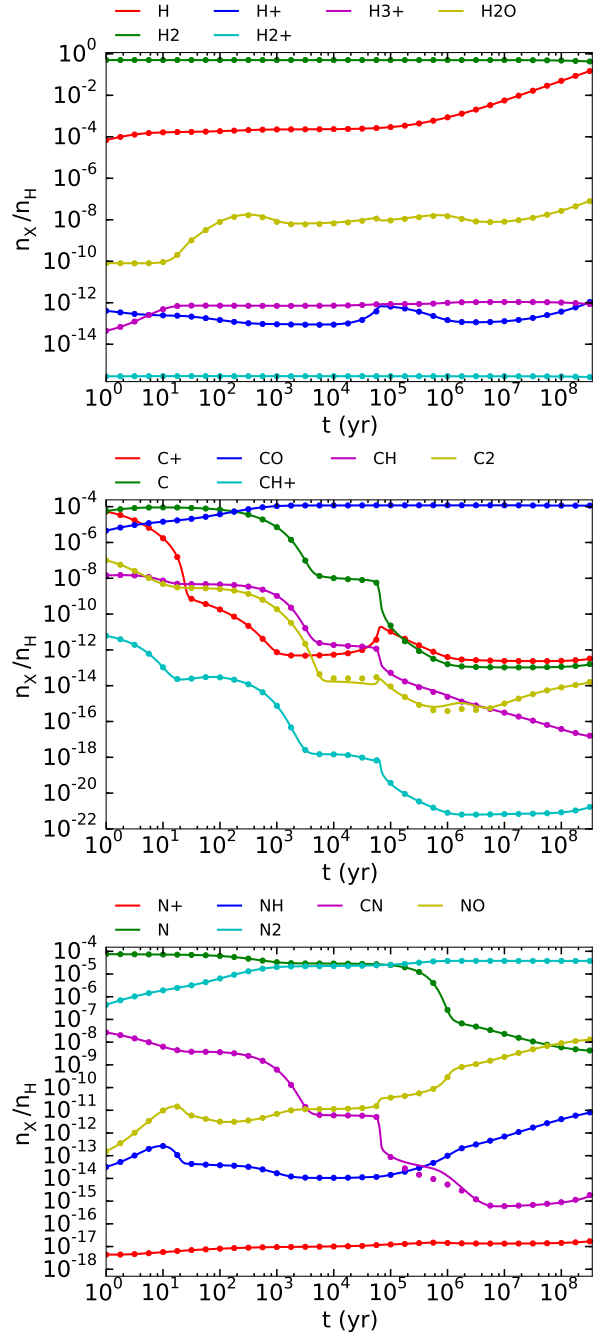
Figure 2.4: Abundances for the Hot Core model obtained with *Saptarsy* (solid lines) and from Semenov et al. (2010) (point markers).
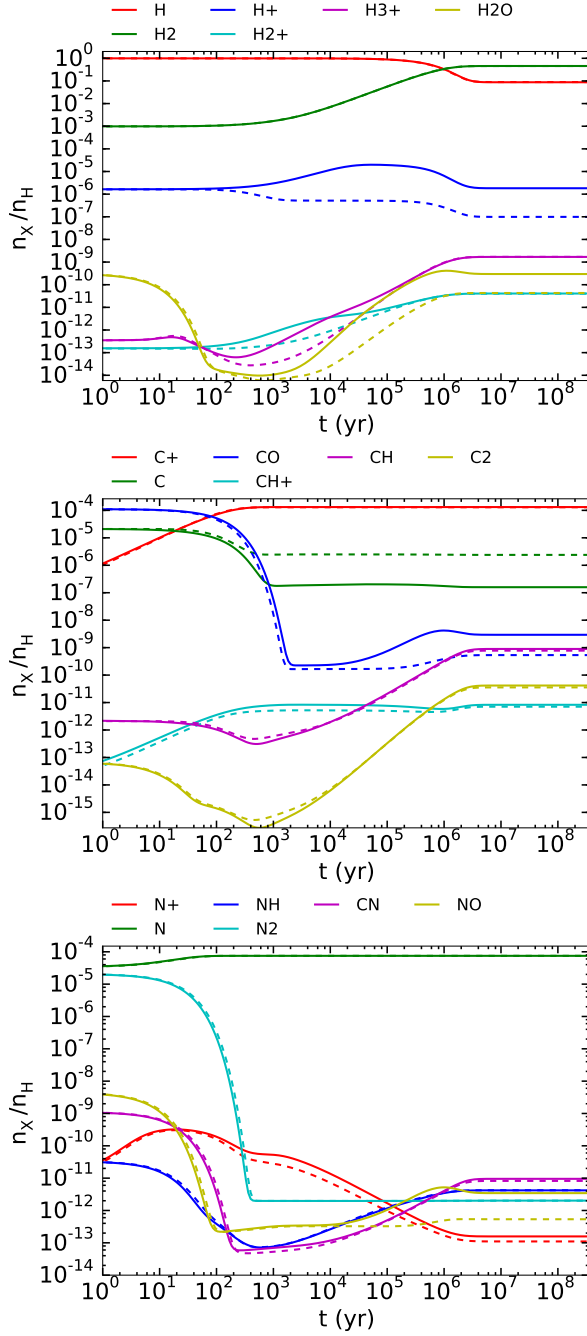
Figure 2.5: Comparison between *Saptarsy* (solid lines) and the TDR code (dashed lines) for a model with $A_V = 10^{-1}$ mag, $n_H = 10^3$ cm^{-3}, $\zeta = 10^{-16}$ s^{-1} and $\chi_0 = 10^1$ Draine unit.
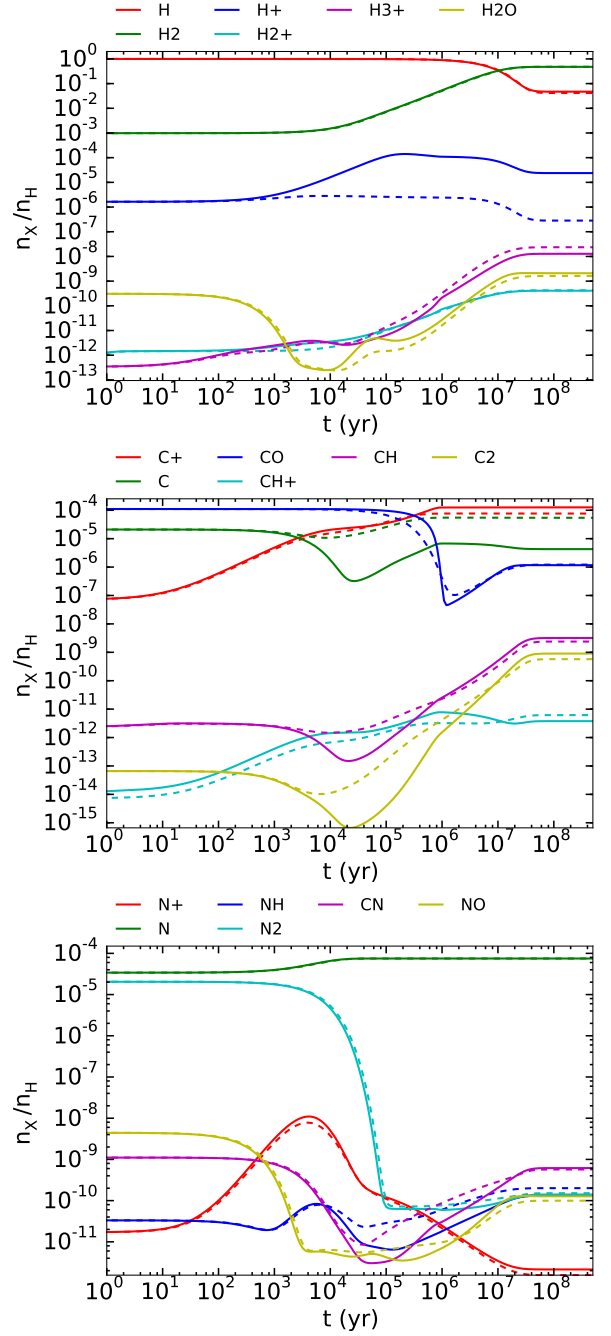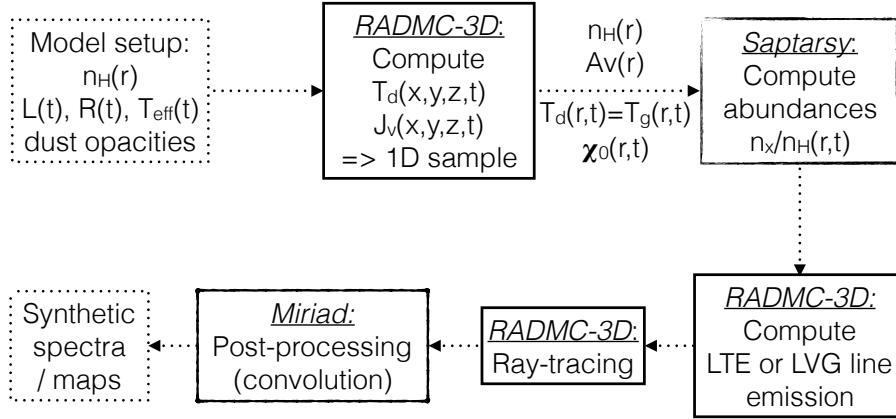
Figure 2.6: Comparison between *Saptarsy* (solid lines) and the TDR code (dashed lines) for a model with $A_V = 1$ mag, $n_H = 10^2$ cm^{-3}, $\zeta = 10^{-16}$ s^{-1} and $\chi_0 = 1$ Draine unit.

3

Pandora

Contents

Pandora is a Python based program which connects the astrochemical code *Saptarsy* to the radiative transfer code *RADMC-3D* (Dullemond 2012). Thus, *Saptarsy* uses the dust temperature and radiation field intensity computed self-consistently by *RADMC-3D* which finally provides synthetic spectra using the detailed chemical modeling obtained with *Saptarsy*. The modeling framework is presented in Fig. 3.1. This flowchart does not include all the capabilities of *Pandora* but only the ones necessary for this work. Indeed, *Pandora* also include the radiative transfer code *LIME* (Brinch & Hogerheijde 2010) or the software *MAGIX* (Möller et al. 2013) used for the optimization of the model inputs parameters. More information about the other capabilities of *Pandora* than the ones described in this manuscript can be found in Schmiedeke et al. (2016). At the beginning of the framework we first have to define the model structure to produce all the inputs required by *RADMC-3D*.

In this chapter we first describe in Sec. 3.1 how the temperature and radiation field intensity are computed with *RADMC-3D*. This requires some explanations of the stellar parameters, the density profile, the grain properties and the structure of the cores. In Sec. 3.2 we explain how we obtain he synthetic spectra via line emission computation and the post-processing applied to the raw images produced by *RADMC-3D*.

```
┌·····················┐   ┌─────────────┐                    ┌─────────────┐
: Model setup:       :   │ RADMC-3D:   │  n_H(r)            │ Saptarsy:   │
:   n_H(r)           :   │ Compute     │  Av(r)             │ Compute     │
: L(t), R(t), T_eff(t) :·▶│ T_d(x,y,z,t)│ T_d(r,t)=T_g(r,t) ▶│ abundances  │
: dust opacities     :   │ J_v(x,y,z,t)│  χ_0(r,t)          │ n_x/n_H(r,t)│
└·····················┘   │ => 1D sample│                    └─────────────┘
                         └─────────────┘                           │
                                                                   ▼
┌·············┐   ┌──────────────┐   ┌─────────────┐   ┌─────────────┐
: Synthetic  :   │ Miriad:      │   │ RADMC-3D:   │   │ RADMC-3D:   │
: spectra   ◀··:│ Post-processing│◀─│ Ray-tracing │◀··│ Compute     │
: / maps     :   │ (convolution)│   └─────────────┘   │ LTE or LVG line│
└·············┘   └──────────────┘                    │ emission    │
                                                      └─────────────┘
```

Figure 3.1: Flowchart of the modeling framework *Pandora*.

3.1   Dust temperature & radiation field computation

The computation by *RADMC-3D* of the dust temperature is performed using an improved thermal Monte-Carlo method of Bjorkman & Wood (2001). It requires at least one luminosity source. *RADMC-3D* uses a number of photon packages emitted one by one by the luminosity source and they are spread isotropically in the cube. The total luminosity per photon package is obtained by dividing the total luminosity of the source by the number of packages. This number of photon packages has to be high enough to ensure that every cell is crossed by photon packages. Once a photon package reaches the edge of the modeling grid it is considered lost and a new photon package is emitted. On their way the photons can be absorbed, and reemitted in a different direction and at a different wavelength but the luminosity fraction it represents remains the same, and they can also be scattered.

The dust temperature is an equilibrium temperature, i.e. each grain absorbs as much energy as it emits. This is a valid approximation as the heating and cooling timescales for dust grains are very short compared to any time-dependent dynamical processes. Indeed, assuming that the specific heat of one grain is $1 \text{ J g}^{-1} \text{ K}^{-1} = 10^7 \text{ erg g}^{-1} \text{ K}^{-1}$ and that the mass density of a grain is 3 g.cm^{-3}, at 20 K the thermal energy of a 0.1 μm size grain is about 2.8×10^{-7} erg. The grain emission equation is developed in Eq. 3.1. Considering an emission from 10^{-3} to 10^3 μm, which is the range we use in the model, and assuming $Q_{abs} = Q_{em}$, with the absorption efficiency Q_{abs} taken from Draine's data (Laor & Draine 1993) the grain emission is about 3.65×10^{-9} erg s^{-1}. The cooling time scale which is the ratio of the thermal energy over the grain emission is then ~ 76 s $\sim 2.4 \times 10^{-6}$ year.

$$P_{em} = 4\pi a^2 \int_0^\infty Q_\lambda^{em} \pi B_\lambda(T_d) d\lambda \qquad (3.1)$$

We assume that the gas temperature is equal to the dust temperature once this one is computed. We know it is not the case everywhere in the core such as for low density or in the PDR where the gas temperature is approximately one order of magnitude higher than the dust temperature from extinction up to ~ 2 mag. Indeed when tests are performed with a light version of the Meudon PDR code we see that the gas temperature goes way above 10^3 K while the dust temperature remains close to 100 K.

RADMC-3D also computes the mean intensity of the radiation field J_ν in $\mathrm{erg\,s^{-1}\,cm^{-2}\,Hz^{-1}}$ (Eq. 3.2) using the monochromatic Monte-Carlo calculation. In this method the scattering has the same effect than in the thermal Monte-Carlo run: it modifies the direction of the photon packages. This computation is done for several frequencies whose number is defined by the user.

$$J_\nu = \frac{1}{4\pi} \oint I_\nu(\Omega) d\Omega \tag{3.2}$$

The mean intensity depends on the specific intensity $I_\nu(\Omega)$ which represents the radiative energy flux per solid angle $d\Omega$ and is computed as in Eq. 3.8.

$$\frac{dI_\nu(\Omega)}{d\tau} = S_\nu(\Omega) - I_\nu(\Omega) \tag{3.3}$$

τ represents the optical depth and is a function of the extinction coefficient χ_ν, the scattering coefficient σ_ν and the radius: $d\tau = (\chi_\nu + \sigma_\nu)dr$. S represents the source function defined in Eq. 3.9 and η_ν is the emissivity, i.e. the energy volume density per solid angle per unit time and per unit frequency.

$$S_\nu = \frac{\eta_\nu + \sigma_\nu J_\nu}{\chi_\nu + \sigma_\nu} \tag{3.4}$$

Before any dust temperature and radiation field intensity computations are performed we have to define several properties of the models required by *RADMC-3D*. Indeed, it needs to know the properties of the heating sources, in our case it is a single proto-star situated at the center of the core, the structure of the core(s) and so the density profile and the dust properties. The heating sources are in our models a single proto-star located at the center of the core and the structure of this core sets up the modeling grid. The dust temperature and mean intensity of the radiation field are computed in a 3D grid and then sampled along one axis to give them to *Saptarsy*.

3.1.1 Luminosity evolution

The time evolution in the model is given by the evolution of the proto-star parameters. These parameters are obtained with the model of an accreting massive proto-star from Hosokawa & Omukai (2009) (model named MD3). In this model the accretion rate is equal to 10^{-3} $\mathrm{M_\odot.yr^{-1}}$, the ratio of deuterium over hydrogen is equal to 2.5×10^{-5} and the metallicity is equal to 0.02. Deuterium burning and the use of primordial or solar metallicity hardly affect the results of the evolution. The mass of the proto-star increases monotonically from 0.05 $\mathrm{M_\odot}$ at ~ 50 years until about 80 $\mathrm{M_\odot}$ at 7.8×10^4 years as seen in the top left panel of Fig. 3.2. This figure also shows the evolution of the total luminosity (bottom left panel), the radius (top right panel), starting at 15.5 $\mathrm{R_\odot}$, and the effective temperature (bottom right panel) obtained with the two other parameters using Eq. 2.25. The stellar radius is actually only used to get the effective temperature of the star as we consider the star is a point source in *RADMC-3D*. The evolution of these parameters shows that the evolution can be divided into four parts: the adiabatic accretion, the swelling, the Kelvin-Helmholtz (KH) contraction, and finally the main-sequence accretion. The mass and time period spent by the proto-star in these different phases are presented in Tab. 3.1.
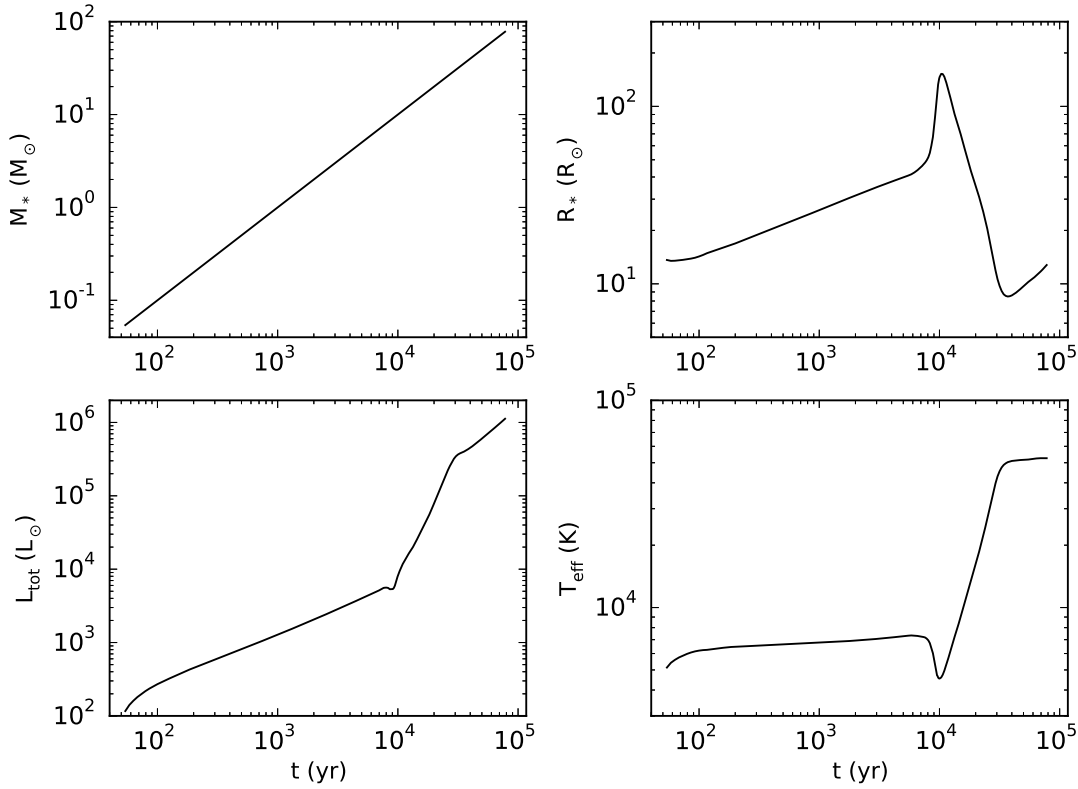
Figure 3.2: Time evolution of the parameters M_* (top left), R_* (top right), L_{tot} (bottom left) and T_{eff} (bottom right) from Hosokawa & Omukai (2009) for an accreting massive protostar (10^{-3} M$_\odot$.s^{-1})

In the first phase, the adiabatic accretion, the radiative energy loss barely affects the proto-star's evolution when the KH timescale t_{KH} (Eq. 3.5) is higher than the accretion timescale t_{acc} (Eq. 3.6). The accreted matter is embedded deep into the stellar interior before the entropy due to the accretion shock is lost radiatively. During this period the opacity is really high but it starts to decrease. Thus, the entropy can be gradually transported to the exterior. The matter at the surface of the proto-star accumulates entropy and when the amount is sufficient the star expands. This is the swelling phase. The consequent energy loss induces an increase of the interior luminosity and the proto-star contraction to preserve the viral equilibrium. This is the KH-contraction phase where the KH timescale is the shorter and is as short as the accretion timescale. Because of the contraction the temperature increases and the hydrogen burning eventually starts and provides energy to stop the contraction. The proto-star enters the zero-age main-sequence (ZAMS).

$$t_{KH} \quad = \quad \frac{GM_*^2}{R_* L_*} \tag{3.5}$$

$$t_{acc} \quad = \quad \frac{M_*}{\dot{M}_*} \tag{3.6}$$

We start the computation of the dust temperature before 50 years, first time provided by Hosokawa and Omukai data. We linearly extrapolate the different parameters from t = 0 year and parameters at 0 to the first point in the data. Furthermore, the data spread until $\sim 7.8 \times 10^4$ years. Afterwards, the stellar parameters are considered constant from

Table 3.1: Phases of the evolution of an accreting massive proto-star with an accretion rate of $10^{-3} M_{\odot}.\mathrm{yr}^{-1}$ (Hosokawa & Omukai 2009).

Phases	Proto-star mass ($M_{\odot}$)	Time (years)
Adiabatic accretion	≤ 6	$\leq 5 \times 10^3$
Swelling	$6 - 10$	$5 \times 10^3 - 10^4$
Kelvin-Helmholz contraction	$10 - 30$	$10^4 - 3 \times 10^4$
Main-sequence accretion	≥ 30	$\geq 3 \times 10^4$

this point and thus the dust temperature and the radiation field intensity are constant.

3.1.2 Density and structure of the cores

The radial evolution in the models is given by the density profile. We use a Plummer-like function defined in Eq. 3.7. In this equation, r_p represents the Plummer radius (in cm) and n_c is half of the central density (in cm^{-3}– and would be the number of hydrogen molecules if atomic hydrogen is in negligible amount). We distinguish two models with different exponent γ as seen in Fig. 3.3. This figure shows the profiles for different sizes of HII regions: 0.015 pc (solid), 0.05 pc (dashed) and 0.10 pc (dashed-dotted). In the first case (black curves), γ is equal to 2.5 and r_p also corresponds to the size of the HII region, $n_c = 2.825 \times 10^X$ cm^{-3} with X being 7, 6 or 5 for instance. It is defined this way so that the density at the ionization front is 10^X cm^{-3} (in Fig. 3.3 $X = 7$). Thus the density decreases as r^{-5}, factor in agreement with Qin et al. (2011) in the case of Sgr B2(N)-SMA1, region close to the UCHII region K2. For the second density profile (red curves), γ is equal to 1 which gives asymptotically a decrease as r^{-2}. This is closer to the results of Didelon et al. (2015) in the case of Monoceros R2 central UCHII region. In this model, n_c is always equal to 2.825×10^7 cm^{-3} and r_p is fixed and equal to 3×10^3 AU whatever the size of the HII region. Thus, the density at the ionization front decreases when the size of the ionized cavity increases as seen in the figure.

$$n(r) \ (\mathrm{cm}^{-3}) = 2n_c \left(1 + \left(\frac{r}{r_p} \right)^2 \right)^{-\gamma} \tag{3.7}$$

The structure of the core(s) is defined by the user and gives the structure of the modeling grid. In our models, we have a single spherical symmetric core, hence we use a spherical grid. Two kind of grids are necessary to produce a hot molecular core, a hollow hot molecular core (HHMC) and a HII region model: one for the HMC model and another for the hollow HMC and the HII region model. In Fig.3.4 we present a scheme of these three models. HII region and HMC models use the same Plummer function but are not directly comparable in the sense that they do not have in particular the same column density due to the presence of the ionized cavity at the center for the HII region. To compare them we expand the HMC models and produce hollow HMC models, with the exact same structure than the HII region models so that these two models can be compared with each other. The only difference between the HII region and the HMC models is that
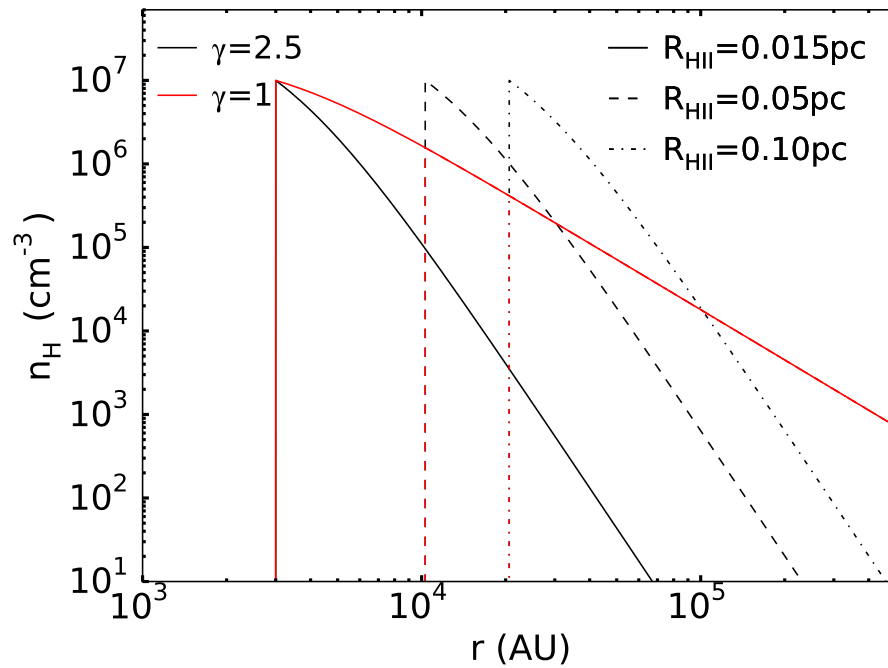
Figure 3.3: Density for two different exponent of the Plummer function (2.5 in black and 1 in red) for three sizes of HII region (0.015 pc in solid line, 0.05 pc in dashed and 0.10 pc in dashed-dotted).
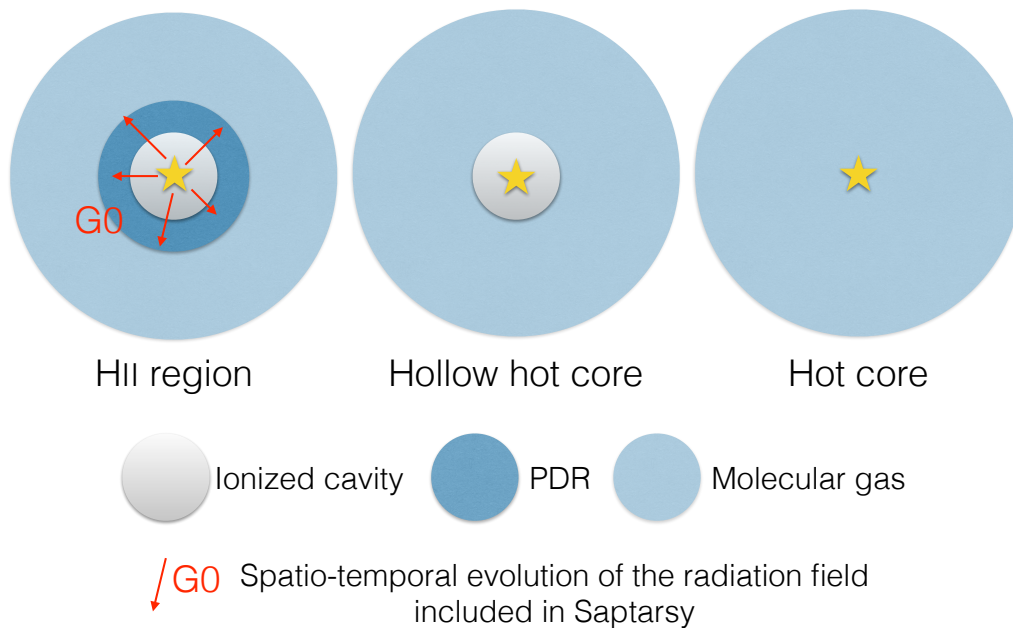
Figure 3.4: Scheme presenting the structure of the HII region, hollow hot core and hot core models. The ionized cavity is filled only with HII and electrons.
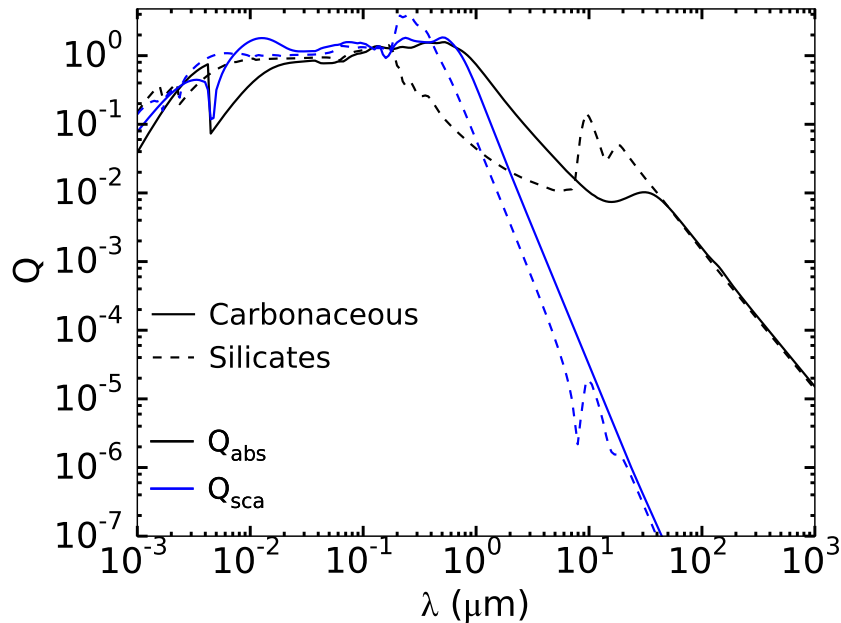
Figure 3.5: Absorption (black line) and scattering (blue) efficiencies for carbonaceous (solid) and silicates (dashed) grains as a function of wavelength.

we use the spatio-temporal evolution of the radiation field in the HII region model to compute the relative abundances.

The ionized cavity in the HII region and hollow HMC models are Strömgren sphere, i.e. they are spherical, fully and uniformly ionized and they contain no dust. Furthermore, no expansion in time of the HII region is implemented as we consider a HII region whose expansion is limited by the high accretion flow (Peters et al. 2010a) and the ionized cavity is present from the beginning of the time evolution. The cavity is assumed to be filled only with HII and electrons whose temperature is set to the typical HII region temperature of 10^4 K and an electron density of 10^5 cm^{-3}.

3.1.3 Dust properties

RADMC-3D requires some dust properties, the absorption and scattering efficiencies. We first included the dust opacities following the standard MRN distribution for the diffuse interstellar medium (Draine & Lee 1984) which are taken from Ossenkopf & Henning (1994). However the wavelength range going from 1 μm to 1.3×10^3 μm does not cover the UV regime required to compute the radiation field strength and only the absorption coefficient are included. So we now use the opacities data from Laor & Draine (1993) for one size of grains covering the wavelengths from 10^{-3} to 10^3 μm and including scattering efficiency (see Fig. 3.5). We adopt a standard grain size of 0.1 μm in *Saptarsy* so we choose the efficiencies for this size. In all the models presented later we use carbonaceous grains' efficiencies and anisotropic scattering for the dust temperature and mean intensity computation.

In Fig. 3.6 we show the effect of the scattering mode on the temperature for carbonaceous, silicates and a mixture of both grains (70% carbonaceous and 30% silicates) for
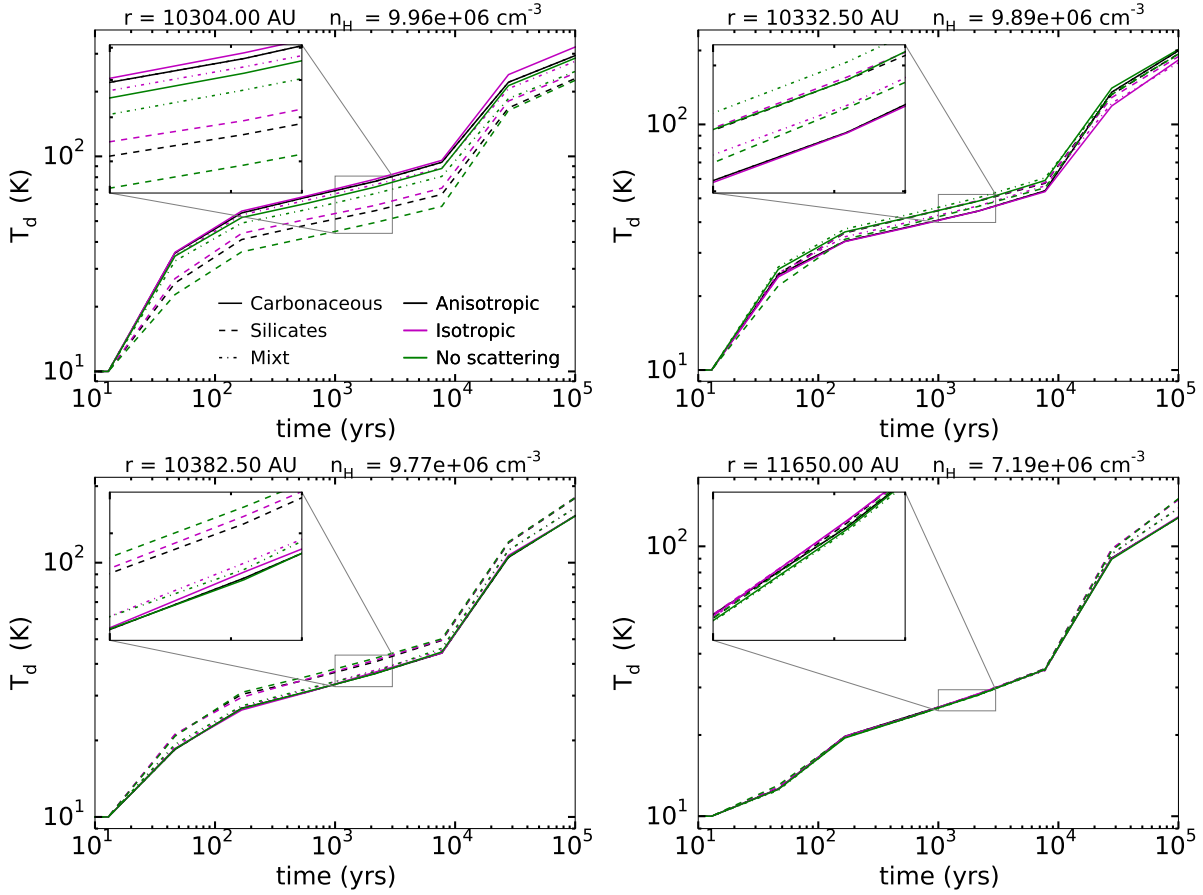
Figure 3.6: Time evolution of the dust temperature for several radii/densities comparing the type of scattering: anisotropic (black), isotropic (purple) or no scattering (green); and comparing carbonaceous (solid lines), silicate grains (dashed) and a mixture of carbonaceous and silicates (dotted dashed). Each plot title gives the radius and density where the dust temperature is computed.

several radii in our reference model (HII region of a size of 0.05 pc $\sim$ 10300 AU). We do not have the anisotropic scattering for the mixture of grains. The different radii shown represent a transition between carbonaceous grains and silicates. At the ionization front (top left panel) the carbonaceous grains temperature is higher. Then, $\sim$ 30 AU further, it becomes similar to silicates temperature (top right) and even further, $\sim$ 80 AU, silicates grains temperature gets higher than carbonaceous grains (left bottom). Finally about 1350 AU after the ionization front they have the same temperature (right bottom).The differences are more important near the ionization front for the silicates and carbonaceous grains as well as for the type of scattering and become more significant with time. This change in the dominant temperature, from carbonaceous to silicates grains, requires further investigations. This behavior is likely due to the difference in the absorption – and scattering when it is included – coefficients (black curves in Fig. 3.5) because this is the only difference between these two types of grains included in the models. Isotropic scattering gives the highest temperature and no scattering induces the lowest dust temperature. 30 AU further, the highest temperature is obtained without scattering in the model for carbonaceous only. Deeper in the core, isotropic, anisotropic and no scattering produce the same temperature. So, whereas anisotropic scattering is the best assumption as more realistic, one could think that the assumption that the grains are fully carbonaceous is

not a good assumption. Molecular clouds are composed by a mixture of carbonaceous and silicates grains with a standard view that 70% are carbonaceous and the rest are silicates. However, we can see that the mixture of grains without or with isotropic scattering gives temperatures really close to the only carbonaceous grains. So we assume that anisotropic scattering with the mixture would give really similar results. We can then choose the efficiencies only for carbonaceous grains.

3.2   Synthetic spectra

Once *Saptarsy* has computed the spatio-temporal evolution of the relative abundances, *RADMC-3D* uses them for the line emission computation in the LTE approximation. Then it performs a ray-tracing to obtain raw images which can then be post-processed, i.e. convolved to the beam of observations we want to compare them with. We finally obtain synthetic map from which we can extract spectra.

3.2.1   Line emission

The line emission is computed without scattering. We are mostly interested in lines in the sub-millimeter regime thus we assume that scattering by a grain of 0.1 μm is not going to affect the line emission in the frequency range. Thus, the radiative transfer equation is modified and becomes:

$$\frac{dI_{ij}(\Omega, \nu)}{d\tau} = S_{ij}(\Omega, \nu) - I_{ij}(\Omega, \nu) \tag{3.8}$$

The optical depth is as well modified: $d\tau = \chi_\nu dr$ and the source function becomes (i: upper level and j: lower level):

$$S_{ij}(\Omega, \nu) = \frac{\eta_{ij}(\Omega, \nu)}{\chi_{ij}(\Omega, \nu)} \tag{3.9}$$

In the LTE approximation it can also be written $S_\nu = B_\nu(T)$ following the Kirchoff's law. The emissivity and extinction coefficient can be written as follows:

$$\eta_{ij}(\Omega, \nu) = \frac{h\nu}{4\pi} N_i A_{ij} \varphi_{ij}(\Omega, \nu) \tag{3.10}$$

$$\chi_{ij}(\Omega, \nu) = \frac{h\nu}{4\pi} \left(N_j B_{ji} - N_i B_{ij} \right) \varphi_{ij}(\Omega, \nu) \tag{3.11}$$

with N_i the number of molecules per unit volume in level i (N_j in level j). In LTE the ratio of N_i and N_j is fixed by the Boltzmann distribution (see Eq. 3.12). ϕ_{ij} is the line profile function described in Eq. 3.13 where a_{tot} is the line width in cm.s^{-1} and ν_{ij} is the line center frequency. The line width a_{tot} is the sum of the thermal and micro-turbulent line widths and can be written as in Eq. 2.9. A_{ij}, B_{ij} and B_{ji} are the Einstein coefficients described in Eq. 3.14 where g_i is the degeneracy of level i, also called statistical weight.

A_{ij} (s^{-1}) the Einstein coefficient for spontaneous emission which gives the probability per unit time for an electron to spontaneously decay from level i to level j. B_{ij} (J^{-1}.m^3.s^{-2}) is the Einstein coefficient for stimulated emission, process where an electron decays from level i to level j induced by a photon whose energy is equal to the level transition energy. B_{ji} (J$^{?1}$.m^3.s$^{?2}$) is the Einstein coefficient for photon absorption where an electron jumps from level j to level i.

$$\frac{N_i}{N_j} = \frac{g_i}{g_j} \exp\left(-\frac{h\nu_{ij}}{k_B T}\right) \tag{3.12}$$

$$\varphi_{ij}(\Omega, \nu) = \frac{c}{a_{tot}\nu_{ij}\sqrt{\pi}} \exp\left(-\frac{c^2(\nu - \nu_{ij})^2}{a_{tot}^2\nu_{ij}^2}\right) \tag{3.13}$$

$$A_{ij} = \frac{2h\nu_{ij}^3}{c^2} B_{ij} \; ; \quad B_{ij}g_i = B_{ji}g_j \tag{3.14}$$

3.2.2   Post-processing

After line emission computation ray-tracing is performed in order to obtain a raw image. It generates a 2D projection of the 3D grid for each frequency channel required by tracing the path of light through each pixel. The image is first produced without the star(s) but with emission from the dust, lines induced by the star. Then, a ray-tracing is done from the star to an imaginary observer with only extinction accounted for and the flux is added to the previous image.

Finally, *Pandora* offers the possibility to convolve the raw synthetic spectra to the beam of observations one wants to compare with. *Miriad* is used to perform the convolution using a fast Fourier transform (FFT)-based algorithm. The algorithm computes the discrete Fourier transform (DFT) $\mathfrak{F}$ of the image and uses the convolution theorem stating that $\mathfrak{F}(f * g) = \mathfrak{F}(f) \times \mathfrak{F}(g)$. In our case, the function f is the image and the function g is a 2D circular symmetric Gaussian G.

$$G = \frac{1}{2\pi\sigma^2} \exp\left(-\frac{x^2 + y^2}{2\sigma^2}\right)$$

To perform the convolution, *Miriad* requires the full-width at half maximum f of the Gaussian to be convolved with the image and a scale factor s which ensures the flux is conserved in the process. Both parameters are defined as follows:

$$
\begin{aligned}
f(rad) &= 1.22 \, \frac{\lambda}{D} \\
f('') &= 1.22 \, \frac{180}{\pi} \, 3600 \, \frac{c(m.s^{-1})}{\nu(Hz)} \, \frac{1}{D(m)}
\end{aligned}
$$

$$s = \left(\frac{\pi}{4\ln 2}\left(\frac{f}{p}\right)^2\right)^{-1}$$

D is the telescope size, c the light speed, ν the central frequency of the line and p is the pixel size in arcsecond. It is also possible if one has interferometric data to perform a uv-filtering and imaging in *Pandora* using *Miriad*.
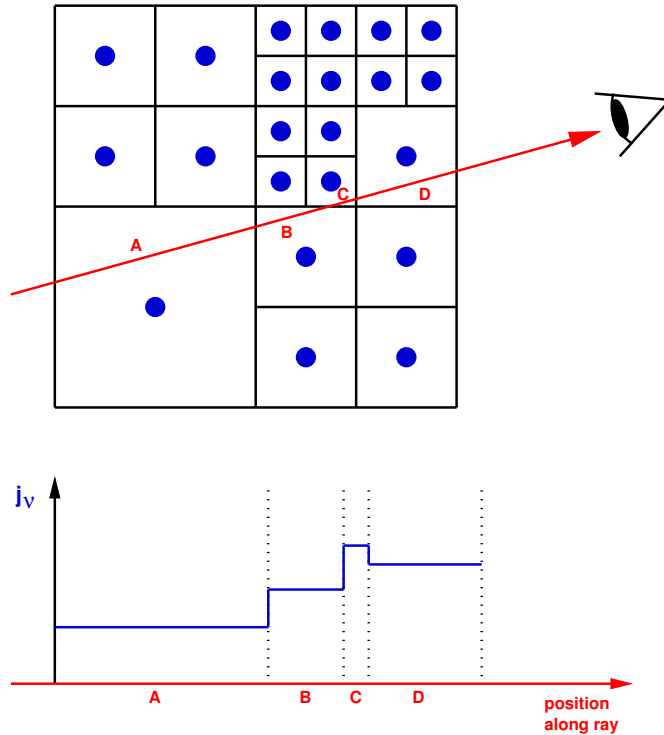
Figure 3.7: Pictographic representation of the integration of the transfer equation along a ray (red arrow) through an AMR grid (black lines) when using first order integration. The grid cuts the ray into ray segments A, B, C and D. At the bottom it is shown how the integrands are assumed to be along these four segments. The emissivity function and extinction function are constant within each cell and thus constant along each ray segment. Credit: *RADMC-3D* manual version 0.39 by Cornelis Dullemond.

In conclusion, *Pandora* is a modeling framework developed to couple *RADMC-3D* to *LIME*, another radiative transfer code, and to produce synthetic spectra and maps in one single step from a model structure defined by the user. For this work, we have used *Pandora* and improved it by coupling *RADMC-3D* to *Saptarsy*.

<div style="text-align: right; font-size: 3em;">4</div>

Semi-analytical model

Contents

The main goal of this work is to study the PDR and how it impacts its surroundings. The investigation of the PDR and its effect on the chemistry is going to be examined in the next chapters. However, it seems also important to understand its main physical characteristics, i.e. the dissociation front. Our model as detailed in Chap. 3 uses the

spatio-temporal evolution of the temperature and radiation field, and the network involves more than a hundred of species, which makes this model hard to analyze because of the huge number of variables. Therefore, we chose to develop a semi-analytical code which aims at deriving the time evolution of H_2 only in a 1D cloud[1]. Physical processes are restricted to formation on grains and photodissociation alone. The UV source is on one side only and the UV radiation is constant. We compare two formulations of the formation rate:

1. Standard constant rate:
$$k_f = R_f \, n_H \, n(H)$$
   with a constant value for R_f, typically $3{\times}10^{-17}$ $cm^{-3}.s^{-1}$.

2. Through computation of H adsorbed on grains:
$$H + Grain \rightarrow H_{ad}$$
$$H + H_{ad} \rightarrow H_2$$
   Relevant rates are taken from Le Bourlot et al. (2012) for the Eley-Rideal mechanism.
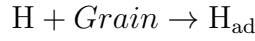
Computation of H_2 column density and dissociation probability are are done using results from all slabs from the illuminated edge to the current point. This imposes the structure of the code (See Sec. 4.5).

   In order to maintain a small fraction of atomic hydrogen throughout the cloud, we include cosmic rays destruction of H_2 only with a constant rate $k_c = 10^{-16}$ s^{-1}:
$$H_2 + C.R. \rightarrow H + H$$
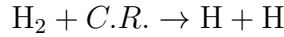
4.1   Equations Case 1

In Case 1, we have two variables, H and H_2, whose evolution is given by:
$$\frac{dn(H_2)}{dt} = R_f \, n_H \, n(H) - (k_d + k_c) \, n(H_2)$$
$$n(H) + 2 \, n(H_2) = n_H$$

Or:
$$\frac{dn(H_2)}{dt} = R_f \, (n_H - 2 \, n(H_2)) - (k_d + k_c) \, n(H_2)$$

   The tricky part comes from the dissociation rate. It reads[2]:
$$k_d = k_d^0 \, I_{UV} \, \exp\left(-\sigma_g \, N_H\right) \, f(N_2)$$

where (from Sternberg et al. 2014):

---

[1]The present derivation corresponds to a plane parallel cloud.

[2]The dilution factor coming from spherical geometry is not accounted for here. It could be added later.

- $k_d^0 = 5.8 \times 10^{-11}\,\mathrm{s}^{-1}$ is the photodissociation rate in free space.

- I_{UV} is the radiation field strength in Draine's field units.

- $\sigma_g = 1.9 \times 10^{-21}\,\mathrm{cm}^2\,\mathrm{H}^{-1}$ is the typical dust extinction coefficient in the far UV.

- N_{H} is the total column density from the edge of the cloud to the current point.

- N_2 is the column density of H_2 from the edge of the cloud to the current point. It is given by:

$$N_2(s_0') = \int_0^{s_0'} n(\mathrm{H}_2)\,ds'$$

  where the distance from the illuminated edge is s' in cm.

The function $f(N_2)$ is taken from Draine & Bertoldi (1996):

$$f(X) = \frac{0.965}{\left(1 + \frac{X}{b_5}\right)^2} + \frac{0.035}{(1+X)^{0.5}}\exp\left(-8.5 \times 10^{-4}\,(1+X)^{0.5}\right) \tag{4.1}$$

where:

- $b_5 = \dfrac{b}{10^5\,\mathrm{cm\,s}^{-1}}$ is a typical line broadening ($b_5 = 2$ in the following).

- $X = \dfrac{N_2}{N_0}$, with $N_0 = 5 \times 10^{14}\,\mathrm{cm}^{-2}$

In this version, we consider a constant density n_{H} and a constant illumination I_{UV}. A time dependent law could be added later.

4.2 Scaling

4.2.1 Length

Using a constant density model, we see that a natural length scale is:

$$\lambda = \frac{N_0}{n_{\mathrm{H}}} \Rightarrow s = \frac{s'}{\lambda}$$

From it, we get:

$$\frac{N_2(s_0')}{N_0} = \int_0^{s_0'/\lambda} \frac{n(\mathrm{H}_2)}{n_{\mathrm{H}}}\,d\left(\frac{s'}{\lambda}\right)$$

From now on, let us write $x = \dfrac{n(\mathrm{H}_2)}{n_{\mathrm{H}}}$ and $X = \dfrac{N_2}{N_0}$. Then:

$$X(s_0) = \int_0^{s_0} x\,ds$$

At position s, the evolution of $x(s)$ is given by:

$$\frac{dx}{dt} = R_f \, n_\mathrm{H} \, (1 - 2\,x) - k_d \, x$$

The total column density is:

$$N_\mathrm{H} = \int_0^{s_0'} n_\mathrm{H} \, ds' = N_0 \, s_0$$

We have also:

$$N_\mathrm{H} = N_0 \, (s_0 - 2\,X) + 2\,N_0 \, X$$

We transform from distance to a magnitude scale by using:

$$C_D = \frac{N_\mathrm{H}}{E_{B-V}} \; ; \quad R_v = \frac{A_\mathrm{V}}{E_{B-V}}$$

Their typical values in the Galaxy are $R_v = 3.1$ and $C_D = 5.8 \times 10^{21}\ \mathrm{cm}^{-2}$. So:

$$A_\mathrm{V} = \frac{R_v}{C_D} \, n_\mathrm{H} \, s_0' \tag{4.2}$$

4.2.2   Time

One needs a common time scale over the whole cloud. A "natural" one is given by:

$$\tau = \frac{1}{R_f \, n_\mathrm{H}} \tag{4.3}$$

Multiplying x evolution equation by τ, we get:

$$\frac{dx}{dt'} = (1 - 2\,x) - k_d' \, x$$

The destruction coefficient reads:

$$k_d' = \alpha \, \exp\left(-\sigma_g \, N_0 \, s\right) \, f(X) + k_c' \tag{4.4}$$

with:

$$\alpha = \frac{k_d^0 \, I_{UV}}{R_f \, n_\mathrm{H}} \; ; \quad k_c' = \frac{k_c}{R_f \, n_\mathrm{H}}$$

The final equation is thus (dropping the prime on t):

$$\frac{dx}{dt} = (1 - 2x) + k_d' \, x \tag{4.5}$$

Steady state corresponds to:

$$x = \frac{1}{2 + k_d'}$$

or, if there is no external radiation:

$$x = \frac{1}{2 + k_c'} \tag{4.6}$$

4.2.3 Logarithmic variables and Jacobian

To avoid going into negative values, we may use logarithmic variables:

$$y = \log(x) \; ; \quad x = \exp(y)$$

$$\frac{dy}{dt} = \frac{d}{dt} \log(x) = \frac{1}{x} \frac{dx}{dt}$$

The resulting equations is thus:

$$F(y) = \frac{dy}{dt} = \exp(-y) - (2 + k'_d)$$

The Jacobian matrix is:

$$\frac{\partial F}{\partial y} = -\exp(-y)$$

4.3 Equations Case 2

4.3.1 Grain properties

To get a model as simple as possible, we use a constant grain radius a, and a constant density ρ. The mass of grains per unit volume is:

$$M_d = \frac{4}{3} \pi a^3 \rho n_d$$

where n_d is the number of dust grains per unit volume,. It is also available through the dust to gas mass ratio G_d:

$$G_d = \frac{M_d}{1.4 m_H n_H}$$

The surface a dust available per unit volume S_d is:

$$S_d = 4 \pi a^2 n_d \tag{4.7}$$

and the total number of sites n_s is:

$$n_s = \frac{4 \pi a^2}{d^2} n_d \tag{4.8}$$

where d is the mean distance between sites. Bringing all expressions together, we have:

$$\frac{n_d}{n_H} = \frac{3 G_d 1.4 m_H}{4 \pi a^3 \rho} \; ; \quad \frac{S_d}{n_H} = \frac{3 G_d 1.4 m_H}{a \rho} \; ; \quad \frac{n_s}{n_H} = \frac{3 G_d 1.4 m_H}{a \rho d^2}$$

We assume the following numerical values: the grain radius $a = 10^{-5}$ cm, the grain density (graphite value) $\rho = 2.24$ g cm^{-3}, the dust to gas mass ratio $G_d = 10^{-2}$ and the mean distance between sites $d = 2.6 \times 10^{-8}$ cm.

4.3.2   Evolution equations

The evolution of H_2 is given by:

$$\frac{dn(H_2)}{dt} = v_{\text{th}}\, S_d\, n(H)\, \frac{n(H_{\text{ad}})}{n_s} - (k_d + k_c)\, n(H_2)$$

where k_c is the cosmic rate dissociation rate, $\dfrac{n(H_{\text{ad}})}{n_s}$ is the fraction of grain occupied by H chemisorbed, and v_{th} is the thermal velocity of H atoms defined in Eq. 2.10. The evolution equation for H_{ad} is:

$$\frac{dn(H_{\text{ad}})}{dt} = v_{\text{th}}\, S_d\, s(T)\, n(H)\, \frac{(n_s - n(H_{\text{ad}}))}{n_s} - v_{\text{th}}\, S_d\, n(H)\, \frac{n(H_{\text{ad}})}{n_s}$$

where $s(T)$ is the sticking coefficient of H on grains, and is a function of the gas temperature only:

$$s(T) = \frac{1}{1 + \left(\frac{T}{T_2}\right)^{\beta}}$$

with $\beta = \frac{3}{2}$ and $T_2 = 464\,\text{K}$ from Le Bourlot et al. (2012).

From Eq. 4.7 and 4.8, we have:

$$\frac{S_d}{n_s} = d^2$$

And conservation reads:

$$n_H = n(H) + n(H_{\text{ad}}) + 2\, n(H_2)\; ; \quad n(H) = n_H - n(H_{\text{ad}}) - 2\, n(H_2)$$

so we can rearrange the evolution equations:

$$\frac{dn(H_{\text{ad}})}{dt} = v_{\text{th}}\, d^2\, (n_H - 2\, n(H_2) - n(H_{\text{ad}}))\, (s(T)\, n_s - s(T)\, n(H_{\text{ad}}) - n(H_{\text{ad}}))$$

$$\frac{dn(H_2)}{dt} = v_{\text{th}}\, d^2\, (n_H - 2\, n(H_2) - n(H_{\text{ad}}))\, n(H_{\text{ad}}) - (k_d + k_c)\, n(H_2)$$

4.3.3   Scaling

To simplify comparisons with Case 1, we use Eq. 4.3 and the same scaling as in Sec. 4.2 for H_2. H_{ad} is usually orders of magnitude smaller, and we scale it relative to n_s. We also drop the T dependance of $s(T)$ below. So, we write:

$$x_1 = \frac{n(H_{\text{ad}})}{n_s}\; ; \quad x_2 = \frac{n(H_2)}{n_H}$$

We have:

$$\frac{dx_1}{dt'} = k_f \left(1 - 2\, x_2 - x_1\, \frac{n_s}{n_H}\right) (s - (1 + s)\, x_1)$$

$$\frac{dx_2}{dt'} = k_f \frac{n_s}{n_{\mathrm{H}}} \left(1 - 2\,x_2 - x_1 \frac{n_s}{n_{\mathrm{H}}}\right) x_1 - k'_d\,x_2 \tag{4.9}$$

where we define:

$$k_f = \frac{v_{\mathrm{th}}\,d^2}{R_f}$$

We have again:

$$k'_d = \frac{k_d + k_c}{R_f\,n_{\mathrm{H}}}$$

In the following, we will drop the prime on t' and we use also logarithmic variables:

$$y_i = \log\left(x_i\right); \quad x_i = \exp\left(y_i\right)$$

$$\frac{dy_i}{dt} = \frac{d}{dt}\log\left(x_i\right) = \frac{1}{x_i}\frac{dx_i}{dt}$$

where the indice i has to be replaced by 1 or 2, for H_2 or H_{ad} evolution equations respectively. It leads to:

$$F_1(y_1, y_2) = \frac{dy_1}{dt} = k_f \left(1 - 2\,\exp\left(y_2\right) - \exp\left(y_1\right) \frac{n_s}{n_{\mathrm{H}}}\right) \left(s\,\exp\left(-y_1\right) - (1+s)\right) \tag{4.10}$$

$$F_2(y_1, y_2) = \frac{dy_2}{dt} = k_f \frac{n_s}{n_{\mathrm{H}}} \left(1 - 2\,\exp\left(y_2\right) - \exp\left(y_1\right) \frac{n_s}{n_{\mathrm{H}}}\right) \exp\left(y_1\right) \exp\left(-y_2\right) - k'_d$$

The Jacobian is:

$$\frac{\partial F_1}{\partial y_1} = -k_f \left(s\,(1 - 2\,\exp\left(y_2\right))\,\exp\left(-y_1\right) - (1+s)\,\exp\left(y_1\right) \frac{n_s}{n_{\mathrm{H}}}\right)$$

$$\frac{\partial F_1}{\partial y_2} = -2\,k_f\,\exp\left(y_2\right)\,\left(s\,\exp\left(-y_1\right) - (1+s)\right)$$

$$\frac{\partial F_2}{\partial y_1} = -k_f \frac{n_s}{n_{\mathrm{H}}}\,\exp\left(y_1\right)\,\left(2 - \left(1 - 2\,\exp\left(y_1\right) \frac{n_s}{n_{\mathrm{H}}}\right)\,\exp\left(-y_2\right)\right)$$

$$\frac{\partial F_2}{\partial y_2} = -k_f \frac{n_s}{n_{\mathrm{H}}}\,\exp\left(y_1\right)\,\left(1 - \exp\left(y_1\right) \frac{n_s}{n_{\mathrm{H}}}\right)\,\exp\left(-y_2\right)$$

Initial conditions are molecular, i.e. steady state without radiation but with a remnant of cosmic rays. From Eq. 4.10, we get:

$$k_f \left(1 - 2\,x_2 - x_1 \frac{n_s}{n_{\mathrm{H}}}\right) (s - (1+s)\,x_1) = 0 \quad \Rightarrow \quad x_1 = \frac{s}{1+s}$$

It is remarkable that, once established, this steady states remains. So, for a constant sticking coefficient, the number of equations is reduced to 1. Nevertheless, we solve both equations to allow for tests with different initial conditions.

For H_2, we have:

$$x_2 = \frac{1}{\left(2 + \frac{k'_d}{k_f}\frac{(1+s)\,n_{\mathrm{H}}}{s\,n_s}\right)}\left(1 - \frac{s\,n_s}{(1+s)\,n_{\mathrm{H}}}\right) \tag{4.11}$$

If photo-destruction is negligible, we recover $x_2 = \frac{1}{2}$.

Using the steady state, we have for adsorbed H abundance:

$$\frac{dx_2}{dt} = k_f \frac{s}{1+s} \frac{n_s}{n_H} \left(1 - \frac{s}{1+s} \frac{n_s}{n_H} - 2\,x_2\right) - k'_d\,x_2$$

We may compare that equation to Eq. 4.5 of the previous case. Neglecting the factor $\frac{s}{1+s} \frac{n_s}{n_H}$ compared to 1, we see that we recover the same evolution if:

$$\frac{v_{\text{th}}\,d^2}{R_f} \frac{s}{1+s} \frac{n_s}{n_H} = 1$$

Using $T = 10^3\,\text{K}$, which gives $v_{\text{th}} \simeq 4.6 \times 10^5\,\text{cm s}^{-1}$ and $s = 0.24$, $d = 2.6 \times 10^{-8}\,\text{cm}$, $R_f = 3 \times 10^{-17}\,\text{cm}^3\,\text{s}^{-1}$ and $\dfrac{n_s}{n_H} = 4.6 \times 10^{-6}$, we have:

$$\frac{v_{\text{th}}\,d^2}{R_f} \frac{s}{1+s} \frac{n_s}{n_H} = 9.2$$

So the evolution should be somewhat more rapid.

4.4   Sums

To compute the UV photodissociation rate, we need to compute the following sum:

$$X(s_0) = \int_0^{s_0} x\,ds$$

It is computed using a standard integration scheme. We begin with a trapezoidal rule, which may easily be changed for a more complex scheme if needed. The point is that:

$$X(s_0) = X(s_0 - \delta) + \int_{s_0-\delta}^{s_0} x\,ds$$

$$X(s_0) = X(s_0 - \delta) + \frac{\delta}{2} \left(x(s_0 - \delta) + x(s_0)\right)$$

Hence, this is a function of $x(s_0)$ only, if computation proceeds from 0 to s_0 for each time step, and the state of the system is known up to $(s_0 - \delta)$.

4.5   Integration

4.5.1   Discretization

Thanks to the very specific dependence in space of the problem if radiation comes from one direction only, it can be solved using only a ODE integrator, without the need of an PDE solver. Let us assume a space and time discretization, s_i with $i \in [0, N]$, so $\delta_i = s_i - s_{i-1}$, t_j with $j \in [0, M]$, so $h_j = t_j - t_{j-1}$, then we set $x_{i,j} = x(s_i, t_j)$, $X_{i,j} = X(s_i, t_j)$ and $k_{i,j} = k'_d(s_i, t_j)$.

4.5.2   Algorithm

Integration goes thus:

1. Start from $x_{i,0}$ taken from Eq 4.6 or 4.11. I.e., the cloud is initially fully molecular, with no UV photons, but accounting for cosmic rays. Set $X_{0,j} = 0$ and $k_{0,j} = \alpha = \dfrac{k_d^0 \, I_{UV}}{R_f \, n_{\mathrm{H}}} + \dfrac{k_c}{R_f \, n_{\mathrm{H}}}$ for all time steps j.

2. Loop over space index i

   (a) Loop over time index j

      i. The system to solve is given by Eq 4.5 or 4.9, where k_d' is computed using the known values of x up to $i - 1$ for all j.

      ii. Use a predictor $\tilde{X}_{i,j} = X_{i-1,j} + \dfrac{\delta_i}{2} \, (x_{i-1,j} + x_{i,j-1})$.

      iii. Compute $k_d'\left(\tilde{X}_{i,j}\right)$.

      iv. Solve the ODE for one step h_j to get $x_{i,j}$.

      v. Find a better value $X_{i,j} = X_{i-1,j} + \dfrac{\delta_i}{2} \, (x_{i-1,j} + x_{i,j})$.

      vi. If needed, an iteration may be done until some convergence criterium is met.

The hard part is in the choice of $\{\delta_i\}$ and $\{h_j\}$. The differential equations are solved using the VODE package.

4.5.3   Time step

Using a logarithmic scale, we have, for a total integration time T reached in N steps:

$$\tau_{i+1} = a \, \tau_i$$

$$\tau_1 = t_1 \ \text{ and } \ \tau_N = T \ \Rightarrow \ a = \left(\frac{T}{t_1}\right)^{\frac{1}{N-1}}$$

t_1 is chosen to get a sensible first step. At the edge, $k_d' = \alpha$ (see Eq. 4.4), so Eq. 4.5 in Case 1 gives:

$$x(t) = \frac{2 + \alpha \, \exp\left(-\left(2 + \alpha\right) t\right)}{2 \, (2 + \alpha)}$$

We verify that setting $t = 0$ gives $x = \dfrac{1}{2}$. The evolution goes at a characteristic time scale of $\dfrac{1}{2 + \alpha}$. Hence, we may chose:

$$t_1 = \frac{10^{-2}}{2 + \alpha}$$

The same scaling is kept for Case 2.
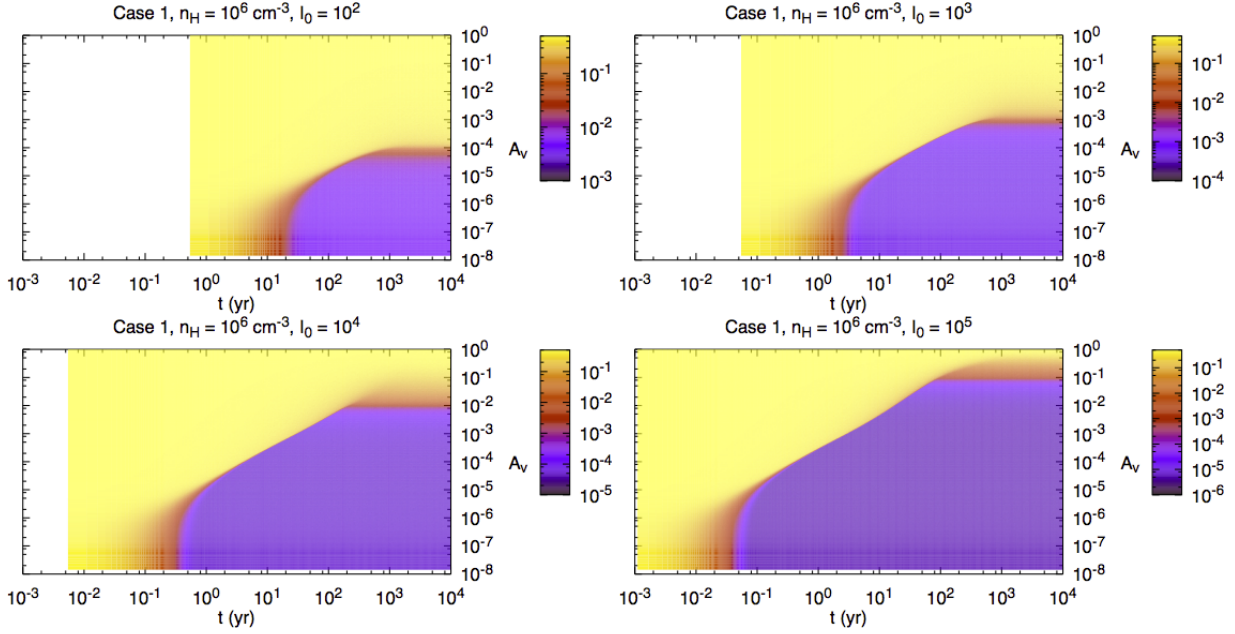
Figure 4.1: Case 1: Spatio-temporal evolution of H_2 (defined in Eq 4.5) with $n_H = 10^6$ cm^{-3}. The time evolution is in x-axis and the extinction in y-axis. From left to right, top to bottom, we have radiation field of $I_0 = 10^2$, $I_0 = 10^3$, $I_0 = 10^4$ and $I_0 = 10^5$.

4.6   Results

4.6.1   2D plots

Fig. 4.1 and 4.2 show the spatio-temporal evolution (time in x-axis and extinction in y-axis) of H_2 and chemisorbed H, respectively, for a cloud at $n_H = 10^6$ cm^{-3} and with a radiation field of $I_0 = 10^2$ (upper left panel), $I_0 = 10^3$ (upper right), $I_0 = 10^4$ (bottom left) and $I_0 = 10^5$ (bottom right). The colorbar represents the relative abundance of H_2, from purple for low abundances to yellow for high abundances. This calculation does not depend on the temperature.

Looking along the t axis, one sees that, for small distances into the cloud, there is a characteristic time scale for the dissociation of H_2. This can be read for very small A_V. As A_V increases, the dissociation front progresses deeper and deeper into the cloud. Then, we reach a stage where all UV photons have been absorbed, and the gas stays completely molecular. That distance is a function of the radiation field intensity.

4.6.2   Transition values

Dissociation time at the edge

Dissociation is best seen on Fig. 4.3 where we show the time evolution of H_2 (in purple) at the edge of the cloud, $A_V = 0$, and determine the time scale for Case 1 with $I_0 = 10^3$. We find $\tau = 0.565$ year when we fit the beginning of the evolution (green line). The time
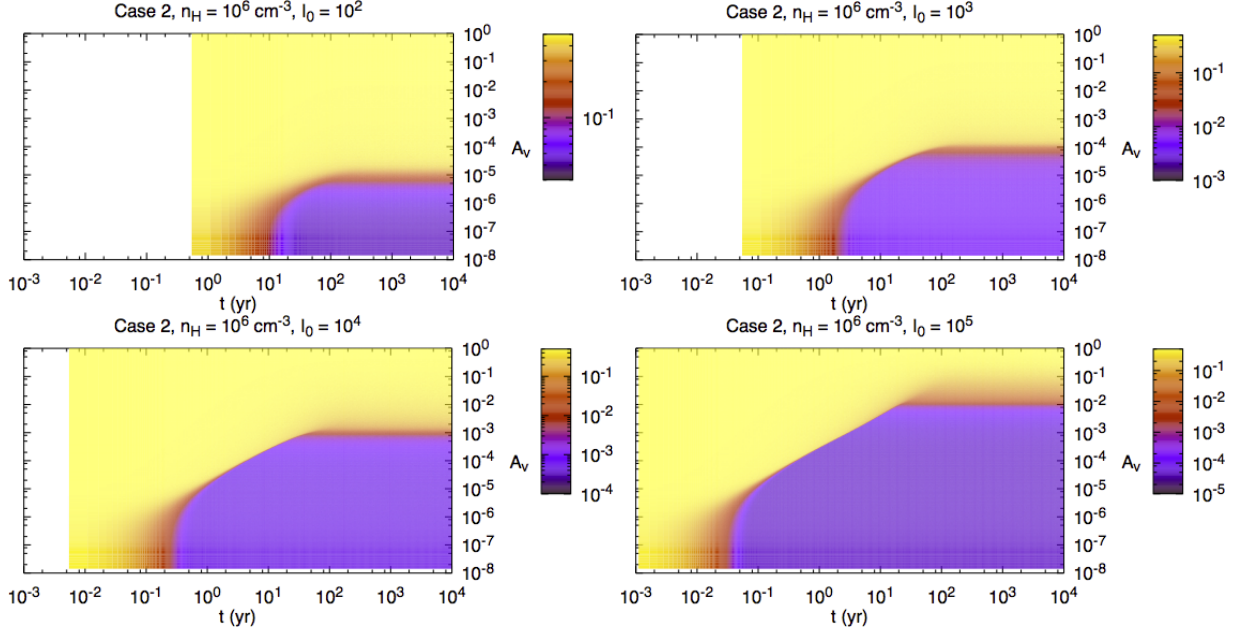
Figure 4.2: Case 2: Spatio-temporal evolution of chemisorbed H (defined in Eq 4.9) with $n_H = 10^6$ cm^{-3}. The time evolution is in x-axis and the extinction in y-axis. From left to right, top to bottom, we have radiation field of $I_0 = 10^2$, $I_0 = 10^3$, $I_0 = 10^4$ and $I_0 = 10^5$.

scale computed at Sec. 4.5.3 is $\dfrac{1}{2+\alpha}$. Back in "real" time, this gives a perfect match:

$$\frac{\tau}{2+\alpha} = \frac{1}{2\,R_f\,n_H + k_d^0\,I_{UV}} = 0.546 \text{ year}$$

Size of atomic region

The size of the atomic region x_s obtained from the situation in steady state is:

$$x(s) = \frac{1}{2 + k_d'(s)}$$

where s is the natural length scale and $k_d'(s)$ is the destruction coefficient (see Eq. 4.4).

At $s = 0$, $k_d' \simeq \alpha$, which is usually large. For large values of s, k_d' goes to 0. Neglecting cosmic rays, we see that x varies from $\dfrac{1}{2+\alpha}$ to $\dfrac{1}{2}$. We may define the transition by the point s_c where the column density is, say, $2\,N_0$ (or $X = 2$), and we compute it using a constant value of x, taken at the edge:

$$s_c = 2\,(2 + \alpha)$$

So, neglecting 2 compared to α in the above equation, we obtain for the extinction $A_{V,c}$ at the transition:

$$A_{V,c} = \frac{2\,R_v}{C_D}\,N_0\,\frac{k_d^0}{R_f\,n_H}\,I_{UV} \simeq 10^{-6}\,I_0 \qquad (4.12)$$
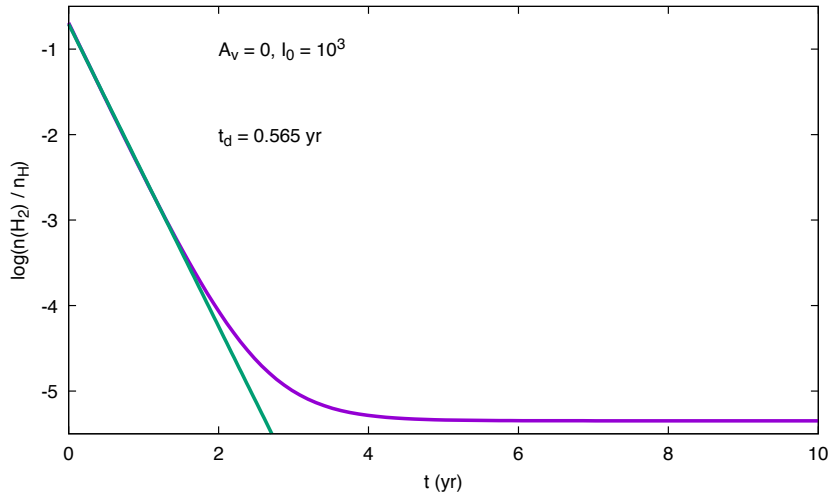
Figure 4.3: Logarithmic relative H_2 abundance at the edge of the cloud as a function of time (purple). The green line corresponds to the fit of the of the beginning of the evolution of the H_2 abundance.
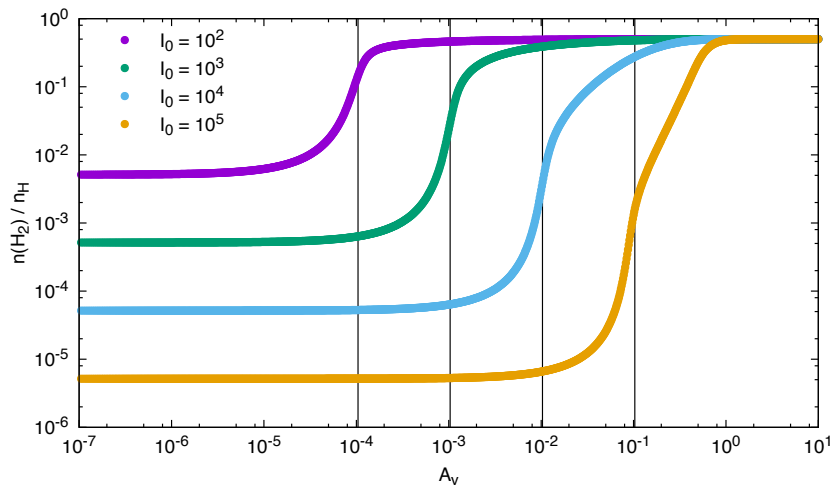
Figure 4.4: Relative abundance of H_2 for Case 1 as a function of extinction showing the H/H_2 transition as a function of the radiation field: $I_0 = 10^2$ (purple), $I_0 = 10^3$ (green), $I_0 = 10^4$ (blue) and $I_0 = 10^5$ (orange). Vertical bars are the values of $A_{V,c}$ from Eq 4.12.
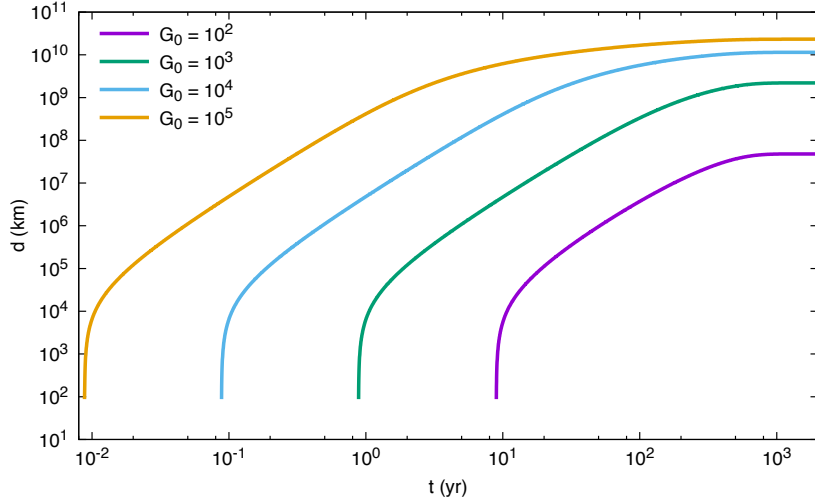
Figure 4.5: Time evolution of the dissociation front position, defined for $x = 0.1$, as a function of the radiation field: $I_0 = 10^2$ (purple), $I_0 = 10^3$ (green), $I_0 = 10^4$ (blue) and $I_0 = 10^5$ (orange).

In Fig. 4.4 we show the evolution of H_2 abundance as a function of extinction, at steady-state, with a radiation field varying from $I_0 = 10^2$ to $I_0 = 10^5$. Here again, the agreement with the figure is excellent.

Eq. 4.12 is used later in this work (Chap. 6.8) to study the dissociation front in the models using *Saptarsy* and *RADMC-3D* and including the spatio-temporal evolution of the temperature and radiation field intensity.

Dissociation front

We define, rather arbitrarily, the position of the dissociation front by the point where $x = \dfrac{n(H_2)}{n_H} = 0.1$. Fig. 4.5 shows the evolution of this front as a function of the radiation field intensity for Case 1. After the initial sharp rising of the front position, we find that the value $x = 0.1$ has a position varying as:

$$A_V(t) = b\,t^a$$

during the progression phase of the dissociation front.

Fig. 4.6 shows the time evolution of the dissociation front position (in purple) for Case 2 and $I_0 = 10^5$ and the fit (in green) made on the period going from 10^{-1} to 5×10^1 years approximately. We see that the exponent is $a = 1.2$ (and $b = 2.9 \times 10^{-4}$), which is significantly different from a constant velocity front:

$$\frac{dA_V}{dt} = a\,b\,t^{a-1}$$

This result is not particularly obvious physically, and deserves further exploration. To get back to more standard units, with s in cm and t in s, and using Eq. 4.2, we have:

$$s'_0(t) = \frac{C_D}{R_v\,n_H}\,b\left(\frac{t}{yr}\right)^a = 5.45 \times 10^2 \left(\frac{10^6\,\mathrm{cm}^{-3}}{n_H}\right)t^{1.2}$$

$$\frac{ds'}{dt} = 6.54 \times 10^2 \left(\frac{10^6\,\mathrm{cm}^{-3}}{n_H}\right)\left(\frac{t}{1\,yr}\right)^{0.2}(1\,yr)^{0.2}$$
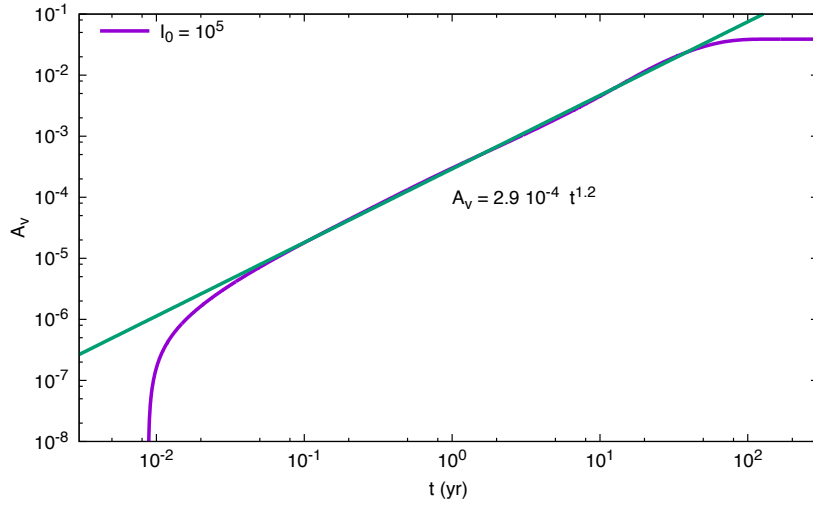
Figure 4.6: Time evolution of the dissociation front position (purple) for Case 2, when $I_0 = 10^5$. The green line represents the fit of the purple curve between 10^{-1} and 5×10^1 years approximately.
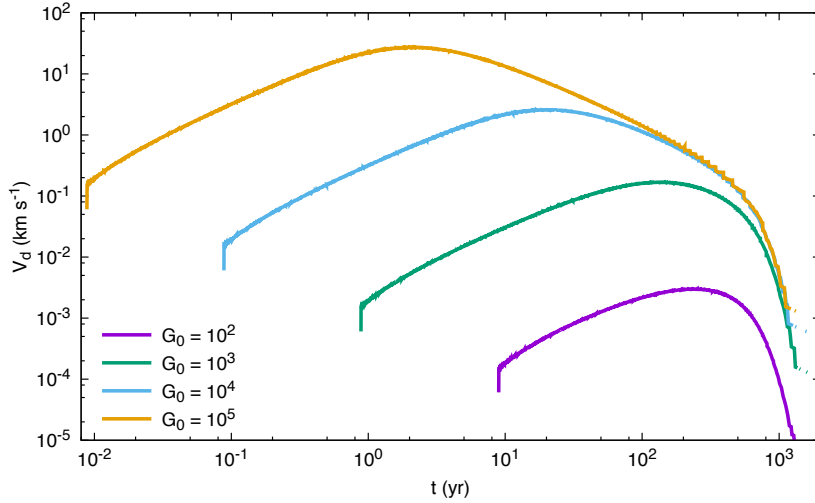
Figure 4.7: Time evolution of the dissociation front velocity ($x = 0.1$) as a function of radiation field: $I_0 = 10^2$ (purple), $I_0 = 10^3$ (green), $I_0 = 10^4$ (blue) and $I_0 = 10^5$ (orange).

So, the front velocity is:

$$\frac{ds}{dt} = 0.2 \left(\frac{10^6 \, \text{cm}^{-3}}{n_\text{H}} \right) \left(\frac{t}{1 \, \text{yr}} \right)^{0.2} \text{km} \, \text{s}^{-1}$$

In Fig. 4.7, we show a better evaluation of the front velocity, obtained from a numerical derivative of the curves shown on Fig. 4.5. We see that there is a first phase where the front progresses with a fast rising velocity (rather like an explosion). This corresponds to the fact that at a given position in space the radiation field intensity is an increasing function of time. Then, once the maximum is reached, the front velocity decreases until it stops. This is a consequence of the decreasing amount of radiative energy with position as the front progresses. Note that the first phase is a direct consequence of the choice of initial conditions (fully molecular).

Analytical expression

We may try to look how the point where $x = 0.1$ moves with time. Let us write it $z(t)$. So we have:

$$x\left(z(t)\right) = 0.1$$

A instant Δt later, that point is at $z + \Delta z$. With:

$$x(z + \Delta z, t + \Delta t) = x(z, t) + \left.\frac{\partial x}{\partial s}\right|_{z,t} \Delta z + \left.\frac{\partial x}{\partial t}\right|_{z,t} \Delta t$$

By hypothesis we must have:

$$\left.\frac{\partial x}{\partial s}\right|_{z,t} \Delta z + \left.\frac{\partial x}{\partial t}\right|_{z,t} \Delta t = 0 = \frac{\partial x}{\partial s} \Delta z + \left(1 - (2 + k_d') \, x\right) \Delta t$$

So, the required velocity of the front is:

$$V(z) = \frac{\Delta z}{\Delta t} = \left((2 + k_d') \, x - 1\right) \left(\frac{\partial x}{\partial s}\right)^{-1} \tag{4.13}$$

with $x = 0.1$, but where we still do not know the value of the gradient $\dfrac{\partial x}{\partial s}$.

It is not possible to derive directly an expression for $\dfrac{\partial x}{\partial s}$. But we have:

$$\frac{\partial}{\partial s}\left(\frac{\partial x}{\partial t}\right) = -\frac{\partial k_d'}{\partial s} \, x - (2 + k_d') \, \frac{\partial x}{\partial s}$$

With the approximate relation Eq. 4.4, assuming there is no CR dissociation,:

$$k_d' = \alpha \, f(X) \quad \Rightarrow \quad \frac{\partial k_d'}{\partial s} = \alpha \, x \, \frac{\partial f(X)}{\partial X}$$

So:

$$\frac{\partial}{\partial t}\left(\frac{\partial x}{\partial s}\right) = -\alpha \, x^2 \, \frac{\partial f(X)}{\partial X} - (2 + \alpha \, f(X)) \, \frac{\partial x}{\partial s}$$

with:

$$\frac{\partial f(X)}{\partial X} = -2 \frac{b_1}{b_5} \left(1 + \frac{X}{b_5}\right)^{-3} - \frac{b_2}{2 \, (1 + X)} \left(\frac{1}{(1 + X)^{0.5}} + b_3\right) \exp\left(-b_3 \, (1 + X)^{0.5}\right)$$

where $b_1 = 0.965$, $b_2 = 0.035$ and $b_3 = 8.5 \times 10^{-4}$ (see Eq. 4.1).

Physically, we know that the gradient of x is positive. It starts from 0 at $t = 0$ and reaches an asymptotic value when the dissociation front becomes stationary. At that time, we have:

$$\frac{\partial}{\partial t}\left(\frac{\partial x}{\partial s}\right) = 0$$

With $\dfrac{\partial k_d'}{\partial s} < 0$ and $(2 + k_d') > 0$ we may seek a condition for the duration of the evolution by setting:

$$-\frac{\partial k_d'}{\partial s} \, x - (2 + k_d') \, \frac{\partial x}{\partial s} = 0$$

Using Eq. 4.6 we obtain:

$$\frac{\partial x}{\partial s} = -\frac{1}{(2 + k_d')^2} \, \frac{\partial k_d'}{\partial s}$$
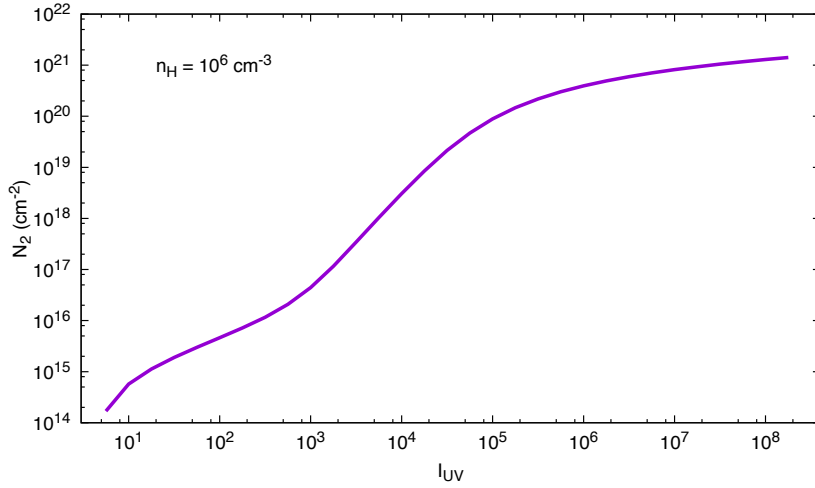
Figure 4.8: Dissociation front final position for Case 1, with $n_{\mathrm{H}} = 10^6 \mathrm{cm}^{-3}$, as a function of radiation field intensity.

Discussion

From the initial conditions, we know that:

- $\forall t$ we have $\dfrac{\partial x}{\partial s} \geqslant 0$ (that is: the abundance of H_2 increases with distance to the source at any time).

- $\forall s$ we have $\dfrac{\partial x}{\partial t} \leqslant 0$ (that is: the abundance of H_2 decreases with time at a fixed distance to the source).

Therefore, in Eq 4.13 the velocity of the front has a sign fixed by the sign of $(2 + k'_d)\, x - 1$. Since that velocity cannot become negative, we deduce that the front stops if (using $x = 0.1$):

$$(2 + k'_d)\, x - 1 = 0$$

$$k'_d = 8$$

or (neglecting cosmic rays):

$$\alpha \exp\left(-\sigma_g N_0\, s\right) f(X) = 8$$

If we write $N_{\mathrm{H}} = N_1 + 2\, N_2 = N_0\, s$, we have (with $2\,\sigma_g N_0 = \beta = 1.9 \times 10^{-6}$):

$$\alpha \exp\left(-\beta\, \frac{N_1}{2\, N_0}\right) \exp\left(-\beta\, X\right) f(X) = 8$$

Since the cloud evolves from a purely molecular state, the column density of H is always smaller than the limiting column density found from Sternberg et al. (2014). Thus, most of the time, we may neglect $\exp\left(-\beta\, \frac{N_1}{2\, N_0}\right)$. Then, the limiting column density of H_2 at the front is such that:

$$\exp\left(-\beta\, X\right) f(X) = \frac{8}{\alpha}$$

$$\exp\left(-\beta\,X\right)\left(\frac{b_1}{\left(1+\frac{X}{b_5}\right)^2}+\frac{b_2}{(1+X)^{0.5}}\,\exp\left(-b_3\,(1+X)^{0.5}\right)\right)=\frac{8}{\alpha}=\frac{8\,R_f}{k_d^0}\,\frac{n_{\rm H}}{I_{UV}}$$

$$\exp\left(-\beta\,X\right)\left(\frac{b_1}{\left(1+\frac{X}{b_5}\right)^2}+\frac{b_2}{(1+X)^{0.5}}\,\exp\left(-b_3\,(1+X)^{0.5}\right)\right)=4.14\times10^{-6}\,\frac{n_{\rm H}}{I_{UV}}$$

This expression can be solved numerically. The result is shown on Fig. 4.8. As expected, the dissociated region size increases with the radiation field. However, it is striking from Fig. 4.7 that the time required to establish steady state seems to be constant: the vertical asymptote is at a few thousand years in all cases. We did not find a satisfying analytical explanation for this fact.

PART II:

RESULTS

5

Models

Contents

We produce several models for hot molecular cores, hollow hot molecular cores and HII regions (see Sec. 3.1.2). Each of these models have a different temperature as well as density and visual extinction profiles. HII region models also have a radiation field intensity profile obtained thanks to *RADMC-3D*.

In this chapter we first describe in Sec. 5.1 the initial abundances obtained thanks to *Saptarsy* and used for the models. In Sec. 5.2 we introduce the molecules we have chosen to study in this work. In Sec. 5.3 we describe the different figures presented in the next chapter and how to read them. Then, in Sec. 6.1 we describe the density profile and the temperature profile for the hollow hot molecular core (HHMC) and the hot molecular core (HMC) model and how they compare to each other. In Sec. 6.2 we do the same for the HII region and HHMC models, including the description of the radiation field intensity profile used in the HII region models. Then, we describe those profiles for models where we changed some of the parameters, e.g., density at the ionization front, size of the ionized cavity, etc.

5.1   Computation of the initial abundances

The initial abundances for the different models are obtained using *Saptarsy* for a starless core model. We consider a cold core with a temperature of 10 K and a visual extinction of 10 mag. No temporal evolution of the temperature and the radiation field is included and no spatial (i.e., density) evolution is considered. The radiation field is assumed to be inexistent so its intensity is set to 10^{-20} Draine unit. We start the models with elemental abundances based on the abundances set named EA2 taken from Wakelam & Herbst (2008). This set is based on the high-metal abundances as observed in the diffuse cloud ζ Ophiucus. To compute the initial abundances, and for the different models, we use the diffusion to desorption ratio of 0.50 (see Sec. 2.1.1 – neutral-neutral reaction part). Two different sets of initial abundances, *ini1* of and *ini2*, were obtained:

1. *ini1*: For the first initial abundances we simulate a collapsing core and its density increase in two phases. We start with a density of 10^4 cm^{-3}. We let the chemistry evolve until 10^5 years and we use the results of this phase for the next one. In the next step we increase the density to 10^7 cm^{-3} and again we let the chemistry evolve until 10^5 years.

2. *ini2*: For this set of initial abundances we fix the density to 10^7 cm^{-3} and we let the chemistry evolve until we reach the stationary state around 10^{10} years.

The results of these two models are shown in Tab. 5.1 with the second column corresponding to the abundances *ini1* and the third column of *ini2*. For both sets the molecules are frozen on the grain surface except for hydrogen which is mainly found in molecular hydrogen in the gas phase. For S-bearing molecules the dominant species is s-H$_2$S in both models but in *ini1* the abundance is much lower as s-HS and s-CS are also very abundant.

The carbon is found mostly in s-CO in *ini1*, even if s-CH$_4$ also has high abundance, and in s-CH$_4$ in *ini2*. When we let the chemistry evolve to stationary state in both models we see that we form mostly methane but we stop the model before and reach this state for *ini1*. The formation of methane on ice is due to the following reactions chain on the grain surface: shortly after 10^5 years methanol is destroyed to form formaldehyde by CRs dissociation which is then also destroyed by the same process and produce carbon monoxide. The latter is then dissociated by CRs and the resulting atomic carbon reacts with hydrogen to form the radical s-CH. It is followed by a hydrogenation chain until we obtain methane. Before this time s-CO is the dominant C-bearing species in the medium.

In *ini2*, most of the oxygen is found in s-H$_2$O whereas it is more spread in different species in *ini1* like s-OH and s-O in addition to s-H$_2$O which is still the main O-bearing species. Before 10^5 years in *ini2* s-O and s-OH are also very abundant but after that time s-O reacts with s-H to form s-OH which is also hydrogenated to form s-H$_2$O. The hydrogenation reactions chain does not have the time to happen in model *ini1*.

As for nitrogen, for *ini1* the dominant species is s-HNO and s-N$_2$ and for the second set it is s-NH3. s-HNO abundance remains quite high until 10^9 years because it is mainly destroyed by CRs to form s-NO but immediately reformed by hydrogenation. However s-NO abundances drops after 10^5 years because of CR dissociation and later formation of s-NO by accretion also decreases leading to a second drop at 10^9 years and thus it is not able to sustain the formation of s-HNO. For the other species, the same process as

Table 5.1: Initial abundances of the principal species for the two sets. The annotation a(b) for the abundances refers to $a \times 10^b$ through the thesis.

Species	n_X/n_H: ini1	n_X/n_H: ini2
H_2	4.99(-1)	4.99(-1)
He	9.00(-2)	9.00(-2)
s-H_2	1.24(-4)	1.24(-4)
s-H_2O	9.87(-5)	2.46(-4)
s-CO	9.19(-5)	9.58(-6)
s-OH	1.91(-5)	7.24(-14)
s-HNO	2.89(-5)	3.12(-7)
s-N_2	1.33(-5)	6.14(-12)
s-O	1.16(-5)	2.74(-16)
s-HCN	6.23(-6)	4.17(-7)
s-CH_4	6.20(-6)	1.10(-4)
s-NH_3	8.03(-6)	7.53(-5)
s-H_2CO	3.20(-7)	7.12(-9)
s-CH_3OH	1.29(-7)	2.67(-17)
s-CO_2	9.83(-8)	5.91(-10)
s-H_2S	3.09(-8)	7.93(-8)
s-Si	8.00(-9)	8.00(-9)
s-Fe	3.00(-9)	3.00(-9)

for C-bearing species is happening for N-bearing species. s-N_2 is the second dominant species at 10^5 years but is dissociated by CRs to form atomic nitrogen which produces then the radical s-NH by hydrogenation. The hydrogenation chain follows until s-NH_3 is the dominant species at the stationary state.

Whether the density is 10^4 or 10^7 cm^{-3}, the same processes happen and we end up with methane and ammonia at the steady-state. For *ini1* after increasing the density to 10^7 cm^{-3}, if we let the chemistry evolve until steady-state, we also reach the same state. But stopping the process by simulating the collapse allow to have higher abundances for other species and mainly for methanol. In the first initial abundances set the elemental abundances are more spread into different species whereas in the second they are found mainly in one.

In Choudhury et al. (2015) two hot core models are produced: one starting with the canonical dark cloud temperature of 10 K and the other with a temperature of 15 K as some recent studies indicates that starless cores have a temperature of 15 K (Wienen et al. 2012; Hoq et al. 2013). It appears that more COMs are produced in a starless core at 15 K. Thus, we also tried to obtain the initial abundances for model *ini1* with a pre-stellar core at 10 and 15 K. But it seems that, in this work, we produce less COMs precursors and less COMs on ice in a medium at 15 K than at 10 K and so we expect to get less COMs in warmed up medium. Therefore, we have decided to work with the model at 10 K. In the first phase of the collapse when the density is 10^4 cm^{-3}, two times more s-CH_3OH is produced at 15 K as the main formation reactions are more efficient: (1) s-H + s-CH_2OH $\longrightarrow$ s-CH_3OH and (2) s-OH + s-CH_3 $\longrightarrow$ s-CH_3OH; reaction (2) being a bit less efficient. In the second phase of the collapse, density of 10^7 cm^{-3}, the main

Table 5.2: List of the selected species and one of their transition and its frequency in GHz.

Species	Transition	Frequency (GHz)
NH_3	$5(5,1) - 5(5,0)$	24.53
$HC^{15}N$	$1 - 0$	86.06
HCO	$1(0,1) - 0(0,0)$	86.71
$HN^{13}C$	$1 - 0$	87.09
HCO^+	$1 - 0$	89.19
N_2H^+	$1 - 0$	93.17
H_2CO	$2(0,2) - 1(0,1)$	101.33
CN	$1 - 0$	113.12
CH_3OH	$2(2,1) - 3(1,2)$	335.13
$H_2^{18}O$	$4(1,4) - 3(2,1)$	390.61
C	$^3P_1 - {}^3P_0$	492.16
C^+	$^2P_{3/2} - {}^2P_{1/2}$	1900.54
O	$^3P_1 - {}^3P_2$	4744.78

formation reaction at 15 K, reaction (1), is a bit more efficient than at 10 K but the main formation reaction at 10 K is not this one anymore but reaction (2) and it becomes more efficient than reaction (1). In this phase, s-CH_2OH is mainly destroyed by reaction (1) at 15 K while at 10 K it is formed via the reactions: s-OH + s-CH_2 $\longrightarrow$ s-CH_2OH and s-O + s-CH_3 $\longrightarrow$ s-CH_2OH.

5.2   Selected species

The chemical network considered in our models has over 150 species. We have selected a subsample of species to focus the analysis on. Similar studies can be performed for all the species in the network. The relevant species for this work are: $HC^{15}N$, $HN^{13}C$, CN, $H_2^{18}O$, HCO, HCO^+, H_2CO, CH_3OH, N_2H^+, NH_3, C, C^+ and O. A summary of the molecules, the selected transitions and the respective frequencies is presented in Tab. 5.2. The transitions are mainly chosen within the 1, 2 and 3 mm wavelength regime because we have the project to compare our models to the observations of the UCHII region Monoceros R2. For this region a survey using the IRAM 30 m telescope was done (Treviño-Morales et al. 2014, Treviño-Morales et al. in prep), hence observational data are obtained in the 1, 2 and 3 mm wavelength regime. In addition, for each of the molecules we choose one transition which is optically thin for most of the time steps. Thus, we decide to use isotopologues of HCN, HNC and H_2O as they all give optically thick lines after 10^4 years. As no isotopologue is included in the chemical network, to obtain synthetic spectra for them we use the local ISM isotopologue ratios from Wilson & Rood 1994: $^{12}C/^{13}C = 70$, $^{14}N/^{15}N = 450$ and $^{16}O/^{18}O = 500$. For CN we consider the whole hyperfine structure of the chosen transition.

Detectability of the lines: In the results presented later, we assume that all lines with an integrated intensity below 5×10^{-2} K km s^{-1} can not be detected as well as lines with a peak intensity following this criterium $I_{peak} < 15$ mK (if we consider a rms noise
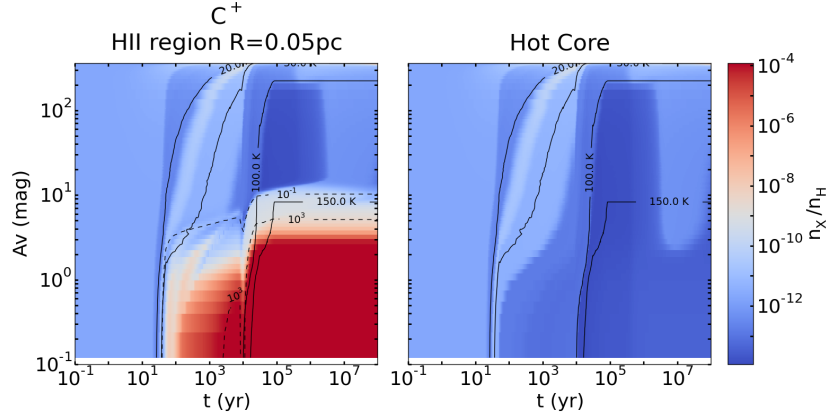
Figure 5.1: Diagnostic tool: Example of a "bacon plot" showing the spatio-temporal evolution of relative abundance, here for C^+ in a HII region and HHMC model.

of about 3 mK, which is for example the rms noise found at approximately 100 GHz in the IRAM 30 m telescope survey from Treviño-Morales et al. 2014, Treviño-Morales et al. 2016 in prep).

5.3   Diagnostic tools

In the following we present and describe all the figures that are used throughout the thesis to present and analyze the data.

Abundance profiles: All abundance profiles will be presented in figures like Fig. 5.1. The x-axis shows the temporal evolution from 10^{-1} to 10^8 years but the principal time . The y-axis shows the spatial evolution in density n_H (cm^{-3}) or in visual extinction A_V (mag). The density will be used to compare the abundances of the HMC model with the ones of the HHMC model and from 6×10^6 cm^{-3} at the bottom of the figure to 10^4 cm^{-3} at the top. For all the other comparisons we will use the visual extinction, starting at 10^{-1} mag at the bottom until the highest extinction of the compared models at the top. When we go from low extinction to high ones, we move away from the central protostar. We use visual extinction instead of the density because all the figures compare HII regions and their internal PDRs to other HII regions or to HHMC models. Because the internal PDRs are extremely thin (e.g., ~ 100 AU, corresponding to $A_V = 5$ mag when the density at the ionization front is 10^7 cm^{-3} using the standard Milky-Way values R_v = 3.1 and $N_H/E(B-V) = 5.8 \times 10^{21}$ cm^{-2}) and end when the density is still very high ($\sim$ 9.8×10^6 cm^{-3} if the density at the ionization front is 10^7 cm^{-3}) the figures are clearer if we use the visual extinction to scale the spatial evolution. The colorbar on the right side of the figure represents the variation of the relative abundances, from low abundances in blue to high abundances in red. The title on top of a panel indicates the model represented in this panel. In addition on top of the first panel of each figure we indicate the name of the molecule for which the abundances are plotted. As these figures look like bacon slices we decide to call them "Bacon plots".
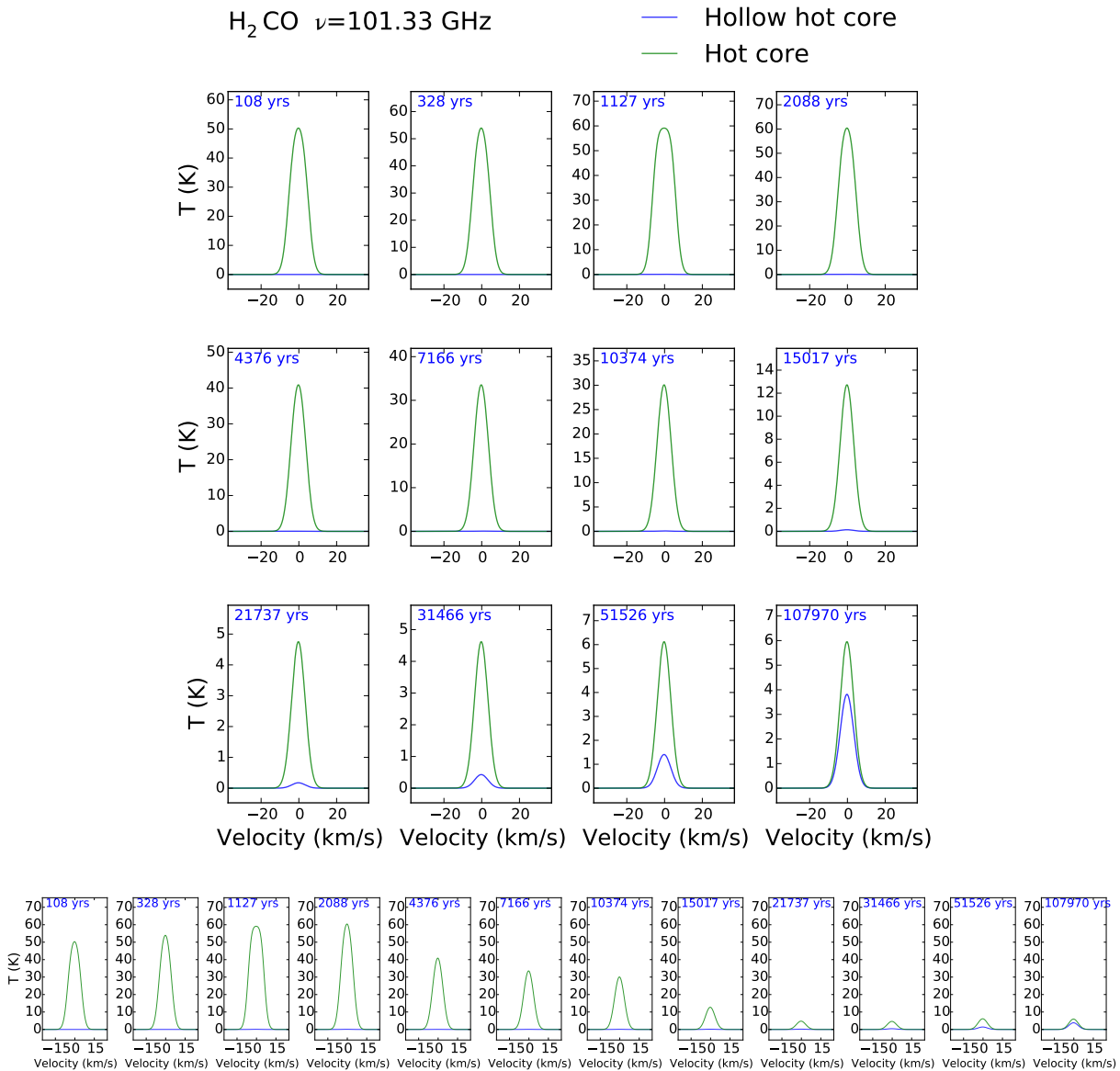
Figure 5.2: Diagnostic tool: Example of a figure showing the time evolution of synthetic spectra. The figures on the bottom panel have the same y-axis level.

In some cases the panels may show a white area for high extinctions, it means that the highest extinction is reached for the model. As the modeling grid does not extend further than a cut-off density (10^1 cm^{-3} in most models), depending on the density in the medium and the size of the grid, we have a maximal extinction.

Temperature and radiation field profiles: The temperature and radiation field intensity figures shown in this chapter (e.g. Fig. 5.8 or 5.10) are also "Bacon plots". The x-axis represents the time evolution from 10^{-1} to 10^8 years and the y-axis represents the visual extinction evolution. No title is given in these figures. These profiles are represented as a function of extinction for the same reason as for the abundance profiles in HII region models. The medium is really dense so the IR and UV radiation do no penetrate deep. Thus, in few hundred astronomical units the temperature and radiation field intensity are equal to their initial values, 10 K and 10^{-20} Draine unit respectively.
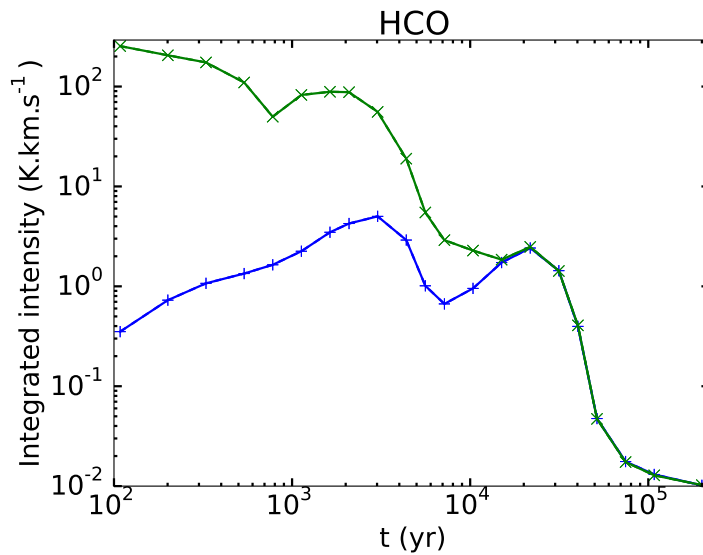
Figure 5.3: Diagnostic tool: Example of a figure showing the time evolution of an integrated intensity. The colored represent integrated intensity for different models.

All figures presenting spectra, integrated intensities, integrated intensity ratios and integrated intensity ratio vs integrated intensity ratio are shown from 10^2 to $2{\times}10^5$ years. This is the range where we have data for the stellar parameters (from Hosokawa & Omukai 2009). We consider that the models are not physical enough if we consider constant dust temperature and radiation field intensity due to the lack of data for further times. Thus it is not relevant to produce synthetic spectra after $2{\times}10^5$ years. The same can apply to the times before 10^2 years and in addition, as all molecules in the medium are frozen onto the grain surface before this time, no lines are detectable.

Synthetic spectra: All figures showing synthetic spectra display twelve panels with increasing times from left to right from top to bottom as show in the example of Fig. 5.2. Annotations indicating the time in years when the spectra are produced are situated on the top left corner of each panel. The x-axis represents the velocity in $\mathrm{km\,s^{-1}}$ with the peak intensity being at $0\ \mathrm{km\,s^{-1}}$ and the y-axis represents the temperature in Kelvin. The legend indicates the name of the molecule, the frequency of the considered transition in GHz and the color used for each model.

Integrated intensities: The time evolution of integrated intensities is presented in figures like Fig. 5.3. The x-axis represents the time in years, the y-axis represents the integrated intensity in $\mathrm{K\,km\,s^{-1}}$. The title on top of the figure indicates the name of the molecule we plot the integrated intensities. The color lines represent the intensity evolution for different models.

Integrated intensity ratios: We can also obtain integrated intensity ratios to investigate the chemical temporal evolution of HII regions and HMCs. In Tab. 5.3 we present the abbreviations used for each ratio. All ratios consider the integrated intensity of $HC^{15}N$ as the denominator. We choose to use this species because for every time step the $HC^{15}N$ lines are detectable. Furthermore, always using the same denominator simplify the comparison of the ratios. An example of a figure showing the time evolution of the integrated intensity ratio is shown in Fig. 5.4. The x-axis represents the time in years, the y-axis represents the
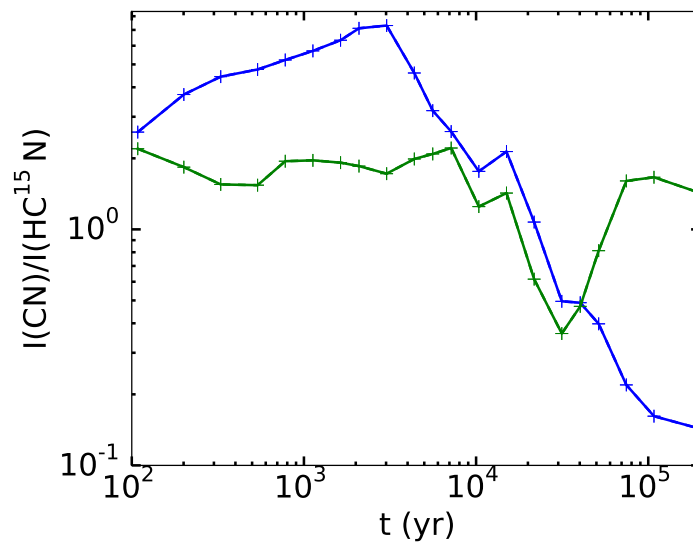
Figure 5.4: Diagnostic tool: Example of a figure showing the time evolution of an integrated intensity ratio. The colored line represent integrated intensity ratio for different models.

integrated intensity ratio. The y-label indicates the molecules used for the ratio profile.
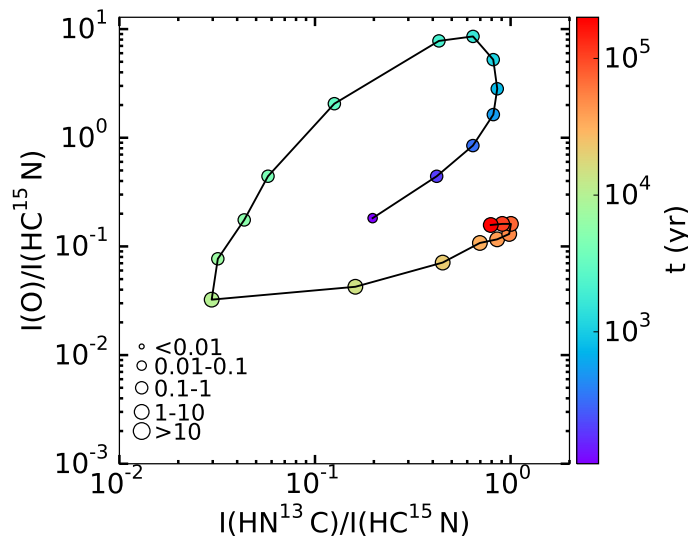
Figure 5.5: Diagnostic tool: Example of a figure showing an integrated intensity ratio as a function of another integrated intensity ratio, with the time evolution in color. The colored line represent integrated intensity for different models. The different time steps are as follows: 1.08×10^2, 2.01×10^2, 3.29×10^2, 5.38×10^2, 7.79×10^2, 1.13×10^3, 1.63×10^3, 2.09×10^3, 3.02×10^3, 4.38×10^3, 5.60×10^3, 7.17×10^3, 1.04×10^4, 1.50×10^4, 2.17×10^4, 3.15×10^4, 4.03×10^4, 5.15×10^4, 7.46×10^4, 1.08×10^5 and 2×10^5 years.

Integrated intensity ratio VS integrated intensity ratio: We also compare in one single plot the variation of two integrated intensity ratios for different couples of species. Fig. 5.5 shows an example. The x-axis represents the ratio $I(\mathrm{HN^{13}C})$ / $I(\mathrm{HC^{15}N}\,(1\text{–}0))$ and the y-axis represents the ratio $I(\mathrm{X}_i)$ / $I(\mathrm{HC^{15}N}\,(1\text{–}0))$ where X_i is one of selected molecules except $\mathrm{HN^{13}C}$ and $\mathrm{HC^{15}N}$. Each time step is represented by a marker of a certain color.

Table 5.3: Abbreviations used for the integrated intensity ratios.

Integrated intensity ratio	Abbreviation
$\frac{I(\mathrm{HN^{13}C})}{I(\mathrm{HC^{15}N})}$	raHNC
$\frac{I(\mathrm{C^+})}{I(\mathrm{HC^{15}N})}$	raC+
$\frac{I(\mathrm{C})}{I(\mathrm{HC^{15}N})}$	raC
$\frac{I(\mathrm{O})}{I(\mathrm{HC^{15}N})}$	raO
$\frac{I(\mathrm{CN})}{I(\mathrm{HC^{15}N})}$	raCN
$\frac{I(\mathrm{H_2^{18}O})}{I(\mathrm{HC^{15}N})}$	raH2O
$\frac{I(\mathrm{HCO^+})}{I(\mathrm{HC^{15}N})}$	raHCO+
$\frac{I(\mathrm{HCO})}{I(\mathrm{HC^{15}N})}$	raHCO
$\frac{I(\mathrm{H_2CO})}{I(\mathrm{HC^{15}N})}$	raH2CO
$\frac{I(\mathrm{CH_3OH})}{I(\mathrm{HC^{15}N})}$	raCH3OH
$\frac{I(\mathrm{N_2H^+})}{I(\mathrm{HC^{15}N})}$	raN2H+
$\frac{I(\mathrm{NH_3})}{I(\mathrm{HC^{15}N})}$	raNH3

The colorbar shows the color corresponding to each time step, from blue for early times to red for late times. In addition each model presented in these figures has a different marker (circle, triangle and diamond). The size of these markers is correlated to the value of the peak intensity of the line. It goes from small sizes for low peak intensity values to big size for high values: < 0.01 K, $0.01 - 0.1$, $0.1 - 1$, $1 - 10$ and > 10 K. The smallest size corresponds to undetectable lines. This kind of figures is extremely useful as it can be compared to observational data, assuming we have knowledge on the integrated intensity for at least three molecules, to provide the age of the observed region.

5.4   Hollow hot core vs Hot core

In order to understand the impact of strong radiation field onto the chemistry in dense cores we want to compare a model of HC/UCHII region with a hot molecular core (HMC) model. We can not directly compare them together as they do not have the same den-
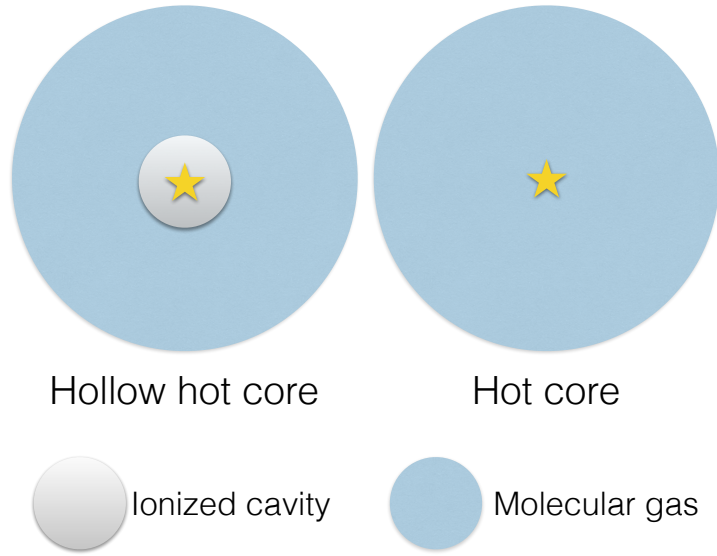
Figure 5.6: Scheme showing the differences between an hot core model and a hollow hot core model. The proto-star is situated at the centre of the core. In the HHMC model an ionized cavity (grey) is included between the star and the molecular cloud (blue).
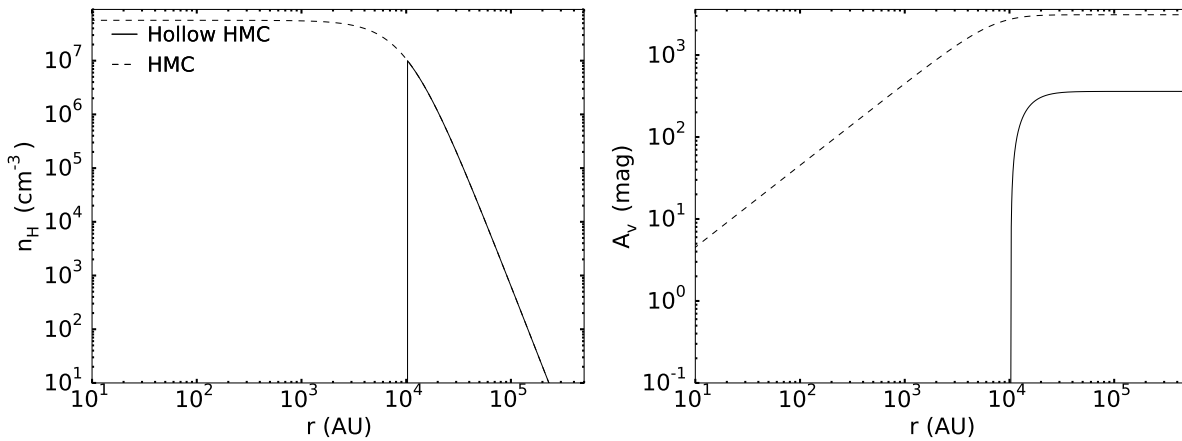
Figure 5.7: Density (left panel) and visual extinction (right) as a function of radius for the HHMC (solid line) and HMC (dashed) model.

sity/column density and the same temperature profile. So, we have built a model of hollow hot molecular core (HHMC) which has the same properties than the HC/UCHII region as it also hosts an ionized cavity in its centre as seen in the right picture in Fig. 5.6. This hollow HMC is compared the standard HMC model.

Density profile: In the left panel of Fig. 5.7 we show the evolution of the density as a function of radius for the HHMC (solid) and the HMC (dashed) models. The profiles are the same after a radius of 0.05 pc (10^4 AU). Before this radius, we assume that the density is zero in the HHMC model. Thus the maximum density for the HHMC model is the density at the ionization front 10^7 cm^{-3} and the maximum density for the HMC model corresponds to the Plummer peak density, 5.65×10^7 cm^{-3}. On the right panel of this figure we also present the visual extinction as a function of radius. Due to the cavity included in the HHMC model the extinction profile is quite different and of course lower
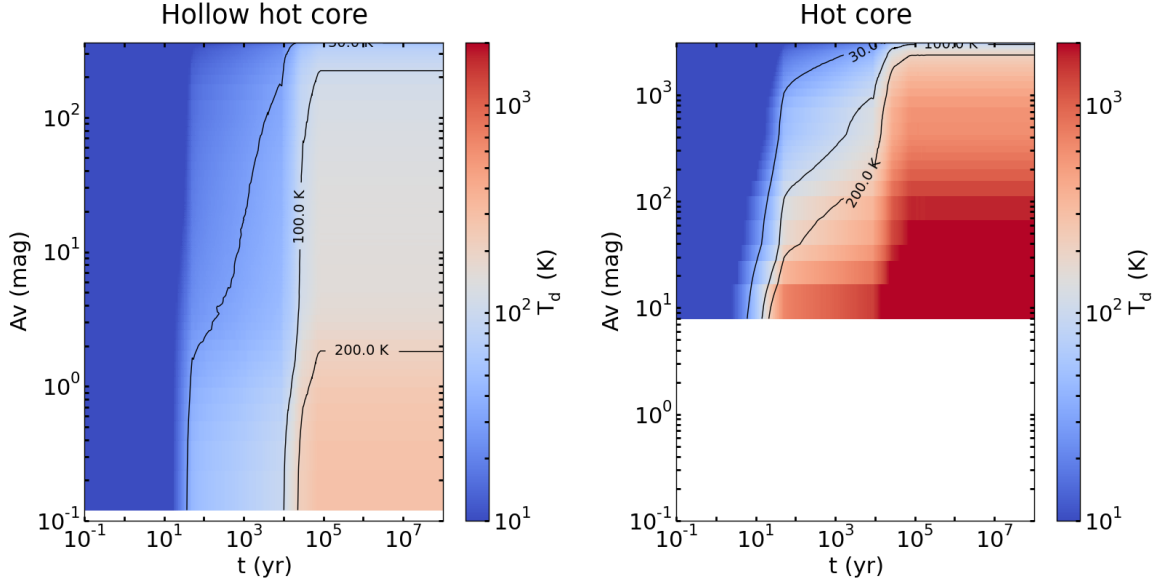
Figure 5.8: Temperature as a function of time (x-axis) and visual extinction (y-axis) for the HHMC (left) and the HMC model (right). The black lines represent the contours for the temperature: 30, 100 and 200 K.

than for the HMC model by one order of magnitude for radii higher than 10^4 AU. The maximal extinction for the HHMC model is 360 mag and is ~ 3100 mag for the HMC model

Temperature profile: The temperature profiles for the HHMC and HMC models are shown in Fig. 5.8, left and right panel respectively. The dust temperature seems higher for the HMC model but the temperature is in fact about two times lower at the edge of the ionized cavity ($\sim 10^4$ AU in this figure) and then they become similar as the density decreases and radius increases.

5.5   HC/UCHII region vs Hollow hot core

Now we compare the hollow hot core model to the HC/UCHII region model. In Fig. 5.9 we show the scheme of these two models. They both have the same density profile (solid lines in Fig. 5.7) and the same spatio-temporal evolution of the temperature. The difference between these two models is that for the HII region model we form an internal PDR as we include the radiation field and its spatio-temporal evolution (red arrows) when computing the relative abundances.

Temperature and radiation field profiles: The temperature profile and the radiation field intensity obtained for the reference model of UCHII region ($R_{HII} = 10^4$ AU, density at the ionization front $n_H = 10^7$ cm^{-3}, $\gamma = 2.5$) and the HHMC model are shown in Fig. 5.10. All models start with an initial temperature of 10 K and it increases to $\geq$ 200 K. We can define three phases in the time evolution: the first one where T_d remains
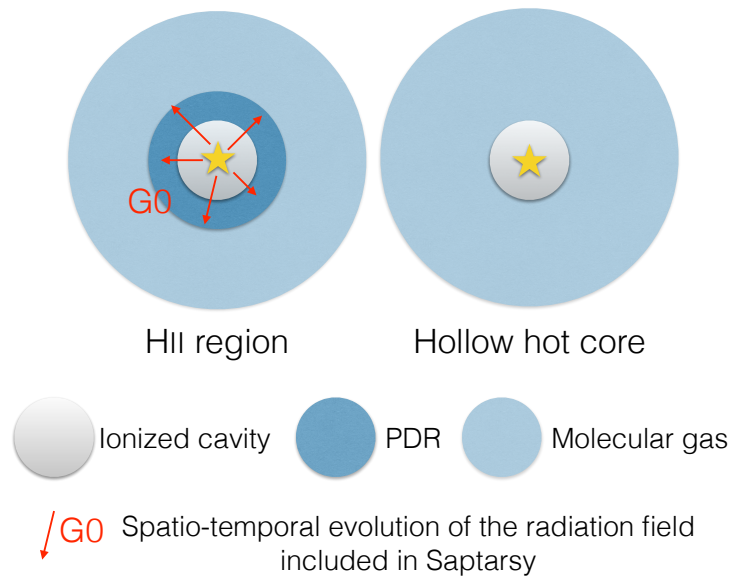
Figure 5.9: Scheme showing the differences between a hollow hot core model and a HC/UCHII region model. The latter presents an internal PDR (dark blue) between the ionized cavity (grey) and the molecular gas (light blue). The red arrows represent the radiation field intensity included only in the HII region model.
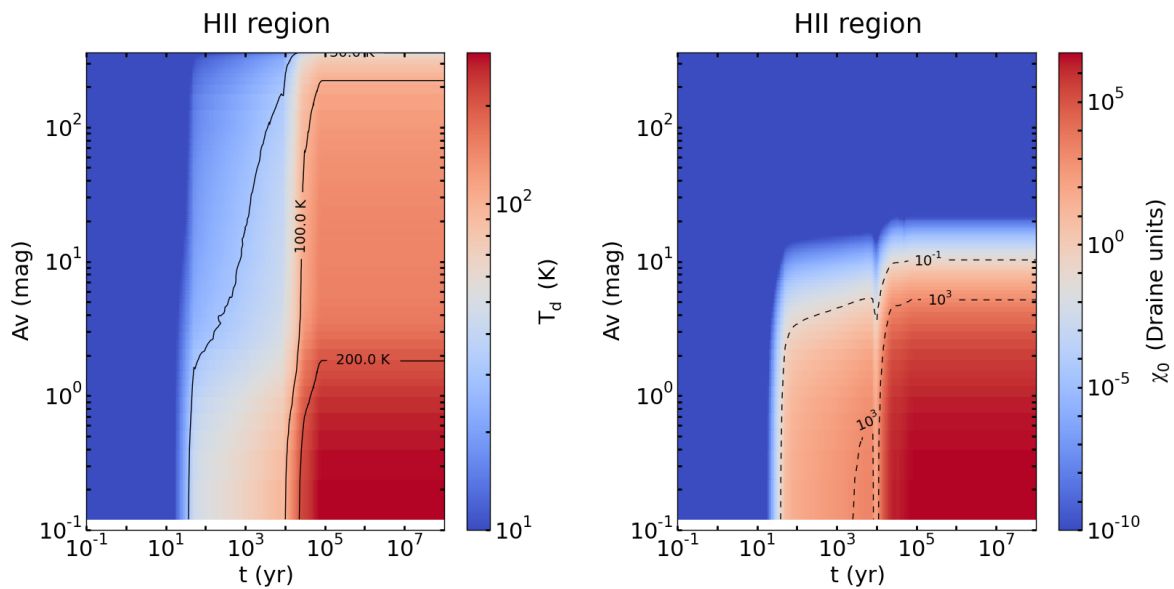
Figure 5.10: Temperature (left panel) and radiation field intensity (right) as a function of time (x-axis) and visual extinction (y-axis) for the HC/UCHII region. On the left panel the contours are shown for 30, 100 and 200 K. On the right panel the contours are shown for 10^{-1} and 10^3 Draine unit.
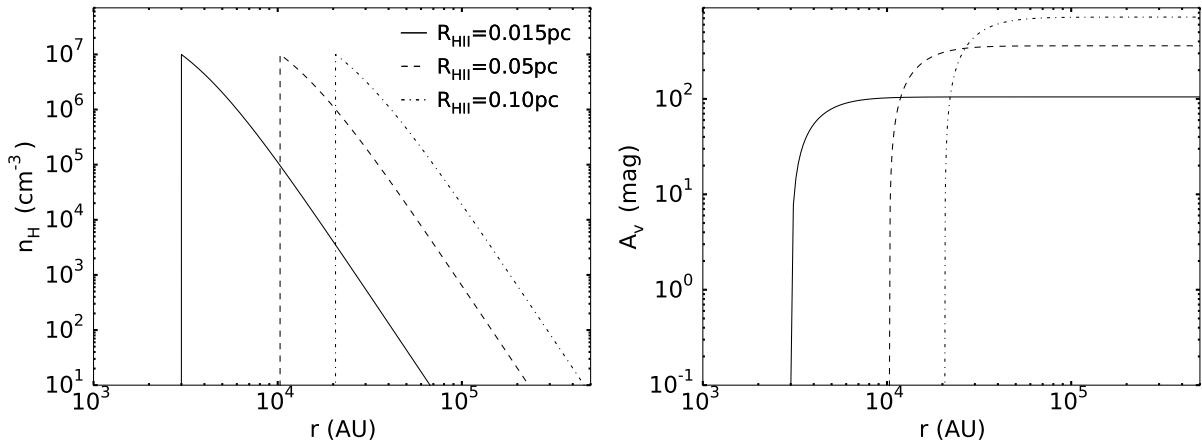
Figure 5.11: Density (left panel) and visual extinction (right) as a function of radius for HII region models for different sizes: 0.015 pc (solid line) and 0.05 pc (dashed) and 0.10 pc (dashed dotted).

at 10 K up to 10^1 years, the second up to 10^4 years where it reaches 100 K and the last one. From the ionization front to the edge of the cloud the temperature decreases to 10 K for density lower than 10^6 cm^{-3}. At 10^4 years a temperature decrease occurs because the luminosity of the proto-star drops when it becomes bloated. The same event happens for the radiation field intensity. For this parameter we start the time evolution at 10^{-20} Draine unit and it can go to intensity higher than 10^7 depending on the HII region size. The same time zone than for the temperature can be seen. As for the radial evolution after an extinction of ~ 20 mag we have no radiation field.

5.5.1   Size of the ionized cavity

We can vary the size of the ionized cavity and produce models. We have done it for three sizes of ionized cavity R_c: 0.015 pc, 0.05 pc and 0.10 pc (3000, 10300 and 20600 AU respectively). The reference model is the HII region with a size of 0.05 pc and a density of 10^7 cm^{-3} at the ionization front. According to Tab. 1.3 this is a UCHII region at least by its size. As for the two other sizes, $R_c = 0.015$ pc is clearly a HCHII region but the one with a size of 0.10 pc is at the transition from a UC to a Compact HII region.

Density profile: The density and the visual extinction profiles for these three models are represented as a function of radius in Fig. 5.11. All models start with a density of 10^7 cm^{-3} at the ionization front and only the Plummer radius changes because it is equal to the size of the ionized cavity. The extinction is higher when the size of the cavity increases as we increase the amount of material (see Eq. 2.32). The maximal extinction for each size of cavity is: 105, 360 and 720 mag for the size of 0.015, 0.05 and 0.10 pc respectively.

Temperature and radiation field profiles: In Fig. 5.12 we show the temperature profiles (upper panels) and the radiation field intensity profiles (bottom panels) for models with different size of ionized cavity: 0.015 pc (left), 0.05 pc (middle) and 0.10 pc (right). The temperature and the radiation field intensity are higher for smaller sizes of HII regions as it is closer to the star. The values for the temperature and the radiation field intensity
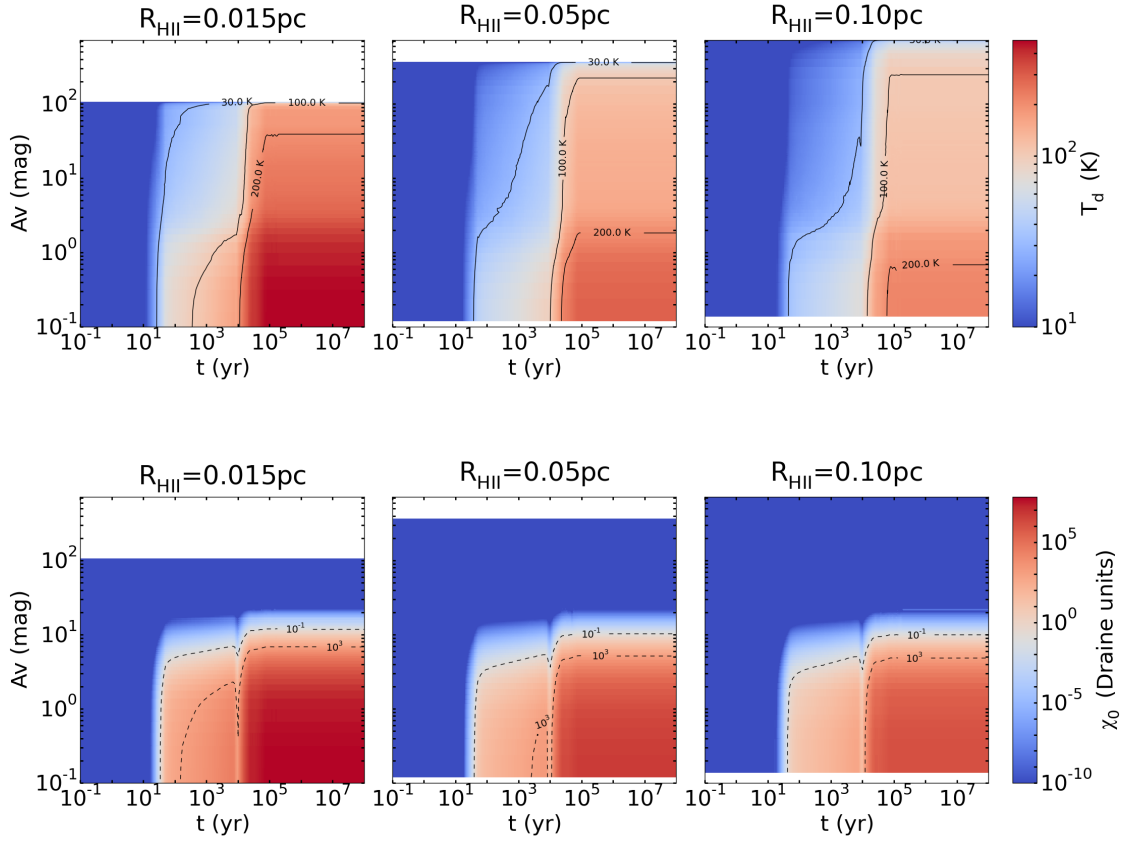
Figure 5.12: Temperature (left) and radiation field intensity (right) as a function of time (x-axis) and visual extinction (y-axis) for HC/UCHII region models with different sizes: 0.015 pc (left), 0.05 pc (middle) and 0.10 pc (right). On the upper panels the contours are shown for 30, 100 and 200 K. On the bottom panels the contours are shown for 10^{-1} and 10^3 Draine unit. The temperature evolution is the same for the corresponding HHMC models.

Table 5.4: Temperature and radiation field intensity values at the ionization front at 10^5 years for the different sizes of HII region.

R (pc)	R (AU)	T (K)	χ_0 (Draine unit)
0.015	3000	475	6.5×10^7
0.05	10300	290	5.2×10^6
0.10	20600	220	1.3×10^6

at 10^5 years are presented in Tab. 5.4. Furthermore, it takes more time for the temperature to increase as we go deeper into the core for models with bigger ionized cavity.

5.5.2   Density at the ionization front

Density profile: The density at the ionization front is a also free parameter that we change and compare the results. In addition to a model with a density at the ionization
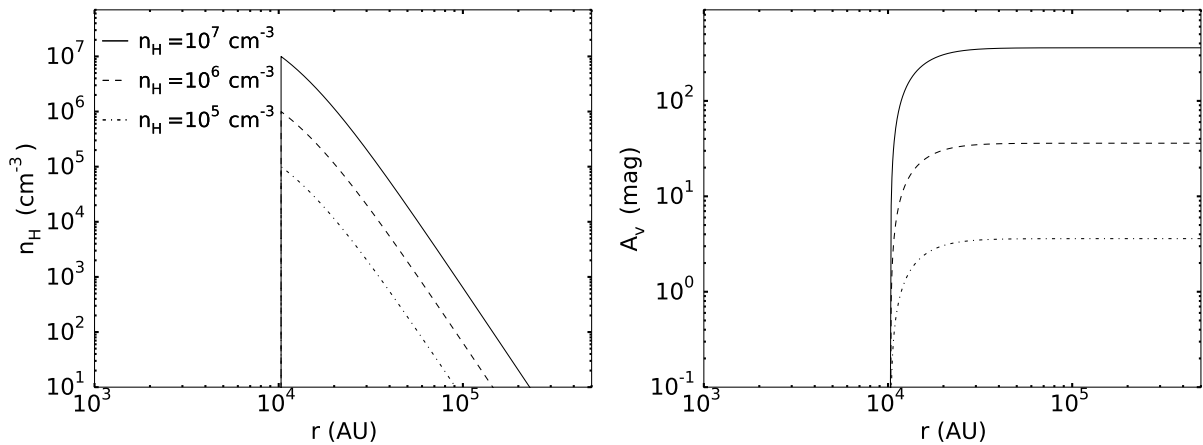
Figure 5.13: Density (left panel) and visual extinction (right) as a function of radius for UC/HCHII region models with different densities at the ionization front: 10^7 cm^{-3} (solid line), 10^6 cm^{-3} (dashed) and 10^5 cm^{-3} (dashed dotted).
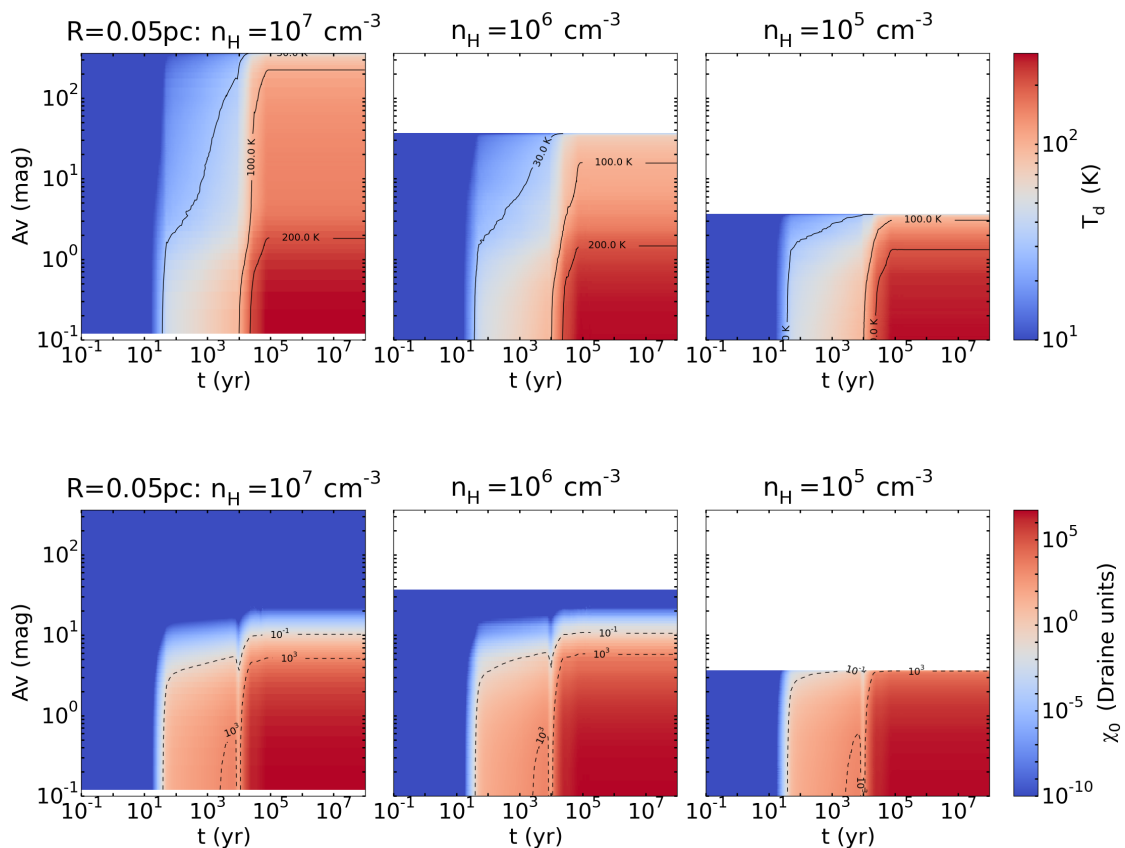
Figure 5.14: Temperature (left) and radiation field intensity (right) as a function of time (x-axis) and visual extinction (y-axis) for HC/UCHII region models with different densities at the ionization front: 10^7 cm^{-3} (left), 10^6 cm^{-3} (middle) and 10^5 cm^{-3} (right). On the upper panels the contours are shown for 30, 100 and 200 K. On the bottom panels the contours are shown for 10^{-1} and 10^3 Draine unit. The temperature evolution is the same for the corresponding HHMC models.
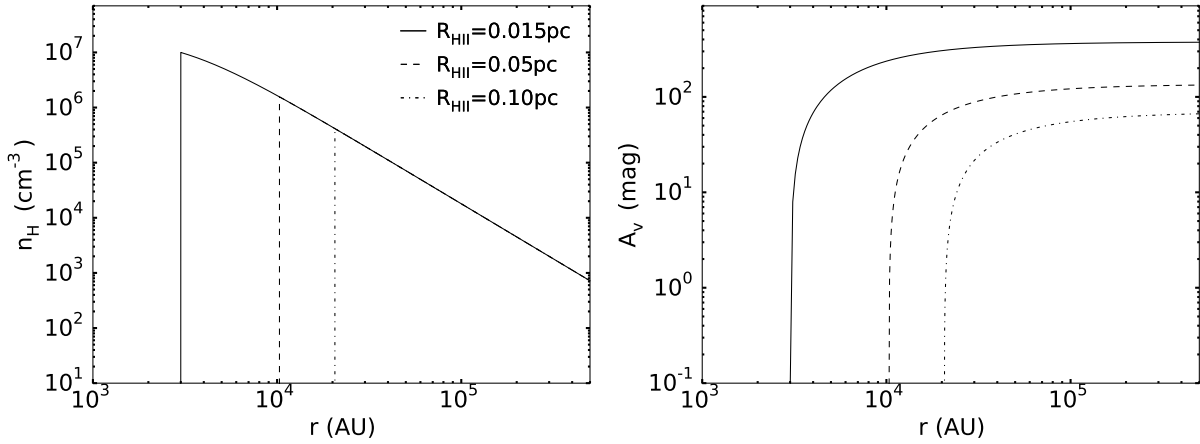
Figure 5.15: Density (left panel) and visual extinction (right) as a function of radius for HII region models using for the second density profile ($\gamma = 1$) and with different sizes of ionized cavity: 0.015 pc (solid line) and 0.05 pc (dashed) and 0.10 pc (dashed dotted).

front of 10^7cm^{-3} we produce models with densities of 10^6 and 10^5 cm^{-3}, when the size of the HII region is equal to 0.05 pc, as seen in the left panel of Fig. 5.13). The cut-off density is reached for a lower radius when the density is decreased. The visual extinction profiles for these models are shown on the right panel of the same figure. Higher densities at the ionization front induce higher visual extinction as we have more material on the line of sight. The maximal extinctions are: 3.6, 36 and 360 for models with density of 10^5, 10^6 and 10^7cm^{-3} respectively.

Temperature and radiation field profiles: In Fig. 5.14 we show the temperature (upper panels) and the UV radiation field intensity (bottom) profiles for the different densities: 10^7 cm^{-3} (left panel), 10^6 cm^{-3} (middle) and 10^5 cm^{-3} (right). All models have the same temperature and same radiation field intensity at the ionization front. We see that when we decrease the density the UV radiation can penetrate deeper into the core. The radiation even goes through the whole core in the case of a density of 10^5 cm^{-3}. To define the atomic-to-molecular transition we can use the dimensionless parameter αG, where α is also a dimensionless variable representing the ratio of H_2 photo-dissociation in a free space to H_2 formation and G is the average H_2 self-shielding factor (αG is proportional to $\frac{\chi_0}{n_H}$; see Sternberg et al. 2014 for the H/H_2 transition).

5.5.3   Plummer exponent

Density profile: We also obtain models for a second density profile using an exponent of the Plummer function $\gamma = 1$. The density profile is less steep than with an exponent of 2.5 (see Fig. 5.15). The density at the ionization front is the same as for the model with $\gamma = 2.5$ for the model with a cavity size of 0.015 pc, 10^7 cm^{-3}. For the other sizes, we have a density of $1.56 \times 10^6 \text{ cm}^{-3}$ when the size of the cavity is 0.05 pc. And for a model with a size of 0.10 pc, the density at the ionization front is $4.15 \times 10^5 \text{ cm}^{-3}$. Thus, the model with the smallest cavity size has a maximal extinction of 376 mag. The ones with a size of 0.05 pc and 0.10 pc have maximal extinctions of 135 and 69 mag respectively.

Temperature and radiation field profiles: The temperature and radiation field profiles are quite similar to the first density profile for a HII region of a size of 0.015 pc. At 10^5 years and at the ionization front the temperature and radiation field intensity are the same, 475 K and 6.5×10^7 Draine unit respectively. They decrease a bit faster when we go deeper into the core because the density is higher for the same radius. For the other HII regions sizes as the density is decreased when we increase the size of the ionized cavity the temperature and radiation field intensity are lower for this model except at the ionization front where they are equal.

6

Results and analysis

Contents

We produce several models that we compare with a reference one. The reference model is a HII region with a size of 0.05 pc, a density of 10^7 cm^{-3} at the ionization front and a Plummer exponent of 2.5. It also has a cut-off density of 10^1 cm^{-3}. The various comparisons with this reference model are enumerated below:

1. The first comparison is between HHMC and HMC models to study the impact of the ionized cavity onto the lines emission; then we compare HII regions models and HHMC models to study the impact of the radiation field on the chemistry.

2. We also study the impact of a change of the size of the HII region. In addition to $R_{HII} = 0.05$ pc (10300 AU), which seems to be a UCHII region according to Tab. 1.3, we have produced models with $R_{HII} = 0.015$ and 0.10 pc (or 3000 and 20600 AU, respectively). The model where $R_{HII} = 0.015$ pc is clearly a HCHII region and the one with a size of 0.10 pc is at the transition from a UC to a Compact HII region.

3. As the reference model has a density closer to the density of a HCHII region we compare it to models with lower density at the ionization front to be closer to the density of a UCHII region: 10^6 and 10^5 cm^{-3}.

Table 6.1: Abbreviations used for the models.

Item	Parameter	Value	Abbreviation
1	UCHII region model		*mHII*
	HMC model		*mHC*
	HHMC model		*mHHC*
2	Size of the HII region (pc)	0.05	*r0.05*
		0.015	*r0.015*
		0.10	*r0.10*
3	Density at the	10^5	*n5*
	ionization front (cm^{-3})	10^6	*n6*
		10^7	*n7*
4	Plummer exponent γ	1	*p1*
		5/2	*p2.5*
5	Initial abundances		*ini1*
	(see Sec. 5.1)		*ini2*
6	Cut-off density (cm^{-3})	10^1	c1
		10^6	c6
7	Number of species	183	*s183*
	in the network	334	*s334*

4. We compare models with different exponent of the Plummer function: $\gamma = 2.5$ or 1. We also perform this comparison as in Chap. 3.1.2 we have shown that the steepness of the Plummer function varies from one astrophysical object to another (Sgr B2(N)-SMA(1): $\gamma = 2.5$; Mon-R2: $\gamma = 1$). In addition the models where $\gamma = 1$ also include a decrease of the density as the size of the HII region increases. This seems to be a more realistic view of the evolution of the HII region.

5. We compare models starting with different initial abundances: *ini1* and *ini2*. This is done to observe the impact of the initial chemical composition of the medium has on the final results.

6. A model with a smaller grid, i.e. the cut-off density at 10^6 cm^{-3} instead of 10^1 cm^{-3}, is also produced to trace the emission coming from the inner core only.

7. We have two gas-grain networks: one contains 183 species and 2437 reactions and the other has 334 species and 3684 reactions. They have 50 and 100 grain species, respectively. The network with 334 species is an extension of the other one and it contains more complex molecules such as dimethyl ether or methyl formate in the molecular, ionized and icy state.

The abbreviations for the different models are presented in Tab. 6.1. We annotate the
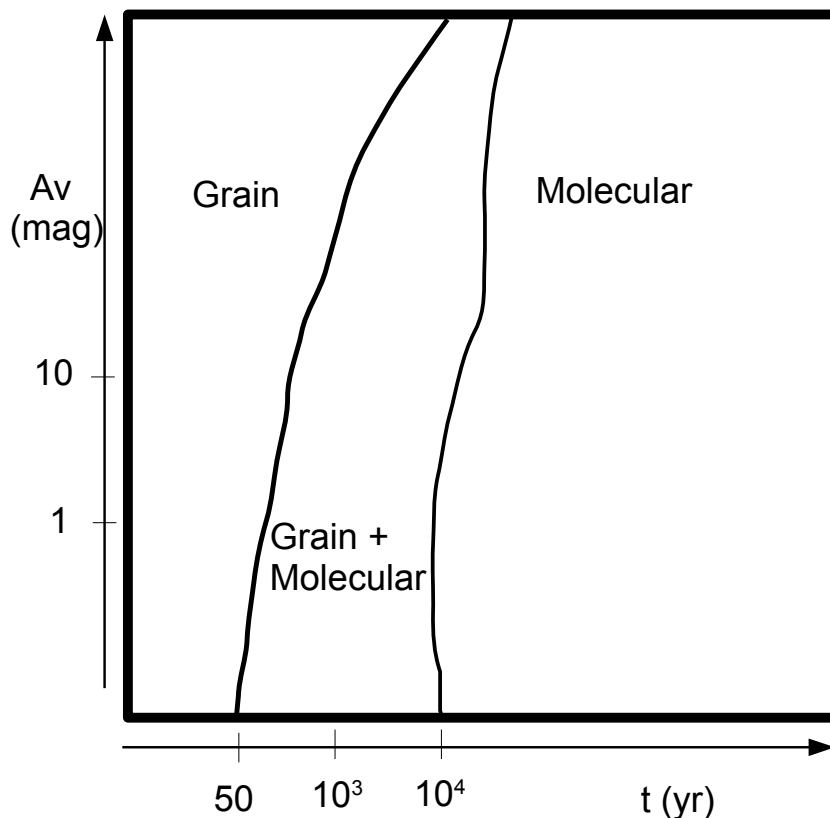
Figure 6.1: Scheme showing the different regions in the HII region reference model. The different regions/areas appear due to the thermal desorption of species, and some desorb later than others. The processes of reactive desorption seems to be also at play for some species (e.g., CH_3OH).

reference model as *mHII:r0.05n7p2.5ini1c1s183*. If none of these items is mentioned for a particular model it possesses the reference one.

In this chapter we compare the HHMC model with the HMC model and in Sec. 6.2 we compare the HII regions to HHMC models. In Sec. 6.3 we compare models with different cavity sizes and in Sec. 6.4 we do it for models with different density at the ionization front. Then in Sec. 6.5 models with different Plummer function exponents are compared followed by the Sec. 6.6 where we compare models using different initial abundances. Finally in Sec. 6.7 model with no envelope emission is compared to the reference model.

The abundances, integrated intensity and integrated intensity ratio–ratio figures are shown in the Appendix A for all the selected molecules.

6.1 Hollow hot core vs Hot core

Abundance profiles: The spatio-temporal evolution of the relative abundances of CH_3OH for the HHCM (left panel) and HMC (right) models is shown in Fig. 6.2. For this comparison the spatial evolution is presented as a function of density, from 10^7 cm^{-3}, bottom, to 10^4 cm^{-3}, top. The black lines appearing on the figures represent the contours for
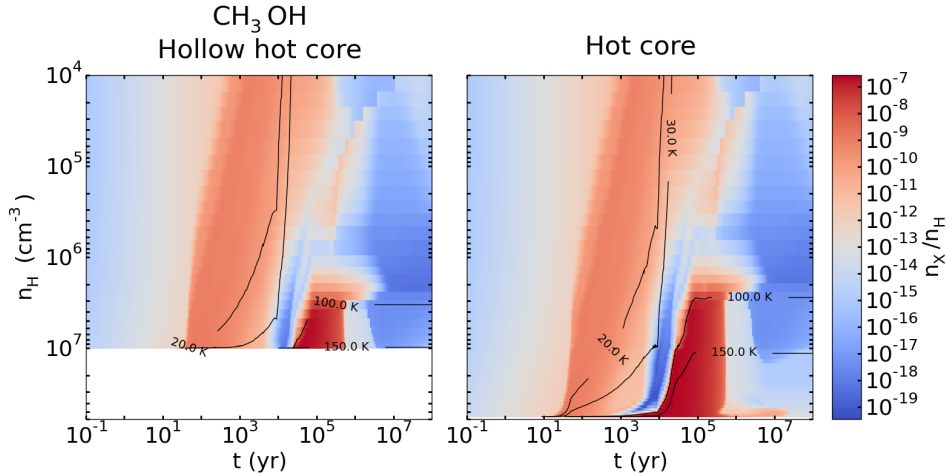
Figure 6.2: Abundance of CH$_3$OH as a function of time (x-axis) and density (y-axis) for the HHMC (left) and HMC (right) models.

the temperature: 20, 30, 100 and 150 K. For all molecules after 10^7 cm^{-3}, i.e. the density at the ionization front, the abundances for the HHMC and HMC models are very similar as the decrease of the temperature as a function of radius becomes quickly the same. We can define several regions/areas from the abundances profiles of the different species. In Fig. 6.1 we show a scheme of these regions. At early times when the temperature is still cold, lower than 20 K, molecules are frozen on the surface of the grains. Thus we have a grain surface region. Later, the temperature increases and some species desorbs while other are still on the grain surface. We have then a grain-molecular region. Finally, we find a molecular regions once the temperature is high enough for all molecules to desorb. The molecular region could as well be divided in several areas as some molecules like CH$_3$OH, NH$_3$ or H$_2$O appear only for density higher than about 10^6 cm^{-3}.

The grain species are more abundant at the beginning of the time evolution where the dust temperature is lower than 20 K, until approximately 50 years at 10^7 cm^{-3} and 10^4 years at a density of 10^4 cm^{-3}. We see that the abundances of some grain species decrease faster compared to others. For instance, it happens at 50 years for s-C, 100 years for s-CO and 10^4 years for s-CH$_3$OH in the inner core around 10^7 cm^{-3}, and at approximately 2000 years, 10^4 years and 2×10^4 years, respectively, in the envelope. This is the case for the HHMC and HMC models. In the HCM model where there is no cavity the time period when grains species are dominant is shorter because the decrease in the abundances starts even before 10^1 years near the star. This decrease in the grain species abundances is due to thermal desorption and some of them desorb faster than others because of their lower desorption energy. s-C, s-O and s-OH desorb before 20 K or s-CO and s-CH$_4$ desorb for T_d between 20 and 30 K. More complex molecules like s-H$_2$CO, s-NH$_3$ or s-CH$_3$OH desorbs around 100 K. The desorption is delayed by one to two orders of magnitude in time when the radius increases because the radiation emitted by the proto-star and causing the increase of the temperature in the medium is attenuated. After 10^5 years and for density below 10^6 cm^{-3} s-H$_2$O is very abundant and the main O-bearing species in the medium. It has an abundance of 9.8×10^{-5} at the beginning of the evolution and of 10^{-4} at the end.

The rest of the time evolution is mainly molecular. For instance, CH_4 is very abundant, $\sim 10^{-5}$, from 10^4 to 10^6 years and then it is destroyed and has abundance of about 10^{-8} whereas CO abundance continuously increases from 10^4 years to almost reach 1.2×10^{-4} after $\sim 5 \times 10^5$ years. Because of this high abundance CO is the main C-bearing molecule in the medium at the end of the evolution. For N-bearing molecules it is N_2 with an abundance of 3.7×10^{-5}. H_2O is the main O-bearing molecules but only for density higher than 10^6 cm^{-3} (see Fig. A.174). Carbon chains have high abundances, higher than 10^{-7} for C_4H_2 or C_3H for example, from approximately 10^4 and 10^6 years and then the carbon is transferred into CO.

Ions, mainly the light ones like C^+, N^+, H^+ or H_2^+ are more abundant in the envelope mostly due to CRs. For instance C^+ has an abundance of about 10^{-12} at 10^7 cm^{-3} and 10^{-8} at 10^4 cm^{-3} see Fig. A.214. These ions form principally by reaction with He$^+$ which is itself formed by direct CR dissociation. This reaction becomes significant only when the density is lower than 10^5 cm^{-3}. The second formation route of ions at low density is secondary photon processes. However a few ions appear to be more abundant by one to two orders of magnitude like H_2S^+ where T_d is close to 30 K; or like H_2NC^+ or NH_4^+ when the temperature reaches 100 K at 2×10^4 years before being destroyed around 2×10^5 years by dissociative recombination.

In the case of CH_3OH as presented in Fig. 6.2, we can see that the abundance starts to increase at 10 years. This is due to the dissociative recombination reaction $CH_5O^+ + e \longrightarrow CH_3OH + H$, and to the reactive desorption reaction for the HHMC model: s-H + s-$CH_2OH \longrightarrow CH_3OH$. CH_5O^+ is formed by reaction of methanol with cations like H_3^+ or H_3O^+. Then the methanol abundance decreases from $\geq 10^3$ years to 10^4 years because of accretion reactions and reactive desorption is not sustained due to the temperature. At about 10^4 years the abundances increase again as the dust temperature is high enough to allow thermal desorption before decreasing again at 5×10^5 years by bimolecular gas phase reactions with H_3O^+ and H^+ in particular as well as secondary photon processes.

Synthetic spectra and Integrated intensity profiles: In Fig. 6.3 the time evolution of the synthetic spectra of $H_2CO\,(2(0,2)-1(0,1))$ for the HHMC (blue) and HMC (green) models are presented. In 6.4 the integrated intensities of HC^{15}N (1–0) (top left panel), HN^{13}C (1–0) and $CH_3OH\,(2(2,1)-3(1,2))$ (bottom) for the HHMC (blue) and HMC (green) models are shown as a function of time. For H_2CO, HC^{15}N and CH_3OH we see that the HMC model emission is stronger by several orders of magnitude sometimes. For N_2H^+, HCO and HCO$^+$ the HMC and HHMC emissions tend to be equal after 10^4 years (see Fig. A.155, A.35 and A.55 respectively) and after 5×10^4 years for HN^{13}C. For CN they are equal between 10^4 and 2×10^4 years. Only for C the HHMC emission is stronger and only after 10^4 years (see Fig. A.195). This is because the line is in absorption for the HMC model after this time. Both C$^+$ and O are in absorption for the HMC model, and also for the HHMC model at the end of the time evolution. These molecules have higher line intensity in the HMC model because they are abundant at high density and their column density is higher in this model as there is no cavity.

In Fig. 6.4 we see that the integrated intensities of both models increase in time for HC^{15}N. This is also happening for $H_2^{18}O$, HN^{13}C and NH_3 but not for the other selected species (see Fig. A.175, A.15 and A.135 respectively). For instance the intensities of H_2CO in the HMC model are decreasing from 500 to 10 K km s^{-1}. For CN, until 10^4 years the HMC intensities decrease while the HHMC intensity increase, and then they decrease and
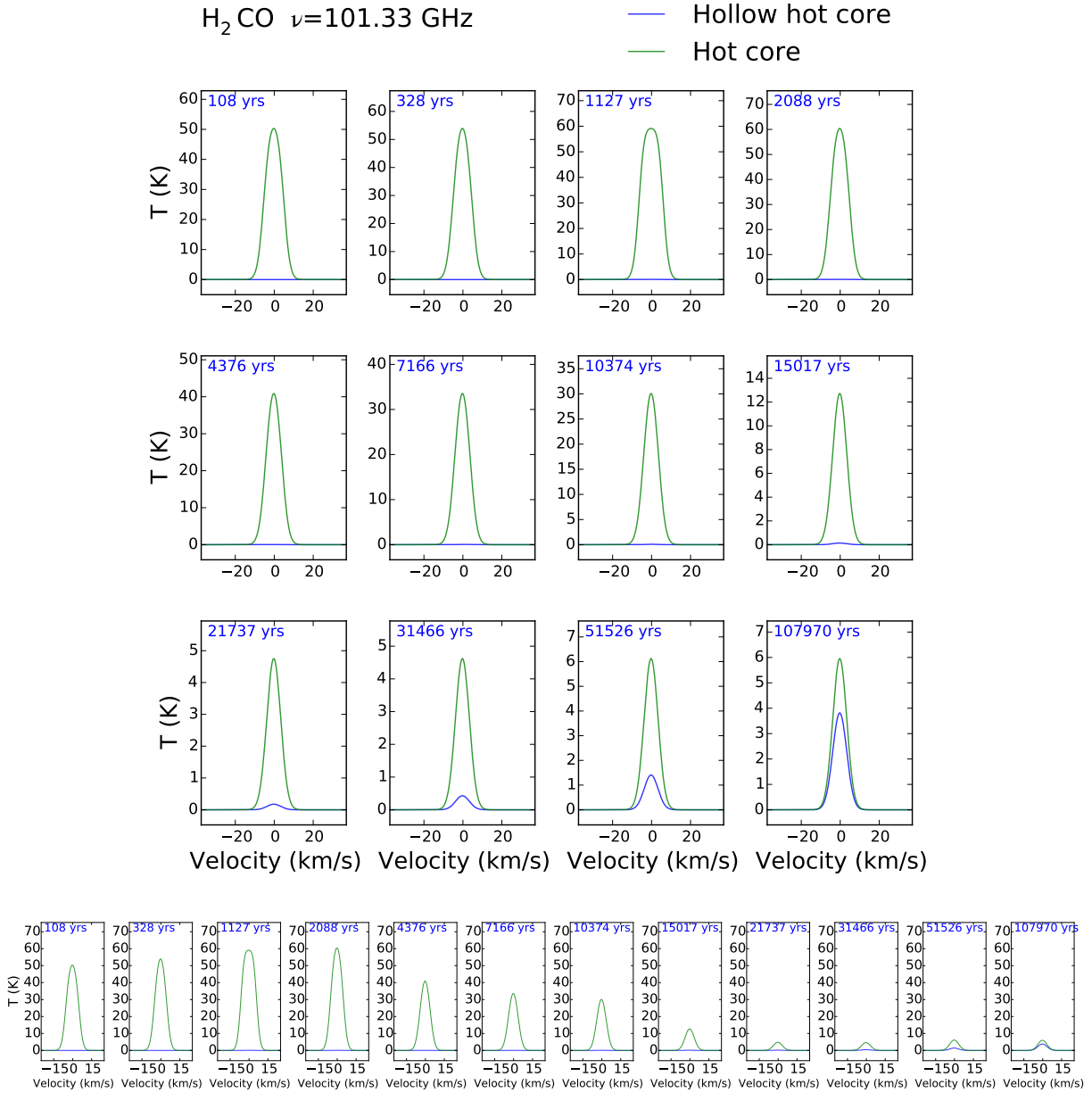
Figure 6.3: Time evolution of $H_2CO\,(2(0,2){-}1(0,1))$ spectra for the HHMC model in blue and the HMC model in green. The bottom panel shows the same spectra but with the same scale on the y-axis.

increase respectively. For CH_3OH, the HMC emission increases until 10^4 years and then decrease while the opposite happens for the HHMC emission. As for N_2H^+ for instance, both models emission are constant until 10^4 years and then they decrease. In general, a radical change in the time evolution of the integrated intensities occurs at 10^4 years time when the star is bloated. At 8×10^3 years, its radius suddenly increase from about 50 to 150 $R_\odot$ at 10^4 years inducing a decrease in the effective temperature, from 7500 to 4500 K. Therefore, the proto-star emits less and the medium cools down a bit, less than 10 K, inducing a low formation for some molecules or low destruction. The latter might be the case for methanol which goes through a period of accretion onto the grains. And as the abundances increase again at 10^4 years, the integrated intensity of the line also
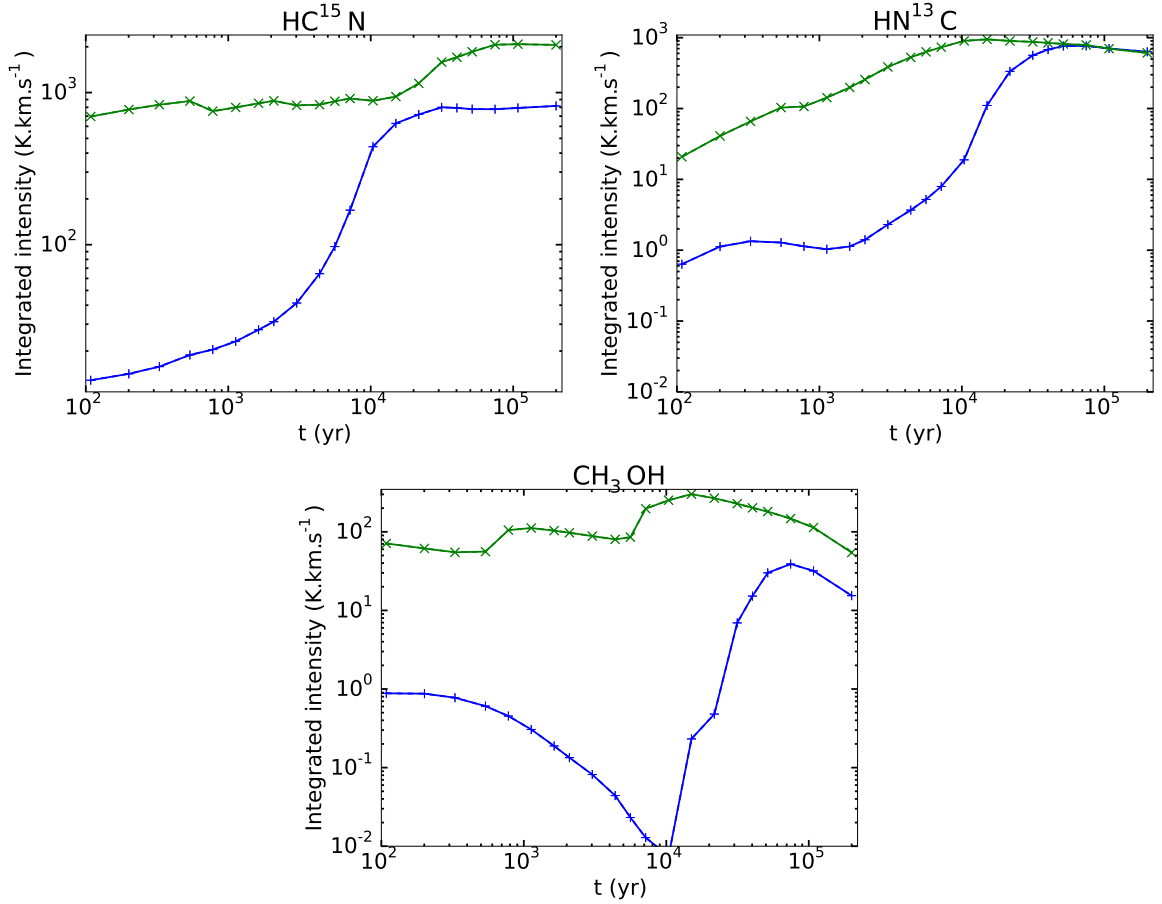
Figure 6.4: Time evolution of integrated intensities for $HC^{15}N$ (1–0) (top left panel), $HN^{13}C$ (1–0) (top right) and CH_3OH (2(2,1)–3(1,2)) (bottom). The blue lines represent the HHMC model and the green ones represent the HMC model.

increases. The intensity of $HC^{15}N$ or $H_2^{18}O$ increases in time for both models because the abundance of HCN, or H_2O, also increases. Thus, integrated intensities increase are due to an increase in the abundance of the species and they decrease because the abundance decreases.

Integrated intensity ratios: We can also investigate the time evolution of the chemical species using integrated intensity ratios. In Fig. 6.5 we present the temporal evolution of the integrated intensity ratios of `raHNC` and `raCH3OH` (see Tab. 5.3) as a function of time. The blue lines represent the HHMC model and the green lines represent the HMC model.

For the ratio `raHNC` we can see that the HMC model ratio is stronger between 300 and 3×10^4 years, with the strongest difference of one order of magnitude at 10^4 years. The ratio for the HHMC model is about 1.5 times higher before this time range, and 2.5 times higher after it. We can also see that the ratio for the HMC model increases from 0.03 to 1 until 10^4 years and then decreases to 0.3. The HHMC model ratio does not have the same trend. It also starts to increase from 0.05 to 0.08 until about 3×10^2 years, then it decreases to 0.04 until 2×10^3 years. This is the first bump. It increases again to 0.05 at 5×10^3 years and decreases back to 0.04 at 10^4 years. This is the second bump. After that it goes through a considerable increase up to 1 at 7×10^4 years and finally it slightly
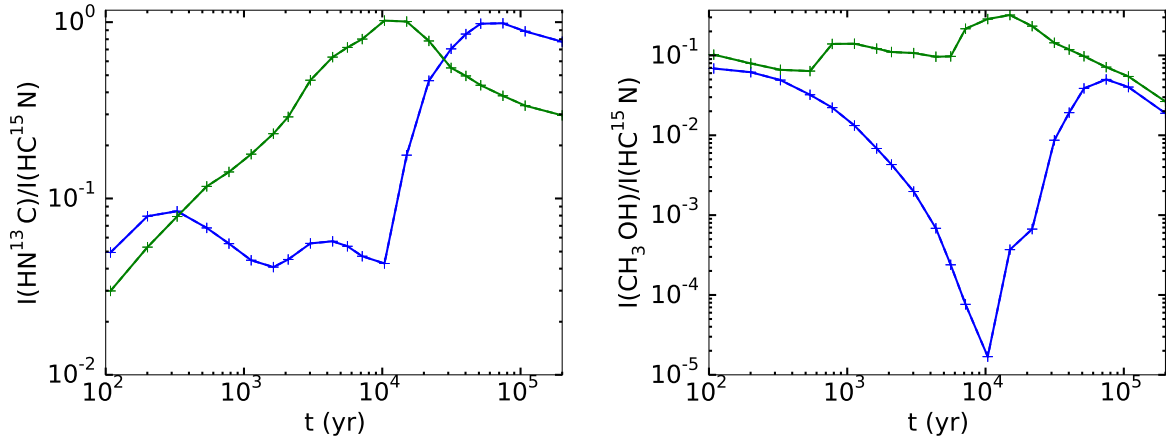
Figure 6.5: Time evolution for HHMC (blue) and HMC (green) models of integrated intensity ratio $(I(X_i) / I(HC^{15}N (1–0)))$. X_i is $HN^{13}C (1–0)$ (left panel) and $CH_3OH (2(2,1)–3(1,2))$ (right).
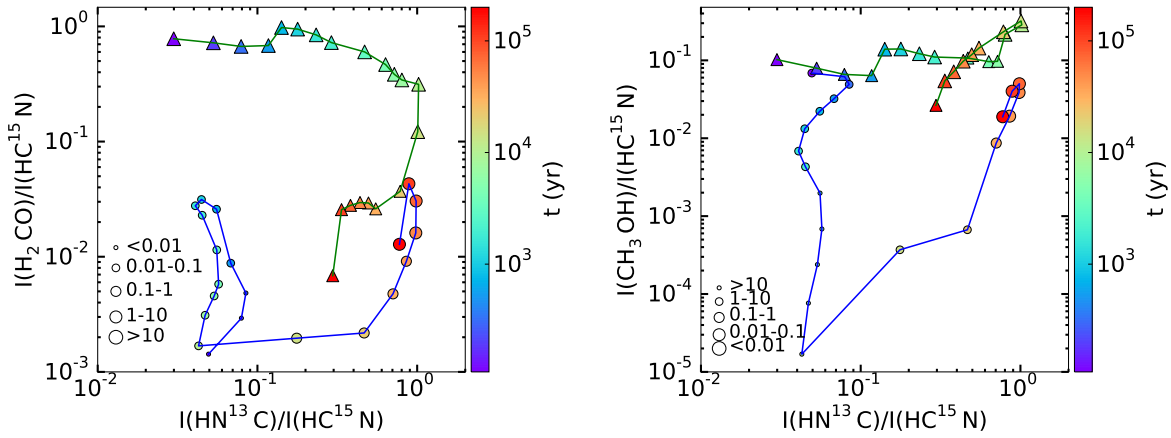
Figure 6.6: Time evolution for the HHMC (blue line and circle markers) and HMC (green line and triangle markers) models of the integrated intensity ratio $(I(X_i) / I(HC^{15}N (1–0)))$ as a function of the integrated intensity ratio $(I(HN^{13}C (1–0)) / I(HC^{15}N (1–0)))$. X_i represents $H_2CO (2(0,2)–1(0,1))$ (left panel) and $CH_3OH (2(2,1)–3(1,2))$ (right). The size of the markers corresponds to the range value of the peak intensity in Kelvin of H_2CO and CH_3OH.

decreases to 0.8. In the HMC model, the increase of the ratio is due to the increase of the integrated intensity of $HN^{13}C$ which is faster than the increase of the integrated intensity of $HC^{15}N$. The decrease is due to the fact that the intensity of $HC^{15}N$ becomes stronger, and remains constant, than to one of $HN^{13}C$ which slightly decreases from about 800 to 600 K km s^{-1}. For the HHMC model, the first bump is produced by a faster increase of the intensity of $HN^{13}C$ and then a decrease in its intensity. The second bump is due to a faster increase of $HN^{13}C$ and then a slower increase compared to $HC^{15}N$. Finally the intensity of $HC^{15}N$ barely increases and the intensity of $HN^{13}C$ goes from 20 to 800 K km s^{-1} so the ratio increases to then decrease as the $HN^{13}C$ intensity decrease and the $HC^{15}N$ intensity is constant.

As for the ratio `raCH3OH`, the HMC model ratio is always higher than the ratio the HHCM model and it does not fluctuate tremendously. It starts at 0.1, has a maximum of 0.3 at 10^4 years and a minimum of 0.03 at the end of the time evolution. The evolution of the ratio for the HHMC model presents high variations. It starts at 0.07 and continuously

decrease to 2×10^{-5} at 10^4 years, then it increases up to 0.05 at 7×10^4 years and decreases again to 0.02. Th ratios' behavior follows closely the behavior of the integrated intensity of CH_3OH.

Some other ratios go through such significant fluctuations mostly for the HHMC model. This is the case for example for `raNH3` which is constant and at $\sim 2\times10^{-4}$ until 7×10^3 and then suddenly increase to 2 in less than 4×10^4 years whereas this ratio for the HMC model starts at 2 and remains constant. Both models have the same trend and same fluctuations for the ratio `raHCO`. They decrease from $\sim 10^{-1}$ to 10^{-5}. The ratios `raH2O` has, like for `raCH3OH`, a ratio for the HMC model, which is constant in time, higher than the HHMC model. This is the opposite for `raC` where the HHMC model ratios are higher; as well as for `raN2H+` and `raHCO+` where the difference between the two models is the biggest, of about one order of magnitude, at the beginning of the evolution and then both ratios decrease and tend to be equal. The ratio which presents the less variations for the two models is `raCN`. They both start at 2 then the HHMC model ratio increase to 7 at 3×10^3 years and decrease until about 0.15 and the HMC model is constant except at 3×10^4 years where it decreases to 0.3 before increasing back to where it started.

Integrated intensity ratio − ratio: Using these ratios we can also produce figures like Fig. 6.6 showing on the left panel `raH2CO` as a function of `raHNC` and on the right panel `raCH3OH` as a function of `raHNC`. The time evolution is given by the color of the markers which are circles for the HHMC model and triangles for the HMC model.

We can see significant differences between the time evolution of the two models, with the HHMC model ratio lower than the ratio of the HMC model as explained in the previous "Integrated intensity ratios" paragraphs. Each ratio produces a different pattern. Loops, as the one appearing for `raH2CO` for the HHMC model (in blue), do not facilitate the determination of the age of the region; even more when they are as narrow as the one for `raH2CO`. In addition, we notice that H_2CO and CH_3OH are undetectable at the beginning of the evolution for the first one and around 10^4 years for the second.

For `raH2CO` as a function of `raHNC` for the HHMC model, we start the evolution on the bottom left corner with a loop. The loop appears because the curve increases and decreases in x-axis 10^3 years, and only increases in y-axis. Then until 10^4 years, it decreases in y-axis, and increase and decrease in x-axis and as the ratio `raHNC` is a bit lower on this second increase – decrease the curve forms the loop, as mentioned in the previous paragraph. The increase-decrease behavior on the x-axis is due to the bumps seen in the time evolution of the integrated intensity ratio `raHNC`. And due to the behavior of `raH2CO` the curve increases and decreases in y-axis. The rest of the evolution can be explained in a similar manner thanks to the figures of the time evolution of ratios.

Summary of the section:

The abundance profiles for the HMC and HHMC models are very similar for density lower than 10^7 cm^{-3}, i.e. after 0.05 pc, size of the ionized cavity.

They present the same distribution of the species with first a grain region, later a grain-molecular region and finally a molecular region. In the HMC model from 10^7 to 5.75×10^7 cm^{-3} the species start to desorb at early times. The abundances of most gas phase species is then high in this region.

For C^+ and O there is no emission for the HHMC and HMC models and for C the HMC emission becomes weaker at 10^4 years as the line is in absorption from this time. After this time, the emission of both models are equal for HCO and HCO^+. Otherwise,
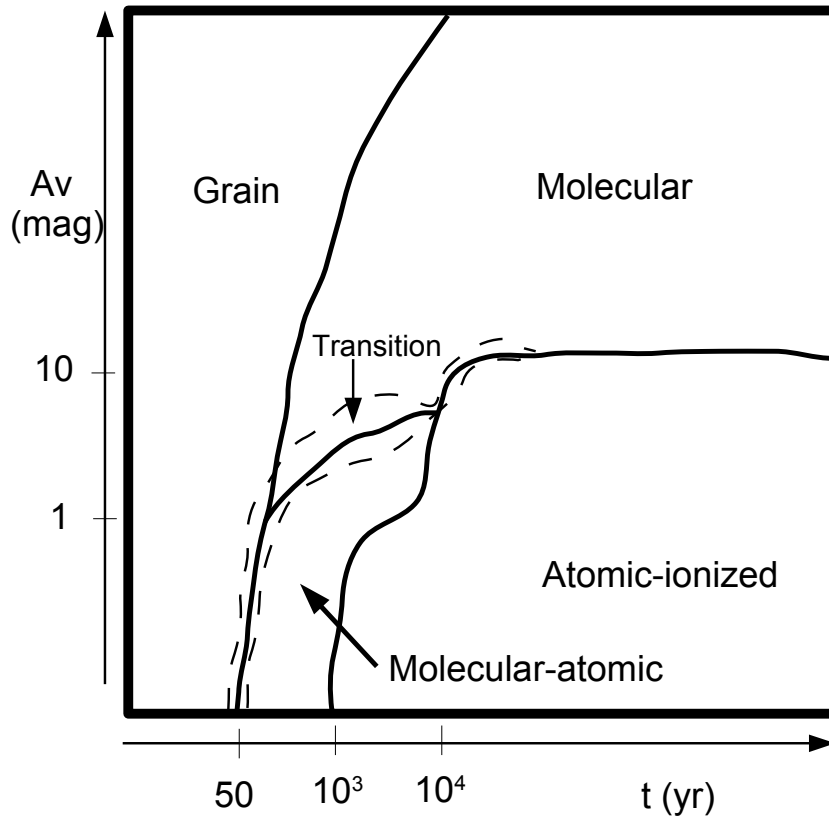
Figure 6.7: Scheme showing the different regions in the HII region reference model. The transition form the grain to the molecular area happens due to thermal desorption mainly, and also reactive desorption. The transition from the grain to the molecular-atomic area is caused by photo-desorption mainly, and a bit of photo-dissociation, and the transition from the molecular-atomic to atomic-ionized is due to photo-dissociation and photo-ionization.

for most species the HMC model emission is stronger than the HHMC model all along the time evolution due to the matter present close to star.

6.2   H$_{\text{II}}$ region vs Hollow hot core

Abundance profiles: Similarly to what we did for the HHMC and HMC models, we can produce spatio-temporal profiles of abundances for the HII region and HHMC models. In Fig. 6.8 we display those profiles for C$^+$ (upper panels) and CH$_3$OH (lower panels). Despite the title on the right panel indicating "hot core", we show the hollow hot core model in this panel. We can identify from the HII region model what we call a grain region, a molecular region, a molecular-atomic region and an atomic-ionized region. A scheme showing the different regions is shown in Fig. 6.7. These regions are variable in time and extinction and depend on the species chosen to define them. The grain region ends at 50 years for low extinction and at 10^4 years for higher ones. The molecular-atomic region extends from 50 years to 10^3 years and from 0 to 7 mag. The molecular region goes from 50 years at A_{V} around 1 mag and from 10^4 years deeper into the core to the end of
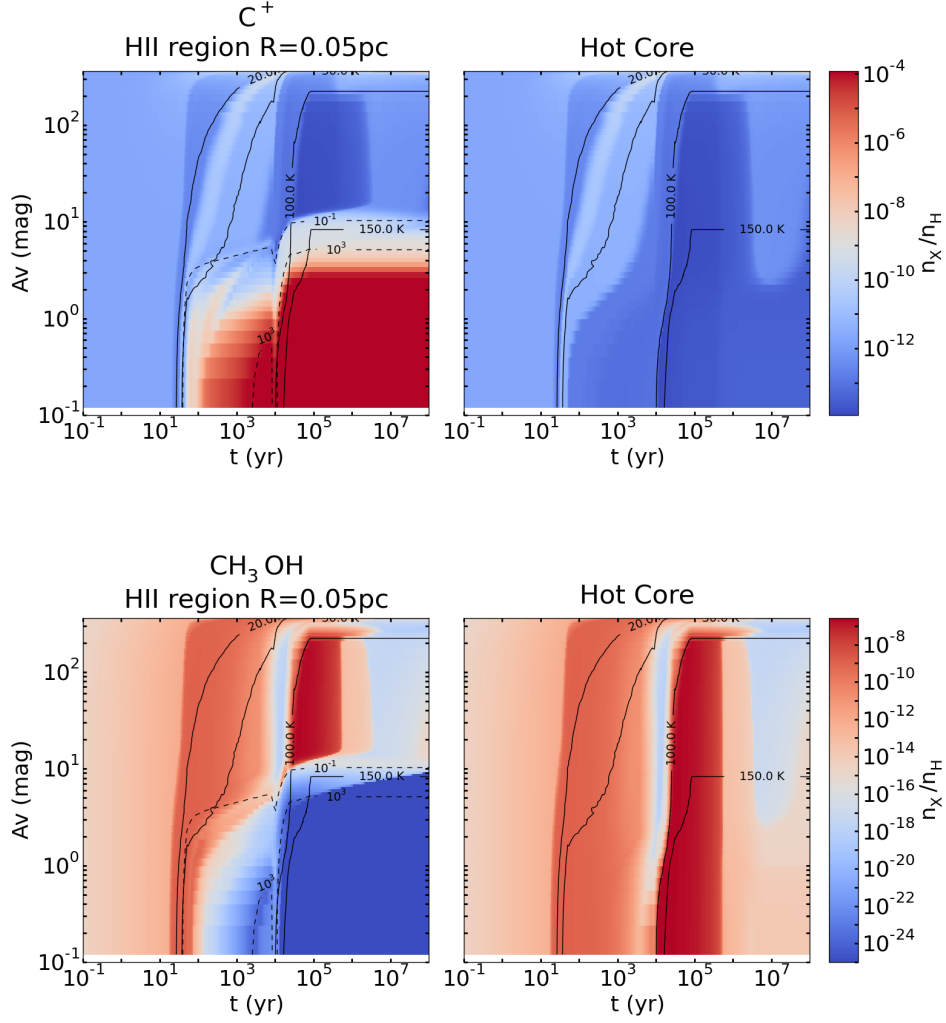
Figure 6.8: Abundances of C^+ and CH_3OH as a function of time (x-axis) and visual extinction (y-axis) for the HII region (left panel) and HHMC (right) models. The solid black lines represent the contours for the temperature: 20, 30, 100 and 150 K and the dashed black lines represent some contours for the radiation field intensity: 10^{-1} and 10^3 Draine unit.

the evolution. The atomic-ionized region extends from 0 to 10 mag, from about 10^3 years for $A_V < 1$ mag and from 10^4 years between 1 and 10 mag. The transition from the grain region to the molecular-atomic region is sudden close to the HII region, up to 1 mag, as the radiation field increases extremely fast and smoother deeper in the core as only the temperature influences the chemistry there. This is called the transition region. This atomic-ionized region starts earlier (t $\sim$ 200 years) for N-bearing and O-bearing species for $A_V < 5$ mag, and is mainly atomic.

In both cases, for C^+ because it is very abundant $- \sim 10^{-4} -$ and for methanol as it is not abundant $- < 10^{-20}$, we clearly see the period when the PDR appears in the HII region model and the extinction until which it extends. It is formed at approximately 10^2 years, and extends up to 1 mag until 10^4 years and up to 10 mag later. The formation of the PDR and the molecules specific to it like C^+ arises from the increase in the radiation field intensity χ_0. Stronger the radiation field is, higher the abundance of C^+ is. The radiation

field induces photo-dissociation reactions which are not happening in the HHMC model because $\chi_0 = 10^{-20}$ Draine unit.

It does not emerge from these two species abundances profiles but in the HHMC model the desorption of molecules, in the region where the extinction is lower than 10 mag, is delayed by at most 10^4 years compared to the HII region model. For instance, it is the case for one of the main O-bearing molecule, H_2O, and one of the main N-bearing molecule, NH_3. But for molecules like CO which has a low desorption energy the desorption is not delayed. The desorption happens earlier for the HII region model as it is not only thermal desorption taking place but also photo-desorption.

In the PDR, the main formation mechanism for C^+ is of course the photo-dissociation of C. The photo-dissociation of methanol is the main destruction reaction for CH_3OH until 10^4 years when reaction with C^+ becomes the main destruction reaction. But at this time the dominant reaction is the following formation reaction: $CH_5O^+ + e \longrightarrow CH_3OH + H$, hence the slight increase in the abundance near the ionization front, up to 10^{-20} which is still negligible as it remains really low.

In Sec. 6.1 we detailed the reasons of the increased abundance of methanol around 50 years. For the HII region model another reactive desorption reaction is involved: s-$OH + s\text{-}CH_3 \longrightarrow CH_3OH$. It becomes significant around 60 years even if it is still less than the two other reactions. But at the same time, destruction of methanol by photo-dissociation occurs and the abundance decrease from about 10^{-9} at 20 years to 10^{-13} at 100 years.

Synthetic spectra and Integrated intensity profiles: In Fig. 6.9 we show the time evolution of the synthetic spectra for H_2CO (2(0,2)–1(0,1)) for the HII region (black) and HHMC (blue) models. We see that the intensity of the lines for the HII region model is higher until 10^4 years (by ~ 0.2 K at the beginning and then ~ 0.03 K), equal at this time and then higher again (by ~ 0.03 K) until $\sim 4\times10^4$ years. After the HHMC model intensity is about $0.10 - 0.20$ K higher. Before 10^4 years there is a region where H_2CO is very abundant, almost 10^{-6}, which follows the temporal evolution of the radiation field when it is higher than 10^{-1} Draine unit (see Fig.A.74). This is the transition region (Fig. 6.7) and it delimits the PDR from the grain surface region and from the molecular region. At 10^3 years a region with higher abundance of H_2CO appears for the HHMC model, inducing higher line intensities. But this region in the HHMC model is more constrained spatially, $A_V < 1$ mag, and thus the intensity remains lower than for the HII region model. At 10^4 years, the abundance of H_2CO decreases in the aforementioned region but increases deeper into the core. The intensity of the line still increases but it is now equal to the intensity of the HHMC model. After 10^4 years H_2CO is photo-dissociated until $A_V \sim 5$ mag but the region where the abundance are higher and follow the radiation field is still present around $A_V \sim 10$ mag and until 10^5 years. This region is not present anymore for the HHMC model. The intensity of H_2CO is then higher for the HII region model.

In Fig. 6.10 we present the integrated intensities as a function of time for $HC^{15}N$ (left panel) and CH_3OH (right). The HII region model is represented by the black lines and the HHMC model by the blue lines. For both molecules the evolution is similar for the HII region and HHMC models except at the beginning of the evolution for $HC^{15}N$ where the HHMC model has a stronger emission, of about one order of magnitude around 2×10^3 years; and from 10^4 to 3×10^4 years for CH_3OH where the HHMC emission is higher by almost two orders of magnitude. The trend of the curves has already been detailed in
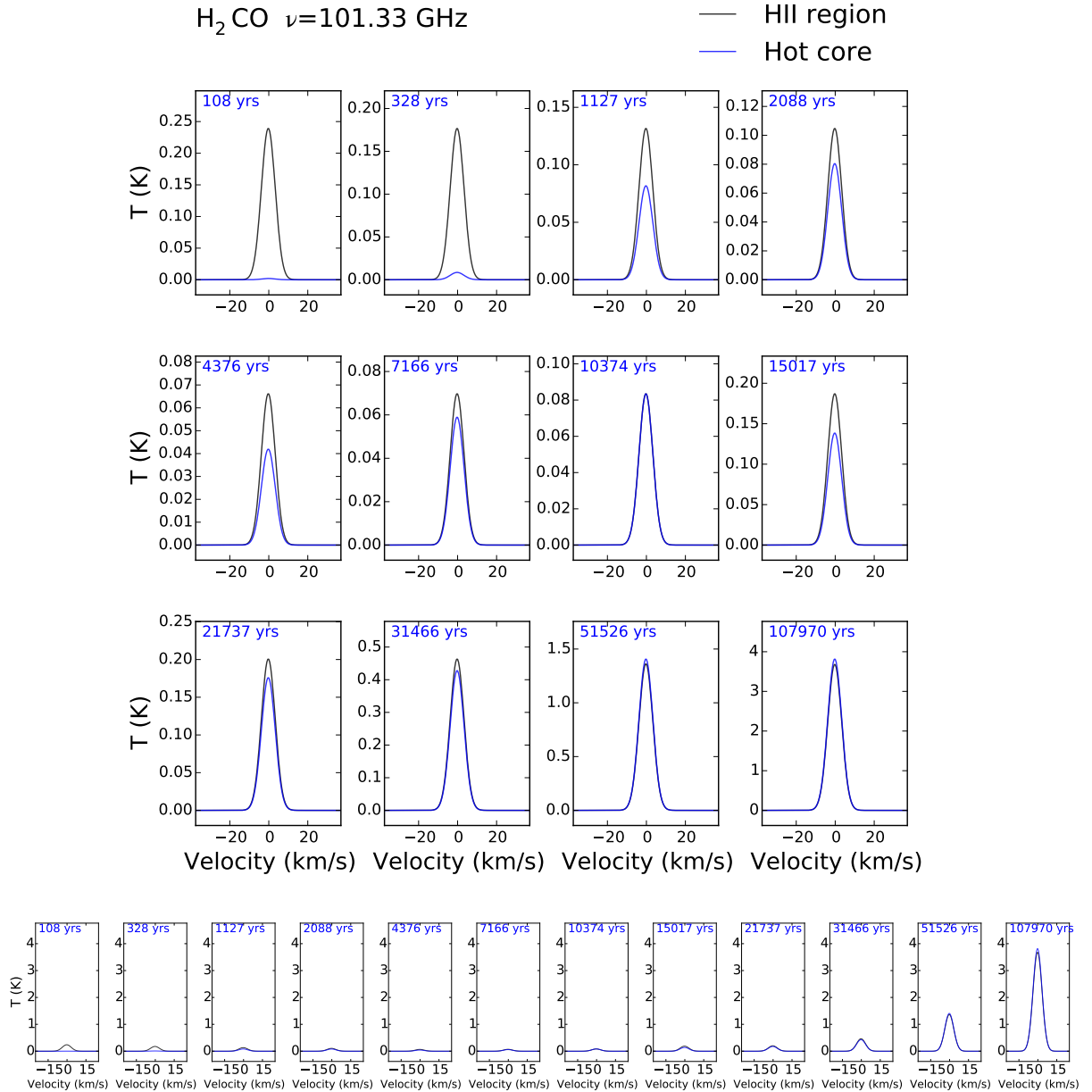
Figure 6.9: Time evolution of H_2CO (2(0,2)–1(0,1)) spectra for the HHMC model in blue and the HII region model in black. The bottom panel shows the same spectra but with the same scale on the y-axis.

Sec. 6.1 for the HHMC model and the HII region model trend is similar. In general the HHMC model emission is higher, about one order of magnitude, at the beginning of the evolution except for C and H_2CO. This is because the PDR starts to form at 10^2 years and the abundance of these species starts to decrease due to photo-dissociation. For C, the HII region emission is more than order of magnitude higher than the HHMC model until 2×10^4 years (see Fig. A.198), because the abundance of C in the forming PDR is two orders of magnitude higher (see Fig. A.197), and then they have similar emission as C is ionized. Only C^+ and O exhibit extremely different results as they are undetectable for the HHMC model (see Fig. A.216 and A.234 respectively) but have integrated intensities going from 10^{-2} to $100\,\mathrm{K\,km\,s^{-1}}$ for C^+ and from 0.6 to $100\,\mathrm{K\,km\,s^{-1}}$ for O. The latter is
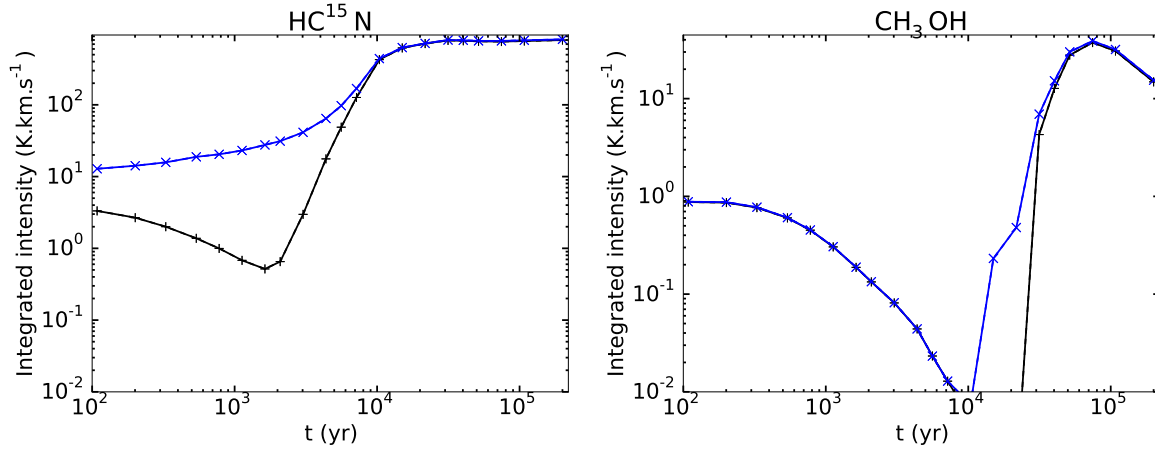
Figure 6.10:   Time evolution of integrated intensities for $HC^{15}N\,(1\text{--}0)$ (left panel) and $CH_3OH\,(2(2,1)\text{--}3(1,2))$ (right). The black lines represent the HII region model and the blue one the HHMC model.
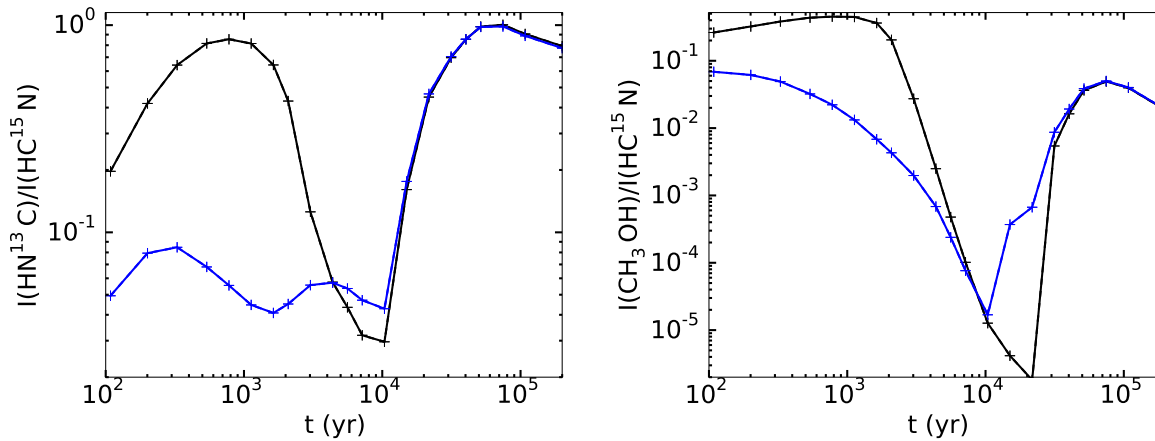
Figure 6.11: Time evolution for HII region (black) and HHMC (blue) models of integrated intensity ratio $(I(X_i)\,/\,I(HC^{15}N\,(1\text{--}0)))$. X_i is $HN^{13}C\,(1\text{--}0)$ (left panel) and $CH_3OH\,(2(2,1)\text{--}3(1,2))$ (right). The black lines represent the HII region model and the blue ones represent the HHMC model.

actually optically thick after 10^4 years. The emission of these two atoms comes from the PDR where they are the dominant species along with N.

Integrated intensity ratios: We present the time evolution of the integrated intensity ratios `raHNC` and `raCH3OH` in Fig. 6.11. The black lines represent the HII region model and the blue lines the HHMC model. We note that the late evolution for both models is similar for these two molecules. This is also the case for all the other molecules except for C^+ and O. For `raH2CO`, the HII region models ratio is higher by one to two orders of magnitude before 10^4 years when it becomes equal to the HHMC model ratio (see Fig. A.79). The other ratios presenting this behavior are `raC`, `raCN`, `raHCO`, `raHCO+` and `raN2H+` (see Fig. A.199, A.119, A.39, A.59 and A.159 respectively). This is because the integrated intensity of $HC^{15}N$ in the HII region model is lower than for the HHMC model whereas the integrated intensities for the other molecules are equal or superior to the HHMC model. For the other ratios, the ratio of the HII region model is also bigger until 10^4 years, then the ratio of the HHMC model becomes higher also by one to two
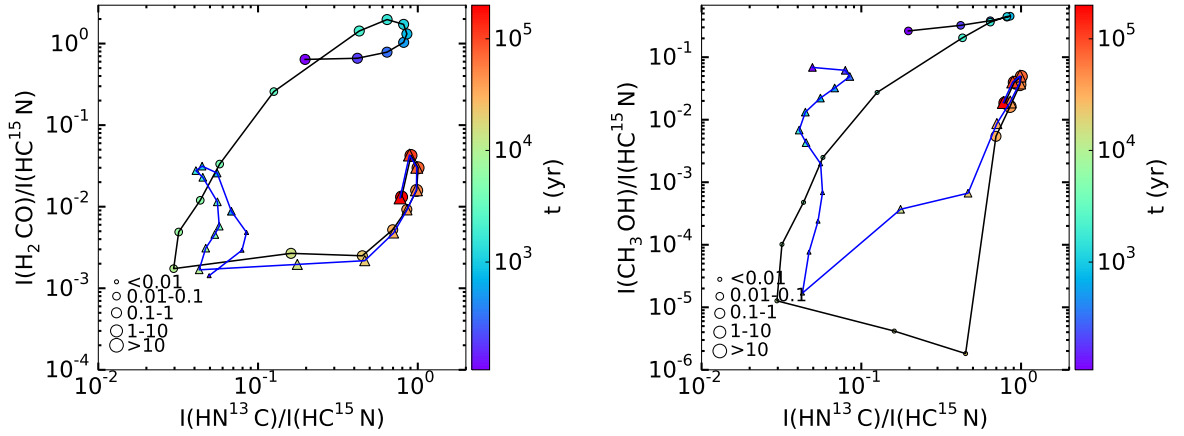
Figure 6.12: Time evolution for the HII region (black line and circle markers) and HHMC (blue line and triangle markers) models of the integrated intensity ratio ($I(\mathsf{X}_i)$ / $I(\mathrm{HC^{15}N}\,(1\text{--}0))$) as a function of the integrated intensity ratio ($I(\mathrm{HN^{13}C}\,(1\text{--}0))$ / $I(\mathrm{HC^{15}N}\,(1\text{--}0))$). X_i represents $\mathrm{H_2CO}\,(2(0,2)\text{--}1(0,1))$ (left panel) and $\mathrm{CH_3OH}\,(2(2,1)\text{--}3(1,2))$ (right). The size of the markers corresponds to the range value of the peak intensity in Kelvin of $\mathrm{H_2CO}$ and $\mathrm{CH_3OH}$.

orders of magnitude until 3×10^4 years and finally they are both equal. The ratio for the HHMC model is higher during this short period because the intensities for the HHMC model are higher.

For `raH2CO`, `raC`, `raCN`, `raHCO`, `raHCO+` and `raN2H+`, the ratio of the HII region model increases until approximately 3×10^3 years then it decreases because the integrated intensity of $\mathrm{HC^{15}N}$ increase and decrease. The ratio of the HHMC model slowly increases compared to the HII region ratio, from 2 to 7 for CN for instance in the HHMC and from 10 to 300 for the HII region model. It starts to decrease at the same time as the ratio of the HII region model decrease. This decrease covers two orders of magnitude at least except for `raC` for which it is less than one. This behavior is due to the fact that the integrated intensity of $\mathrm{HC^{15}N}$ slowly increases but it is a bit faster after $\sim 3\times10^3$ years. Only the ratio `raH2CO` shows a different behavior after 10^4 years because instead of decreasing the ratio increases by one and half order of magnitude because the integrated intensity of $\mathrm{H_2CO}$ increases. For the rest of the ratios, they start with an increase until 3×10^3 years because the intensity of $\mathrm{HC^{15}N}$ decreases or slowly increase compared to the intensity of the other molecules. This is followed by a decrease of several orders of magnitude for the HII region model. The ratio for the HHMC model are constant or slightly decreasing by less than one order of magnitude. For `raCH3OH` as shown in Fig. 6.11 the decrease for the HHMC model covers at least three orders of magnitude but is still less important than the decrease for the HII region model of about five orders of magnitude. Then from 10^4 years they all increase.

Integrated intensity ratio – ratio: In Fig. 6.12 we show the integrated intensity ratios `raH2CO` and `raCH3OH` as a function of the ratio `raHNC` for the HII region (black lines and circle markers) and the HHMC models (blue lines and triangle markers). In the same way as for the time evolution of the integrated intensity ratios, the late evolution is similar for both models because of similar integrated intensities. The ratios `raH2CO` and `raCH3OH` vary less for the HHMC model and this is the same for the other ratios, except `raHNC`, of the HHMC model. If we do not consider $\mathrm{C^+}$ and O for which both models have totally

different behaviors, the patterns showing the biggest differences between the HII region and the HHMC models are for CH_3OH, $H_2^{18}O$ and NH_3. These two last molecules are unfortunately undetectable until $\sim 10^4$ years for the HHMC model and $\sim 3\times10^4$ years for the HII region model. And methanol is not detectable from $\sim 4\times10^3$ years to 10^4 years for the HHMC model and 3×10^4 years. And when it can be considered detectable its intensity remains really low (< 1 K) most of the time.

Except for CH_3OH and C^+, all patterns for the HII region model look like a "c" or an unclosed "e". The end of the evolution varies a bit from one figure to another. For NH_3 and $H_2^{18}O$ the tail of the "c" goes up closing the pattern. For HCO and CN it goes down. The pattern related to C^+ has more the shape of a "9" we would start from the bottom. For CH_3OH the shape looks more like a "u". The patterns for the HHMC model are more diverse. The one that resembles the most the pattern of the HII region is for CH_3OH with the shape of a "v".

If we relate this comparison to the one done in Sec. 6.1, using the integrated intensities, we see that C^+, O are undetectable in the HMC model and have high intensities, increasing with time, in the HII region. C emission is stronger in the HII regions more than two times until 10^4 years and then more than one order in magnitude. On the contrary CH_3OH and $H_2^{18}O$ have a stronger emission for the HMC model, more than two orders of magnitude at the beginning of the evolution and more than three times higher at the end. The trend they present with high differences for early times and less at the end is common to H_2CO, NH_3 and $HC^{15}N$ as well. After $\sim 10^4$ years the intensities tend to equality and the difference between the HMC and the HII region models is of a factor $2-3$ or less. For CN, the emission of both models becomes equal from 9×10^3 to 3×10^4 years approximately. HCO and $HN^{13}C$ have the same emission after 10^4 years, even before for HCO^+ and N_2H^+ has the same intensity for the HII region and the HMC during the whole evolution.

Only five of the studied molecules present a clear distinction between the HII region and the HMC model. C^+, C and O seems to trace the HII regions and the PDR whereas CH_3OH and $H_2^{18}O$ may trace the HMC and a medium where the radiation field is weak and does not influence the chemistry. In the assumption that the object is young, less than 10^4 years, we could use CN, $HN^{13}C$, HCO, H_2CO, NH_3 and $HC^{15}N$ to trace the HMC. The non detection of these species could indicate that the HII region is not formed yet. NH_3 and HCO^+ appear to not be good tracers for any of the regions.

Summary of the section:

In this section we compare a HII region model to the previous section HHMC model.

Once we include the evolution of the radiation field to compute the relative abundances with *Saptarsy* an internal PDR is formed at the interface between the HII region and the molecular cloud. We can see that typical PDR species like C^+ are formed by ionization in the region with a strong UV field while some others like HCN or CH_3OH are not.

The line emission for C^+ and O are stronger in the HII region model. This is also the case for C despite weaker lines and the same emission for both models after 2×10^4 years. Thus, C^+, O and C seems to be potential tracers of internal PDRs. For other species their emission in both models are equal or their emission in the HHMC model is slightly stronger, and the HMC model emission is stronger than the HII region model emission.
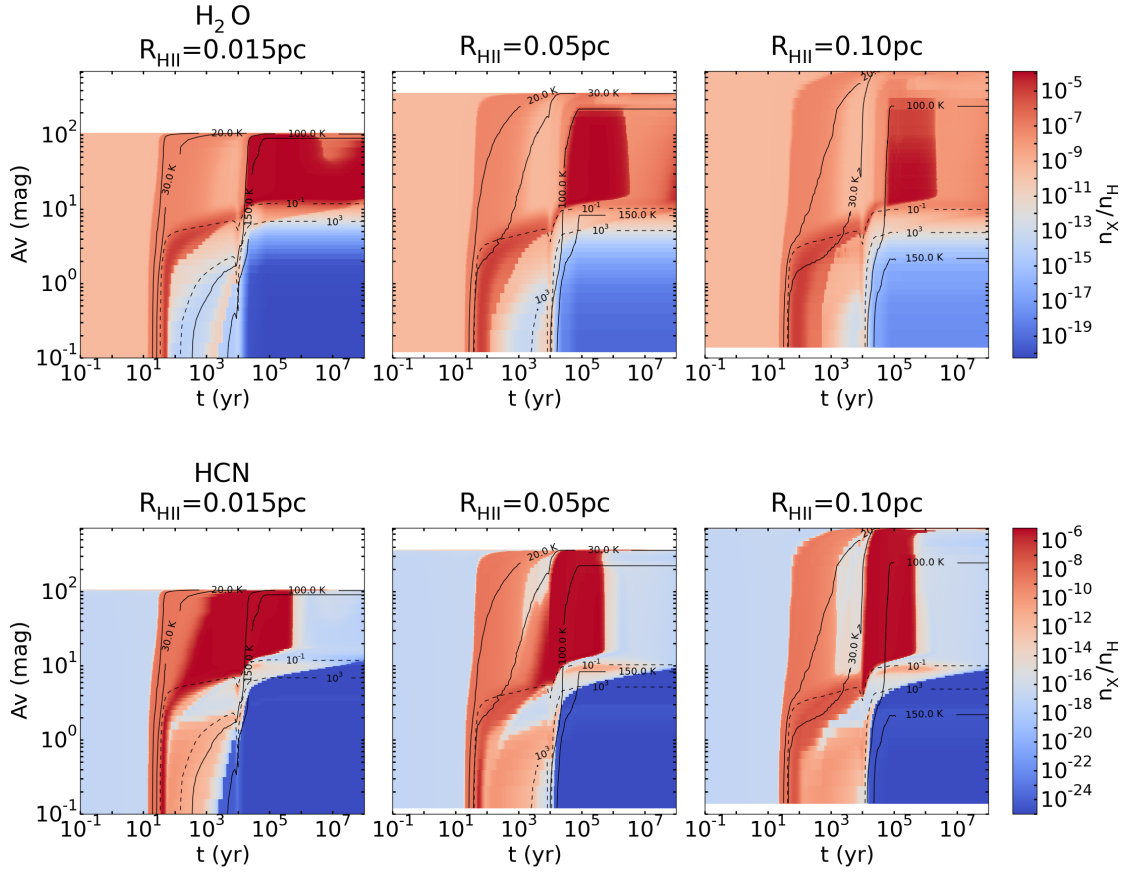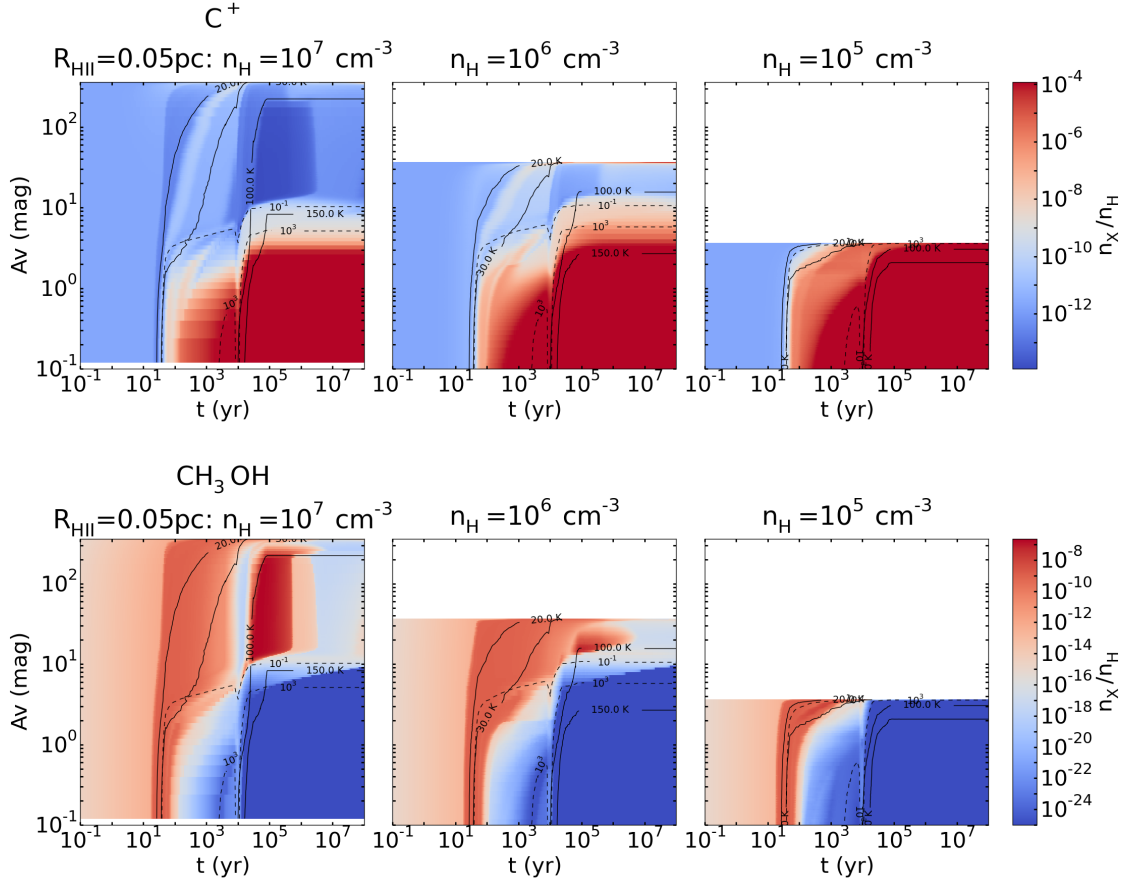
Figure 6.13: Abundances of H_2O and HCN as a function of time (x-axis) and visual extinction (y-axis) for HII region models with different sizes: 0.015 pc (left panels), 0.05 pc (middle) and 0.10 pc (right). The solid black lines appearing on the figures represent the contours for the temperature: 20, 30, 100 and 150 K and the dashed black lines represent some contours for the radiation field intensity: 10^{-1} and 10^3 Draine unit.

6.3 HII region size

Abundance profiles: In Fig. 6.13 we present the abundances profiles for H_2O (upper panels) and for HCN (lower). For the smallest size of HII region, i.e. $R_c = 0.015$ pc, the desorption at $A_V \sim 100$ mag happens at the same time as for $A_V = 1$ mag, but for the biggest size model, i.e. $R_c = 0.10$ pc, the desorption of species occurs at ~ 50 years at $A_V = 1$ mag and at approximately 10^3 years at $A_V = 100$ mag. Because the temperature increases slower into the core for models with bigger sizes of ionized cavity, the desorption of species is delayed in time.

We see that the molecular area, approximately defined as $10 \leq A_V \leq 200$ mag and $t \geq 10^4$ years, is more extended when the size of the ionized cavity decreases. We have high abundances of H_2O and HCN, $> 10^{-6}$ and $> 10^{-7}$ respectively, for a longer period of time for extinction above ~ 10 mag. For H_2O this period extends from approximately 2×10^4 to 5×10^6 years for a size of 0.015 pc, from 3×10^4 to 3×10^6 years for 0.05 pc and from 6×10^4 to 2×10^6 years for a size of 0.10 pc. For HCN, it extends from approximately 6×10^2 to 6×10^5 years for a size of 0.015 pc, from 10^4 to 5×10^5 years for 0.05 pc and from
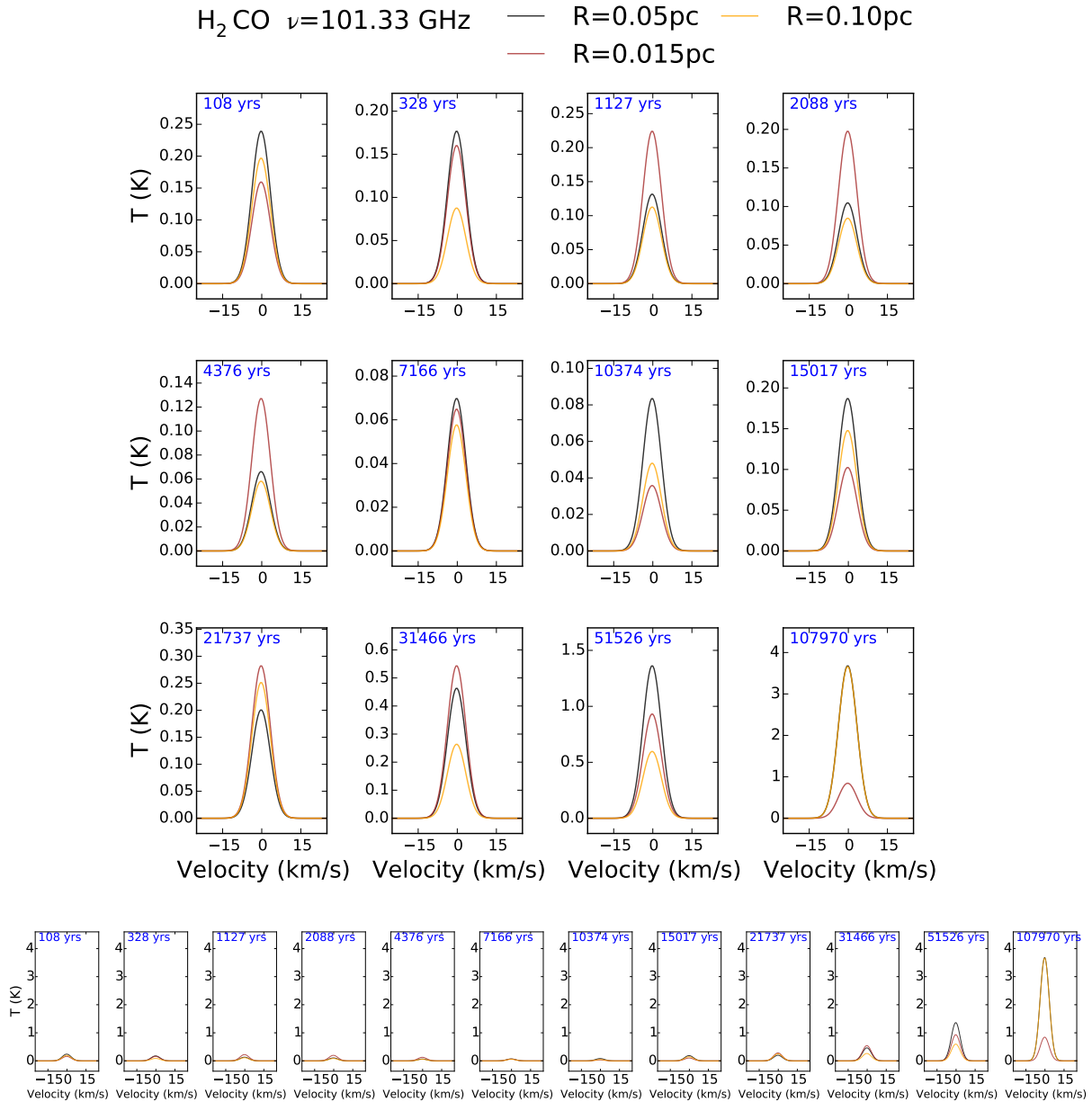
Figure 6.14: Time evolution of $H_2CO\,(2(0,2)$–$1(0,1))$ spectra for different HII region sizes: 0.05 pc in black, 0.015 pc in brown and 0.10 pc in orange. The bottom panel shows the same spectra but with the same scale on the y-axis.

10^4 to $5{\times}10^5$ years for a size of 0.10 pc. The reason is that for the same extinction the temperature is higher and increases faster for the smallest cavity because this is closer to the star.

In the case of H_2O, we can see that the abundances near the ionization front, up to 10 mag, are higher when the size of the ionized cavity increases – at 10^3 years: $\sim 10^{-12}$ for a size of 0.015 pc, 10^{-10} for 0.05 pc and 10^{-9} for 0.10 pc. This is also the case for a lot of species like CO, CH_3OH, CS or HCO and even grain surface species (see also for example Fig. A.100 for CH_3OH, B.8 for CO or A.40 for HCO). But few others, mostly small ionized species like C^+, C_2^+, C_2H^+ or CN^+, exhibit the opposite behavior (see Fig. A.218 for C^+). This is because the formation of the PDR is delayed for bigger sizes of cavity as the
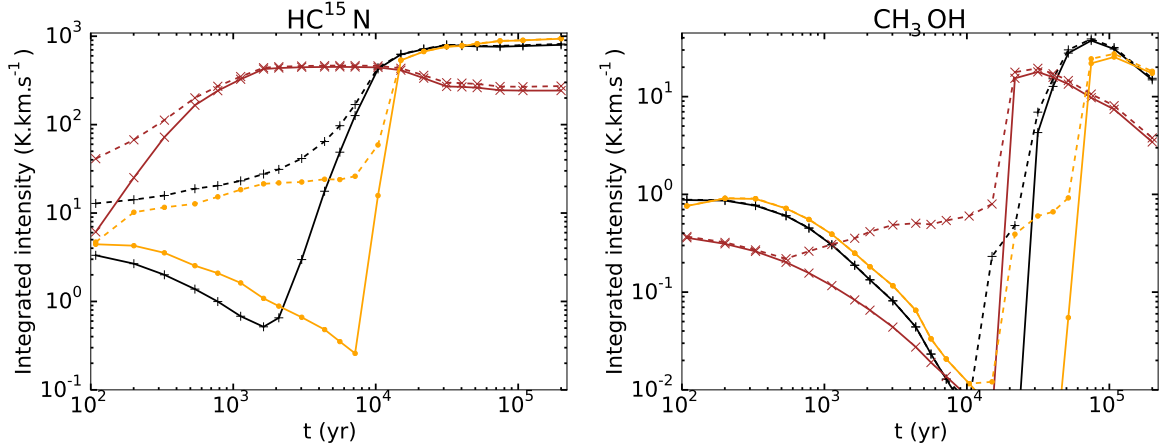
Figure 6.15:   Time evolution of integrated intensities for $HC^{15}N\,(1–0)$ (left panel) and $CH_3OH\,(2(2,1)–3(1,2))$ (right) for models with different sizes of ionized cavity: 0.015 pc (left), 0.05 pc (middle) and 0.10 pc (right). The solid lines represent the HII region models and the dashed lines the HHMC models.

radiation field is less strong.

In the case of HCN, we can notice a decrease of about four orders of magnitude in the abundance, for $A_V > 10$ mag and between 10^3 and 10^4 years, for the model with the biggest size of ionized cavity $R_c = 0.10$ pc. It becomes less important for a size of 0.05 pc and does not appear for the model with the smallest size. This is also seen for H_2O but the decrease in the abundances is only of about one order of magnitude. Other species such as HNC, HNC^+ or CH_3OH also present the same gap. The reason for this gap is that during this period of time the molecules harbouring the gap react first with H_3^+ and then N_2H^+, principally, and second with HCO^+ because these two species have an increased abundance. In addition, accretion is still a dominant reaction during that period. HCO^+ is also formed by reaction with N_2H^+ which is formed on a short period around 300 years by reaction with H_3^+. And because they react with other species N_2H^+ and then HCO^+ have lower abundances after 10^3 years for the model with $R_c = 0.015$ pc, 10^4 years for R_c = 0.05 pc and $\sim 2 \times 10^4$ years for $R_c = 0.10$ pc.

Synthetic spectra and Integrated intensity profiles: In Fig. 6.14 we show the time evolution of the synthetic spectra for $H_2CO\,(2(0,2)–1(0,1))$ for HII region models with different sizes of ionized cavity: 0.015 pc (brown), 0.05 pc (black) and 0.10 pc (orange). This molecule has the hardest behavior to describe, compared to the other selected molecules, because the intensities fluctuate a lot and one model is never dominant compared to another. It seems that at the beginning of the evolution until 8×10^3 years the intensity is higher when the size of the cavity is smaller, with a difference of 0.05 K between the models *r0.015* and *r0.05*, but the first hundred years do not show it. After 8×10^3 years no clear trend can be seen. All the intensities increase but not at the same rate, hence one model can have a stronger H_2CO emission for some time and then it is another one.

In Fig. 6.15, we present the integrated intensities as a function of time for the same models (same colors) for $HC^{15}N$ and CH_3OH. The HII region models are represented with solid lines and the HHMC model with dashed lines. We do not observe a general trend in the evolution of the integrated intensities from one molecule to another. Along with

H_2CO, CN is also a molecule which does not show a clear trend (see also for example Fig. A.121). Intensities for C^+ and O are stronger for the smallest HII regions, by one order of magnitude at the beginning and two times higher at 10^5 years, and they increase with time and there is no emission coming from the HHMC models (see Fig. A.219 and A.237). The smallest cavity has a stronger C^+ emission as the PDR form earlier due to stronger radiation. Because of the stronger radiation the PDR is also more extended and so the intensity at 10^5 years is also higher. In addition a small gap at 10^4 years appears for C^+ and is due to the decrease of radiations as the proto-star is bloated.

For every molecule there is a change in the trend around 10^4 years. Intensities for the smallest cavity suddenly decreases, the ones for the model with a size of 0.05 pc go through a maximum and for a size of 0.10 pc they suddenly increases. It seems that for most molecules, except CH_3OH, $HN^{13}C$ and N_2H^+, the emission for the smallest size of ionized cavity is stronger, until this critical time, by one order of magnitude compared to the emission of model *r0.05* which has an emission really similar to model *r0.10*. For CH_3OH and $HN^{13}C$, the intensity of *r0.015* is lower before 10^4 years. After 10^4 years, the emission of model *r0.10* seems to dominate. It is not very strong compared to model *r0.05* but is one to two orders of magnitude higher than model *r0.015* because the size of its molecular region is smaller. In the case of N_2H^+, the emission is always stronger for the biggest cavity model (about twice bigger at 10^2 years and five times higher at 10^5 years) and lower for the smallest cavity (about two times and ten times lower at 10^2 years and 10^5 years respectively).

We notice that for $HC^{15}N$, $HN^{13}C$, H_2CO and CH_3OH the lines intensity increase and this increase is delayed when the HII region size increases. In the case of $HC^{15}N$ it happens at 10^4 years for a size of 0.10 pc whereas it happens at 2×10^3 years for a size of 0.05 pc and seems to start before 100 years for the smallest cavity. This is related to the delay in the desorption of the corresponding grain species. Furthermore, after this increase in the intensity, the emission for the smallest cavity model seems to be the smallest, about five times smaller for $HC^{15}N$ and CH_3OH as seen in Fig. 6.15. This is likely due to the smaller size of the molecular region of this model.

The comparison between the HHMC and the HII region models does not differ from the one made in the previous section. When changing the size of the ionized cavity we only change the time when the intensity increase or decrease as well as the difference of intensity between the two models. For example, if we look at CH_3OH, the HHMC intensity becomes stronger than the HII region intensity at 10^3 years for model *0.015* instead of 10^4 years for model *r0.05*. This is because methanol is destroyed earlier in the HII region model due to a higher radiation field.

Integrated intensity ratios: The time evolution of integrated intensity ratios for model *r0.015* (brown), *r0.05* (black) and *r0.10* (orange) is shown in Fig. 6.16 for `raHNC` (left panel) and `raCH3OH` (right). The ratio `raHNC` is similar for the models *r0.05* and *r0.10* and lower by two orders of magnitude for model *r0.015* until 10^3 years. Then `raHNC` seems higher for the biggest HII region model until $\sim 10^4$ years and the ratio for model *r0.05* becomes the smallest at 3×10^3 years. The ratio seems smaller for bigger HII regions. After 5×10^4 years the ratio is again bigger for bigger HII regions. In addition all sizes seem to have the same trend but with a time delay. For `raHNC` a minima appears at 4×10^2 years for *r0.015*, at 8×10^3 years for *r0.05* and at $\sim 1.5\times10^4$ years for *r0.10*. And for `raCH3OH` a minima appears at about 1.5×10^4 years for *r0.015*, at 2×10^4 years for *r0.05* and at $\sim 4\times10^4$ years for *r0.10*. Delays in minima and maxima of ratios is also
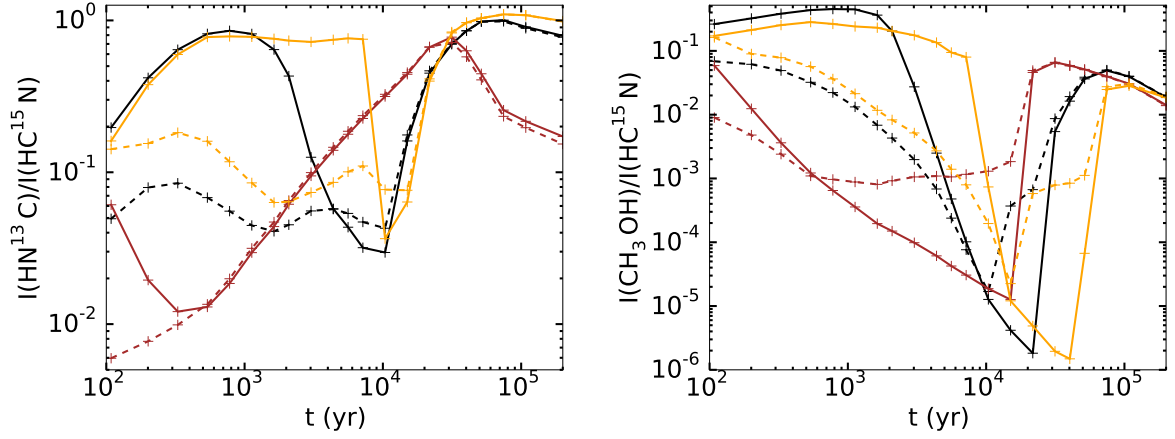
Figure 6.16: Time evolution of integrated intensity ratio $(I(X_i) / I(HC^{15}N\,(1\text{–}0)))$ for models with different sizes of ionized cavity: 0.015 pc (brown), 0.05 pc (black) and 0.10 pc (orange). X_i is $HN^{13}C\,(1\text{–}0)$ (left panel) and $CH_3OH\,(2(2,1)\text{–}3(1,2))$ (right). The solid lines represent the HII region models and the dashed lines the HHMC models.
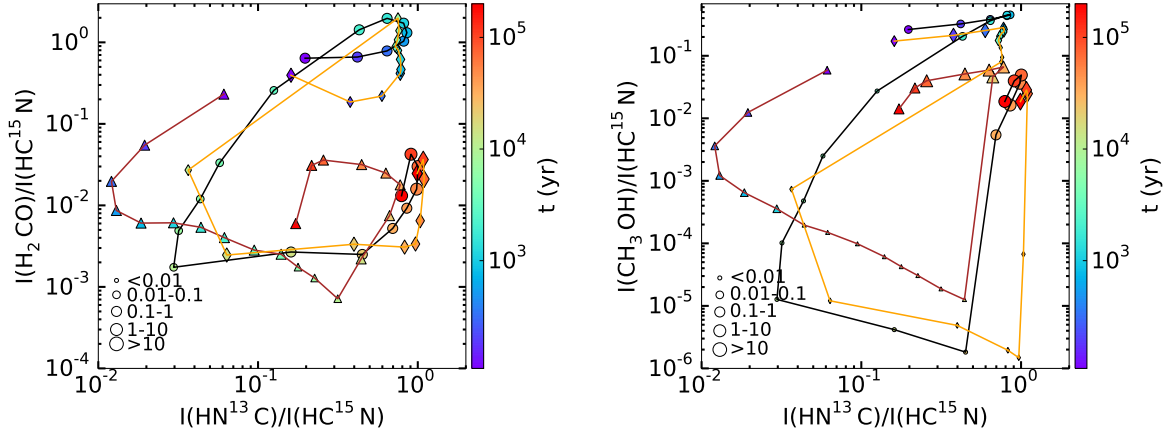
Figure 6.17: Time evolution of the integrated intensity ratio $(I(X_i) / I(HC^{15}N\,(1\text{–}0)))$ as a function of the integrated intensity ratio $(I(HN^{13}C\,(1\text{–}0)) / I(HC^{15}N\,(1\text{–}0)))$ for HII region models with different sizes of ionized cavity: 0.015 pc (brown line and triangle markers), 0.05 pc (black line and circle markers) and 0.10 pc (orange line and diamond markers). X_i represents $H_2CO\,(2(0,2)\text{–}1(0,1))$ (left panel) and $CH_3OH\,(2(2,1)\text{–}3(1,2))$ (right). The size of the markers corresponds to the range value of the peak intensity in Kelvin of H_2CO and CH_3OH.

seen in the HHMC models. The same way than for the integrated intensity this is likely due to the delay in the desorption of the species when the size of the cavity increases as the radiation is not as strong inducing a lower temperature and radiation field intensity.

Integrated intensity ratio – ratio: In Fig. 6.17 we show the integrated intensity ratios `raH2CO` and `raCH3OH` as a function of the ratio `raHNC` for the HII region models. The different sizes of ionized cavity are represented as follows: 0.015 pc (brown lines and triangle markers), 0.05 pc (black lines and circle markers) and 0.10 pc (orange lines and diamond markers). The pattern is very similar for each model. They are just scaled as a function of ratios obtained for each of them.

Summary of the section:

In this section we have compared the chemistry for HII region models with sizes of ionized cavity: one closer to the HCHII region size (0.015 pc), the reference one (0.05 pc) being a UCHII region and the last one (0.10 pc) being at the transition between UCHII region and Compact HII region.

A bigger size of the ionized cavity implies a lower incident radiation field and a slower increase of the temperature and radiation field in the core. The internal PDR is formed a bit later for bigger HII region models and the molecular region/area is smaller.

A lower radiation field intensity for bigger ionized cavities models induces a weaker emission of C^+ and O. In the case of N_2H^+ the emission is stronger for the models with bigger HII region. For the other studied species the emission varies in time.

6.4   Density at the ionization front

Abundance profiles: We compare in Fig. 6.18 models with different densities at the ionization front: 10^7 (left panels), 10^6 (middle) and 10^5 cm^{-3} (right) for models *mHII:n7*, *mHII:n6* and *mHII:n5*) respectively. The upper panels display C^+ abundance and the lower panels show CH_3OH abundance. We see that the PDR is more ionized for lower densities as most of the ions abundances are higher at lower densities. This is also true in other regions of the core as seen for C^+ between the 20 and 30 K contours for an extinction higher than 3 mag. The abundance for model *n7* is between one to two orders of magnitude lower than for model *n6*. This could be due to CR reactions being more significant at lower densities. Radicals also have higher abundances everywhere in the core and during the whole evolution when the density is smaller.

In the forming PDR, from 100 to 10^4 years and for extinction up to $2 - 3$ mag, the abundances of gas phase molecules such as CH_3OH or HCN as well as grain species is slightly lower when the density of the core is lower because the ions and radicals are more abundant. In addition the size of the molecular area is smaller. As seen for methanol, the abundance are high after 100 K from 10 to 200 mag (which corresponds to approximately from 10400 AU to 14500 AU) for model *n7* and from about 15 mag to 25 mag (i.e., from 12800 AU to 16100 AU) for model *n6*. This region does not appear for model *n5* as it is almost fully ionized. This is because the size of the PDR, which does not depend on the temperature, is bigger. The radiation penetrates further as they are less attenuated and so we reach a temperature of 100 K, temperature when methanol desorbs, when we just crossed of the PDR.

Synthetic spectra and Integrated intensity profiles: In Fig. 6.19 we show the time evolution of the synthetic spectra for H_2CO (2(0,2)–1(0,1)) for HII region models with different density at the ionization front: 10^5 cm^{-3} (pink), 10^6 cm^{-3} (red) and 10^7 cm^{-3} (black). We see that the H_2CO emission of model *n5* is very low, always inferior to 0.05 K until about 10^4 years and then it is undetectable for all the other times. This is also the case for the other selected molecules except C^+ and O as the medium is almost entirely ionized after 10^3 years. Otherwise, we see that the emission for model *n6* is stronger than for model *n7* from 3×10^2 years, with a difference of about 0.1 K, to 2×10^4 years, with a slightly bigger difference of 0.15 K. This is due to higher abundance of H_2CO in the transition region. After 2×10^4 years, the line for model *n7* becomes higher, more than
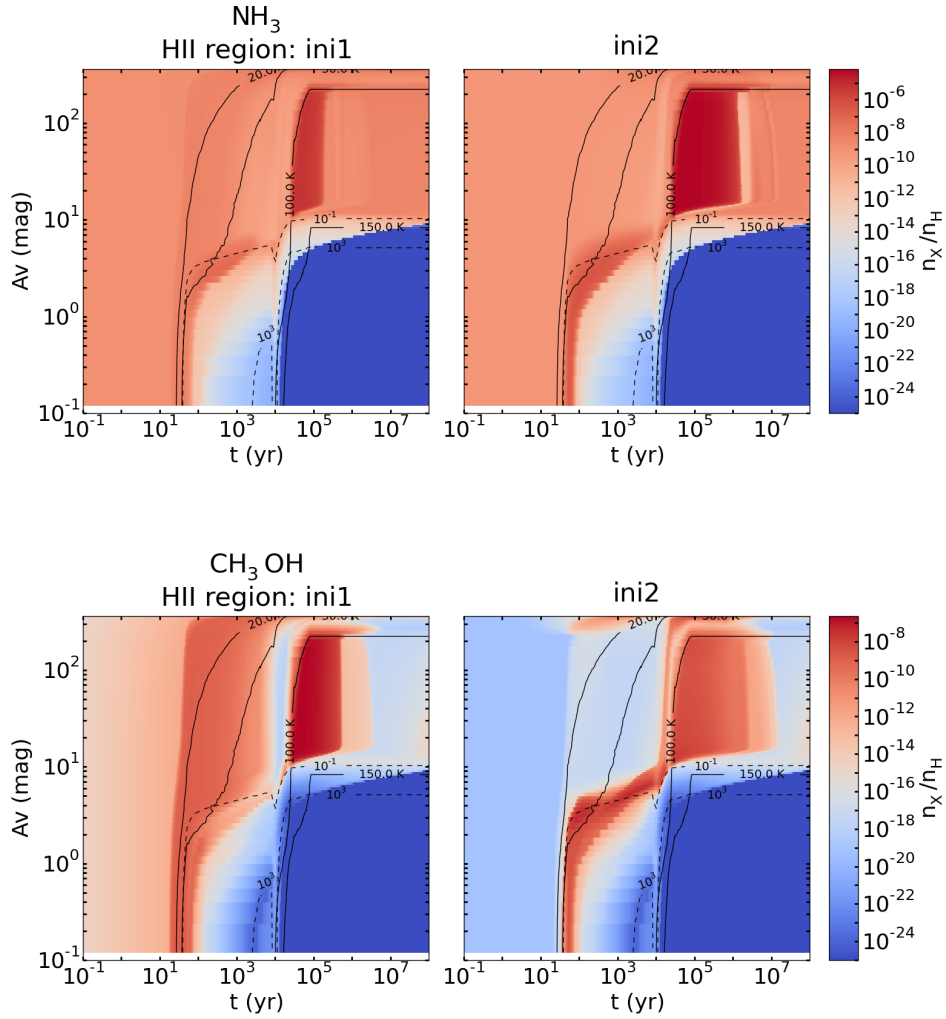
Figure 6.18: Abundances of C^+ and CH_3OH as a function of time (x-axis) and visual extinction (y-axis) for HII region models with different densities at the ionization front: 10^7 cm^{-3} (left), 10^6 cm^{-3} (middle) and 10^5 cm^{-3} (right). The solid black lines appearing on the figures represent the contours for the temperature: 20, 30, 100 and 150 K and the dashed black lines represent some contours for the radiation field intensity: 10^{-1} and 10^3 Draine unit.

0.3 K at 3×10^4 and 3 K at 10^5 years. This is because the abundances of H_2CO are a bit higher but more importantly it spreads on a larger (spatial) scale.

In Fig. 6.20 we show the time evolution of the integrated intensity of HC^{15}N and CH_3OH for the different density at the ionization front: 10^5 cm^{-3} (pink), 10^6 cm^{-3} (red) and 10^7 cm^{-3} (black). The HII region models are represented with solid lines and the HHMC models with dashed lines. The line intensities behave similarly to models described in the previous sections. Only the intensity is scaled as a function of density. For model *mHII:n5*, the intensity drops of one to more orders in magnitude until $\sim 10^3$ years. Then, no lines are detectable except for $C^+$and O because the medium is atomic and ionized (see Fig. A.222 and A.240). Thus, *mHHC:n5* emission is always stronger, by several orders of magnitude for HC^{15}N or HN^{13}C, than *mHII:n5*, except before 500 years for H_2CO, HCO and C (see Fig. A.84, A.44 and A.204 respectively).

After 10^4 years, except for HCO, O and C^+, the intensities are stronger for higher densities, up to one oder of magnitude for CH_3OH for instance, for the HII region and HHMC models. The molecules have larger column densities for models with higher density in the medium. After 10^4 years, the *mHHC:n7* emission is equal to *mHII:n7* emission as seen in Sec.6.2 but this is not true for *mHHC:n6* which has a stronger emission for
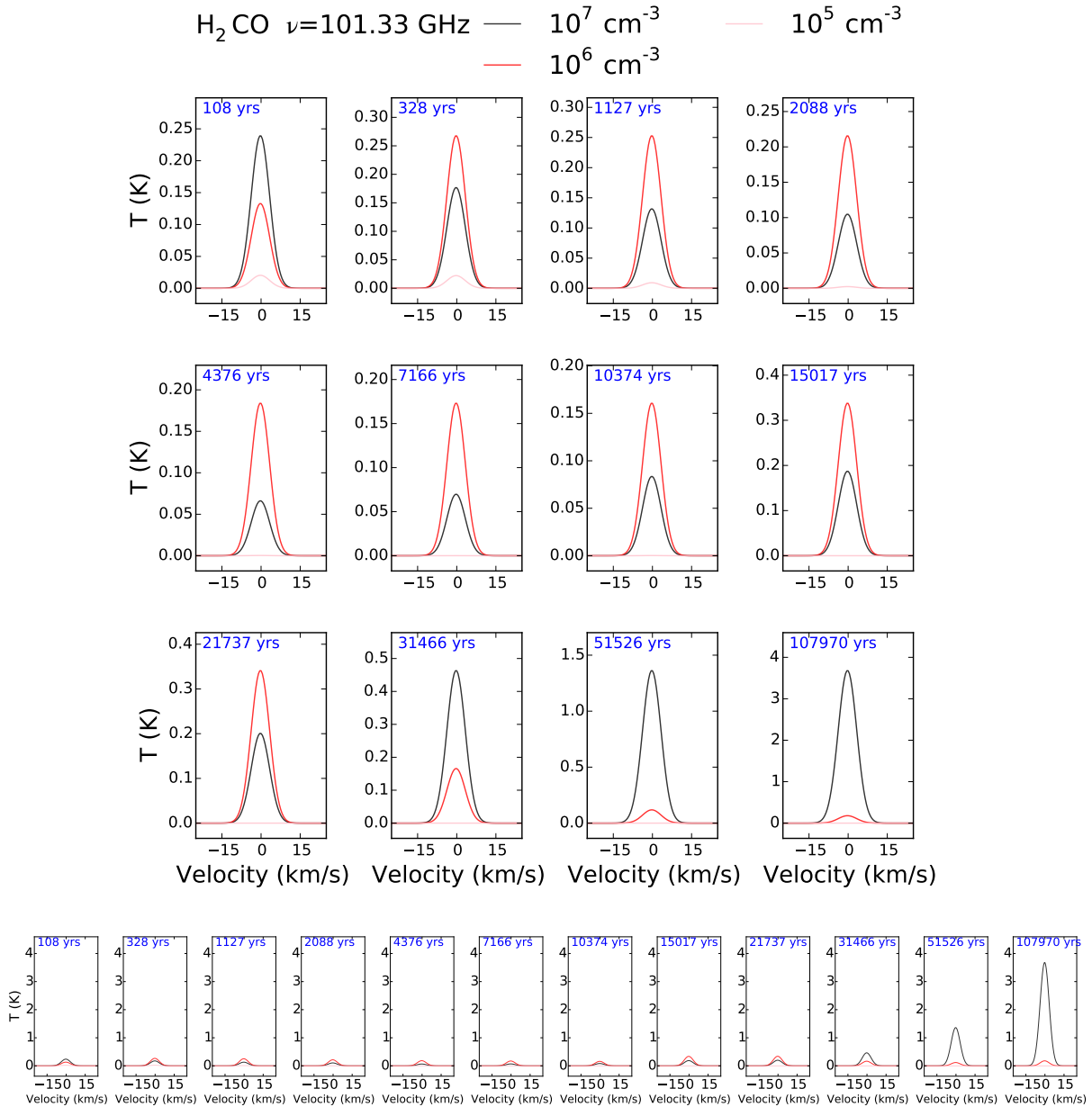
Figure 6.19: Time evolution of $H_2CO\,(2(0,2)-1(0,1))$ spectra for HII region models with different densities at the ionization front: 10^7 cm^{-3} (black), 10^6 cm^{-3} (red) and 10^5 cm^{-3} (pink). The bottom panel shows the same spectra but with the same scale on the y-axis.

CH_3OH, $HN^{15}C$, $HN^{13}C$, $H_2^{18}O$ and NH_3. The presence of the PDR, which is wider and more ionized (more O^+ and N^+), reduces the column density for these molecules.

From 500 years up to 10^4 years, the HHMC emission is stronger for $HC^{15}N$ (about ten times), $HN^{13}C$ (up to eight times) and CN (less than two times); even before 500 years in the case of $HC^{15}N$. This is the contrary for H_2CO which has intensities for the HHMC models about 5 times lower than for the HII region. In the first case, the presence of the PDR decrease the abundance on the line of sight and so the column density. In the second case, the radiation field enhances the formation of H_2CO in the transition region, region which does not exist in the HHMC model.

Integrated intensity ratios: The time evolution of integrated intensity ratios for
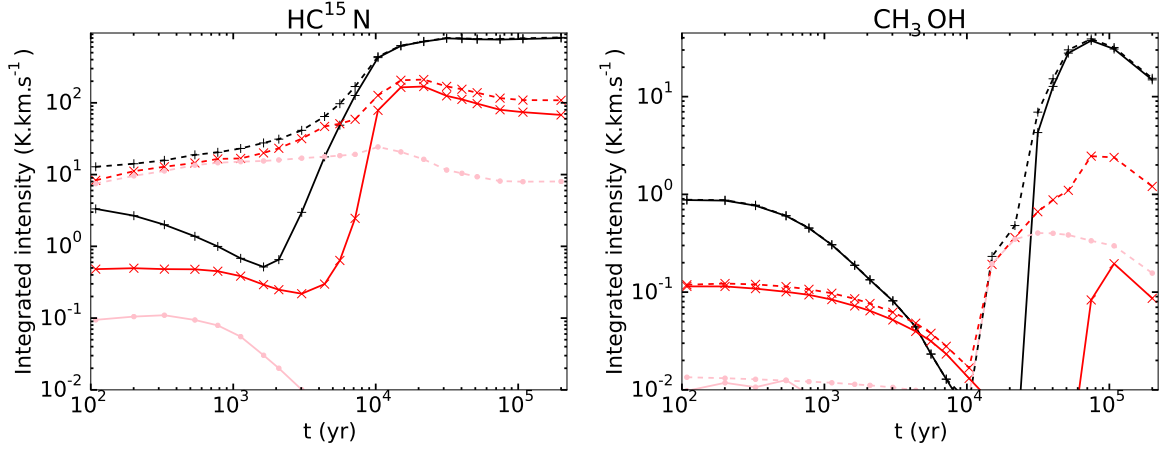
Figure 6.20: Time evolution of integrated intensities for $HC^{15}N\,(1\text{–}0)$ (left panel) and $CH_3OH\,(2(2,1)\text{–}3(1,2))$ (right) for models with different densities at the ionization front: 10^7 cm^{-3} (black), 10^6 cm^{-3} (red) and 10^5 cm^{-3} (pink). The solid lines represent the HII region models and the dashed lines the HHMC models.
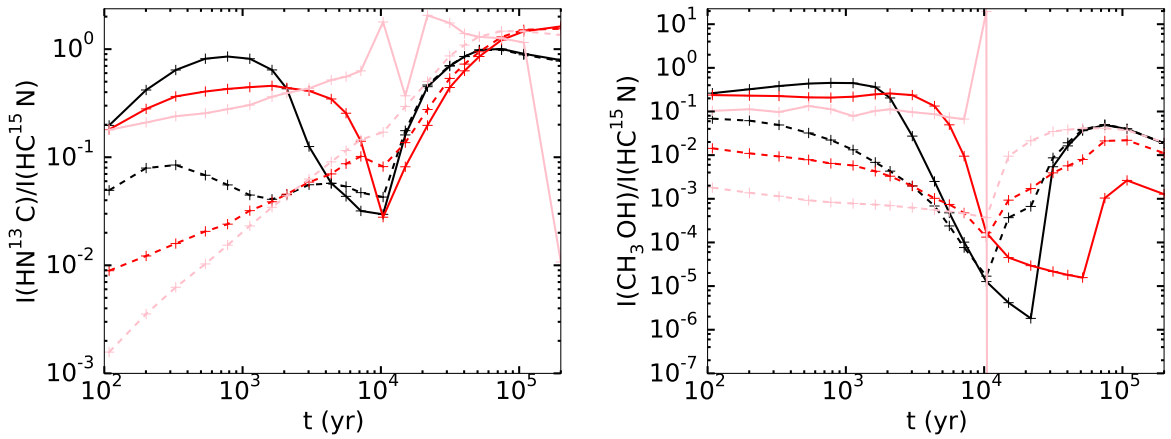
Figure 6.21: Time evolution of integrated intensity ratio $(I(X_i)\,/\,I(HC^{15}N\,(1\text{–}0)))$ for models with different sizes of ionized cavity: 10^7 cm^{-3} (black), 10^6 cm^{-3} (red) and 10^5 cm^{-3} (pink). X_i is $HN^{13}C\,(1\text{–}0)$ (left panel) and $CH_3OH\,(2(2,1)\text{–}3(1,2))$ (right). The solid lines represent the HII region models and the dashed lines the HHMC models.

model $n7$ (black), $n6$ (red) and $n5$ (pink) is shown in Fig. 6.21 for `raHNC` (left panel) and `raCH3OH` (right). For model $mHII{:}n5$, the ratios can not be trusted after $\sim 4{\times}10^3$ years because the integrated intensities are close to zero, except for C$^+$ and O but `raC+` and `raO` are still affected by the absence of HN^{15}C emission. Before this time the ratios for this model is smaller than the others except for HCO$^+$, HCO, C$^+$ and O.

At the beginning of the evolution the ratio `raHNC` is smaller in the HHMC models until $4{\times}10^3$ years for $n7$ and a bit later, at $9{\times}10^3$ years, for $n6$. Then the $mHII{:}n6$ ratio is slightly higher, less than one order of magnitude, and 1.5 times lower for $n7$. At 10^4 years for $n7$ and $\sim 4{\times}10^4$ years for $n6$ HII region and HHMC ratios tend to be equal. For `raCH3OH`, the HII region models have higher ratios before 10^4 years and lower (for $n6$) or equal (for $n7$) after. This behavior is similar to `raNH3`, `raH2O` and `H2CO` (see Fig. A.145, A.185 and A.85). For the other ratios, the ratio of $mHHC{:}n6$ is about two times lower than the ratio for $mHII{:}n6$.
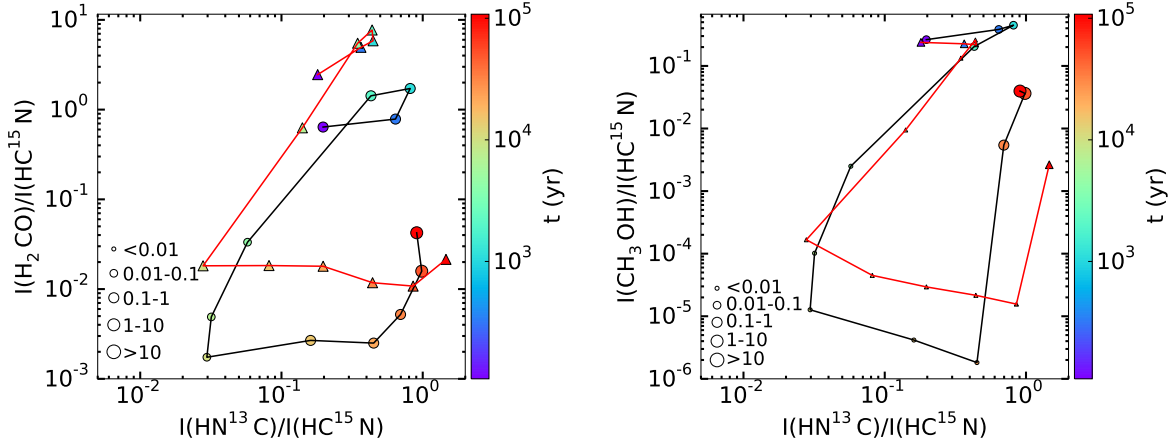
Figure 6.22: Time evolution of the integrated intensity ratio ($I(\mathrm{X}_i)$ / $I(\mathrm{HC^{15}N}\,(1\text{–}0)))$ as a function of the integrated intensity ratio ($I(\mathrm{HN^{13}C}\,(1\text{–}0))$ / $I(\mathrm{HC^{15}N}\,(1\text{–}0)))$ for HII region models with different density at the ionization front: 10^7 cm^{-3} (black line and circle markers), 10^6 cm^{-3} (red line and triangle markers) and 10^5 cm^{-3} (pink line and diamond markers). X_i represents $\mathrm{H_2CO}\,(2(0,2)\text{–}1(0,1))$ (left panel) and $\mathrm{CH_3OH}\,(2(2,1)\text{–}3(1,2))$ (right). The size of the markers corresponds to the range value of the peak intensity in Kelvin of $\mathrm{H_2CO}$ and $\mathrm{CH_3OH}$.

For every ratio, there is a maximum around 10^3–2×10^3 years that seems to be delayed by ≤ 2000 years when we decrease the density of one order of magnitude. This is because the integrated intensity of $\mathrm{HC^{15}N}$ decreases until these times. In addition, all ratios are higher for models with lower densities, by one order of magnitude between all models, due to a larger PDR, except for `raHNC` and `raCH3OH`. For these two ratios, the difference between $n6$ and $n7$ is lower than one order of magnitude; and after the maximum of the ratio model $n7$ has a stronger ratio (about one order of magnitude).

Integrated intensity ratio − ratio: As in Sec. 6.3 the pattern, as presented in Fig. 6.22 is very similar for each model. This figure shows the integrated intensity ratios `raH2CO` and `raCH3OH` as a function of the ratio `raHNC` for the HII region models. The different sizes of ionized cavity are represented as follows: 10^7 cm^{-3} (black lines and circle markers), 10^6 cm^{-3} (red lines and triangle markers) and 10^5 cm^{-3} (pink lines and diamond markers).

Summary of the section:

In this section we studied the chemistry in HII region models with different densities: the reference model having a density of 10^7 cm^{-3} at the ionization front, density of a HCHII region but with a size of a UCHII region, we produce models with lower densities: 10^6 and 10^5 cm^{-3}.

We see that for lower densities the PDR contains more ionized species mainly during the time period where it forms, from 100 to 10^4 years. The molecular area is less spread in time and space and the PDR is bigger for models with smaller densities.

The emission of C$^+$ and O is stronger for models with lower densities. The emission of the other studied species is weaker except for $\mathrm{H_2CO}$ before 10^4 years approximately and HCO after this time.
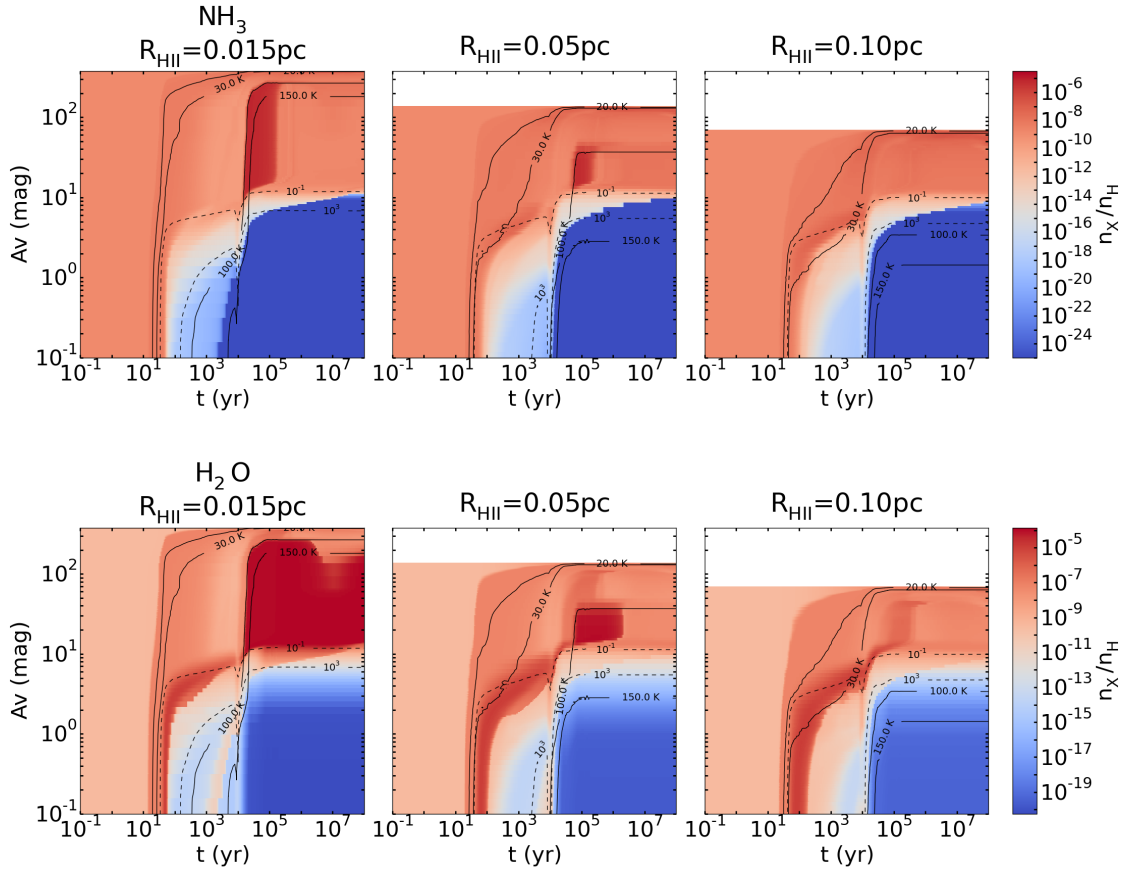
Figure 6.23: Abundances of NH_3 and H_2O as a function of time (x-axis) and visual extinction (y-axis) for HII region models using for the second density profile ($\gamma = 1$) and with different sizes of ionized cavity: 0.015 pc (left panel), 0.05 pc (middle) and 0.10 pc (right). The solid black lines appearing on the figures represent the contours for the temperature: 20, 30, 100 and 150 K and the dashed black lines represent some contours for the radiation field intensity: 10^{-1} and 10^3 Draine unit.

6.5   Plummer exponent

Abundance profiles: In Fig. 6.23 we show the abundance of NH_3 and H_2O for models with a Plummer exponent $\gamma = 1$. From the left panel to the right one, we show models with increasing sizes of ionized cavity: 0.015, 0.05 and 0.10 pc. The principal difference here compared to Sec. 6.3, comparing the sizes of ionized cavity, is the decrease of the density at the ionization front when the size of the cavity increases. The results for these models are very similar to the ones with $\gamma = 2.5$ presented in Sec. 6.2 comparing HII region and HHMC models and in Sec. 6.4 comparing the density in the medium.

Synthetic spectra and Integrated intensity profiles: In Fig. 6.24 we show the time evolution of the integrated intensity for $HC^{15}N$ (1–0) (left panel) and CH_3OH (2(2,1)–3(1,2)) (right) for HII region models with $\gamma = 1$ and different sizes of ionized cavity: 0.015 pc (brown), 0.05 pc (black) and 0.10 pc (orange). The spectra and the integrated intensities are more influenced by the density in the medium than by the distance of the core from the proto-star because these intensities show the same behavior than the ones
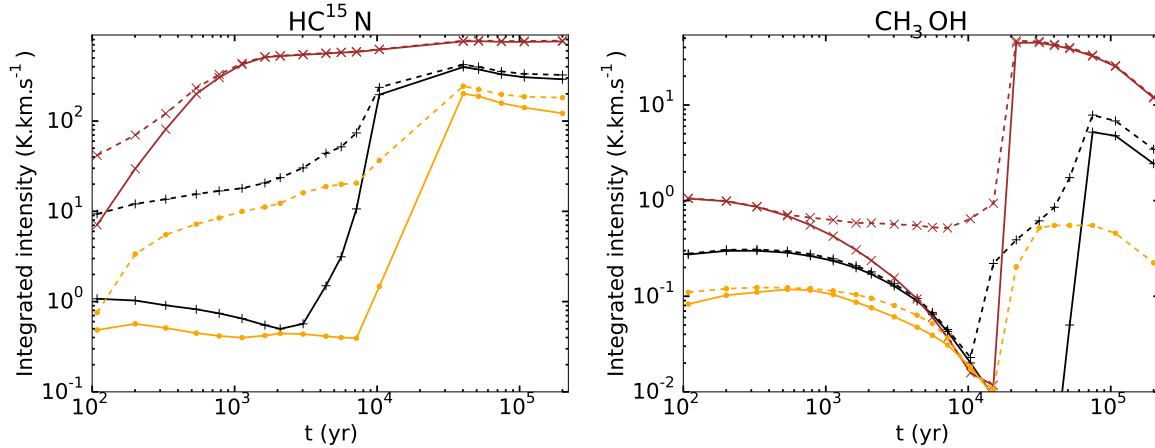
Figure 6.24:   Time evolution of integrated intensities for $HC^{15}N\,(1\text{--}0)$ (left panel) and $CH_3OH\,(2(2,1)\text{--}3(1,2))$ (right) for models using the second density profile ($\gamma = 1$) and with different sizes of ionized cavity: 0.015 pc (brown), 0.05 pc (black) and 0.10 pc (orange). The solid lines represent the HII region models and the dashed lines the HHMC models.

presented in Sec. 6.4.

We compare the integrated intensities of model *r015n7p2.5* with model *r015n7p1*, models where we have the same size of the cavity and the same density at the ionization front and where we only compare the effects of the exponent. We see that the intensities are higher for model *p1* except for C^+ and O which are about 1.2 and 3 times lower, respectively (see Fig. A.225 and A.243 respectively). As for the other molecules, the ones showing the strongest differences are N_2H^+ and CN which are between 2 to 10 times stronger in model *p1* (see Fig. A.167 and A.127 respectively). The differences are due to principally to the amount of matter on the line of sight. The slope is steeper for model *p2.5* so we have less material and thus weaker emission. This steepest slope explains also why this is not the case for O and C^+. The density decreases faster so the radiation penetrates deeper and ionizes a wider region.

Summary of the section:

In this section we study the chemistry in HII region models with a different Plummer exponent γ (1 instead of 2.5). We have three models with different sizes of HII region (0.015, 0.05 and 0.10 pc) and the density at the ionization front (10^7, 1.56×10^6 and 4.15×10^5 cm^{-3}, respectively) because the Plummer radius r_p is the same for the three models (= 0.015 pc).

We find that the PDR is smaller for models with smaller ionized cavities due to the highest density at the ionization front. In, addition, the molecular area when populated with species like CH_3OH, H_2O or NH_3 is wider in time and space for these models.

The emission of molecular species is stronger for models with a smaller HII region whereas the emission atomic and ionized species is weaker.

6.6 Initial abundances

For the models comparing the two sets of initial abundances (*ini1* and *ini2*), all input parameters are the same, hence the spatio-temporal evolution of the temperature and the radiation field intensity are also identical.

Abundance profiles: We compare in Fig. 6.25 models with different initial abundances: *ini1* (left panels) and *ini2* (right). The upper panels show the abundance of NH_3 and the lower panels the abundance of CH_3OH. We notice that complex molecules like CH_3OH are less abundant in *ini2*, by about two orders of magnitude in the case of methanol once the desorption happened at 10^4 years. CO, O_2 and N_2 are also less abundant (approximatively 10, 7 and 25 times less) by at least two orders of magnitude in the region where methanol has its higher abundances, i.e. in the molecular region from 10^4 to 10^6 years. The same is true for HCN and HNC for instance but only from 10^4 to 10^5 years and the difference is a bit less than two orders of magnitude (see Fig. A.11 and A.29 respectively). For HCN, CO, N_2 and methanol for example this happens because we start with lower s-HCN and s-CH_3OH abundances (see Tab. 5.1) and when the desorption occurs we obtain less species. For O we start with the same abundances but then formation of O is more efficient until 10^3 years for model *ini1* (see Fig. A.245). The formation reaction for O in *ini1* is: $HCO_2^+ + e \longrightarrow O + H + CO$. Formation via the reaction $He^+ + CO \longrightarrow O + He + C^+$ occurs for model *ini2*.

On the contrary, in the molecular region and in the transition region too, carbon chains are more abundant by one order of magnitude such as for C_2H_4 or more (three to four orders for C_2H or C_4H). In the grain region, carbon chains are present from the beginning of the evolution in *ini1* but they are formed after 30 K in *ini2*. This also the case of s-CH_3OH. At 30 K, these molecules in model *ini1* go through a similar but less efficient formation process than in model *ini2* leading to lower abundances carbon chains on grain at 2×10^4 years (sC_3H_4 example: a bit lower than 10^{-7} in model *ini1* and 10^{-6} in model *ini2*).

In the gas phase carbon chains, and methanol too for instance, are formed later in model *ini2*, i.e. shortly after the temperature reaches 20 K instead of 15 K in *ini1*. This might be because the initial abundances *ini2* are obtained for the steady-state of the pre-stellar core, hence they are more stable at ~ 10 K. In addition the abundances of the ions forming them, via dissociative recombination, is also lower in model *ini2* and it might take longer to form the carbon chains.

In the transition region, radicals like CH and OH are more abundant by one order of magnitude or less. In the molecular region, the abundances of CH_4, H_2O and NH_3 are also higher (15, 5 and 10 times higher respectively) and for a longer period: from 10^4 to 10^6 years in model *ini2* instead of from 10^4 to 10^5 years for model *ini1*.

With model *mHHC:ini1*, our abundance of methanol are approximately 10^{-7} at 10^5 years when $T \sim 100$ K ($n_H \sim 5 \times 10^6 cm^{-3}$). This is very similar to the ones obtained in Semenov et al. (2010) for the "Hot Core" model ($\sim 2 \times 10^{-7}$ with T = 100 K, $n_H = 2 \times 10^7 cm^{-3}$ and $\chi_0 = 1$) despite that our density is four times lower and we do not have a radiation field. This abundance is also similar to the one observed in the Orion KL hot core (Blake et al. 1987; Sutton et al. 1995), known as a typical hot core. However, in the second set of initial abundances *mHHC:ini2* the methanol abundance, of about 10^{-9}, is too low.

Figure 6.25: Abundances of NH$_3$ and CH$_3$OH as a function of time (x-axis) and visual extinction (y-axis) for HII region with different initial abundances: *ini1* (left panel) and *ini2* (right). The solid black lines appearing on the figures represent the contours for the temperature: 20, 30, 100 and 150 K and the dashed black lines represent some contours for the radiation field intensity: 10^{-1} and 10^3 Draine unit.

When we do the same study with a chemical network including 334 species and obtain the spatio-temporal evolution for other COMs, we get the same conclusion: we do not produce enough of them. However for model *ini1* we have at the same time and same density an abundance of HCN of about 2×10^{-6}. The one obtained withSemenov et al. (2010) data is about 10^{-10}. The difference is very important. With model *ini2* we obtain an abundance of 8×10^{-7}. For this model we have abundances closer to Semenov et al. (2010) and to the Orion KL hot core abundance, $\sim 10^{-9}$ (Schilke et al. 1992).

In the upper panels of Fig. 6.26 we show the spatio-temporal evolution of the sum of the main C-bearing species abundances: C, C$^+$, CO, CH$_4$, s-CO and s-CH$_4$. On the colorbar, the minimal abundances is 10^{-6} and the maximal one is 1.2×10^{-4}, which corresponds to the elemental abundance of C. We see that in both plots we miss some carbon. We miss even more of it in the transition region (one order of magnitude less –
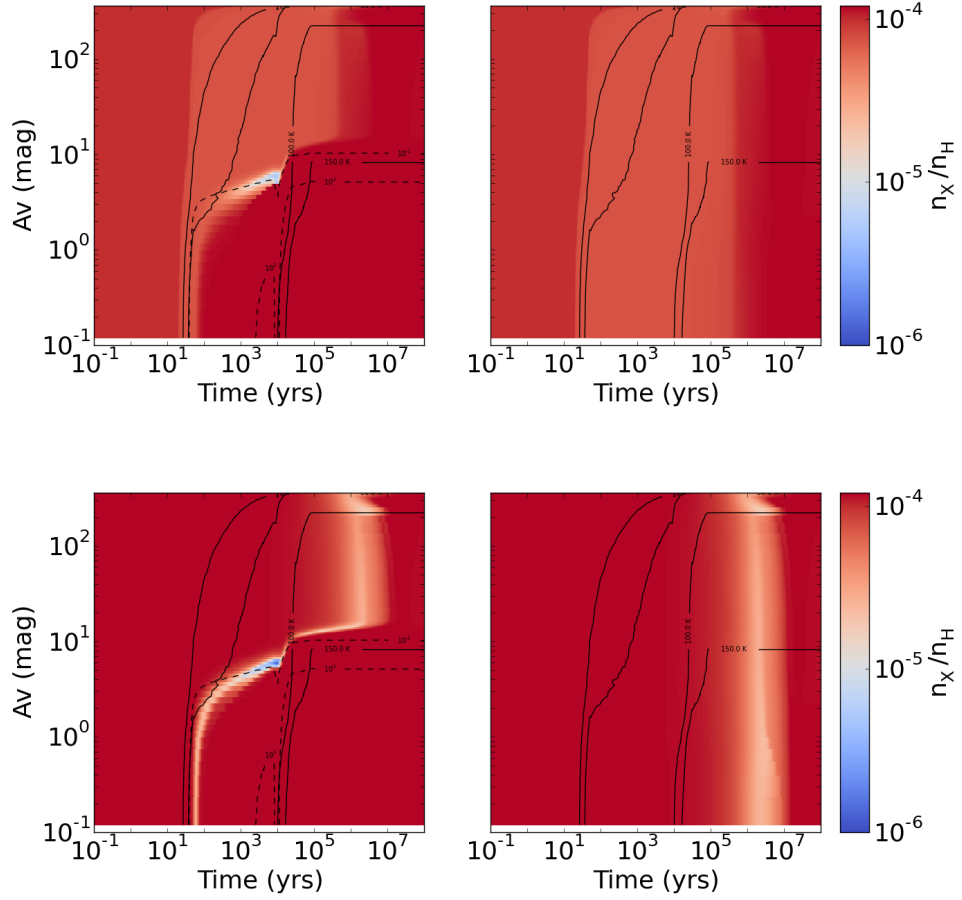
Figure 6.26: Spatio-temporal evolution of the sum of the C-bearing main species abundances (C$^+$, C, CO, CH$_4$, s-CO, s-CH$_4$) in the case of a model HII region model (left panel) and HHMC model (right panel). The upper panels represent the sum of the abundances for the reference model, i.e. *ini1*, and the bottom panels for *ini2*. The solid black lines appearing on the figures represent the contours for the temperature: 20, 30, 100 and 150 K and the dashed black lines represent some contours for the radiation field intensity: 10^{-1} and 10^3 Draine unit.

for $A_V \sim 10$ mag and from 100 to 10^4 years) as well as in the first part of the molecular (from 50 to 5× years for $A_V > 10$ mag) and molecular-atomic (from 50 to 100 years for $A_V < 10$ mag) regions. The rest of the carbon is mainly found in s-CO$_2$ for the grain and transition region, CO$_2$ for the molecular-atomic and part of the molecular region and HCN in the molecular region from 10^4 to 10^5 years. There is no high abundance of s-CO$_2$ in the transition region in the HHMC model. It indicates that the formation of s-CO$_2$ is due to the radiation field.

We produce the same figure for model *ini2* (bottom panels of Fig. 6.26). An interesting result concerning the C-bearing species is that it exists an area, mainly the transition region and from 10^5 to 10^7 years in the molecular region, where the main species do not dominate in the medium. It appears that, for extinctions up to 5 mag, some radicals such as CH, CH$_3$ have larger abundances at the transition from grain surface region to molecular region. But given the short period of time when they pop up it is unlikely to detect them during this transition. For extinctions from 5 to 10 mag, more complex grain
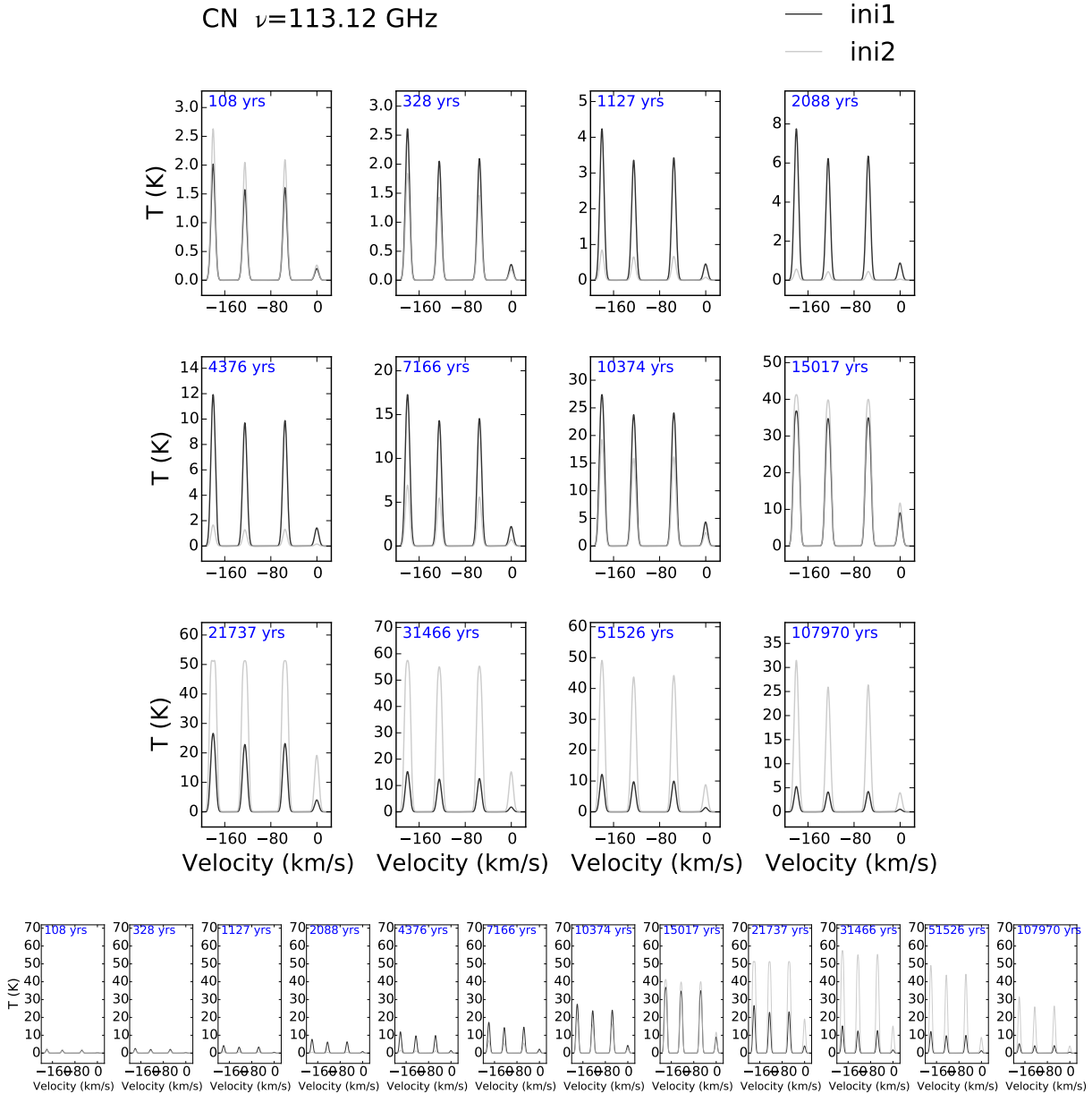
Figure 6.27: Time evolution of CN (1–0) spectra for HII region models with different initial abundances: *ini1* (black) and *ini2* (grey). The bottom panel shows the same spectra but with the same scale on the y-axis.

species like s-CO_2, s-C_2H_2, s-C_3H_2 or s-CH_3OH prevail. The radiation field is almost 10^{-2} in this region but it seems to be enough to trigger diffusion of radicals and then formation of complex molecules. At higher extinctions few other molecules such as HCN are the dominant species. For $A_V > 300$ mag, as there is no radiation field but the temperature is still higher than 30 K, carbon chains, s-C_4H_2 being foremost among them, are formed on the grain surface. Furthermore, when we use the network with 334 species, this decrease of the main C-bearing species is less important in this region. In general, the abundances of the transition molecules are higher with a network of 183 species except for CO_2, s-HCN.

Although no observational constraint can be derived from it, this result shows nicely that the transition from one dominant regime to another is characterized by the spreading
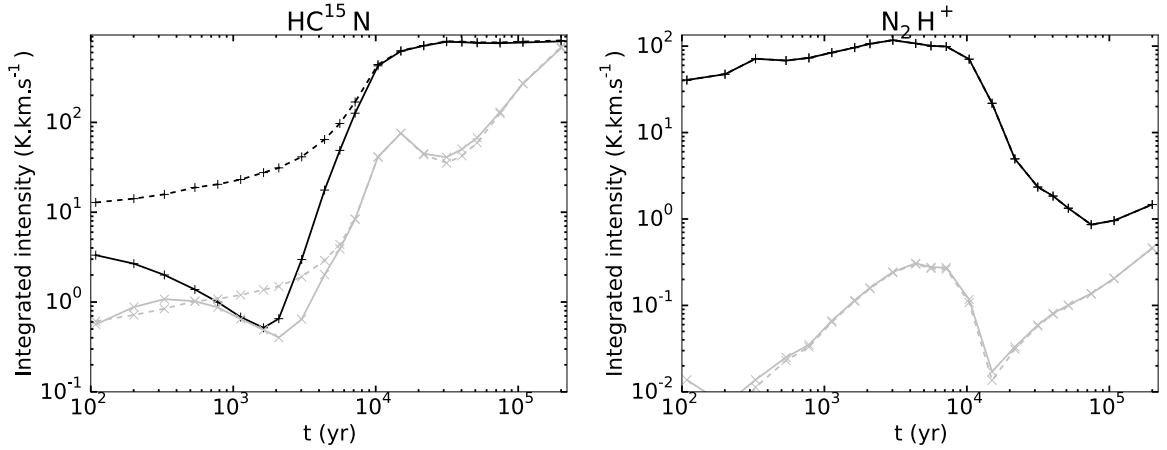
Figure 6.28: Time evolution of integrated intensities for HC^{15}N (1–0) (left panel) and N$_2$H$^+$ (1–0) (right) for models with different initial abundances: *ini1* (black) and *ini2* (grey). The solid lines represent the HII region models and the dashed lines the HHMC models.

of an atom (here C) on a large number of different species.

Synthetic spectra and Integrated intensity profiles: In Fig. 6.27 we show the time evolution of the synthetic spectra for CN (1–0) in black for model *ini1* and in grey for model *ini2*. We see that the emission for model *ini2* is first ~ 1.25 times higher than for model *ini1* until about 10^2 years, Then it is lower until 10^4 years, with differences of more than 5 K and less than 10 K between the two models. Finally, it is higher again by 5 K at 1.5×10^4 years up to 40 K at 3×10^4 years. The abundance of CN are a bit higher in the transition region around 100 years and decrease later and at the beginning of the molecular region CN is already formed in model *ini1* and not in *ini2* inducing higher intensities for model *ini1*. After 10^4 years, just like for many other species, CN abundance are bigger for model *ini2* and thus the intensities becomes stronger.

In Fig. 6.28 we present the temporal evolution of the integrated intensity for HC^{15}N (1–0) and N$_2$H$^+$ (1–0) with model *ini1* in black and model *ini2* in grey. The HII region intensities are represented with solid lines and the HHMC intensities with dashed lines. Compared to the HC^{15}N intensity of model *ini1* (analyzed in Sec. 6.2), the intensity of the HII region is five times lower before 10^4 years, except at 10^3 years where they are equal, and one order of magnitude lower after. The intensity of the HHMC model is equal to the HII region intensity except between 500 years and 8×10^3 years. Its emission is always is lower by more than one order of magnitude than the HHMC emission of model *ini1* before $\sim 7 \times 10^4$ years and a bit less later. As for the intensity of N$_2$H$^+$, emission of model *ini2* is at least three orders of magnitude lower. This is the biggest difference we can observe between the two models. HN^{13}C presents the same behavior than HC^{15}N. HCO and CH$_3$OH also have lower intensities, except after 10^4 years for HCO, and from 2×10^3 years to 2×10^4 years for methanol (see Fig. A.50 and A.110 respectively). C$^+$ and O have the same integrated intensities (see Fig. A.228 and A.246 respectively). For all the other molecules the emission of model *ini2* behaves similarly to *ini1* model but it is stronger (five times higher for HCO$^+$ and only 1.5 times higher for H$_2$^{18}O for instance). We observe in the abundances profiles that H$_2$O, NH$_3$, N$_2$H$^+$, H$_2$CO have larger abundances and thus they have larger intensities (see Fig. A.189, A.149, A.169 and A.89 respectively).

Integrated intensity ratios: In Fig. 6.29 we show the time evolution of the inte-
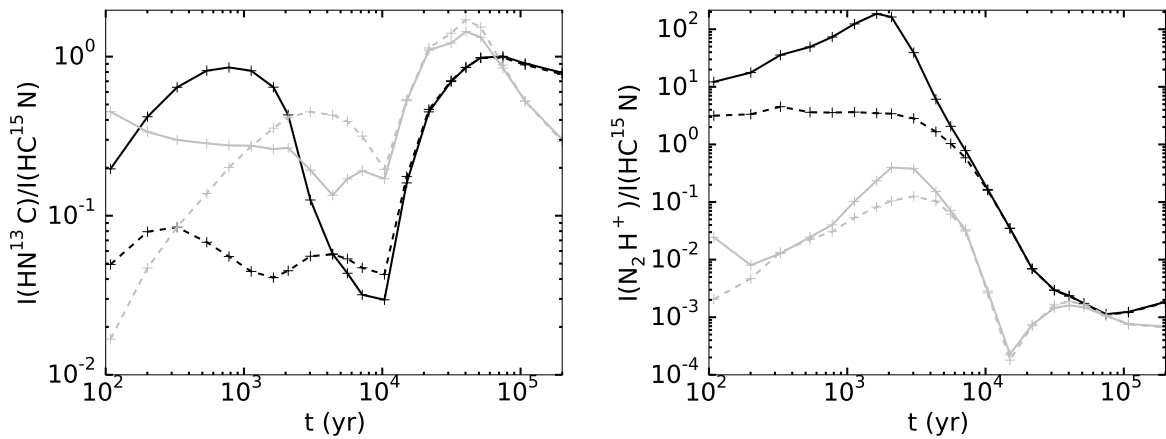
Figure 6.29: Time evolution of integrated intensity ratio ($I(X_i)$ / $I(HC^{15}N\,(1\text{–}0))$) for models with different initial abundances: *ini1* (black) and *ini2* (grey). X_i is $HN^{13}C\,(1\text{–}0)$ (left panel) and $N_2H^+\,(1\text{–}0)$ (right panel). The solid lines represent the HII region models and the dashed lines the HHMC models.

grated intensity ratio `raHNC` and `raN2H+` in black for model *ini1* and in grey for model *ini2*. The HII region ratios are represented with solid lines and the HHMC ratios with dashed lines. The trend of the evolution is similar for most ratios in model *ini2* and *ini1* but the fluctuations of the ratios for model *ini2* are less important than for model *ini1*. For N_2H^+ for instance the variations cover five orders of magnitude in model *ini* which two orders more than model *ini2*. The ratios for model *ini2* are stronger during the whole evolution, up to two orders of magnitude, except for CN (after 3×10^3 years – Fig. A.131), HCO (after 4×10^3 years – Fig. A.51), CH_3OH (between 2×10^3 years and 2×10^4 years), $HN^{13}C$ (between 2×10^3 years and 6×10^4 years) and N_2H^+ (always lower – Fig. A.171).

`raHNC` is one of the ratio for which the trend is the most different between model *ini1* and model *ini2*, principally at the beginning of the evolution. Instead of the bump shown by *mHII:ini1* between 10^2 years and 10^4 years with the maximum around 10^3 years the ratio for model *mHII:ini2* decreases from 0.04 to ~ 0.02. Then the ratio increases in both models but the maximum at 4×10^5 years is higher for model *mHII:ini2*. For *mHHC:ini2* we do not have two bumps before 10^4 years but a single one which is about ten times stronger. After this time the evolution is the same than the HII region for both models. `raCN` ratios shows a similar behavior than `raHNC` at the beginning of the evolution.

Integrated intensity ratio – ratio: Fig. 6.30 shows the integrated intensity ratios `raHCO+` and `raCH3OH` as a function of the ratio `raHNC` for the HII region models (upper panels) and HHMC models (bottom panels) with different initial abundances: *ini1* (black lines and circle markers) and *ini2* (grey lines and triangle markers). The patterns are really different between the two HII region models and between the HHMC models, principally due to the differences in the evolution of the ratio `raHNC`. On the contrary of model *ini1* no similar pattern emerged for model *ini2* when we compare the molecules.

Summary of the section:

In this section, we have compared the abundances and emissions for two models starting with different initial abundances.

We find that the abundances, and so the species' emissions as well as the pattern in
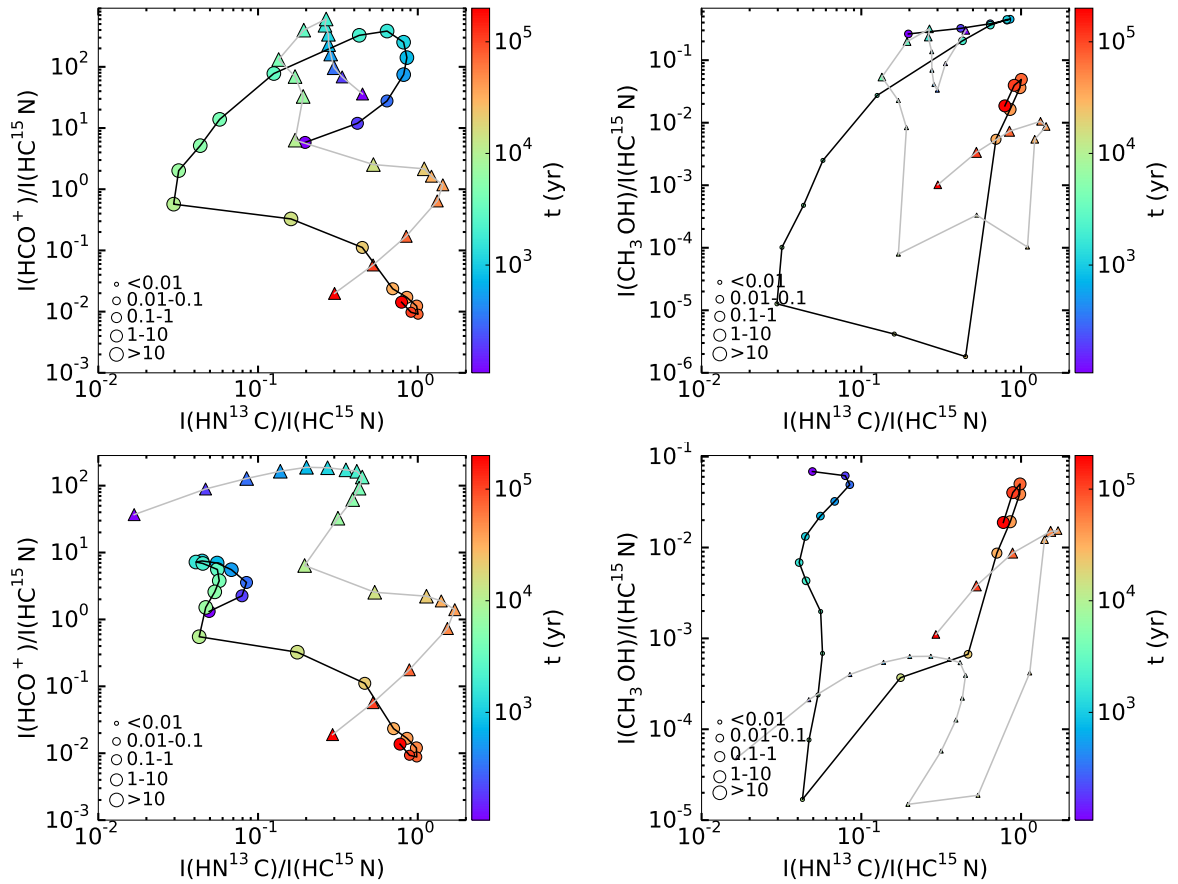
Figure 6.30: Time evolution of the integrated intensity ratio ($I(X_i)$ / $I(HC^{15}N\,(1–0))$) as a function of the integrated intensity ratio ($I(HN^{13}C\,(1–0))$ / $I(HC^{15}N\,(1–0))$) for models with different initial abundances: *ini1* (black line and circle markers) and *ini2* (grey line and triangle markers). X_i represents $HCO^+\,(1–0)$ (left panel) and $CH_3OH\,(2(2,1)–3(1,2))$ (right). The upper panels show the HII region models and the lower panels show the HHMC models. The size of the markers corresponds to the range value of the peak intensity in Kelvin of HCO^+ and CH_3OH.

the ratio-ratio plots, are highly influenced by the choice of the initial conditions. Each species is affected in a different way, less methanol in one case but more water, or barely affected like C^+.

6.7 Effect of the envelope

For this section we do not present any "Bacon plots" because the models we compare have the same density, the same temperature, the same radiation field evolution and so the same spatio-temporal evolution of the relative abundances. Only the spectra, the integrated intensities and the ratios are going to be affected as the models do not have the same column density because we have a model with a smaller modeling grid. The grid is stopped for a cut-off density of 10^6 cm^{-3} (shown in light blue in all the figures presented in the section) instead of 10^1 cm^{-3} (shown in black in the figures).
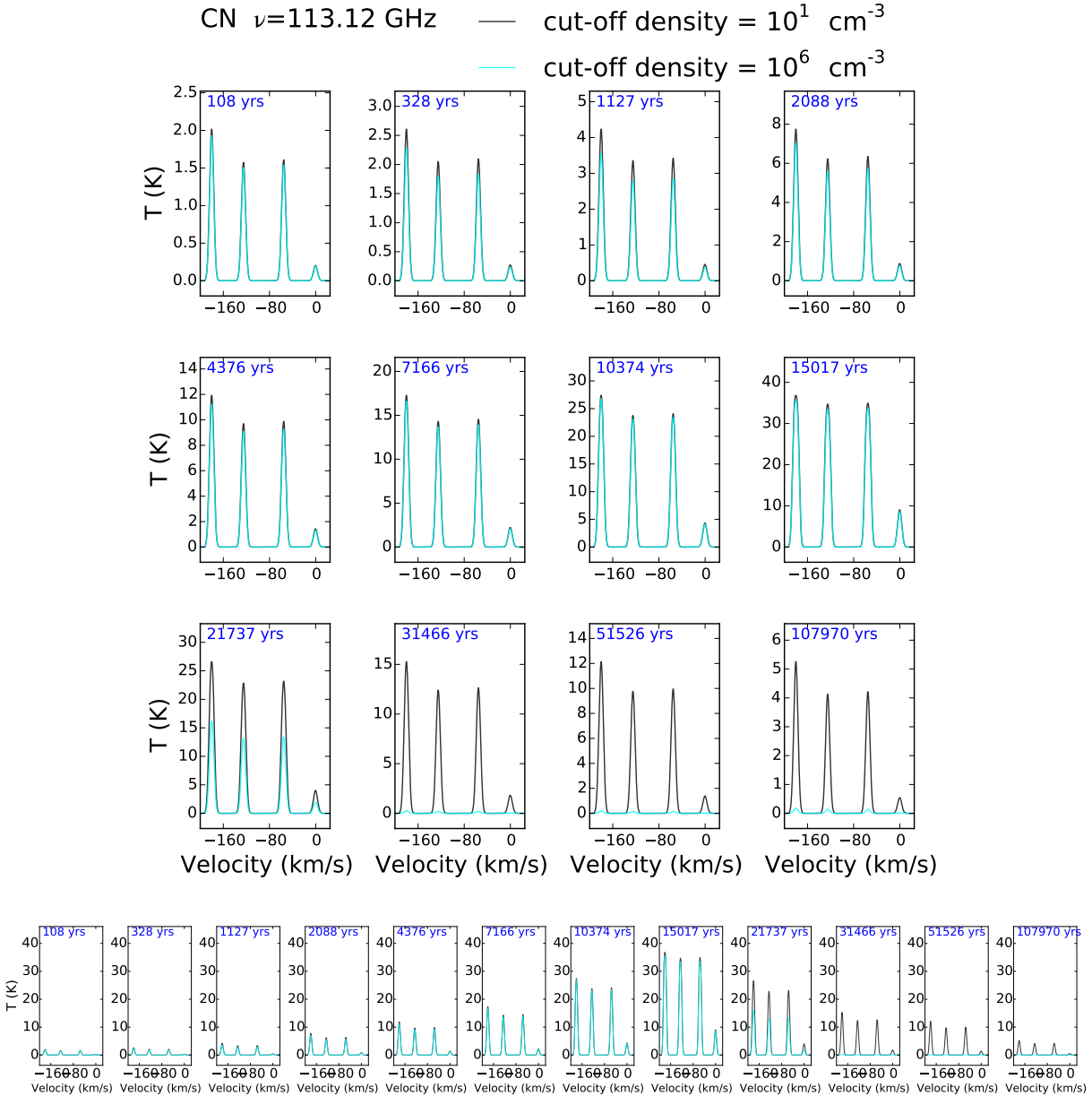
Figure 6.31: Time evolution of CN (1–0) spectra for HII region models with different cut-off density: 10^1 cm^{-3} (black) and 10^6 cm^{-3} (light blue). The bottom panel shows the same spectra but with the same scale on the y-axis.

Synthetic spectra and Integrated intensity profiles: In Fig. 6.31 we show the time evolution of the synthetic spectra for CN (1–0) in black for model *mHII:c1*, with a cut-off density of 10^1 cm^{-3}, and in light blue for model *mHII:c6*, with a cut-off density of 10^6 cm^{-3}. We notice that the early evolution is almost identical for both models. Model *c6* is less than ~ 0.5 K lower than model *c1*. After $1.5{\times}10^4$ years the model with the smallest modeling grid *c6* decreases to be lower than 1 K strong after $3{\times}10^4$ years whereas the intensity for model *c1* has decreased but remains higher than 5 K. This indicates that the emission of CN comes principally from the envelope, at least at the end.

In Fig. 6.32 we present the time evolution of the integrated intensity for HC^{15}N (1–0) and N$_2$H$^+$ (1–0) with model *c1* in black and model *c6* in light blue. The HII region
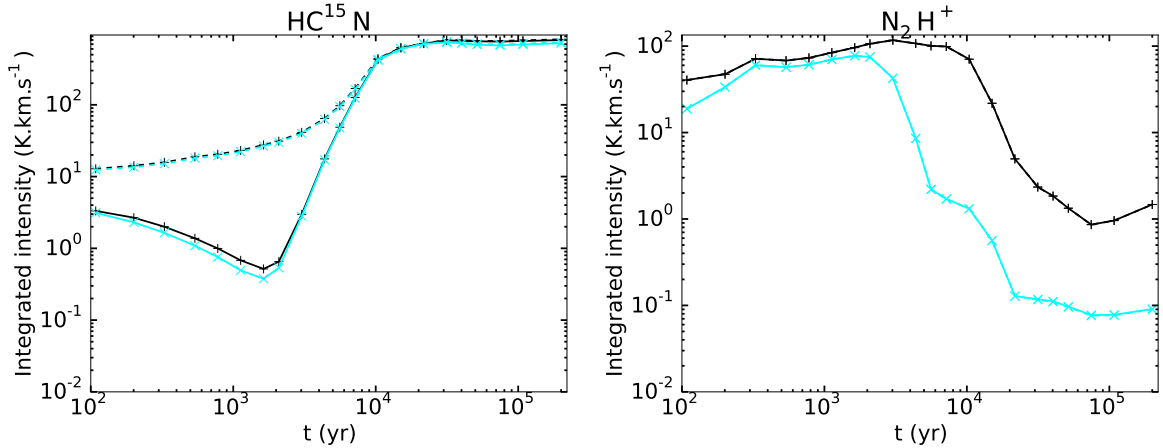
Figure 6.32: Time evolution of integrated intensities for $HC^{15}N$ (1–0) (left panel) and N_2H^+ (1–0) (right) for models with different cut-off density: 10^1 cm^{-3} (black) and 10^6 cm^{-3} (light blue). The solid lines represent the HII region models and the dashed lines the HHMC models.

intensities are represented with solid lines and the HHMC intensities with dashed lines. In the case of $HC^{15}N$ there is no difference between models *c1* and *c6* aside from the lower intensity before 10^3 years. However this difference is smaller than 1.2. C^+, $H_2^{18}O$, NH_3 and $HN^{13}C$ also have identical integrated intensities (see Fig. A.230, A.192, A.152 and A.32 respectively). The intensity of H_2CO is the same in both models for all times except from 10^4 to 3×10^4 years where model *c6* intensity decreases from 1.5 to 0.5 K km s^{-1} (see Fig. A.92). For CH_3OH the emission is slightly lower, less than two times, until 3×10^4 years and then it is the same (see Fig. A.112).

For the other molecules, the emission of model *c6* becomes lower by one order of magnitude after $\sim 1.5\times10^4$ years. It starts to be lower at 7×10^3 years for HCO^+ (see Fig. A.72). For N_2H^+ it is always lower but the intensity is only two times smaller until 2×10^3 years. For C and HCO (see Fig. A.212 and A.52 respectively), the lines become undetectable after 2×10^4 years. In the same way as for CN (see Fig. A.132), these molecules emission arises mostly from the envelope. Therefore, they can not be considered as good tracers of the HII region and its internal PDR.

The intensity of O is always ~ 1.2 times higher for model *c6* during the evolution. This should not happen because all parameters are the same (same temperature, same radiation field, same abundances) we just decrease the column density of the species by taking out the emission coming from the envelope, region with densities lower than 10^6 cm^{-3}. The intensities must be equal or lower for model *c6*. This difference probably arises from the line emission computation by *RADMC-3D*. It is not coming from the computation of the integrated intensities as the intensities in the synthetic spectra for model *c6* are also higher than for model *c1*. This is a good estimation of the uncertainties we have for every time step in the models.

Integrated intensity ratios and Integrated intensity ratio − ratio: In Fig. 6.33 we show the time evolution of the integrated intensity ratio `raHNC` and `raN2H+` in black for model *c1* and in light blue for model *c6*. The HII region ratios are represented with solid lines and the HHMC ratios with dashed lines. In Fig. 6.34 we show the integrated intensity ratios `raHCO+` and `raHCO` as a function of the ratio `raHNC` for the HII region models with different cut-off density: *c1* (black lines and circle markers) and *c6* (light
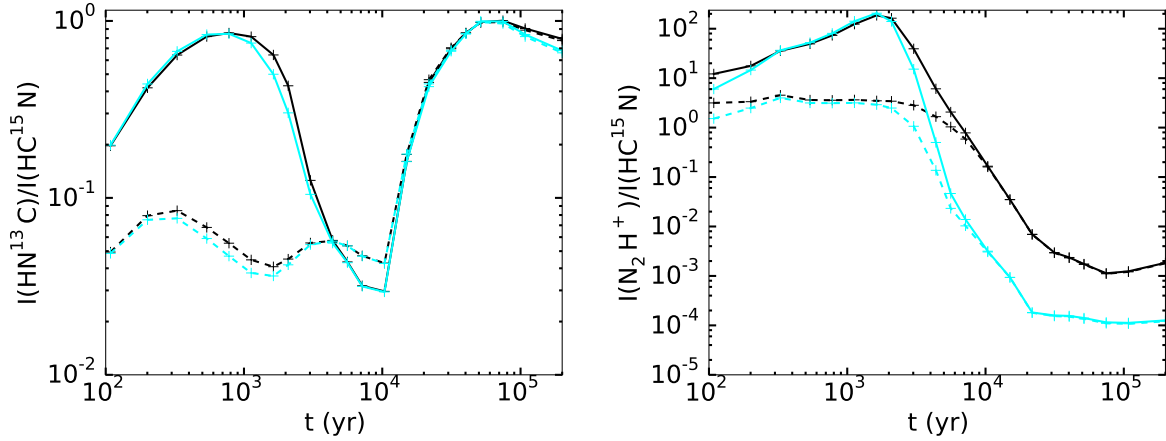
Figure 6.33: Time evolution of integrated intensity ratio $(I(X_i) \, / \, I(HC^{15}N\,(1{-}0)))$ for models with different cut-off density: 10^1 cm^{-3} (black) and 10^6 cm^{-3} (light blue). X_i is HN^{13}C (1–0) (left panel) and N$_2$H$^+$ (1–0) (right). The solid lines represent the HII region models and the dashed lines the HHMC models.
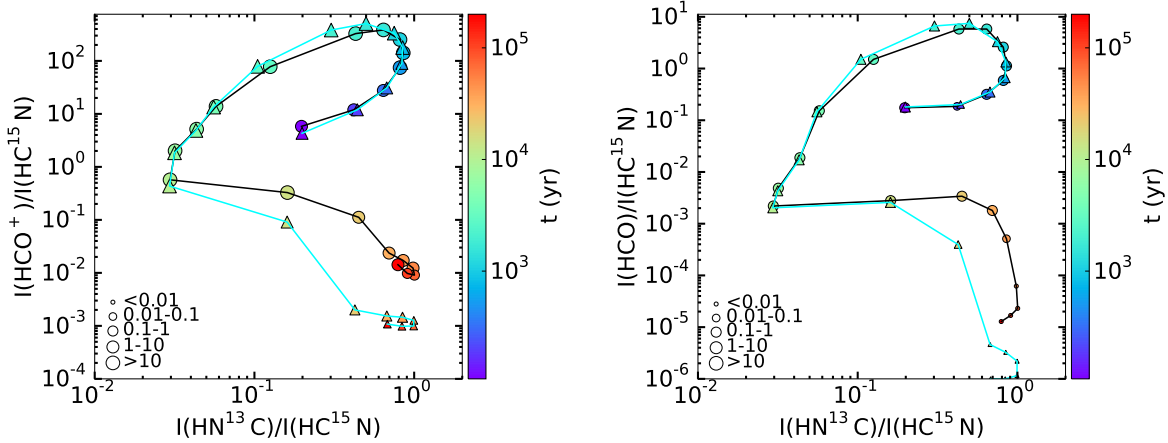
Figure 6.34: Time evolution of the integrated intensity ratio $(I(X_i) \, / \, I(HC^{15}N\,(1{-}0)))$ as a function of the integrated intensity ratio $(I(HN^{13}C\,(1{-}0)) \, / \, I(HC^{15}N\,(1{-}0)))$ for HII regions models with different cut-off density: 10^1 cm^{-3} (black line and circle markers) and 10^6 cm^{-3} (light blue line and triangle markers). X_i represents HCO$^+$ (1–0) (left panel) and HCO (1(0,1)–0(0,0)) (right). The size of the markers corresponds to the range value of the peak intensity in Kelvin of H$_2$CO and HCO.

blue lines and triangle markers). The ratios are only affected by the integrated intensity of the species at the numerator. The explanation regarding their behavior is the same as commented in the "Synthetic spectra and Integrated intensity profiles" part. The same conclusion applies to the integrated intensity ratios as a function of `raHCN`.

Summary of the section:

In this section we have compared the emission for two models with different sizes of modeling cube. The reference model includes the emission from the envelope and we compare it to a model where we filter out the envelope.

We find that the emission of several species are affected when we cut out the envelope as their emission decreases. This implies that the emission of these species comes, partly or mainly, from the envelope. These species are C, HCO, HCO$^+$, CN and N$_2$H$^+$.
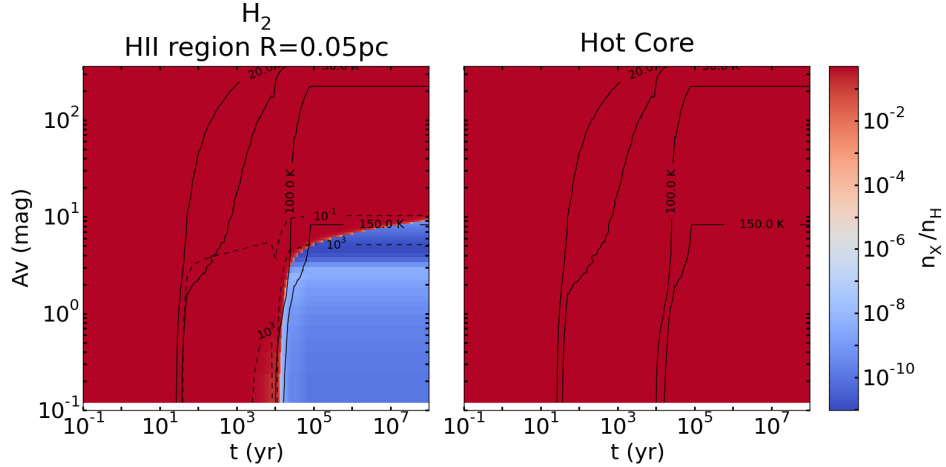
Figure 6.35: Abundance of H_2 as a function of time (x-axis) and visual extinction (y-axis) for HII region (left panel) and HHCM (right panel) model. The solid black lines appearing on the figures represent the contours for the temperature: 20, 30, 100 and 150 K and the dashed black lines represent some contours for the radiation field intensity: 10^{-1} and 10^3 Draine unit.

6.8 Dissociation front

For each of the HII region models we obtain, we can determine the size of the PDR using the rule assumed in Chap. 4.6.2. In this chapter, we considered that the dissociation front is located where $\frac{n(H_2)}{n_H} = 0.1$. In Fig. 6.35 we compare the abundance of H_2 for the reference HII region model with the HHMC model. We see the propagation of the dissociation front in the HII region model, i.e. separation between the PDR in blue and the molecular region in red.

In Tab. 6.2 we present the position of the dissociation front at 10^5 years for all our models involving a change in the physical parameters which affect the size of PDR. The second and fourth columns of the table indicate the visual extinction and the density at the dissociation front. The third column indicates the size of the PDR, or size of the atomic region, r_{PDR}. Knowing the position of the ionization front r_c: at 3×10^3 AU for models *r0.015*, at 1.03×10^3 AU for models *r0.05* and at 2.06×10^4 AU for models *r0.10*, to obtain the position of the dissociation front we have to add r_{PDR} to r_c.

We see that for the models *mHII:p2.5* the size of the PDR decreases with the size of the HII regions and it increases when the density at the ionization front decreases. We can also notice that the density at the dissociation front is higher when the size of the PDR is smaller. This is because the radiation field is less strong at the ionization front for bigger sizes of HII regions and because it penetrates deeper into the core for lower densities. In the case of model *mHII:r0.05n5* almost all the core is the PDR. For the models *mHII:p1*, the distance between the ionization front and the dissociation front increases when we increase the size of the HII region. The density at the ionization front is lower for bigger HII regions and despite the lower radiation field impacting the PDR the density parameter affects more the PDR size.

Except for model *mHII:r0.05n5p2.5s183ini1*, the size of the PDR is extremely thin. It

Table 6.2: H_2 dissociation front position from the ionization front at 10^5 years for the different models. The dissociation front position is defined at $\frac{n(H_2)}{n_H} = 0.1$.

Models	A_V (mag)	r_{PDR} (AU)	n_H (cm^{-3})
mHII:r0.015n7p2.5s183ini1	6.8	88.7	9.26×10^6
mHII:r0.05n7p2.5s183ini1 (ref)	5.2	64.2	9.82×10^6
mHII:r0.10n7p2.5s183ini1	4.8	59.2	9.90×10^6
mHII:r0.05n6p2.5s183ini1	5.5	758.3	8.30×10^5
mHII:r0.05n5p2.5s183ini1	3.6	54568.4	5.46×10^1
mHII:r0.015n7p1s183ini1	6.8	86.4	9.72×10^6
mHII:r0.05n7p1s183ini1	5.5	455.3	1.44×10^6
mHII:r0.10n7p1s183ini1	4.7	1508.2	3.62×10^5

is always lower than 1500 AU. Therefore, the observation of this kind of objects requires high angular resolution if we want to investigate the PDR and distinguish the phase of the region: HII region or hot molecular core. Assuming a source at a distance of 1 kpc, we would need an angular resolution of about $0.04 - 0.05''$. This is currently the best resolution we could get with ALMA[1], in good weather conditions, to reach the required sensitivity. Despite the first aim of SKA[2] is not high-mass star formation and it focuses on the centimeter wavelength range, we could reach the required resolution.

With the semi-analytical code in Sec. 4.6.2 we have found that the size of the atomic region is defined by Eq. 4.12 ($A_{V,c} \approx 10^{-6} I_0$). When we apply this equation to model *mHII:r0.05n7p2.5* where the density and the radiation field at the ionization front are 10^7 cm^{-3} and 5.2×10^6 Draine unit (seen in Sec. 5.5.1), respectively, we have a size of the atomic region of $A_{V,c} = 5.2$ mag which is equal to the value shown in the Tab. 6.2. Using Eq. 2.32, with the approximation that the density is constant and so the column density is the factor of the density and the size of the atomic region r_{PDR} we get:

$$r_{PDR} = \frac{5.8 \times 10^{21} \, A_{V,c}}{3.1 \, n_H}$$

We obtain $r_{PDR} = 65$ AU for model *mHII:r0.05n7p2.5* which is the same as in Tab. 6.2.

When we do it for model *mHII:r0.05n6p2.5* we find $A_{V,c} = 5.4$ mag as the radiation field is equal to 5.4×10^6 Draine unit and $r_{PDR} = 668.5$ AU. These values are really close to the ones in the table although r_{PDR} is 100 AU smaller. When applied to model *mHII:r0.05n5p2.5* we do not find the same results as we get $A_{V,c} = 5.4$ mag (the radiation field is also equal to $\sim 5.4 \times 10^6$ Draine unit) and $r_{PDR} = 6684.5$ AU. This size is about eight times shorter that the value reported in Tab. 6.2. It might be because the density as a function of radius is not constant and it decreases faster as the density at the ionization front gets smaller. Thus it affects a bit model *mHII:r0.05n6p2.5* and much more model *mHII:r0.05n5p2.5*.

---

[1]The Atacama Large Millimeter/sub-millimeter Array (ALMA) is a radio-telescope observing in the millimeter, sub-millimeter range (about $80 - 600$ GHz in frequency) as its name indicates. It is located in Chile, on the Chajnantor plateau at 5000 m altitude.

[2]The Square Kilometer Array (SKA) is a radio-telescope which will be composed of thousand antennas located in Africa and Australia. It will achieve both high resolution and high sensitivity images in the $0.10 - 25$ GHz frequency regime.

For the two other models with different size of HII region *mHII:r0.015n7p2.5* and *mHII:r0.10n7p2.5*, we have a radiation field of 6.5×10^7 and 1.3×10^6 Draine unit respectively. This gives $A_{V,c} = 65$ and 1.3 mag and then $r_{PDR} = 802.1$ and 16.7 AU, respectively. For these models it does not match.

7

Conclusions & Outlook

Contents

7.1 Conclusions

Hot molecular cores and HC/UCHII regions are two successive evolutionary stages of massive star formation. We have investigated the spatio-temporal chemical evolution in HMCs as well as in HC/UC HII regions with internal PDRs to understand the impact of the radiation field and its effects on the chemistry and on the emission of several molecules.

We have optimized and improved the astrochemical code *Saptarsy* (Choudhury et al. 2015). Moreover, we have coupled *Saptarsy* to work along with the radiative transfer code *RADMC-3D* via the Python based program *Pandora* (Schmiedeke et al. 2016). This has been done in order to obtain synthetic spectra using the detailed spatio-temporal evolution of species abundances. The produced spectra can provide us with information on the detectability of a molecule and they are also directly comparable to observations. Several HII region, hollow HMC and HMC models have been produced by changing physical parameters such as the size of the ionized cavity or the density at the ionization front. *Saptarsy* has also been used to obtain two sets of initial abundances used in the models. Hollow HMC models are meant to describe HMCs but they have an ionized cavity at the center like in HII region models. They do not represent a physical object but have been produced because they are directly comparable to the HII region models due to the same source structure. They have the same density and column density, and the same temperature evolution. We include the evolution of the radiation field in the HII region models and thus we can study its influence on the chemistry.

First, we have found that the following species: C, HCO, HCO^+, CN and N_2H^+ do not make good tracers of the HII regions or the HMCs because their emission seems to arise mostly from the envelope of the core. They do not allow us to distinguish between the HC/UCHII region and the hot core phase and can not help us investigate the influence of the radiation field which affects only the inner core.

Second, while comparing the HMC, HHMC and HII region models we have observed that only few species, among the dozen we have investigated, show a distinct difference between their emission in the HII region and in the HMC models. They are C^+, C, O, CH_3OH and $H_2^{18}O$. CH_3OH and $H_2^{18}O$ seem to trace the hot molecular core whereas it looks like C^+, C, O trace the UC/HCHII region phase. However, from this result we can exclude C as a tracer of UC/HCHII regions and the internal PDR because its emission mostly comes from the envelope. In addition we did not include an external radiation field in the model. Adding one might enhance the abundances of C^+ and O in the envelope for the HMC and HII region models and make it harder to differentiate the emission coming from these two evolutionary phases. To overcome this, we should observe these regions with an interferometer to make sure we only observed the compact emission, emission coming from the inner core.

We also have noticed that the size of the internal PDR is extremely thin, less than 1500 AU for all the models except for the one with the lowest density 10^5 cm^{-3}. Observing this kind of narrow regions requires high angular resolution data (at most $0.05''$ at 1 kpc). In the ALMA era this is fortunately possible as large baseline interferometers can provide the required resolution. Nevertheless, C^+ and O can not be observed with ALMA, or even with SKA, as their transitions are in the THz range. The GREAT receiver onboard SOFIA could be used as it covers this frequency range. However, Leurini et al. (2015) have shown that the emission of O at 4.75 THz, observed in the UCHII region G5.89–0.39 with the GREAT receiver, is highly contaminated by absorption from the source envelope. Once again we need observations from interferometers to filter out the extended emission and this is currently not possible in this frequency range. Thus, even though the models indicate than C^+ and O trace the internal PDR, we do not have found any species currently observable to trace the HC/UCHII region phase and the internal PDR.

Furthermore, we have seen that the size of the PDR increases when the ionized cavity gets smaller or when the density decreases. While comparing the density profiles with different Plummer exponents, we have noted that the density in the medium seems to have a bigger impact on the size of the PDR than the distance between the star and the ionization front. The density, either because of its value or its profile, also appears to have a stronger effect on the molecular emission. Finally, the density profile, either an asymptotic decrease of r^{-5} or r^{-2}, does not change the difference between the HII region emission and the HMC emission.

We have noted the critical dependance of the abundances, and therefore the intensities and the integrated intensity ratios, on the initial conditions. The choice of the physical processes happening during the pre-stellar phase, i.e. no evolution whatsoever compared to a crude simulation of a collapse, generates two highly different initial abundances sets. These abundances consequently lead to very dissimilar results during the proto-star evolution. Additionally, when producing the initial abundances, for model *ini1*, we have tested two pre-stellar core models, one with a temperature of 10 K and the other with 15 K. It looks like we produce less precursors to complex organic molecules and less complex organic molecules in a medium at 15 K than at 10 K.

The selected molecules for this work are just a small sample, so we have just begun to analyze all the possible cases. A spectral survey at 3, 2 and 1 mm of Monoceros R2 have been done recently using the IRAM 30 m telescope (Treviño-Morales et al. 2014, Treviño-Morales in prep.). Monoceros R2 is the closest UCHII region, $d = 830$ pc (Herbst & Racine 1976), which can therefore be spatially resolved using sub-mm and far-IR instruments. This UCHII region is ionized by a B0 star (Downes et al. 1975), has a size of about 0.08 pc and it is surrounded by a dense PDR, $n_{H_2} = 2\times10^5$ cm^{-3} (Pilleri et al. 2012). These parameters are very close to the ones used in our models. We can then use the detected molecules in this region to extend our model study: for example molecules such as CS, SO, OCS or some carbon chain molecules like C_2H, C_3H_2. The abundances of these species are shown in Appendix B. We can then compare the integrated intensities of our models to the observations. This is not done yet as we chose to produce spectra only for the central position and reduced the size of the synthetic maps to the minimum. The maps being too small the spectra can not be convolved to beam of the observations. It is extremely time-consuming to produce bigger synthetic maps for all the models and for a dozen of molecules but it will be done in the near future.

Some other chemical species could be used to trace one phase or the other. For instance, observations suggest that CO^+ is an important species in PDRs. This reactive ion is also observed in Monoceros R2 and appears to be a proof of the existence of high-density PDRs (Rizzo et al. 2003; Trevino-Morales et al. 2016). CO^+ abundance is enhanced by strong UV irradiation of the core. This molecule was a possible candidate to obtain synthetic spectra but we could not obtained detectable lines. The abundance of CO^+ are in fact rather low, less than 5×10^{-13}, and the region where the abundance are high is extremely thin. Higher abundances are observed: 3×10^{-11} in the PDR of NGC 7023, 3×10^{-11} in the Orion Bar Fuente et al. (2003) and a few 10^{-11} in the main PDR IRS 1 surrounding the UCHII region in Monoceros R2 (Trevino-Morales et al. 2016). Nevertheless, the radiation field in NGC 7023 and in the Orion Bar is quite weak: 2.4×10^3, 4×10^4 Habing unit, respectively. It is higher in Monoceros R2, around 5×10^5 Habing unit, but these values are one to three orders of magnitude stronger in our model, about 8.5×10^6 Habing unit. Such a strong radiation field could lead to the destruction of the molecule. (2) Furthermore, the PDR is extremely thin, because the radiation field does not penetrate far into the core, and so the emission of CO^+ is extremely weak. The issue of the low CO^+ abundances in models has been discussed in Bruderer et al. (2009b). They circumvent it by modeling a proto-star embedded in a cavity produced by a bipolar outflow. This provides a larger surface to UV radiation.

This work lays the foundations of the tools necessary for the study of internal PDRs, and the new observational instruments will allow to reach the required resolution to observe these regions. Nevertheless we are still far from having a realistic representation of the processes happening there. In particular, it seems essential to include dynamics in the pre-stellar core models to fix the initial conditions.

7.2 Outlook

This work can be completed and improved in many different ways. We list below the future work we would like to carry out. This is a non-exhaustive list but it summarizes the main points.

1. In the current models I assume that the gas temperature is equal to the dust temperature. Although this is a good assumption in the case of HMCs due to their high densities and the gas being strongly coupled to dust, it is no longer valid in the internal PDR. From the edge of the cloud to an extinction of ~ 2 mag UV radiation is extremely strong ($\geq 10^5$ Draine unit) and heats the gas intensely. Thanks to the Meudon PDR code we know that the gas reaches temperatures above a thousand Kelvin while the dust temperature is between 50 and 70 K. Therefore, implementing in *Saptarsy* a simple and self-consistent computation of the gas temperature, based on heating and cooling processes, for a better treatment of the PDR in the HII region models, would be a significant progress.

2. Currently, the stellar parameters given by Hosokawa & Omukai (2009) correspond to a bloated O-type star. We could investigate the chemistry around a different type of star. We would need stellar parameters provided by a different model such as models developed in Smith (2014). They produce several models considering different kind of accretion: hot/cold, fast/slow. Studying the effect of the accretion, via the change in the radiation, onto the chemistry would be an interesting work.

3. We would like to investigate HC/UCHII regions in the context of large ionized cavities (Peters et al. 2010a) or PDRs on outflow cavities (Visser et al. 2012) which create large surfaces and thus a more easily observable chemistry. We could then investigate CO^+ chemical evolution like Bruderer et al. (2009b) did. This implies to implement in *Pandora* different geometries than the spherical symmetric core. Additionally, we could improve the model by adding multiple proto-star in the core to simulate a cluster and/or by adding multiple cores. While column density is simple to compute in a single spherical symmetric core, it is currently done in *Saptarsy*, it becomes harder once you change the geometry and it is different from one line of sight to another. Therefore, the major difficulty of adding an outflow or more cores will be the treatment of H_2 and CO self-shielding which should be computed directly in *RADMC-3D* before the computation of the relative abundances by *Saptarsy*. And as *RADMC-3D* does not know about the abundance of H_2 and CO several iterations might then be necessary to converge to a result.

4. In the current model the only source of radiation is the central proto-star. Nonetheless, the interstellar medium surrounding the core is also radiating and influencing the medium. We could include an external radiation field in the model in order to make it more complete/realistic even if, when the extinction is large, its effect on the internal PDR will be negligible.

5. Some new improvements in *Saptarsy* are as follows: the first one is to develop the ice chemistry by building an ice mantle (D. Schaefer, work in progress); the second one is to include dynamics in the chemical code and implement the temporal evolution

of the density (S. Pols, future work). This could be done by including infall and following the parcels of gas or by post-processing data obtained with a MHD code. The last point would be really useful to simulate the collapse of the pre-stellar core and obtain more accurate initial abundances.

6. Another possible outlook would be to expand the chemical network and include isotopologues focusing on deuterated species (Taquet et al. 2012a, 2013). In addition, Monoceros R2 seems to present a rich deuterated chemistry (Treviño-Morales et al. 2014). Nevertheless, this would be a tricky task as it means to add hundreds of new species and therefore thousands of reactions. This might cause some stability issues in the chemical code. A group in Bordeaux, from Laboratoire d'Astrophysique de Bordeaux with Liton Majumdar as the principal investigator, already started about a year ago to include into their network the deuterated species as well as ortho-para ratio and spin chemistry. This network involves now not less than 10^4 species.

A

Additional figures: Selected molecules

Contents

A.1   HC^{15}N

HMC vs HHMC model
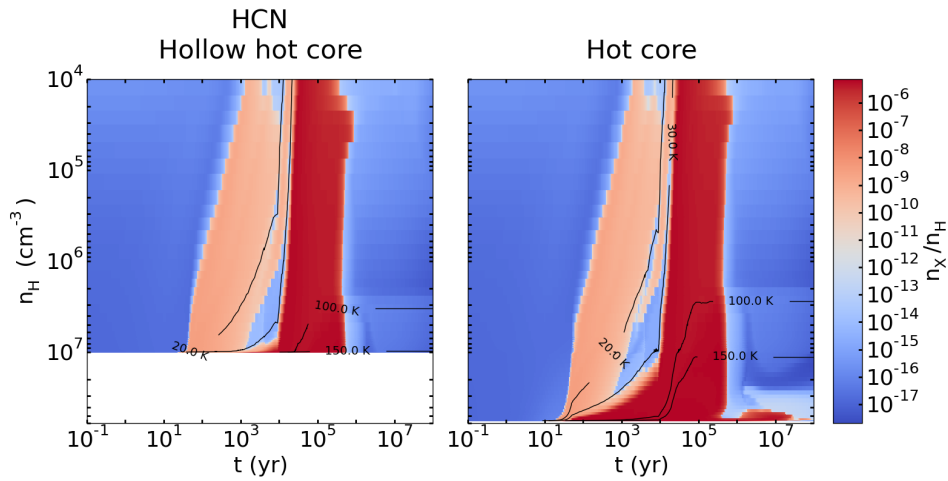
Figure A.1: Abundance of HCN in function of time (x-axis) and density (y-axis) for the HHMC (left) and HMC (right) models.
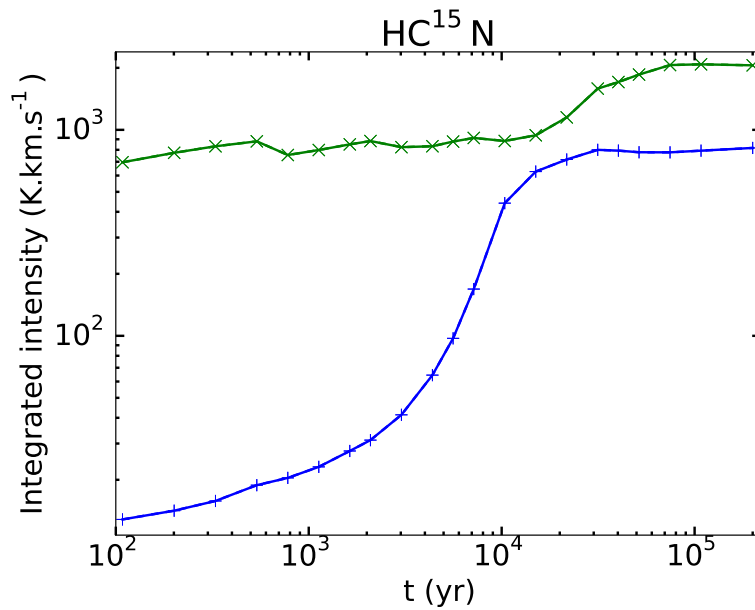
Figure A.2: Time evolution of integrated intensities for HC^{15}N (1–0). The blue line represents the HHMC model and the green one represents the HMC model.

H$\scriptstyle\rm II$ region vs HHMC model
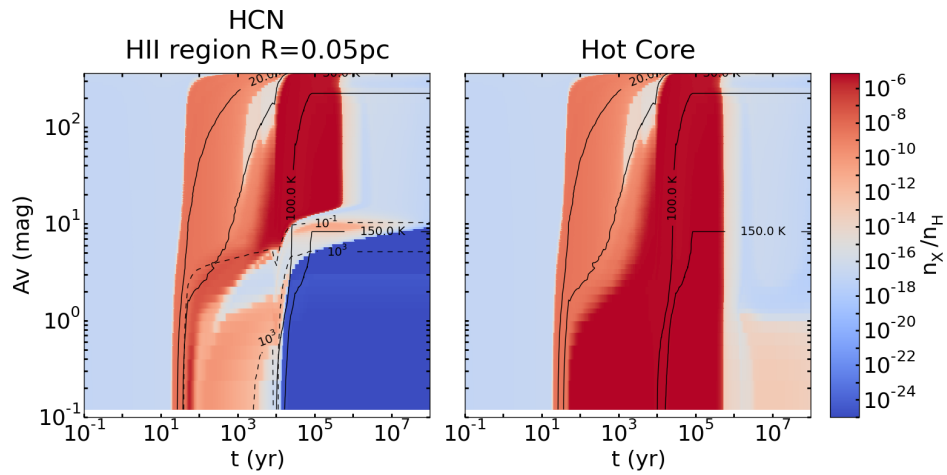
Figure A.3: Abundances of HCN in function of time (x-axis) and visual extinction (y-axis) for the HII region (left panel) and HHMC (right) models. The solid black lines represent the contours for the temperature: 20, 30, 100 and 150 K and the dashed black lines represent some contours for the radiation field intensity: 10^{-1} and 10^{3} Draine unit.
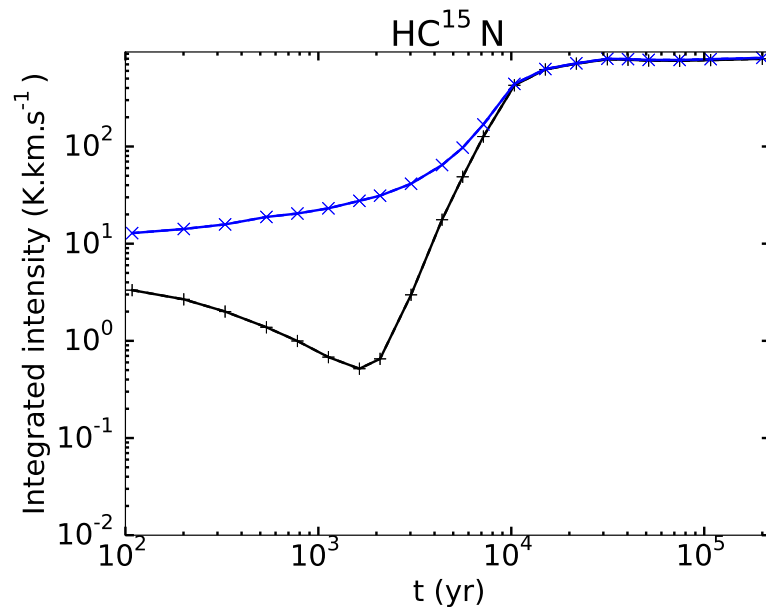
Figure A.4: Time evolution of integrated intensities for HC^{15}N (1–0). The black line represents the HII region model and the blue line represents the HHMC model.

H$_{\text{II}}$ region size
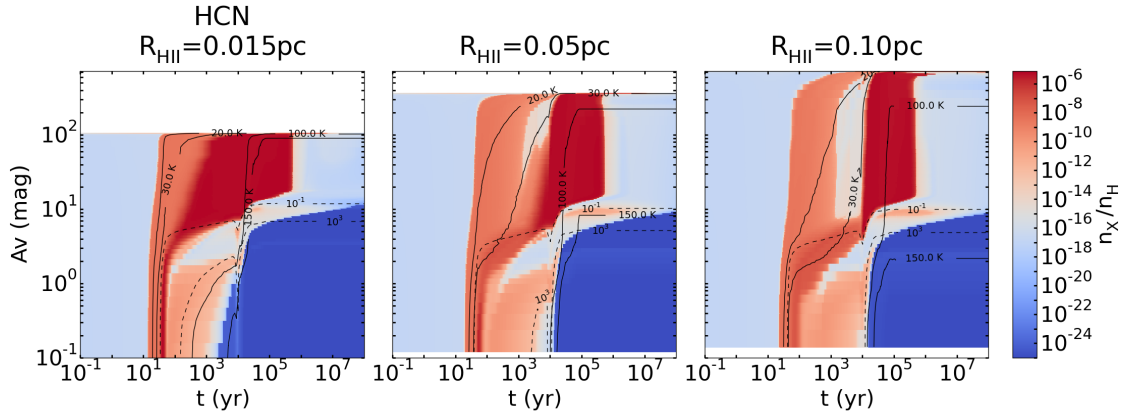
Figure A.5: Abundances of HCN in function of time (x-axis) and visual extinction (y-axis) for HII region models with different sizes: 0.015 pc (left panels), 0.05 pc (middle) and 0.10 pc (right). The solid black lines appearing on the figures represent the contours for the temperature: 20, 30, 100 and 150 K and the dashed black lines represent some contours for the radiation field intensity: 10^{-1} and 10^3 Draine unit.
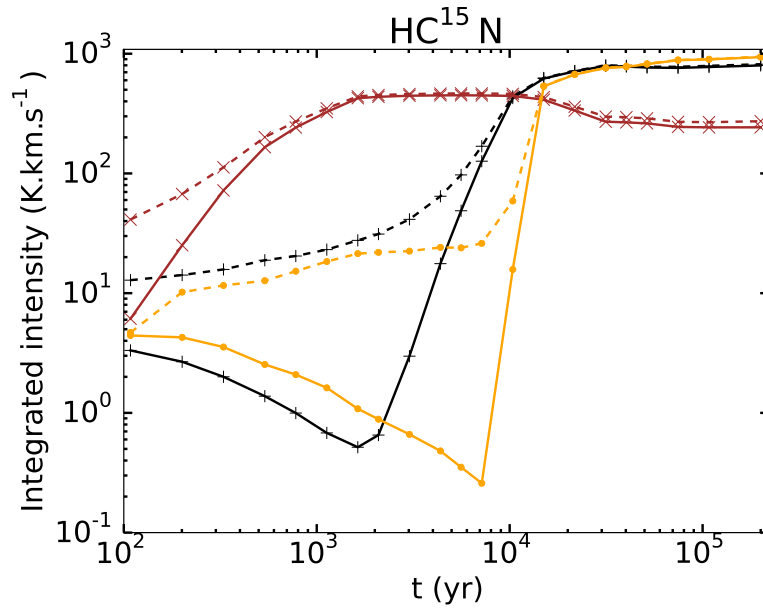
Figure A.6: Time evolution of integrated intensities for HC^{15}N (1–0) for models with different sizes of ionized cavity: 0.015 pc (orange), 0.05 pc (black) and 0.10 pc (brown). The solid lines represent the HII region models and the dashed lines the HHMC models.
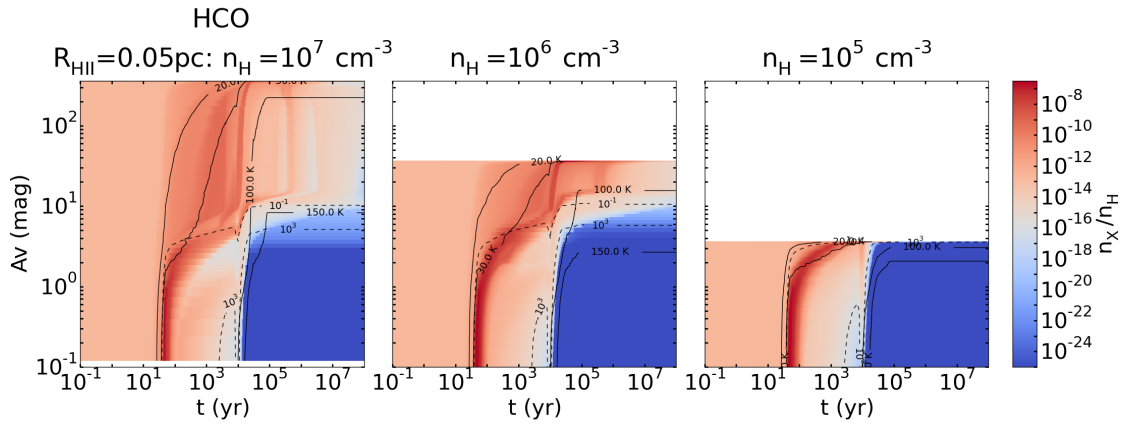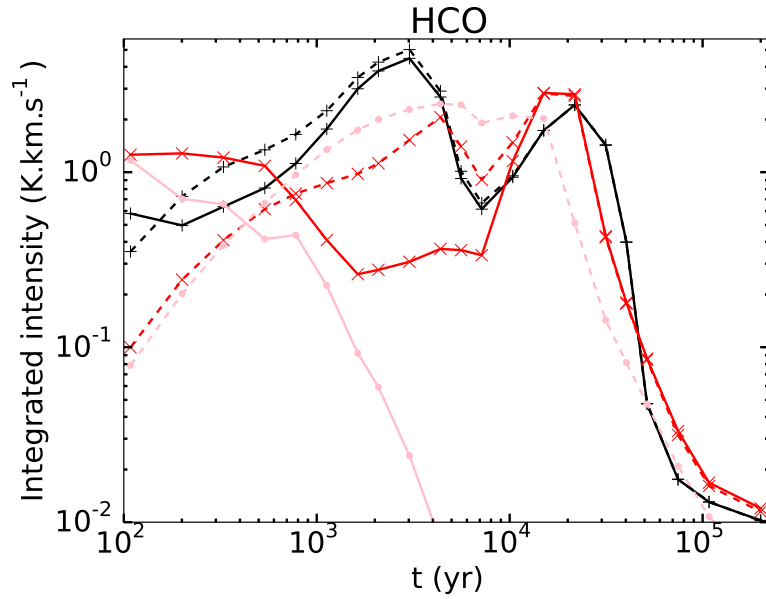
Density at the ionization front
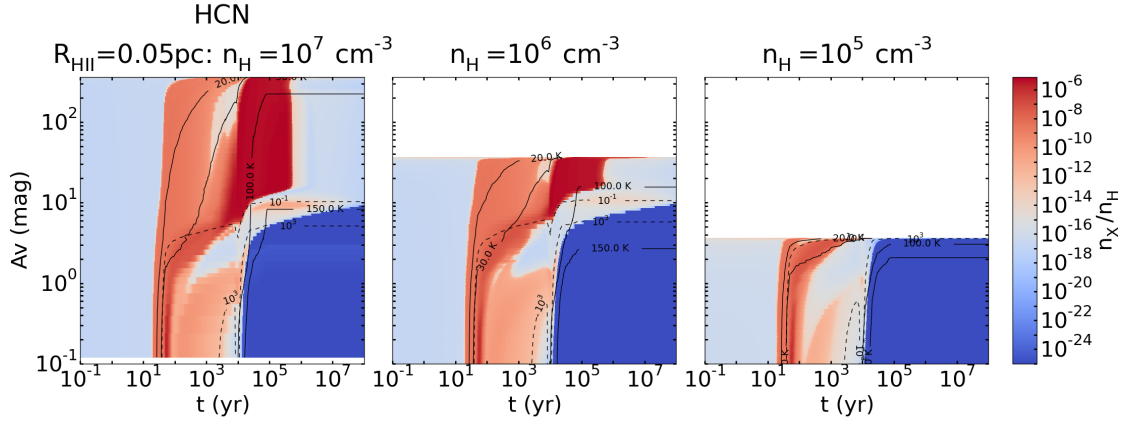
Figure A.7: Abundances of HCN in function of time (x-axis) and visual extinction (y-axis) for HII region models with different densities at the ionization front: 10^7 cm^{-3} (left), 10^6 cm^{-3} (middle) and 10^5 cm^{-3} (right). The solid black lines appearing on the figures represent the contours for the temperature: 20, 30, 100 and 150 K and the dashed black lines represent some contours for the radiation field intensity: 10^{-1} and 10^3 Draine unit.
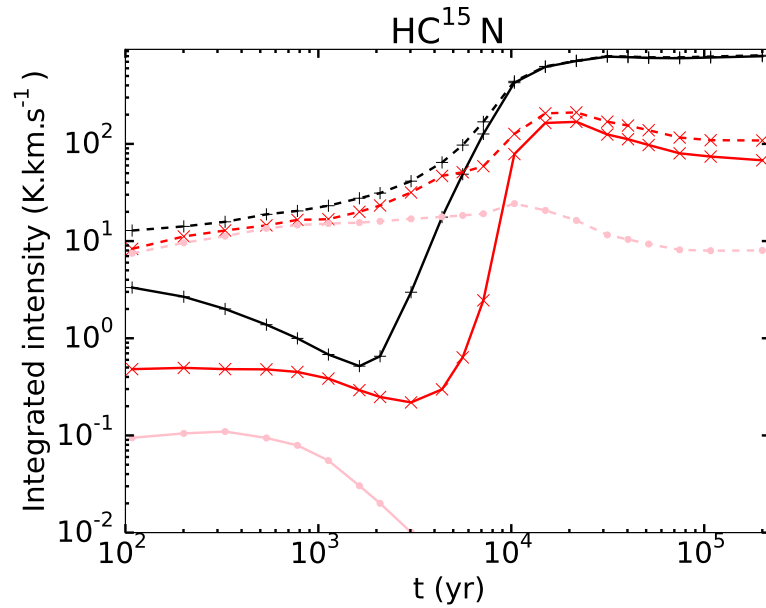
Figure A.8: Time evolution of integrated intensities for HC^{15}N (1–0) for models with different densities at the ionization front: 10^7 cm^{-3} (black), 10^6 cm^{-3} (red) and 10^5 cm^{-3} (pink). The solid lines represent the HII region models and the dashed lines the HHMC models.

Plummer exponent
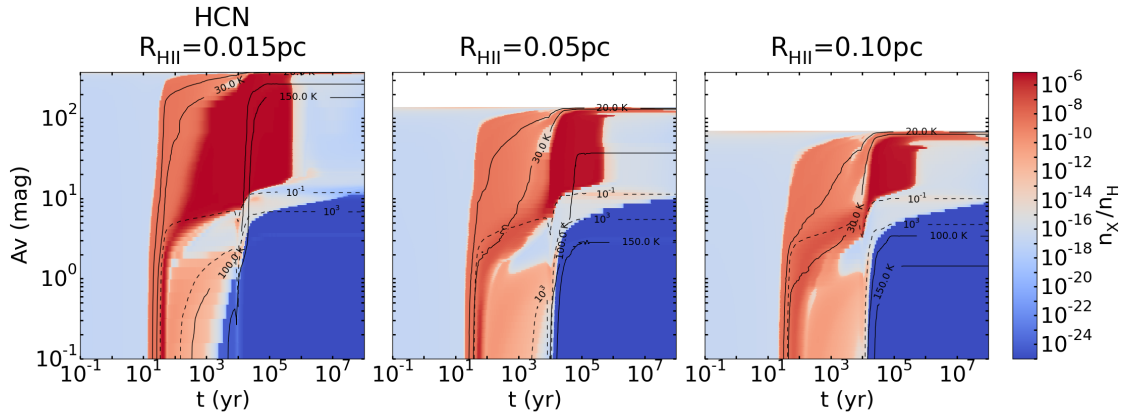
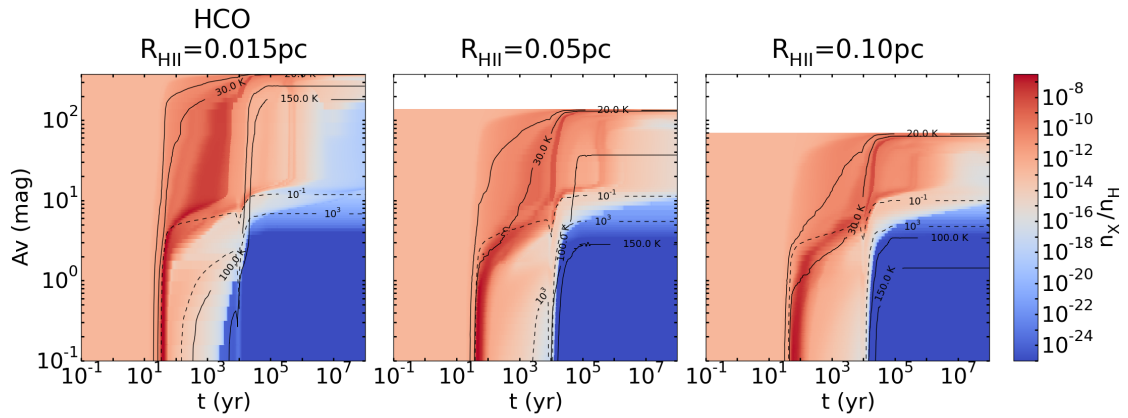

Figure A.9: Abundances of HCN in function of time (x-axis) and visual extinction (y-axis) for HII region models using for the second density profile ($\gamma = 1$) and with different sizes of ionized cavity: 0.015 pc (left panel), 0.05 pc (middle) and 0.10 pc (right). The solid black lines appearing on the figures represent the contours for the temperature: 20, 30, 100 and 150 K and the dashed black lines represent some contours for the radiation field intensity: 10^{-1} and 10^3 Draine unit.
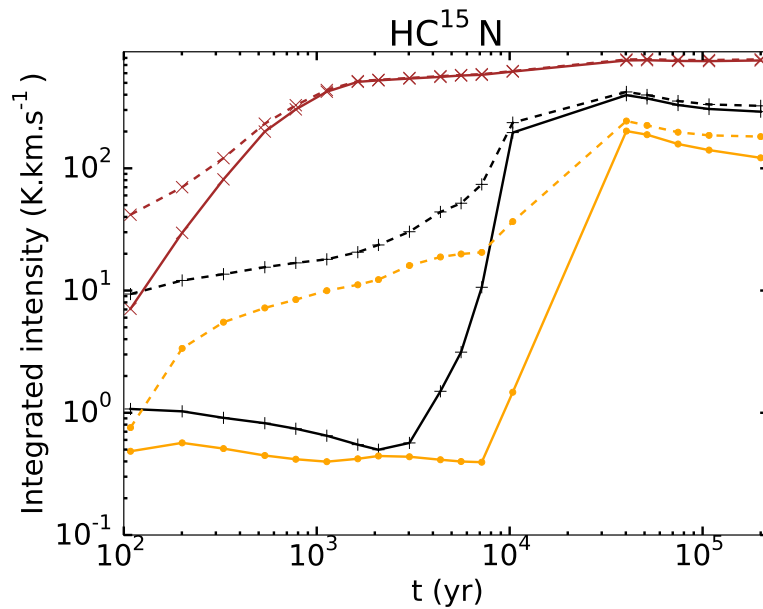
Figure A.10: Time evolution of integrated intensities for $HC^{15}N$ (1–0) (left panel) for models using the second density profile ($\gamma = 1$) and with different sizes of ionized cavity: 0.015 pc (brown), 0.05 pc (black) and 0.10 pc (orange). The solid lines represent the HII region models and the dashed lines the HHMC models.

Initial abundances
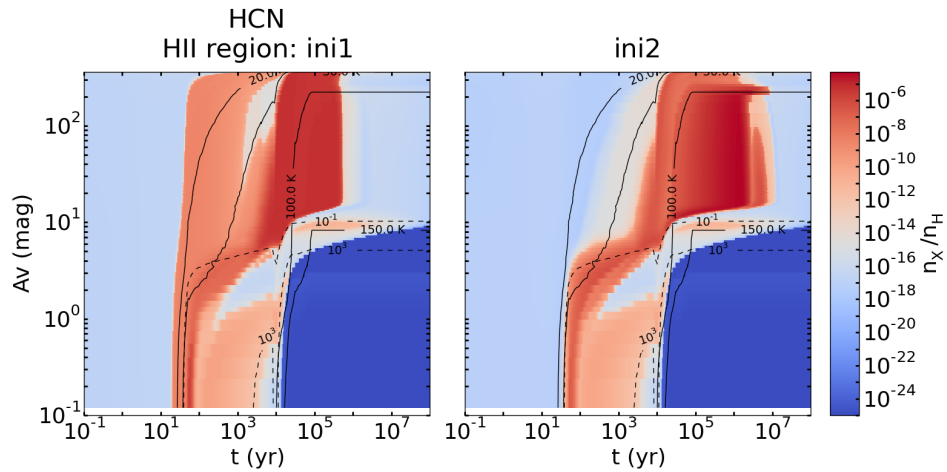
Figure A.11: Abundances of HCN in function of time (x-axis) and visual extinction (y-axis) for HII region with different initial abundances: *ini1* (left panel) and *ini2* (right). The solid black lines appearing on the figures represent the contours for the temperature: 20, 30, 100 and 150 K and the dashed black lines represent some contours for the radiation field intensity: 10^{-1} and 10^3 Draine unit.
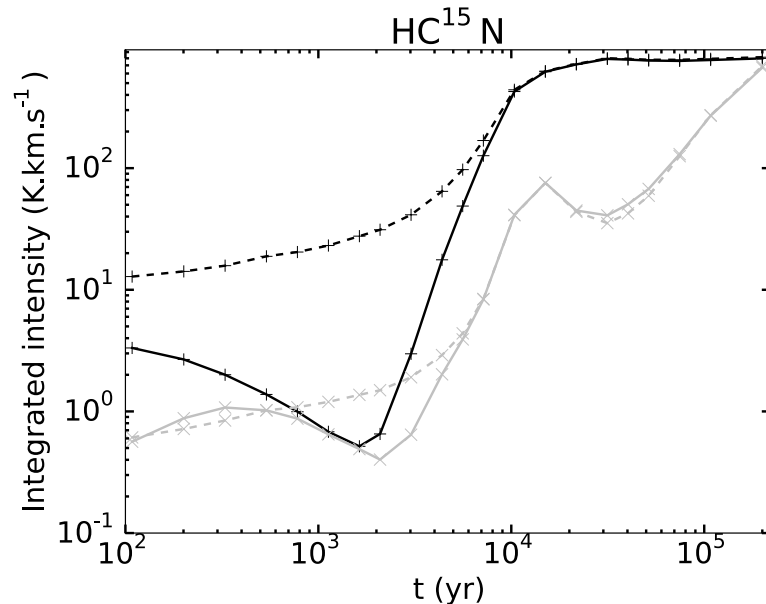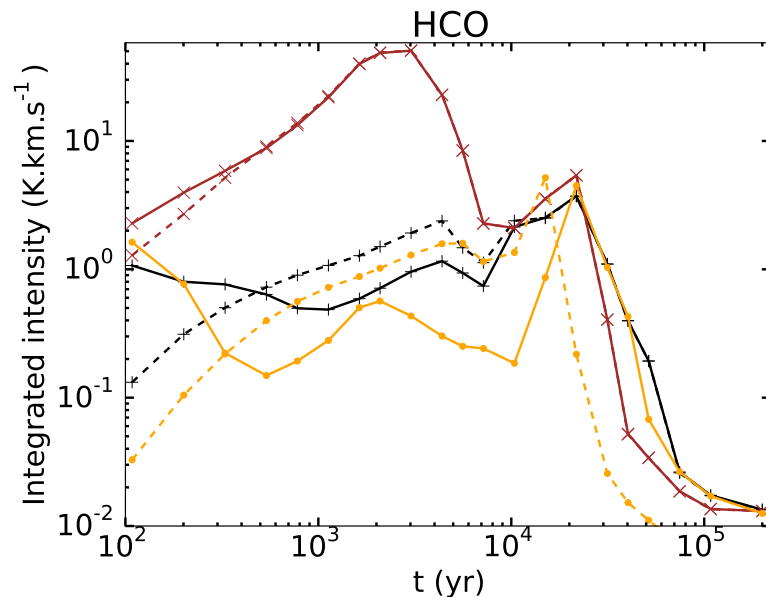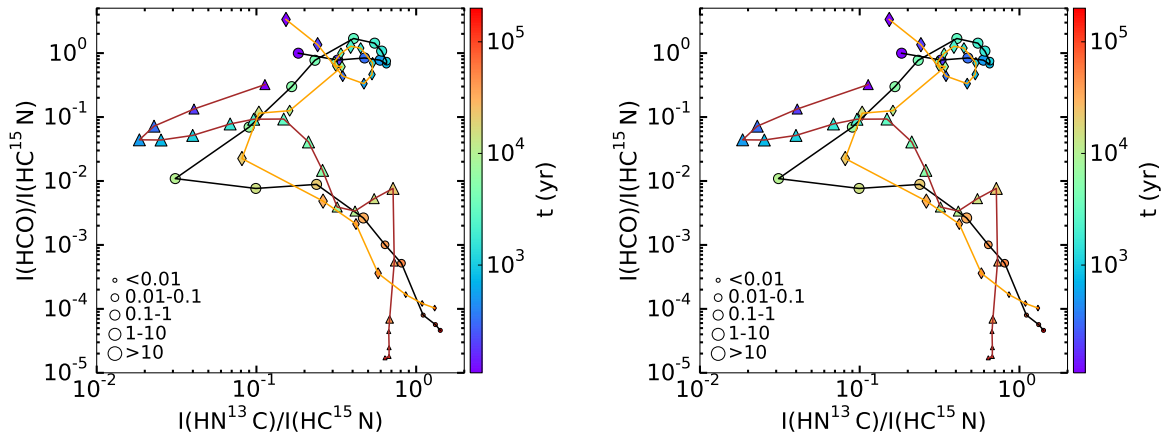

Figure A.12: Time evolution of integrated intensities for HC^{15}N (1–0) (left panel) for models with different initial abundances: *ini1* (black) and *ini2* (grey). The solid lines represent the HII region models and the dashed lines the HHMC models.

Effect of the envelope
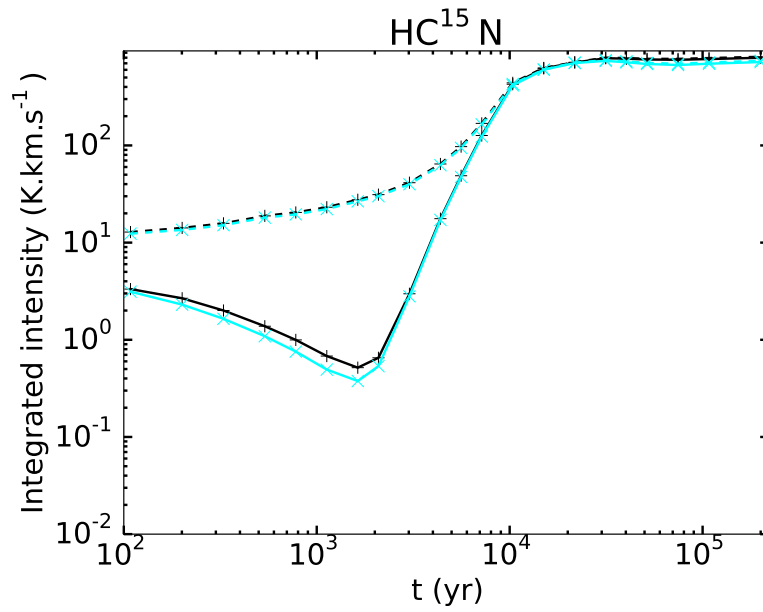
Figure A.13: Time evolution of integrated intensities for $HC^{15}N$ (1–0) for models with different cut-off density: 10^1 cm^{-3} (black) and 10^6 cm^{-3} (light blue). The solid lines represent the HII region models and the dashed lines the HHMC models.

A.2   HN^{13}C

HMC vs HHMC model
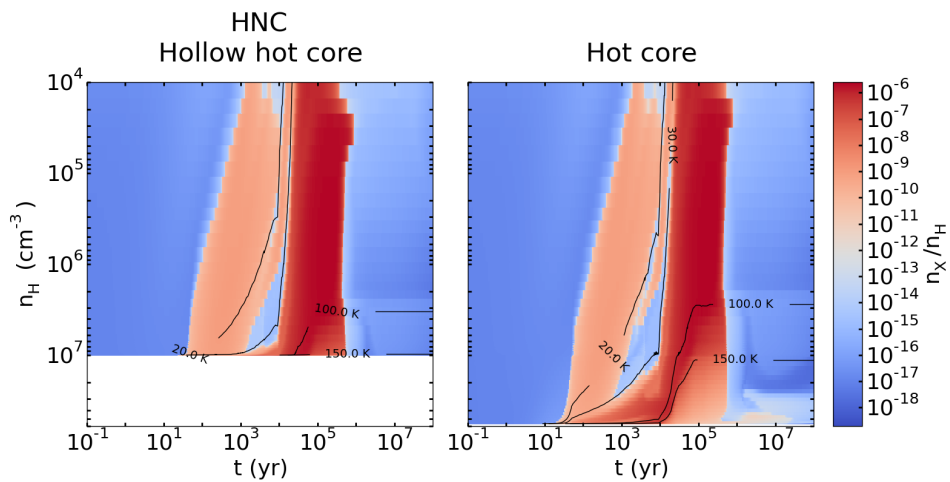
Figure A.14: Abundance of HCN in function of time (x-axis) and density (y-axis) for the HHMC (left) and HMC (right) models.
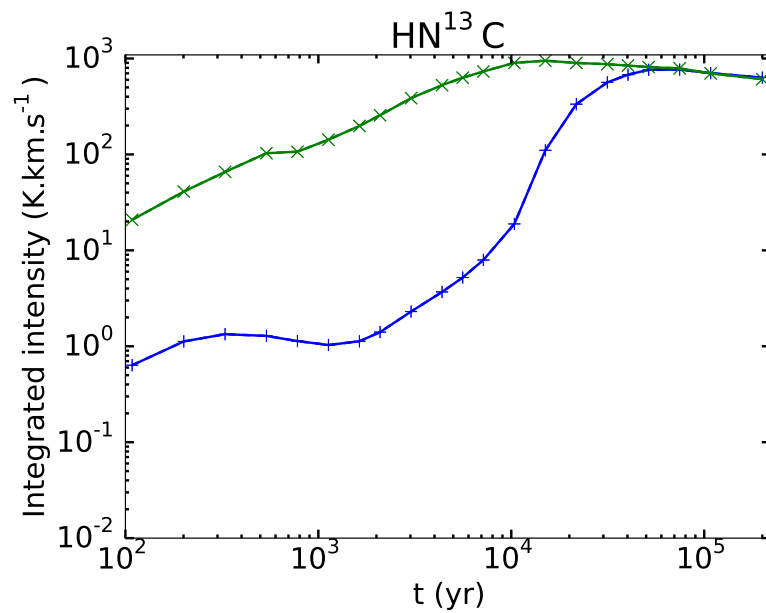
Figure A.15: Time evolution of integrated intensities for HN^{13}C (1–0). The blue lines represent the HHMC model and the green ones represent the HMC model.
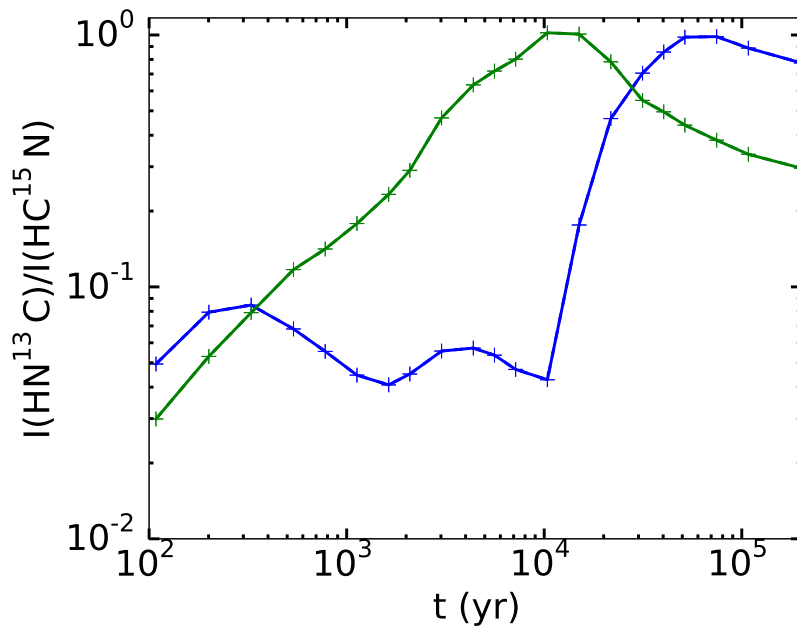
Figure A.16: Time evolution for the HHMC (blue) and HMC (green) models of integrated intensity ratio ($I(\text{HN}^{13}\text{C}\,(1\text{--}0))$ / $I(\text{HC}^{15}\text{N}\,(1\text{--}0))$).

H$\textsc{ii}$ region vs HHMC model
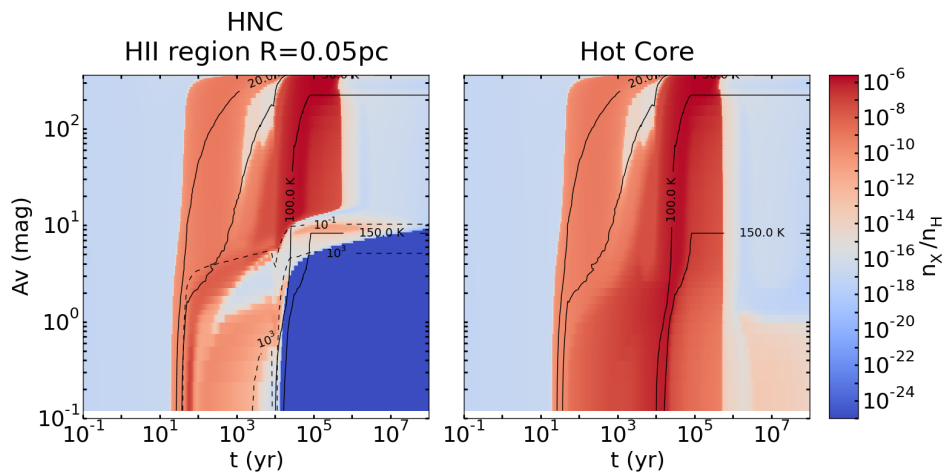
Figure A.17: Abundances of HNC in function of time (x-axis) and visual extinction (y-axis) for the HII region (left panel) and HHMC (right) models. The solid black lines represent the contours for the temperature: 20, 30, 100 and 150 K and the dashed black lines represent some contours for the radiation field intensity: 10^{-1} and 10^{3} Draine unit.
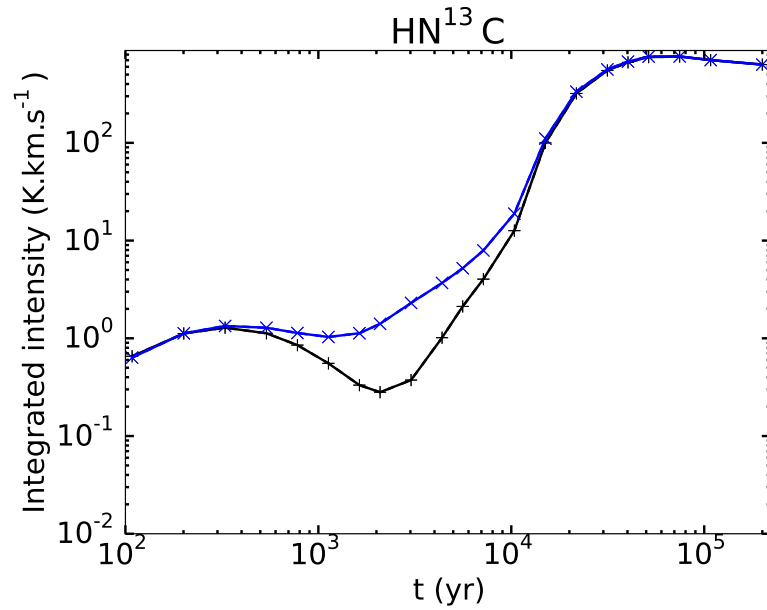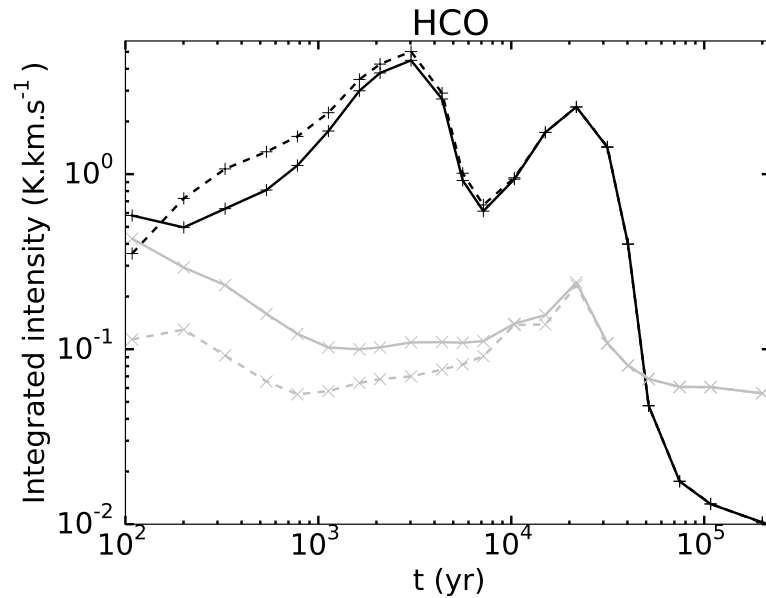
Figure A.18: Time evolution of integrated intensities for HN^{13}C (1–0). The black line represent the HII region model and the blue line represents the HHMC model
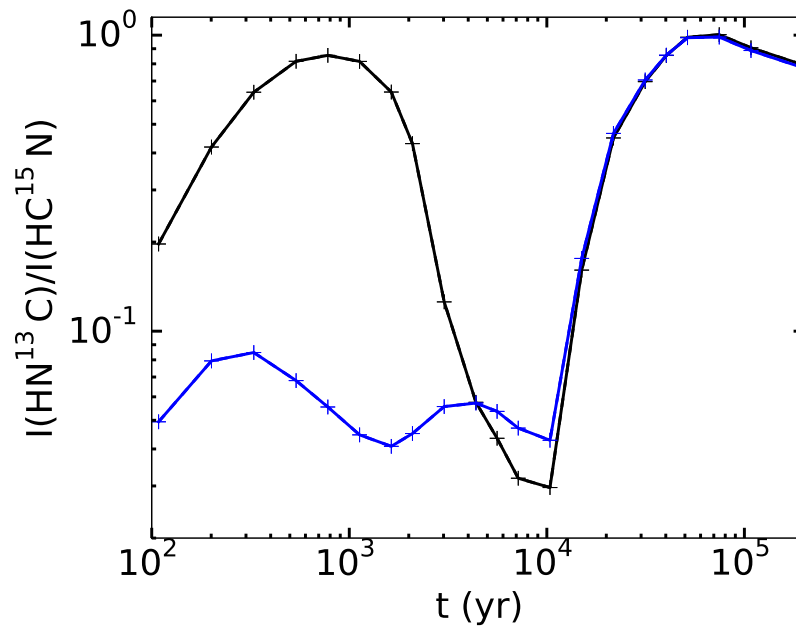
Figure A.19: Time evolution for HII region (black) and HHMC (blue) models of integrated intensity ratio (I(HN^{13}C (1–0)) / I(HC^{15}N (1–0))).

H II region size
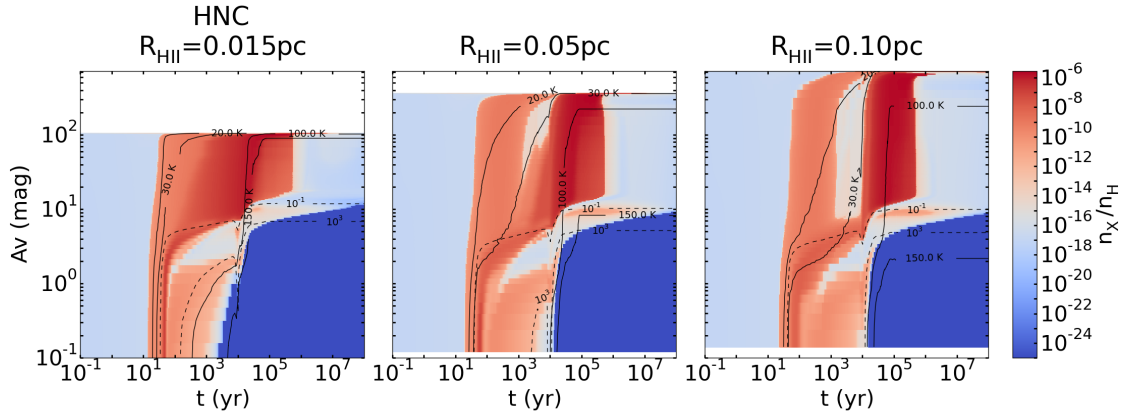
Figure A.20: Abundances of HNC in function of time (x-axis) and visual extinction (y-axis) for HII region models with different sizes: 0.015 pc (left panels), 0.05 pc (middle) and 0.10 pc (right). The solid black lines appearing on the figures represent the contours for the temperature: 20, 30, 100 and 150 K and the dashed black lines represent some contours for the radiation field intensity: 10^{-1} and 10^3 Draine unit.
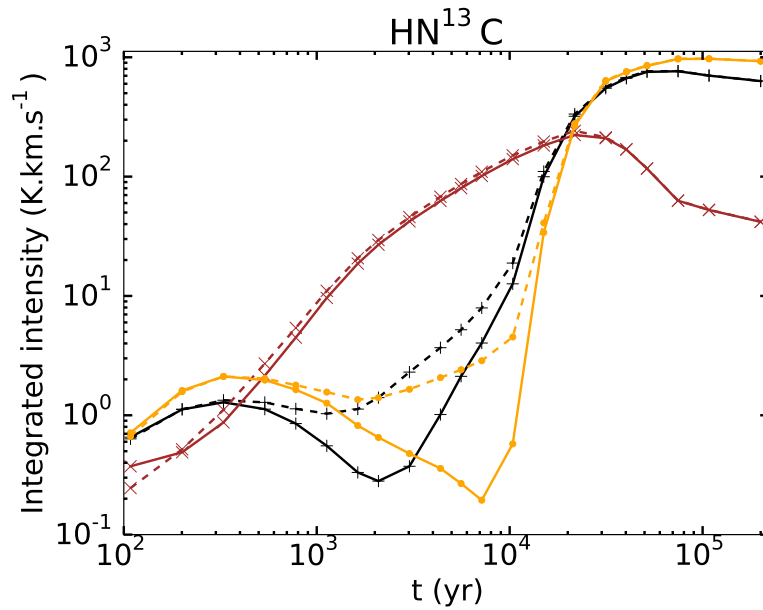
Figure A.21: Time evolution of integrated intensities for $HN^{13}C$ (1–0) for models with different sizes of ionized cavity: 0.015 pc (orange), 0.05 pc (black) and 0.10 pc (brown). The solid lines represent the HII region models and the dashed lines the HHMC models.
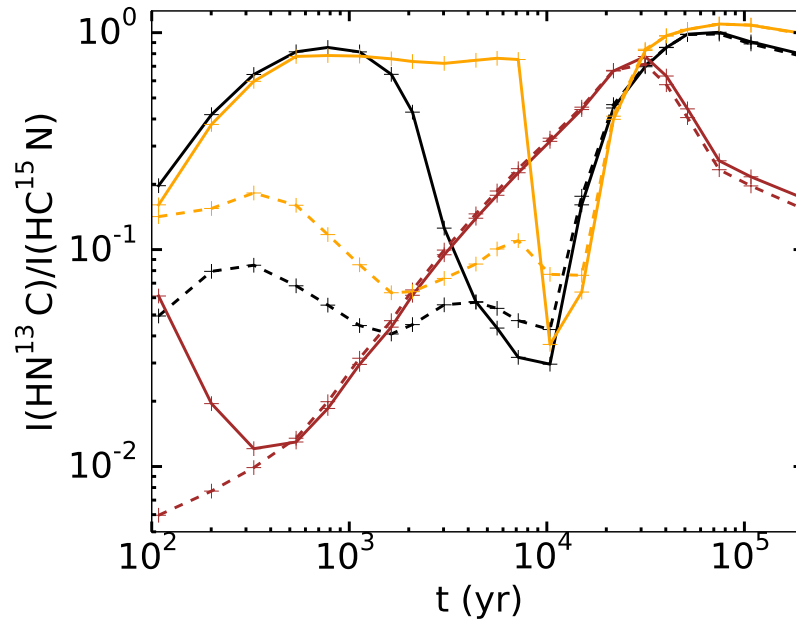
Figure A.22: Time evolution of integrated intensity ratio ($I(\mathrm{HN}^{13}\mathrm{C}\,(1\text{--}0))$ / $I(\mathrm{HC}^{15}\mathrm{N}\,(1\text{--}0))$) for models with different sizes of ionized cavity: 0.015 pc (brown), 0.05 pc (black) and 0.10 pc (orange). The solid lines represent the HII region models and the dashed lines the HHMC models.

Density at the ionization front
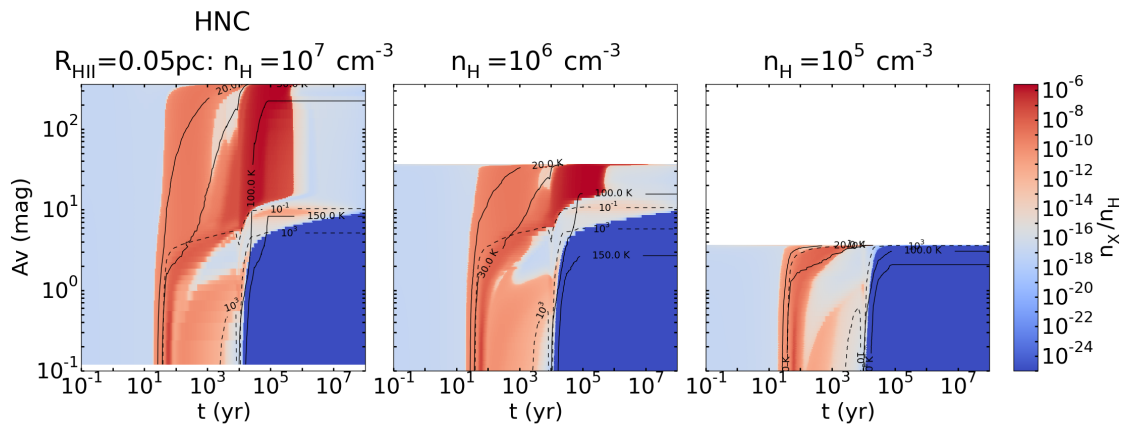
Figure A.23: Abundances of HNC in function of time (x-axis) and visual extinction (y-axis) for HII region models with different densities at the ionization front: 10^7 cm^{-3} (left), 10^6 cm^{-3} (middle) and 10^5 cm^{-3} (right). The solid black lines appearing on the figures represent the contours for the temperature: 20, 30, 100 and 150 K and the dashed black lines represent some contours for the radiation field intensity: 10^{-1} and 10^3 Draine unit.
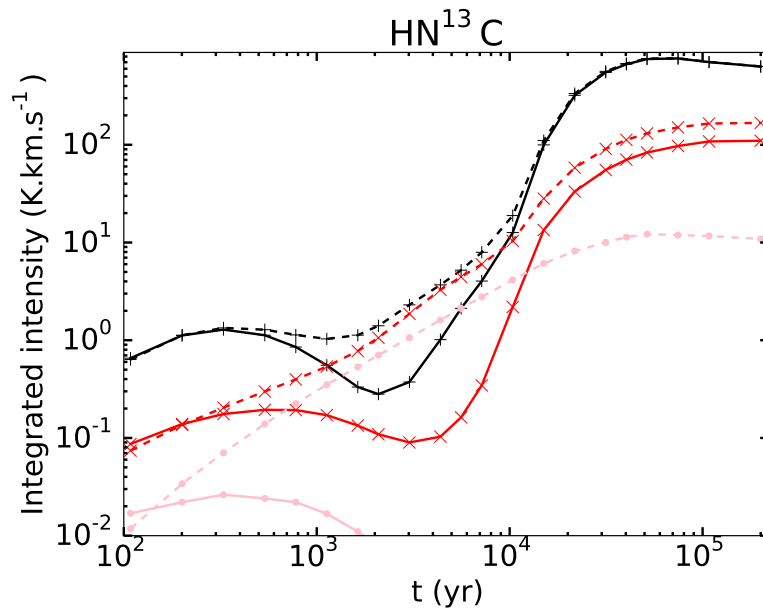
Figure A.24: Time evolution of integrated intensities for $HN^{13}C\,(1\text{–}0)$ for models with different densities at the ionization front: 10^7 cm^{-3} (black), 10^6 cm^{-3} (red) and 10^5 cm^{-3} (pink). The solid lines represent the HII region models and the dashed lines the HHMC models.
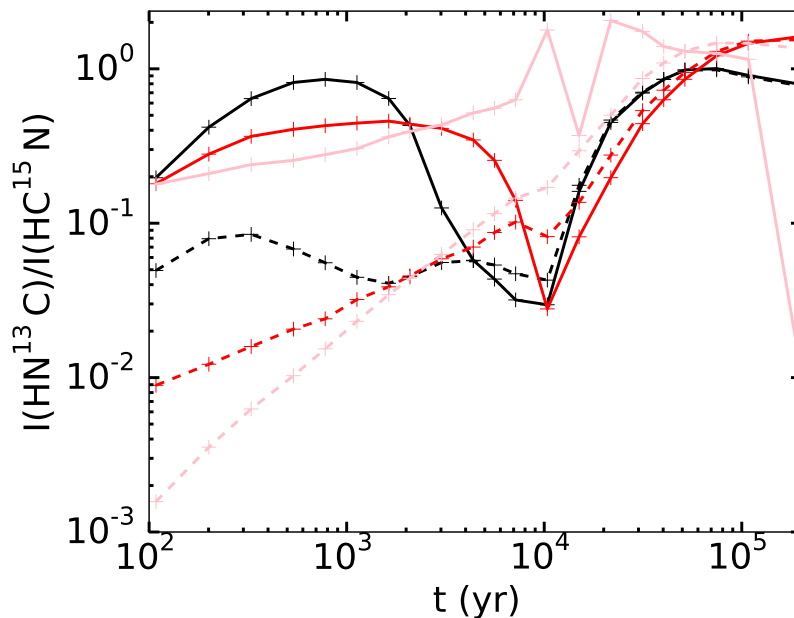
Figure A.25: Time evolution of integrated intensity ratio $(I(HN^{13}C\,(1\text{–}0))\,/\,I(HC^{15}N\,(1\text{–}0)))$ for models with different sizes of ionized cavity: 10^7 cm^{-3} (black), 10^6 cm^{-3} (red) and 10^5 cm^{-3} (pink). The solid lines represent the HII region models and the dashed lines the HHMC models.

Plummer exponent
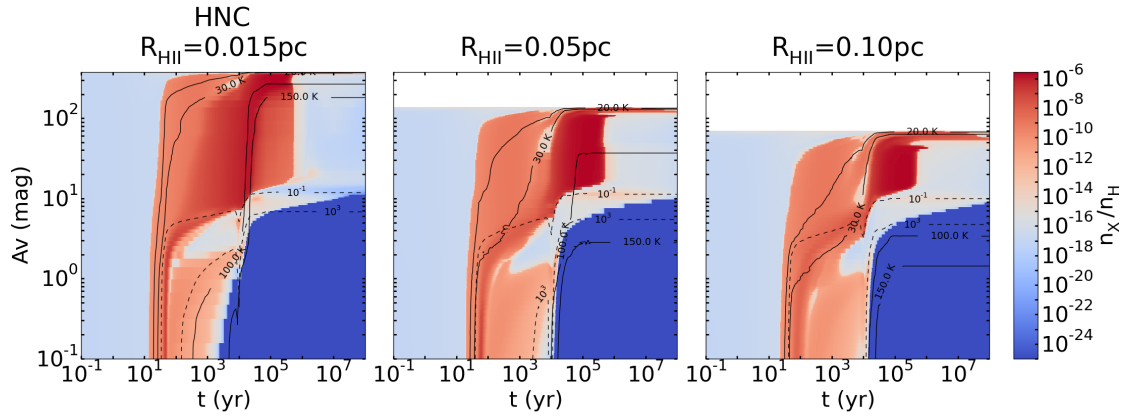
Figure A.26: Abundances of HNC in function of time (x-axis) and visual extinction (y-axis) for HII region models using for the second density profile ($\gamma = 1$) and with different sizes of ionized cavity: 0.015 pc (left panel), 0.05 pc (middle) and 0.10 pc (right). The solid black lines appearing on the figures represent the contours for the temperature: 20, 30, 100 and 150 K and the dashed black lines represent some contours for the radiation field intensity: 10^{-1} and 10^3 Draine unit.
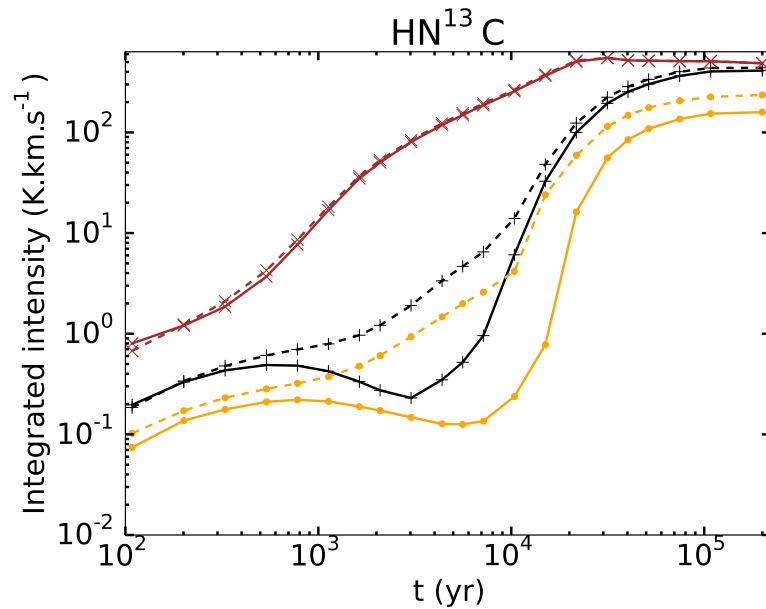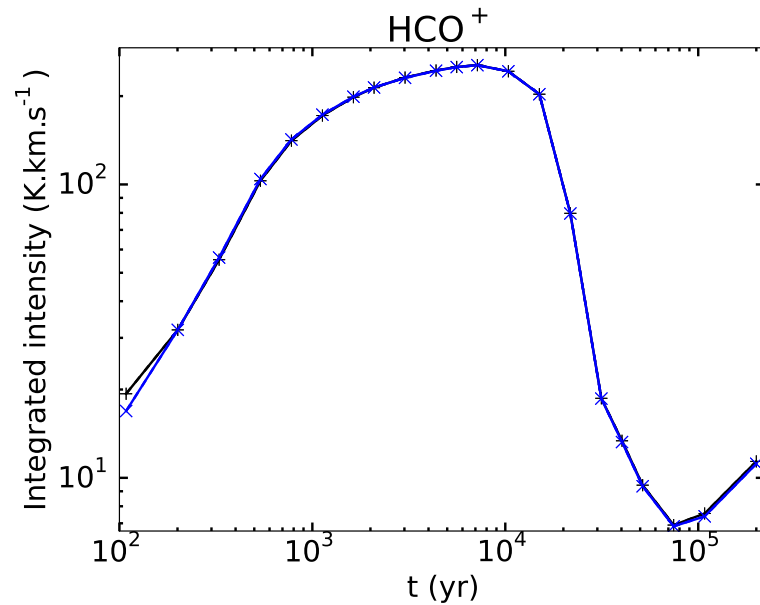

Figure A.27: Time evolution of integrated intensities for HN¹³C (1–0) (left panel) for models using the second density profile ($\gamma = 1$) and with different sizes of ionized cavity: 0.015 pc (brown), 0.05 pc (black) and 0.10 pc (orange). The solid lines represent the HII region models and the dashed lines the HHMC models.
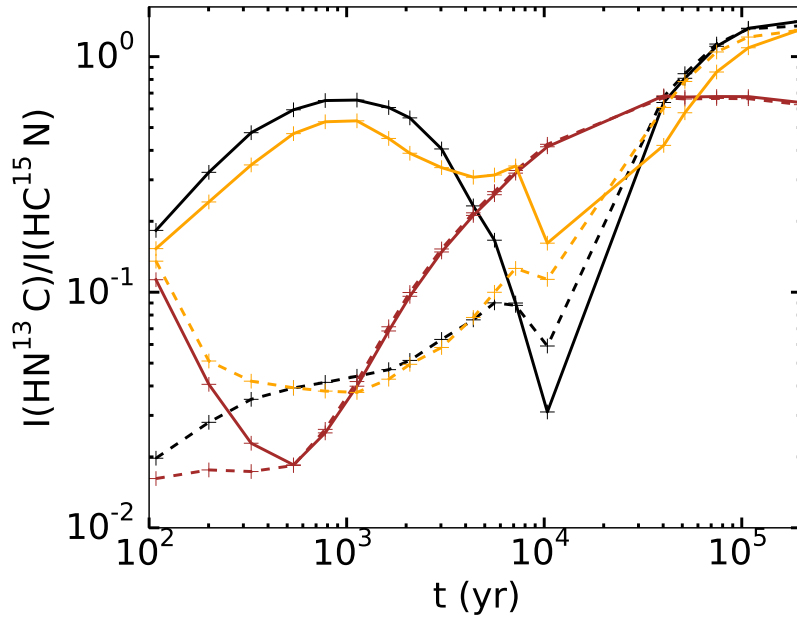
Figure A.28: Time evolution of integrated intensity ratio ($I(\mathrm{HN^{13}C}\,(1\text{–}0))$ / $I(\mathrm{HC^{15}N}\,(1\text{–}0))$) for models using the second density profile ($\gamma = 1$) and with different sizes of ionized cavity: 0.015 pc (brown), 0.05 pc (black) and 0.10 pc (orange). The solid lines represent the HII region models and the dashed lines the HHMC models.

Initial abundances
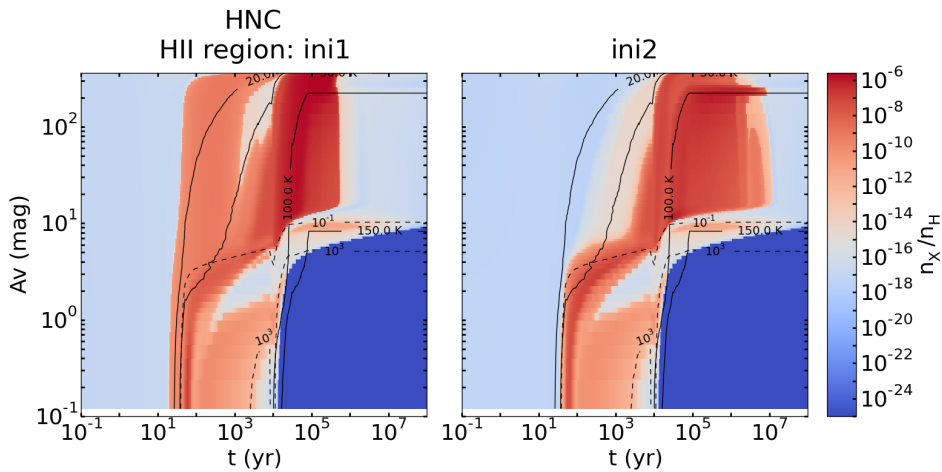
Figure A.29: Abundances of HNC in function of time (x-axis) and visual extinction (y-axis) for HII region with different initial abundances: *ini1* (left panel) and *ini2* (right). The solid black lines appearing on the figures represent the contours for the temperature: 20, 30, 100 and 150 K and the dashed black lines represent some contours for the radiation field intensity: 10^{-1} and 10^{3} Draine unit.
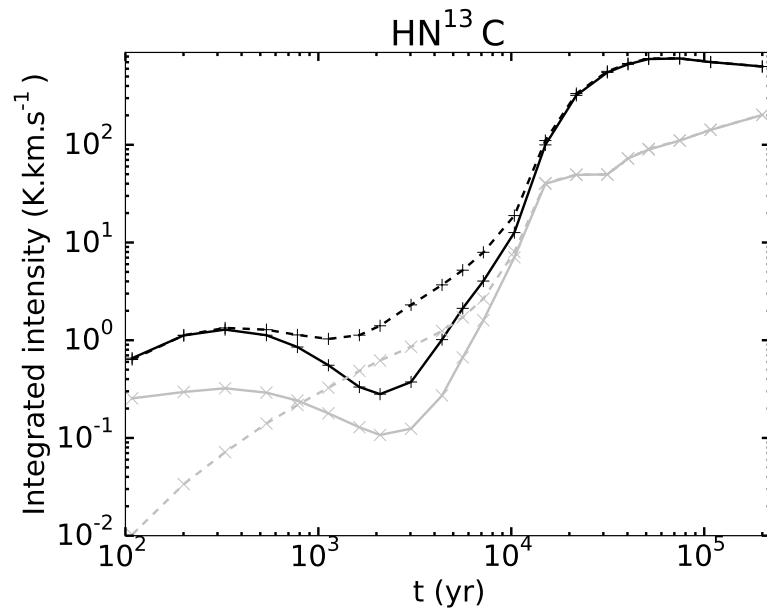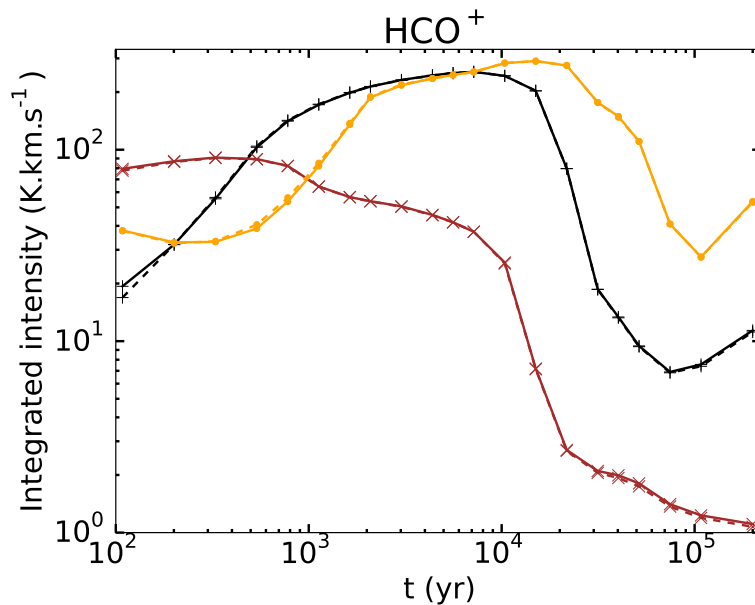
Figure A.30: Time evolution of integrated intensities for HN^{13}C (1–0) (left panel) for models with different initial abundances: *ini1* (black) and *ini2* (grey). The solid lines represent the HII region models and the dashed lines the HHMC models.
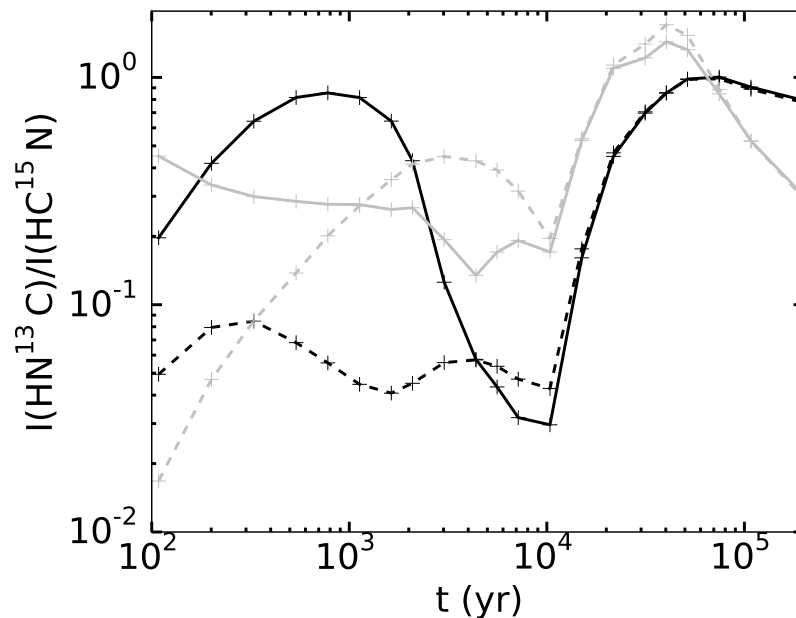
Figure A.31: Time evolution of integrated intensity ratio (I(HN^{13}C (1–0)) / I(HC^{15}N (1–0))) for models with different initial abundances: *ini1* (black) and *ini2* (grey). The solid lines represent the HII region models and the dashed lines the HHMC models.

Effect of the envelope
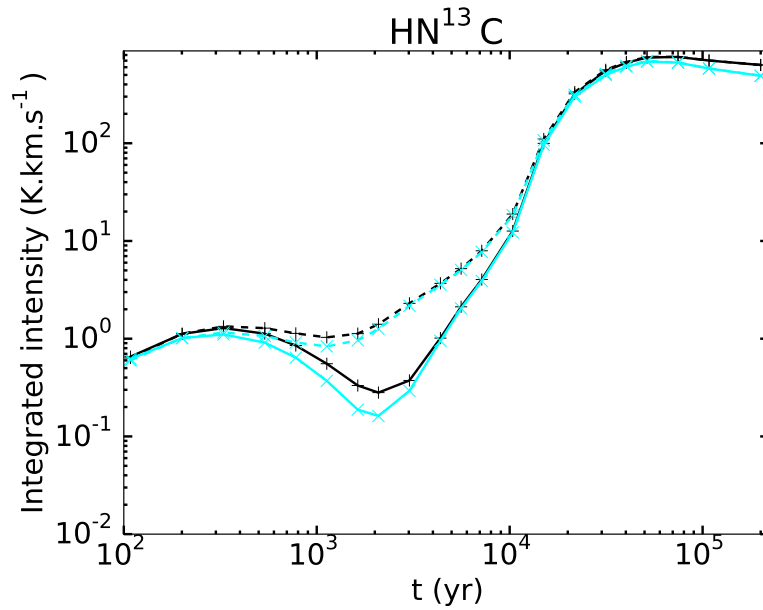
Figure A.32: Time evolution of integrated intensities for $HN^{13}C$ (1–0) for models with different cut-off density: 10^1 cm^{-3} (black) and 10^6 cm^{-3} (light blue). The solid lines represent the HII region models and the dashed lines the HHMC models.
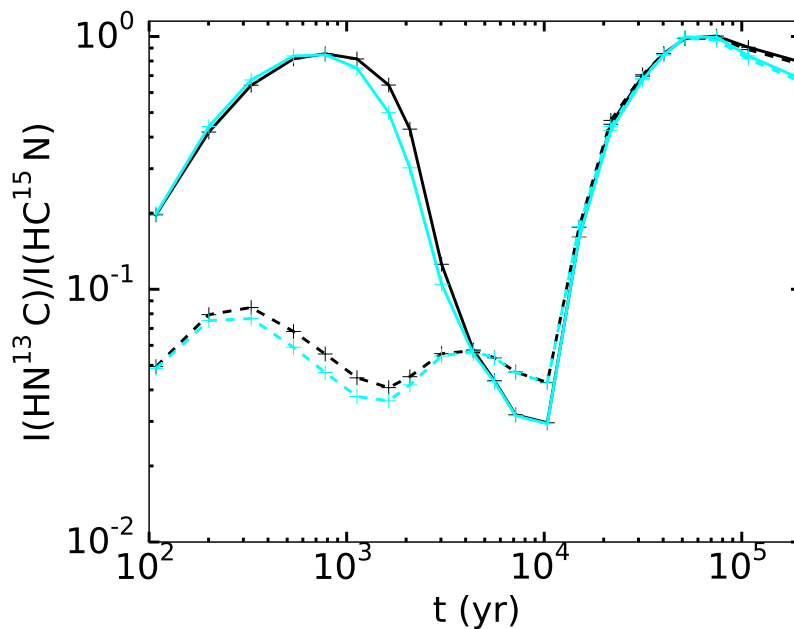
Figure A.33: Time evolution of integrated intensity ratio ($I(HN^{13}C$ (1–0)) / $I(HC^{15}N$ (1–0))) for models with different cut-off density: 10^1 cm^{-3} (black) and 10^6 cm^{-3} (light blue). The solid lines represent the HII region models and the dashed lines the HHMC models.

A.3   HCO

HMC vs HHMC model
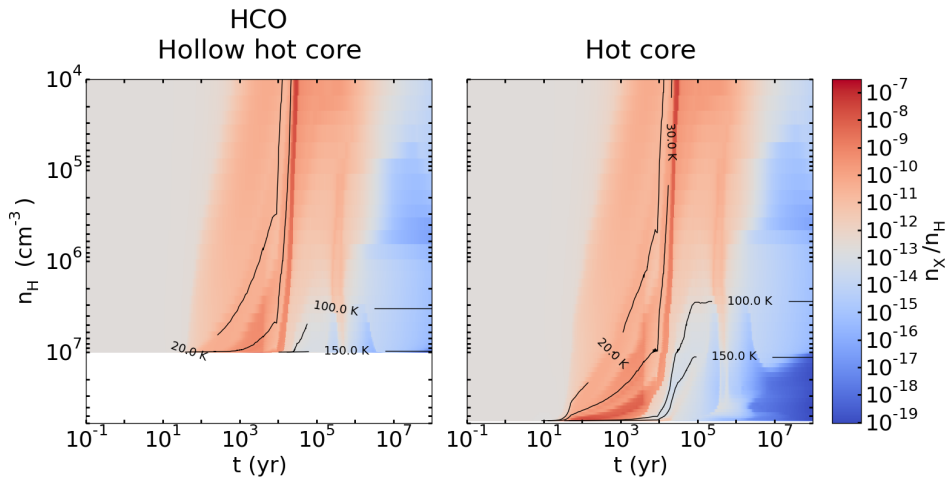
Figure A.34: Abundance of HCN in function of time (x-axis) and density (y-axis) for the HHMC (left) and HMC (right) models.
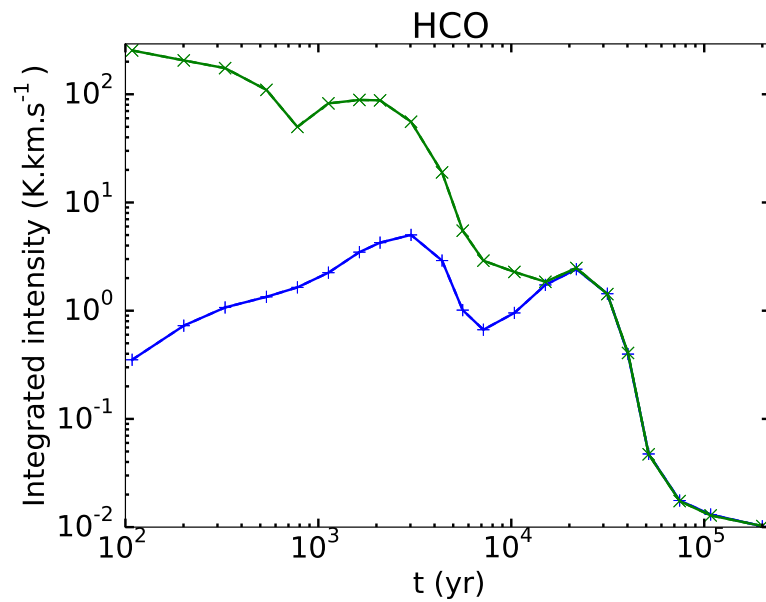
Figure A.35: Time evolution of integrated intensities for HCO (1(0,1)–0(0,0)). The blue lines represent the HHMC model and the green one represents the HMC model.
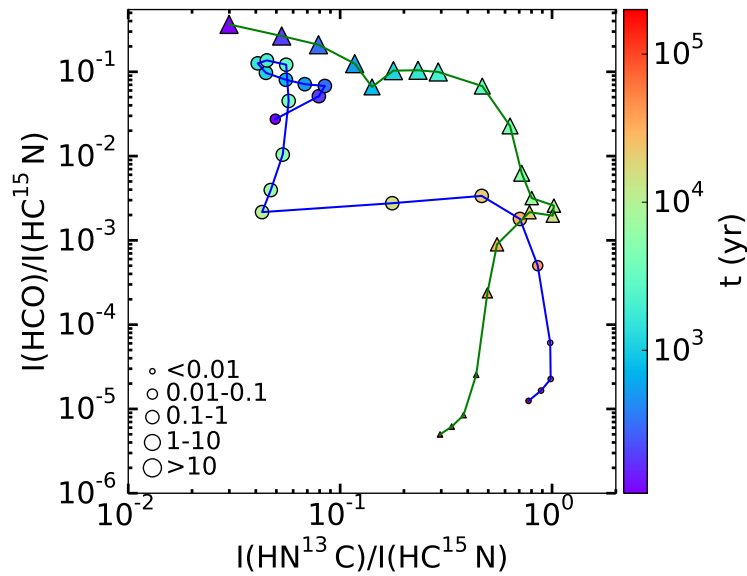
Figure A.36: Time evolution of the integrated intensity ratio (I(HCO (1(0,1)–0(0,0))) / I(HC^{15}N (1–0))) in function of the integrated intensity ratio (I(HN^{13}C (1–0)) / I(HC^{15}N (1–0))) for the HHMC (blue line and circle markers) and HMC (green line and triangle markers) models. The size of the markers corresponds to the range value of the peak intensity in Kelvin of HCO.

H II region vs HHMC model
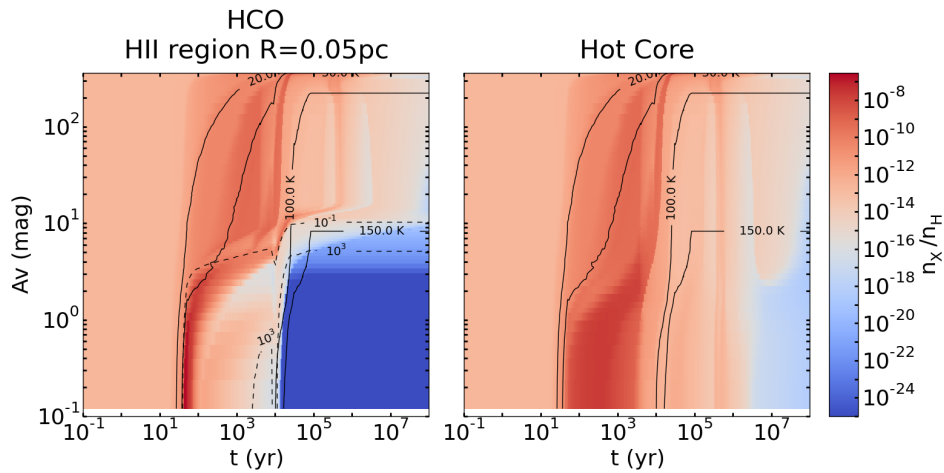
Figure A.37: Abundances of HCO in function of time (x-axis) and visual extinction (y-axis) for the HII region (left panel) and HHMC (right) models. The solid black lines represent the contours for the temperature: 20, 30, 100 and 150 K and the dashed black lines represent some contours for the radiation field intensity: 10^{-1} and 10^{3} Draine unit.
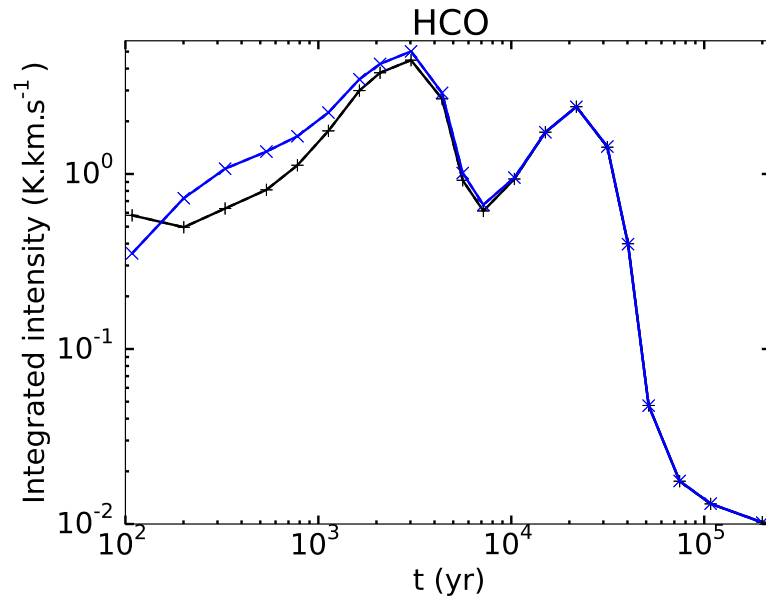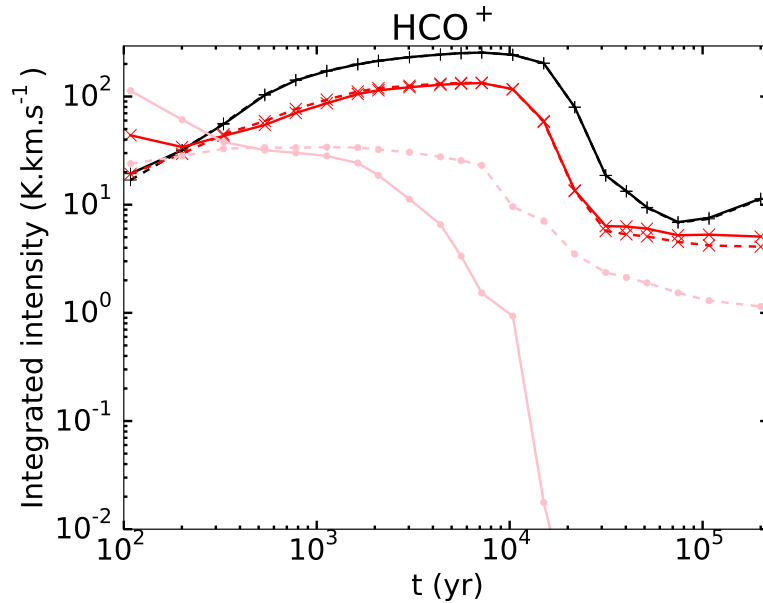
Figure A.38: Time evolution of integrated intensities for HCO (1(0,1)–0(0,0)). The black line represents the HII region model and the blue lines represent the HHMC model.
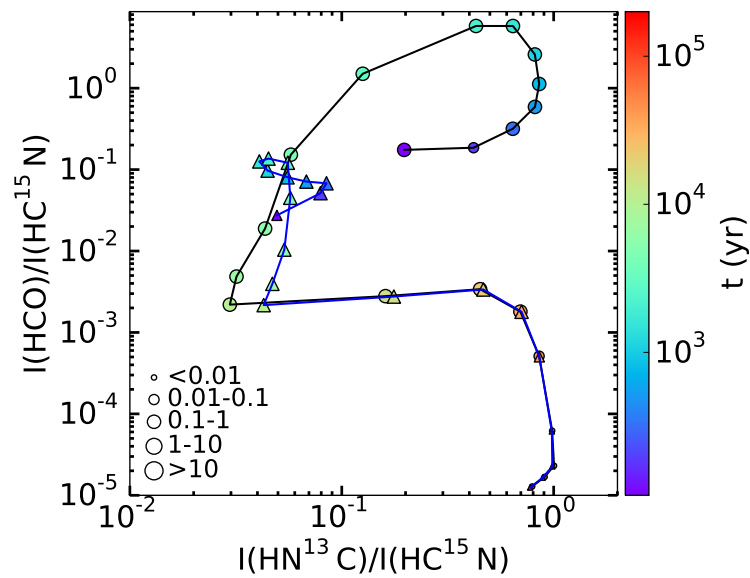
Figure A.39: Time evolution of the integrated intensity ratio ($I(HCO\,(1(0,1)$–$0(0,0)))$ / $I(HC^{15}N\,(1$–$0)))$) in function of the integrated intensity ratio ($I(HN^{13}C\,(1$–$0))$ / $I(HC^{15}N\,(1$–$0)))$) for the HII region (black line and circle markers) and HHMC (blue line and triangle markers) models. The size of the markers corresponds to the range value of the peak intensity in Kelvin of HCO.
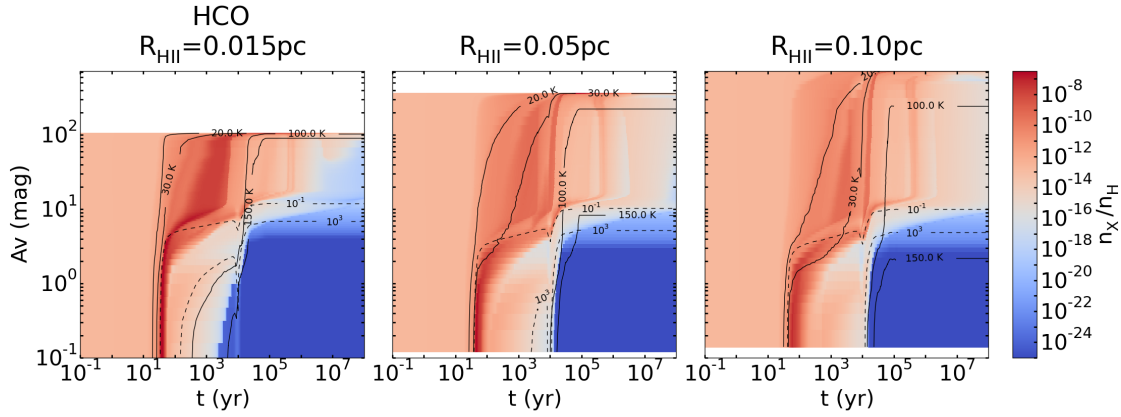
H$_{II}$ region size
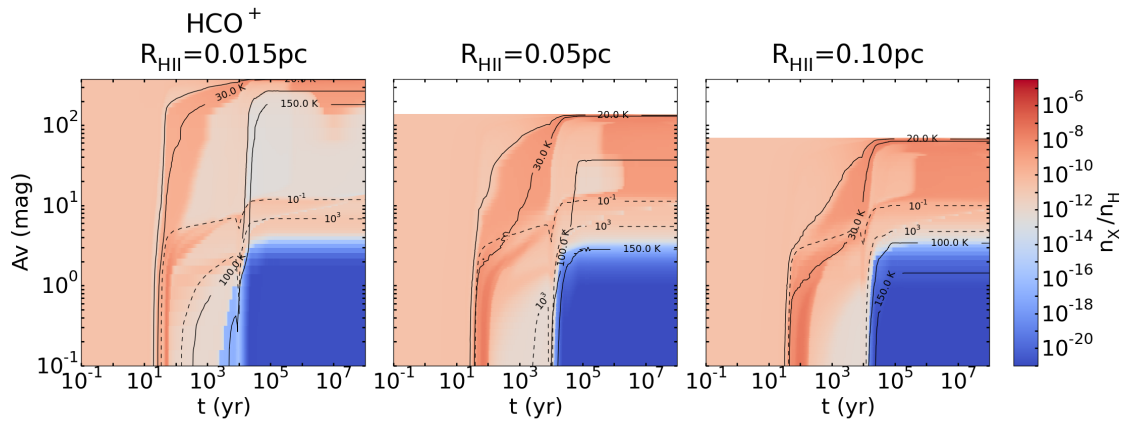

Figure A.40: Abundances of HCO in function of time (x-axis) and visual extinction (y-axis) for HII region models with different sizes: 0.015 pc (left panels), 0.05 pc (middle) and 0.10 pc (right). The solid black lines appearing on the figures represent the contours for the temperature: 20, 30, 100 and 150 K and the dashed black lines represent some contours for the radiation field intensity: 10^{-1} and 10^3 Draine unit.
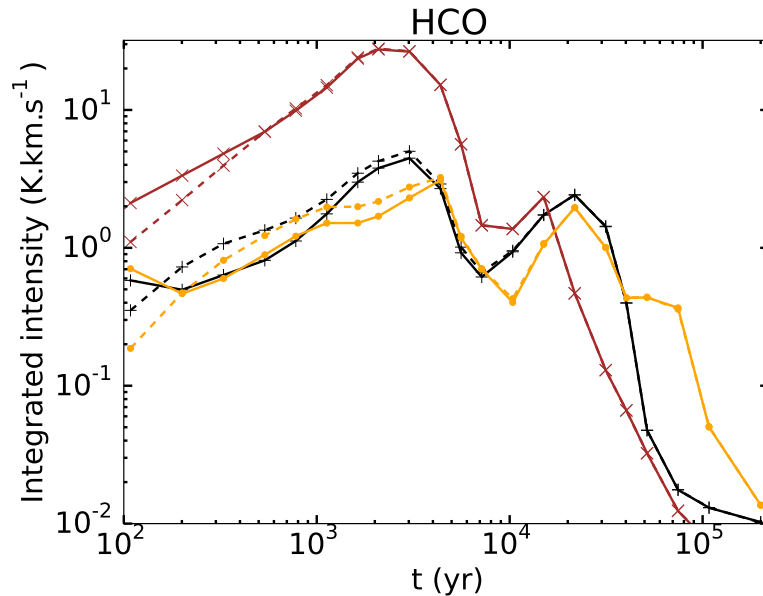
Figure A.41: Time evolution of integrated intensities for HCO (1(0,1)–0(0,0)) for models with different sizes of ionized cavity: 0.015 pc (orange), 0.05 pc (black) and 0.10 pc (brown). The solid lines represent the HII region models and the dashed lines the HHMC models.
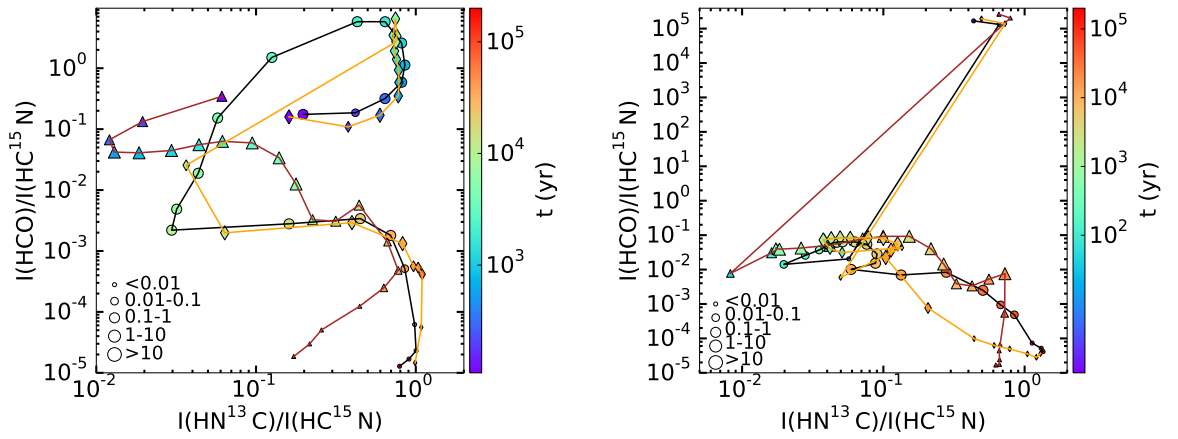
Figure A.42: Time evolution of the integrated intensity ratio $(I(\mathrm{HCO}\,(1(0,1)\text{--}0(0,0))) / I(\mathrm{HC}^{15}\mathrm{N}\,(1\text{--}0)))$ in function of the integrated intensity ratio $(I(\mathrm{HN}^{13}\mathrm{C}\,(1\text{--}0)) / I(\mathrm{HC}^{15}\mathrm{N}\,(1\text{--}0)))$ for models with different sizes of ionized cavity: 0.015 pc (brown line and triangle markers), 0.05 pc (black line and circle markers) and 0.10 pc (orange line and diamond markers). The HII region models are shown on the left panel and the HHMC models on the right panel. The size of the markers corresponds to the range value of the peak intensity in Kelvin of HCO.

Density at the ionization front

Figure A.43: Abundances of HCO in function of time (x-axis) and visual extinction (y-axis) for HII region models with different densities at the ionization front: 10^7 cm^{-3} (left), 10^6 cm^{-3} (middle) and 10^5 cm^{-3} (right). The solid black lines appearing on the figures represent the contours for the temperature: 20, 30, 100 and 150 K and the dashed black lines represent some contours for the radiation field intensity: 10^{-1} and 10^3 Draine unit.
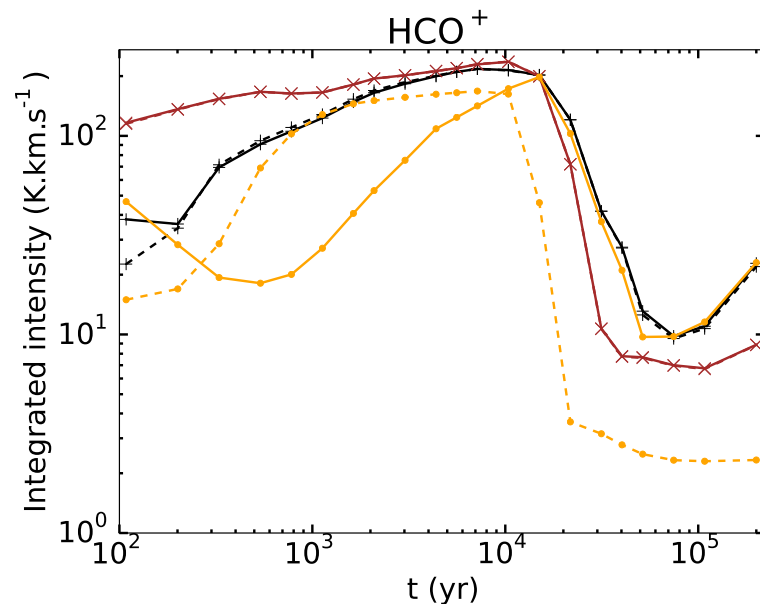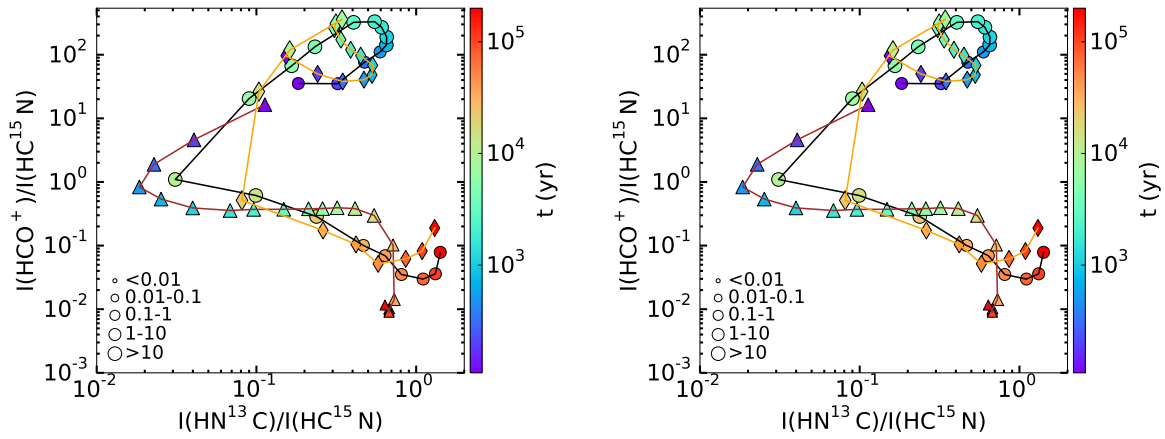
Figure A.44: Time evolution of integrated intensities for HCO (1(0,1)–0(0,0)) for models with different densities at the ionization front: 10^7 cm^{-3} (black), 10^6 cm^{-3} (red) and 10^5 cm^{-3} (pink). The solid lines represent the HII region models and the dashed lines the HHMC models.
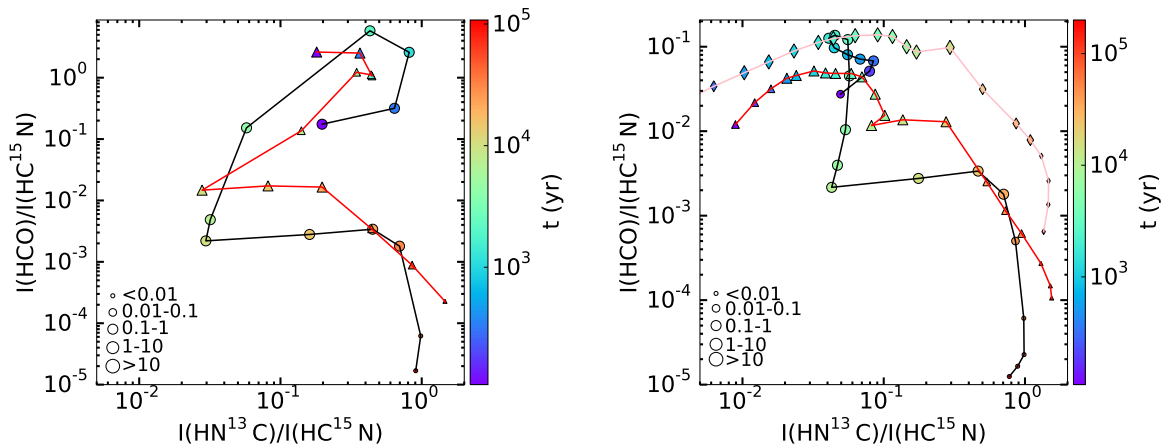
Figure A.45: Time evolution of the integrated intensity ratio (I(HCO (1(0,1)–0(0,0))) / I(HC^{15}N (1–0))) in function of the integrated intensity ratio (I(HN^{13}C (1–0)) / I(HC^{15}N (1–0))) for models with different density at the ionization front: 10^7 cm^{-3} (black line and circle markers), 10^6 cm^{-3} (red line and triangle markers) and 10^5 cm^{-3} (pink line and diamond markers). The HII region models are shown on the left panel and the HHMC models on the right panel. The size of the markers corresponds to the range value of the peak intensity in Kelvin of HCO.
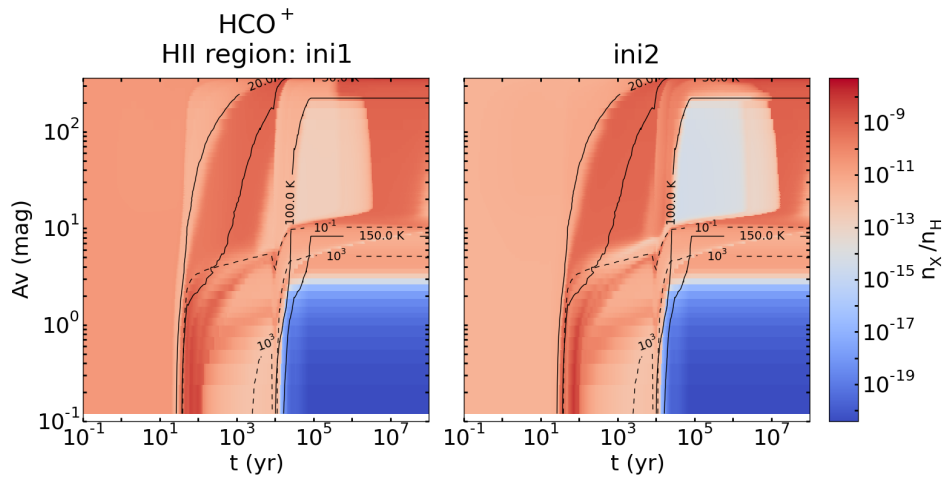
Plummer exponent

Figure A.46: Abundances of HCO in function of time (x-axis) and visual extinction (y-axis) for HII region models using for the second density profile ($\gamma = 1$) and with different sizes of ionized cavity: 0.015 pc (left panel), 0.05 pc (middle) and 0.10 pc (right). The solid black lines appearing on the figures represent the contours for the temperature: 20, 30, 100 and 150 K and the dashed black lines represent some contours for the radiation field intensity: 10^{-1} and 10^{3} Draine unit.

Figure A.47: Time evolution of integrated intensities for HCO (1(0,1)–0(0,0)) (left panel) for models using the second density profile ($\gamma = 1$) and with different sizes of ionized cavity: 0.015 pc (brown), 0.05 pc (black) and 0.10 pc (orange). The solid lines represent the HII region models and the dashed lines the HHMC models.

Figure A.48: Time evolution of the integrated intensity ratio ($I(\text{HCO}\,(1(0,1)\text{–}0(0,0)))$ / $I(\text{HC}^{15}\text{N}\,(1\text{–}0))$) in function of the integrated intensity ratio ($I(\text{HN}^{13}\text{C}\,(1\text{–}0))$ / $I(\text{HC}^{15}\text{N}\,(1\text{–}0))$) for models using the second density profile ($\gamma = 1$) and with different sizes of ionized cavity: 0.015 pc (brown and triangle markers), 0.05 pc (black and circle markers) and 0.10 pc (orange and diamond markers). The HII region models are shown on the left panel and the HHMC models on the right panel. The size of the markers correspond to the range value of the peak intensity in Kelvin of HCO.

Initial abundances
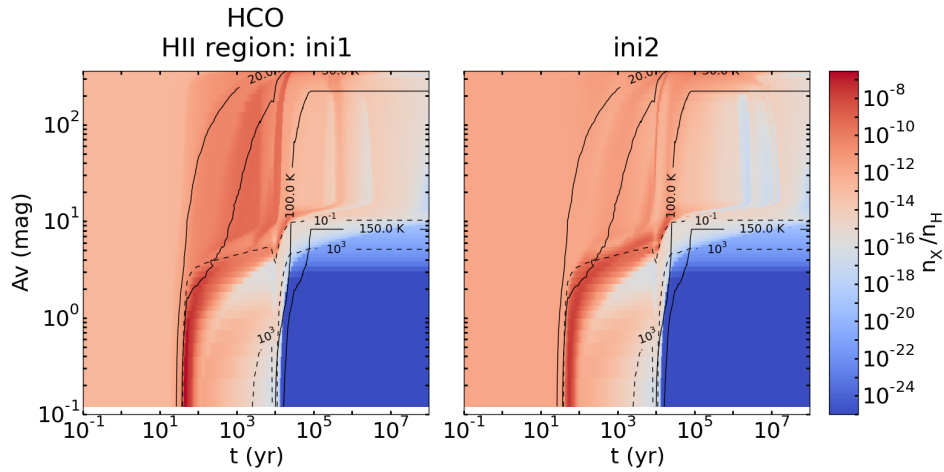


Figure A.49: Abundances of HCO in function of time (x-axis) and visual extinction (y-axis) for HII region with different initial abundances: *ini1* (left panel) and *ini2* (right). The solid black lines appearing on the figures represent the contours for the temperature: 20, 30, 100 and 150 K and the dashed black lines represent some contours for the radiation field intensity: 10^{-1} and 10^{3} Draine unit.

Figure A.50: Time evolution of integrated intensities for HCO (1(0,1)–0(0,0)) (left panel) for models with different initial abundances: *ini1* (black) and *ini2* (grey). The solid lines represent the HII region models and the dashed lines the HHMC models.
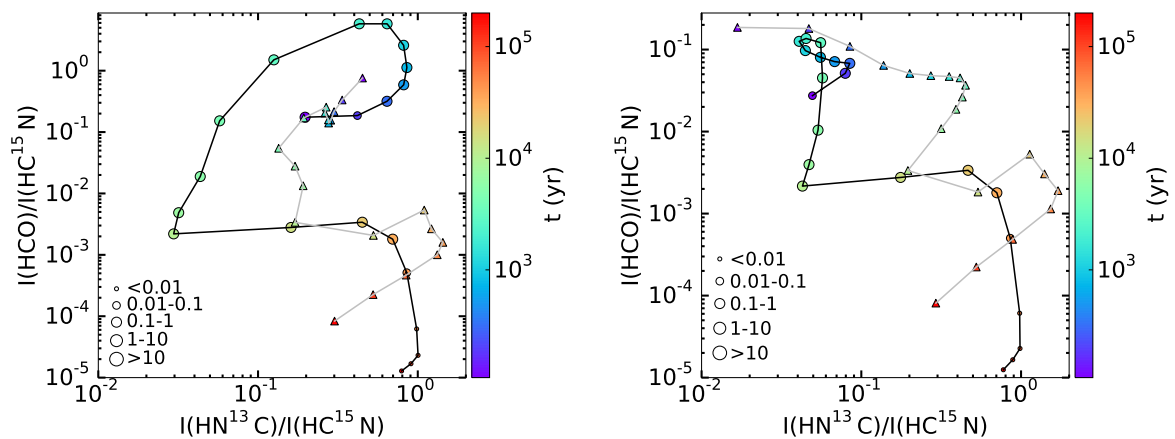
Figure A.51: Time evolution of the integrated intensity ratio (I(HCO (1(0,1)–0(0,0))) / I(HC^{15}N (1–0))) in function of the integrated intensity ratio (I(HN^{13}C (1–0)) / I(HC^{15}N (1–0))) for models with different initial abundances: *ini1* (black line and circle markers) and *ini2* (grey line and triangle markers). The HII region models are shown on the left panel and the HHMC models on the right panel. The size of the markers corresponds to the range value of the peak intensity in Kelvin of HCO.

Effect of the envelope
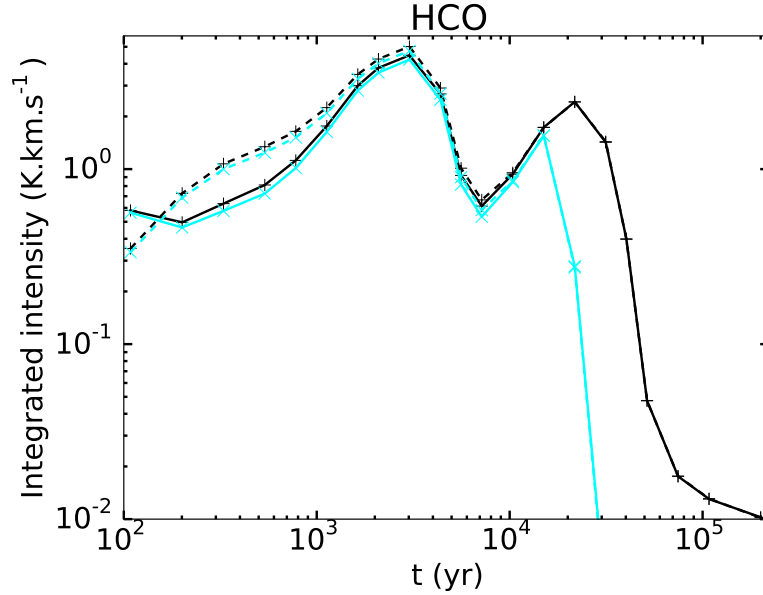
Figure A.52: Time evolution of integrated intensities for HCO (1(0,1)–0(0,0)) for models with different cut-off density: 10^1 cm^{-3} (black) and 10^6 cm^{-3} (light blue). The solid lines represent the HII region models and the dashed lines the HHMC models.
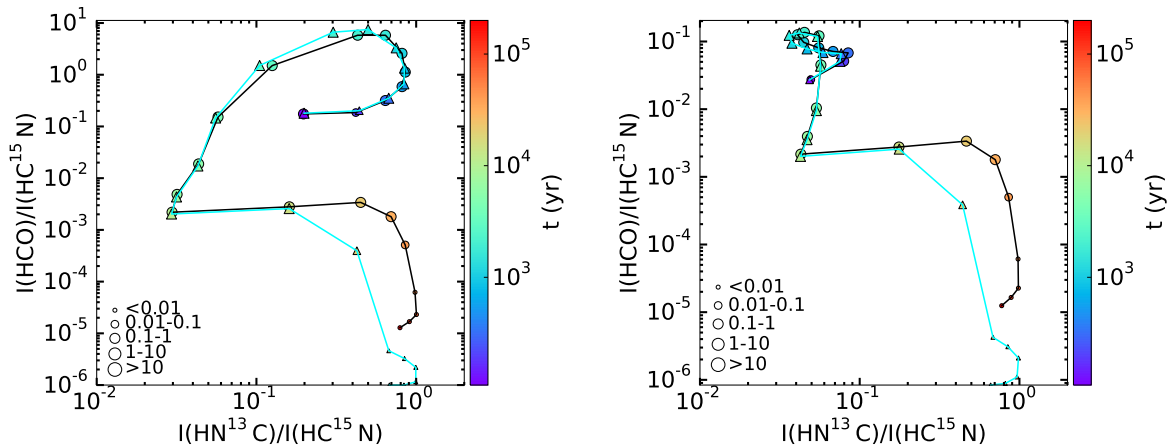
Figure A.53: Time evolution of the integrated intensity ratio (I(HCO (1(0,1)–0(0,0))) / I(HC^{15}N (1–0))) in function of the integrated intensity ratio (I(HN^{13}C (1–0)) / I(HC^{15}N (1–0))) for models with different cut-off density: 10^1 cm^{-3} (black line and circle markers) and 10^6 cm^{-3} (light blue line and triangle markers). The HII region models are shown on the left panel and the HHMC models on the right panel. The size of the markers corresponds to the range value of the peak intensity in Kelvin of HCO.

A.4 HCO$^+$

HMC vs HHMC model
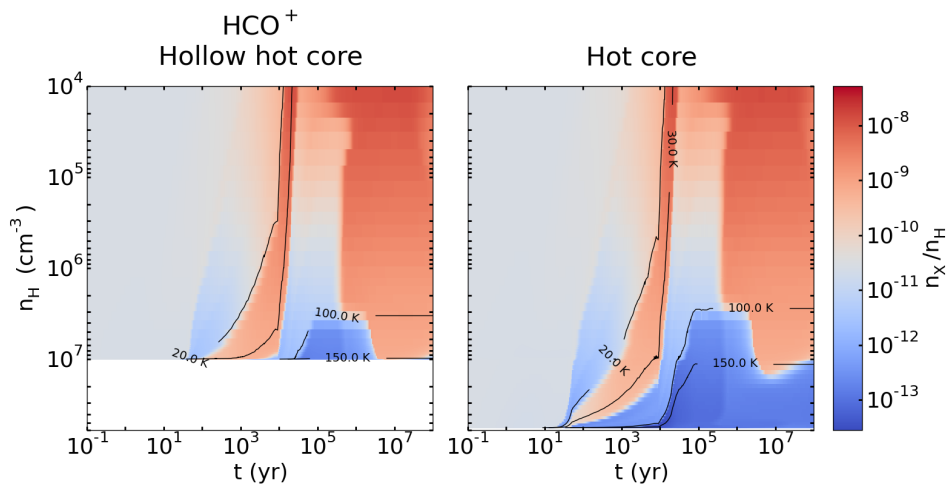
Figure A.54: Abundance of HCO$^+$ in function of time (x-axis) and density (y-axis) for the HHMC (left) and HMC (right) models.
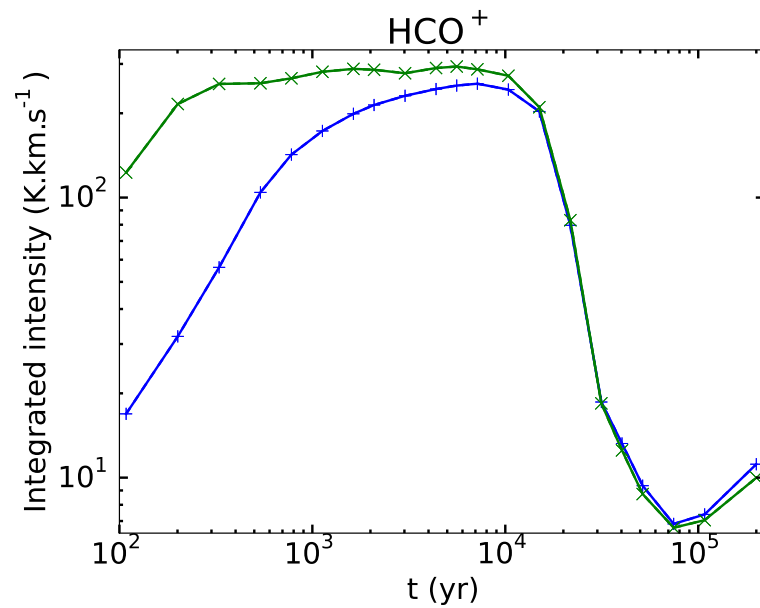
Figure A.55: Time evolution of integrated intensities for HCO$^+$ (1–0). The blue lines represent the HHMC model and the green one represents the HMC model.
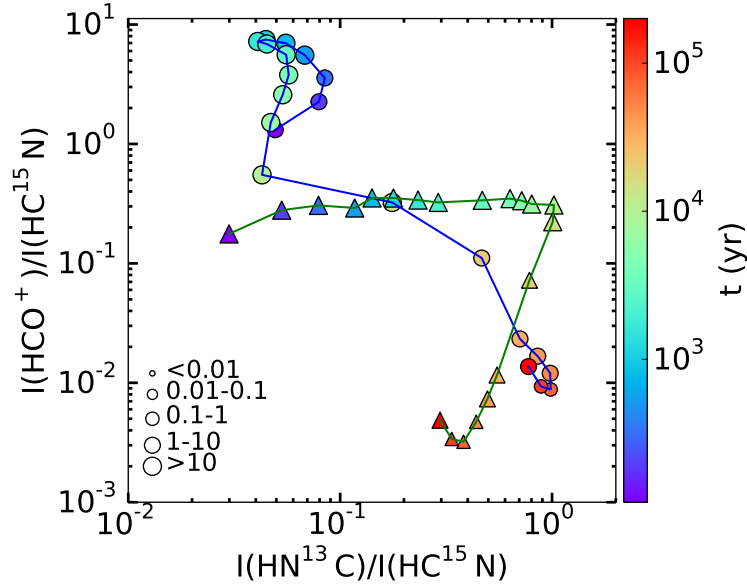
Figure A.56: Time evolution of the integrated intensity ratio ($I(\mathrm{HCO^+}\,(1\text{–}0))$ / $I(\mathrm{HC^{15}N}\,(1\text{–}0))$) in function of the integrated intensity ratio ($I(\mathrm{HN^{13}C}\,(1\text{–}0))$ / $I(\mathrm{HC^{15}N}\,(1\text{–}0))$) for the HHMC (blue line and circle markers) and HMC (green line and triangle markers) models. The size of the markers corresponds to the range value of the peak intensity in Kelvin of $\mathrm{HCO^+}$.

## HII region vs HHMC model
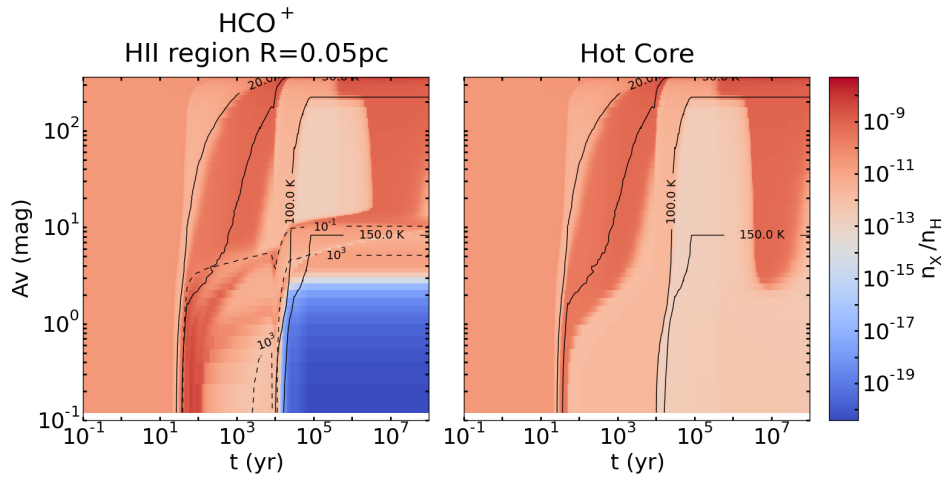
Figure A.57: Abundances of $\mathrm{HCO^+}$ in function of time (x-axis) and visual extinction (y-axis) for the HII region (left panel) and HHMC (right) models. The solid black lines represent the contours for the temperature: 20, 30, 100 and 150 K and the dashed black lines represent some contours for the radiation field intensity: 10^{-1} and 10^{3} Draine unit.
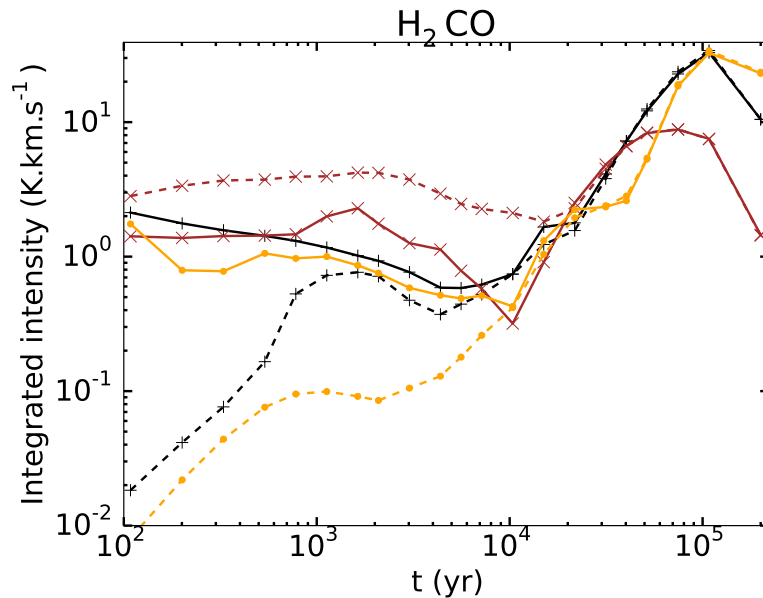
Figure A.58: Time evolution of integrated intensities for HCO+ (1–0). The black line represents the HII region model and the blue lines represent the HHMC model.
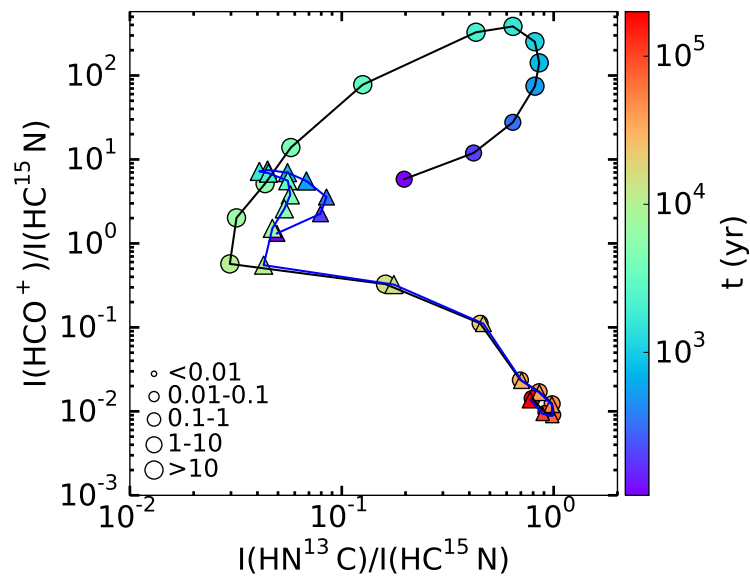
Figure A.59: Time evolution of the integrated intensity ratio (I(HCO+ (1–0)) / I(HC^{15}N (1–0))) in function of the integrated intensity ratio (I(HN^{13}C (1–0)) / I(HC^{15}N (1–0))) for the HII region (black line and circle markers) and HHMC (blue line and triangle markers) models. The size of the markers corresponds to the range value of the peak intensity in Kelvin of HCO+.
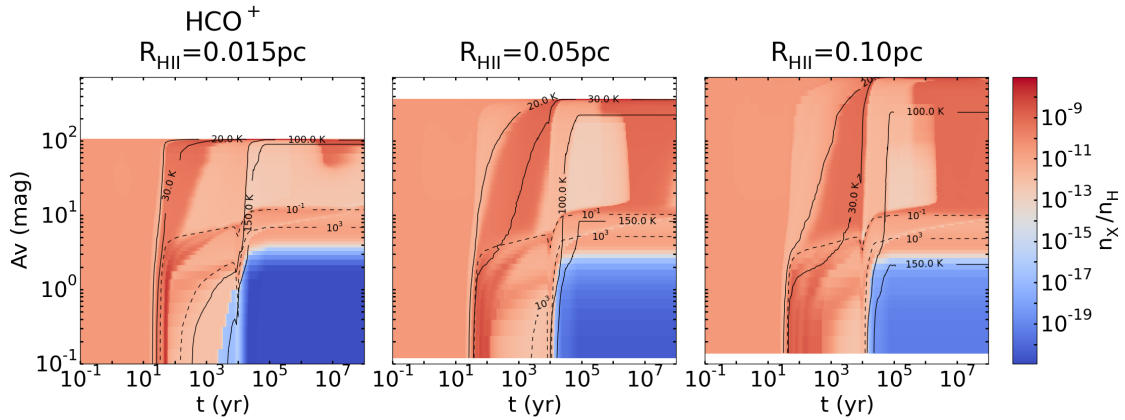
HII **region size**

Figure A.60: Abundances of HCO^+ in function of time (x-axis) and visual extinction (y-axis) for HII region models with different sizes: 0.015 pc (left panels), 0.05 pc (middle) and 0.10 pc (right). The solid black lines appearing on the figures represent the contours for the temperature: 20, 30, 100 and 150 K and the dashed black lines represent some contours for the radiation field intensity: 10^{-1} and 10^3 Draine unit.

Figure A.61: Time evolution of integrated intensities for HCO^+ (1–0) for models with different sizes of ionized cavity: 0.015 pc (orange), 0.05 pc (black) and 0.10 pc (brown). The solid lines represent the HII region models and the dashed lines the HHMC models.
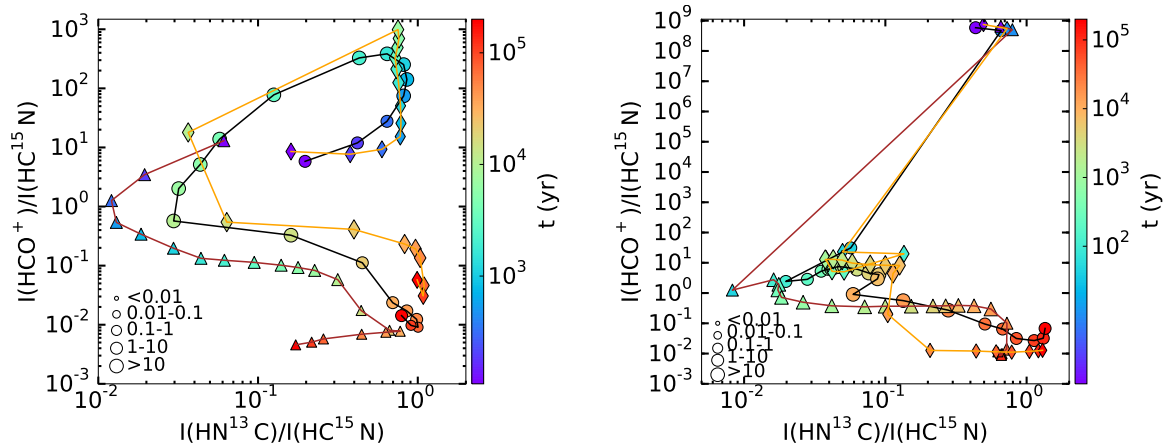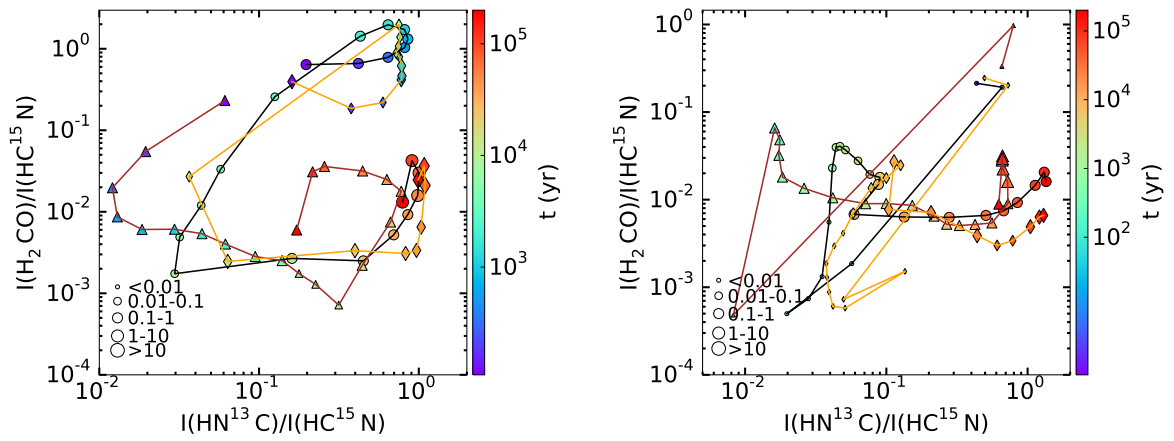
Figure A.62: Time evolution of the integrated intensity ratio ($I(\text{HCO}^+\,(1\text{–}0))$ / $I(\text{HC}^{15}\text{N}\,(1\text{–}0))$) in function of the integrated intensity ratio ($I(\text{HN}^{13}\text{C}\,(1\text{–}0))$ / $I(\text{HC}^{15}\text{N}\,(1\text{–}0))$) for models with different sizes of ionized cavity: 0.015 pc (brown line and triangle markers), 0.05 pc (black line and circle markers) and 0.10 pc (orange line and diamond markers). The HII region models are shown on the left panel and the HHMC models on the right panel. The size of the markers corresponds to the range value of the peak intensity in Kelvin of HCO$^+$.

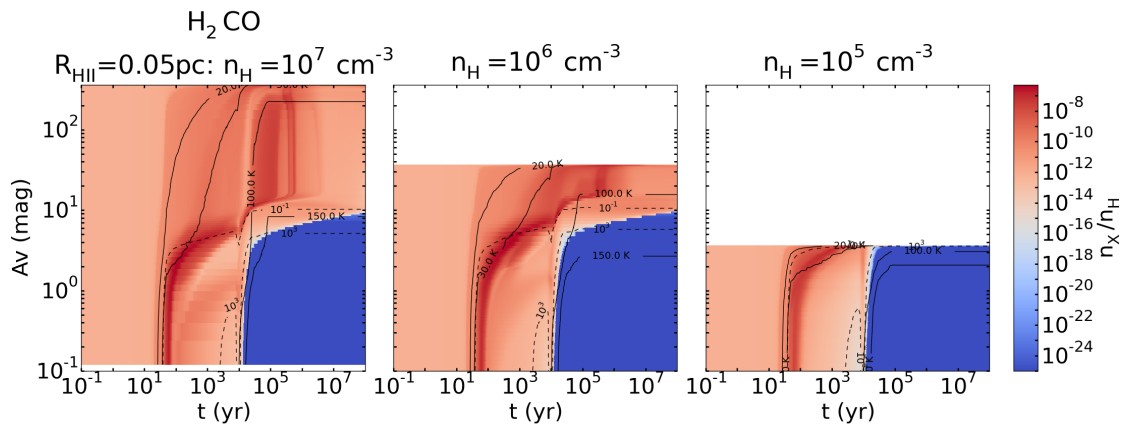## Density at the ionization front
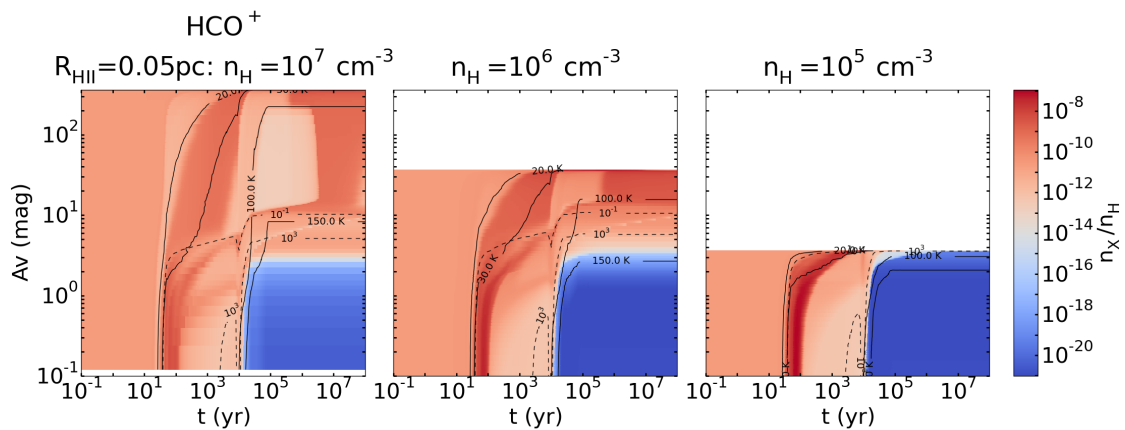
Figure A.63: Abundances of HCO$^+$ in function of time (x-axis) and visual extinction (y-axis) for HII region models with different densities at the ionization front: 10^7 cm^{-3} (left), 10^6 cm^{-3} (middle) and 10^5 cm^{-3} (right). The solid black lines appearing on the figures represent the contours for the temperature: 20, 30, 100 and 150 K and the dashed black lines represent some contours for the radiation field intensity: 10^{-1} and 10^3 Draine unit.
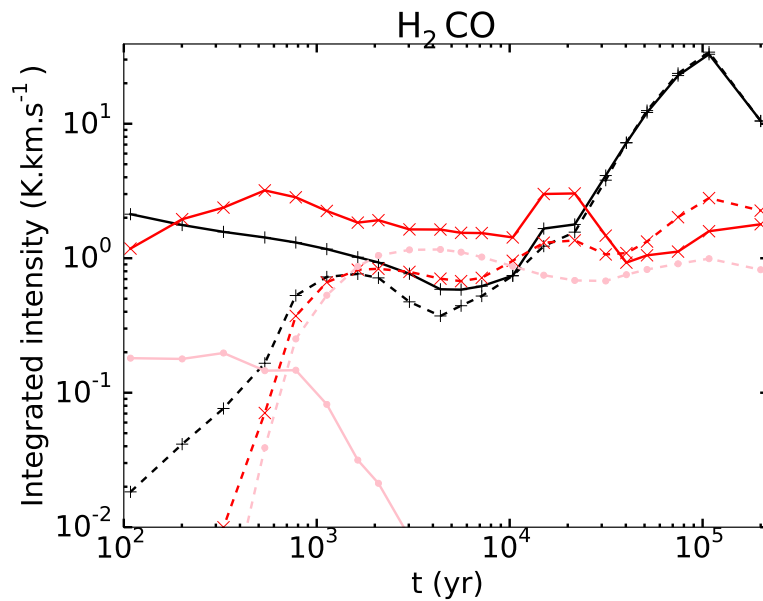
Figure A.64: Time evolution of integrated intensities for HCO^+ (1–0) for models with different densities at the ionization front: 10^7 cm^{-3} (black), 10^6 cm^{-3} (red) and 10^5 cm^{-3} (pink). The solid lines represent the HII region models and the dashed lines the HHMC models.
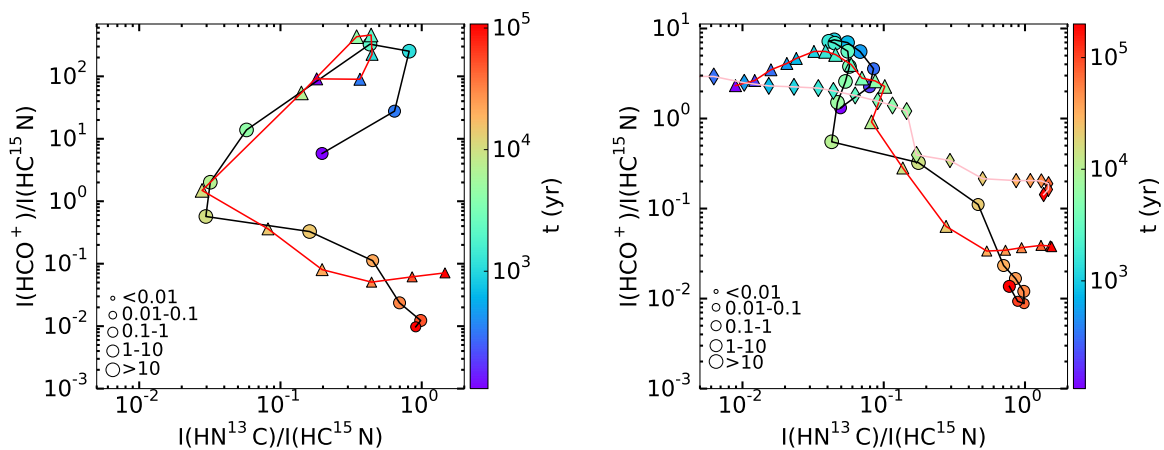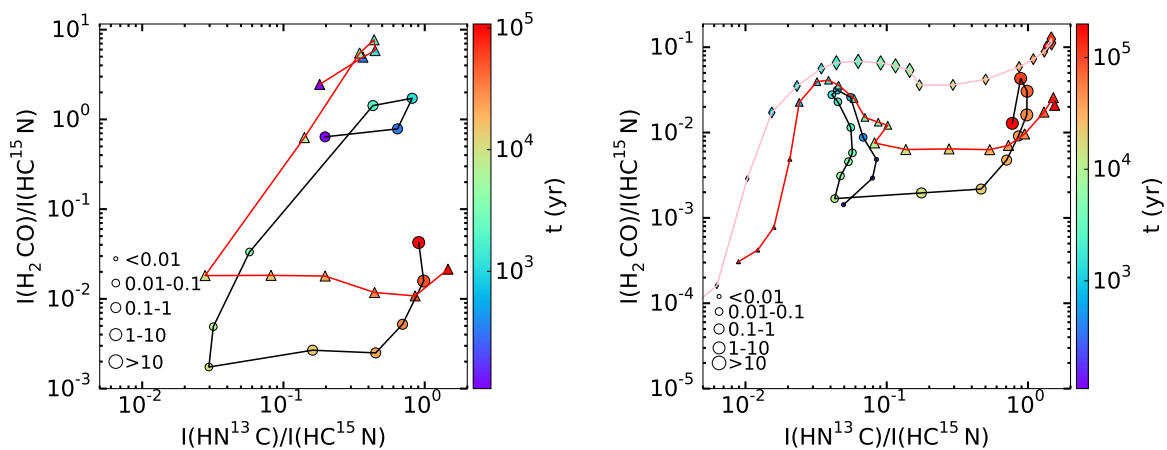

Figure A.65: Time evolution of the integrated intensity ratio ($I(HCO^+$ (1–0)) / $I(HC^{15}N$ (1–0))) in function of the integrated intensity ratio ($I(HN^{13}C$ (1–0)) / $I(HC^{15}N$ (1–0))) for models with different density at the ionization front: 10^7 cm^{-3} (black line and circle markers), 10^6 cm^{-3} (red line and triangle markers) and 10^5 cm^{-3} (pink line and diamond markers). The HII region models are shown on the left panel and the HHMC models on the right panel. The size of the markers corresponds to the range value of the peak intensity in Kelvin of HCO^+.
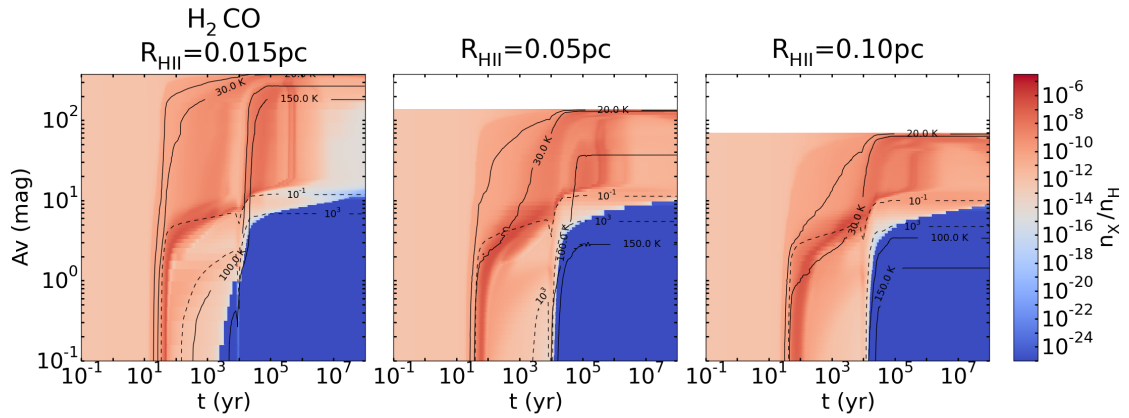
Plummer exponent

Figure A.66: Abundances of HCO$^+$ in function of time (x-axis) and visual extinction (y-axis) for HII region models using for the second density profile ($\gamma = 1$) and with different sizes of ionized cavity: 0.015 pc (left panel), 0.05 pc (middle) and 0.10 pc (right). The solid black lines appearing on the figures represent the contours for the temperature: 20, 30, 100 and 150 K and the dashed black lines represent some contours for the radiation field intensity: 10^{-1} and 10^3 Draine unit.
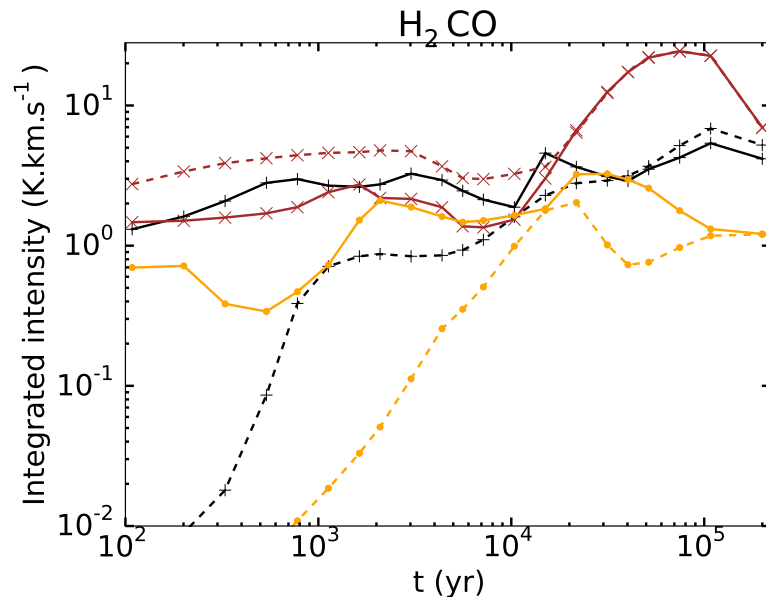

Figure A.67: Time evolution of integrated intensities for HCO$^+$ (1–0) (left panel) for models using the second density profile ($\gamma = 1$) and with different sizes of ionized cavity: 0.015 pc (brown), 0.05 pc (black) and 0.10 pc (orange). The solid lines represent the HII region models and the dashed lines the HHMC models.
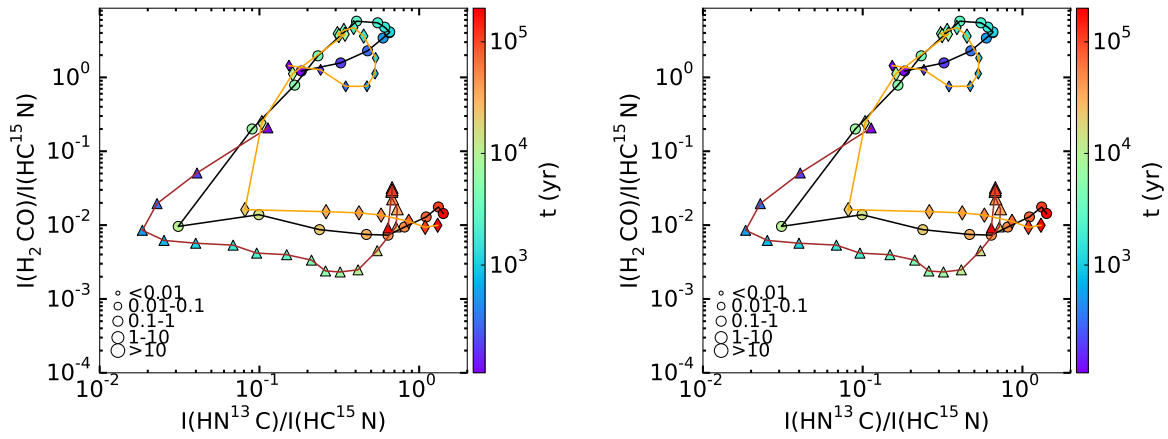
Figure A.68: Time evolution of the integrated intensity ratio ($I(\mathrm{HCO}^+\,(1\text{--}0))$ / $I(\mathrm{HC}^{15}\mathrm{N}\,(1\text{--}0))$) in function of the integrated intensity ratio ($I(\mathrm{HN}^{13}\mathrm{C}\,(1\text{--}0))$ / $I(\mathrm{HC}^{15}\mathrm{N}\,(1\text{--}0))$) for models using the second density profile ($\gamma = 1$) and with different sizes of ionized cavity: 0.015 pc (brown and triangle markers), 0.05 pc (black and circle markers) and 0.10 pc (orange and diamond markers). The HII region models are shown on the left panel and the HHMC models on the right panel. The size of the markers correspond to the range value of the peak intensity in Kelvin of HCO^+.

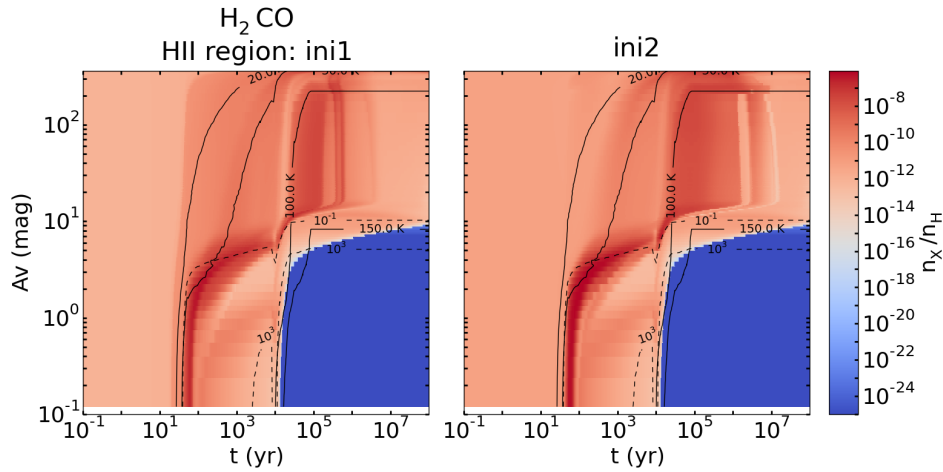## Initial abundances

Figure A.69: Abundances of HCO^+ in function of time (x-axis) and visual extinction (y-axis) for HII region with different initial abundances: *ini1* (left panel) and *ini2* (right). The solid black lines appearing on the figures represent the contours for the temperature: 20, 30, 100 and 150 K and the dashed black lines represent some contours for the radiation field intensity: 10^{-1} and 10^3 Draine unit.
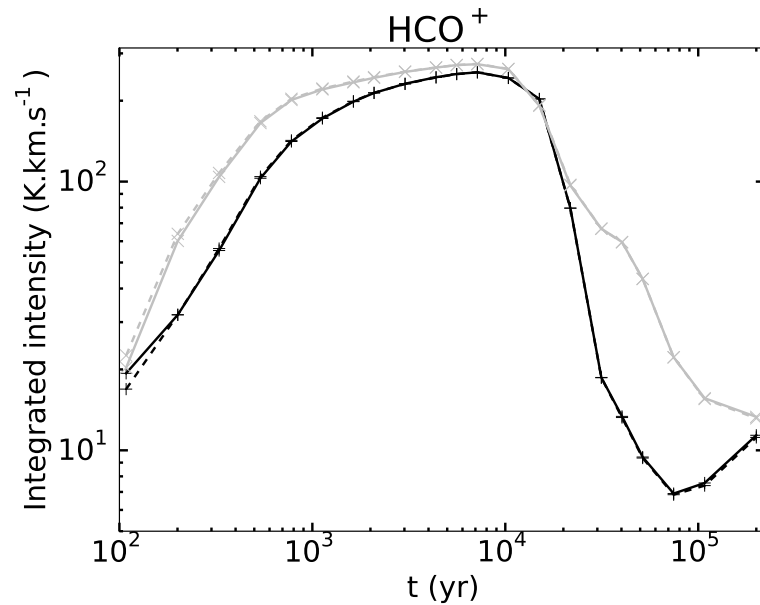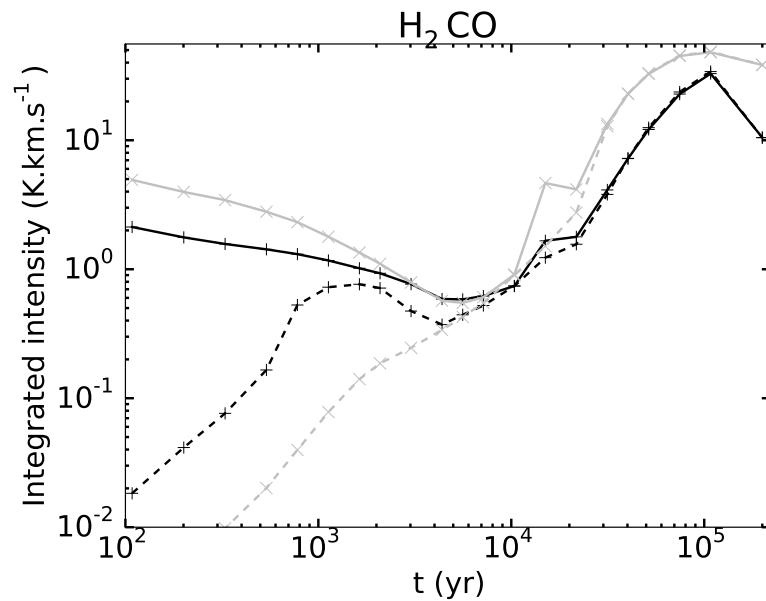
Figure A.70: Time evolution of integrated intensities for HCO$^+$ (1–0) (left panel) for models with different initial abundances: *ini1* (black) and *ini2* (grey). The solid lines represent the HII region models and the dashed lines the HHMC models.
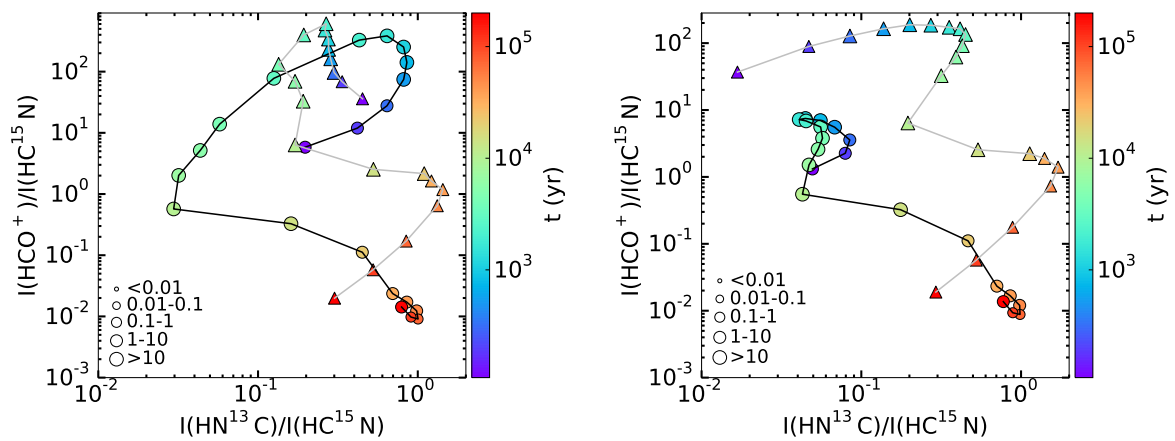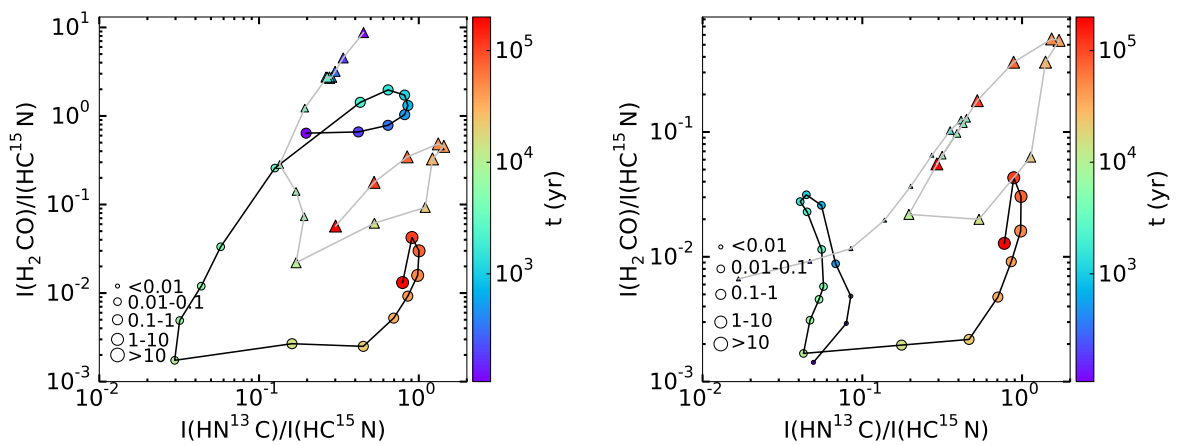

Figure A.71: Time evolution of the integrated intensity ratio ($I(\text{HCO}^+ (1–0)) / I(\text{HC}^{15}\text{N} (1–0))$) in function of the integrated intensity ratio ($I(\text{HN}^{13}\text{C} (1–0)) / I(\text{HC}^{15}\text{N} (1–0))$) for models with different initial abundances: *ini1* (black line and circle markers) and *ini2* (grey line and triangle markers). The HII region models are shown on the left panel and the HHMC models on the right panel. The size of the markers corresponds to the range value of the peak intensity in Kelvin of HCO$^+$.
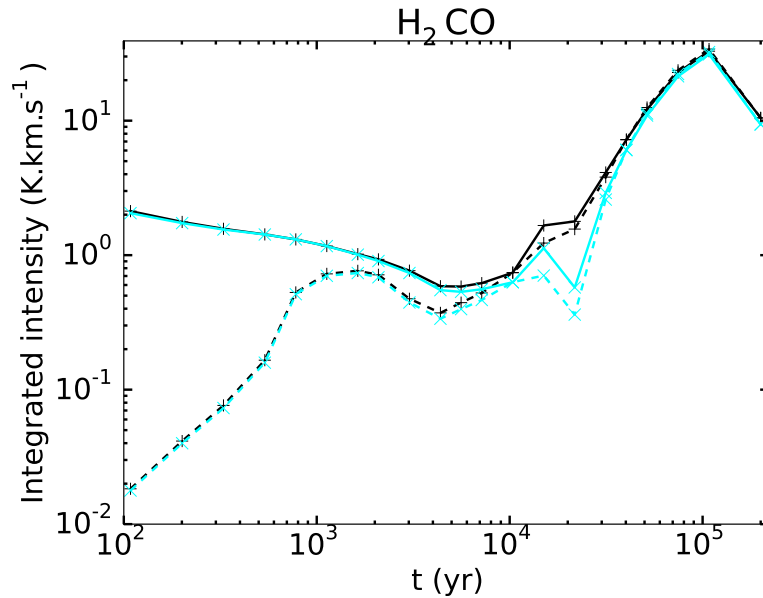
Effect of the envelope
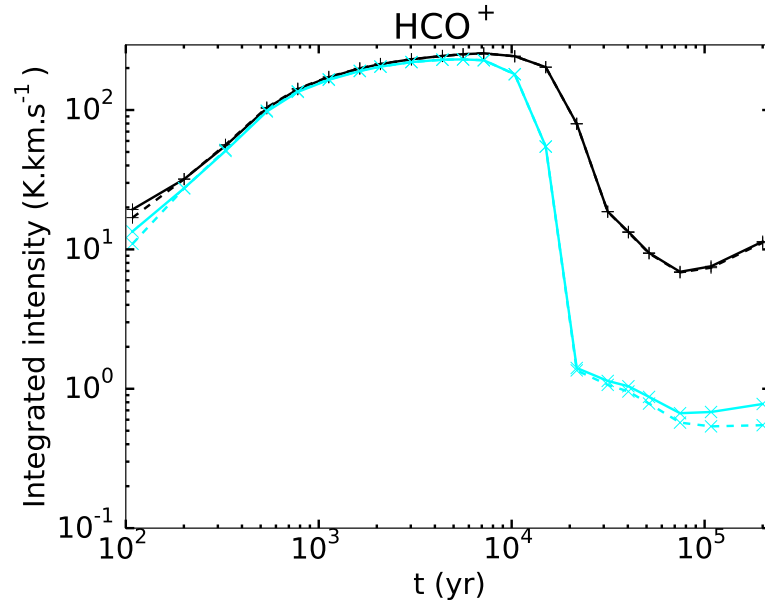
Figure A.72: Time evolution of integrated intensities for HCO^+ (1–0) for models with different cut-off density: 10^1 cm^{-3} (black) and 10^6 cm^{-3} (light blue). The solid lines represent the HII region models and the dashed lines the HHMC models.
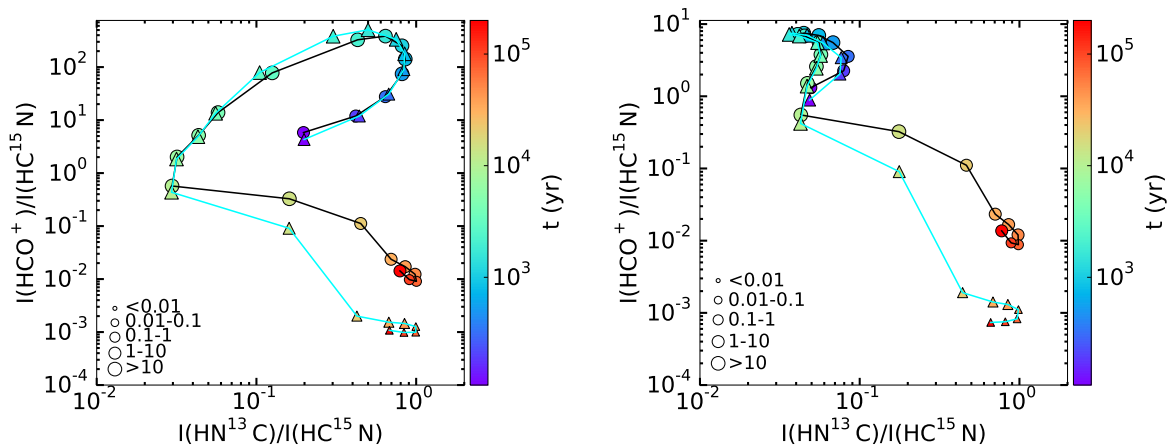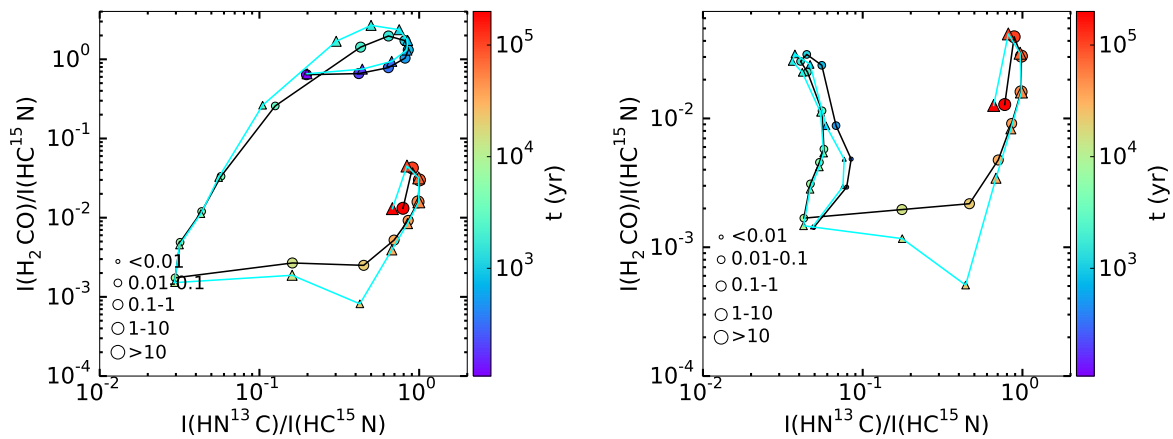

Figure A.73: Time evolution of the integrated intensity ratio ($I(HCO^+ (1–0))$ / $I(HC^{15}N (1–0))$) in function of the integrated intensity ratio ($I(HN^{13}C (1–0))$ / $I(HC^{15}N (1–0))$) for models with different cut-off density: 10^1 cm^{-3} (black line and circle markers) and 10^6 cm^{-3} (light blue line and triangle markers). The HII region models are shown on the left panel and the HHMC models on the right panel. The size of the markers corresponds to the range value of the peak intensity in Kelvin of HCO^+.
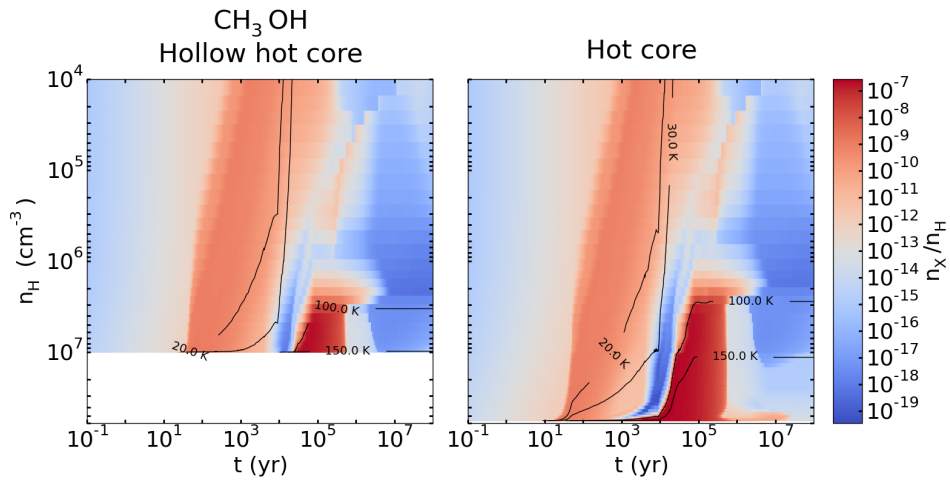
A.5 H$_2$CO

HMC vs HHMC model
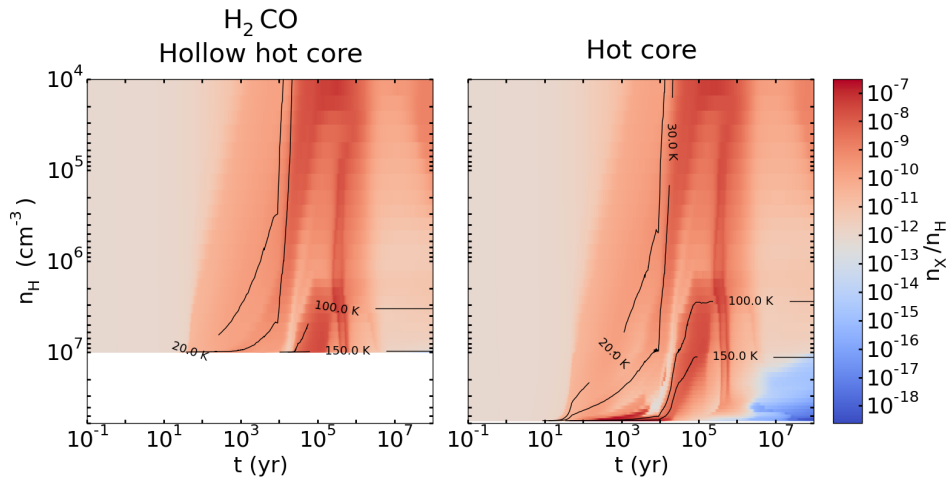
Figure A.74: Abundance of H$_2$CO in function of time (x-axis) and density (y-axis) for the HHMC (left) and HMC (right) models.
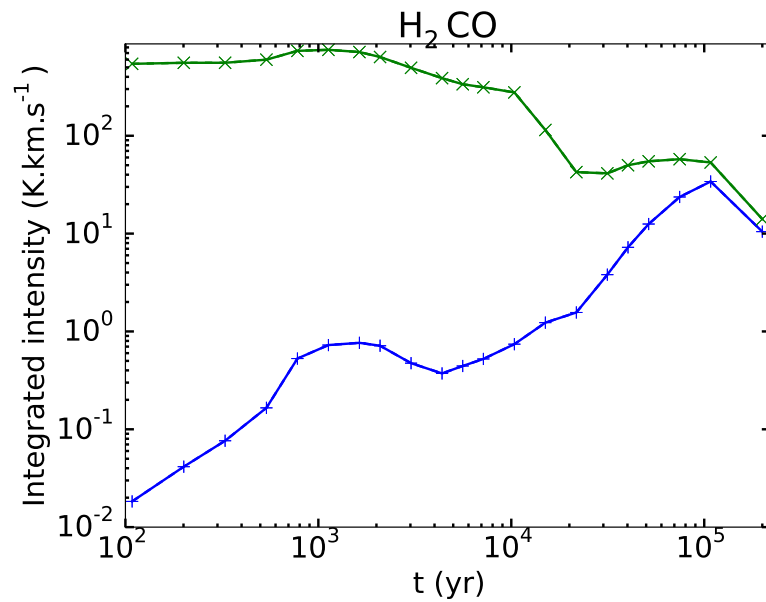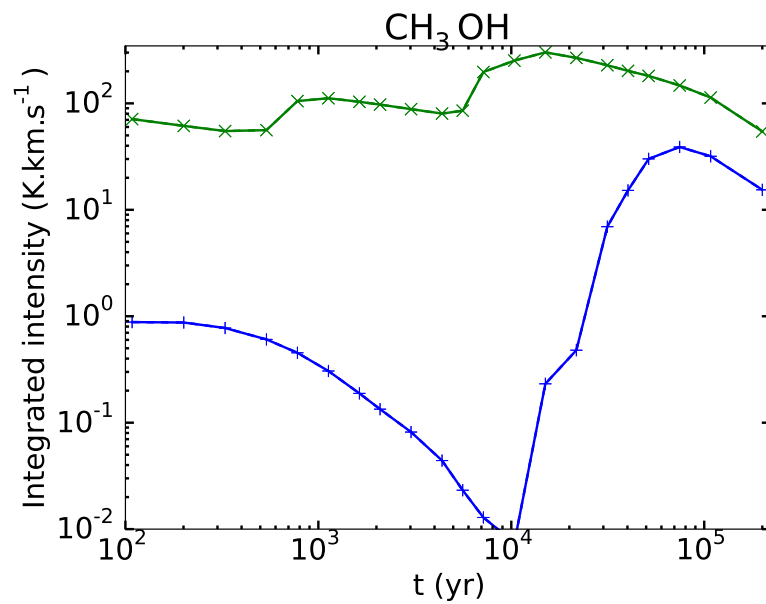

Figure A.75: Time evolution of integrated intensities for H$_2$CO (2(0,2)–1(0,1)). The blue lines represent the HHMC model and the green one represents the HMC model.
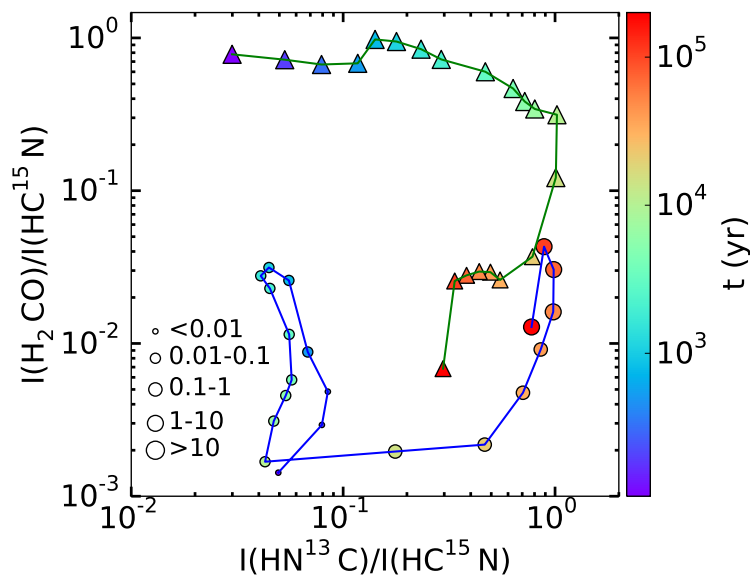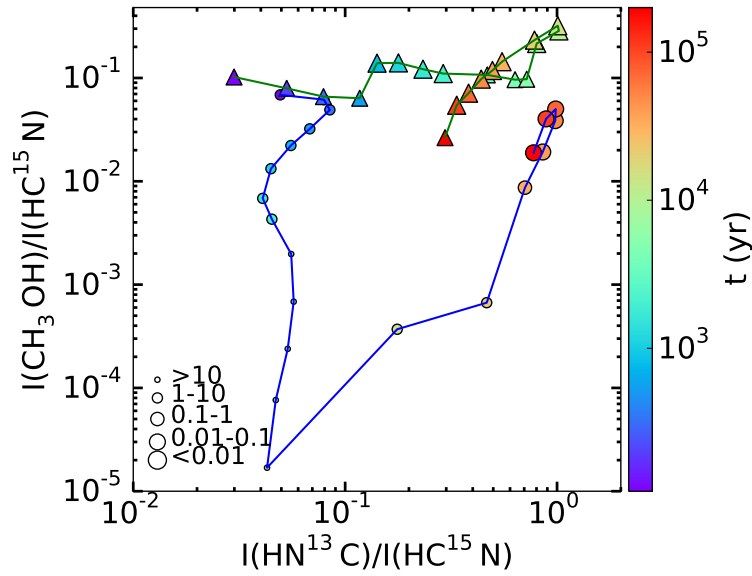
Figure A.76:   Time evolution of the integrated intensity ratio $(I(H_2CO\,(2(0,2)\text{--}1(0,1)))$ / $I(HC^{15}N\,(1\text{--}0)))$ in function of the integrated intensity ratio $(I(HN^{13}C\,(1\text{--}0))$ / $I(HC^{15}N\,(1\text{--}0)))$ for the HHMC (blue line and circle markers) and HMC (green line and triangle markers) models. The size of the markers corresponds to the range value of the peak intensity in Kelvin of H_2CO.
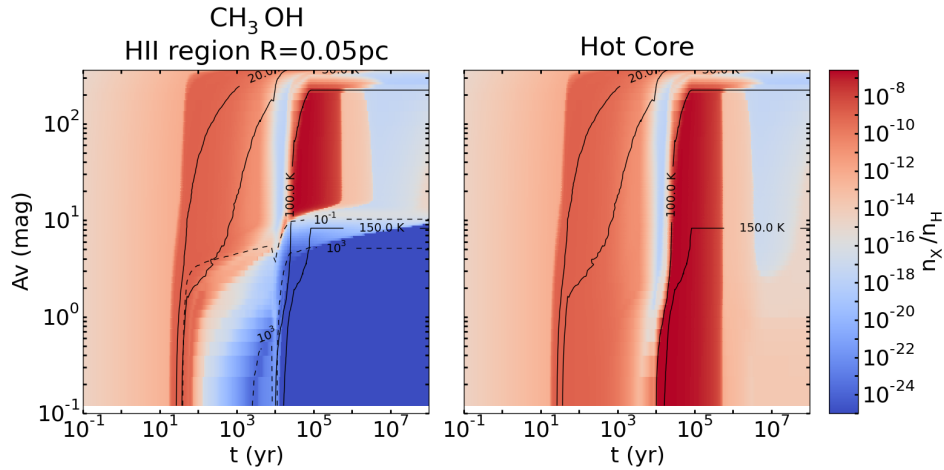
HII region vs HHMC model
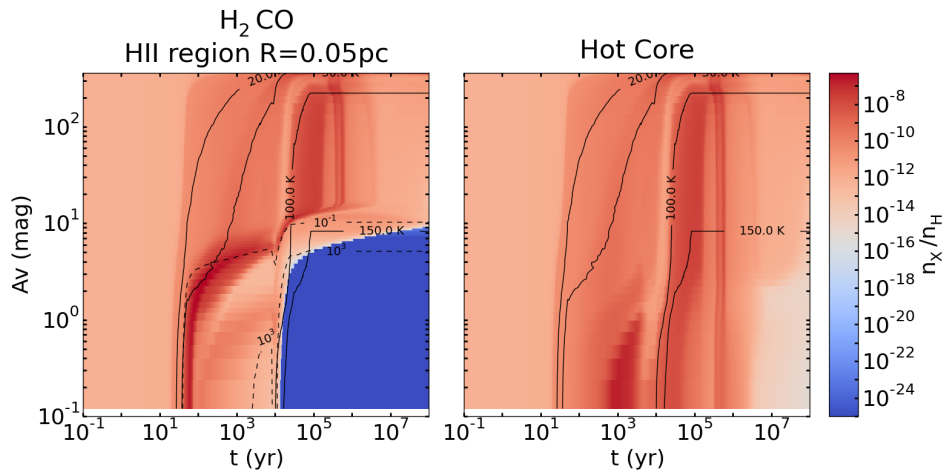
Figure A.77: Abundances of H_2CO in function of time (x-axis) and visual extinction (y-axis) for the HII region (left panel) and HHMC (right) models. The solid black lines represent the contours for the temperature: 20, 30, 100 and 150 K and the dashed black lines represent some contours for the radiation field intensity: 10^{-1} and 10^3 Draine unit.
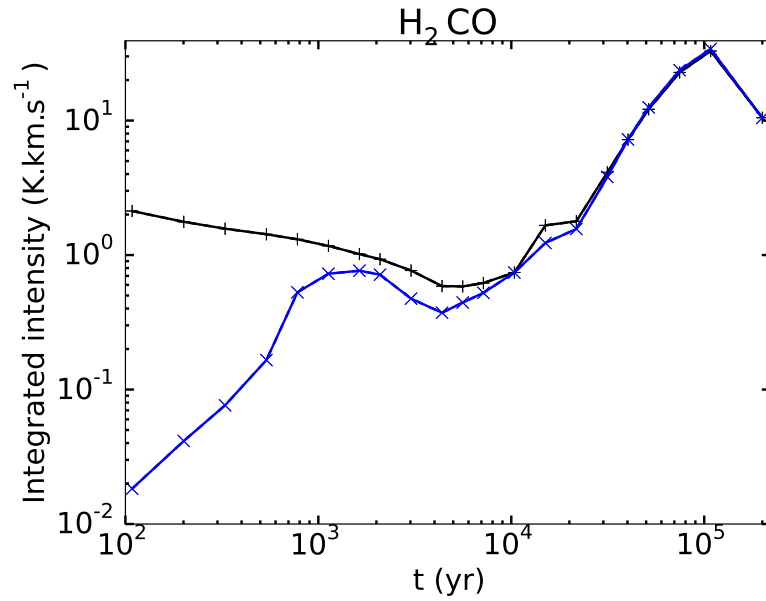
Figure A.78: Time evolution of integrated intensities for $H_2CO\,(2(0,2)–1(0,1))$. The black line represents the HII region model and the blue lines represent the HHMC model.
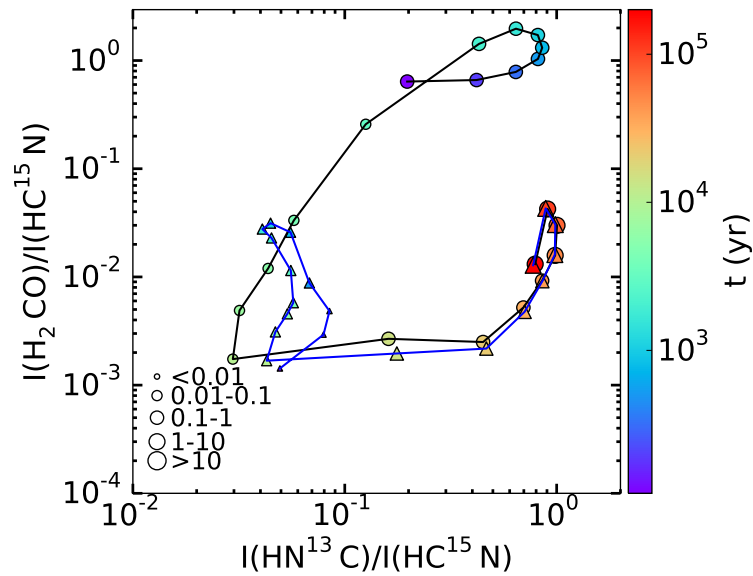
Figure A.79: Time evolution of the integrated intensity ratio $(I(H_2CO\,(2(0,2)–1(0,1)))$ / $I(HC^{15}N\,(1–0)))$ in function of the integrated intensity ratio $(I(HN^{13}C\,(1–0))$ / $I(HC^{15}N\,(1–0)))$ for the HII region (black line and circle markers) and HHMC (blue line and triangle markers) models. The size of the markers corresponds to the range value of the peak intensity in Kelvin of H_2CO.

HII region size
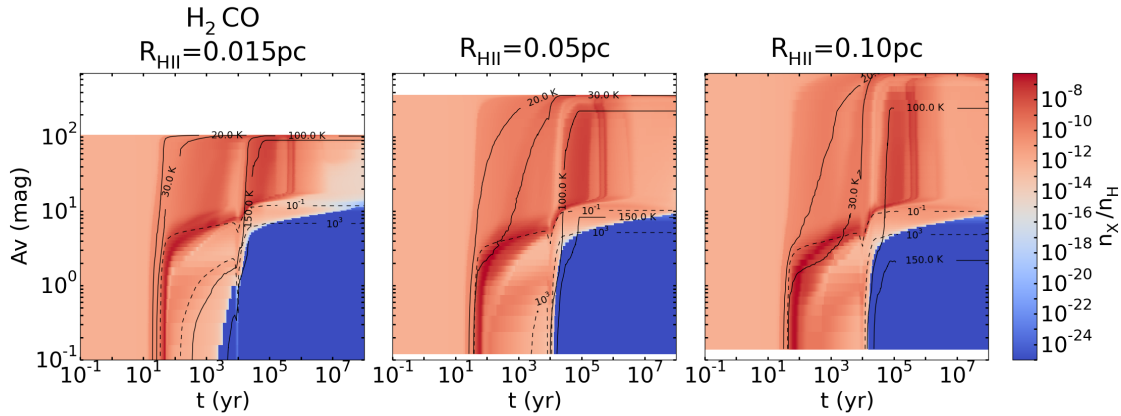
Figure A.80: Abundances of H$_2$CO in function of time (x-axis) and visual extinction (y-axis) for HII region models with different sizes: 0.015 pc (left panels), 0.05 pc (middle) and 0.10 pc (right). The solid black lines appearing on the figures represent the contours for the temperature: 20, 30, 100 and 150 K and the dashed black lines represent some contours for the radiation field intensity: 10^{-1} and 10^3 Draine unit.
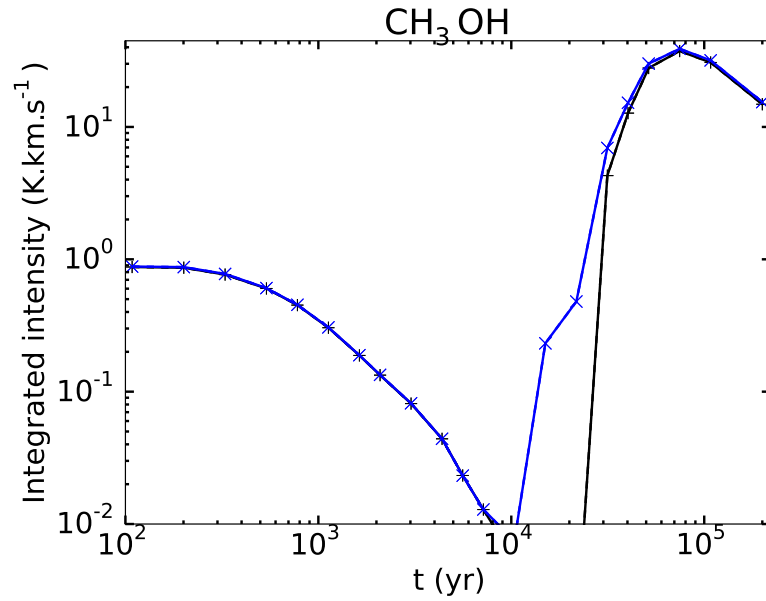

Figure A.81: Time evolution of integrated intensities for H$_2$CO (2(0,2)–1(0,1)) for models with different sizes of ionized cavity: 0.015 pc (orange), 0.05 pc (black) and 0.10 pc (brown). The solid lines represent the HII region models and the dashed lines the HHMC models.

Figure A.82: Time evolution of the integrated intensity ratio $(I(\text{H}_2\text{CO}\,(2(0,2)\text{–}1(0,1)))$ / $I(\text{HC}^{15}\text{N}\,(1\text{–}0)))$ in function of the integrated intensity ratio $(I(\text{HN}^{13}\text{C}\,(1\text{–}0))$ / $I(\text{HC}^{15}\text{N}\,(1\text{–}0)))$ for models with different sizes of ionized cavity: 0.015 pc (brown line and triangle markers), 0.05 pc (black line and circle markers) and 0.10 pc (orange line and diamond markers). The HII region models are shown on the left panel and the HHMC models on the right panel. The size of the markers corresponds to the range value of the peak intensity in Kelvin of H₂CO.
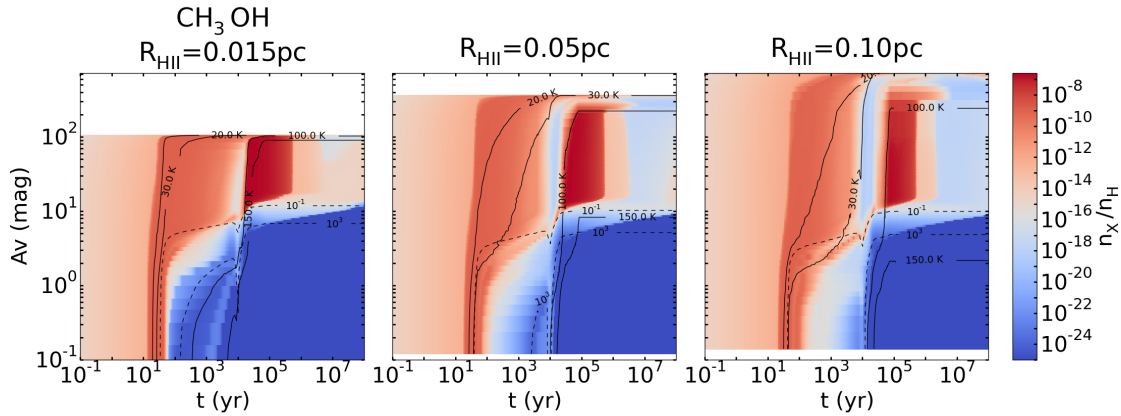
Density at the ionization front

Figure A.83: Abundances of H₂CO in function of time (x-axis) and visual extinction (y-axis) for HII region models with different densities at the ionization front: 10^7 cm^{-3} (left), 10^6 cm^{-3} (middle) and 10^5 cm^{-3} (right). The solid black lines appearing on the figures represent the contours for the temperature: 20, 30, 100 and 150 K and the dashed black lines represent some contours for the radiation field intensity: 10^{-1} and 10^3 Draine unit.
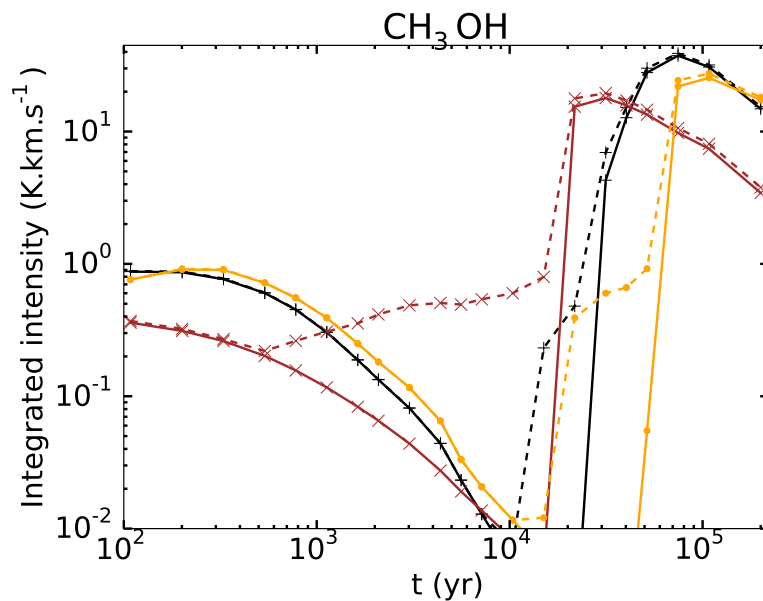
Figure A.84: Time evolution of integrated intensities for $H_2CO\,(2(0,2)\text{--}1(0,1))$ for models with different densities at the ionization front: 10^7 cm^{-3} (black), 10^6 cm^{-3} (red) and 10^5 cm^{-3} (pink). The solid lines represent the HII region models and the dashed lines the HHMC models.

Figure A.85:   Time evolution of the integrated intensity ratio $(I(H_2CO\,(2(0,2)\text{--}1(0,1)))$ / $I(HC^{15}N\,(1\text{--}0)))$ in function of the integrated intensity ratio $(I(HN^{13}C\,(1\text{--}0))$ / $I(HC^{15}N\,(1\text{--}0)))$ for models with different density at the ionization front: 10^7 cm^{-3} (black line and circle markers), 10^6 cm^{-3} (red line and triangle markers) and 10^5 cm^{-3} (pink line and diamond markers). The HII region models are shown on the left panel and the HHMC models on the right panel. The size of the markers corresponds to the range value of the peak intensity in Kelvin of H_2CO.

Plummer exponent

Figure A.86: Abundances of H$_2$CO in function of time (x-axis) and visual extinction (y-axis) for HII region models using for the second density profile ($\gamma = 1$) and with different sizes of ionized cavity: 0.015 pc (left panel), 0.05 pc (middle) and 0.10 pc (right). The solid black lines appearing on the figures represent the contours for the temperature: 20, 30, 100 and 150 K and the dashed black lines represent some contours for the radiation field intensity: 10^{-1} and 10^3 Draine unit.
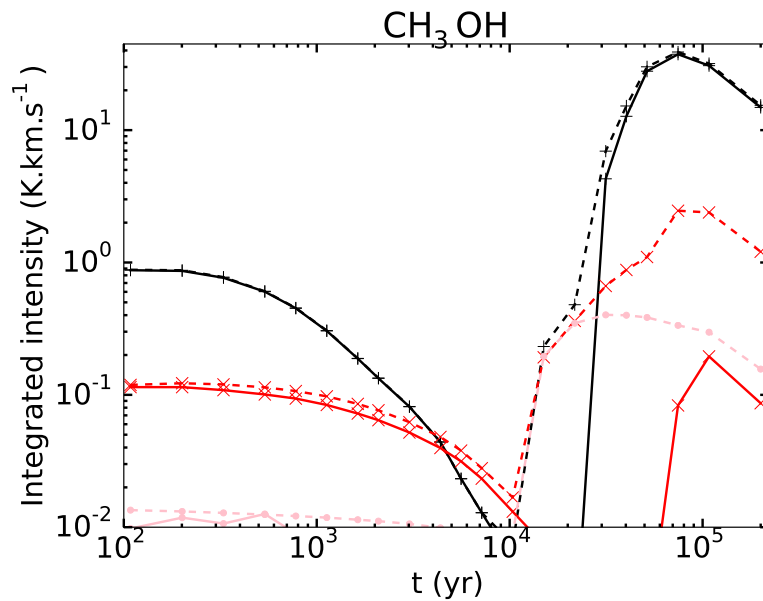

Figure A.87: Time evolution of integrated intensities for H$_2$CO (2(0,2)–1(0,1)) (left panel) for models using the second density profile ($\gamma = 1$) and with different sizes of ionized cavity: 0.015 pc (brown), 0.05 pc (black) and 0.10 pc (orange). The solid lines represent the HII region models and the dashed lines the HHMC models.

Figure A.88:   Time evolution of the integrated intensity ratio $(I(H_2CO\,(2(0,2)\text{--}1(0,1)))$ / $I(HC^{15}N\,(1\text{--}0)))$ in function of the integrated intensity ratio $(I(HN^{13}C\,(1\text{--}0))$ / $I(HC^{15}N\,(1\text{--}0)))$ for models using the second density profile $(\gamma = 1)$ and with different sizes of ionized cavity: 0.015 pc (brown and triangle markers), 0.05 pc (black and circle markers) and 0.10 pc (orange and diamond markers). The HII region models are shown on the left panel and the HHMC models on the right panel. The size of the markers correspond to the range value of the peak intensity in Kelvin of H_2CO.

Initial abundances

Figure A.89: Abundances of H_2CO in function of time (x-axis) and visual extinction (y-axis) for HII region with different initial abundances: *ini1* (left panel) and *ini2* (right). The solid black lines appearing on the figures represent the contours for the temperature: 20, 30, 100 and 150 K and the dashed black lines represent some contours for the radiation field intensity: 10^{-1} and 10^{3} Draine unit.
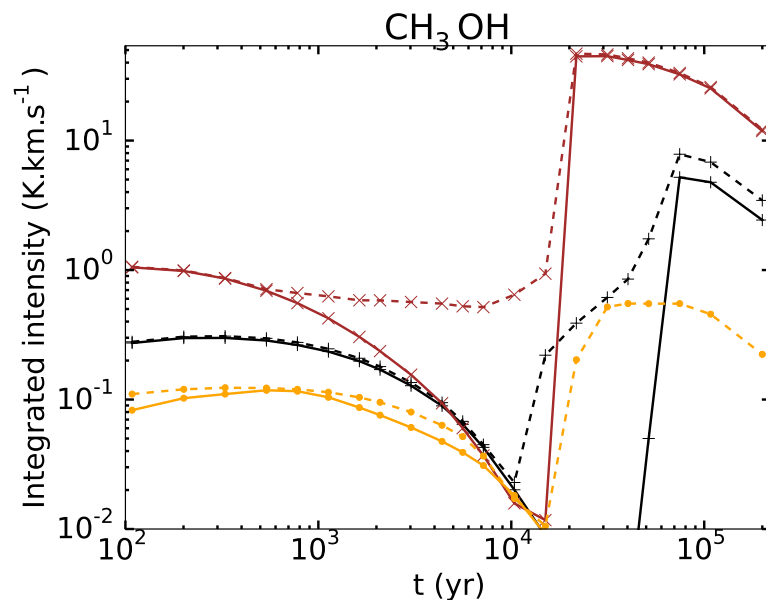
Figure A.90: Time evolution of integrated intensities for H$_2$CO (2(0,2)–1(0,1)) (left panel) for models with different initial abundances: *ini1* (black) and *ini2* (grey). The solid lines represent the HII region models and the dashed lines the HHMC models.

Figure A.91: Time evolution of the integrated intensity ratio $(I(\text{H}_2\text{CO}\,(2(0,2)\text{–}1(0,1)))$ / $I(\text{HC}^{15}\text{N}\,(1\text{–}0)))$ in function of the integrated intensity ratio $(I(\text{HN}^{13}\text{C}\,(1\text{–}0))$ / $I(\text{HC}^{15}\text{N}\,(1\text{–}0)))$ for models with different initial abundances: *ini1* (black line and circle markers) and *ini2* (grey line and triangle markers). The HII region models are shown on the left panel and the HHMC models on the right panel. The size of the markers corresponds to the range value of the peak intensity in Kelvin of H$_2$CO.

Effect of the envelope

Figure A.92: Time evolution of integrated intensities for $H_2CO\,(2(0,2)-1(0,1))$ for models with different cut-off density: 10^1 cm^{-3} (black) and 10^6 cm^{-3} (light blue). The solid lines represent the HII region models and the dashed lines the HHMC models.

Figure A.93:   Time evolution of the integrated intensity ratio $(I(H_2CO\,(2(0,2)-1(0,1)))$ / $I(HC^{15}N\,(1-0)))$ in function of the integrated intensity ratio $(I(HN^{13}C\,(1-0))$ / $I(HC^{15}N\,(1-0)))$ for models with different cut-off density: 10^1 cm^{-3} (black line and circle markers) and 10^6 cm^{-3} (light blue line and triangle markers). The HII region models are shown on the left panel and the HHMC models on the right panel. The size of the markers corresponds to the range value of the peak intensity in Kelvin of H_2CO.

A.6 CH$_3$OH

HMC vs HHMC model

Figure A.94: Abundance of CH$_3$OH in function of time (x-axis) and density (y-axis) for the HHMC (left) and HMC (right) models.

Figure A.95: Time evolution of integrated intensities for CH$_3$OH (2(2,1)–3(1,2)). The blue lines represent the HHMC model and the green one represents the HMC model.

Figure A.96:   Time evolution of the integrated intensity ratio $(I(CH_3OH\,(2(2,1)\text{–}3(1,2)))$ / $I(HC^{15}N\,(1\text{–}0)))$ in function of the integrated intensity ratio $(I(HN^{13}C\,(1\text{–}0))$ / $I(HC^{15}N\,(1\text{–}0)))$ for the HHMC (blue line and circle markers) and HMC (green line and triangle markers) models. The size of the markers corresponds to the range value of the peak intensity in Kelvin of CH_3OH.

H II region vs HHMC model

Figure A.97: Abundances of CH_3OH in function of time (x-axis) and visual extinction (y-axis) for the HII region (left panel) and HHMC (right) models. The solid black lines represent the contours for the temperature: 20, 30, 100 and 150 K and the dashed black lines represent some contours for the radiation field intensity: 10^{-1} and 10^3 Draine unit.

Figure A.98: Time evolution of integrated intensities for CH$_3$OH (2(2,1)–3(1,2)). The black line represents the HII region model and the blue lines represent the HHMC model.
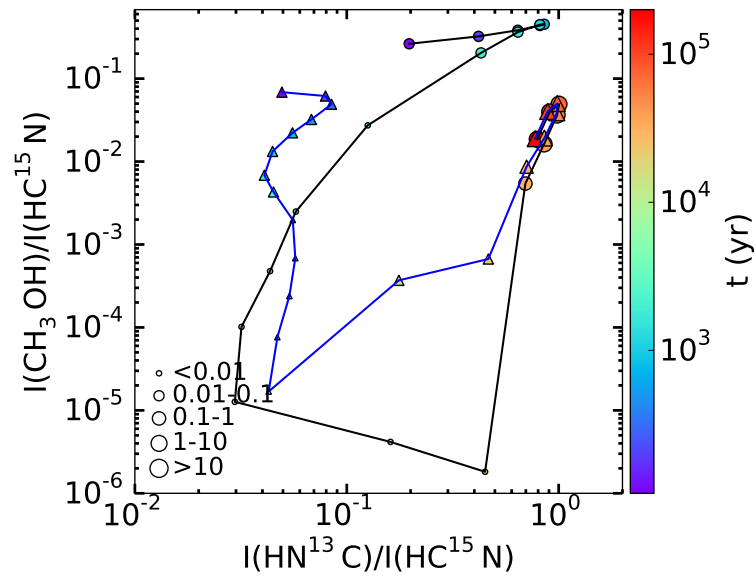
Figure A.99: Time evolution of the integrated intensity ratio $(I(\mathrm{CH_3OH\,(2(2,1)\text{–}3(1,2))))}$ / $I(\mathrm{HC^{15}N\,(1\text{–}0)))}$ in function of the integrated intensity ratio $(I(\mathrm{HN^{13}C\,(1\text{–}0))}$ / $I(\mathrm{HC^{15}N\,(1\text{–}0)))}$ for the HII region (black line and circle markers) and HHMC (blue line and triangle markers) models. The size of the markers corresponds to the range value of the peak intensity in Kelvin of CH$_3$OH.

HII region size

Figure A.100: Abundances of CH_3OH in function of time (x-axis) and visual extinction (y-axis) for HII region models with different sizes: 0.015 pc (left panels), 0.05 pc (middle) and 0.10 pc (right). The solid black lines appearing on the figures represent the contours for the temperature: 20, 30, 100 and 150 K and the dashed black lines represent some contours for the radiation field intensity: 10^{-1} and 10^3 Draine unit.

Figure A.101: Time evolution of integrated intensities for $CH_3OH\,(2(2,1)–3(1,2))$ for models with different sizes of ionized cavity: 0.015 pc (orange), 0.05 pc (black) and 0.10 pc (brown). The solid lines represent the HII region models and the dashed lines the HHMC models.
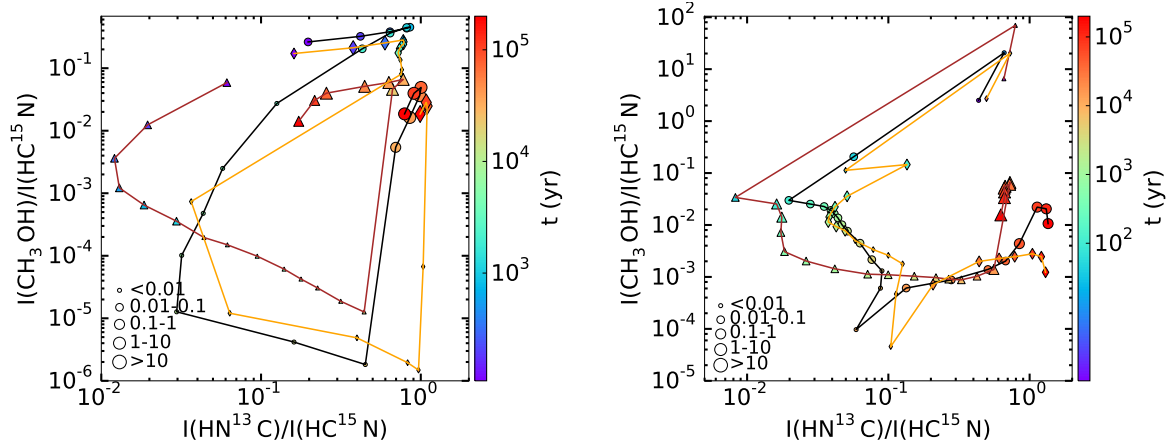
Figure A.102: Time evolution of the integrated intensity ratio $(I(CH_3OH\,(2(2,1)-3(1,2))))$ / $I(HC^{15}N\,(1-0)))$ in function of the integrated intensity ratio $(I(HN^{13}C\,(1-0))$ / $I(HC^{15}N\,(1-0)))$ for models with different sizes of ionized cavity: 0.015 pc (brown line and triangle markers), 0.05 pc (black line and circle markers) and 0.10 pc (orange line and diamond markers). The HII region models are shown on the left panel and the HHMC models on the right panel. The size of the markers corresponds to the range value of the peak intensity in Kelvin of CH$_3$OH.

Density at the ionization front
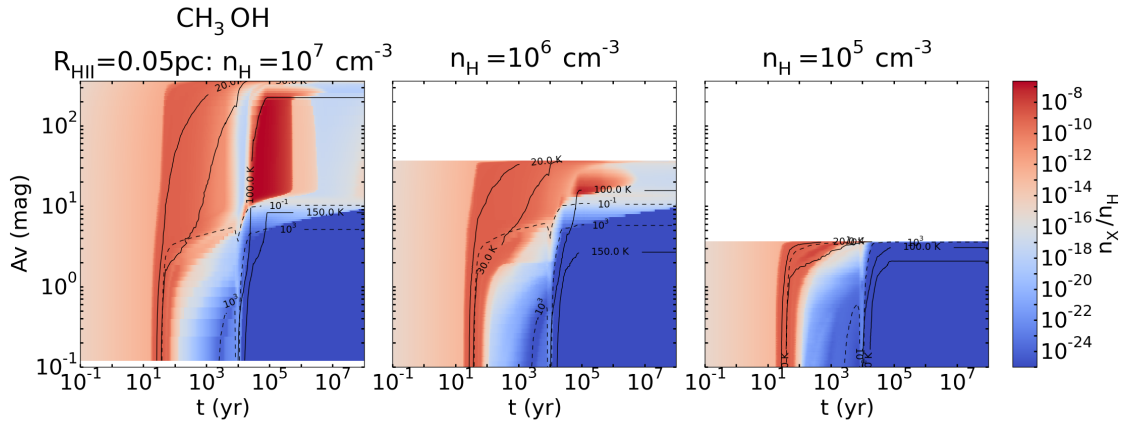
Figure A.103: Abundances of CH$_3$OH in function of time (x-axis) and visual extinction (y-axis) for HII region models with different densities at the ionization front: 10^7 cm^{-3} (left), 10^6 cm^{-3} (middle) and 10^5 cm^{-3} (right). The solid black lines appearing on the figures represent the contours for the temperature: 20, 30, 100 and 150 K and the dashed black lines represent some contours for the radiation field intensity: 10^{-1} and 10^3 Draine unit.
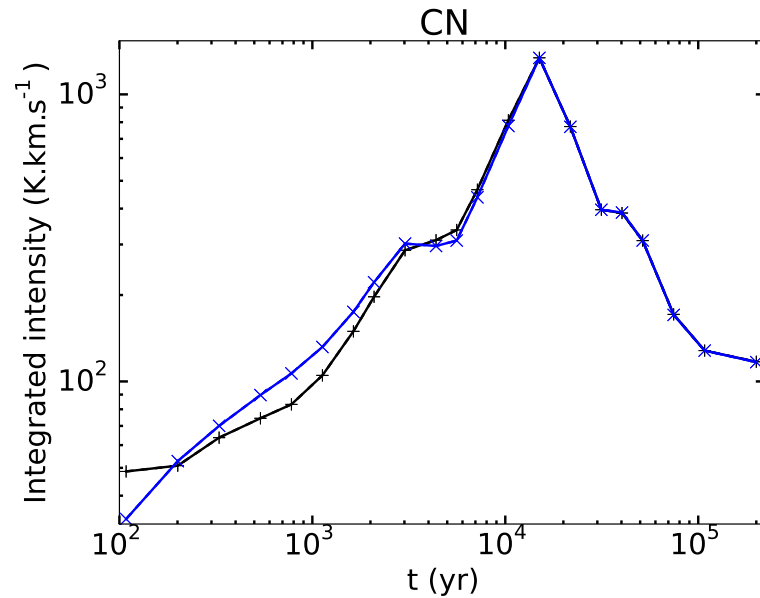
Figure A.104: Time evolution of integrated intensities for $CH_3OH\,(2(2,1)-3(1,2))$ for models with different densities at the ionization front: 10^7 cm^{-3} (black), 10^6 cm^{-3} (red) and 10^5 cm^{-3} (pink). The solid lines represent the HII region models and the dashed lines the HHMC models.
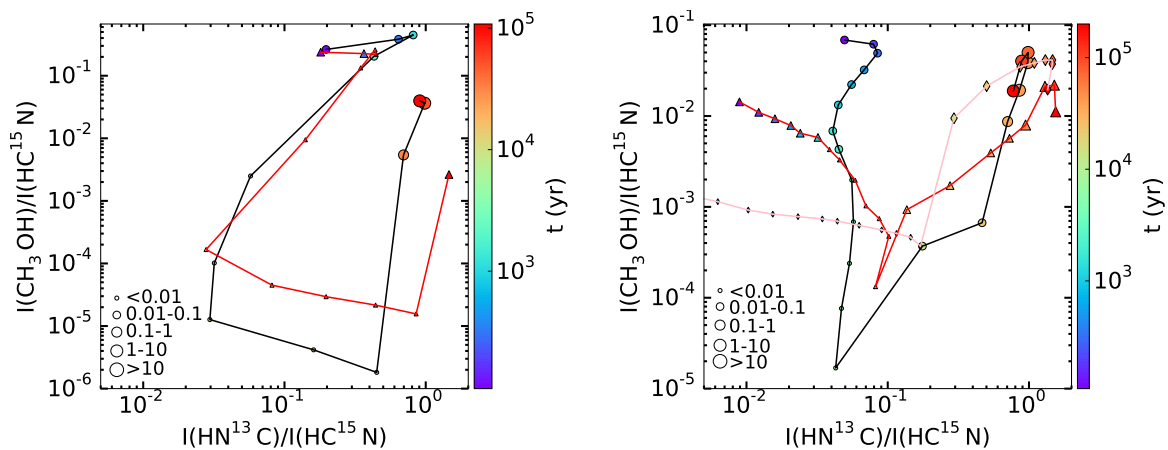
Figure A.105: Time evolution of the integrated intensity ratio $(I(CH_3OH\,(2(2,1)-3(1,2)))$ / $I(HC^{15}N\,(1-0)))$ in function of the integrated intensity ratio $(I(HN^{13}C\,(1-0))$ / $I(HC^{15}N\,(1-0)))$ for models with different density at the ionization front: 10^7 cm^{-3} (black line and circle markers), 10^6 cm^{-3} (red line and triangle markers) and 10^5 cm^{-3} (pink line and diamond markers). The HII region models are shown on the left panel and the HHMC models on the right panel. The size of the markers corresponds to the range value of the peak intensity in Kelvin of CH_3OH.

Plummer exponent
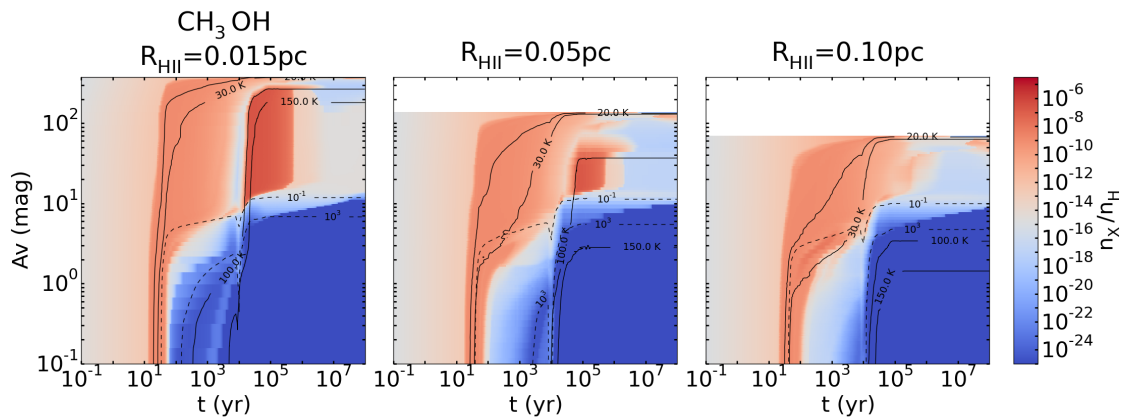
Figure A.106: Abundances of CH$_3$OH in function of time (x-axis) and visual extinction (y-axis) for HII region models using for the second density profile ($\gamma = 1$) and with different sizes of ionized cavity: 0.015 pc (left panel), 0.05 pc (middle) and 0.10 pc (right). The solid black lines appearing on the figures represent the contours for the temperature: 20, 30, 100 and 150 K and the dashed black lines represent some contours for the radiation field intensity: 10^{-1} and 10^3 Draine unit.
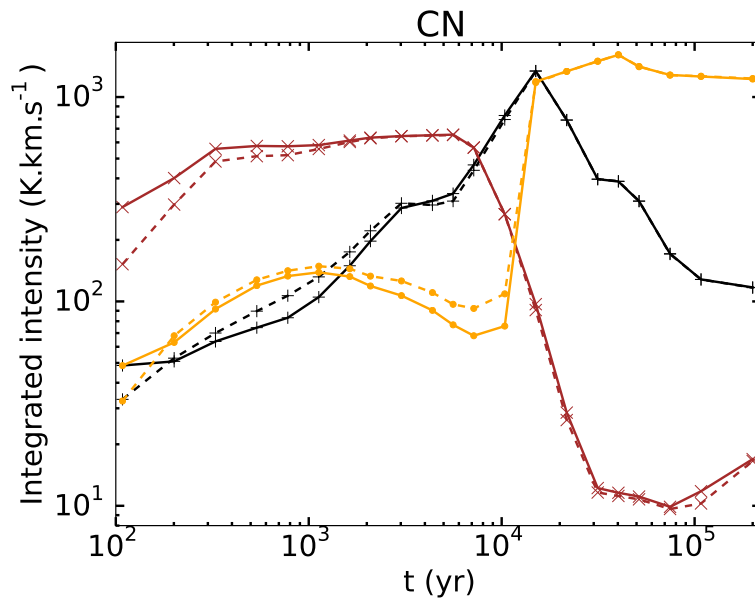

Figure A.107: Time evolution of integrated intensities for CH$_3$OH (2(2,1)–3(1,2)) (left panel) for models using the second density profile ($\gamma = 1$) and with different sizes of ionized cavity: 0.015 pc (brown), 0.05 pc (black) and 0.10 pc (orange). The solid lines represent the HII region models and the dashed lines the HHMC models.
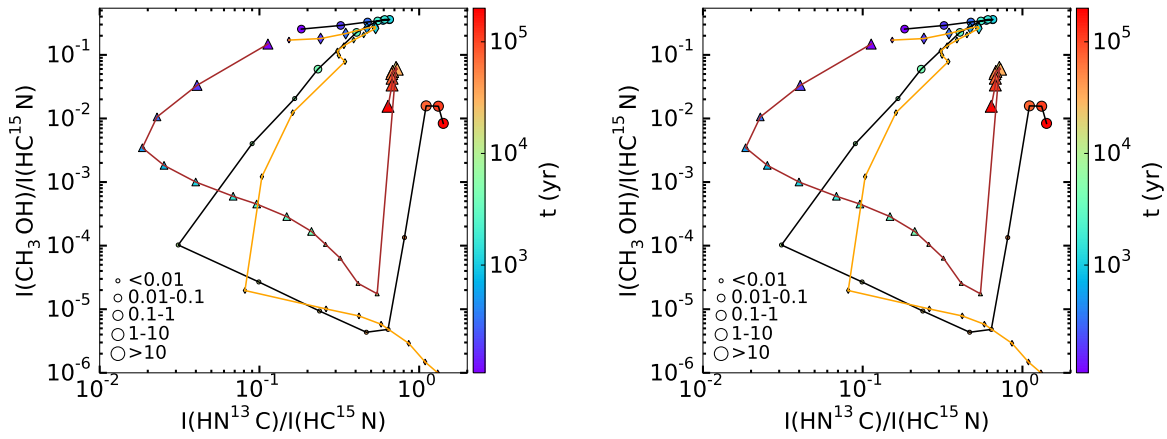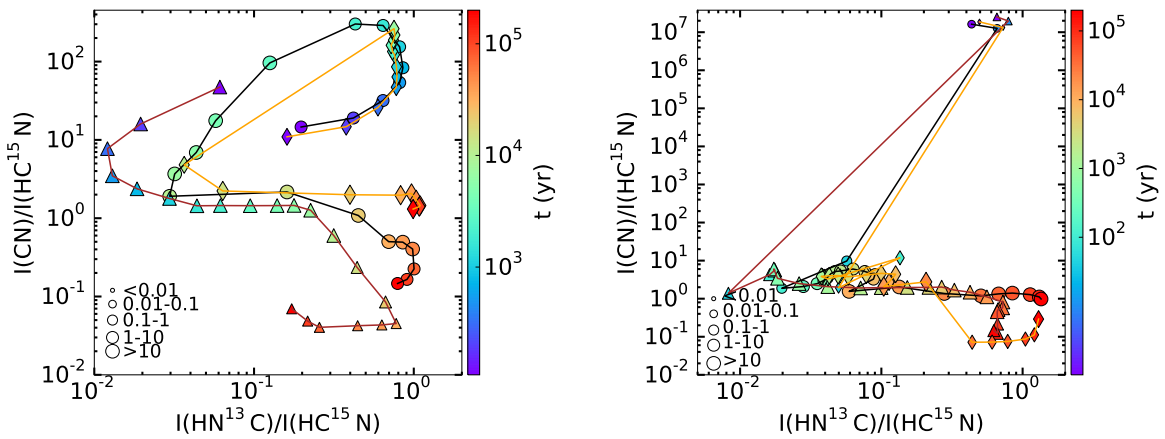
Figure A.108: Time evolution of the integrated intensity ratio $(I(CH_3OH\,(2(2,1)–3(1,2)))$ / $I(HC^{15}N\,(1–0)))$ in function of the integrated intensity ratio $(I(HN^{13}C\,(1–0))$ / $I(HC^{15}N\,(1–0)))$ for models using the second density profile $(\gamma = 1)$ and with different sizes of ionized cavity: 0.015 pc (brown and triangle markers), 0.05 pc (black and circle markers) and 0.10 pc (orange and diamond markers). The HII region models are shown on the left panel and the HHMC models on the right panel. The size of the markers correspond to the range value of the peak intensity in Kelvin of CH_3OH.

Initial abundances
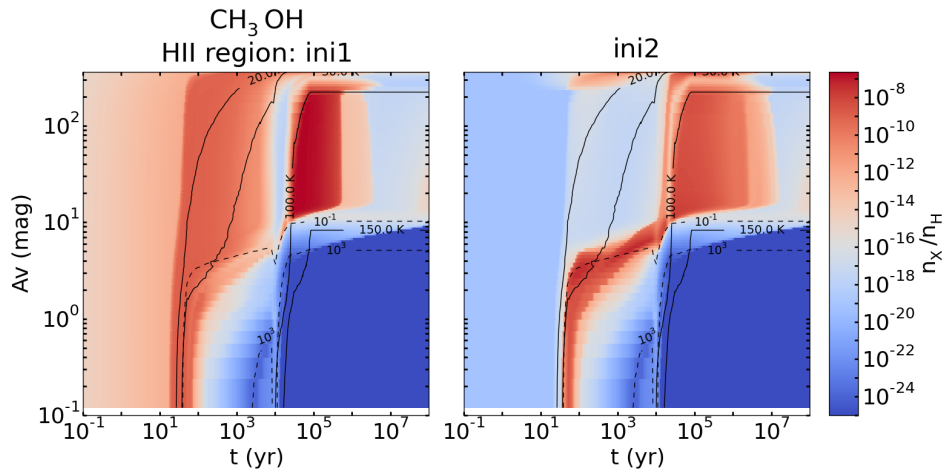
Figure A.109: Abundances of CH_3OH in function of time (x-axis) and visual extinction (y-axis) for HII region with different initial abundances: *ini1* (left panel) and *ini2* (right). The solid black lines appearing on the figures represent the contours for the temperature: 20, 30, 100 and 150 K and the dashed black lines represent some contours for the radiation field intensity: 10^{-1} and 10^3 Draine unit.
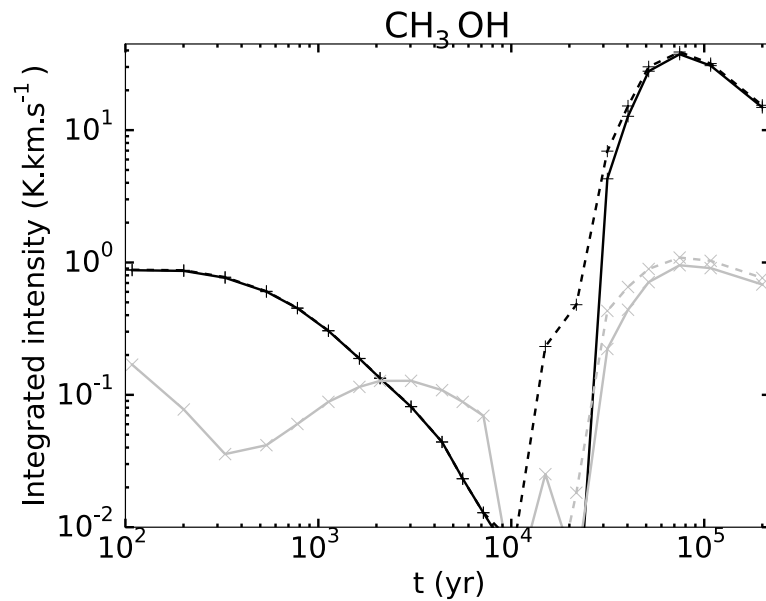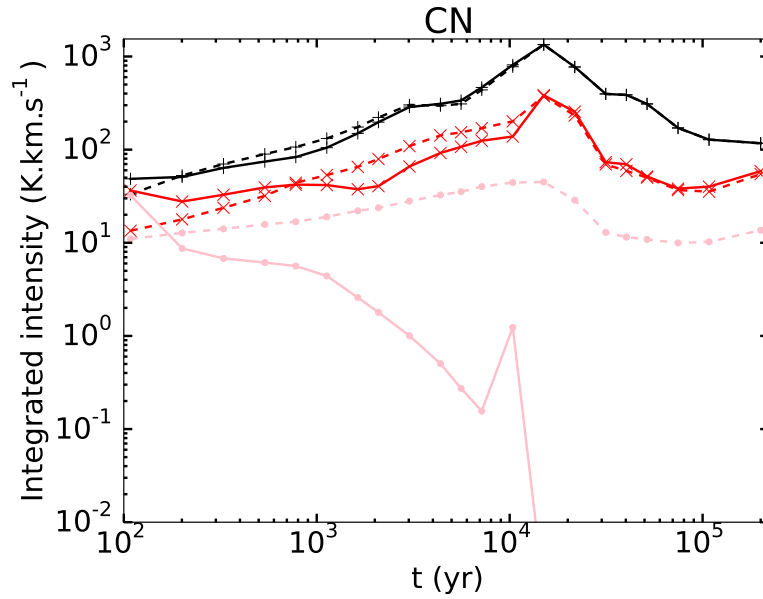
Figure A.110: Time evolution of integrated intensities for CH$_3$OH (2(2,1)–3(1,2)) (left panel) for models with different initial abundances: *ini1* (black) and *ini2* (grey). The solid lines represent the HII region models and the dashed lines the HHMC models.
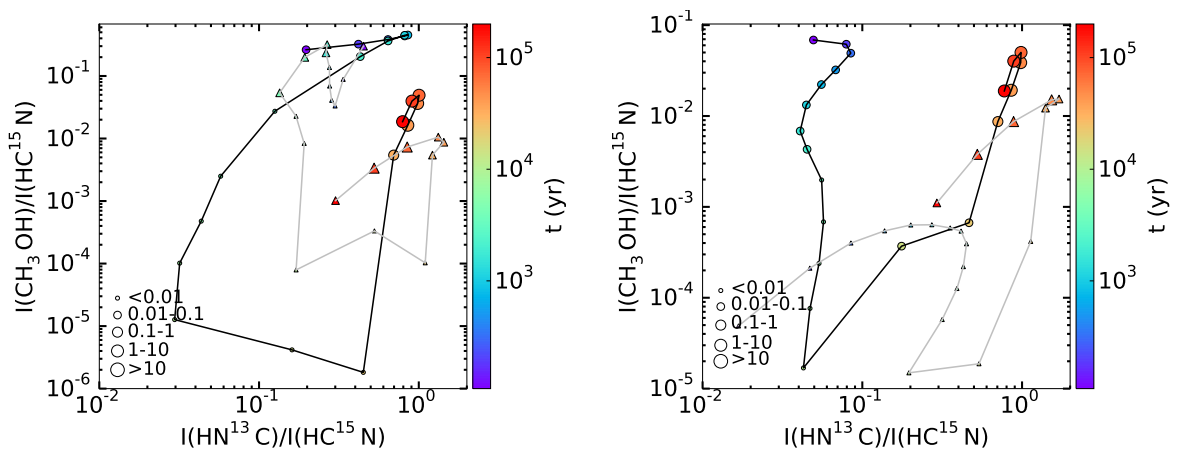
Figure A.111: Time evolution of the integrated intensity ratio (I(CH$_3$OH (2(2,1)–3(1,2))) / I(HC^{15}N (1–0))) in function of the integrated intensity ratio (I(HN^{13}C (1–0)) / I(HC^{15}N (1–0))) for models with different initial abundances: *ini1* (black line and circle markers) and *ini2* (grey line and triangle markers). The HII region models are shown on the left panel and the HHMC models on the right panel. The size of the markers corresponds to the range value of the peak intensity in Kelvin of CH$_3$OH.

Effect of the envelope
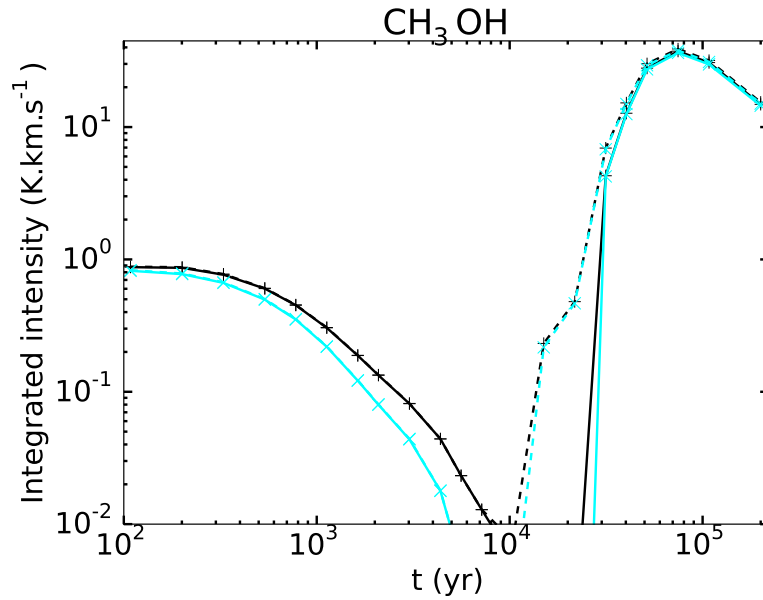
Figure A.112: Time evolution of integrated intensities for $CH_3OH\,(2(2,1)–3(1,2))$ for models with different cut-off density: 10^1 cm^{-3} (black) and 10^6 cm^{-3} (light blue). The solid lines represent the HII region models and the dashed lines the HHMC models.
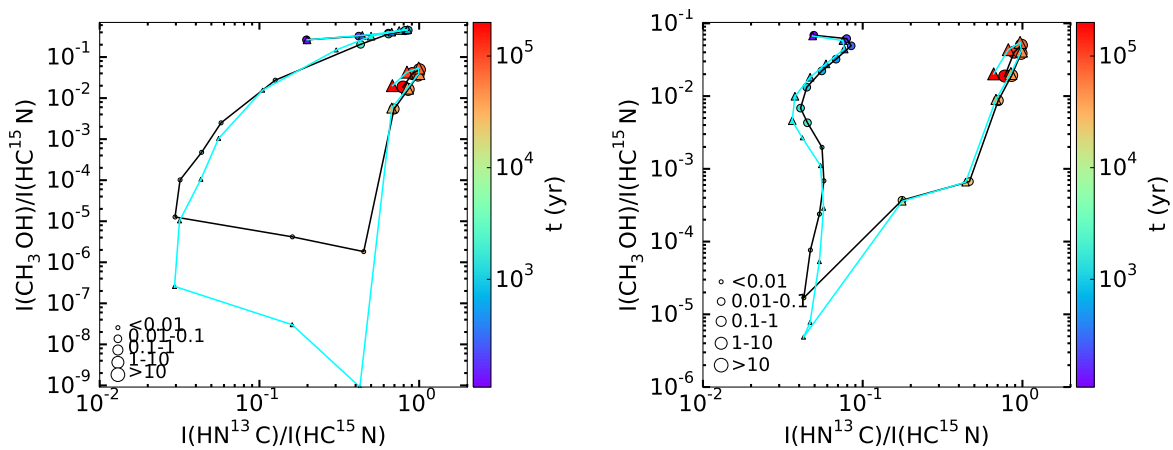
Figure A.113: Time evolution of the integrated intensity ratio $(I(CH_3OH\,(2(2,1)–3(1,2)))$ / $I(HC^{15}N\,(1–0)))$ in function of the integrated intensity ratio $(I(HN^{13}C\,(1–0))$ / $I(HC^{15}N\,(1–0)))$ for models with different cut-off density: 10^1 cm^{-3} (black line and circle markers) and 10^6 cm^{-3} (light blue line and triangle markers). The HII region models are shown on the left panel and the HHMC models on the right panel. The size of the markers corresponds to the range value of the peak intensity in Kelvin of CH_3OH.

A.7   CN

HMC vs HHMC model
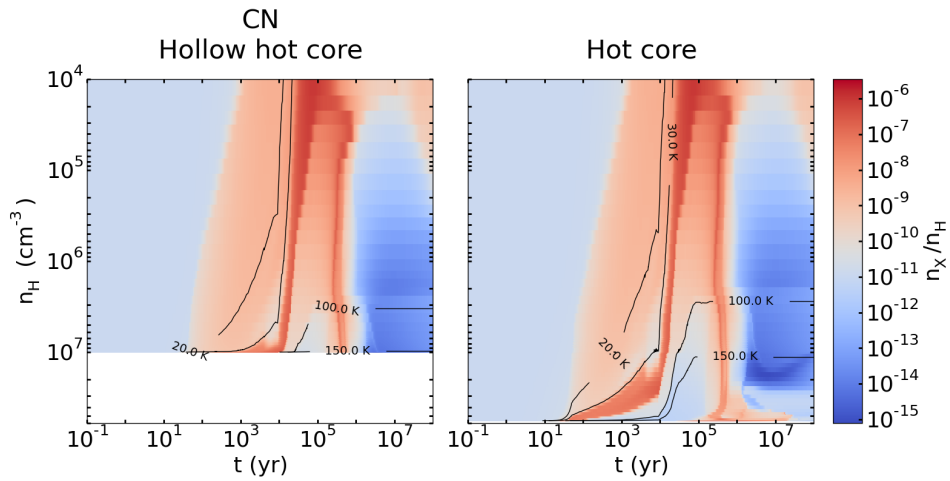
Figure A.114: Abundance of CN in function of time (x-axis) and density (y-axis) for the HHMC (left) and HMC (right) models.
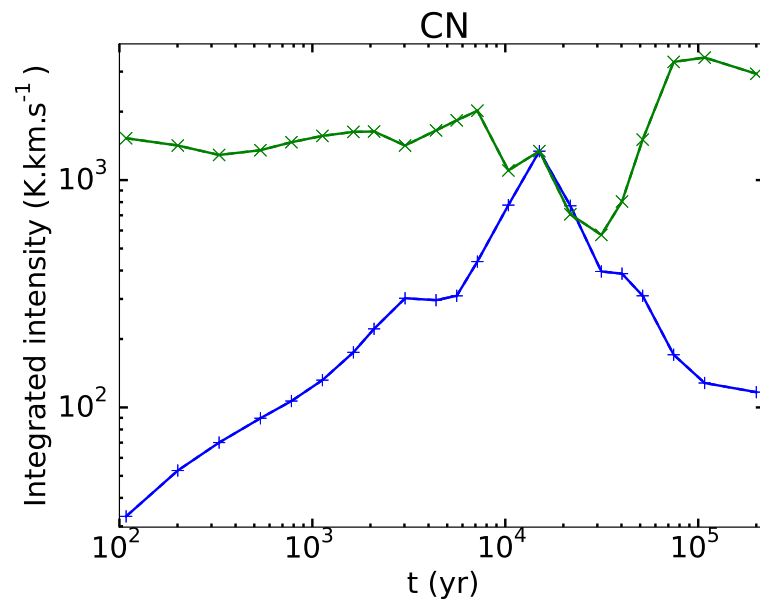
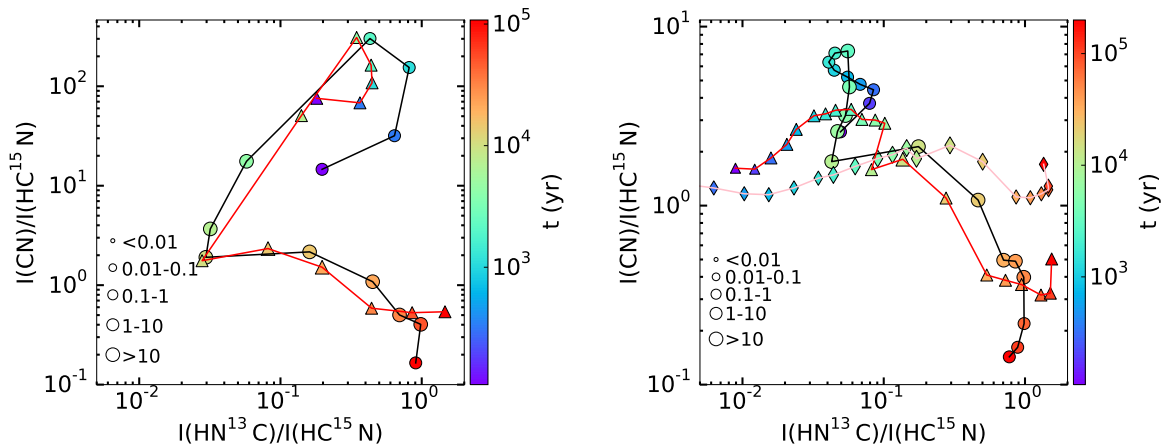Figure A.115: Time evolution of integrated intensities for CN (1–0). The blue lines represent the HHMC model and the green one represents the HMC model.
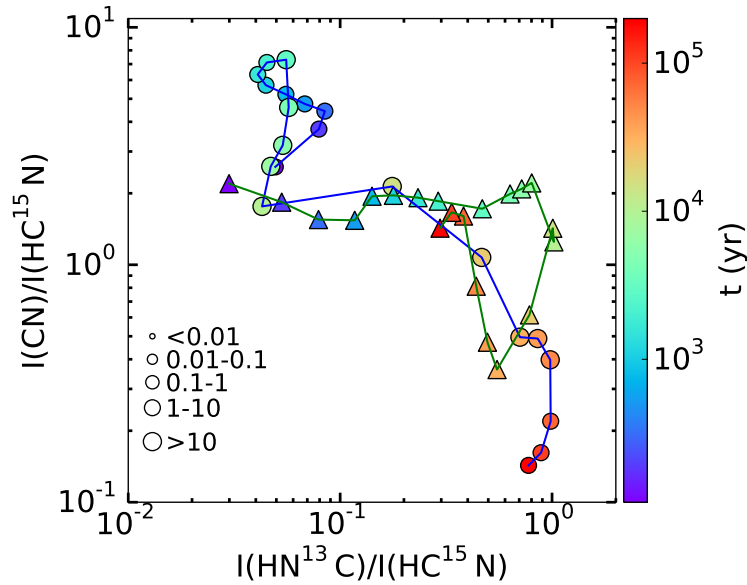
Figure A.116: Time evolution of the integrated intensity ratio ($I(CN(1–0))$ / $I(HC^{15}N(1–0))$) in function of the integrated intensity ratio ($I(HN^{13}C(1–0))$ / $I(HC^{15}N(1–0))$) for the HHMC (blue line and circle markers) and HMC (green line and triangle markers) models. The size of the markers corresponds to the range value of the peak intensity in Kelvin of CN.

HII region vs HHMC model
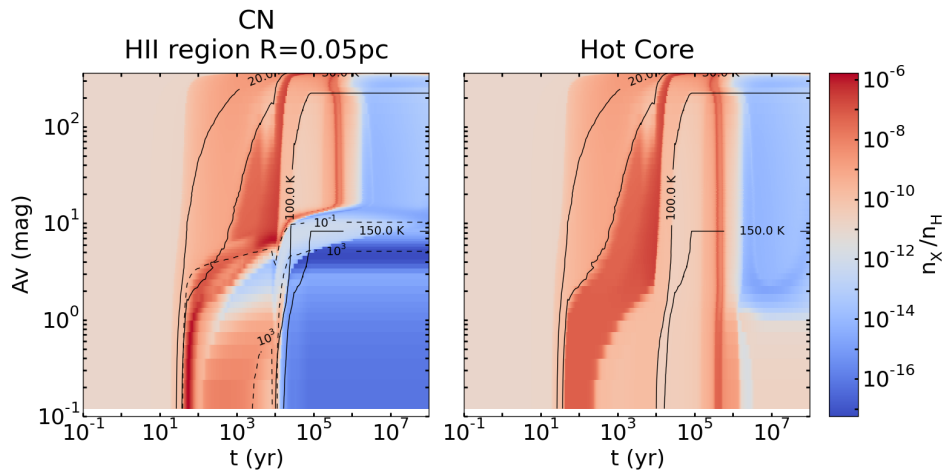
Figure A.117: Abundances of CN in function of time (x-axis) and visual extinction (y-axis) for the HII region (left panel) and HHMC (right) models. The solid black lines represent the contours for the temperature: 20, 30, 100 and 150 K and the dashed black lines represent some contours for the radiation field intensity: 10^{-1} and 10^{3} Draine unit.
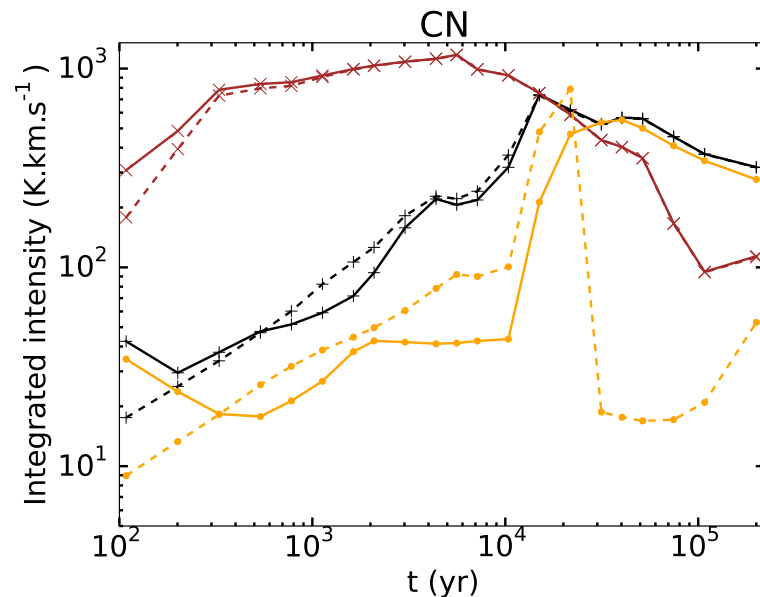
Figure A.118: Time evolution of integrated intensities for CN (1–0). The black line represents the HII region model and the blue lines represent the HHMC model.
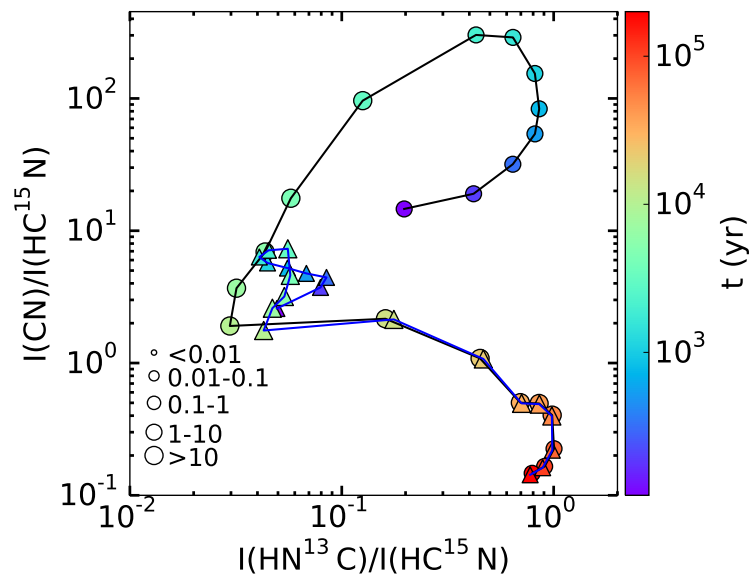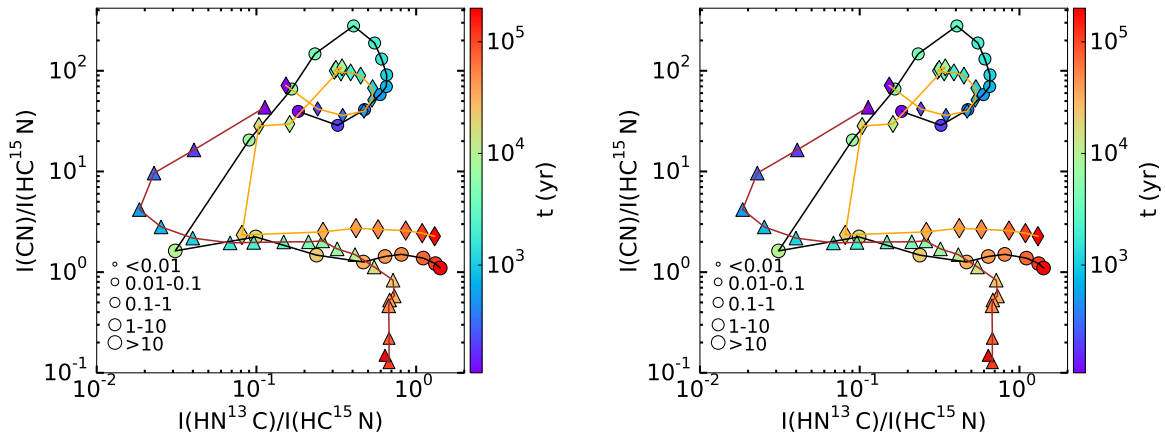

Figure A.119: Time evolution of the integrated intensity ratio ($I(\text{CN}\,(1\text{–}0))$ / $I(\text{HC}^{15}\text{N}\,(1\text{–}0))$) in function of the integrated intensity ratio ($I(\text{HN}^{13}\text{C}\,(1\text{–}0))$ / $I(\text{HC}^{15}\text{N}\,(1\text{–}0))$) for the HII region (black line and circle markers) and HHMC (blue line and triangle markers) models. The size of the markers corresponds to the range value of the peak intensity in Kelvin of CN.
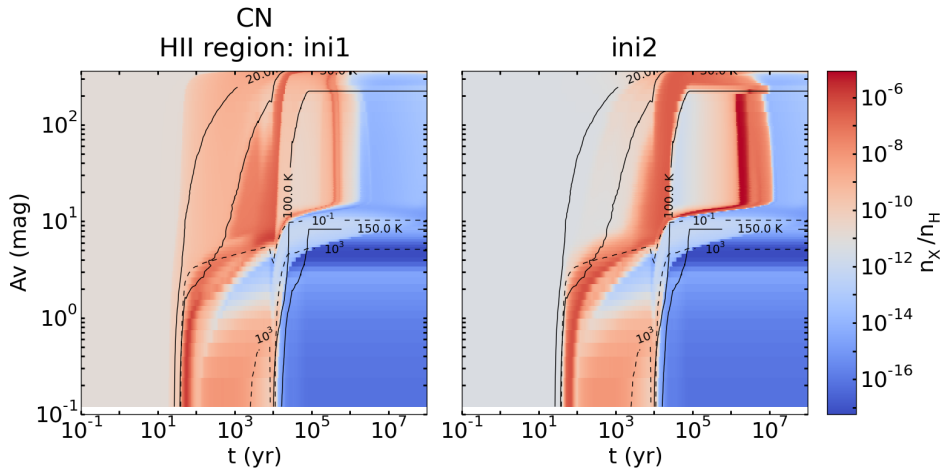
H$_{\text{II}}$ region size
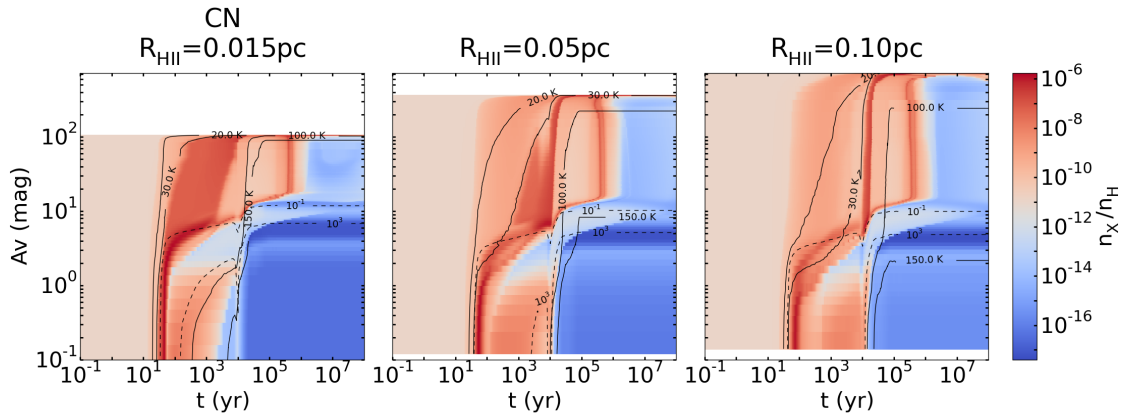
Figure A.120: Abundances of CN in function of time (x-axis) and visual extinction (y-axis) for HII region models with different sizes: 0.015 pc (left panels), 0.05 pc (middle) and 0.10 pc (right). The solid black lines appearing on the figures represent the contours for the temperature: 20, 30, 100 and 150 K and the dashed black lines represent some contours for the radiation field intensity: 10^{-1} and 10^3 Draine unit.
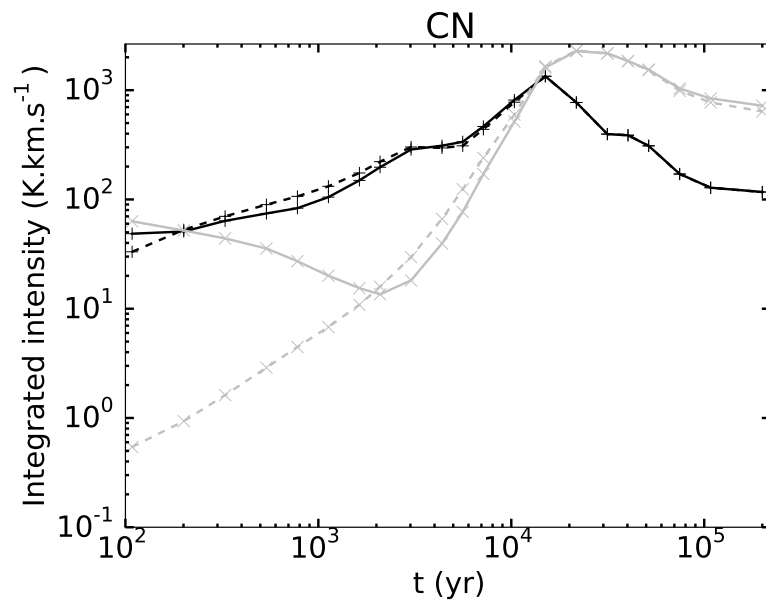

Figure A.121: Time evolution of integrated intensities for CN (1–0) for models with different sizes of ionized cavity: 0.015 pc (orange), 0.05 pc (black) and 0.10 pc (brown). The solid lines represent the HII region models and the dashed lines the HHMC models.

Figure A.122: Time evolution of the integrated intensity ratio ($I(\mathrm{CN}\,(1\text{–}0))$ / $I(\mathrm{HC}^{15}\mathrm{N}\,(1\text{–}0)))$) in function of the integrated intensity ratio ($I(\mathrm{HN}^{13}\mathrm{C}\,(1\text{–}0))$ / $I(\mathrm{HC}^{15}\mathrm{N}\,(1\text{–}0)))$) for models with different sizes of ionized cavity: 0.015 pc (brown line and triangle markers), 0.05 pc (black line and circle markers) and 0.10 pc (orange line and diamond markers). The HII region models are shown on the left panel and the HHMC models on the right panel. The size of the markers corresponds to the range value of the peak intensity in Kelvin of CN.

Density at the ionization front
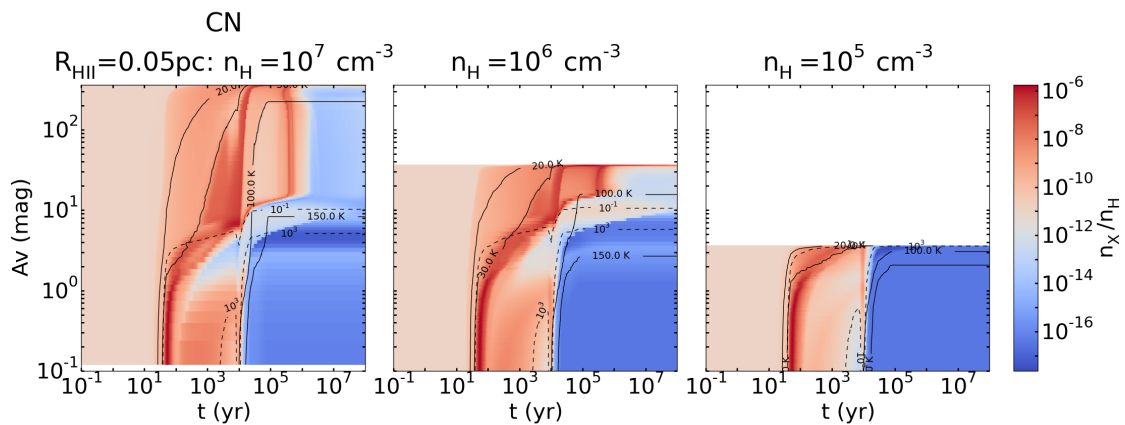
Figure A.123: Abundances of CN in function of time (x-axis) and visual extinction (y-axis) for HII region models with different densities at the ionization front: 10^7 cm^{-3} (left), 10^6 cm^{-3} (middle) and 10^5 cm^{-3} (right). The solid black lines appearing on the figures represent the contours for the temperature: 20, 30, 100 and 150 K and the dashed black lines represent some contours for the radiation field intensity: 10^{-1} and 10^3 Draine unit.

Figure A.124: Time evolution of integrated intensities for CN (1–0) for models with different densities at the ionization front: 10^7 cm^{-3} (black), 10^6 cm^{-3} (red) and 10^5 cm^{-3} (pink). The solid lines represent the HII region models and the dashed lines the HHMC models.
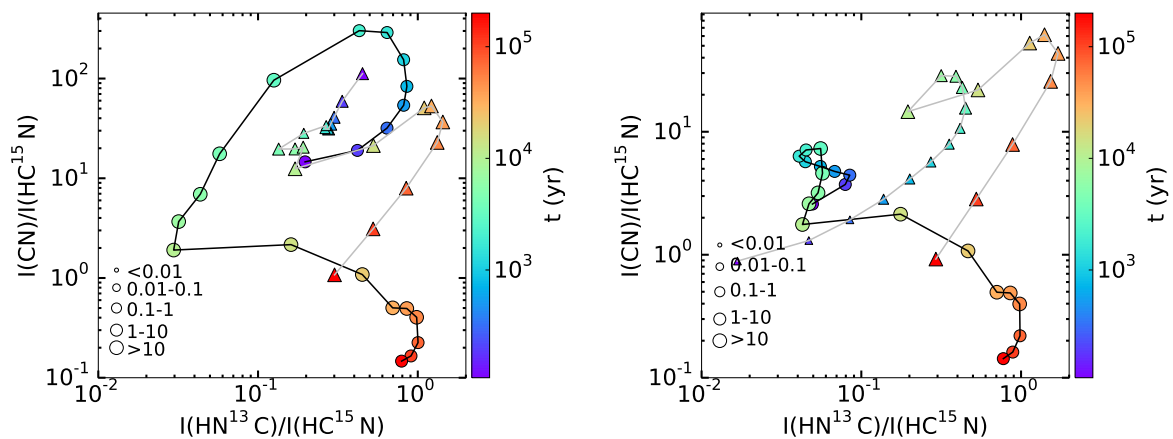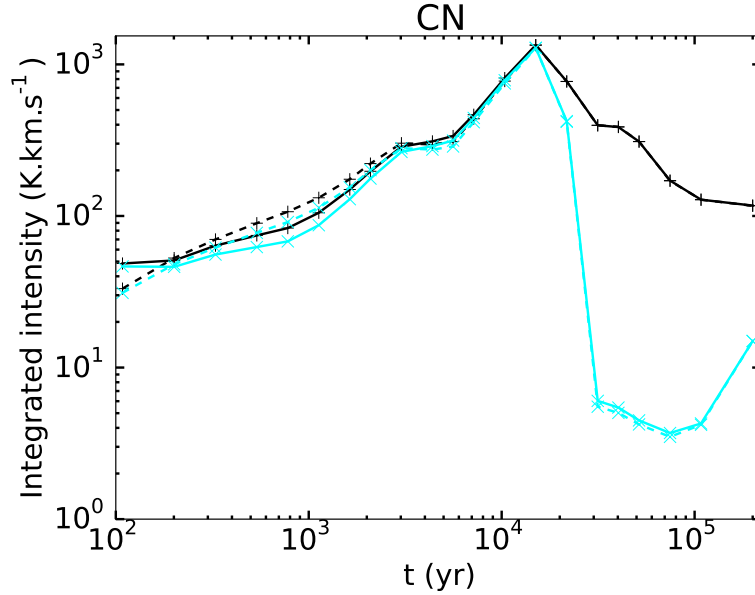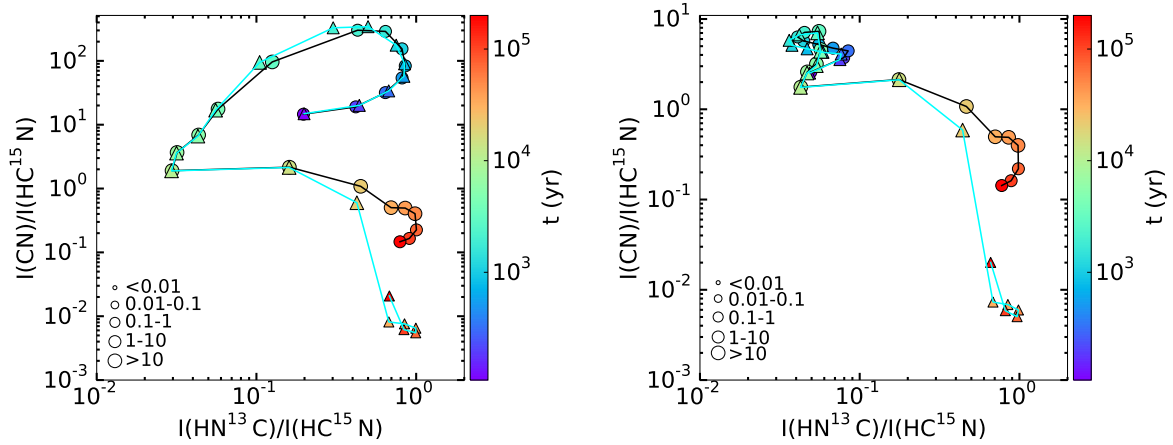

Figure A.125: Time evolution of the integrated intensity ratio (I(CN (1–0)) / I(HC^{15}N (1–0))) in function of the integrated intensity ratio (I(HN^{13}C (1–0)) / I(HC^{15}N (1–0))) for models with different density at the ionization front: 10^7 cm^{-3} (black line and circle markers), 10^6 cm^{-3} (red line and triangle markers) and 10^5 cm^{-3} (pink line and diamond markers). The HII region models are shown on the left panel and the HHMC models on the right panel. The size of the markers corresponds to the range value of the peak intensity in Kelvin of CN.

Plummer exponent
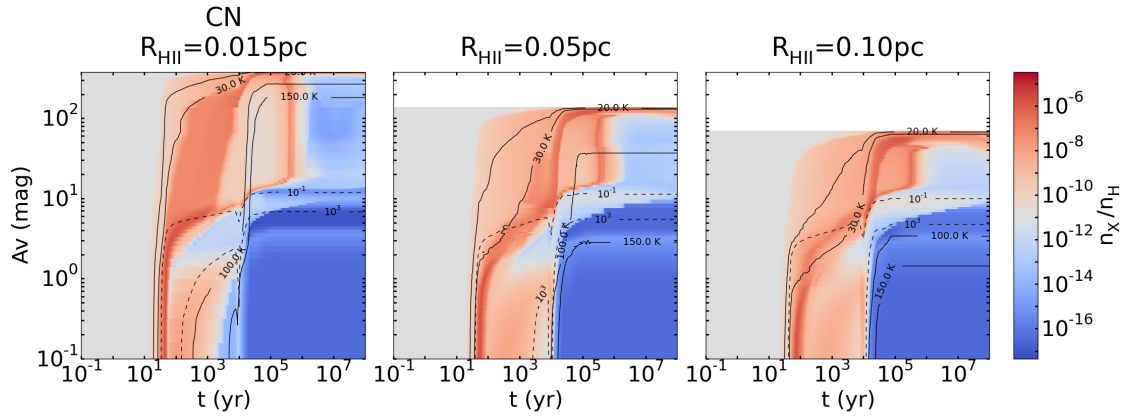
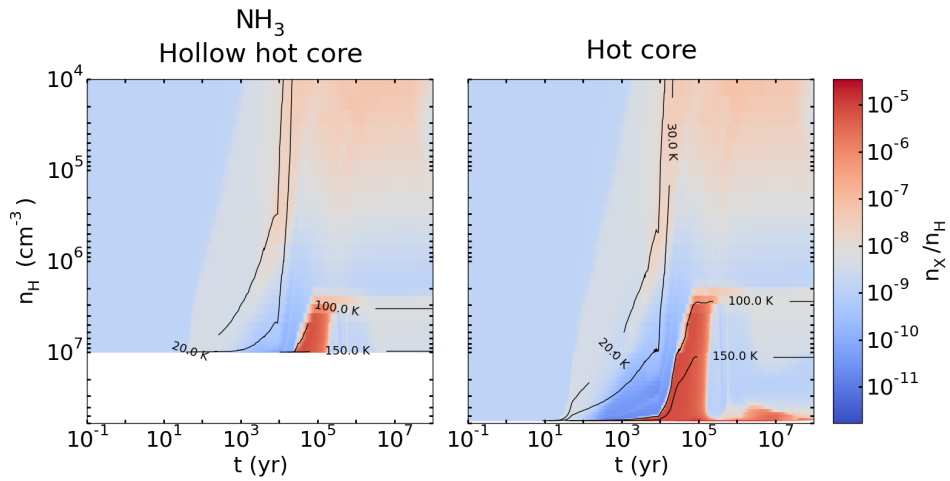Figure A.126: Abundances of CN in function of time (x-axis) and visual extinction (y-axis) for HII region models using for the second density profile ($\gamma = 1$) and with different sizes of ionized cavity: 0.015 pc (left panel), 0.05 pc (middle) and 0.10 pc (right). The solid black lines appearing on the figures represent the contours for the temperature: 20, 30, 100 and 150 K and the dashed black lines represent some contours for the radiation field intensity: 10^{-1} and 10^{3} Draine unit.

Figure A.127: Time evolution of integrated intensities for CN (1–0) (left panel) for models using the second density profile ($\gamma = 1$) and with different sizes of ionized cavity: 0.015 pc (brown), 0.05 pc (black) and 0.10 pc (orange). The solid lines represent the HII region models and the dashed lines the HHMC models.

Figure A.128: Time evolution of the integrated intensity ratio ($I(\mathrm{CN}\,(1\text{–}0))$ / $I(\mathrm{HC}^{15}\mathrm{N}\,(1\text{–}0))$) in function of the integrated intensity ratio ($I(\mathrm{HN}^{13}\mathrm{C}\,(1\text{–}0))$ / $I(\mathrm{HC}^{15}\mathrm{N}\,(1\text{–}0))$) for models using the second density profile ($\gamma = 1$) and with different sizes of ionized cavity: 0.015 pc (brown and triangle markers), 0.05 pc (black and circle markers) and 0.10 pc (orange and diamond markers). The HII region models are shown on the left panel and the HHMC models on the right panel. The size of the markers correspond to the range value of the peak intensity in Kelvin of CN.

Initial abundances

Figure A.129: Abundances of CN in function of time (x-axis) and visual extinction (y-axis) for HII region with different initial abundances: *ini1* (left panel) and *ini2* (right). The solid black lines appearing on the figures represent the contours for the temperature: 20, 30, 100 and 150 K and the dashed black lines represent some contours for the radiation field intensity: 10^{-1} and 10^3 Draine unit.
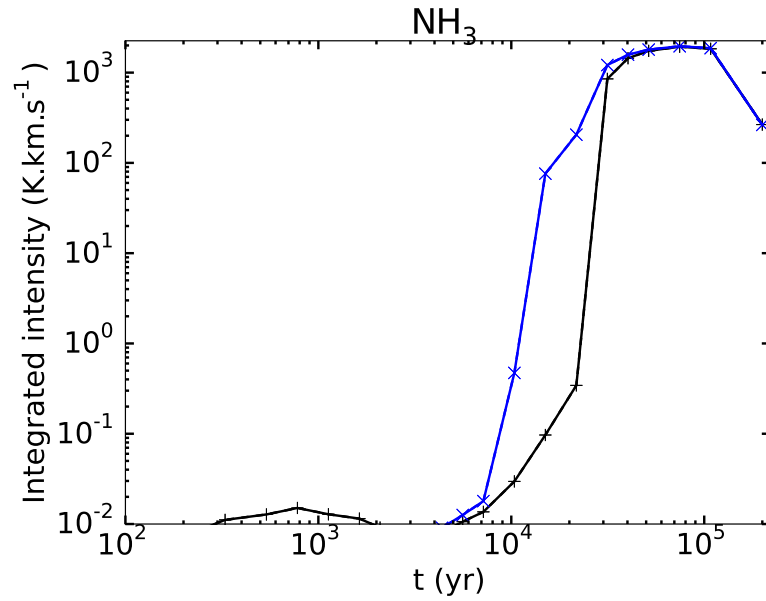
Figure A.130: Time evolution of integrated intensities for CN (1–0) (left panel) for models with different initial abundances: *ini1* (black) and *ini2* (grey). The solid lines represent the HII region models and the dashed lines the HHMC models.
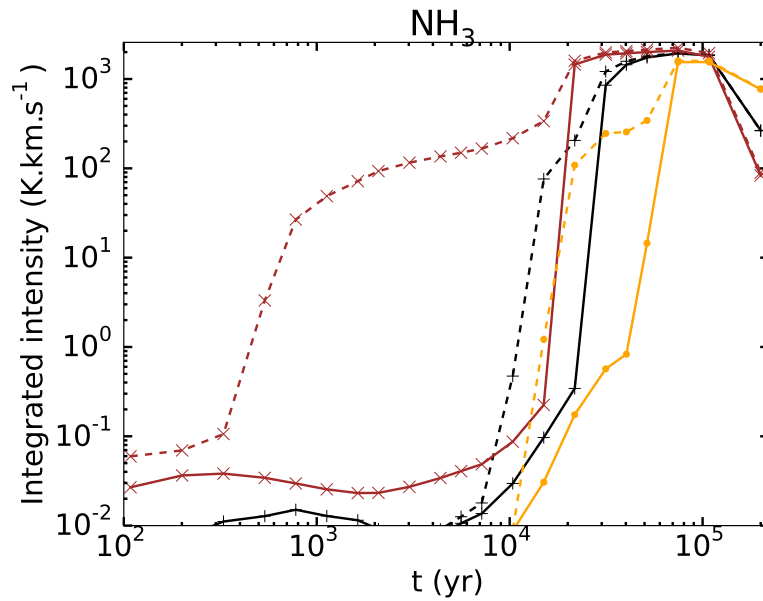

Figure A.131: Time evolution of the integrated intensity ratio $(I(\mathrm{CN}\,(1\text{–}0))\,/\,I(\mathrm{HC}^{15}\mathrm{N}\,(1\text{–}0)))$ in function of the integrated intensity ratio $(I(\mathrm{HN}^{13}\mathrm{C}\,(1\text{–}0))\,/\,I(\mathrm{HC}^{15}\mathrm{N}\,(1\text{–}0)))$ for models with different initial abundances: *ini1* (black line and circle markers) and *ini2* (grey line and triangle markers). The HII region models are shown on the left panel and the HHMC models on the right panel. The size of the markers corresponds to the range value of the peak intensity in Kelvin of CN.

Effect of the envelope

Figure A.132: Time evolution of integrated intensities for $CN\,(1\text{--}0)$ for models with different cut-off density: 10^1 cm^{-3} (black) and 10^6 cm^{-3} (light blue). The solid lines represent the HII region models and the dashed lines the HHMC models.

Figure A.133: Time evolution of the integrated intensity ratio ($I(CN\,(1\text{--}0))\,/\,I(HC^{15}N\,(1\text{--}0))$) in function of the integrated intensity ratio ($I(HN^{13}C\,(1\text{--}0))\,/\,I(HC^{15}N\,(1\text{--}0))$) for models with different cut-off density: 10^1 cm^{-3} (black line and circle markers) and 10^6 cm^{-3} (light blue line and triangle markers). The HII region models are shown on the left panel and the HHMC models on the right panel. The size of the markers corresponds to the range value of the peak intensity in Kelvin of CN.

A.8 NH$_3$

HMC vs HHMC model

Figure A.134: Abundance of NH$_3$ in function of time (x-axis) and density (y-axis) for the HHMC (left) and HMC (right) models.
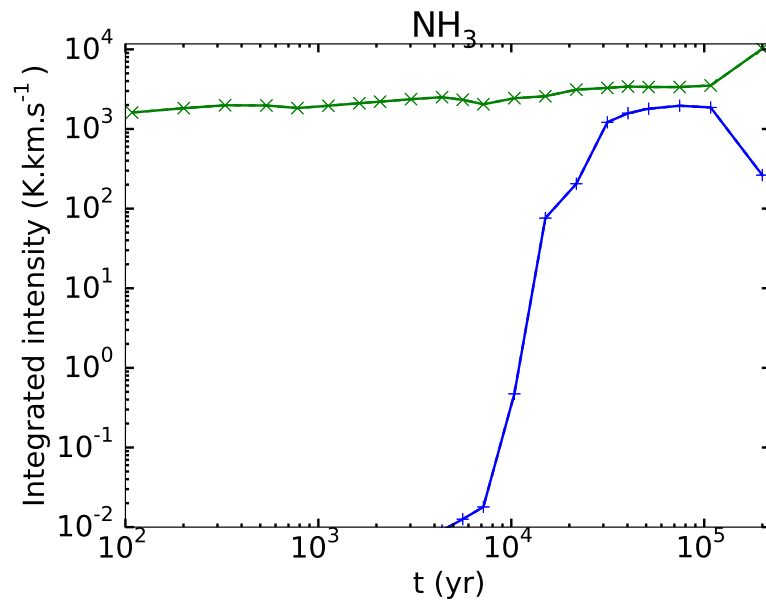
Figure A.135: Time evolution of integrated intensities for NH$_3$ (5(5,1)–5(5,0)). The blue lines represent the HHMC model and the green one represents the HMC model.
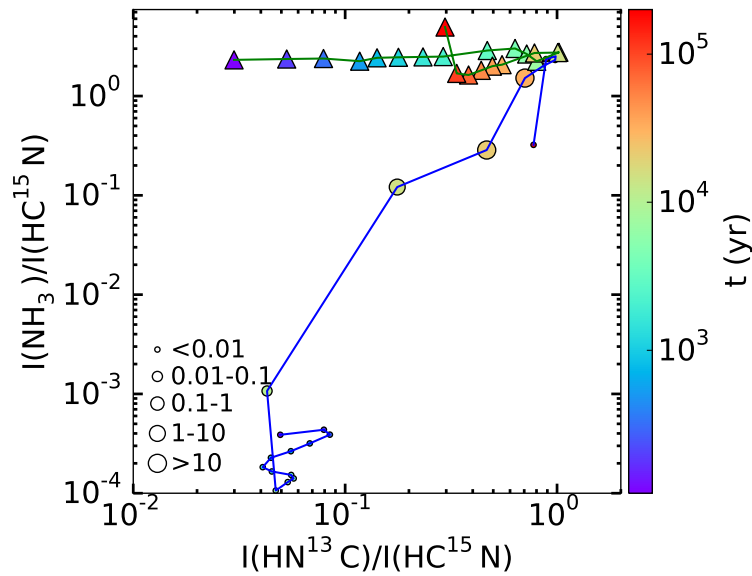
Figure A.136: Time evolution of the integrated intensity ratio ($I(\mathrm{NH}_3\,(5(5,1)\text{–}5(5,0)))$ / $I(\mathrm{HC}^{15}\mathrm{N}\,(1\text{–}0))$) in function of the integrated intensity ratio ($I(\mathrm{HN}^{13}\mathrm{C}\,(1\text{–}0))$ / $I(\mathrm{HC}^{15}\mathrm{N}\,(1\text{–}0))$) for the HHMC (blue line and circle markers) and HMC (green line and triangle markers) models. The size of the markers corresponds to the range value of the peak intensity in Kelvin of NH_3.

H<small>II</small> region vs HMC vs HHMC model
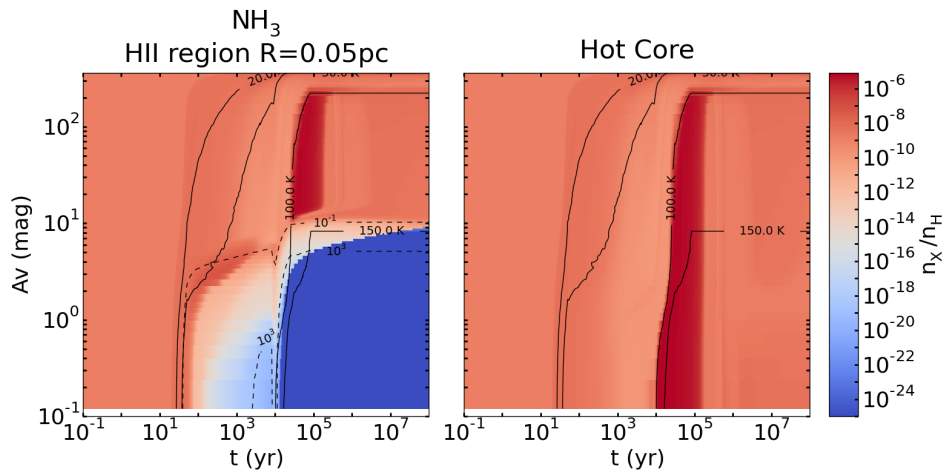
Figure A.137: Abundances of NH_3 in function of time (x-axis) and visual extinction (y-axis) for the HII region (left panel) and HHMC (right) models. The solid black lines represent the contours for the temperature: 20, 30, 100 and 150 K and the dashed black lines represent some contours for the radiation field intensity: 10^{-1} and 10^3 Draine unit.
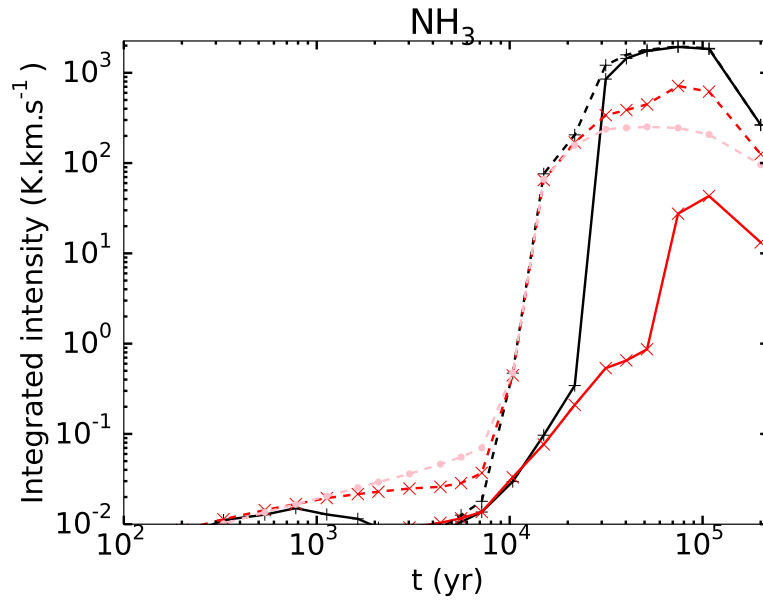
Figure A.138: Time evolution of integrated intensities for NH$_3$ (5(5,1)–5(5,0)). The black line represents the HII region model and the blue lines represent the HHMC model.
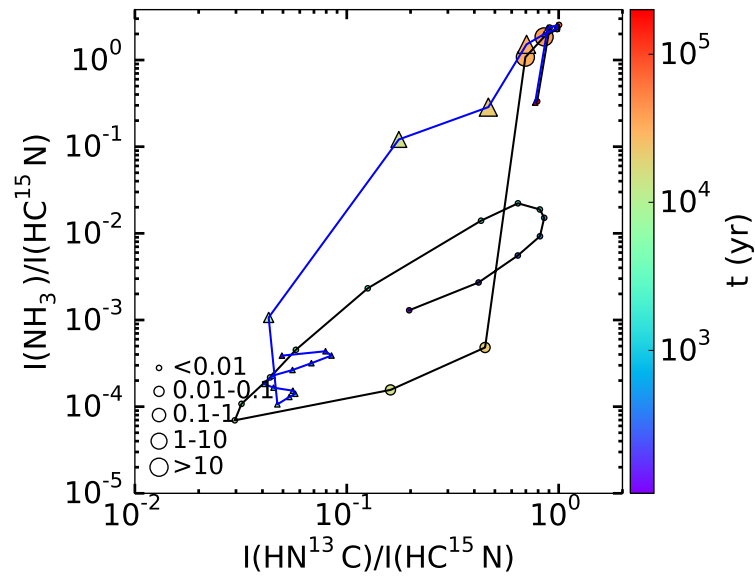
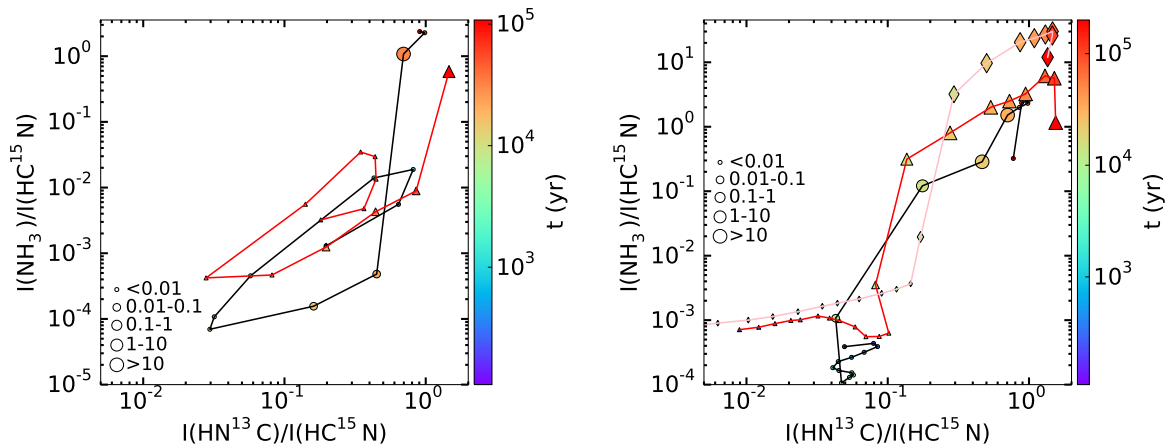Figure A.139: Time evolution of the integrated intensity ratio (I(NH$_3$ (5(5,1)–5(5,0)) / I(HC^{15}N (1–0))) in function of the integrated intensity ratio (I(HN^{13}C (1–0)) / I(HC^{15}N (1–0))) for the HII region (black line and circle markers) and HHMC (blue line and triangle markers) models. The size of the markers corresponds to the range value of the peak intensity in Kelvin of NH$_3$.

HII region size
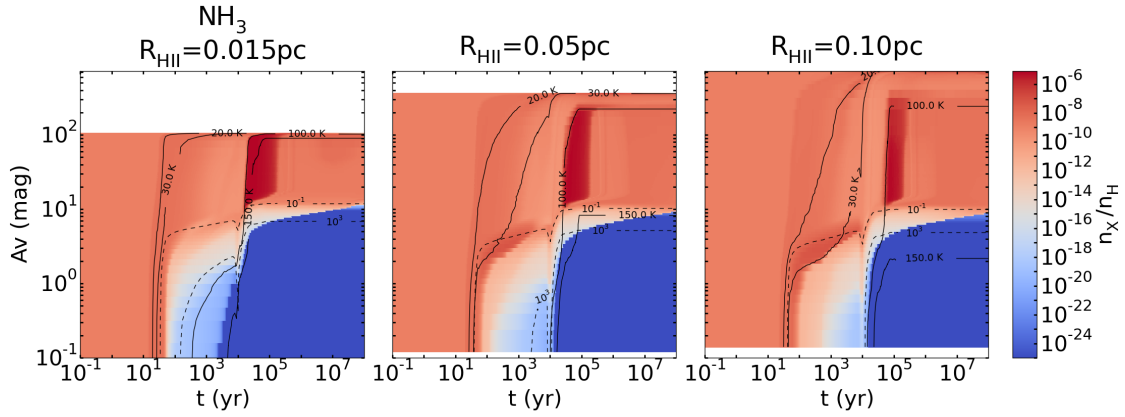
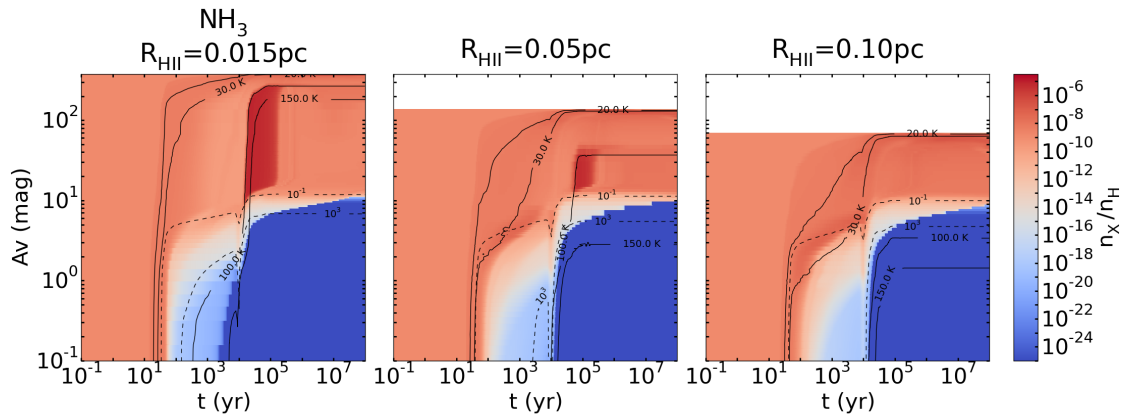Figure A.140: Abundances of NH$_3$ in function of time (x-axis) and visual extinction (y-axis) for HII region models with different sizes: 0.015 pc (left panels), 0.05 pc (middle) and 0.10 pc (right). The solid black lines appearing on the figures represent the contours for the temperature: 20, 30, 100 and 150 K and the dashed black lines represent some contours for the radiation field intensity: 10^{-1} and 10^3 Draine unit.
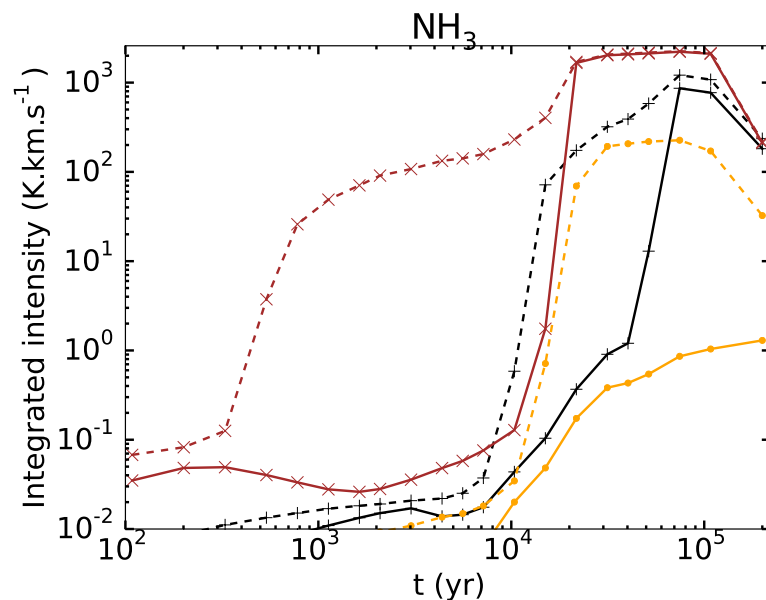

Figure A.141: Time evolution of integrated intensities for NH$_3$ (5(5,1)–5(5,0)) for models with different sizes of ionized cavity: 0.015 pc (orange), 0.05 pc (black) and 0.10 pc (brown). The solid lines represent the HII region models and the dashed lines the HHMC models.
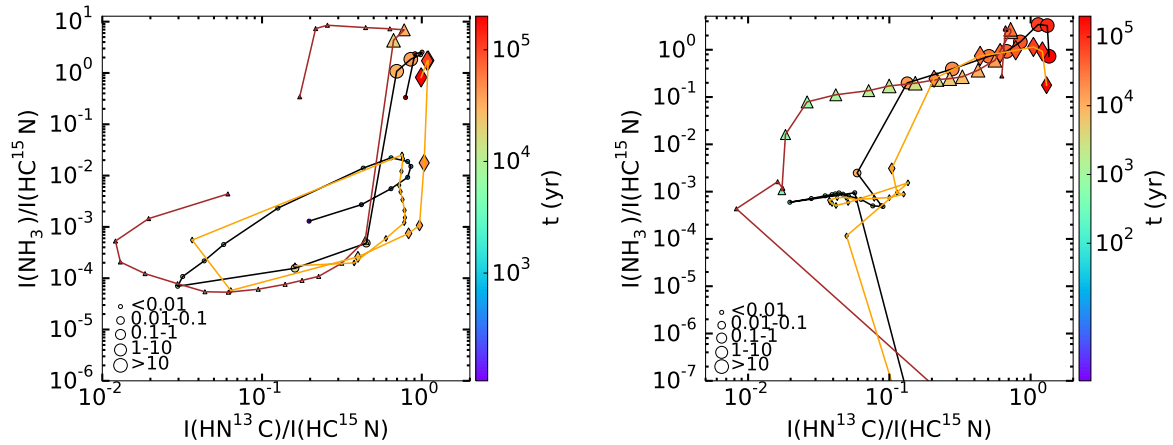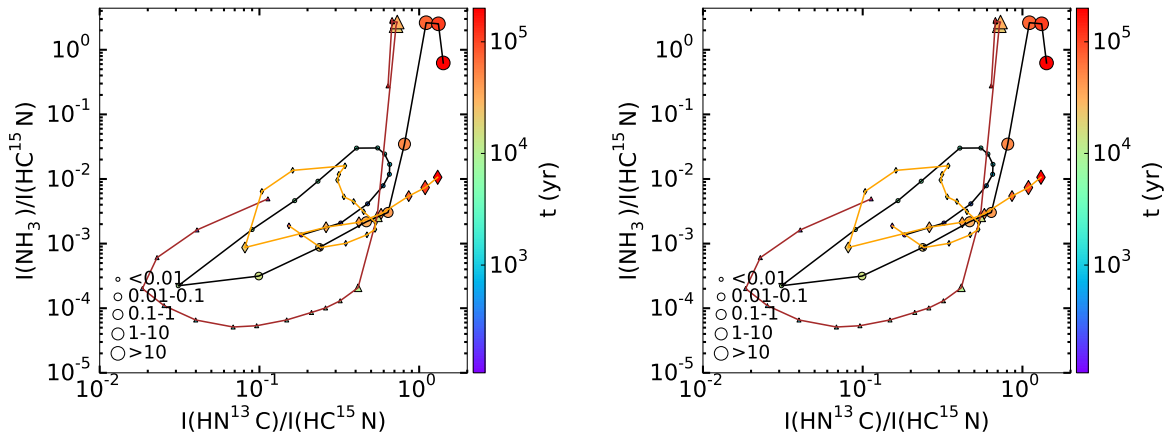
Figure A.142: Time evolution of the integrated intensity ratio ($I(\mathrm{NH_3}\,(5(5,1)-5(5,0)))$ / $I(\mathrm{HC^{15}N}\,(1-0)))$) in function of the integrated intensity ratio ($I(\mathrm{HN^{13}C}\,(1-0))$ / $I(\mathrm{HC^{15}N}\,(1-0)))$) for models with different sizes of ionized cavity: 0.015 pc (brown line and triangle markers), 0.05 pc (black line and circle markers) and 0.10 pc (orange line and diamond markers). The HII region models are shown on the left panel and the HHMC models on the right panel. The size of the markers corresponds to the range value of the peak intensity in Kelvin of $\mathrm{NH_3}$.
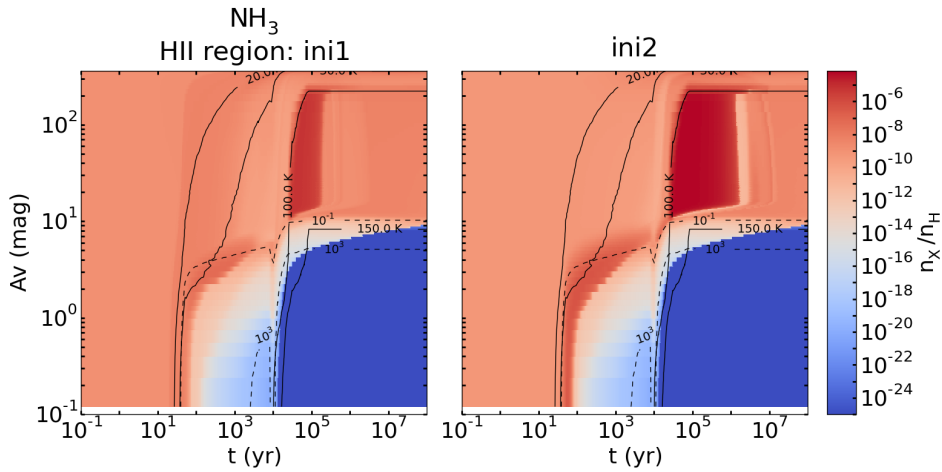
Density at the ionization front
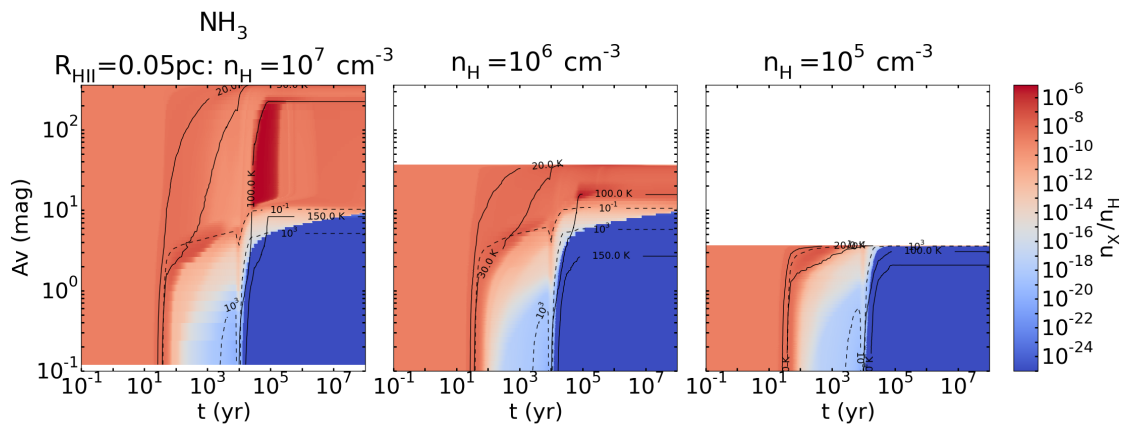
Figure A.143: Abundances of $\mathrm{NH_3}$ in function of time (x-axis) and visual extinction (y-axis) for HII region models with different densities at the ionization front: 10^7 cm^{-3} (left), 10^6 cm^{-3} (middle) and 10^5 cm^{-3} (right). The solid black lines appearing on the figures represent the contours for the temperature: 20, 30, 100 and 150 K and the dashed black lines represent some contours for the radiation field intensity: 10^{-1} and 10^3 Draine unit.
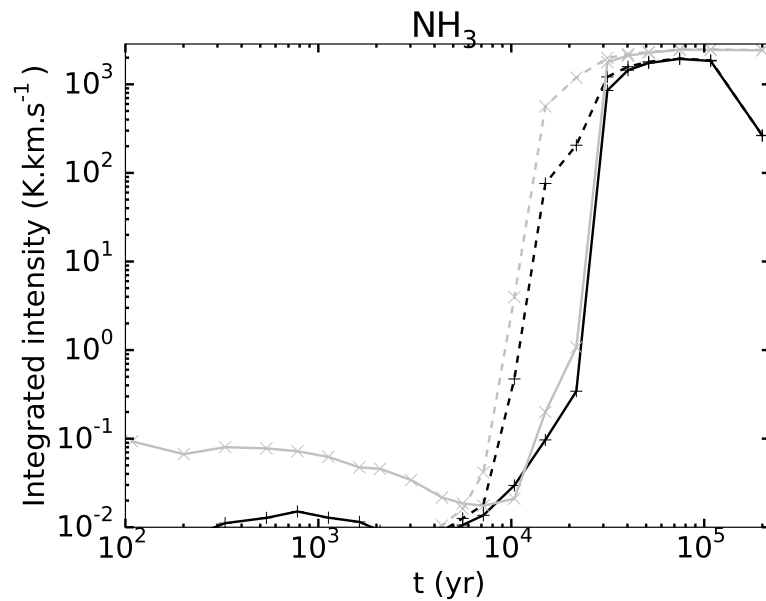
Figure A.144: Time evolution of integrated intensities for NH_3 (5(5,1)–5(5,0)) for models with different densities at the ionization front: 10^7 cm^{-3} (black), 10^6 cm^{-3} (red) and 10^5 cm^{-3} (pink). The solid lines represent the HII region models and the dashed lines the HHMC models.
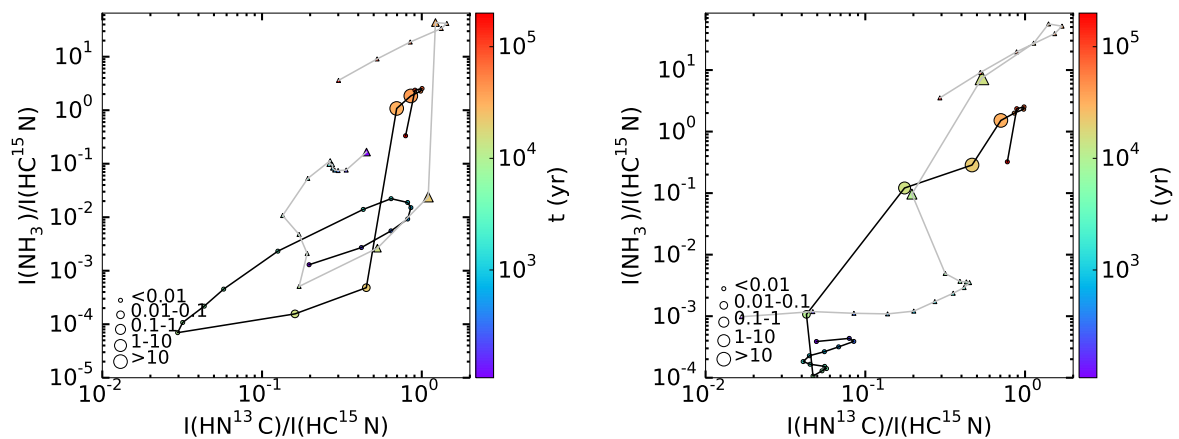

Figure A.145: Time evolution of the integrated intensity ratio ($I(NH_3$ (5(5,1)–5(5,0))) / $I(HC^{15}N$ (1–0))) in function of the integrated intensity ratio ($I(HN^{13}C$ (1–0)) / $I(HC^{15}N$ (1–0))) for models with different density at the ionization front: 10^7 cm^{-3} (black line and circle markers), 10^6 cm^{-3} (red line and triangle markers) and 10^5 cm^{-3} (pink line and diamond markers). The HII region models are shown on the left panel and the HHMC models on the right panel. The size of the markers corresponds to the range value of the peak intensity in Kelvin of NH_3.

Plummer exponent


Figure A.146: Abundances of NH$_3$ in function of time (x-axis) and visual extinction (y-axis) for HII region models using for the second density profile ($\gamma = 1$) and with different sizes of ionized cavity: 0.015 pc (left panel), 0.05 pc (middle) and 0.10 pc (right). The solid black lines appearing on the figures represent the contours for the temperature: 20, 30, 100 and 150 K and the dashed black lines represent some contours for the radiation field intensity: 10^{-1} and 10^3 Draine unit.

Figure A.147: Time evolution of integrated intensities for NH$_3$ (5(5,1)–5(5,0)) (left panel) for models using the second density profile ($\gamma = 1$) and with different sizes of ionized cavity: 0.015 pc (brown), 0.05 pc (black) and 0.10 pc (orange). The solid lines represent the HII region models and the dashed lines the HHMC models.
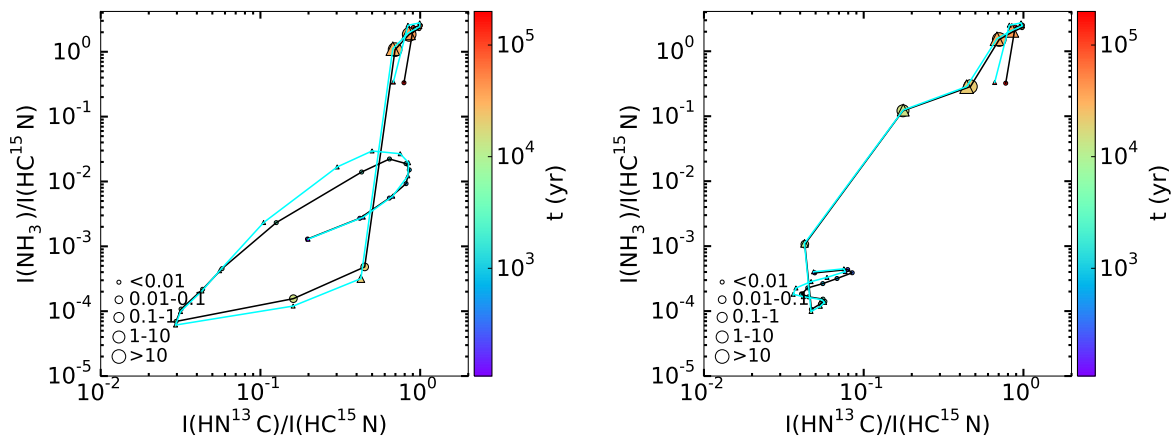
Figure A.148: Time evolution of the integrated intensity ratio ($I(NH_3 (5(5,1)$–$5(5,0)))$ / $I(HC^{15}N (1$–$0)))$ in function of the integrated intensity ratio ($I(HN^{13}C (1$–$0))$ / $I(HC^{15}N (1$–$0)))$ for models using the second density profile ($\gamma = 1$) and with different sizes of ionized cavity: 0.015 pc (brown and triangle markers), 0.05 pc (black and circle markers) and 0.10 pc (orange and diamond markers). The HII region models are shown on the left panel and the HHMC models on the right panel. The size of the markers correspond to the range value of the peak intensity in Kelvin of NH_3.

Initial abundances

Figure A.149: Abundances of NH_3 in function of time (x-axis) and visual extinction (y-axis) for HII region with different initial abundances: *ini1* (left panel) and *ini2* (right). The solid black lines appearing on the figures represent the contours for the temperature: 20, 30, 100 and 150 K and the dashed black lines represent some contours for the radiation field intensity: 10^{-1} and 10^3 Draine unit.

Figure A.150: Time evolution of integrated intensities for NH$_3$ (5(5,1)–5(5,0)) (left panel) for models with different initial abundances: *ini1* (black) and *ini2* (grey). The solid lines represent the HII region models and the dashed lines the HHMC models.

Figure A.151: Time evolution of the integrated intensity ratio $(I(NH_3 (5(5,1)–5(5,0)))) / I(HC^{15}N (1–0)))$ in function of the integrated intensity ratio $(I(HN^{13}C (1–0)) / I(HC^{15}N (1–0)))$ for models with different initial abundances: *ini1* (black line and circle markers) and *ini2* (grey line and triangle markers). The HII region models are shown on the left panel and the HHMC models on the right panel. The size of the markers corresponds to the range value of the peak intensity in Kelvin of NH$_3$.

Effect of the envelope
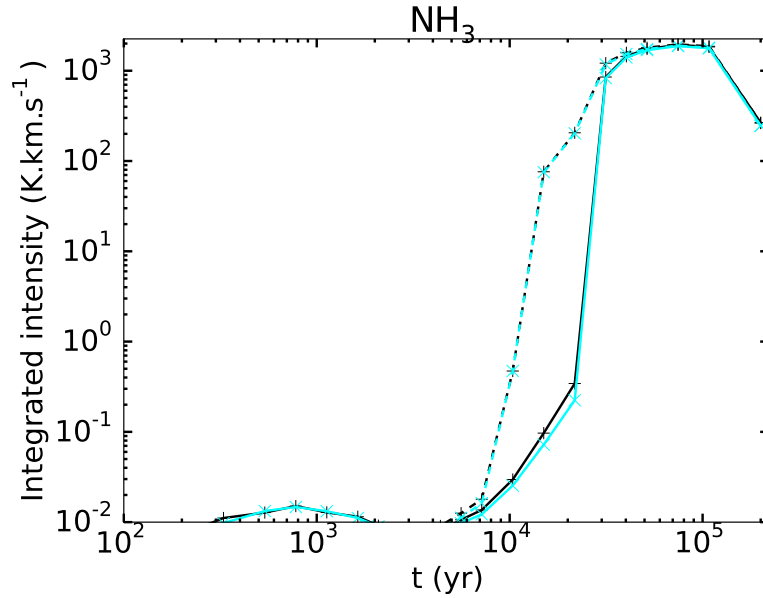
Figure A.152: Time evolution of integrated intensities for NH_3 (5(5,1)–5(5,0)) for models with different cut-off density: 10^1 cm^{-3} (black) and 10^6 cm^{-3} (light blue). The solid lines represent the HII region models and the dashed lines the HHMC models.

Figure A.153: Time evolution of the integrated intensity ratio ($I(NH_3$ (5(5,1)–5(5,0))) / $I(HC^{15}N$ (1–0))) in function of the integrated intensity ratio ($I(HN^{13}C$ (1–0)) / $I(HC^{15}N$ (1–0))) for models with different cut-off density: 10^1 cm^{-3} (black line and circle markers) and 10^6 cm^{-3} (light blue line and triangle markers). The HII region models are shown on the left panel and the HHMC models on the right panel. The size of the markers corresponds to the range value of the peak intensity in Kelvin of NH_3.

A.9 N$_2$H$^+$

HMC vs HHMC model
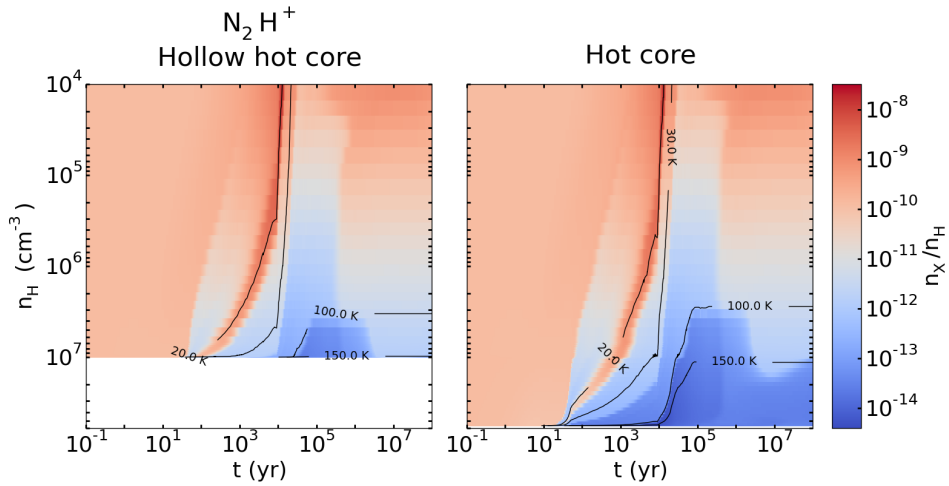
Figure A.154: Abundance of N$_2$H$^+$ in function of time (x-axis) and density (y-axis) for the HHMC (left) and HMC (right) models.
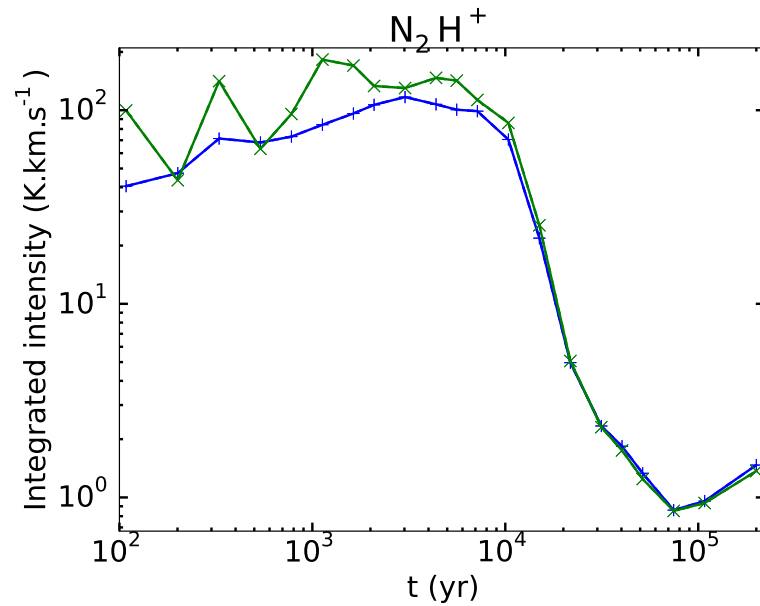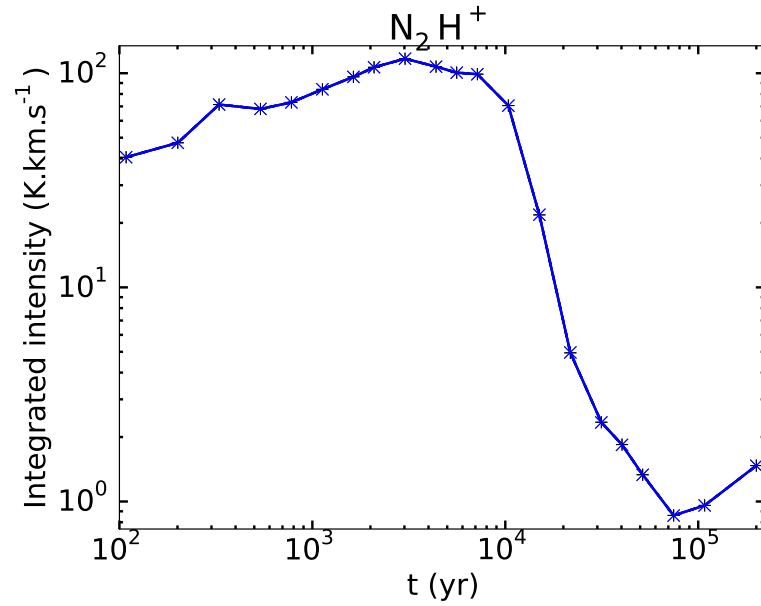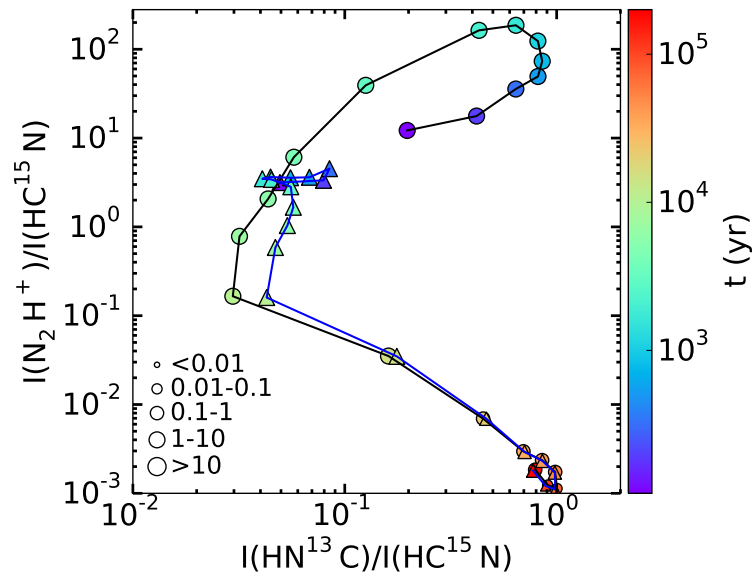

Figure A.155: Time evolution of integrated intensities for N$_2$H$^+$ (1–0). The blue lines represent the HHMC model and the green one represents the HMC model.
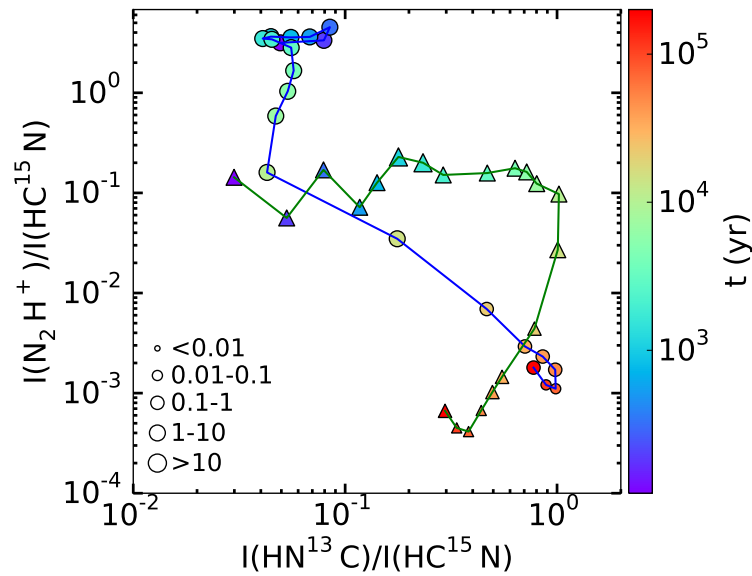
Figure A.156: Time evolution of the integrated intensity ratio $(I(N_2H^+ (1{-}0)) / I(HC^{15}N (1{-}0)))$ in function of the integrated intensity ratio $(I(HN^{13}C (1{-}0)) / I(HC^{15}N (1{-}0)))$ for the HHMC (blue line and circle markers) and HMC (green line and triangle markers) models. The size of the markers corresponds to the range value of the peak intensity in Kelvin of N_2H^+.

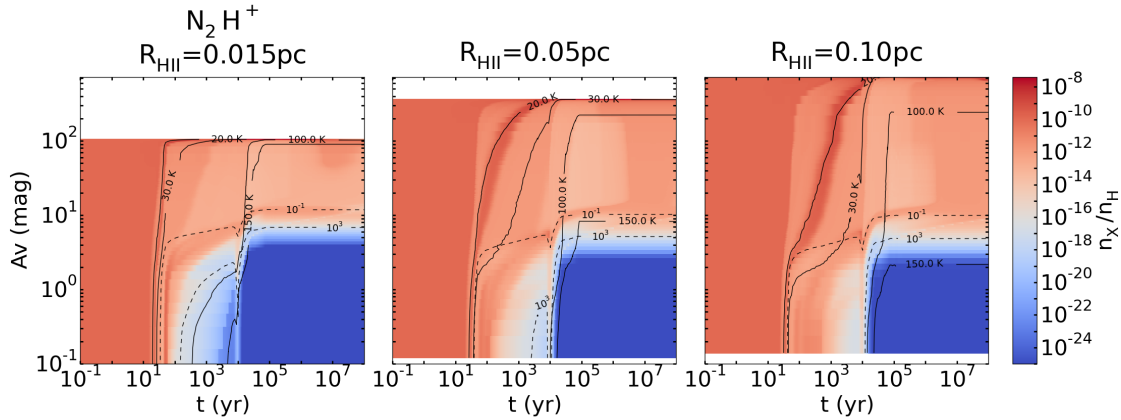## H$_{\mathrm{II}}$ region vs HHMC model
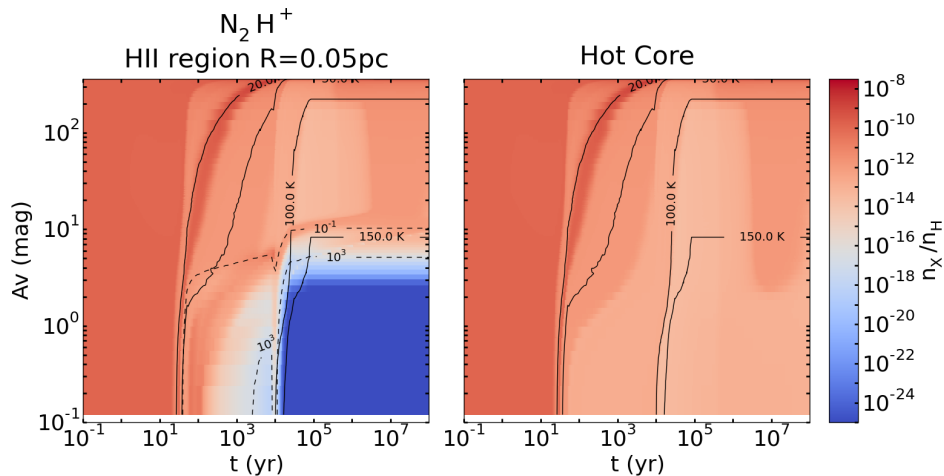
Figure A.157: Abundances of N_2H^+ in function of time (x-axis) and visual extinction (y-axis) for the HII region (left panel) and HHMC (right) models. The solid black lines represent the contours for the temperature: 20, 30, 100 and 150 K and the dashed black lines represent some contours for the radiation field intensity: 10^{-1} and 10^3 Draine unit.
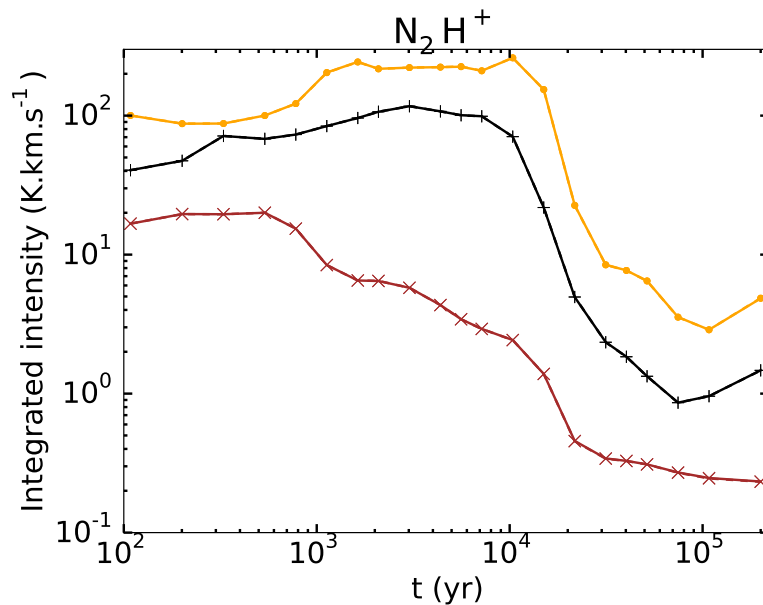
Figure A.158: Time evolution of integrated intensities for N$_2$H$^+$ (1–0). The black line represents the HII region model and the blue lines represent the HHMC model.
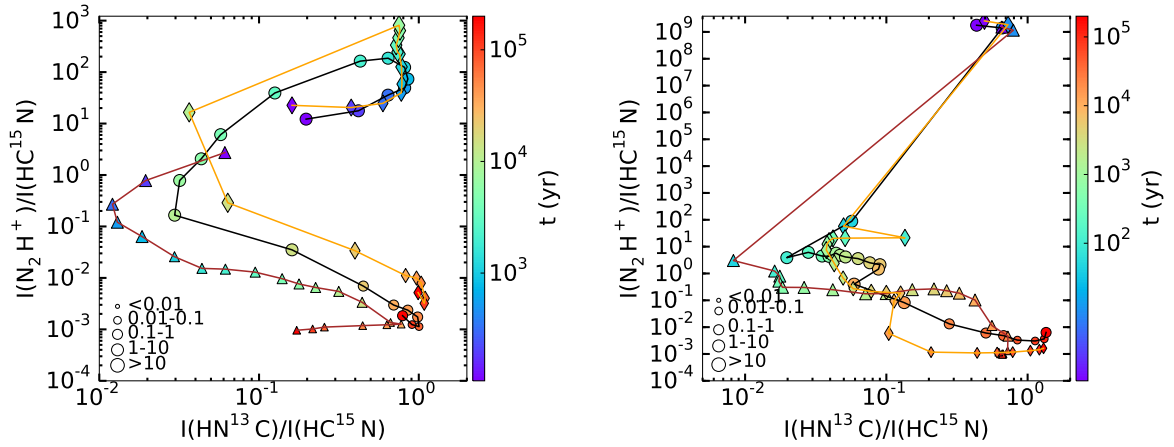

Figure A.159: Time evolution of the integrated intensity ratio (I(N$_2$H$^+$ (1–0)) / I(HC^{15}N (1–0))) in function of the integrated intensity ratio (I(HN^{13}C (1–0)) / I(HC^{15}N (1–0))) for the HII region (black line and circle markers) and HHMC (blue line and triangle markers) models. The size of the markers corresponds to the range value of the peak intensity in Kelvin of N$_2$H$^+$.

H II region size

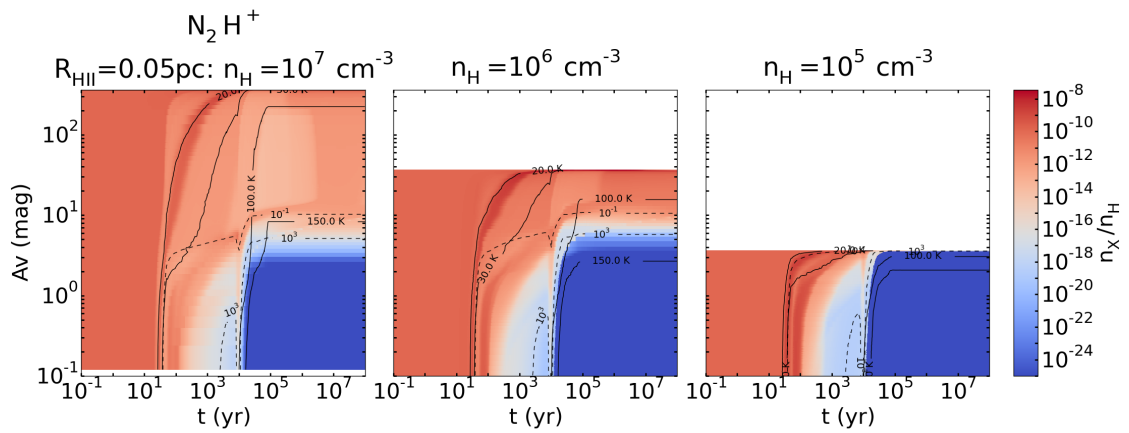
Figure A.160: Abundances of N_2H^+ in function of time (x-axis) and visual extinction (y-axis) for HII region models with different sizes: 0.015 pc (left panels), 0.05 pc (middle) and 0.10 pc (right). The solid black lines appearing on the figures represent the contours for the temperature: 20, 30, 100 and 150 K and the dashed black lines represent some contours for the radiation field intensity: 10^{-1} and 10^3 Draine unit.

Figure A.161: Time evolution of integrated intensities for N_2H^+ (1–0) for models with different sizes of ionized cavity: 0.015 pc (orange), 0.05 pc (black) and 0.10 pc (brown). The solid lines represent the HII region models and the dashed lines the HHMC models.

Figure A.162: Time evolution of the integrated intensity ratio (I(N$_2$H$^+$ (1–0)) / I(HC^{15}N (1–0))) in function of the integrated intensity ratio (I(HN^{13}C (1–0)) / I(HC^{15}N (1–0))) for models with different sizes of ionized cavity: 0.015 pc (brown line and triangle markers), 0.05 pc (black line and circle markers) and 0.10 pc (orange line and diamond markers). The HII region models are shown on the left panel and the HHMC models on the right panel. The size of the markers corresponds to the range value of the peak intensity in Kelvin of N$_2$H$^+$.

Density at the ionization front

Figure A.163: Abundances of N$_2$H$^+$ in function of time (x-axis) and visual extinction (y-axis) for HII region models with different densities at the ionization front: 10^7 cm^{-3} (left), 10^6 cm^{-3} (middle) and 10^5 cm^{-3} (right). The solid black lines appearing on the figures represent the contours for the temperature: 20, 30, 100 and 150 K and the dashed black lines represent some contours for the radiation field intensity: 10^{-1} and 10^3 Draine unit.
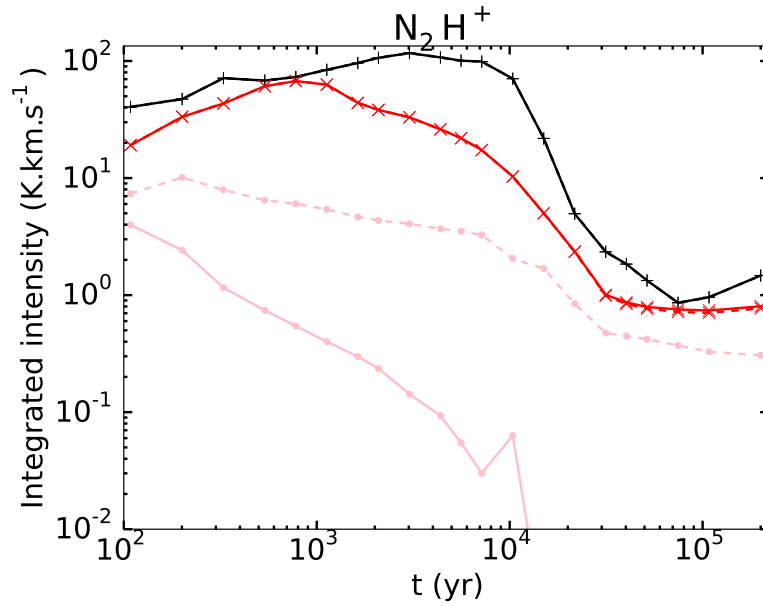
Figure A.164: Time evolution of integrated intensities for N_2H^+ (1–0) for models with different densities at the ionization front: 10^7 cm^{-3} (black), 10^6 cm^{-3} (red) and 10^5 cm^{-3} (pink). The solid lines represent the HII region models and the dashed lines the HHMC models.
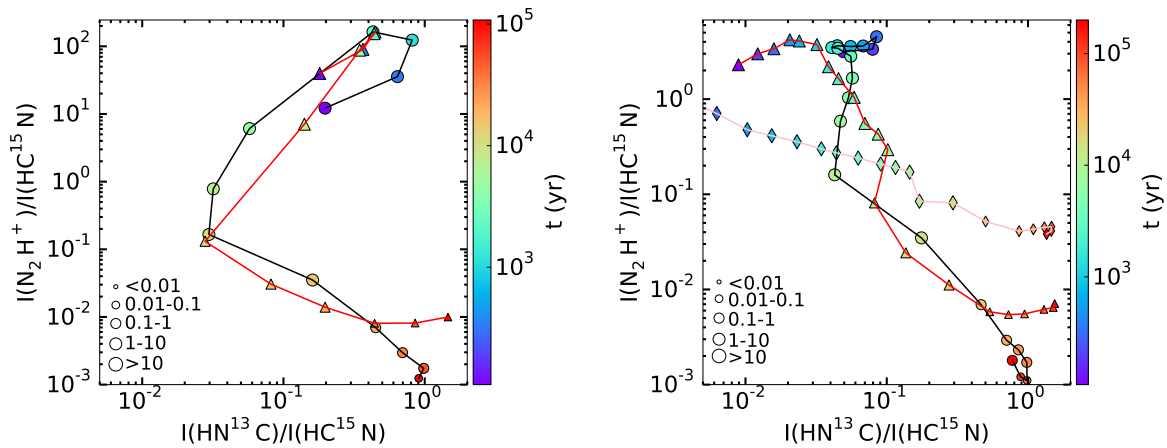

Figure A.165: Time evolution of the integrated intensity ratio ($I(N_2H^+$ (1–0)) / $I(HC^{15}N$ (1–0))) in function of the integrated intensity ratio ($I(HN^{13}C$ (1–0)) / $I(HC^{15}N$ (1–0))) for models with different density at the ionization front: 10^7 cm^{-3} (black line and circle markers), 10^6 cm^{-3} (red line and triangle markers) and 10^5 cm^{-3} (pink line and diamond markers). The HII region models are shown on the left panel and the HHMC models on the right panel. The size of the markers corresponds to the range value of the peak intensity in Kelvin of N_2H^+.
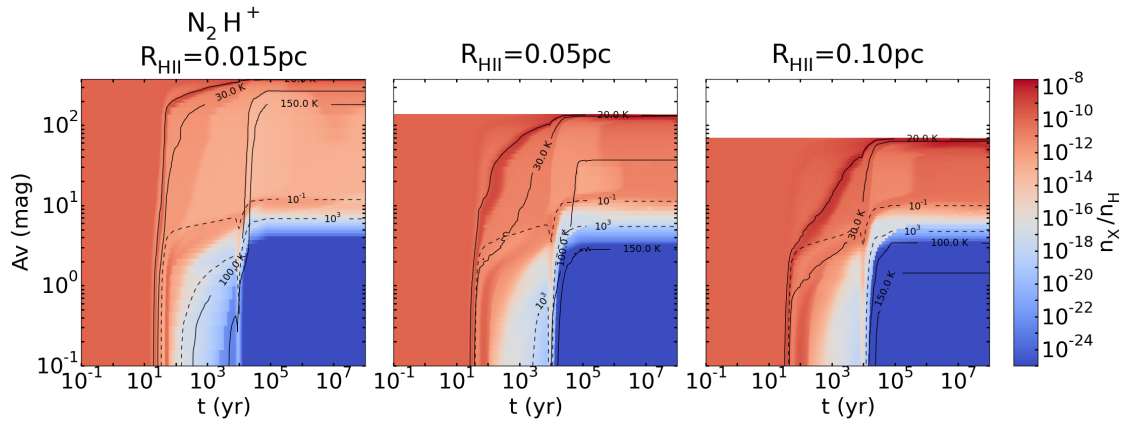
Plummer exponent

Figure A.166: Abundances of N$_2$H$^+$ in function of time (x-axis) and visual extinction (y-axis) for HII region models using for the second density profile ($\gamma = 1$) and with different sizes of ionized cavity: 0.015 pc (left panel), 0.05 pc (middle) and 0.10 pc (right). The solid black lines appearing on the figures represent the contours for the temperature: 20, 30, 100 and 150 K and the dashed black lines represent some contours for the radiation field intensity: 10^{-1} and 10^3 Draine unit.
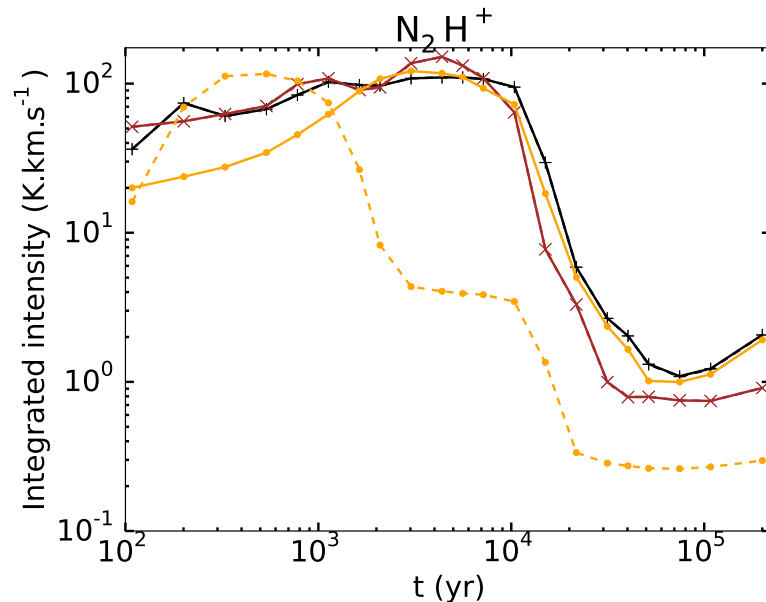
Figure A.167: Time evolution of integrated intensities for N$_2$H$^+$ (1–0) (left panel) for models using the second density profile ($\gamma = 1$) and with different sizes of ionized cavity: 0.015 pc (brown), 0.05 pc (black) and 0.10 pc (orange). The solid lines represent the HII region models and the dashed lines the HHMC models.
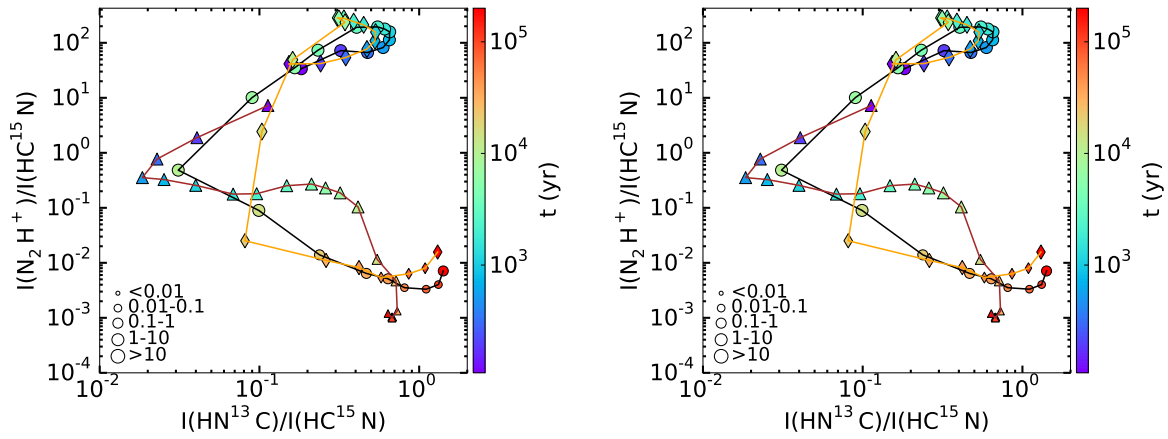
Figure A.168: Time evolution of the integrated intensity ratio $\left(I(N_2H^+(1\text{–}0)) \,/\, I(HC^{15}N(1\text{–}0))\right)$ in function of the integrated intensity ratio $\left(I(HN^{13}C(1\text{–}0)) \,/\, I(HC^{15}N(1\text{–}0))\right)$ for models using the second density profile ($\gamma = 1$) and with different sizes of ionized cavity: 0.015 pc (brown and triangle markers), 0.05 pc (black and circle markers) and 0.10 pc (orange and diamond markers). The HII region models are shown on the left panel and the HHMC models on the right panel. The size of the markers correspond to the range value of the peak intensity in Kelvin of N_2H^+.
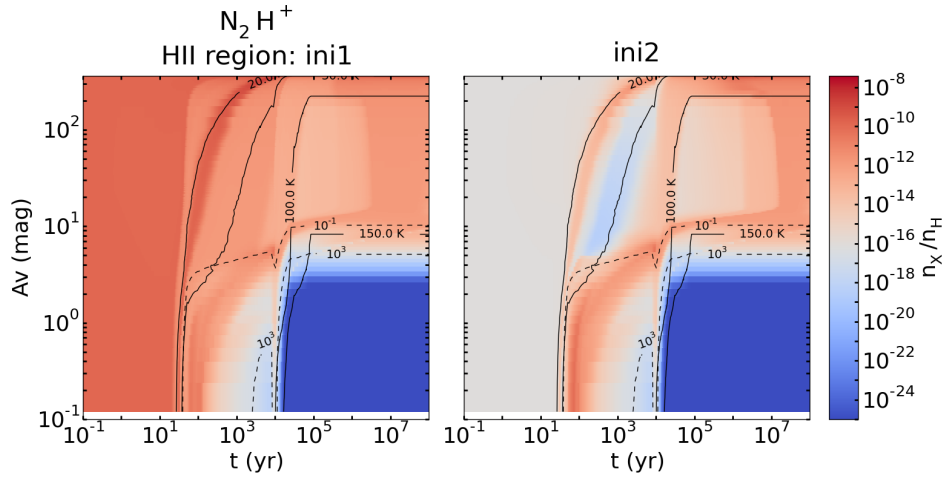
Initial abundances

Figure A.169: Abundances of N_2H^+ in function of time (x-axis) and visual extinction (y-axis) for HII region with different initial abundances: *ini1* (left panel) and *ini2* (right). The solid black lines appearing on the figures represent the contours for the temperature: 20, 30, 100 and 150 K and the dashed black lines represent some contours for the radiation field intensity: 10^{-1} and 10^3 Draine unit.
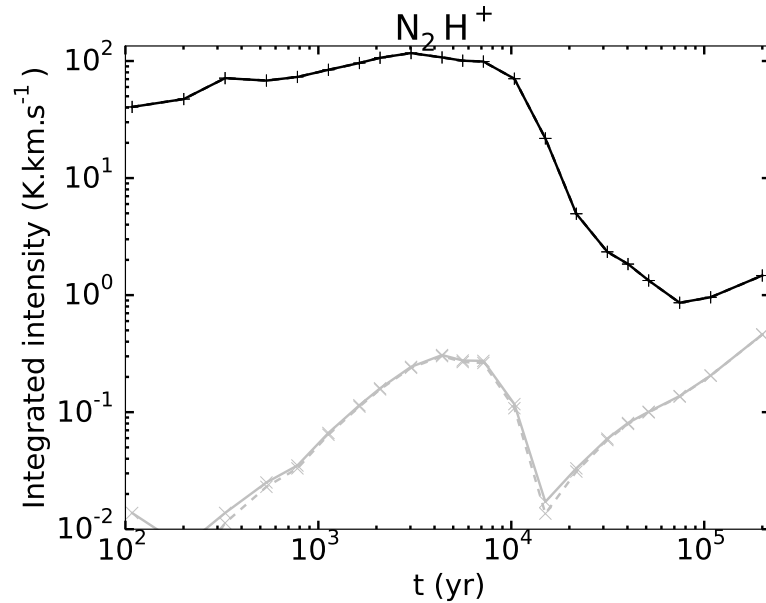
Figure A.170: Time evolution of integrated intensities for N_2H^+ (1–0) (left panel) for models with different initial abundances: *ini1* (black) and *ini2* (grey). The solid lines represent the HII region models and the dashed lines the HHMC models.
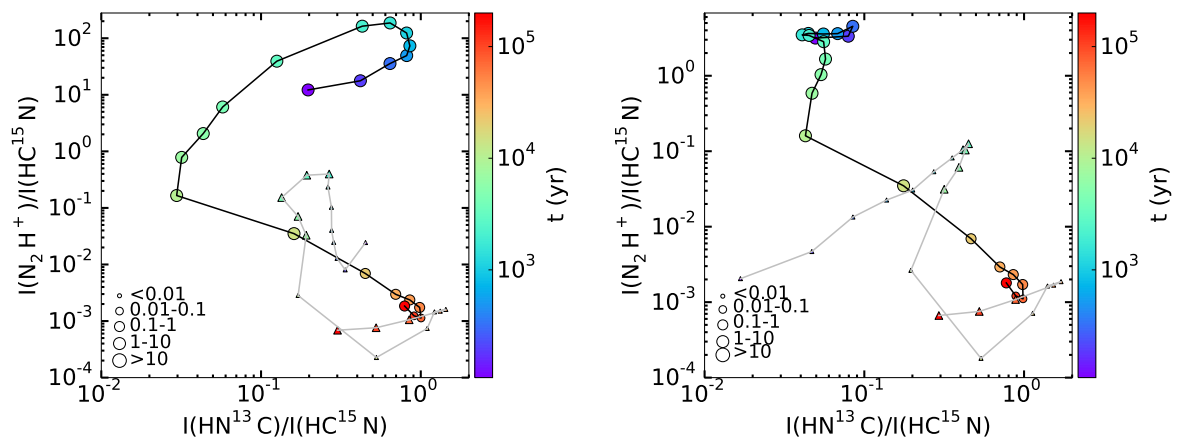

Figure A.171: Time evolution of the integrated intensity ratio ($I(N_2H^+ (1\text{–}0))$ / $I(HC^{15}N (1\text{–}0))$) in function of the integrated intensity ratio ($I(HN^{13}C (1\text{–}0))$ / $I(HC^{15}N (1\text{–}0))$) for models with different initial abundances: *ini1* (black line and circle markers) and *ini2* (grey line and triangle markers). The HII region models are shown on the left panel and the HHMC models on the right panel. The size of the markers corresponds to the range value of the peak intensity in Kelvin of N_2H^+.
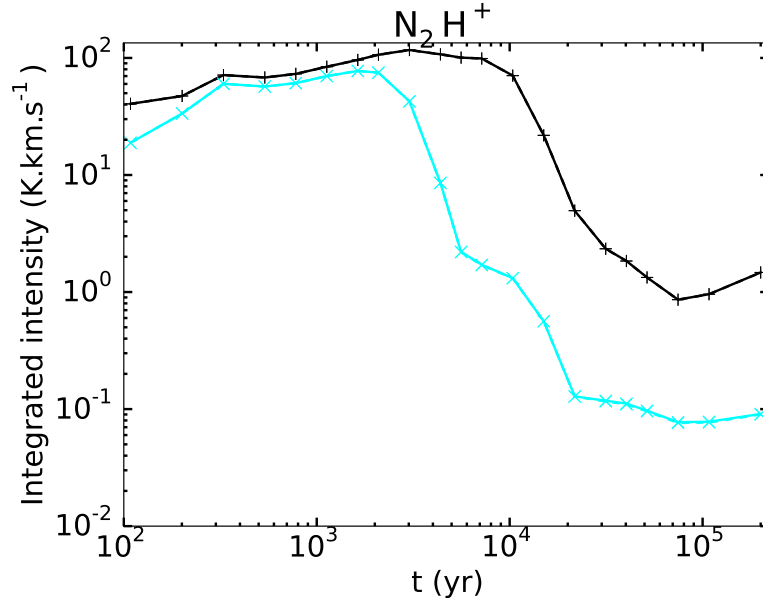
Effect of the envelope

Figure A.172: Time evolution of integrated intensities for N_2H^+ (1–0) for models with different cut-off density: 10^1 cm^{-3} (black) and 10^6 cm^{-3} (light blue). The solid lines represent the HII region models and the dashed lines the HHMC models.
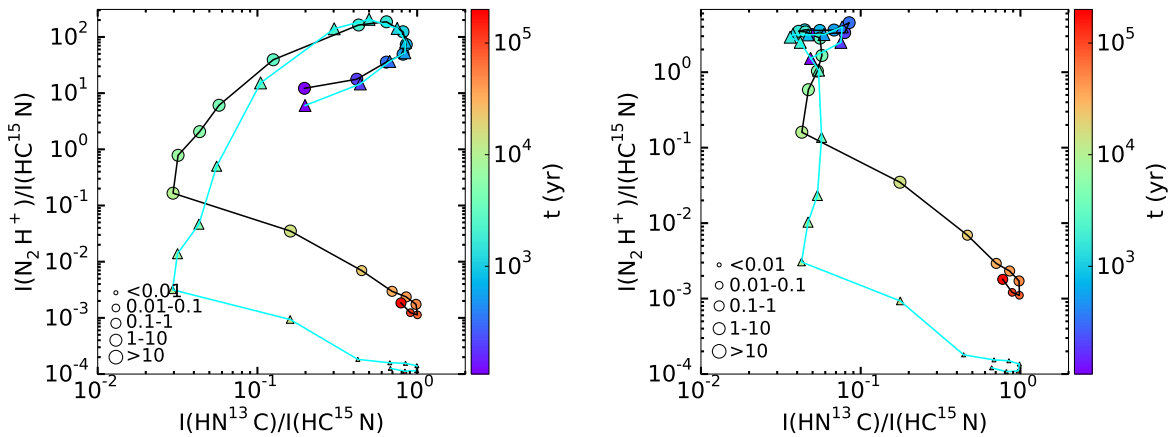

Figure A.173: Time evolution of the integrated intensity ratio ($I(N_2H^+$ (1–0)) / $I(HC^{15}N$ (1–0))) in function of the integrated intensity ratio ($I(HN^{13}C$ (1–0)) / $I(HC^{15}N$ (1–0))) for models with different cut-off density: 10^1 cm^{-3} (black line and circle markers) and 10^6 cm^{-3} (light blue line and triangle markers). The HII region models are shown on the left panel and the HHMC models on the right panel. The size of the markers corresponds to the range value of the peak intensity in Kelvin of N_2H^+.
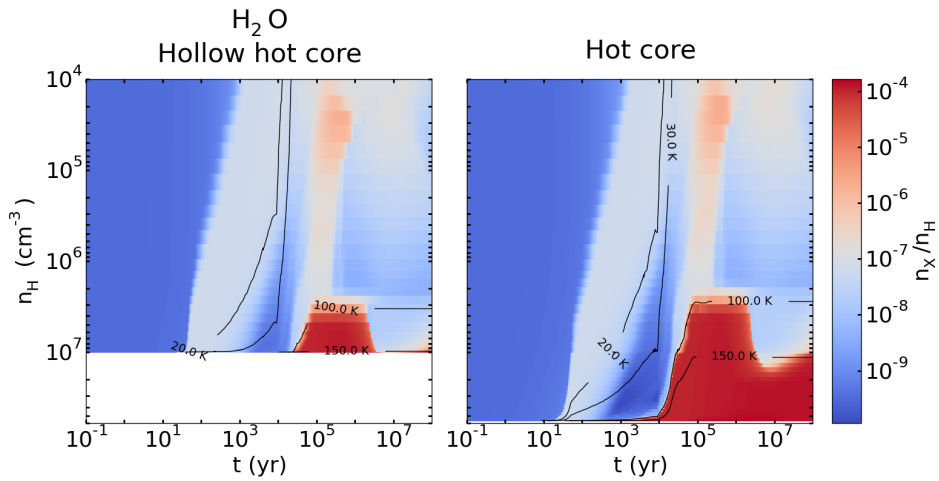
A.10   H$_2^{18}$O

HMC vs HHMC model

Figure A.174: Abundance of H$_2$O in function of time (x-axis) and density (y-axis) for the HHMC (left) and HMC (right) models.
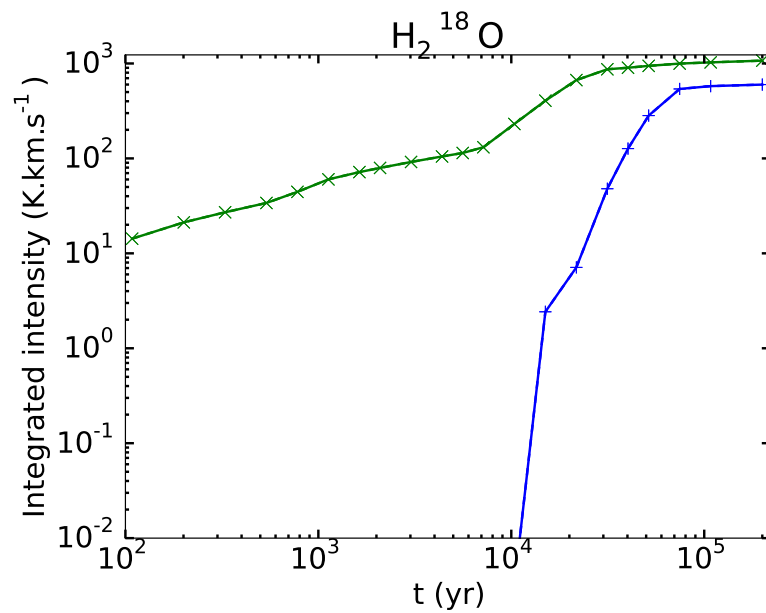

Figure A.175: Time evolution of integrated intensities for H$_2^{18}$O (4(1,4)–3(2,1)). The blue lines represent the HHMC model and the green one represents the HMC model.
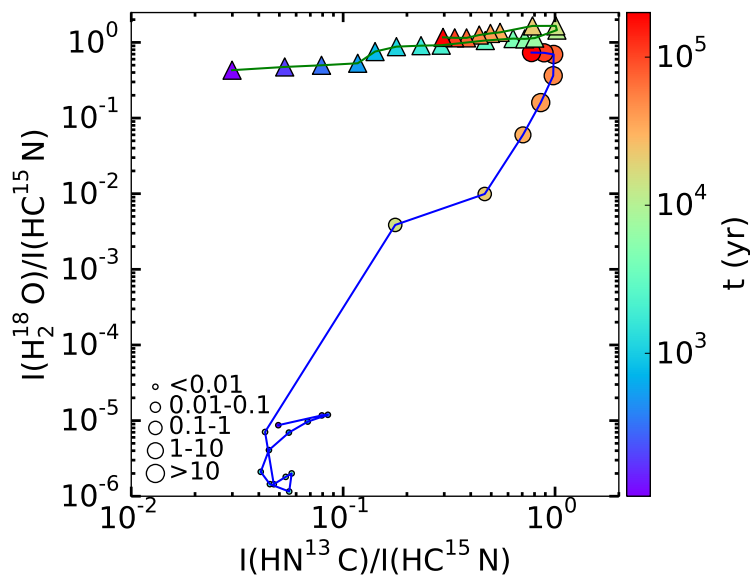
Figure A.176: Time evolution of the integrated intensity ratio $(I(H_2{}^{18}O\,(4(1,4)\text{–}3(2,1)))$ / $I(HC^{15}N\,(1\text{–}0)))$ in function of the integrated intensity ratio $(I(HN^{13}C\,(1\text{–}0))$ / $I(HC^{15}N\,(1\text{–}0)))$ for the HHMC (blue line and circle markers) and HMC (green line and triangle markers) models. The size of the markers corresponds to the range value of the peak intensity in Kelvin of CN.

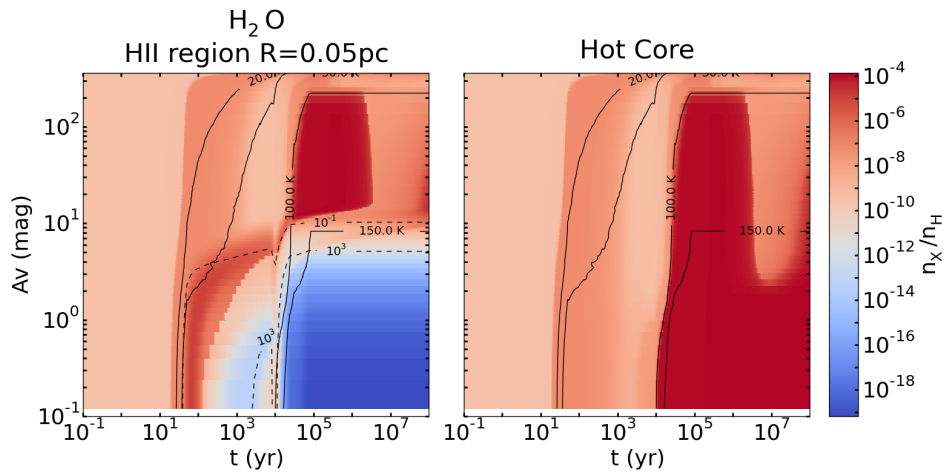## HII region vs HHMC model

Figure A.177: Abundance of H_2O in function of time (x-axis) and density (y-axis) for the HHMC (left) and HMC (right) models.
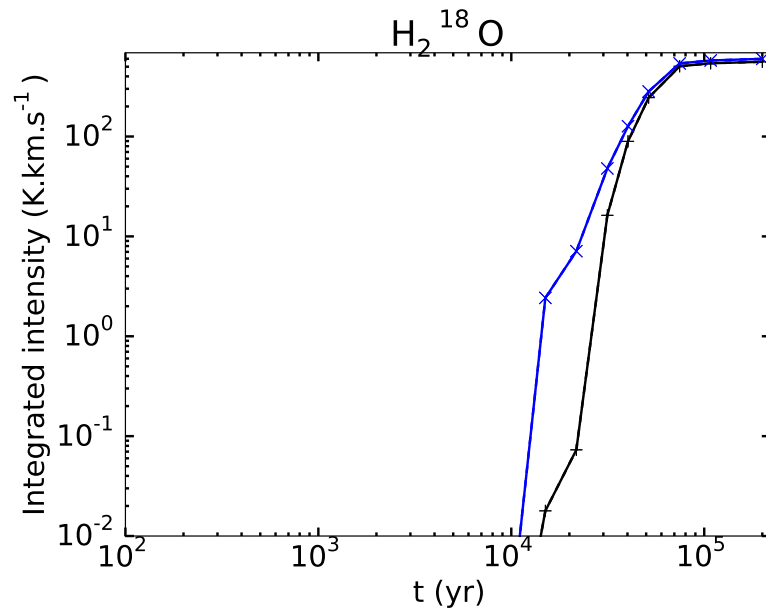
Figure A.178: Time evolution of integrated intensities for $H_2{}^{18}O\,(4(1,4)-3(2,1))$. The black line represents the HII region model and the blue lines represent the HHMC model.
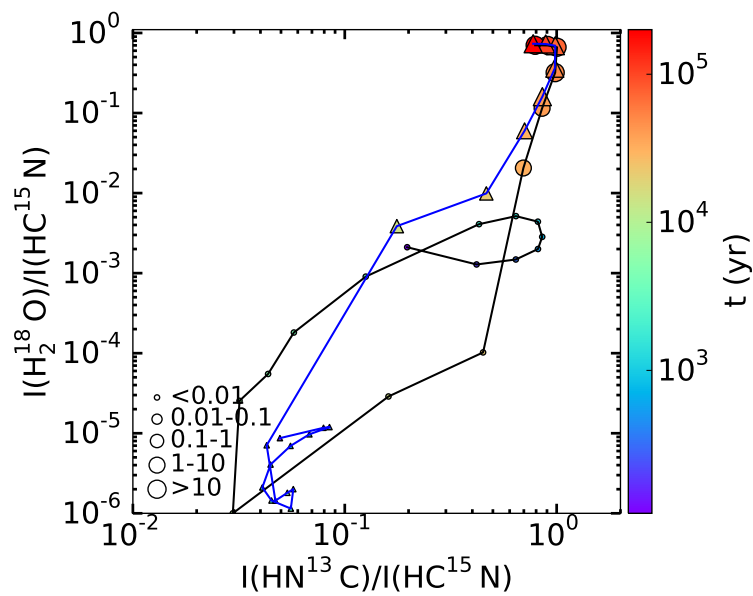
Figure A.179:   Time evolution of the integrated intensity ratio $(I(H_2{}^{18}O\,(4(1,4)-3(2,1)))$ / $I(HC^{15}N\,(1-0)))$ in function of the integrated intensity ratio $(I(HN^{13}C\,(1-0))$ / $I(HC^{15}N\,(1-0)))$ for the HII region (black line and circle markers) and HHMC (blue line and triangle markers) models. The size of the markers corresponds to the range value of the peak intensity in Kelvin of $H_2{}^{18}O$.

HII region size
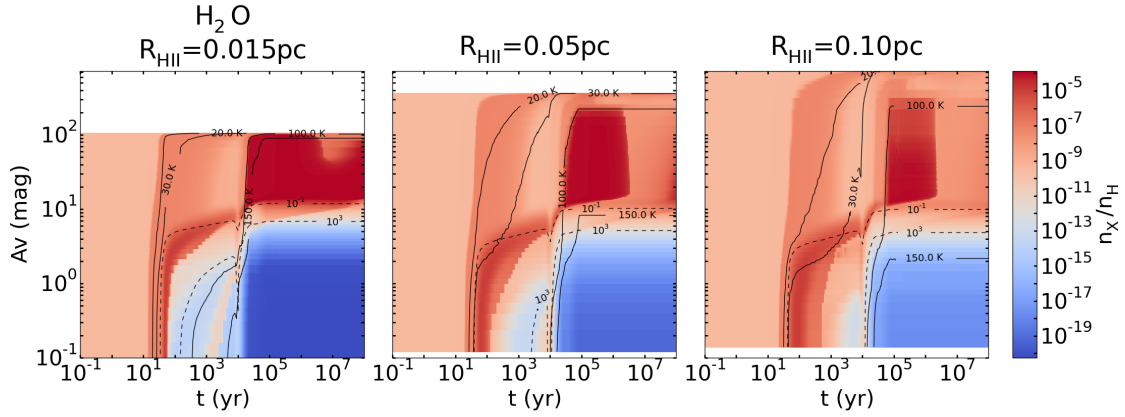
Figure A.180: Abundances of H_2O in function of time (x-axis) and visual extinction (y-axis) for HII region models with different sizes: 0.015 pc (left panels), 0.05 pc (middle) and 0.10 pc (right). The solid black lines appearing on the figures represent the contours for the temperature: 20, 30, 100 and 150 K and the dashed black lines represent some contours for the radiation field intensity: 10^{-1} and 10^3 Draine unit.

Figure A.181: Time evolution of integrated intensities for $H_2^{18}O\,(4(1,4)-3(2,1))$ for models with different sizes of ionized cavity: 0.015 pc (orange), 0.05 pc (black) and 0.10 pc (brown). The solid lines represent the HII region models and the dashed lines the HHMC models.

Figure A.182: Time evolution of the integrated intensity ratio $(I(H_2^{18}O\,(4(1,4)$–$3(2,1)))$ / $I(HC^{15}N\,(1$–$0)))$ in function of the integrated intensity ratio $(I(HN^{13}C\,(1$–$0))$ / $I(HC^{15}N\,(1$–$0)))$ for models with different sizes of ionized cavity: 0.015 pc (brown line and triangle markers), 0.05 pc (black line and circle markers) and 0.10 pc (orange line and diamond markers). The HII region models are shown on the left panel and the HHMC models on the right panel. The size of the markers corresponds to the range value of the peak intensity in Kelvin of H$_2$^{18}O.

Density at the ionization front

Figure A.183: Abundances of H$_2$O in function of time (x-axis) and visual extinction (y-axis) for HII region models with different densities at the ionization front: 10^7 cm^{-3} (left), 10^6 cm^{-3} (middle) and 10^5 cm^{-3} (right). The solid black lines appearing on the figures represent the contours for the temperature: 20, 30, 100 and 150 K and the dashed black lines represent some contours for the radiation field intensity: 10^{-1} and 10^3 Draine unit.
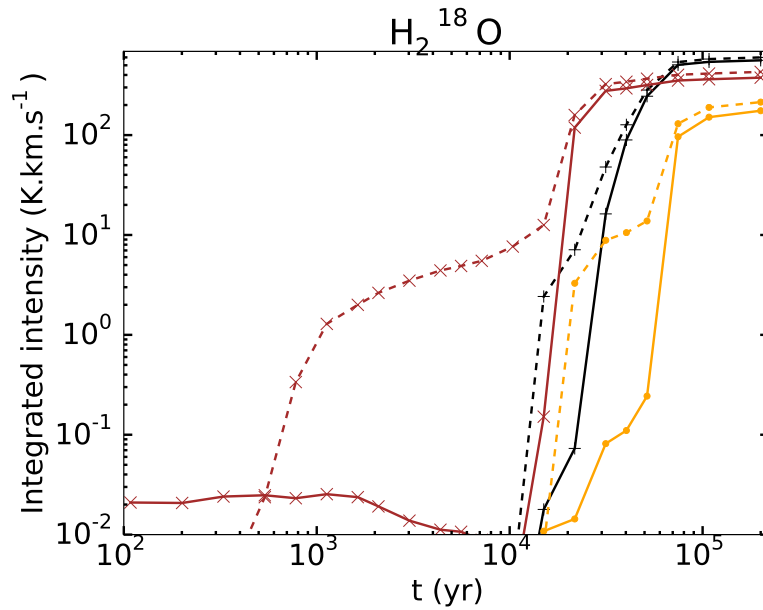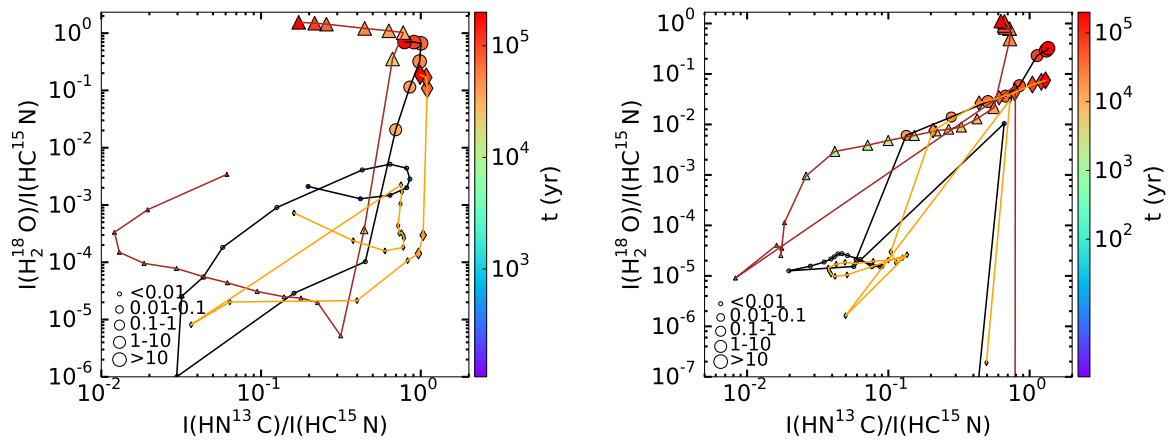
Figure A.184: Time evolution of integrated intensities for $H_2{}^{18}O\,(4(1,4)-3(2,1))$ for models with different densities at the ionization front: 10^7 cm^{-3} (black), 10^6 cm^{-3} (red) and 10^5 cm^{-3} (pink). The solid lines represent the HII region models and the dashed lines the HHMC models.
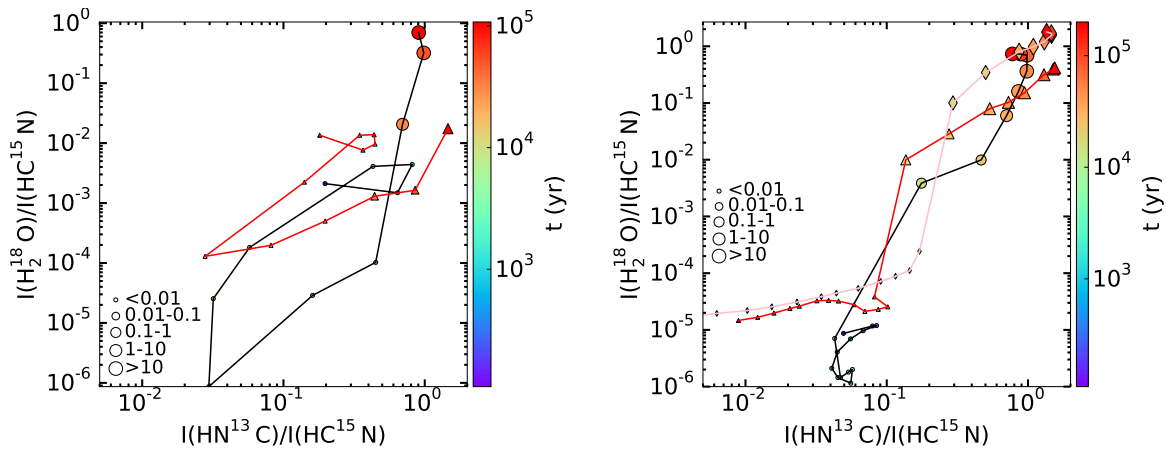
Figure A.185: Time evolution of the integrated intensity ratio $(I(H_2{}^{18}O\,(4(1,4)-3(2,1)))\,/\,I(HC^{15}N\,(1-0)))$ in function of the integrated intensity ratio $(I(HN^{13}C\,(1-0))\,/\,I(HC^{15}N\,(1-0)))$ for models with different density at the ionization front: 10^7 cm^{-3} (black line and circle markers), 10^6 cm^{-3} (red line and triangle markers) and 10^5 cm^{-3} (pink line and diamond markers). The HII region models are shown on the left panel and the HHMC models on the right panel. The size of the markers corresponds to the range value of the peak intensity in Kelvin of $H_2{}^{18}O$.
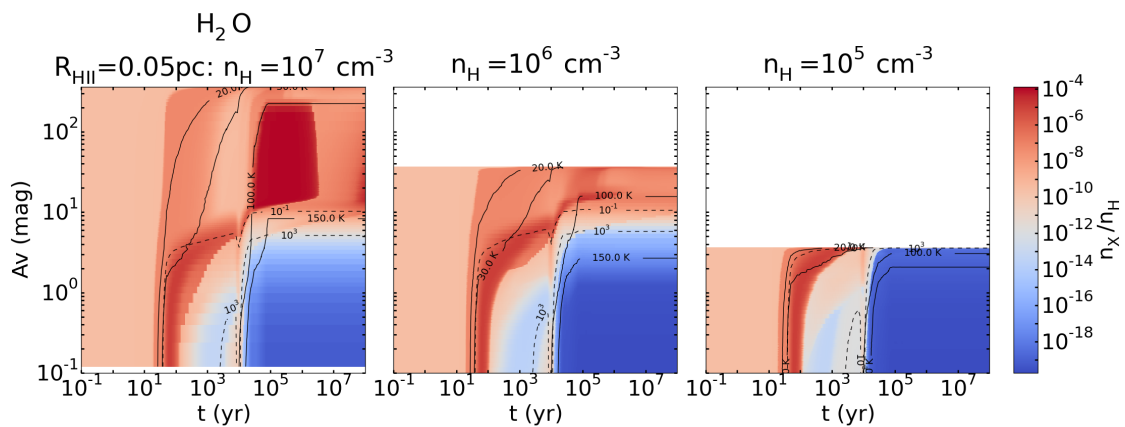
Plummer exponent

Figure A.186: Abundances of H_2O in function of time (x-axis) and visual extinction (y-axis) for HII region models using for the second density profile ($\gamma = 1$) and with different sizes of ionized cavity: 0.015 pc (left panel), 0.05 pc (middle) and 0.10 pc (right). The solid black lines appearing on the figures represent the contours for the temperature: 20, 30, 100 and 150 K and the dashed black lines represent some contours for the radiation field intensity: 10^{-1} and 10^{3} Draine unit.
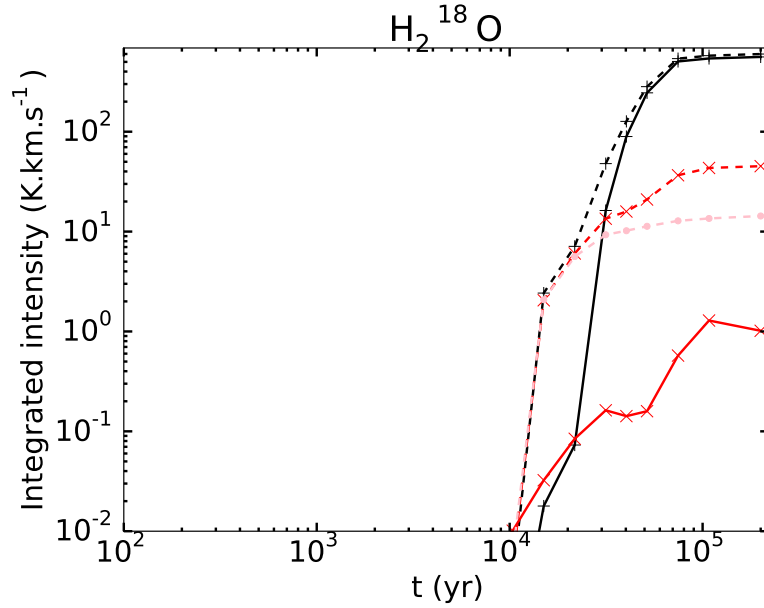

Figure A.187: Time evolution of integrated intensities for $H_2^{18}O$ (4(1,4)–3(2,1)) (left panel) for models using the second density profile ($\gamma = 1$) and with different sizes of ionized cavity: 0.015 pc (brown), 0.05 pc (black) and 0.10 pc (orange). The solid lines represent the HII region models and the dashed lines the HHMC models.
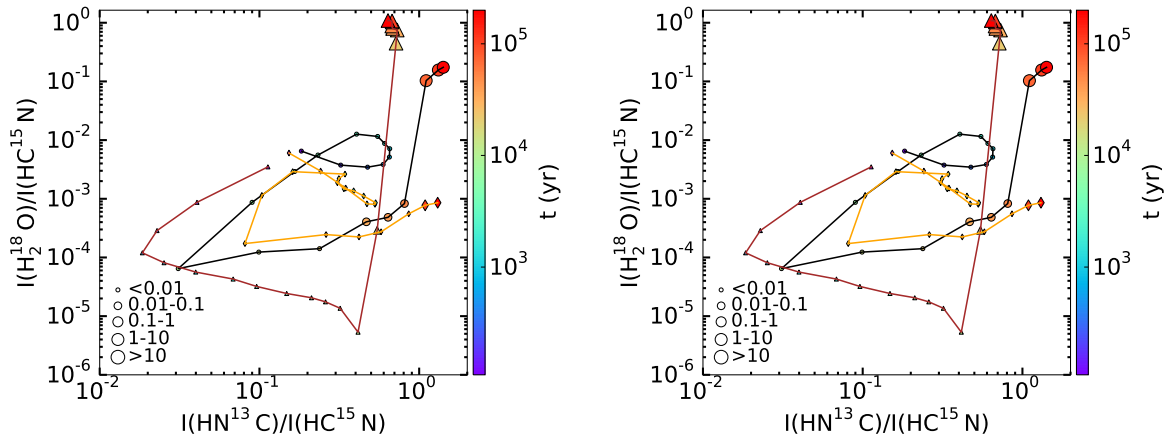
Figure A.188: Time evolution of the integrated intensity ratio $(I(H_2{}^{18}O\,(4(1,4)–3(2,1))))$ / $I(HC^{15}N\,(1–0)))$ in function of the integrated intensity ratio $(I(HN^{13}C\,(1–0))$ / $I(HC^{15}N\,(1–0)))$ for models using the second density profile ($\gamma = 1$) and with different sizes of ionized cavity: 0.015 pc (brown and triangle markers), 0.05 pc (black and circle markers) and 0.10 pc (orange and diamond markers). The HII region models are shown on the left panel and the HHMC models on the right panel. The size of the markers correspond to the range value of the peak intensity in Kelvin of $H_2{}^{18}O$.
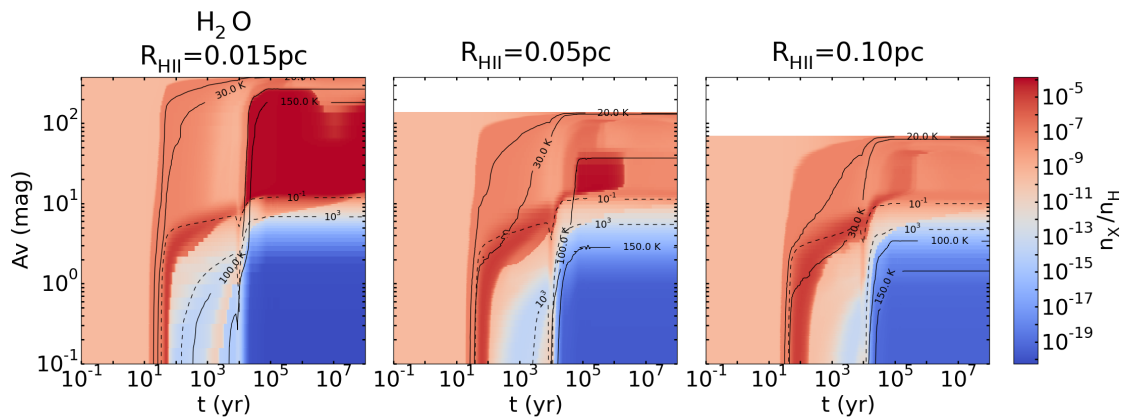
Initial abundances
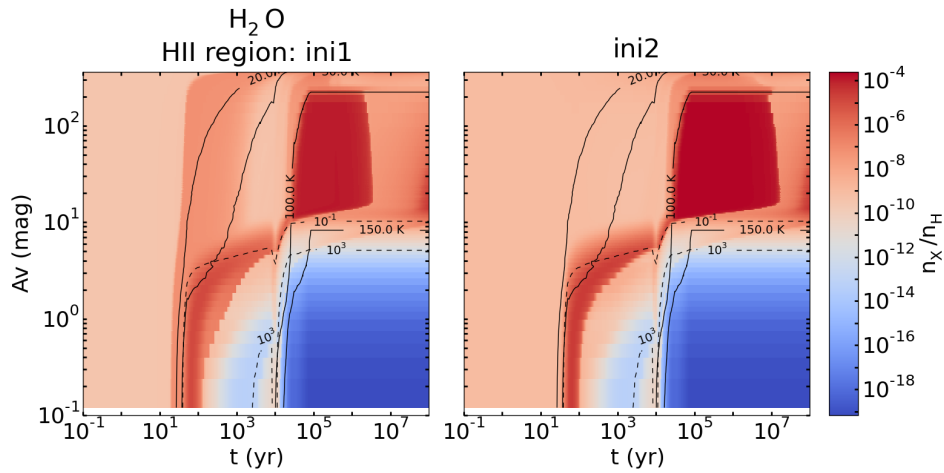
Figure A.189: Abundances of H_2O in function of time (x-axis) and visual extinction (y-axis) for HII region with different initial abundances: *ini1* (left panel) and *ini2* (right). The solid black lines appearing on the figures represent the contours for the temperature: 20, 30, 100 and 150 K and the dashed black lines represent some contours for the radiation field intensity: 10^{-1} and 10^3 Draine unit.
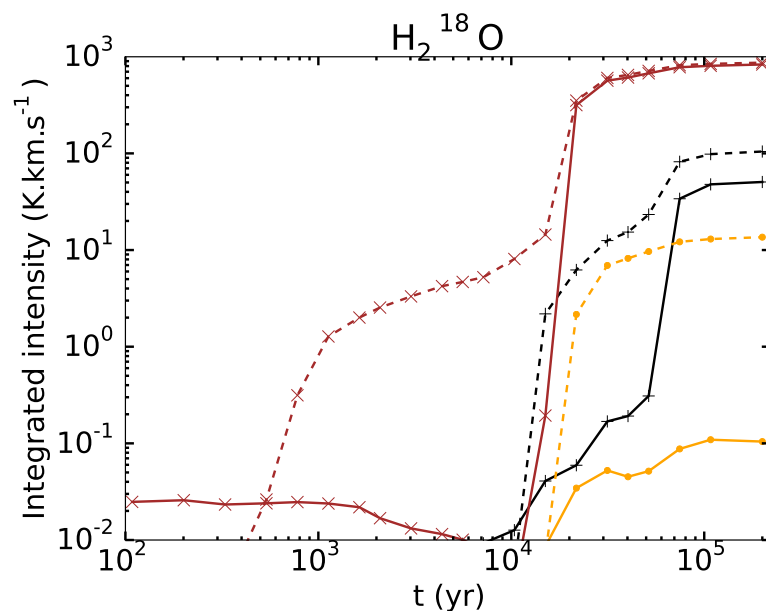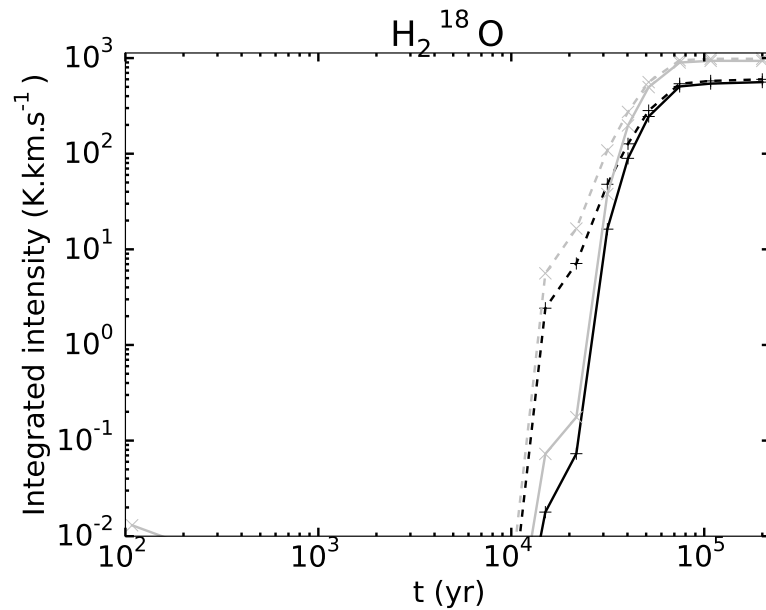
Figure A.190: Time evolution of integrated intensities for H$_2$^{18}O (4(1,4)–3(2,1)) (left panel) for models with different initial abundances: *ini1* (black) and *ini2* (grey). The solid lines represent the HII region models and the dashed lines the HHMC models.
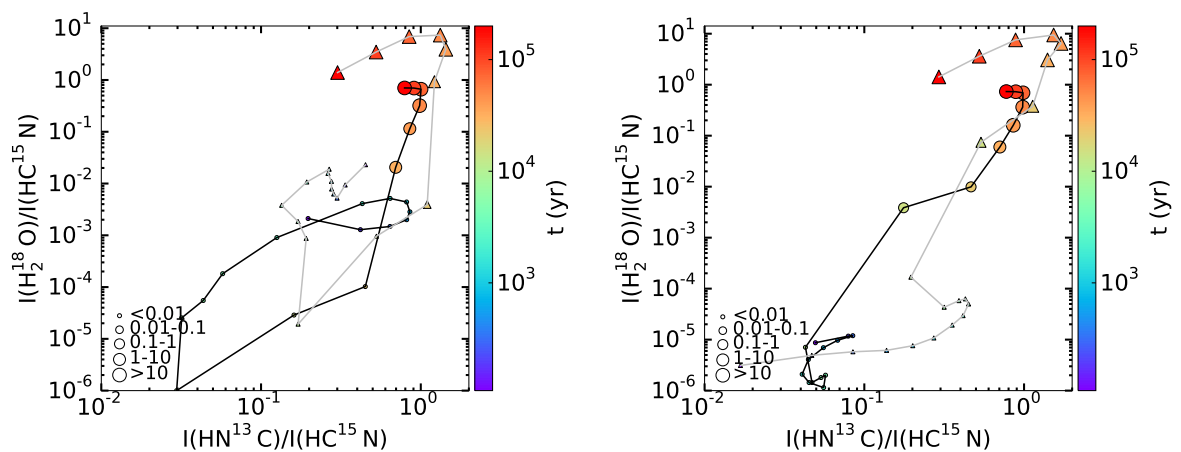
Figure A.191: Time evolution of the integrated intensity ratio (I(H$_2$^{18}O (4(1,4)–3(2,1))) / I(HC^{15}N (1–0))) in function of the integrated intensity ratio (I(HN^{13}C (1–0)) / I(HC^{15}N (1–0))) for models with different initial abundances: *ini1* (black line and circle markers) and *ini2* (grey line and triangle markers). The HII region models are shown on the left panel and the HHMC models on the right panel. The size of the markers corresponds to the range value of the peak intensity in Kelvin of H$_2$^{18}O.

Effect of the envelope
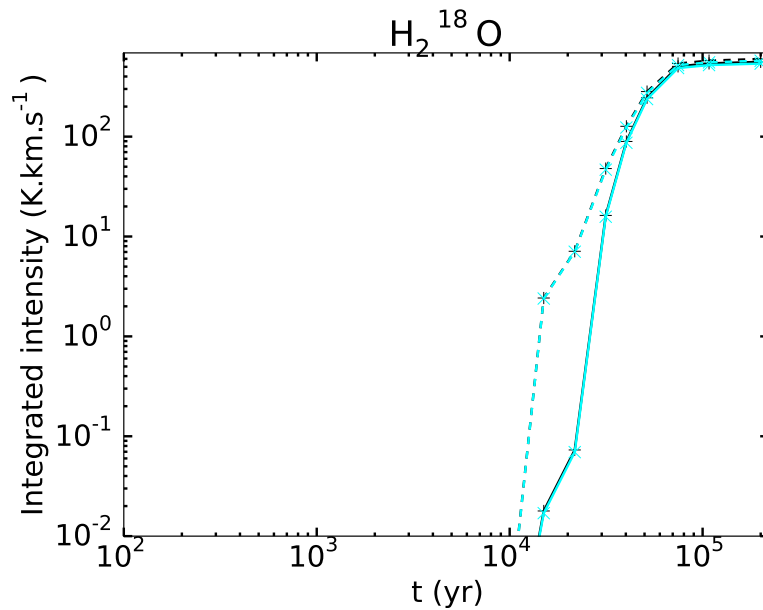
Figure A.192: Time evolution of integrated intensities for $H_2^{18}O\,(4(1,4)–3(2,1))$ for models with different cut-off density: 10^1 cm^{-3} (black) and 10^6 cm^{-3} (light blue). The solid lines represent the HII region models and the dashed lines the HHMC models.
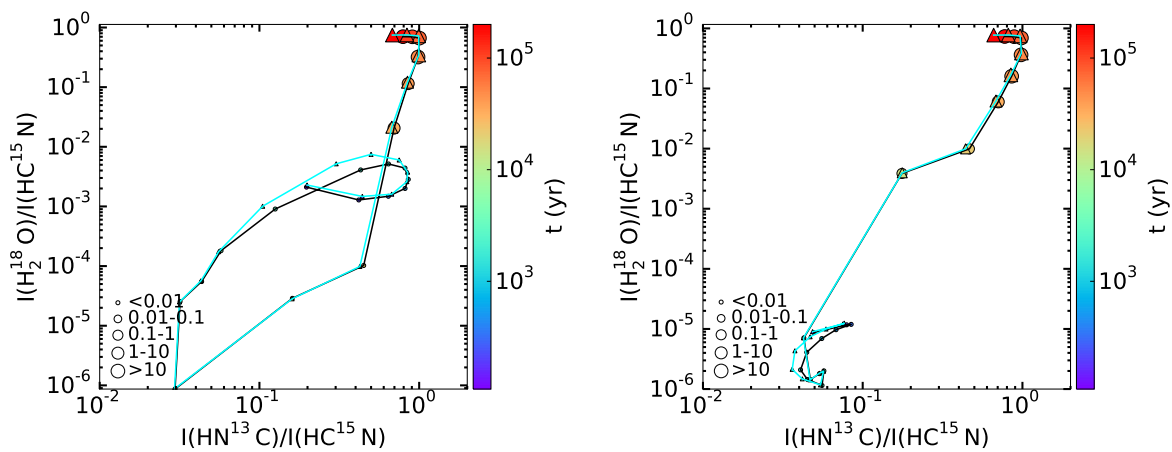
Figure A.193: Time evolution of the integrated intensity ratio $(I(H_2^{18}O\,(4(1,4)–3(2,1)))\ /\ I(HC^{15}N\,(1–0)))$ in function of the integrated intensity ratio $(I(HN^{13}C\,(1–0))\ /\ I(HC^{15}N\,(1–0)))$ for models with different cut-off density: 10^1 cm^{-3} (black line and circle markers) and 10^6 cm^{-3} (light blue line and triangle markers). The HII region models are shown on the left panel and the HHMC models on the right panel. The size of the markers corresponds to the range value of the peak intensity in Kelvin of $H_2^{18}O$.

A.11   C

HMC vs HHMC model
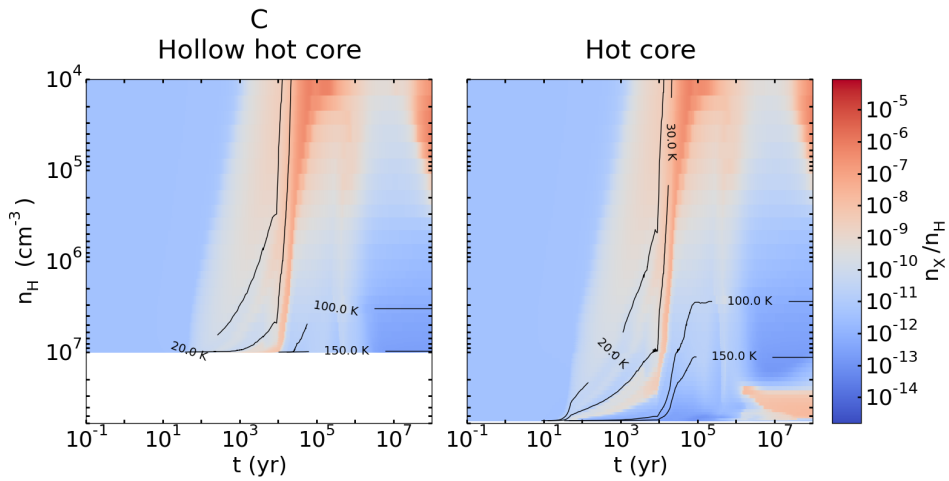
Figure A.194: Abundance of C in function of time (x-axis) and density (y-axis) for the HHMC (left) and HMC (right) models.
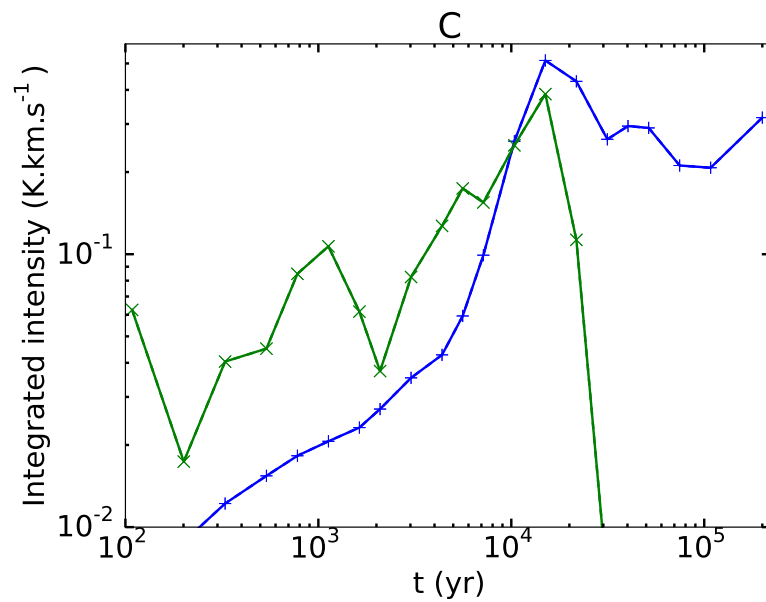
Figure A.195: Time evolution of integrated intensities for $C\left({}^3P_1-{}^3P_0\right)$. The blue lines represent the HHMC model and the green one represents the HMC model.
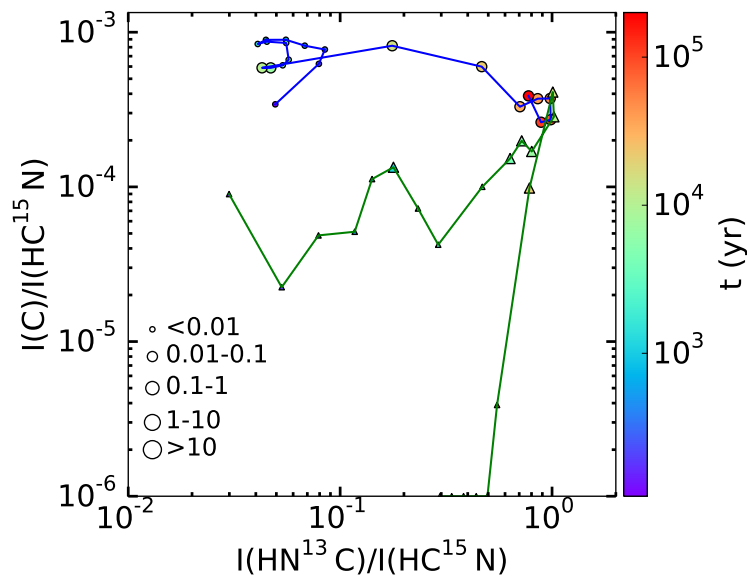
Figure A.196: Time evolution of the integrated intensity ratio $(I(C\,(^3P_1-^3P_0))\,/\,I(HC^{15}N\,(1-0)))$ in function of the integrated intensity ratio $(I(HN^{13}C\,(1-0))\,/\,I(HC^{15}N\,(1-0)))$ for the HHMC (blue line and circle markers) and HMC (green line and triangle markers) models. The size of the markers corresponds to the range value of the peak intensity in Kelvin of C.

H II region vs HHMC model
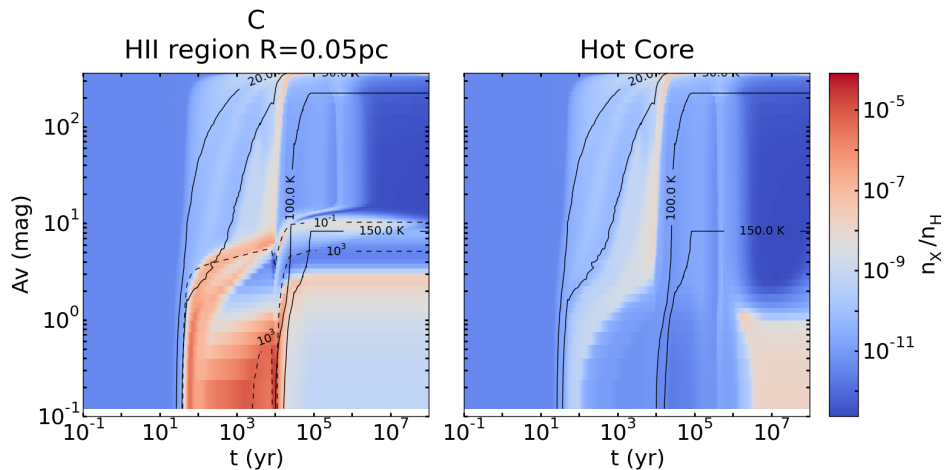
Figure A.197: Abundances of C in function of time (x-axis) and visual extinction (y-axis) for the HII region (left panel) and HHMC (right) models. The solid black lines represent the contours for the temperature: 20, 30, 100 and 150 K and the dashed black lines represent some contours for the radiation field intensity: 10^{-1} and 10^3 Draine unit.

Figure A.198: Time evolution of integrated intensities for $C\,(^3P_1\text{--}^3P_0)$. The black line represents the HII region model and the blue lines represent the HHMC model.

Figure A.199: Time evolution of the integrated intensity ratio $(I(C\,(^3P_1\text{--}^3P_0))\,/\,I(HC^{15}N\,(1\text{--}0)))$ in function of the integrated intensity ratio $(I(HN^{13}C\,(1\text{--}0))\,/\,I(HC^{15}N\,(1\text{--}0)))$ for the HII region (black line and circle markers) and HHMC (blue line and triangle markers) models. The size of the markers corresponds to the range value of the peak intensity in Kelvin of C.

H<small>II</small> **region size**

Figure A.200: Abundances of C in function of time (x-axis) and visual extinction (y-axis) for HII region models with different sizes: 0.015 pc (left panels), 0.05 pc (middle) and 0.10 pc (right). The solid black lines appearing on the figures represent the contours for the temperature: 20, 30, 100 and 150 K and the dashed black lines represent some contours for the radiation field intensity: 10^{-1} and 10^3 Draine unit.

Figure A.201: Time evolution of integrated intensities for C $\left(^3P_1-^3P_0\right)$ for models with different sizes of ionized cavity: 0.015 pc (orange), 0.05 pc (black) and 0.10 pc (brown). The solid lines represent the HII region models and the dashed lines the HHMC models.

Figure A.202: Time evolution of the integrated intensity ratio ($I(C\,(^3P_1-^3P_0))$ / $I(HC^{15}N\,(1–0)))$ in function of the integrated intensity ratio ($I(HN^{13}C\,(1–0))$ / $I(HC^{15}N\,(1–0)))$ for models with different sizes of ionized cavity: 0.015 pc (brown line and triangle markers), 0.05 pc (black line and circle markers) and 0.10 pc (orange line and diamond markers). The HII region models are shown on the left panel and the HHMC models on the right panel. The size of the markers corresponds to the range value of the peak intensity in Kelvin of C.

Density at the ionization front

Figure A.203: Abundances of C in function of time (x-axis) and visual extinction (y-axis) for HII region models with different densities at the ionization front: 10^7 cm^{-3} (left), 10^6 cm^{-3} (middle) and 10^5 cm^{-3} (right). The solid black lines appearing on the figures represent the contours for the temperature: 20, 30, 100 and 150 K and the dashed black lines represent some contours for the radiation field intensity: 10^{-1} and 10^3 Draine unit.
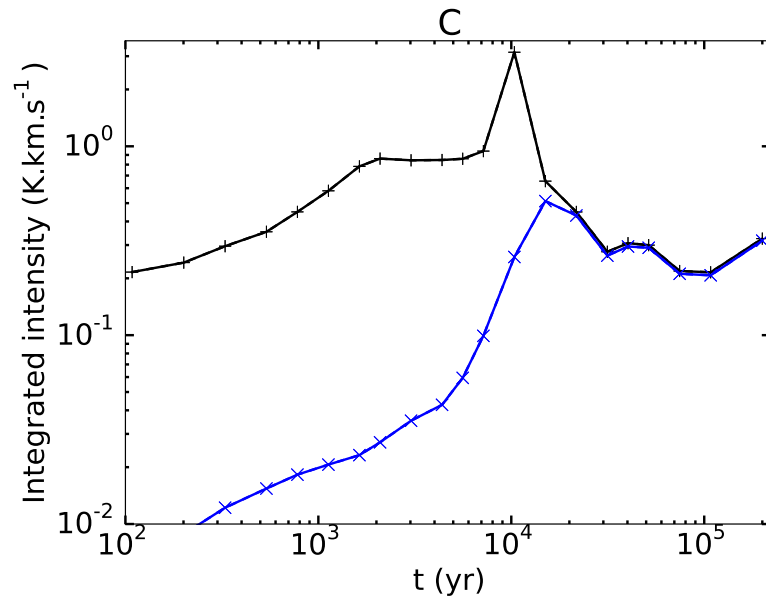
Figure A.204: Time evolution of integrated intensities for $C\left({}^3P_1-{}^3P_0\right)$ for models with different densities at the ionization front: 10^7 cm^{-3} (black), 10^6 cm^{-3} (red) and 10^5 cm^{-3} (pink). The solid lines represent the HII region models and the dashed lines the HHMC models.
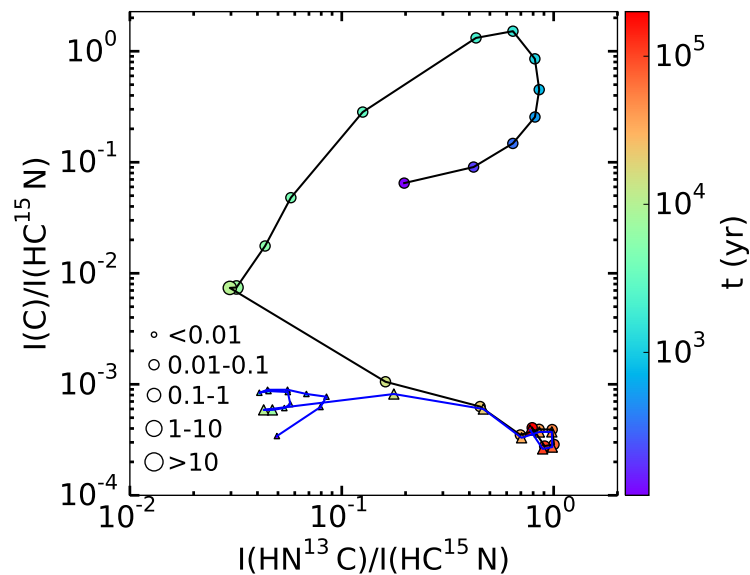

Figure A.205: Time evolution of the integrated intensity ratio $(I(C\left({}^3P_1-{}^3P_0\right)) / I(HC^{15}N\,(1-0)))$ in function of the integrated intensity ratio $(I(HN^{13}C\,(1-0)) / I(HC^{15}N\,(1-0)))$ for models with different density at the ionization front: 10^7 cm^{-3} (black line and circle markers), 10^6 cm^{-3} (red line and triangle markers) and 10^5 cm^{-3} (pink line and diamond markers). The HII region models are shown on the left panel and the HHMC models on the right panel. The size of the markers corresponds to the range value of the peak intensity in Kelvin of C.

Plummer exponent
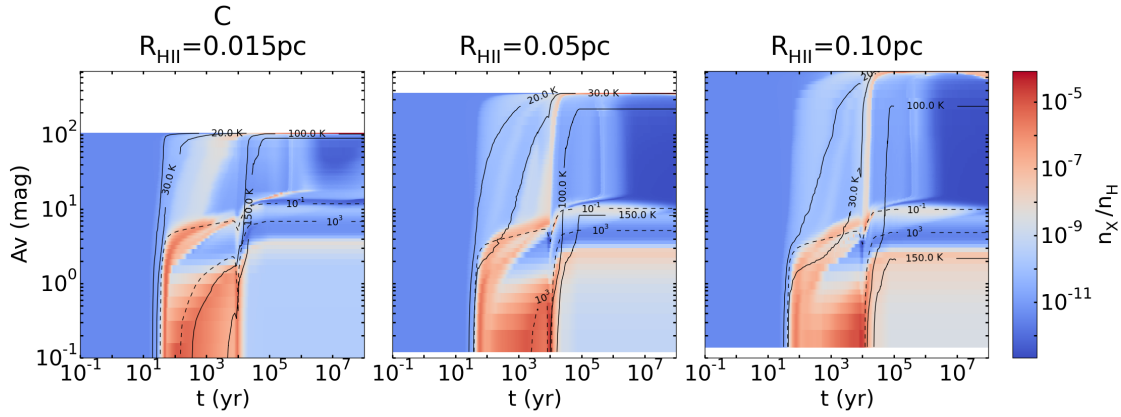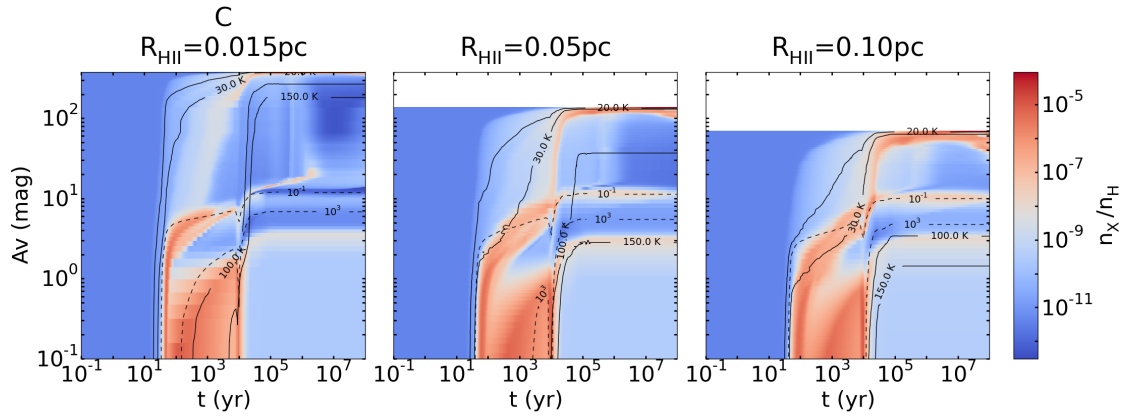

Figure A.206: Abundances of C in function of time (x-axis) and visual extinction (y-axis) for HII region models using for the second density profile ($\gamma = 1$) and with different sizes of ionized cavity: 0.015 pc (left panel), 0.05 pc (middle) and 0.10 pc (right). The solid black lines appearing on the figures represent the contours for the temperature: 20, 30, 100 and 150 K and the dashed black lines represent some contours for the radiation field intensity: 10^{-1} and 10^3 Draine unit.
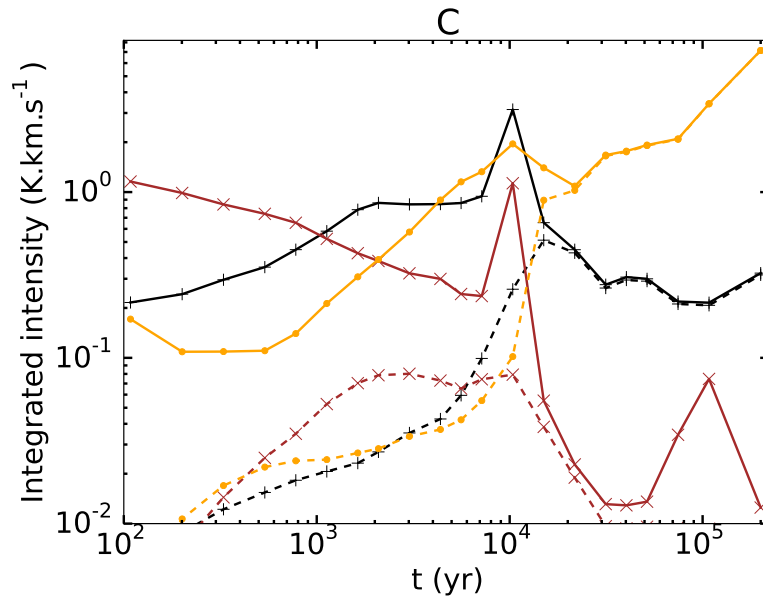

Figure A.207: Time evolution of integrated intensities for $C\left(^3P_1-^3P_0\right)$ (left panel) for models using the second density profile ($\gamma = 1$) and with different sizes of ionized cavity: 0.015 pc (brown), 0.05 pc (black) and 0.10 pc (orange). The solid lines represent the HII region models and the dashed lines the HHMC models.
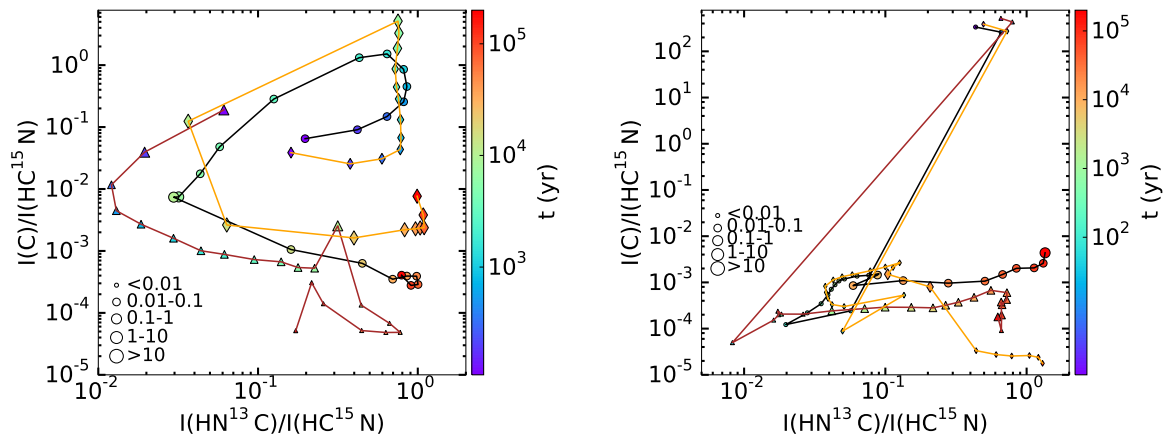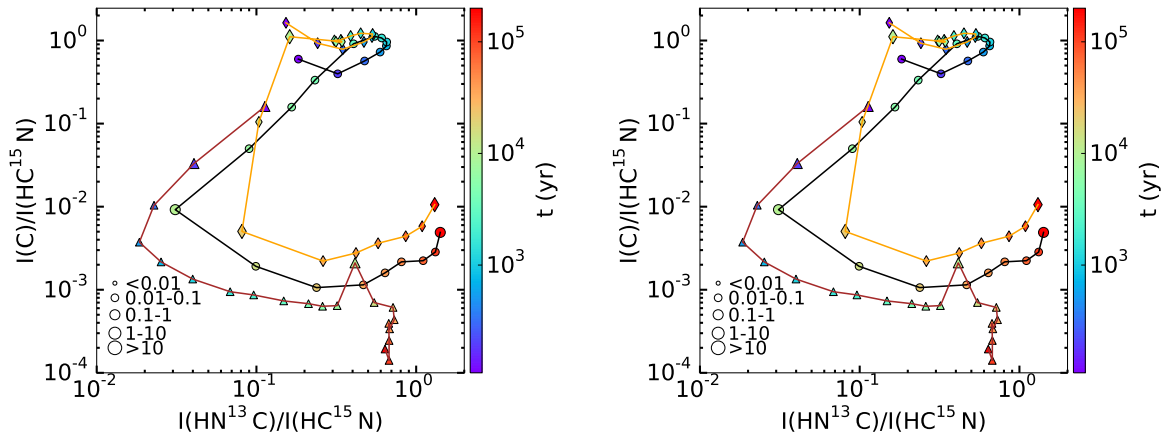
Figure A.208: Time evolution of the integrated intensity ratio ($I(C(^3P_1-^3P_0))$ / $I(HC^{15}N(1-0))$) in function of the integrated intensity ratio ($I(HN^{13}C(1-0))$ / $I(HC^{15}N(1-0))$) for models using the second density profile ($\gamma = 1$) and with different sizes of ionized cavity: 0.015 pc (brown and triangle markers), 0.05 pc (black and circle markers) and 0.10 pc (orange and diamond markers). The HII region models are shown on the left panel and the HHMC models on the right panel. The size of the markers correspond to the range value of the peak intensity in Kelvin of C.

Initial abundances

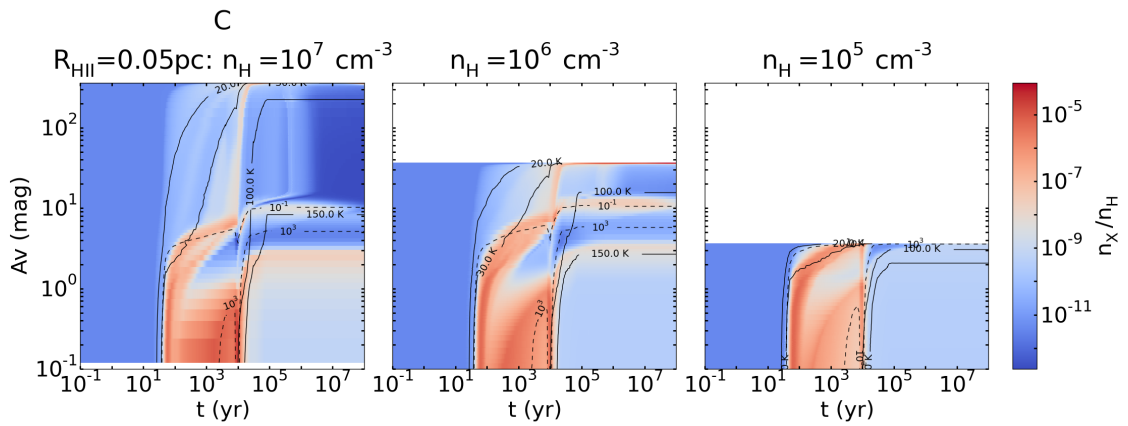Figure A.209: Abundances of C in function of time (x-axis) and visual extinction (y-axis) for HII region with different initial abundances: *ini1* (left panel) and *ini2* (right). The solid black lines appearing on the figures represent the contours for the temperature: 20, 30, 100 and 150 K and the dashed black lines represent some contours for the radiation field intensity: 10^{-1} and 10^3 Draine unit.
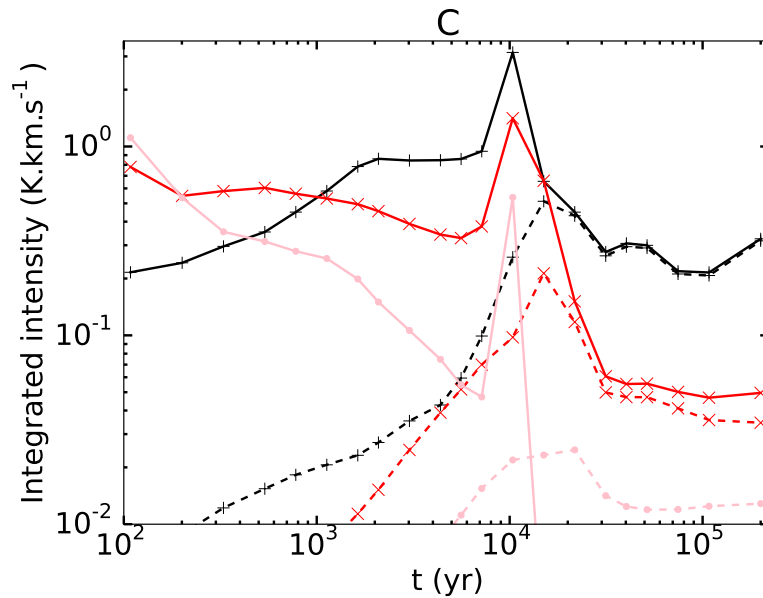
Figure A.210: Time evolution of integrated intensities for C (^{3}P$_1$–^{3}P$_0$) (left panel) for models with different initial abundances: *ini1* (black) and *ini2* (grey). The solid lines represent the HII region models and the dashed lines the HHMC models.
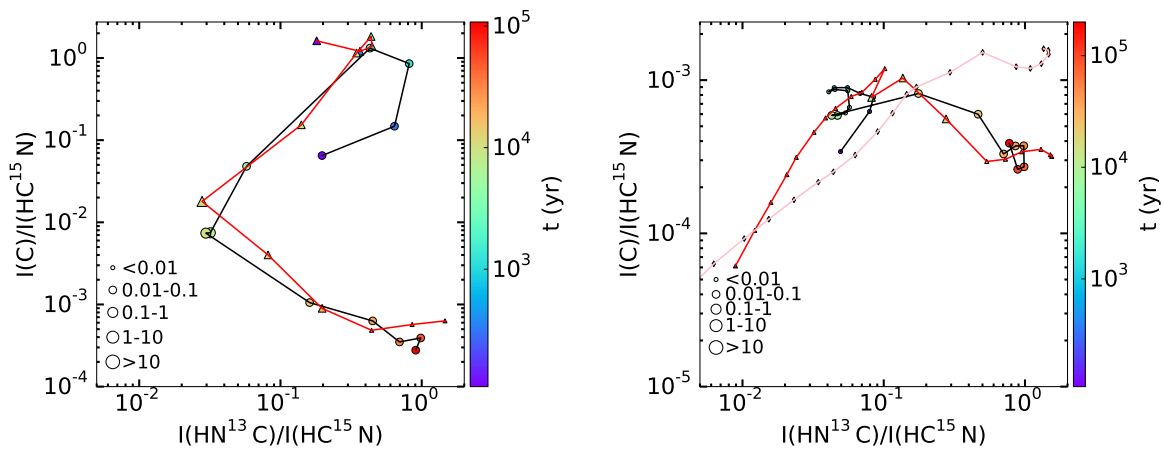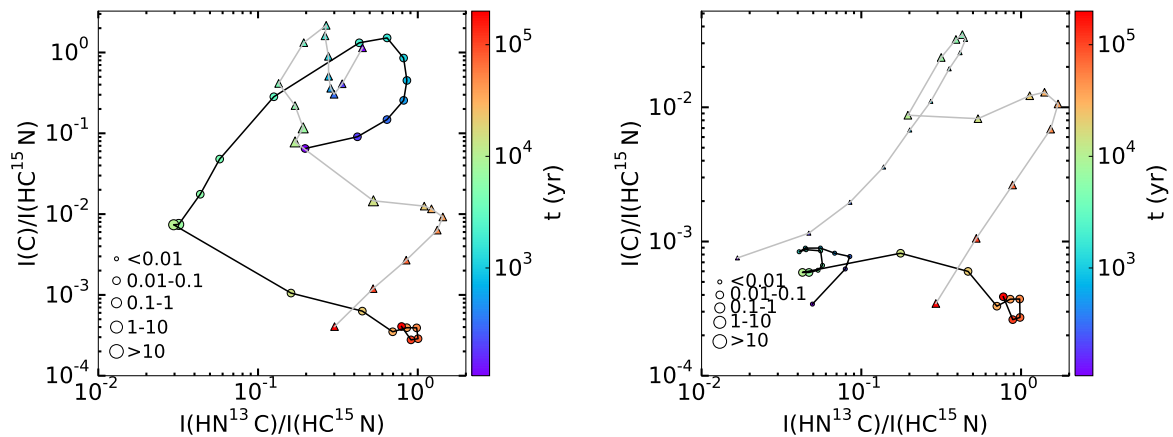

Figure A.211: Time evolution of the integrated intensity ratio (I(C (^{3}P$_1$–^{3}P$_0$)) / I(HC^{15}N (1–0))) in function of the integrated intensity ratio (I(HN^{13}C (1–0)) / I(HC^{15}N (1–0))) for models with different initial abundances: *ini1* (black line and circle markers) and *ini2* (grey line and triangle markers). The HII region models are shown on the left panel and the HHMC models on the right panel. The size of the markers corresponds to the range value of the peak intensity in Kelvin of C.

Effect of the envelope
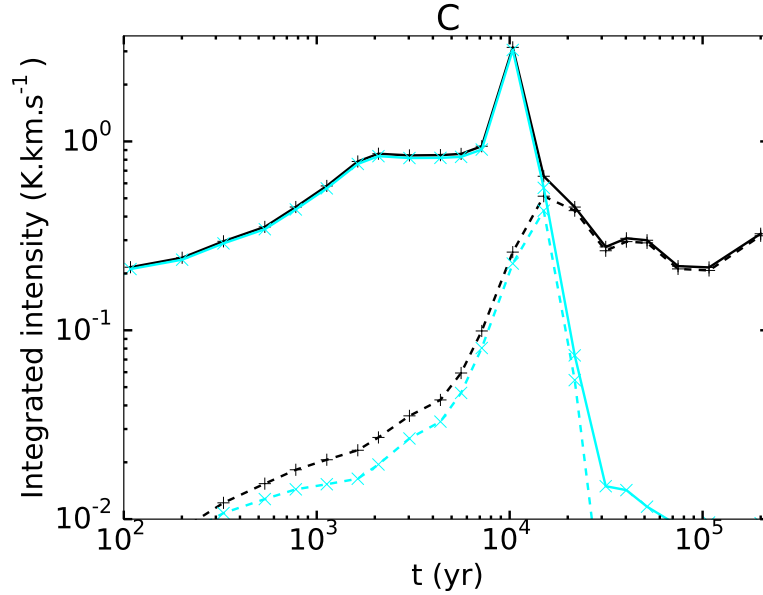
Figure A.212: Time evolution of integrated intensities for $C\left(^{3}P_{1}-^{3}P_{0}\right)$ for models with different cut-off density: 10^{1} cm^{-3} (black) and 10^{6} cm^{-3} (light blue). The solid lines represent the HII region models and the dashed lines the HHMC models.
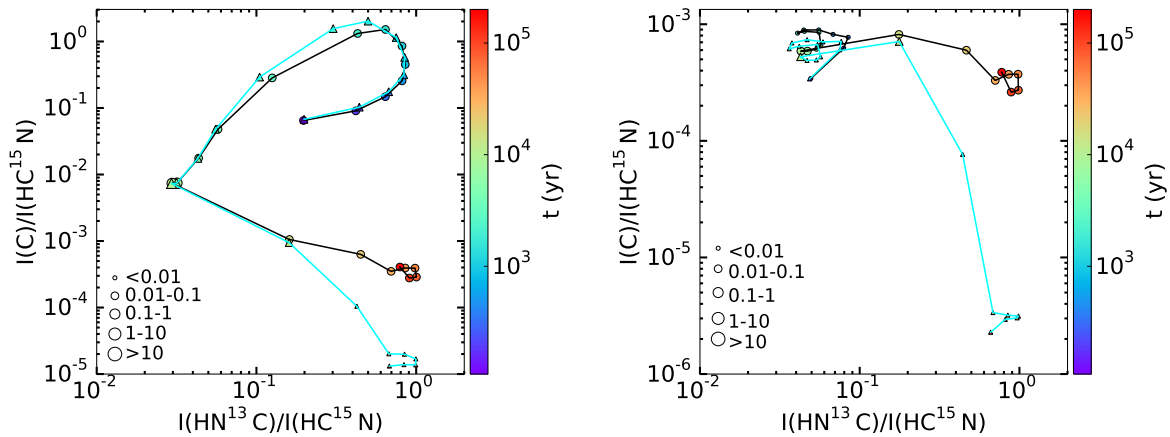
Figure A.213: Time evolution of the integrated intensity ratio $\left(I(C\left(^{3}P_{1}-^{3}P_{0}\right)) \, / \, I(HC^{15}N\,(1–0))\right)$ in function of the integrated intensity ratio $\left(I(HN^{13}C\,(1–0)) \, / \, I(HC^{15}N\,(1–0))\right)$ for models with different cut-off density: 10^{1} cm^{-3} (black line and circle markers) and 10^{6} cm^{-3} (light blue line and triangle markers). The HII region models are shown on the left panel and the HHMC models on the right panel. The size of the markers corresponds to the range value of the peak intensity in Kelvin of C.

A.12 C$^+$

HMC vs HHMC model

In this sub-section we only show the spatio-temporal evolution of the abundance of C$^+$ as the lines, for both the HHMC and HMC models, are undetectable, i.e. the peak intensity is lower than 0.01 K – the integrated intensity is lower than 10^{-2} K km s^{-1}.
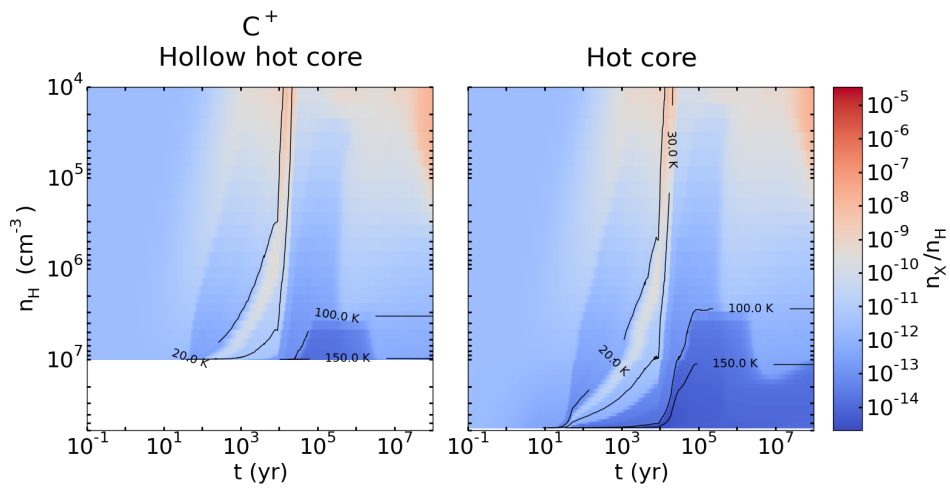
Figure A.214: Abundance of C$^+$ in function of time (x-axis) and density (y-axis) for the HHMC (left) and HMC (right) models. The solid black lines represent the contours for the temperature: 20, 30, 100 and 150 K.

H$_{\text{II}}$ region vs HHMC model
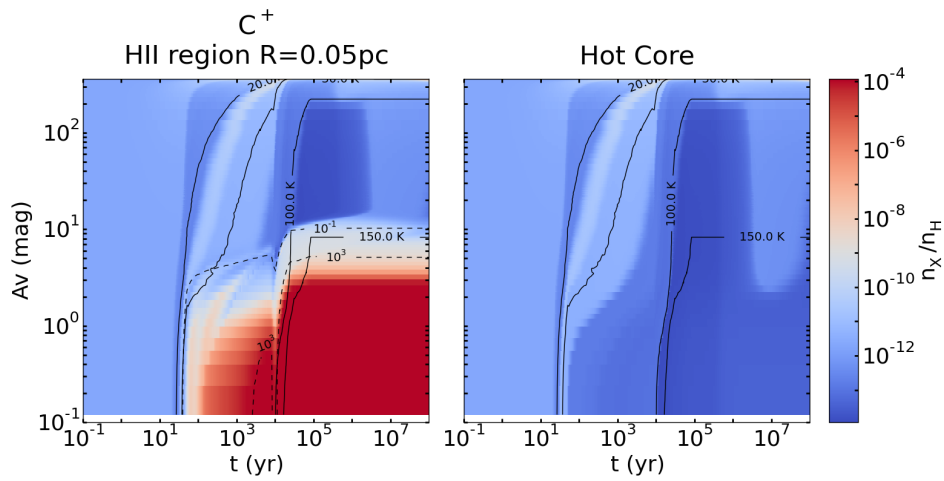
Figure A.215: Abundances of C^+ in function of time (x-axis) and visual extinction (y-axis) for the HII region (left panel) and HHMC (right) models. The solid black lines represent the contours for the temperature: 20, 30, 100 and 150 K and the dashed black lines represent some contours for the radiation field intensity: 10^{-1} and 10^3 Draine unit.
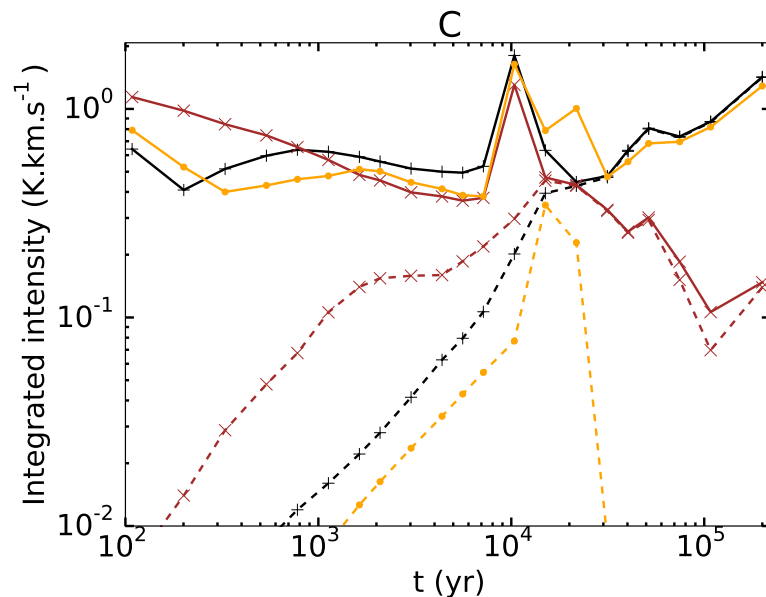

Figure A.216: Time evolution of integrated intensities for C^+ ($^2P_{3/2}$–$^2P_{1/2}$). The black line represents the HII region model and the blue lines represent the HHMC model.
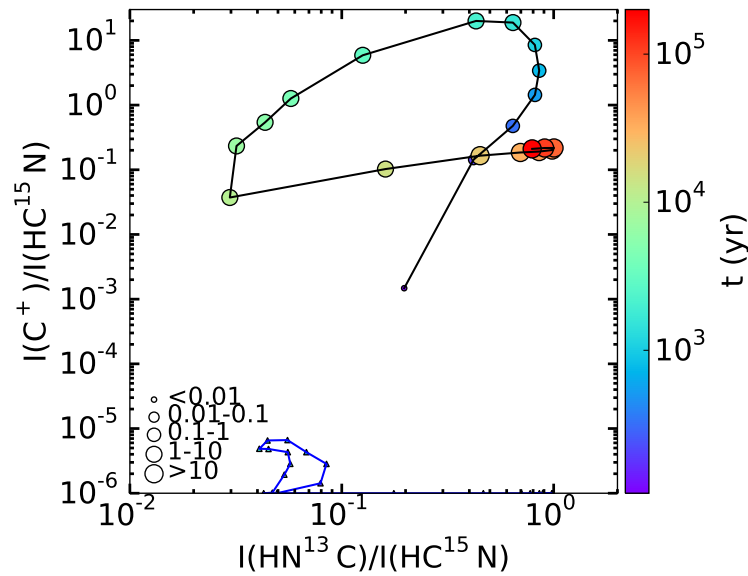
Figure A.217: Time evolution for the HHMC (blue line and circle markers) and HII region (black line and triangle markers) models of the integrated intensity ratio ($I(C^+ (^2P_{3/2}-^2P_{1/2}))$ / $I(HC^{15}N\,(1-0))$)) in function of the integrated intensity ratio ($I(HN^{13}C\,(1-0))$ / $I(HC^{15}N\,(1-0))$)). The size of the markers corresponds to the range value of the peak intensity in Kelvin of C$^+$.
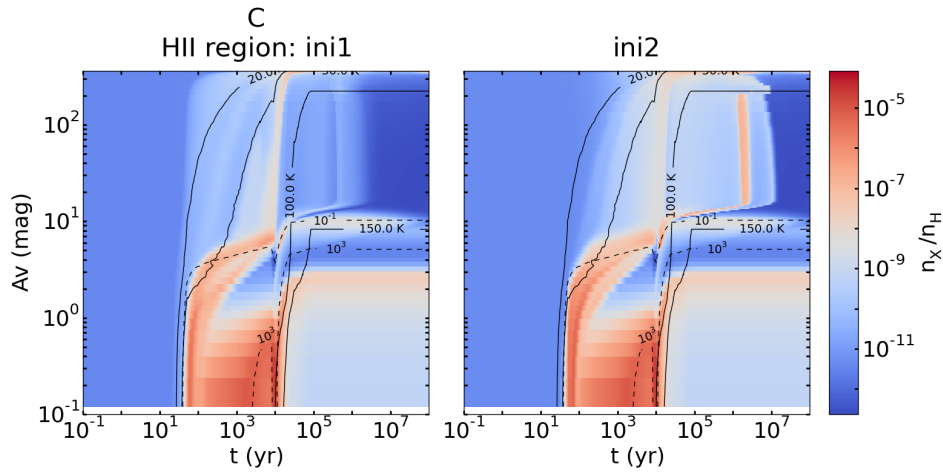
H$_{II}$ region size

Figure A.218: Abundances of C$^+$ in function of time (x-axis) and visual extinction (y-axis) for HII region models with different sizes: 0.015 pc (left panels), 0.05 pc (middle) and 0.10 pc (right). The solid black lines appearing on the figures represent the contours for the temperature: 20, 30, 100 and 150 K and the dashed black lines represent some contours for the radiation field intensity: 10^{-1} and 10^3 Draine unit.
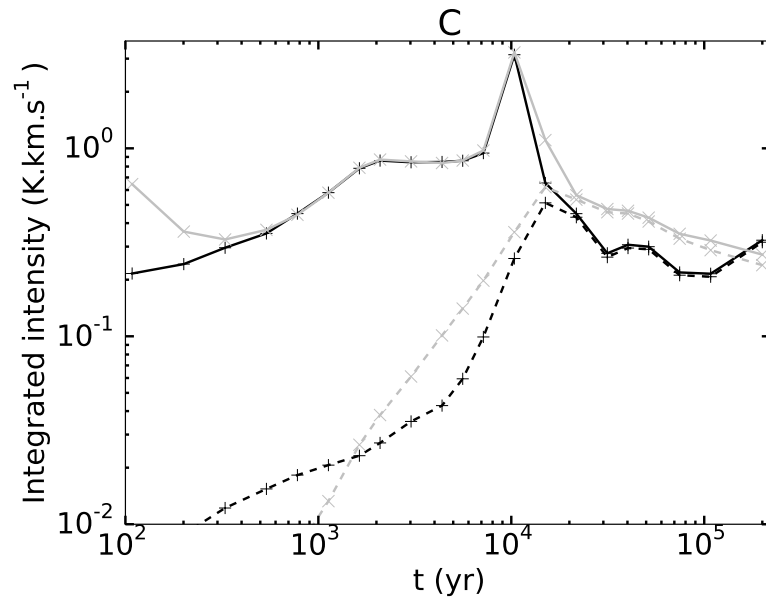
Figure A.219: Time evolution of integrated intensities for C^+ ($^2P_{3/2}$–$^2P_{1/2}$) for models with different sizes of ionized cavity: 0.015 pc (orange), 0.05 pc (black) and 0.10 pc (brown). The solid lines represent the HII region models and the dashed lines the HHMC models.

Figure A.220: Time evolution of the integrated intensity ratio ($I(C^+$ ($^2P_{3/2}$–$^2P_{1/2}$)) / $I(HC^{15}N$ (1–0))) in function of the integrated intensity ratio ($I(HN^{13}C$ (1–0)) / $I(HC^{15}N$ (1–0))) for HII region models with different sizes of ionized cavity: 0.015 pc (brown line and triangle markers), 0.05 pc (black line and circle markers) and 0.10 pc (orange line and diamond markers). The size of the markers corresponds to the range value of the peak intensity in Kelvin of C^+.

Density at the ionization front
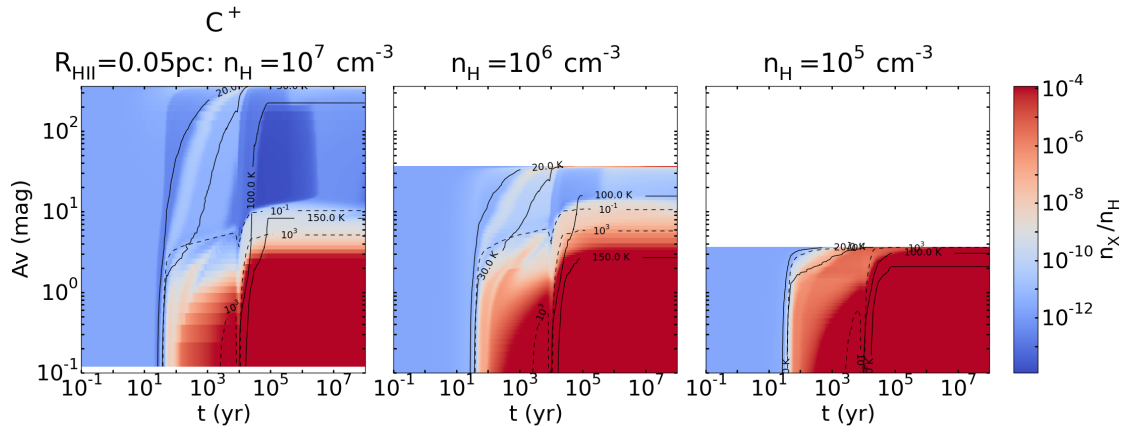
Figure A.221: Abundances of C$^+$ in function of time (x-axis) and visual extinction (y-axis) for HII region models with different densities at the ionization front: 10^7 cm^{-3} (left), 10^6 cm^{-3} (middle) and 10^5 cm^{-3} (right). The solid black lines appearing on the figures represent the contours for the temperature: 20, 30, 100 and 150 K and the dashed black lines represent some contours for the radiation field intensity: 10^{-1} and 10^3 Draine unit.

Figure A.222: Time evolution of integrated intensities for C$^+$ (^{2}P$_{3/2}$–^{2}P$_{1/2}$) for models with different densities at the ionization front: 10^7 cm^{-3} (black), 10^6 cm^{-3} (red) and 10^5 cm^{-3} (pink). The solid lines represent the HII region models and the dashed lines the HHMC models.
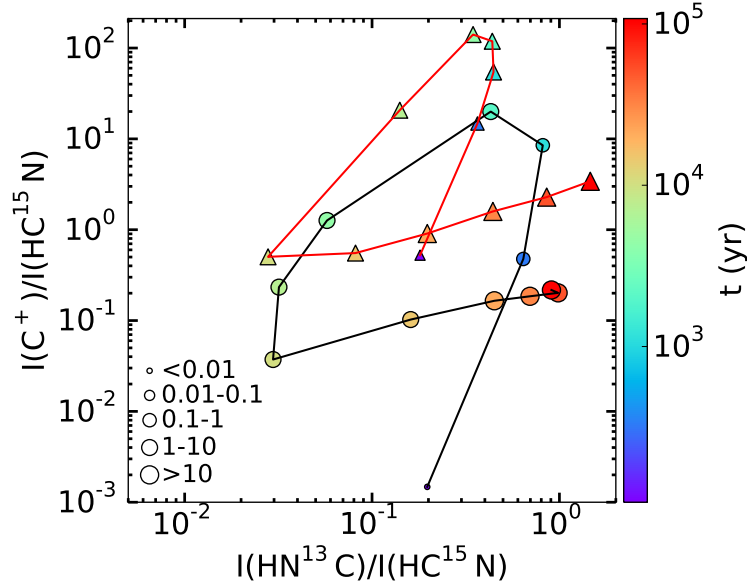
Figure A.223: Time evolution of the integrated intensity ratio ($I(C^+$ ($^2P_{3/2}$–$^2P_{1/2}$)) / $I(HC^{15}N$ (1–0))) in function of the integrated intensity ratio ($I(HN^{13}C$ (1–0)) / $I(HC^{15}N$ (1–0))) for the HII region models with different density at the ionization front: 10^7 cm^{-3} (black line and circle markers), 10^6 cm^{-3} (red line and triangle markers) and 10^5 cm^{-3} (pink line and diamond markers). The size of the markers corresponds to the range value of the peak intensity in Kelvin of C$^+$.

Plummer exponent

Figure A.224: Abundances of C$^+$ in function of time (x-axis) and visual extinction (y-axis) for HII region models using for the second density profile ($\gamma = 1$) and with different sizes of ionized cavity: 0.015 pc (left panel), 0.05 pc (middle) and 0.10 pc (right). The solid black lines appearing on the figures represent the contours for the temperature: 20, 30, 100 and 150 K and the dashed black lines represent some contours for the radiation field intensity: 10^{-1} and 10^3 Draine unit.
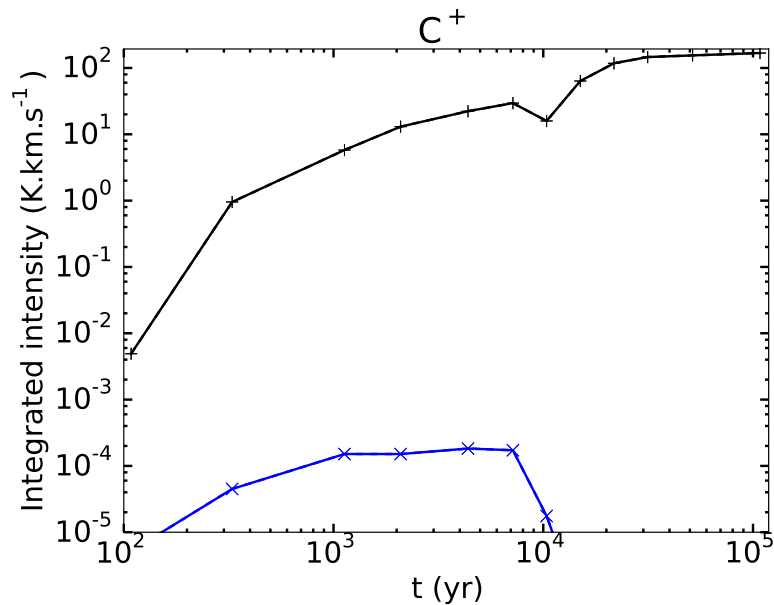
Figure A.225: Time evolution of integrated intensities for C^+ ($^2P_{3/2}$–$^2P_{1/2}$) (left panel) for models using the second density profile ($\gamma = 1$) and with different sizes of ionized cavity: 0.015 pc (brown), 0.05 pc (black) and 0.10 pc (orange). The solid lines represent the HII region models and the dashed lines the HHMC models.

Figure A.226: Time evolution of the integrated intensity ratio ($I(C^+$ ($^2P_{3/2}$–$^2P_{1/2}$)) / $I(HC^{15}N$ (1–0))) in function of the integrated intensity ratio ($I(HN^{13}C$ (1–0)) / $I(HC^{15}N$ (1–0))) for HII region models using the second density profile ($\gamma = 1$) and with different sizes of ionized cavity: 0.015 pc (brown and triangle markers), 0.05 pc (black and circle markers) and 0.10 pc (orange and diamond markers). The size of the markers correspond to the range value of the peak intensity in Kelvin of C^+.

Initial abundances
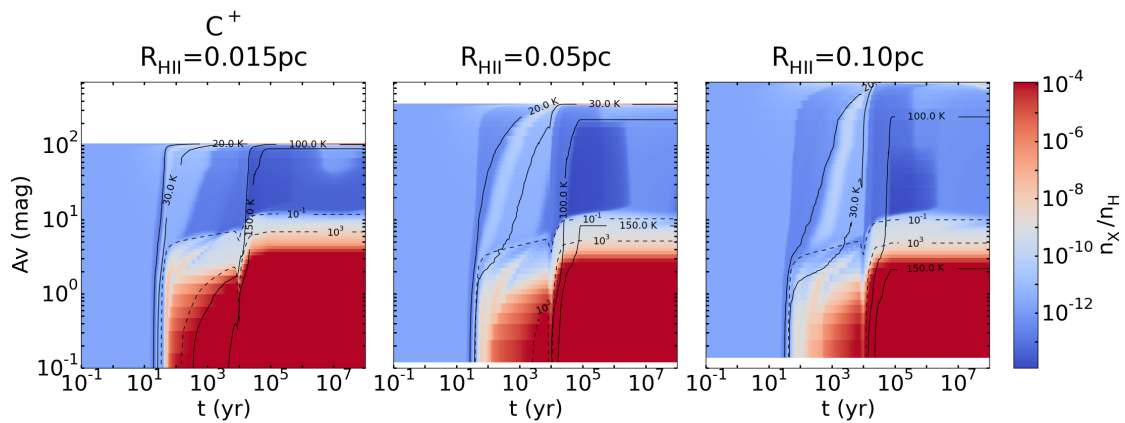

Figure A.227: Abundances of C^+ in function of time (x-axis) and visual extinction (y-axis) for HII region with different initial abundances: *ini1* (left panel) and *ini2* (right). The solid black lines appearing on the figures represent the contours for the temperature: 20, 30, 100 and 150 K and the dashed black lines represent some contours for the radiation field intensity: 10^{-1} and 10^3 Draine unit.

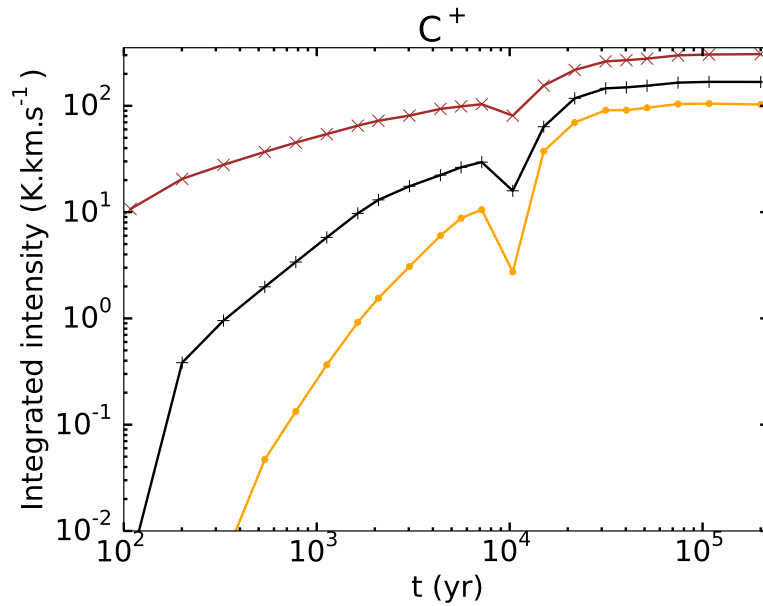Figure A.228: Time evolution of integrated intensities for C^+ ($^2P_{3/2}$–$^2P_{1/2}$) (left panel) for models with different initial abundances: *ini1* (black) and *ini2* (grey). The solid lines represent the HII region models and the dashed lines the HHMC models.
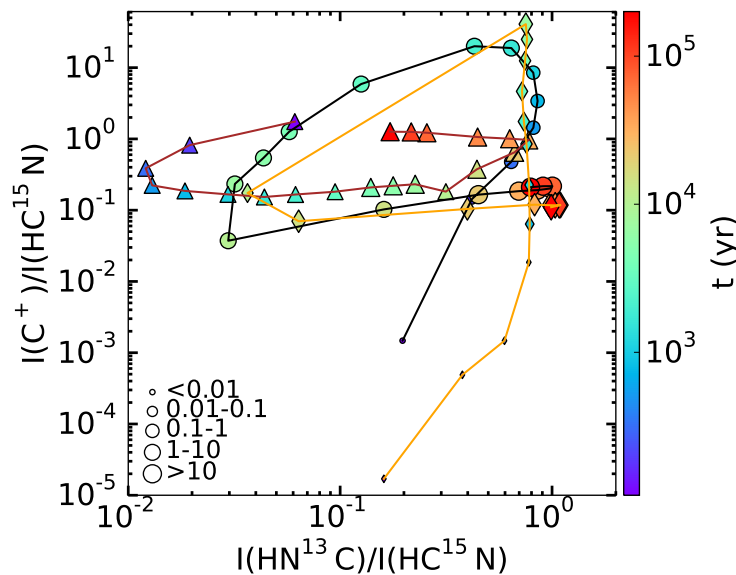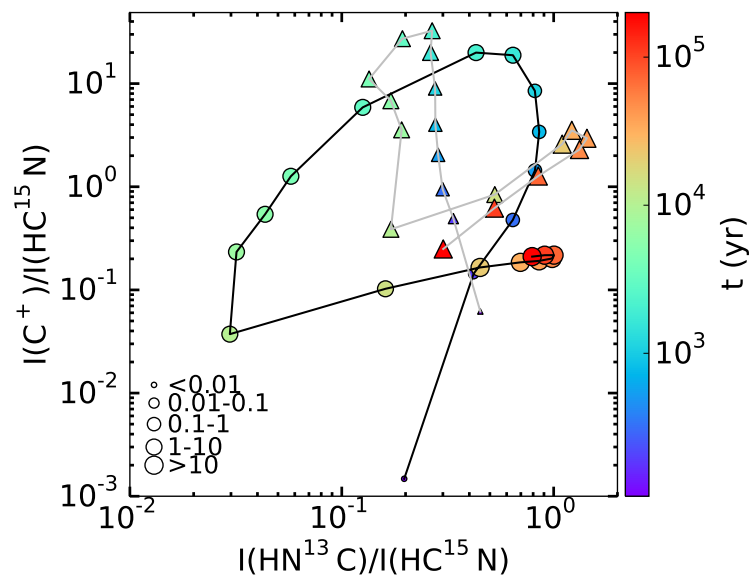
Figure A.229: Time evolution of the integrated intensity ratio (I(C$^+$ (^{2}P$_{3/2}$–^{2}P$_{1/2}$)) / I(HC^{15}N (1–0))) in function of the integrated intensity ratio (I(HN^{13}C (1–0)) / I(HC^{15}N (1–0))) for the HII region models with different initial abundances: *ini1* (black line and circle markers) and *ini2* (grey line and triangle markers). The size of the markers corresponds to the range value of the peak intensity in Kelvin of C$^+$.

Effect of the envelope
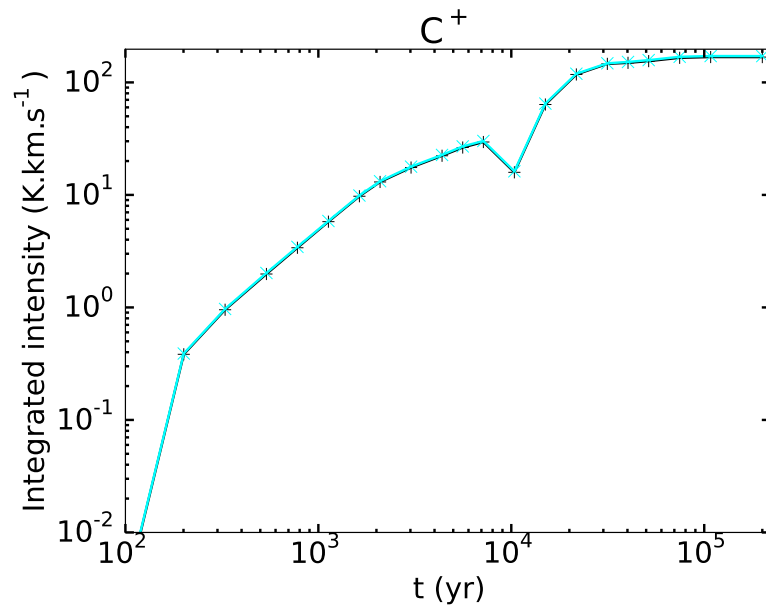
Figure A.230: Time evolution of integrated intensities for C$^+$ (^{2}P$_{3/2}$–^{2}P$_{1/2}$) for models with different cut-off density: 10^1 cm^{-3} (black) and 10^6 cm^{-3} (light blue). The solid lines represent the HII region models and the dashed lines the HHMC models.
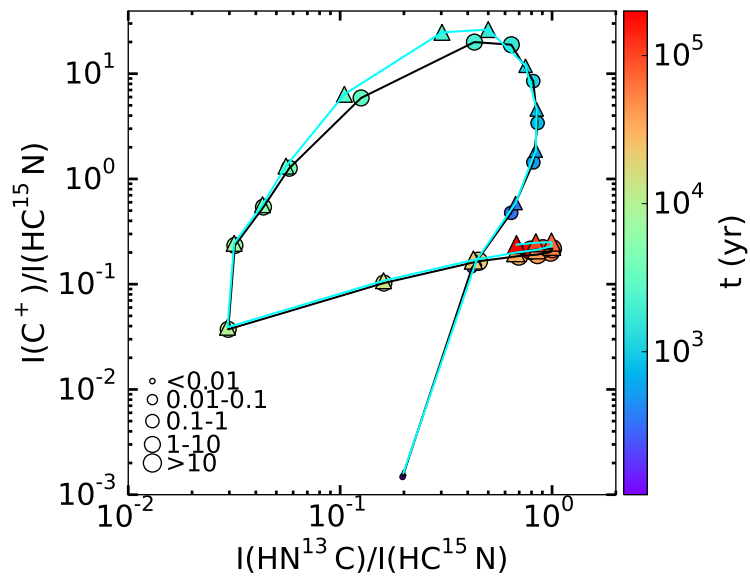
Figure A.231: Time evolution of the integrated intensity ratio ($I(\mathrm{C}^+\,(^2\mathrm{P}_{3/2}\text{--}^2\mathrm{P}_{1/2}))$ / $I(\mathrm{HC}^{15}\mathrm{N}\,(1\text{--}0))$) in function of the integrated intensity ratio ($I(\mathrm{HN}^{13}\mathrm{C}\,(1\text{--}0))$ / $I(\mathrm{HC}^{15}\mathrm{N}\,(1\text{--}0))$) for HII region models with different cut-off density: 10^1 cm^{-3} (black line and circle markers) and 10^6 cm^{-3} (light blue line and triangle markers). The size of the markers corresponds to the range value of the peak intensity in Kelvin of C^+.

A.13   O

HMC vs HHMC model

In this sub-section we only show the spatio-temporal evolution of the abundance of O as the lines, for both the HHMC and HMC models, are undetectable, i.e. the peak intensity is lower than 0.01 K – the integrated intensity is lower than 10^{-2} K km s^{-1}.
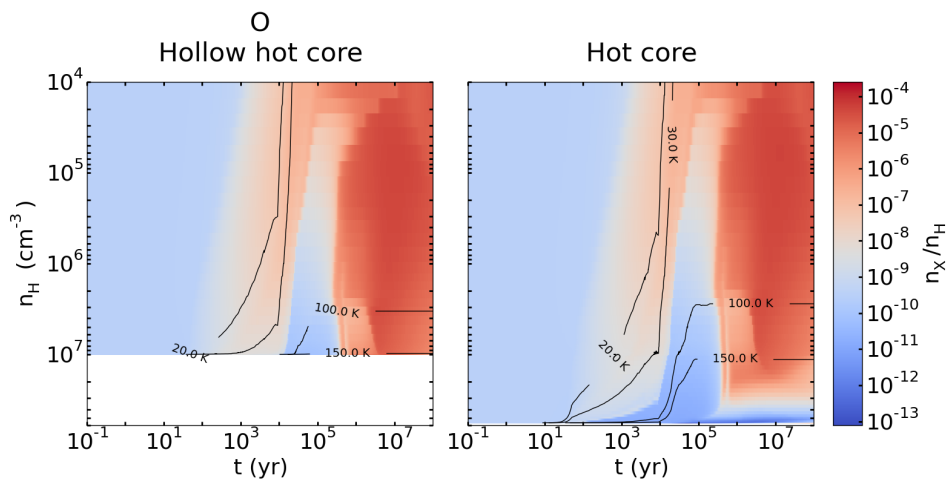
Figure A.232: Abundance of O in function of time (x-axis) and density (y-axis) for the HHMC (left) and HMC (right) models. The solid black lines represent the contours for the temperature: 20, 30, 100 and 150 K.

H$_{II}$ region vs HHMC model
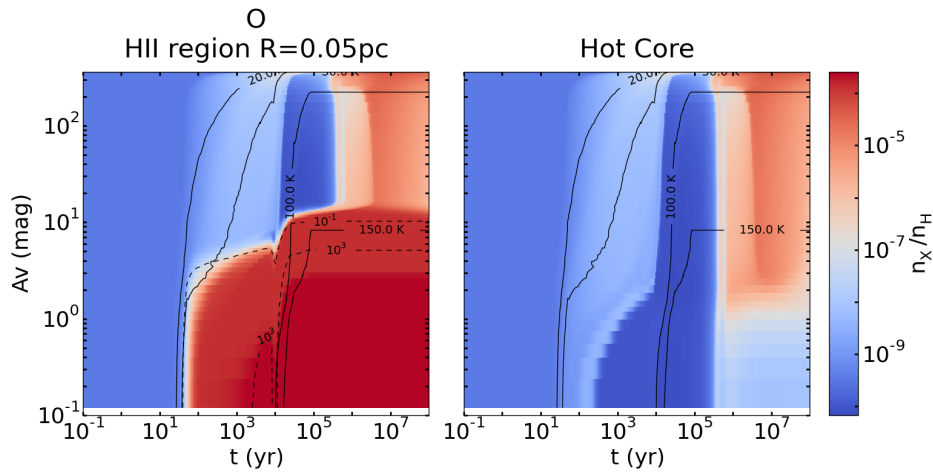
Figure A.233: Abundances of O in function of time (x-axis) and visual extinction (y-axis) for the HII region (left panel) and HHMC (right) models. The solid black lines represent the contours for the temperature: 20, 30, 100 and 150 K and the dashed black lines represent some contours for the radiation field intensity: 10^{-1} and 10^{3} Draine unit.
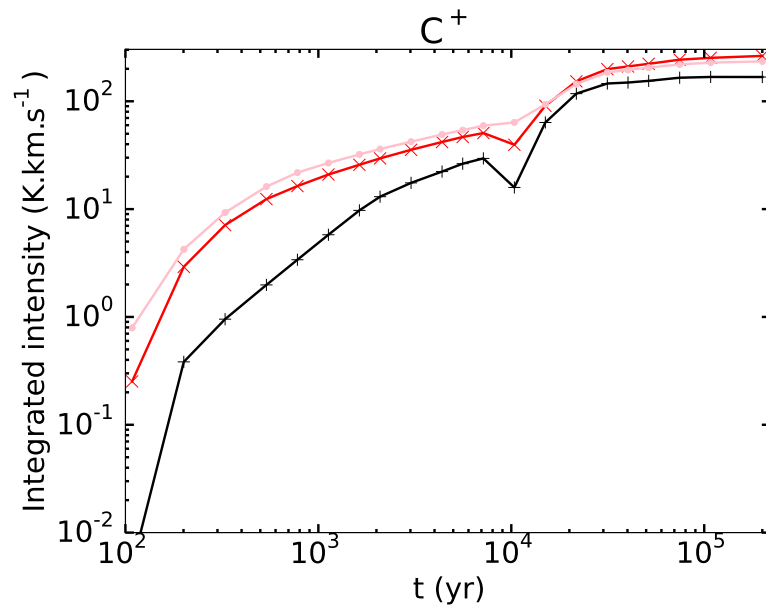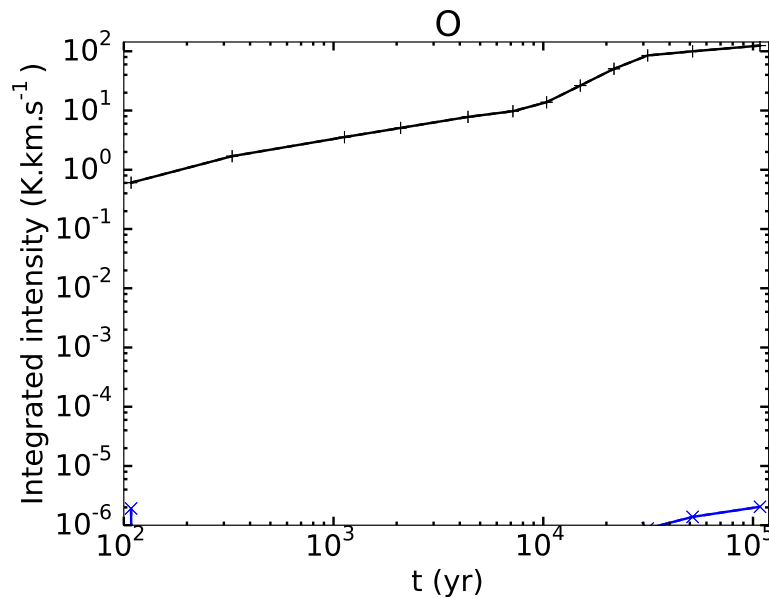

Figure A.234: Time evolution of integrated intensities for $O\left({}^{3}P_{1}-{}^{3}P_{2}\right)$. The black line represents the HII region model and the blue lines represent the HHMC model.
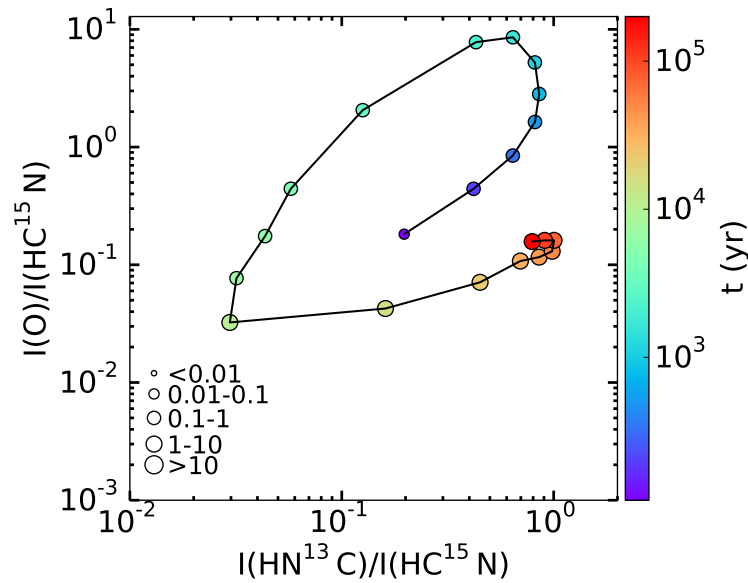
Figure A.235: Time evolution for the HHMC (blue line and circle markers) and HII region (black line and triangle markers) models of the integrated intensity ratio ($I(O\,(^3P_1-^3P_2))$ / $I(HC^{15}N\,(1-0))$) in function of the integrated intensity ratio ($I(HN^{13}C\,(1-0))$ / $I(HC^{15}N\,(1-0))$). The size of the markers corresponds to the range value of the peak intensity in Kelvin of O.

HII region size
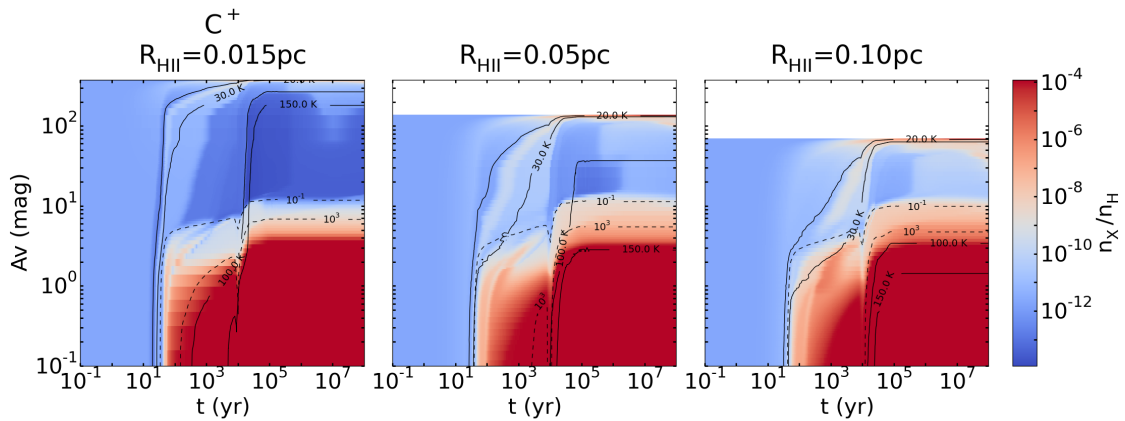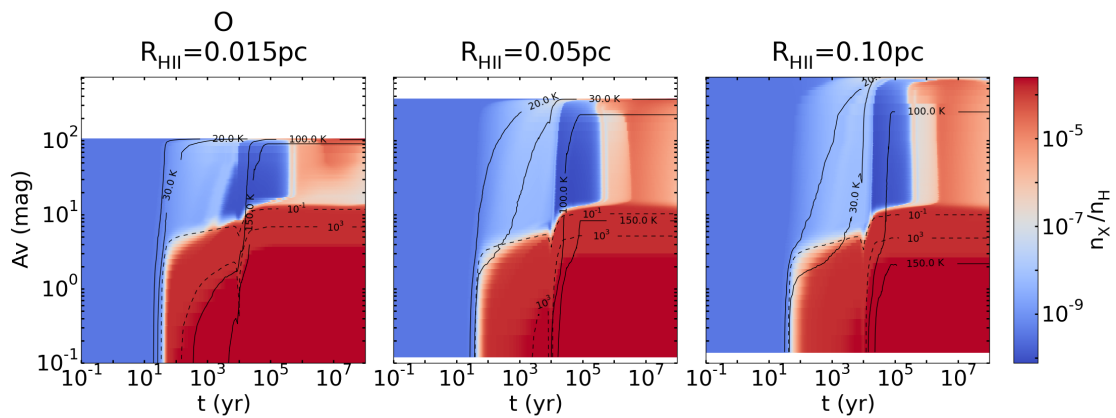

Figure A.236: Abundances of O in function of time (x-axis) and visual extinction (y-axis) for HII region models with different sizes: 0.015 pc (left panels), 0.05 pc (middle) and 0.10 pc (right). The solid black lines appearing on the figures represent the contours for the temperature: 20, 30, 100 and 150 K and the dashed black lines represent some contours for the radiation field intensity: 10^{-1} and 10^3 Draine unit.
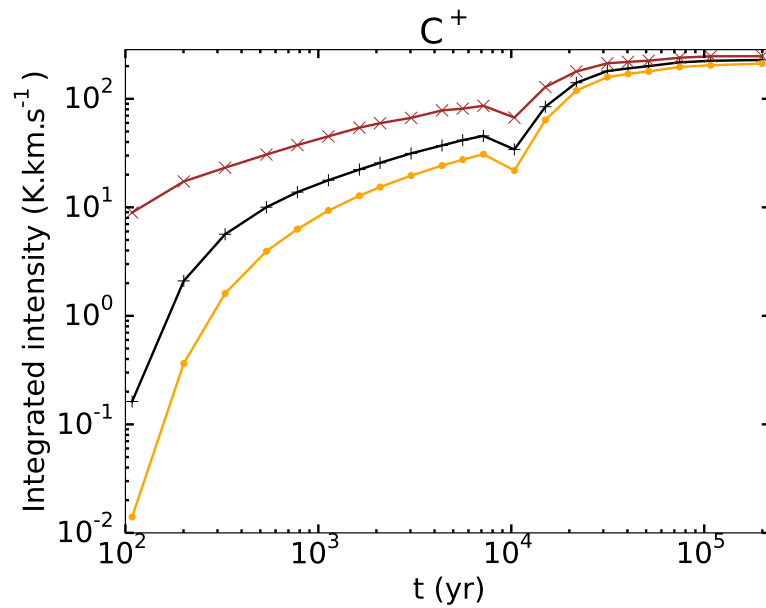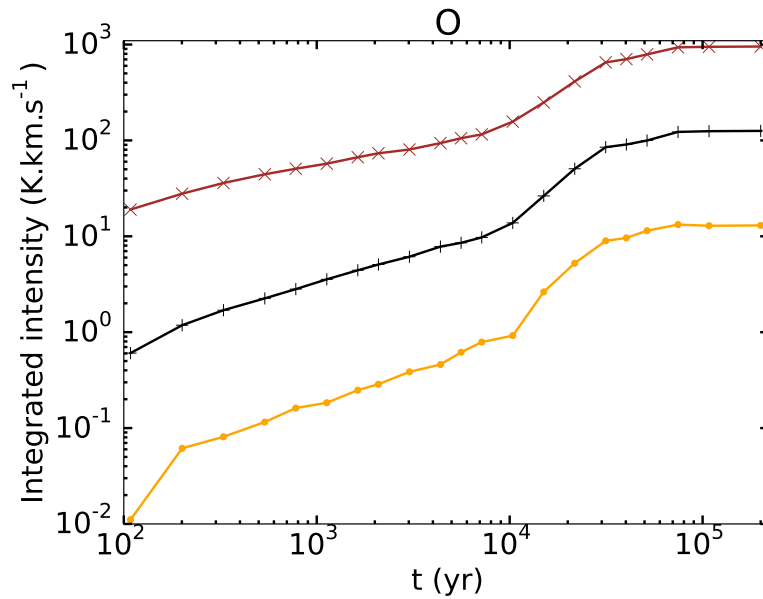
Figure A.237: Time evolution of integrated intensities for O $\left({}^3P_1-{}^3P_2\right)$ for models with different sizes of ionized cavity: 0.015 pc (orange), 0.05 pc (black) and 0.10 pc (brown). The solid lines represent the HII region models and the dashed lines the HHMC models.
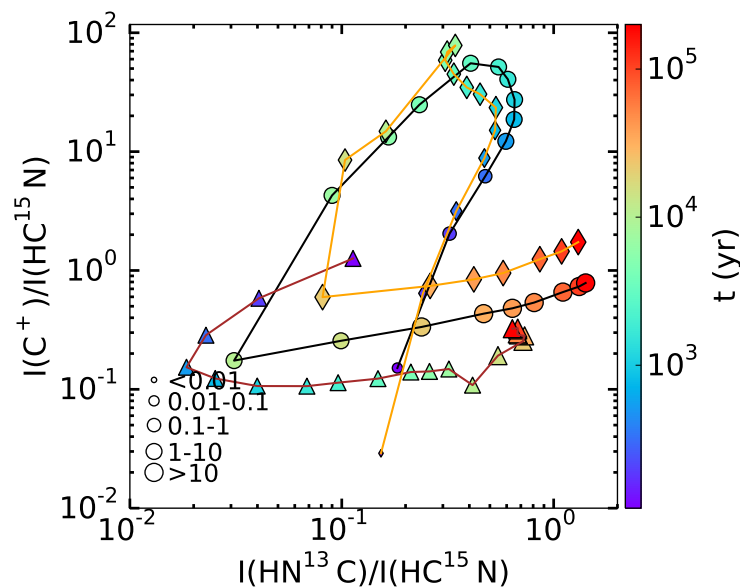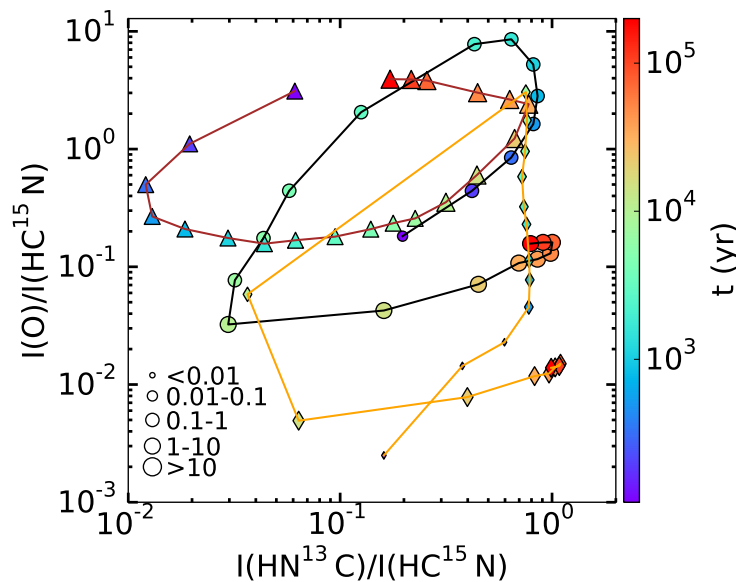

Figure A.238: Time evolution of the integrated intensity ratio $\left(I(O\,({}^3P_1-{}^3P_2))\,/\,I(HC^{15}N\,(1-0))\right)$ in function of the integrated intensity ratio $\left(I(HN^{13}C\,(1-0))\,/\,I(HC^{15}N\,(1-0))\right)$ for HII region models with different sizes of ionized cavity: 0.015 pc (brown line and triangle markers), 0.05 pc (black line and circle markers) and 0.10 pc (orange line and diamond markers). The size of the markers corresponds to the range value of the peak intensity in Kelvin of O.
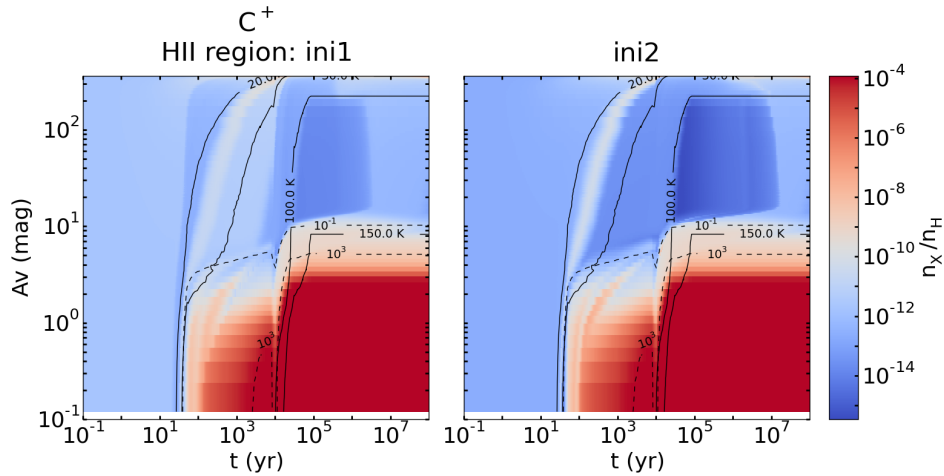
Density at the ionization front
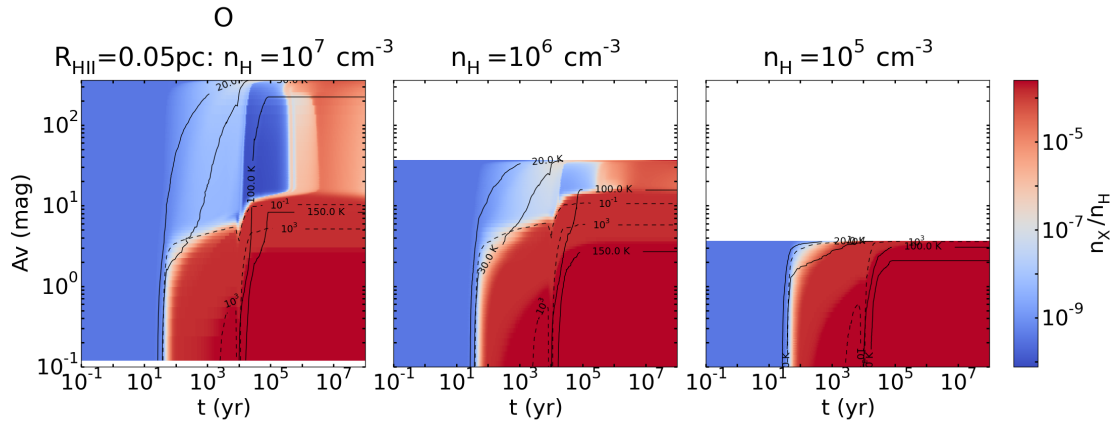
Figure A.239: Abundances of O in function of time (x-axis) and visual extinction (y-axis) for HII region models with different densities at the ionization front: 10^7 cm^{-3} (left), 10^6 cm^{-3} (middle) and 10^5 cm^{-3} (right). The solid black lines appearing on the figures represent the contours for the temperature: 20, 30, 100 and 150 K and the dashed black lines represent some contours for the radiation field intensity: 10^{-1} and 10^3 Draine unit.
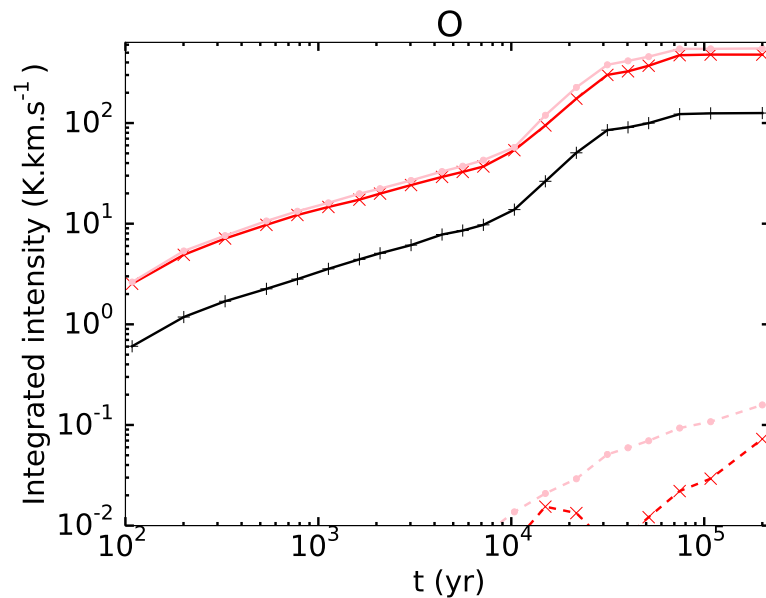
Figure A.240: Time evolution of integrated intensities for O ($^3P_1$–$^3P_2$) for models with different densities at the ionization front: 10^7 cm^{-3} (black), 10^6 cm^{-3} (red) and 10^5 cm^{-3} (pink). The solid lines represent the HII region models and the dashed lines the HHMC models.
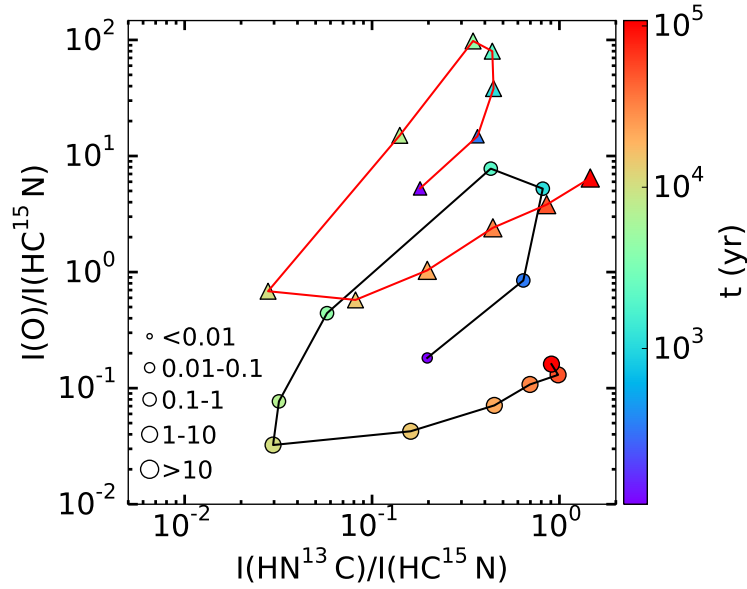
Figure A.241: Time evolution of the integrated intensity ratio $(I(O\,(^3P_1–^3P_2)) / I(HC^{15}N\,(1–0)))$ in function of the integrated intensity ratio $(I(HN^{13}C\,(1–0)) / I(HC^{15}N\,(1–0)))$ for HII region models with different density at the ionization front: 10^7 cm^{-3} (black line and circle markers), 10^6 cm^{-3} (red line and triangle markers) and 10^5 cm^{-3} (pink line and diamond markers). The size of the markers corresponds to the range value of the peak intensity in Kelvin of O.

Plummer exponent
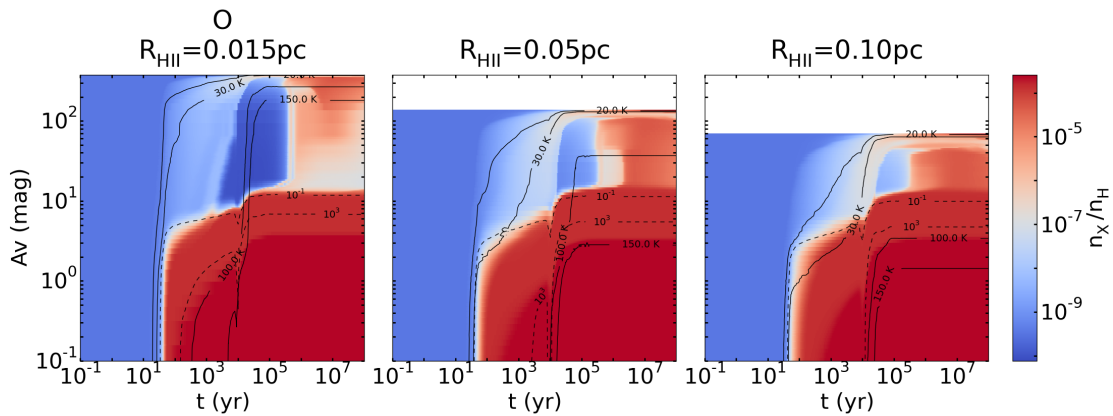
Figure A.242: Abundances of O in function of time (x-axis) and visual extinction (y-axis) for HII region models using for the second density profile ($\gamma = 1$) and with different sizes of ionized cavity: 0.015 pc (left panel), 0.05 pc (middle) and 0.10 pc (right). The solid black lines appearing on the figures represent the contours for the temperature: 20, 30, 100 and 150 K and the dashed black lines represent some contours for the radiation field intensity: 10^{-1} and 10^3 Draine unit.
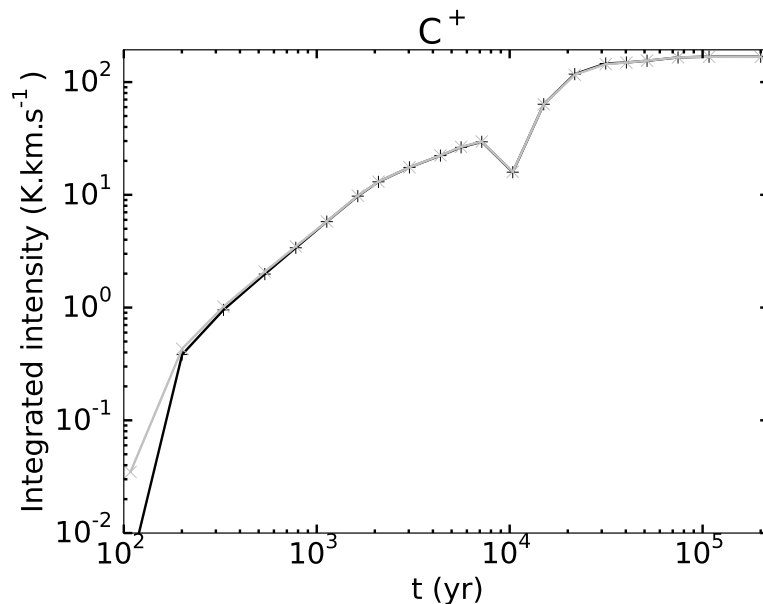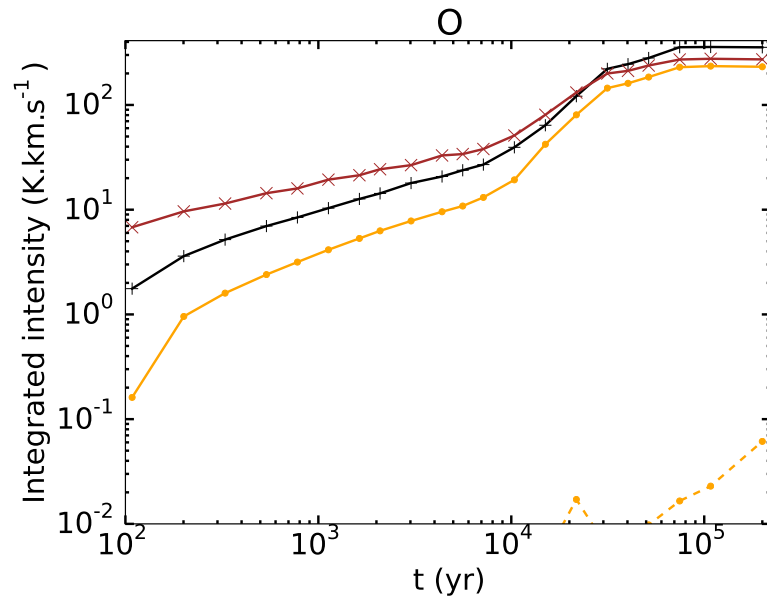
Figure A.243: Time evolution of integrated intensities for O $(^3P_1-^3P_2)$ (left panel) for models using the second density profile ($\gamma = 1$) and with different sizes of ionized cavity: 0.015 pc (brown), 0.05 pc (black) and 0.10 pc (orange). The solid lines represent the HII region models and the dashed lines the HHMC models.
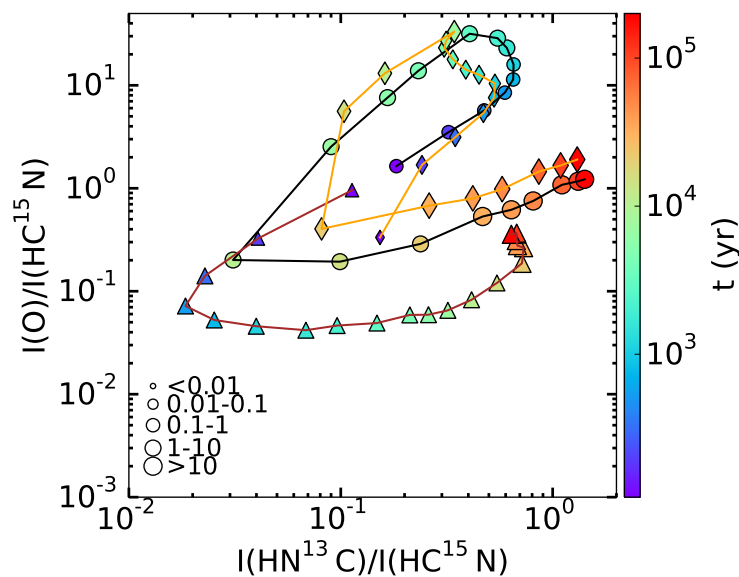
Figure A.244: Time evolution of the integrated intensity ratio $(I(O\,(^3P_1-^3P_2))\,/\,I(HC^{15}N\,(1–0)))$ in function of the integrated intensity ratio $(I(HN^{13}C\,(1–0))\,/\,I(HC^{15}N\,(1–0)))$ for the HII region models using the second density profile ($\gamma = 1$) and with different sizes of ionized cavity: 0.015 pc (brown and triangle markers), 0.05 pc (black and circle markers) and 0.10 pc (orange and diamond markers). The size of the markers correspond to the range value of the peak intensity in Kelvin of O.

Initial abundances
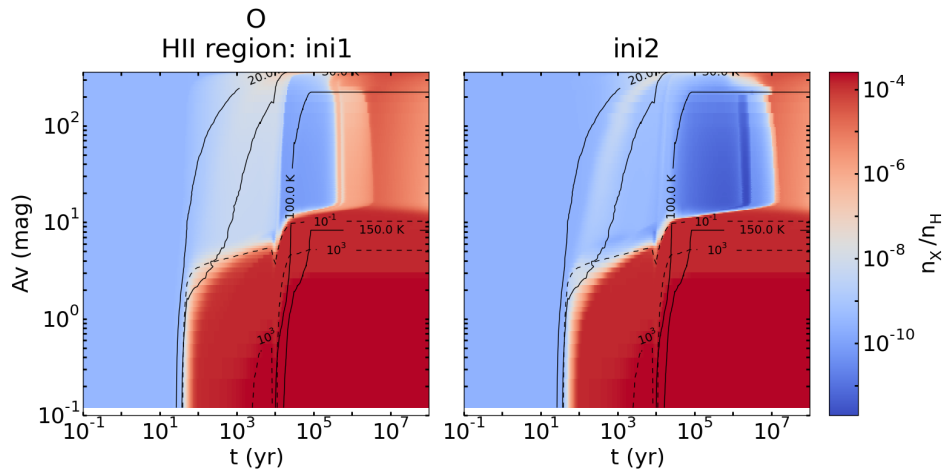
Figure A.245: Abundances of O in function of time (x-axis) and visual extinction (y-axis) for HII region with different initial abundances: *ini1* (left panel) and *ini2* (right). The solid black lines appearing on the figures represent the contours for the temperature: 20, 30, 100 and 150 K and the dashed black lines represent some contours for the radiation field intensity: 10^{-1} and 10^{3} Draine unit.
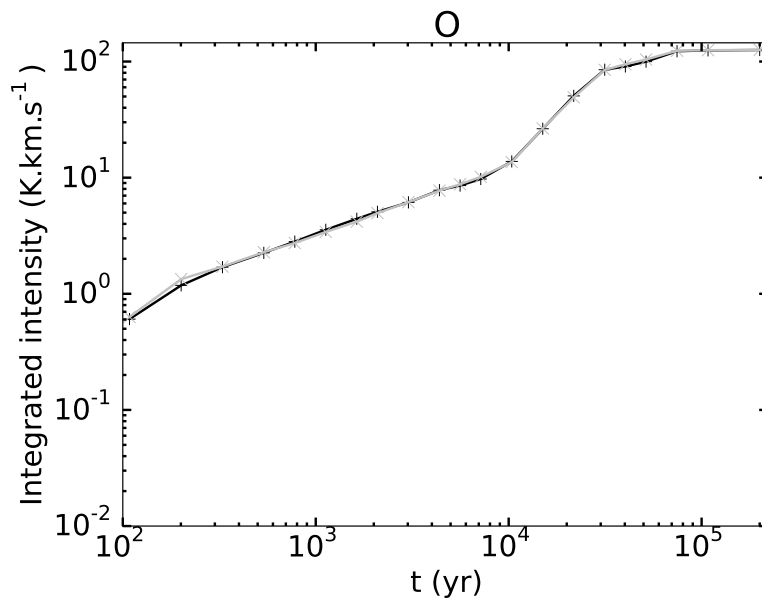
Figure A.246: Time evolution of integrated intensities for $O\left({}^{3}P_{1}-{}^{3}P_{2}\right)$ (left panel) for models with different initial abundances: *ini1* (black) and *ini2* (grey). The solid lines represent the HII region models and the dashed lines the HHMC models.
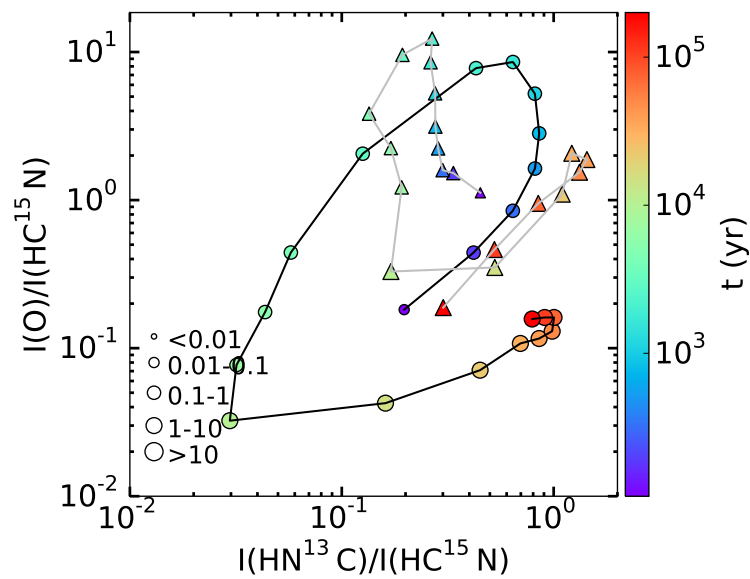
Figure A.247: Time evolution of the integrated intensity ratio $(I(O(^3P_1-^3P_2)) / I(HC^{15}N(1-0)))$ in function of the integrated intensity ratio $(I(HN^{13}C(1-0)) / I(HC^{15}N(1-0)))$ for the HII region models with different initial abundances: *ini1* (black line and circle markers) and *ini2* (grey line and triangle markers). The size of the markers corresponds to the range value of the peak intensity in Kelvin of O.

Effect of the envelope
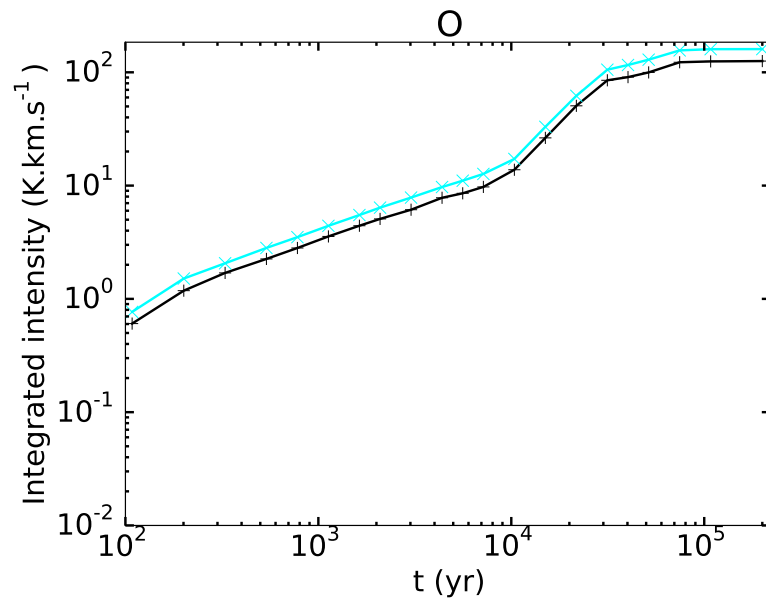
Figure A.248: Time evolution of integrated intensities for $O(^3P_1-^3P_2)$ for models with different cut-off density: 10^1 cm^{-3} (black) and 10^6 cm^{-3} (light blue). The solid lines represent the HII region models and the dashed lines the HHMC models.
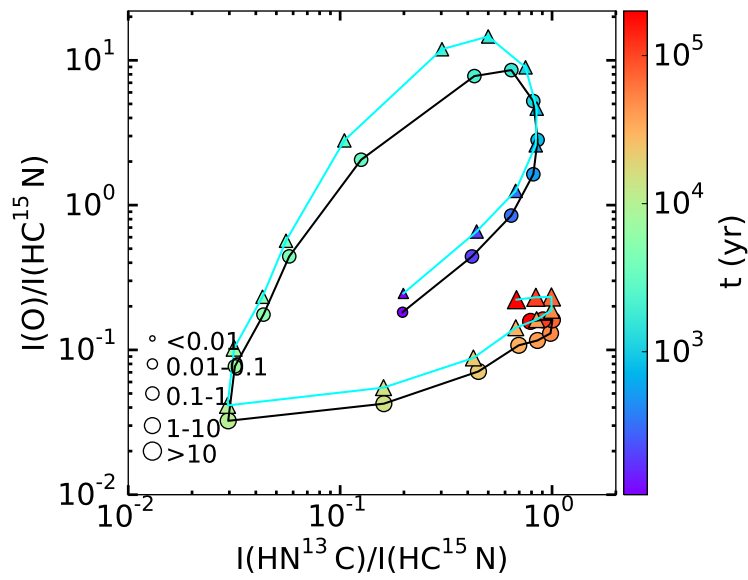
Figure A.249: Time evolution of the integrated intensity ratio $(I(O\,(^3P_1-^3P_2))\,/\,I(HC^{15}N\,(1-0)))$ in function of the integrated intensity ratio $(I(HN^{13}C\,(1-0))\,/\,I(HC^{15}N\,(1-0)))$ for HII region models with different cut-off density: 10^1 cm^{-3} (black line and circle markers) and 10^6 cm^{-3} (light blue line and triangle markers). The size of the markers corresponds to the range value of the peak intensity in Kelvin of O.

B

Additional figures: abundance for other molecules

Contents

For all the sections of this appendix we show the relative abundances of the following molecules: C_3H_2, C_2H, C_4H, CS, SO, S, OCS, CO, CH_2OH, S^+, OH^+, CO^+, s-C_2H, s-CH_3OH and s-OH.

B.1   HMC vs HHMC model
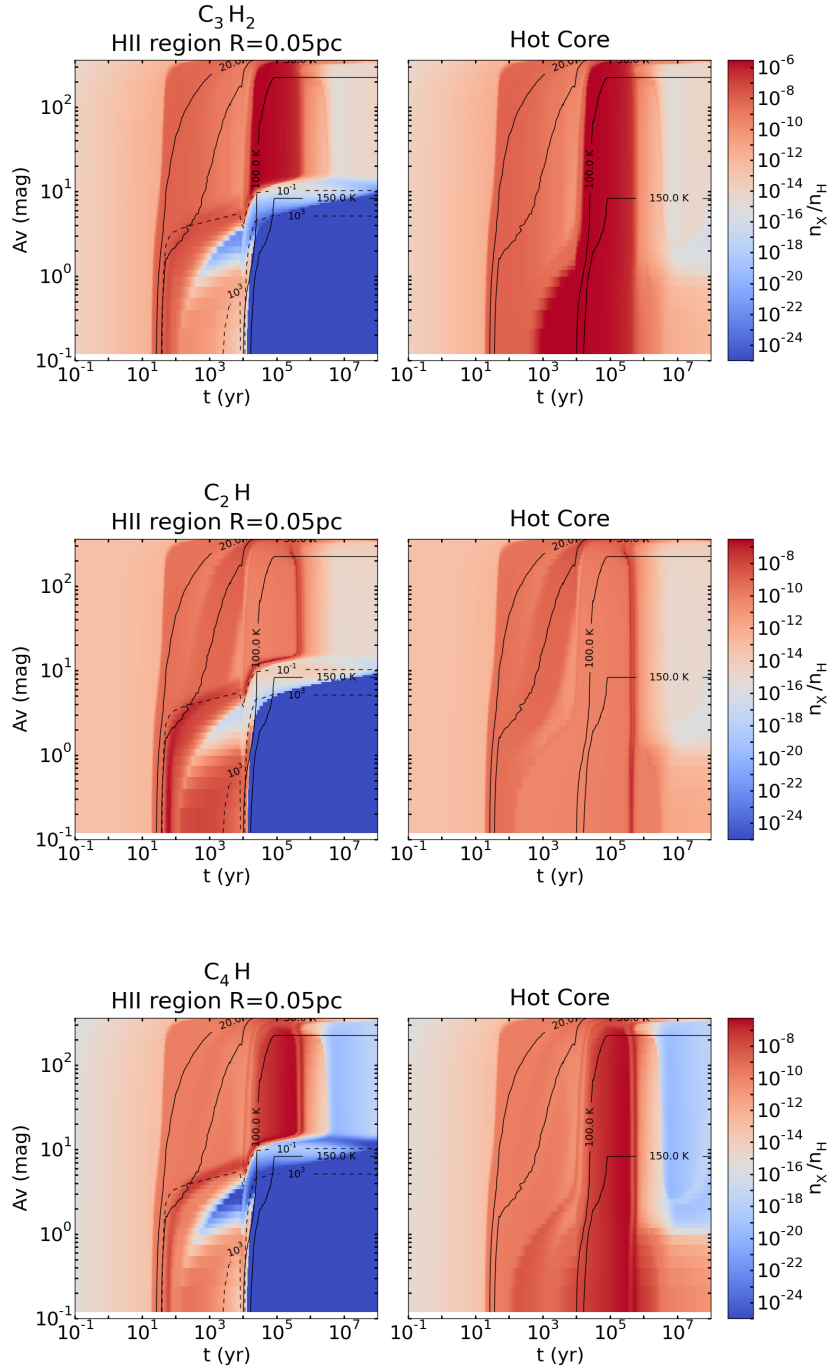
Figure B.1: Abundances of C_3H_2, C_2H and C_4H in function of time (x-axis) and visual extinction (y-axis) for the HII region (left panel) and HHMC (right) models. The solid black lines represent the contours for the temperature: 20, 30, 100 and 150 K and the dashed black lines represent some contours for the radiation field intensity: 10^{-1} and 10^3 Draine unit.
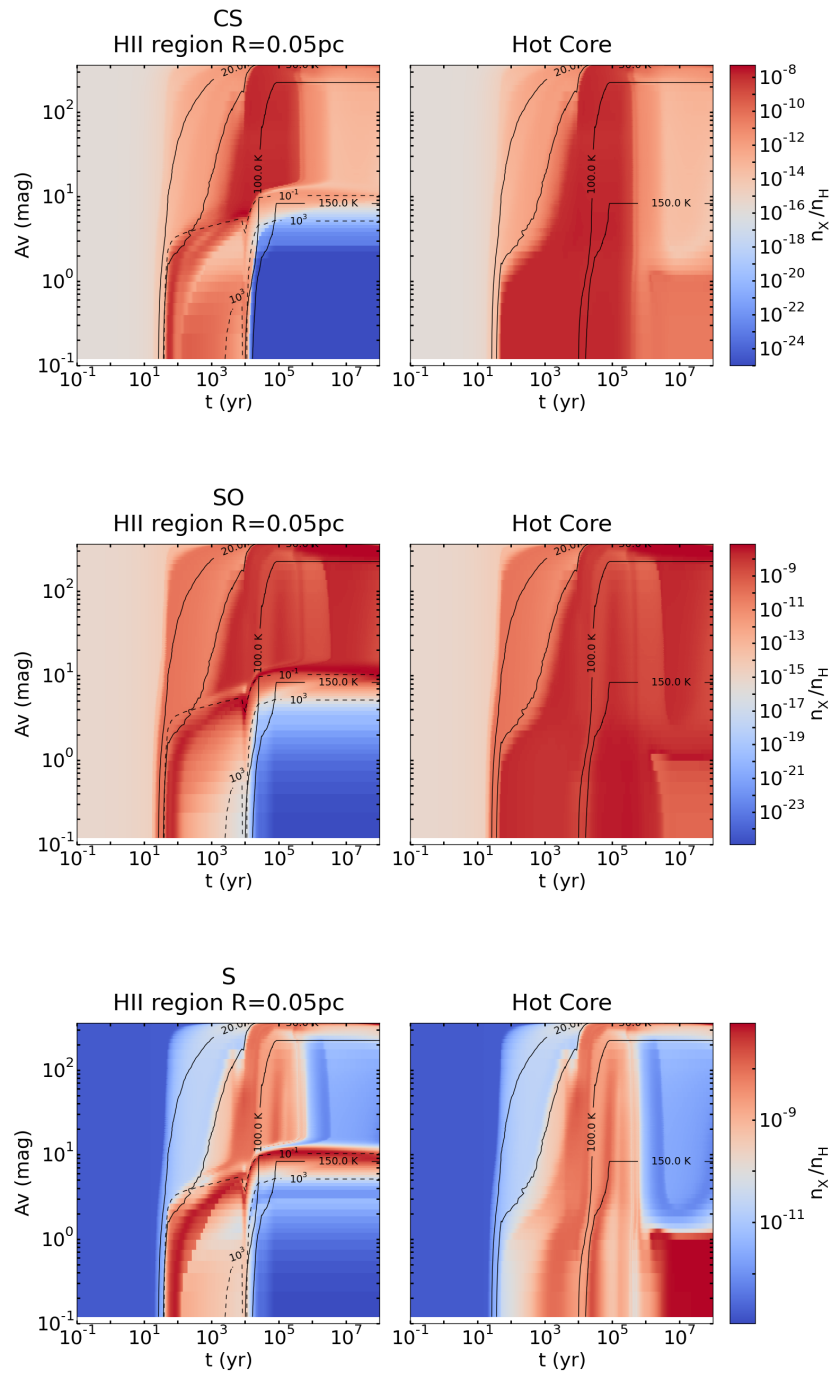
Figure B.2: Abundances of CS, SO and S in function of time (x-axis) and visual extinction (y-axis) for the HII region (left panel) and HHMC (right) models. The solid black lines represent the contours for the temperature: 20, 30, 100 and 150 K and the dashed black lines represent some contours for the radiation field intensity: 10^{-1} and 10^3 Draine unit.
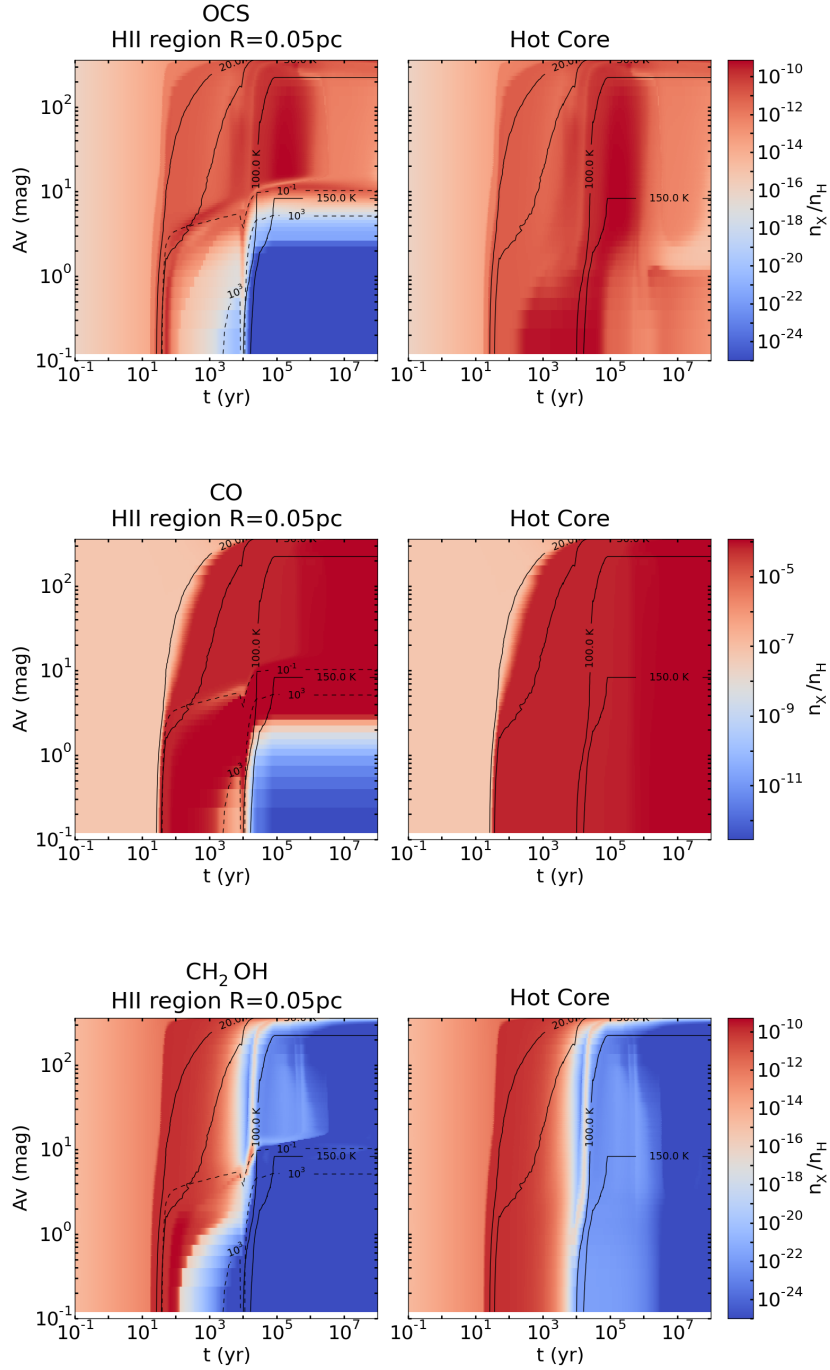
Figure B.3: Abundances of OCS, CO and CH$_2$OH in function of time (x-axis) and visual extinction (y-axis) for the HII region (left panel) and HHMC (right) models. The solid black lines represent the contours for the temperature: 20, 30, 100 and 150 K and the dashed black lines represent some contours for the radiation field intensity: 10^{-1} and 10^3 Draine unit.

Figure B.4: Abundances of S^+, OH^+ and CO^+ in function of time (x-axis) and visual extinction (y-axis) for the HII region (left panel) and HHMC (right) models. The solid black lines represent the contours for the temperature: 20, 30, 100 and 150 K and the dashed black lines represent some contours for the radiation field intensity: 10^{-1} and 10^3 Draine unit.

Figure B.5: Abundances of s-C$_2$H, s-CH$_3$OH and s-OH in function of time (x-axis) and visual extinction (y-axis) for the HII region (left panel) and HHMC (right) models. The solid black lines represent the contours for the temperature: 20, 30, 100 and 150 K and the dashed black lines represent some contours for the radiation field intensity: 10^{-1} and 10^3 Draine unit. The letter "J" in the name of the species in the title means it is a grain species.

B.2   H_{II} region size

Figure B.6: Abundances of C$_3$H$_2$, C$_2$H and C$_4$H in function of time (x-axis) and visual extinction (y-axis) for HII region models with different sizes: 0.015 pc (left panels), 0.05 pc (middle) and 0.10 pc (right). The solid black lines appearing on the figures represent the contours for the temperature: 20, 30, 100 and 150 K and the dashed black lines represent some contours for the radiation field intensity: 10^{-1} and 10^3 Draine unit.
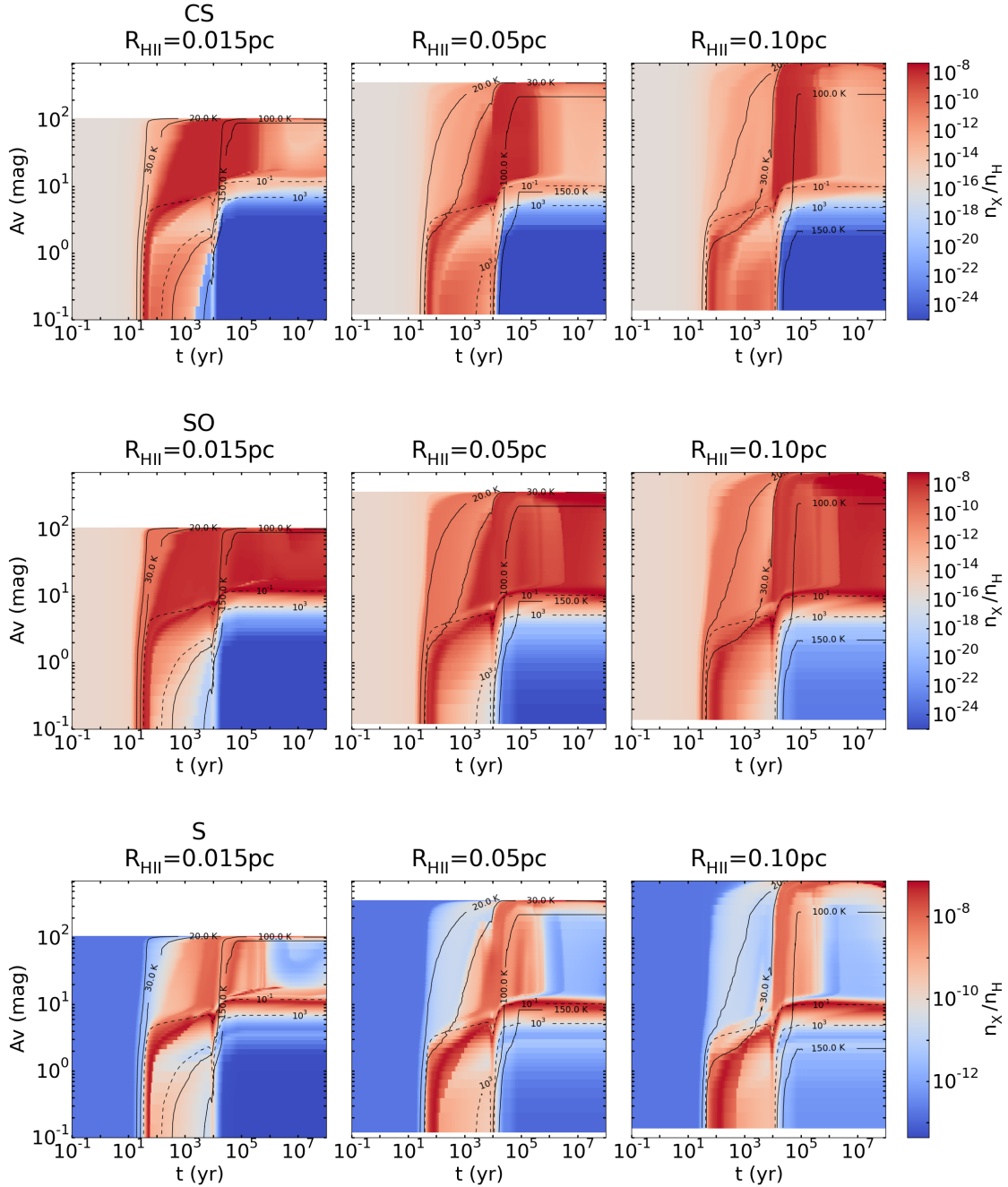
Figure B.7: Abundances of CS, SO and S in function of time (x-axis) and visual extinction (y-axis) for HII region models with different sizes: 0.015 pc (left panels), 0.05 pc (middle) and 0.10 pc (right). The solid black lines appearing on the figures represent the contours for the temperature: 20, 30, 100 and 150 K and the dashed black lines represent some contours for the radiation field intensity: 10^{-1} and 10^3 Draine unit.

Figure B.8: Abundances of OCS, CO and CH$_2$OH in function of time (x-axis) and visual extinction (y-axis) for HII region models with different sizes: 0.015 pc (left panels), 0.05 pc (middle) and 0.10 pc (right). The solid black lines appearing on the figures represent the contours for the temperature: 20, 30, 100 and 150 K and the dashed black lines represent some contours for the radiation field intensity: 10^{-1} and 10^3 Draine unit.
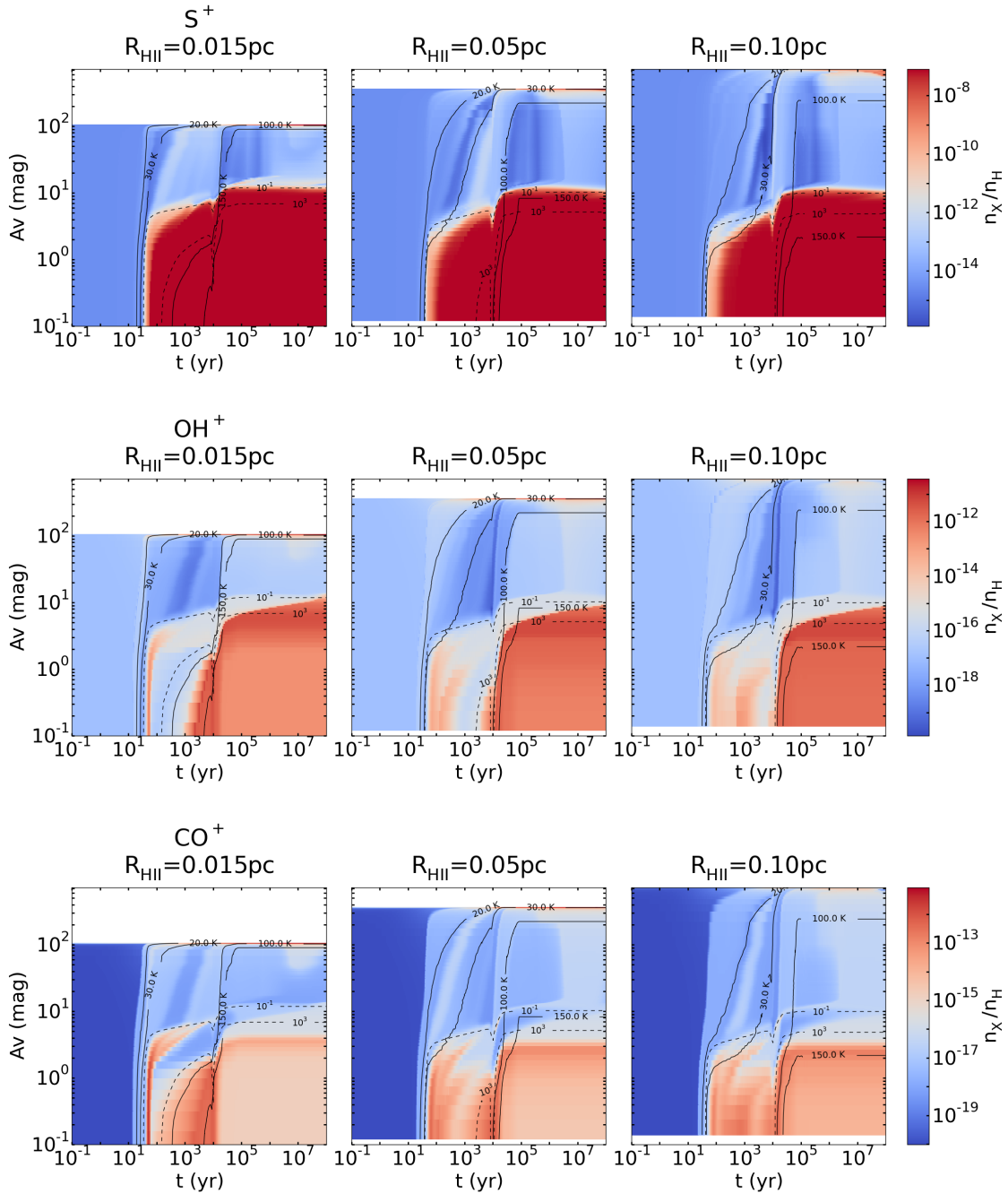
Figure B.9: Abundances of S^+, OH^+ and CO^+ in function of time (x-axis) and visual extinction (y-axis) for HII region models with different sizes: 0.015 pc (left panels), 0.05 pc (middle) and 0.10 pc (right). The solid black lines appearing on the figures represent the contours for the temperature: 20, 30, 100 and 150 K and the dashed black lines represent some contours for the radiation field intensity: 10^{-1} and 10^3 Draine unit.

Figure B.10: Abundances of s-C$_2$H, s-CH$_3$OH and s-OH in function of time (x-axis) and visual extinction (y-axis) for HII region models with different sizes: 0.015 pc (left panels), 0.05 pc (middle) and 0.10 pc (right). The solid black lines appearing on the figures represent the contours for the temperature: 20, 30, 100 and 150 K and the dashed black lines represent some contours for the radiation field intensity: 10^{-1} and 10^3 Draine unit. The letter "J" in the name of the species in the title means it is a grain species.

B.3   Density at the ionization front
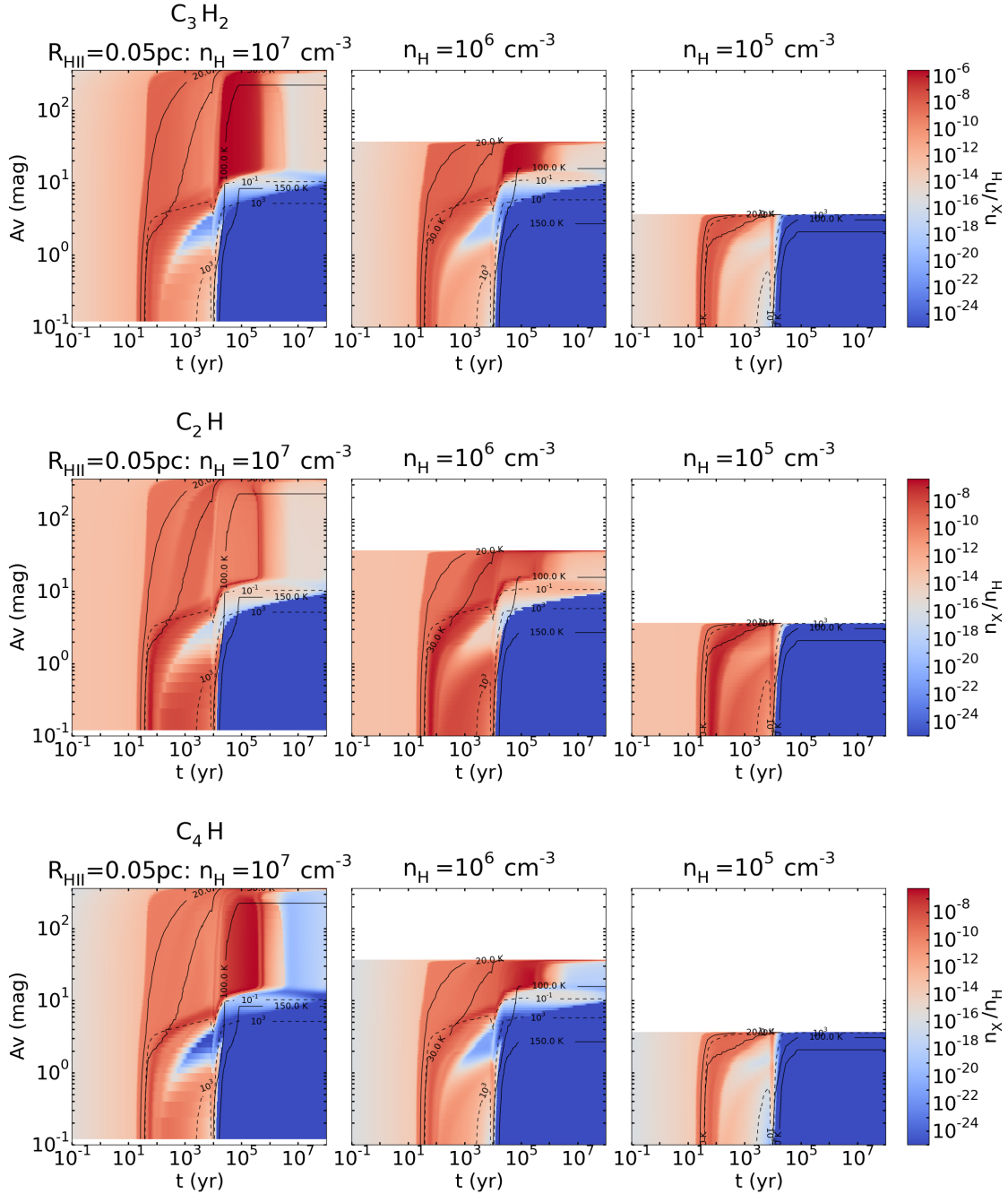
Figure B.11: Abundances of C_3H_2, C_2H and C_4H in function of time (x-axis) and visual extinction (y-axis) for HII region models with different densities at the ionization front: 10^7 cm^{-3} (left), 10^6 cm^{-3} (middle) and 10^5 cm^{-3} (right). The solid black lines appearing on the figures represent the contours for the temperature: 20, 30, 100 and 150 K and the dashed black lines represent some contours for the radiation field intensity: 10^{-1} and 10^3 Draine unit.
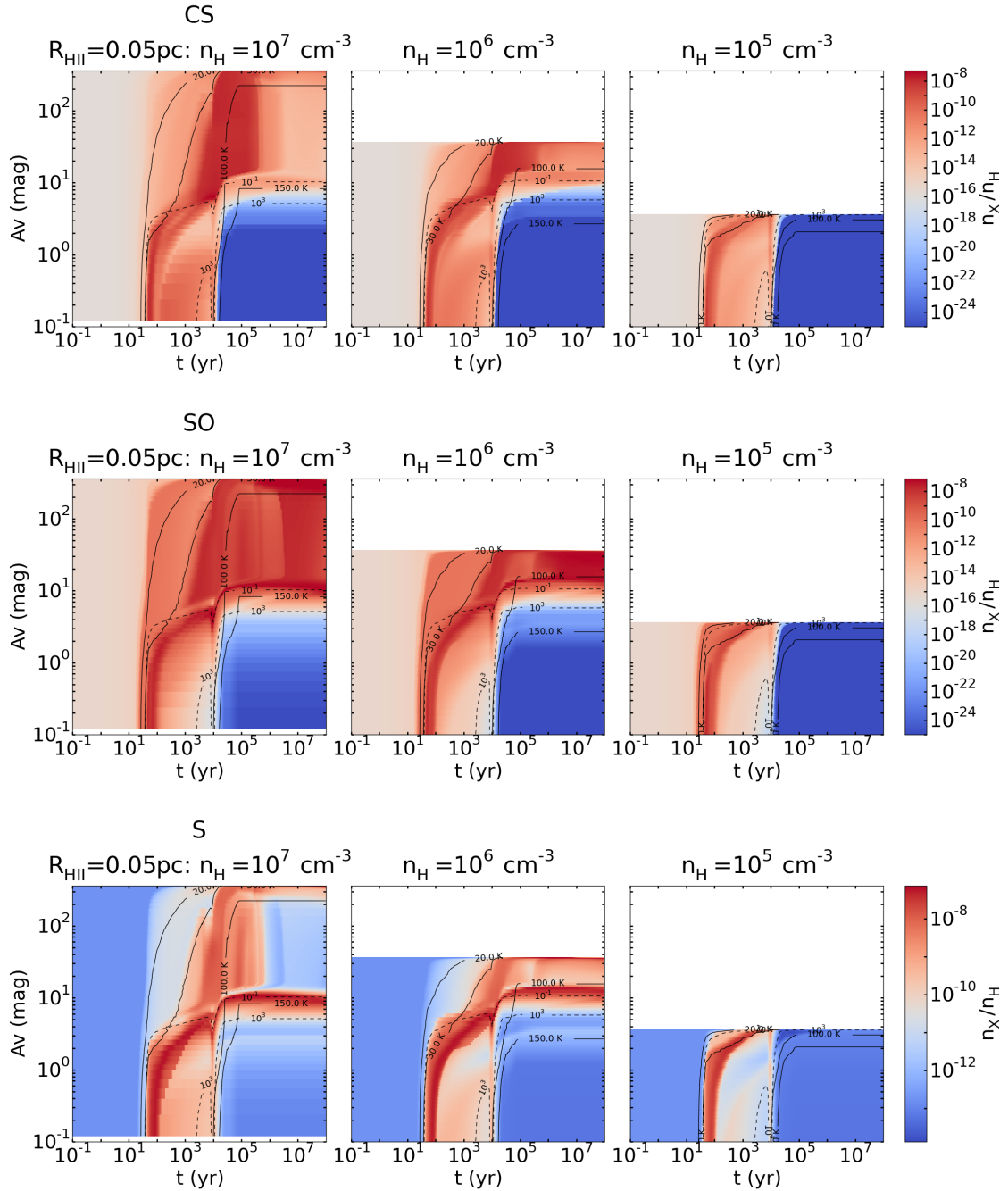
Figure B.12: Abundances of CS, SO and S in function of time (x-axis) and visual extinction (y-axis) for HII region models with different densities at the ionization front: 10^7 cm^{-3} (left), 10^6 cm^{-3} (middle) and 10^5 cm^{-3} (right). The solid black lines appearing on the figures represent the contours for the temperature: 20, 30, 100 and 150 K and the dashed black lines represent some contours for the radiation field intensity: 10^{-1} and 10^3 Draine unit.
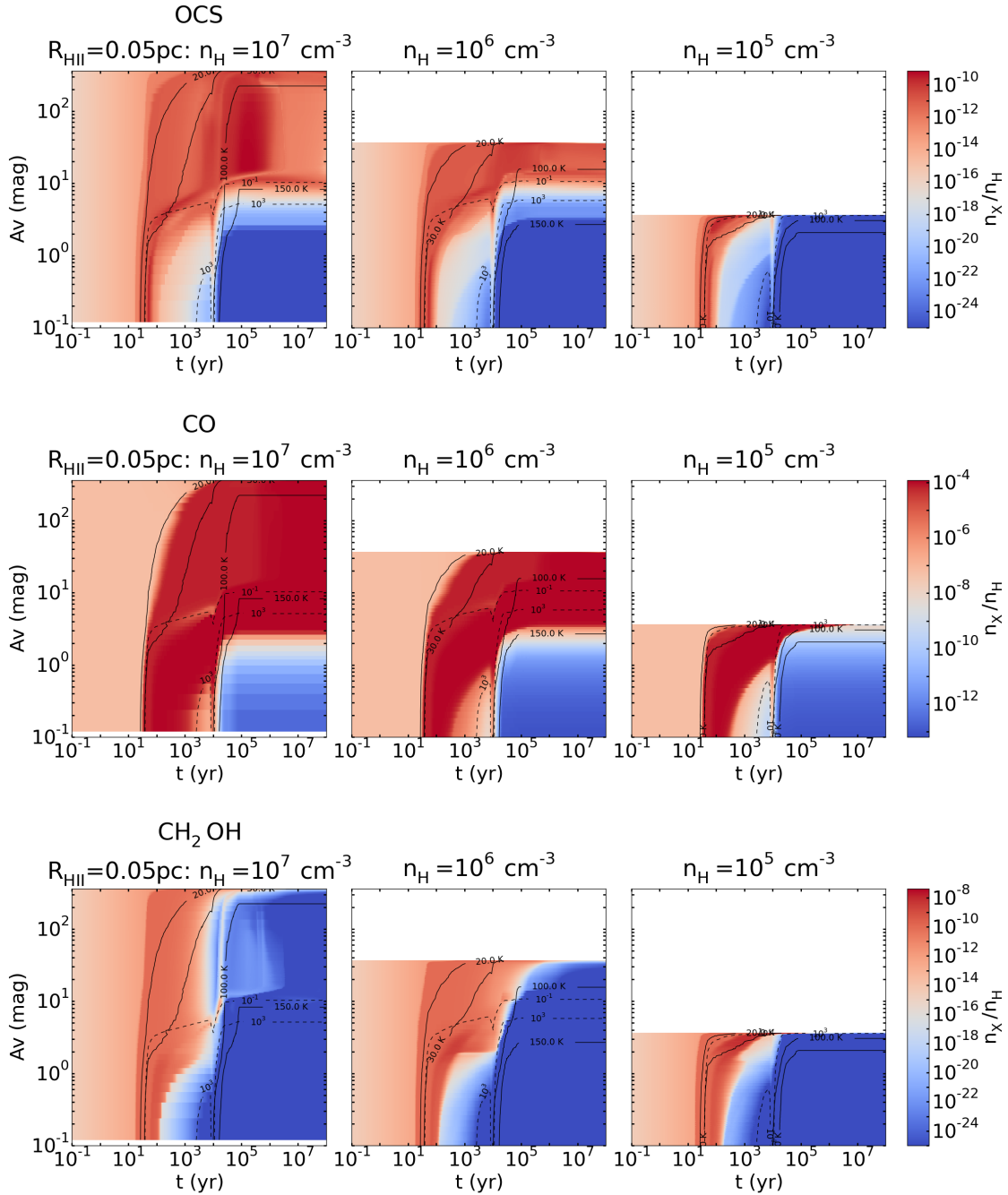
Figure B.13: Abundances of OCS, CO and CH$_2$OH in function of time (x-axis) and visual extinction (y-axis) for HII region models with different densities at the ionization front: 10^7 cm^{-3} (left), 10^6 cm^{-3} (middle) and 10^5 cm^{-3} (right). The solid black lines appearing on the figures represent the contours for the temperature: 20, 30, 100 and 150 K and the dashed black lines represent some contours for the radiation field intensity: 10^{-1} and 10^3 Draine unit.
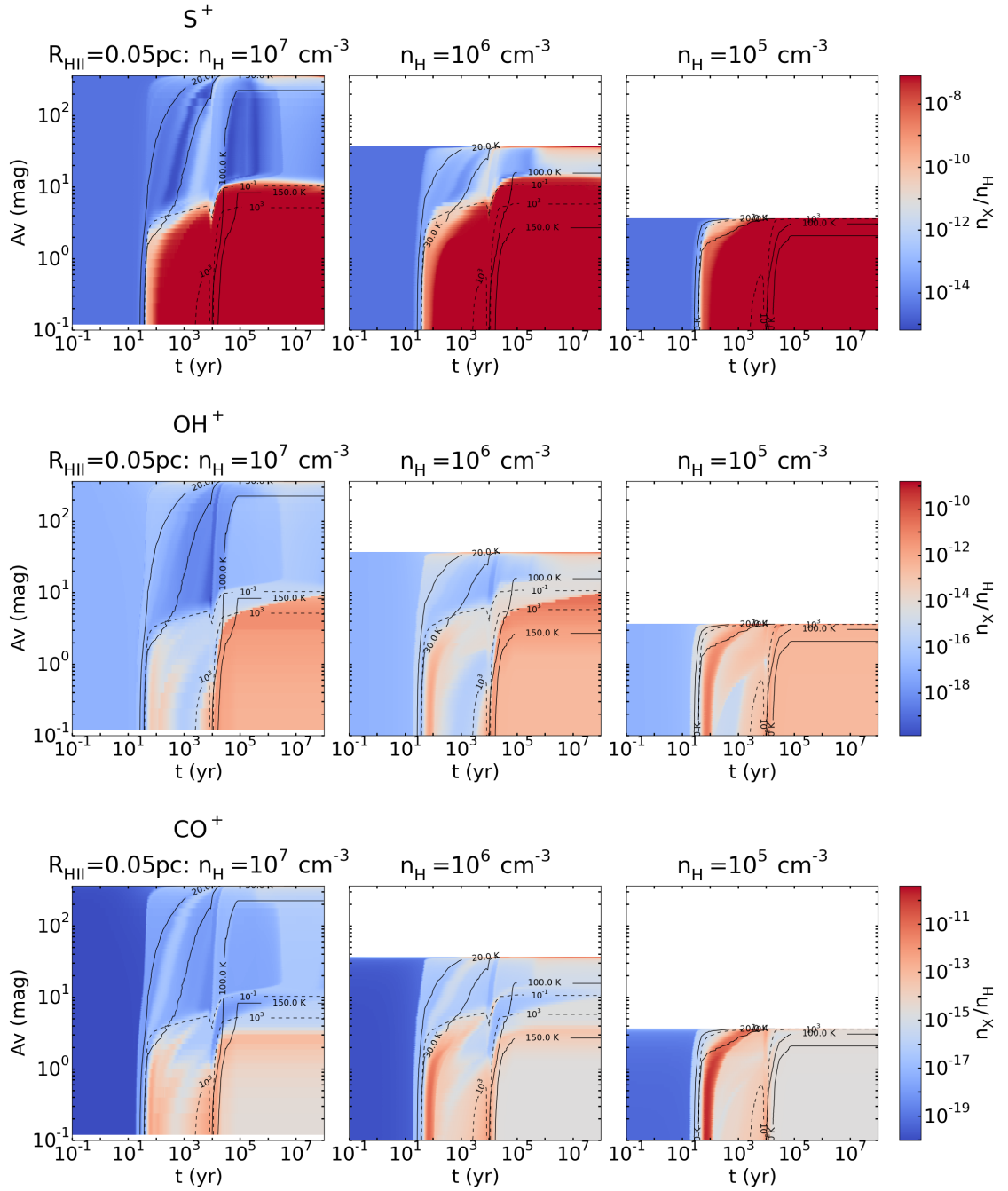
Figure B.14: Abundances of S^+, OH^+ and CO^+ in function of time (x-axis) and visual extinction (y-axis) for HII region models with different densities at the ionization front: 10^7 cm^{-3} (left), 10^6 cm^{-3} (middle) and 10^5 cm^{-3} (right). The solid black lines appearing on the figures represent the contours for the temperature: 20, 30, 100 and 150 K and the dashed black lines represent some contours for the radiation field intensity: 10^{-1} and 10^3 Draine unit.
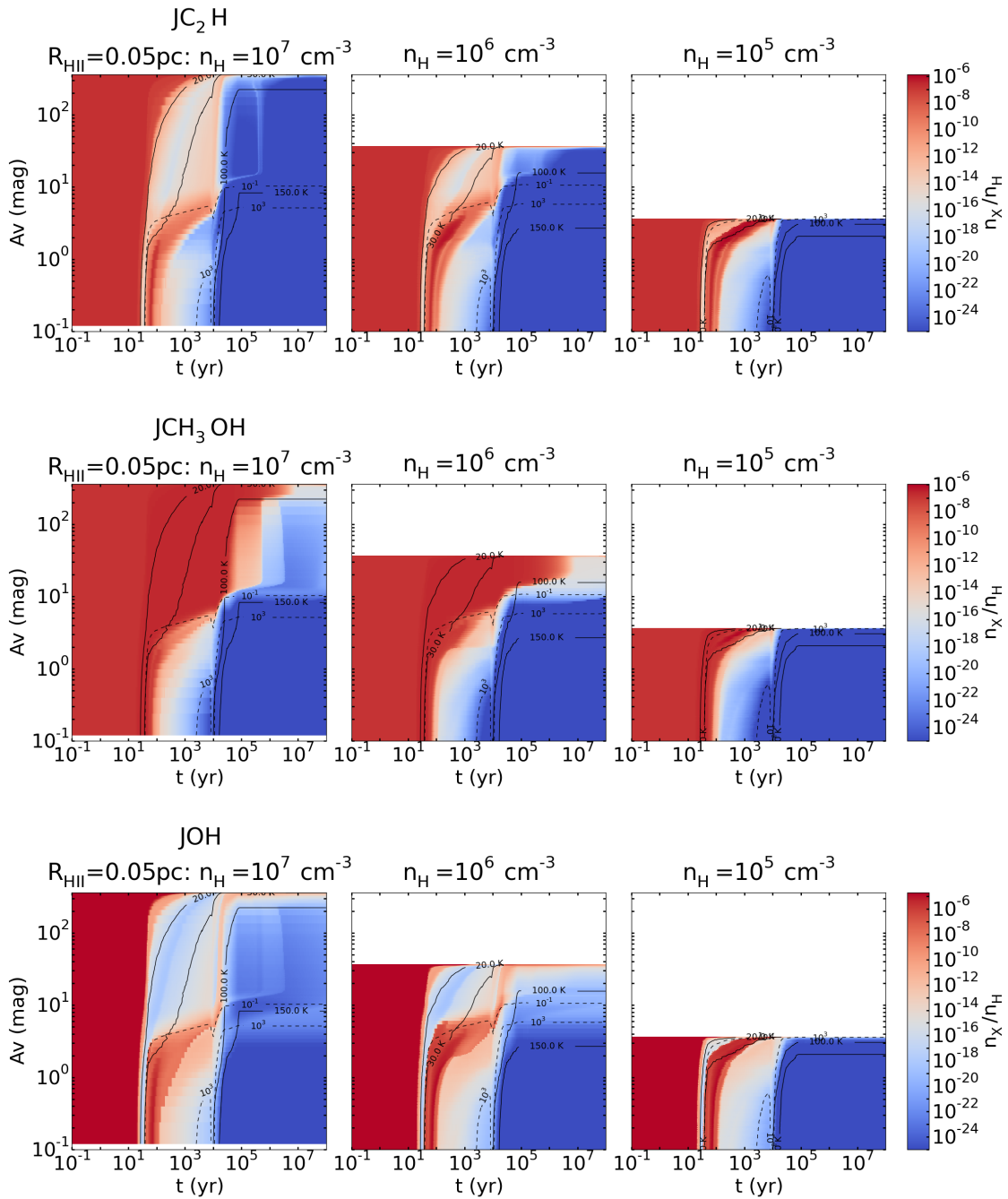
Figure B.15: Abundances of s-C$_2$H, s-CH$_3$OH and s-OH in function of time (x-axis) and visual extinction (y-axis) for HII region models with different densities at the ionization front: 10^7 cm^{-3} (left), 10^6 cm^{-3} (middle) and 10^5 cm^{-3} (right). The solid black lines appearing on the figures represent the contours for the temperature: 20, 30, 100 and 150 K and the dashed black lines represent some contours for the radiation field intensity: 10^{-1} and 10^3 Draine unit. The letter "J" in the name of the species in the title means it is a grain species.

B.4 Plummer exponent
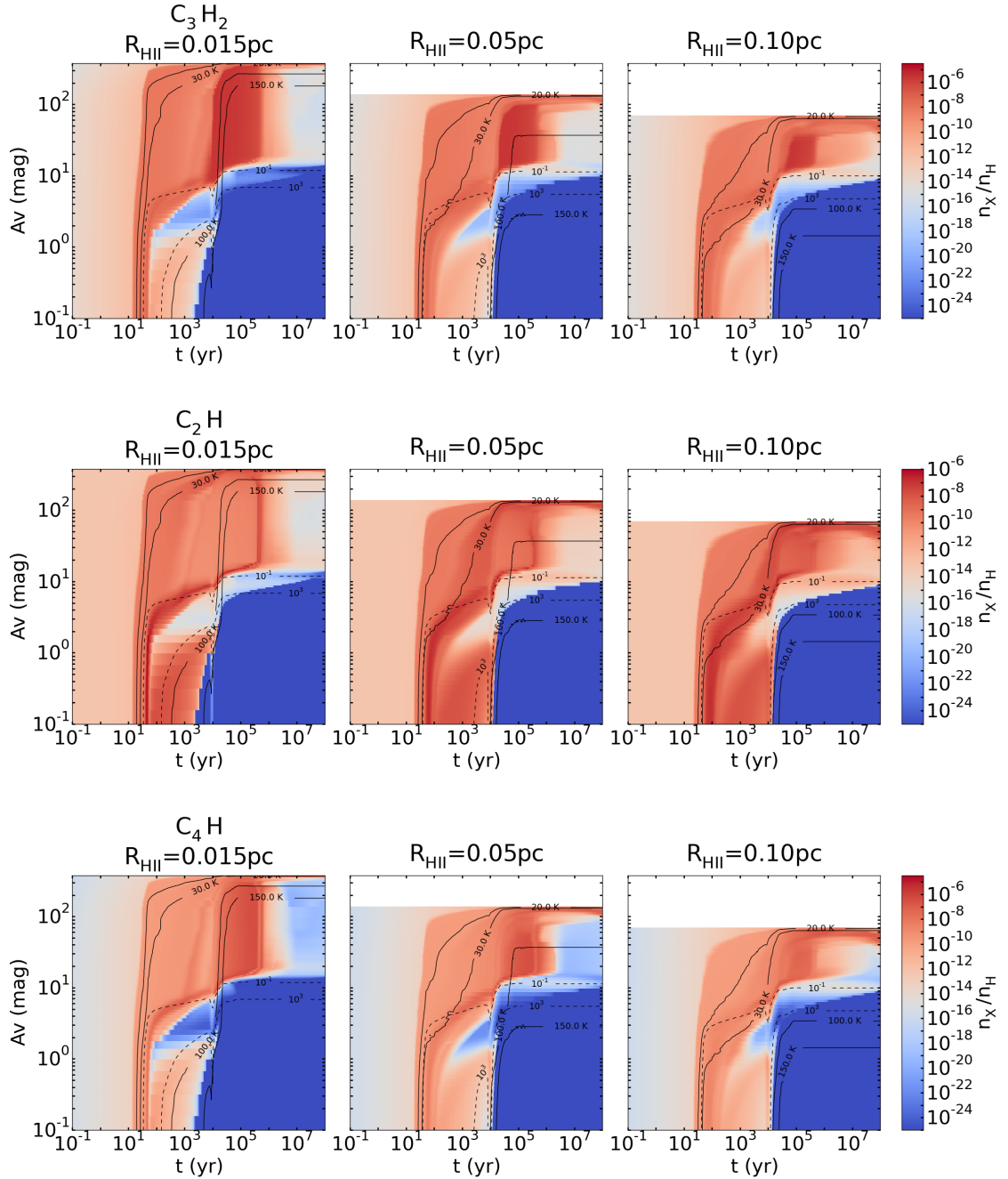
Figure B.16: Abundances of C_3H_2, C_2H and C_4H in function of time (x-axis) and visual extinction (y-axis) for HII region models using for the second density profile ($\gamma = 1$) and with different sizes of ionized cavity: 0.015 pc (left panel), 0.05 pc (middle) and 0.10 pc (right). The solid black lines appearing on the figures represent the contours for the temperature: 20, 30, 100 and 150 K and the dashed black lines represent some contours for the radiation field intensity: 10^{-1} and 10^3 Draine unit.
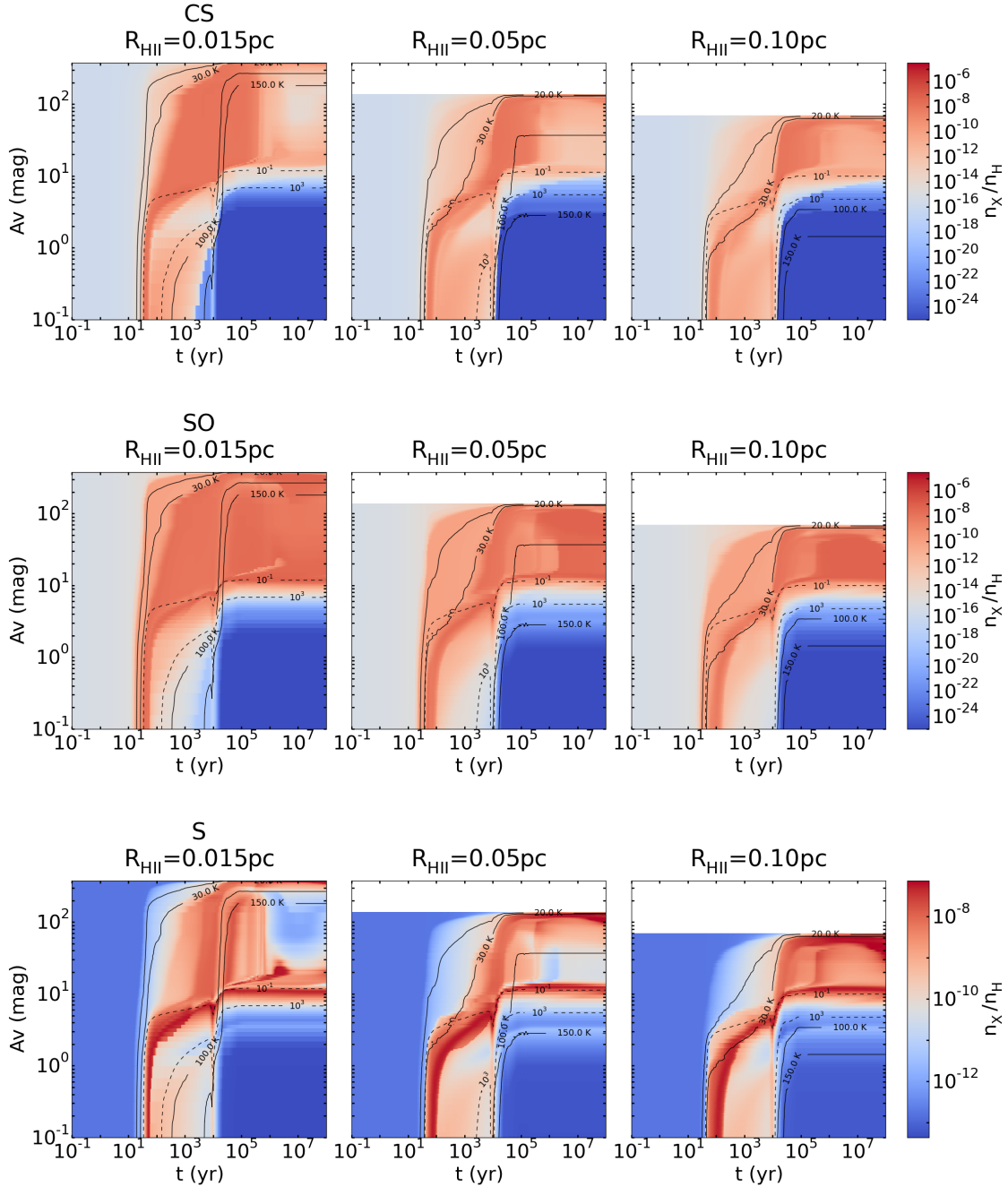
Figure B.17: Abundances of CS, SO and S in function of time (x-axis) and visual extinction (y-axis) for HII region models using for the second density profile ($\gamma = 1$) and with different sizes of ionized cavity: 0.015 pc (left panel), 0.05 pc (middle) and 0.10 pc (right). The solid black lines appearing on the figures represent the contours for the temperature: 20, 30, 100 and 150 K and the dashed black lines represent some contours for the radiation field intensity: 10^{-1} and 10^3 Draine unit.
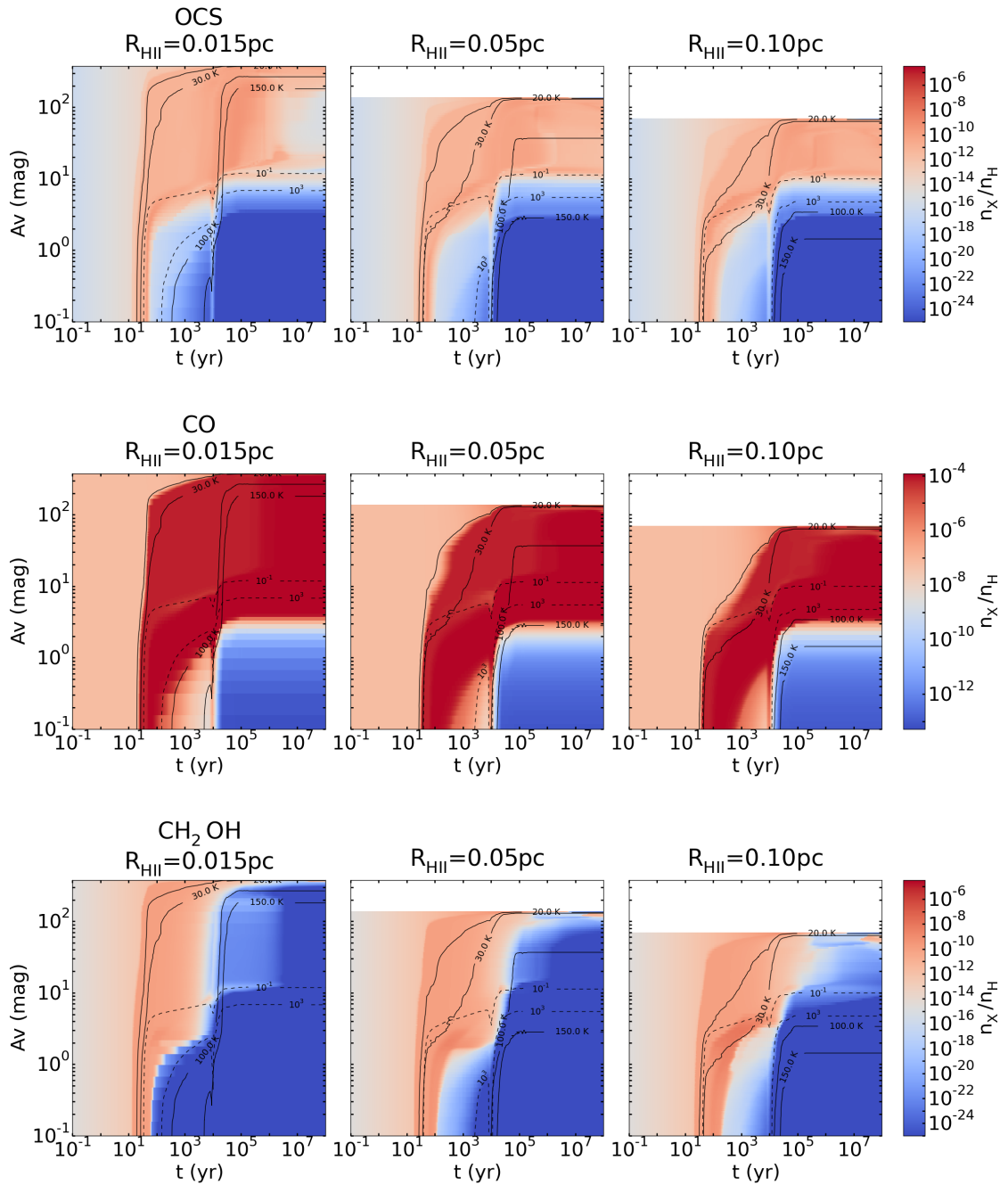
Figure B.18: Abundances of OCS, CO and CH$_2$OH in function of time (x-axis) and visual extinction (y-axis) for HII region models using for the second density profile ($\gamma = 1$) and with different sizes of ionized cavity: 0.015 pc (left panel), 0.05 pc (middle) and 0.10 pc (right). The solid black lines appearing on the figures represent the contours for the temperature: 20, 30, 100 and 150 K and the dashed black lines represent some contours for the radiation field intensity: 10^{-1} and 10^{3} Draine unit.
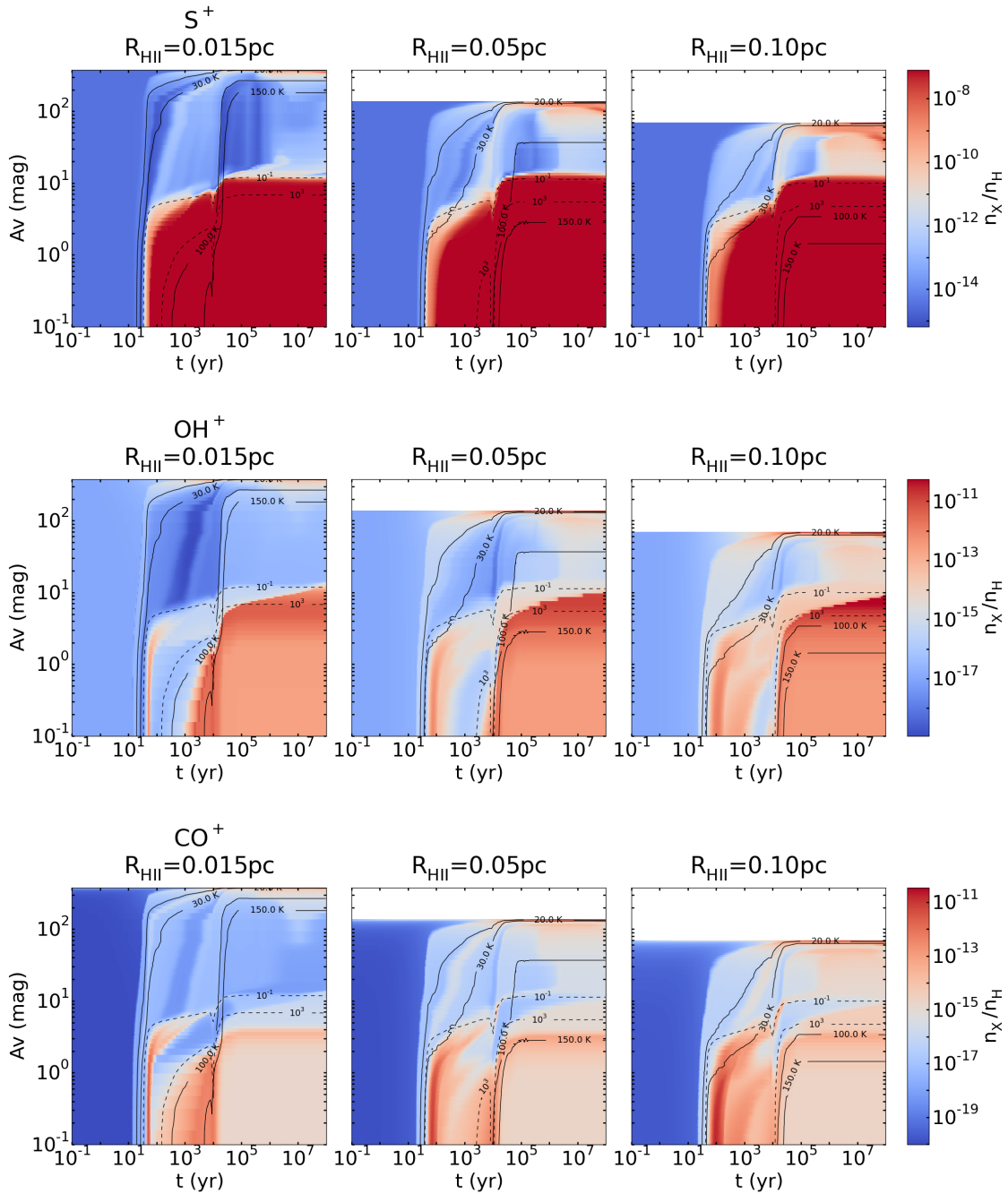
Figure B.19: Abundances of S^+, OH^+ and CO^+ in function of time (x-axis) and visual extinction (y-axis) for HII region models using for the second density profile ($\gamma = 1$) and with different sizes of ionized cavity: 0.015 pc (left panel), 0.05 pc (middle) and 0.10 pc (right). The solid black lines appearing on the figures represent the contours for the temperature: 20, 30, 100 and 150 K and the dashed black lines represent some contours for the radiation field intensity: 10^{-1} and 10^3 Draine unit.
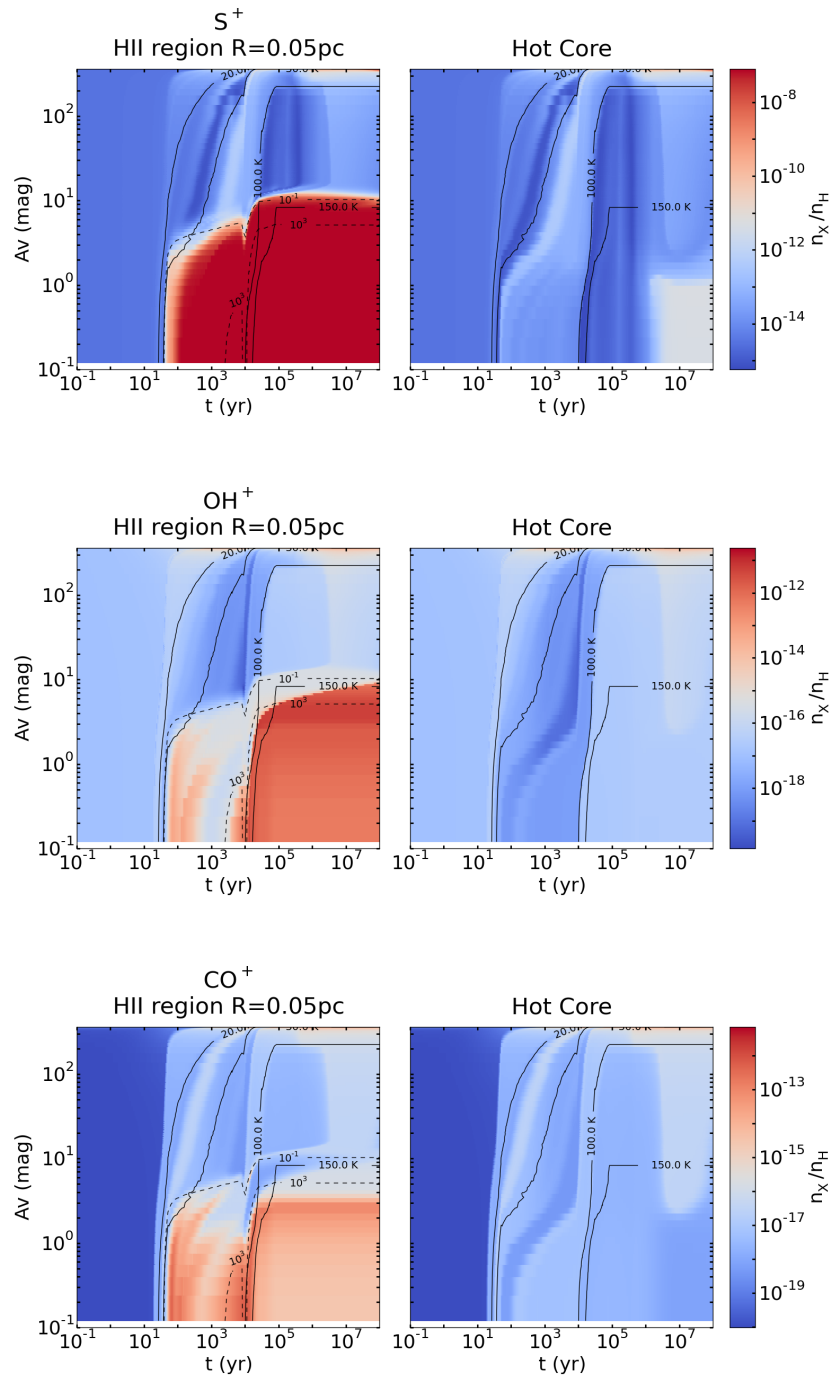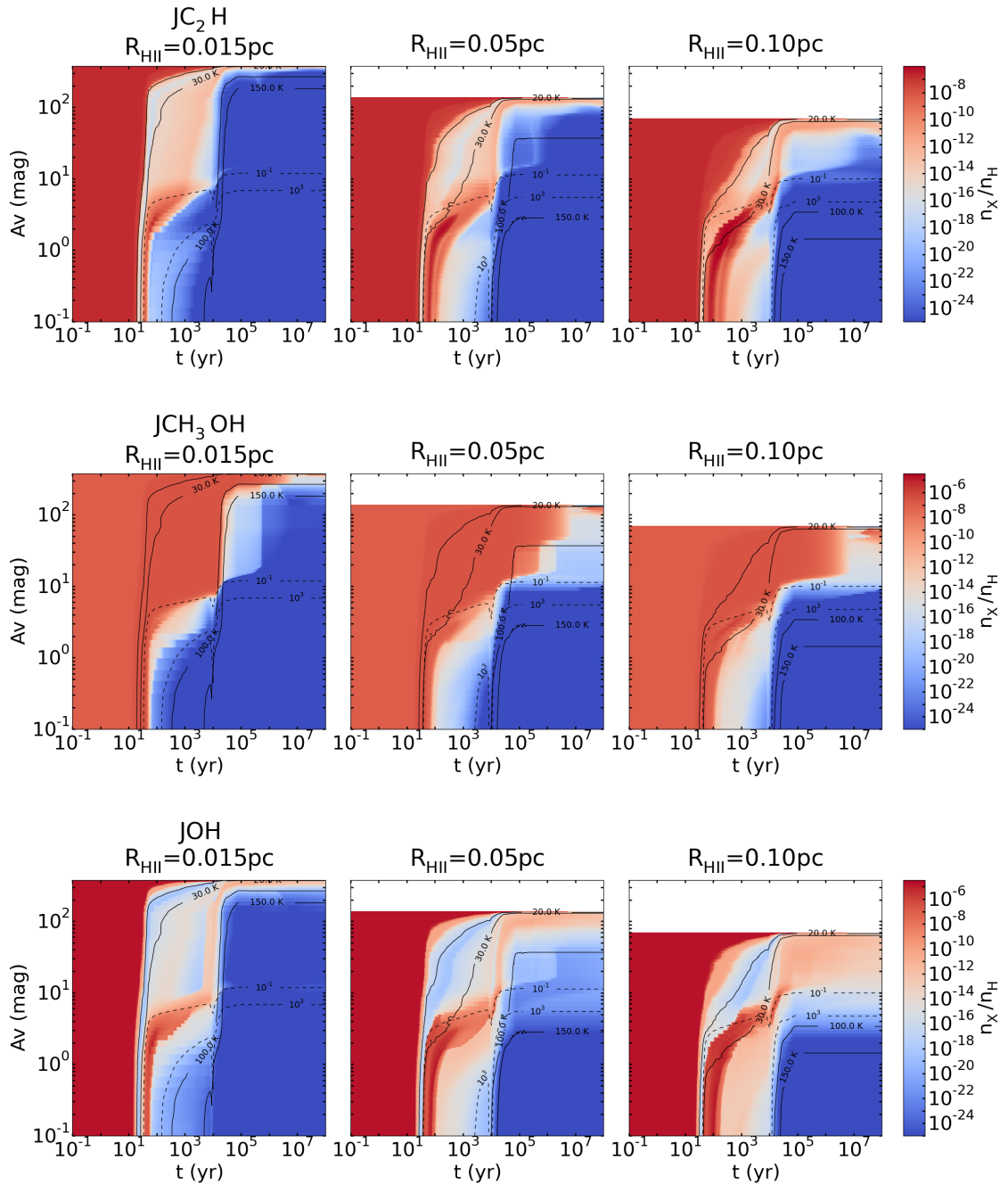
Figure B.20: Abundances of s-C_2H, s-CH_3OH and s-OH in function of time (x-axis) and visual extinction (y-axis) for HII region models using for the second density profile ($\gamma = 1$) and with different sizes of ionized cavity: 0.015 pc (left panel), 0.05 pc (middle) and 0.10 pc (right). The solid black lines appearing on the figures represent the contours for the temperature: 20, 30, 100 and 150 K and the dashed black lines represent some contours for the ra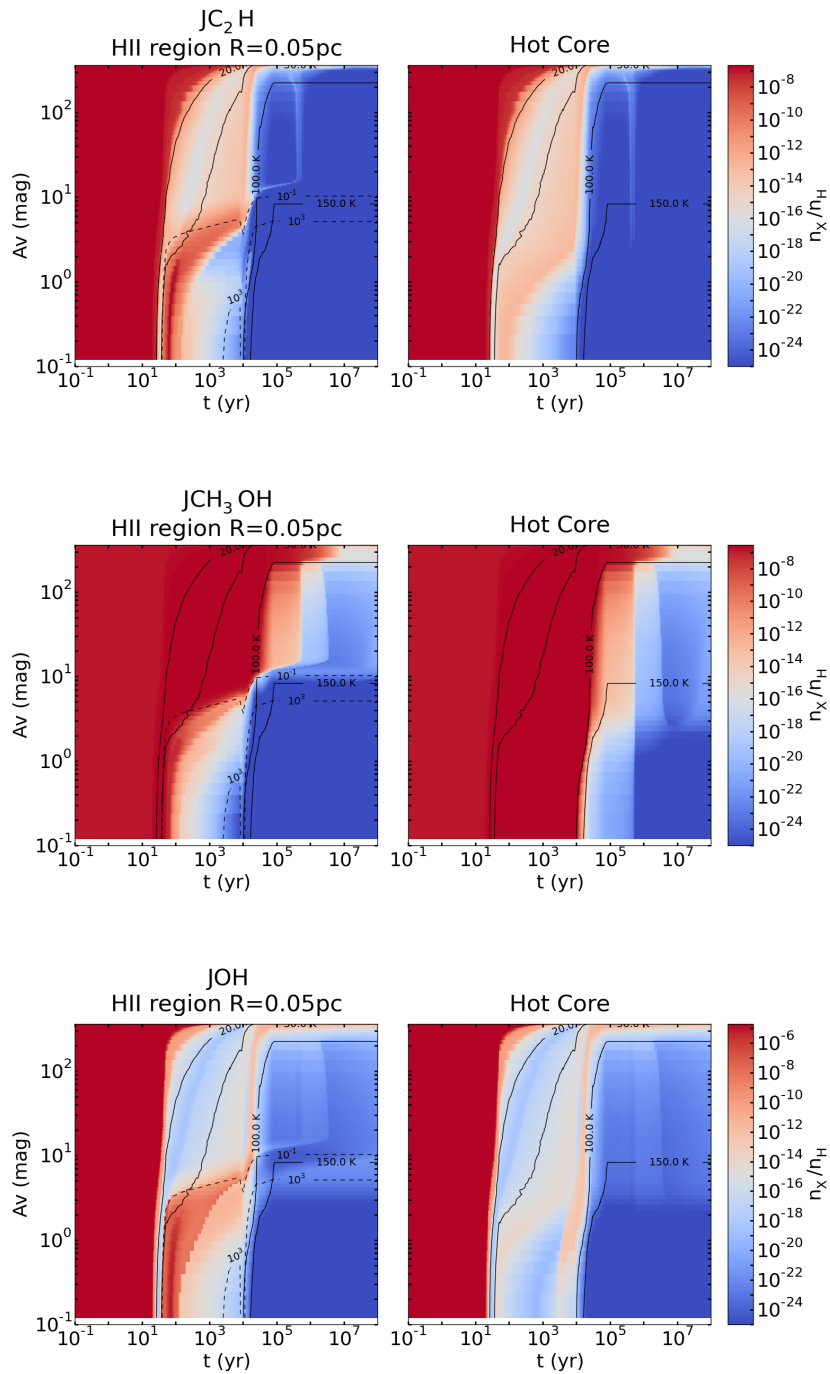diation field intensity: 10^{-1} and 10^3 Draine unit. The letter "J" in the name of the species in the title means it is a grain species.
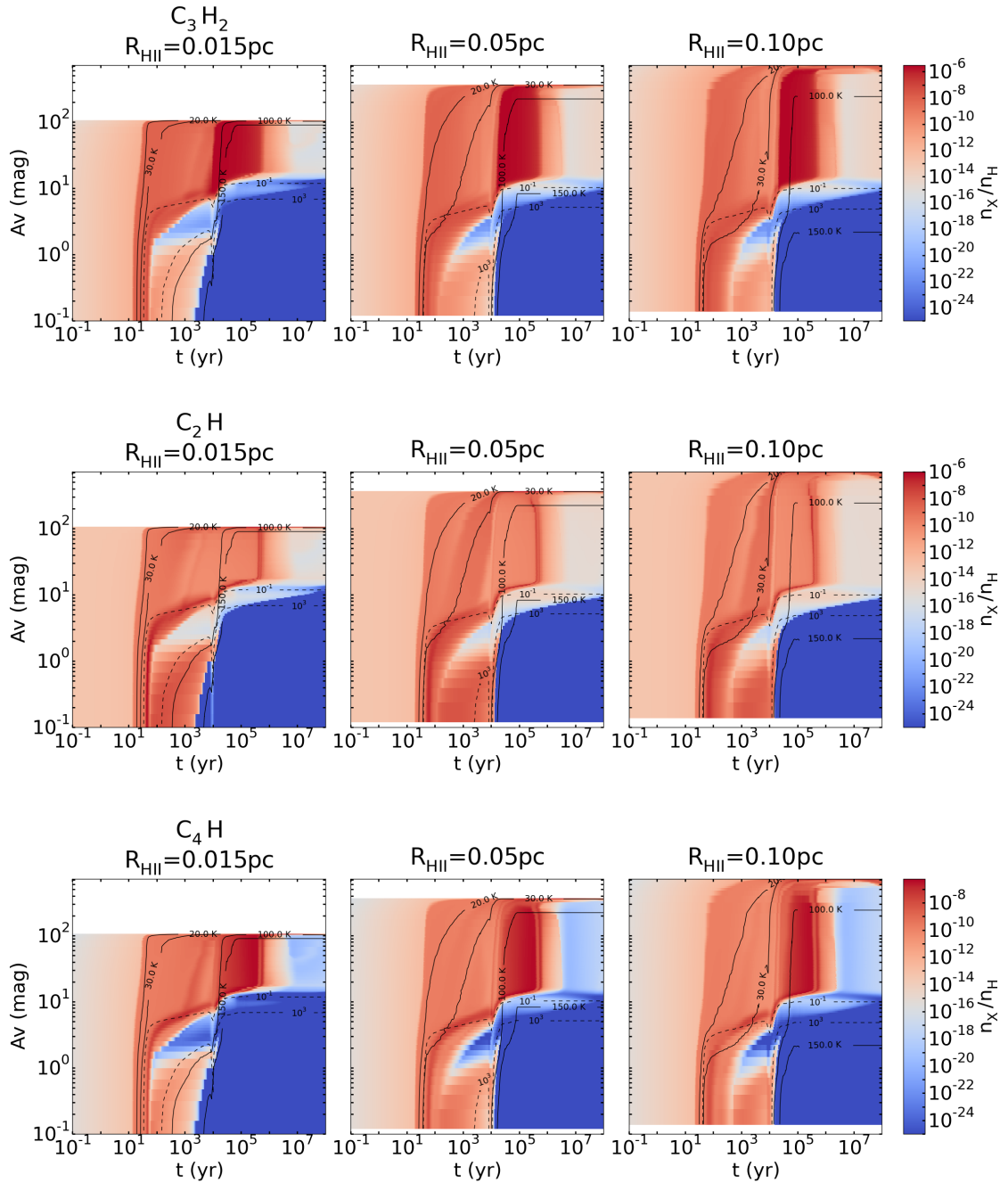
B.5   Initial abundances
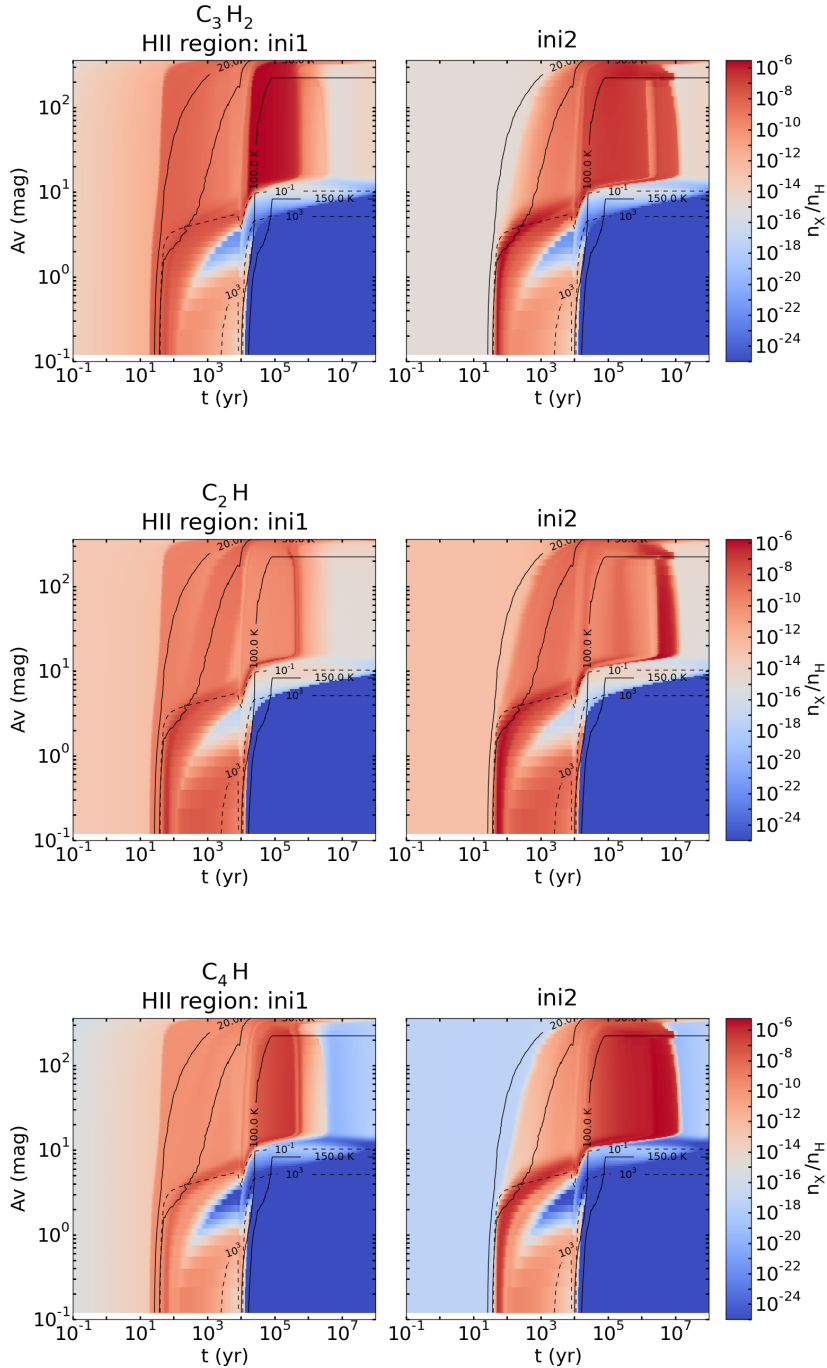
Figure B.21: Abundances of C_3H_2, C_2H and C_4H in function of time (x-axis) and visual extinction (y-axis) for HII region with different initial abundances: *ini1* (left panel) and *ini2* (right). The solid black lines appearing on the figures represent the contours for the temperature: 20, 30, 100 and 150 K and the dashed black lines represent some contours for the radiation field intensity: 10^{-1} and 10^3 Draine unit.
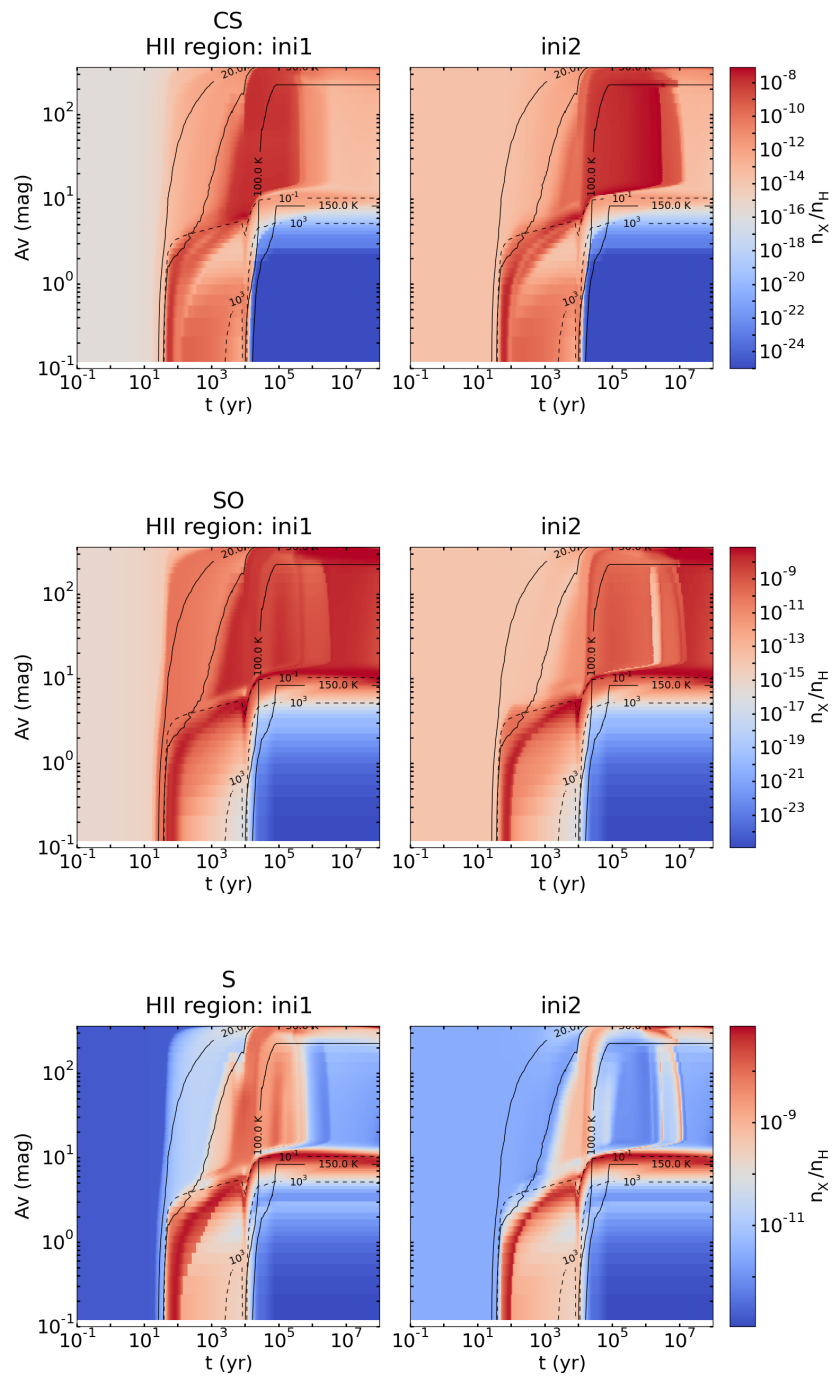
Figure B.22: Abundances of CS, SO and S in function of time (x-axis) and visual extinction (y-axis) for HII region with different initial abundances: *ini1* (left panel) and *ini2* (right). The solid black lines appearing on the figures represent the contours for the temperature: 20, 30, 100 and 150 K and the dashed black lines represent some contours for the radiation field intensity: 10^{-1} and 10^3 Draine unit.
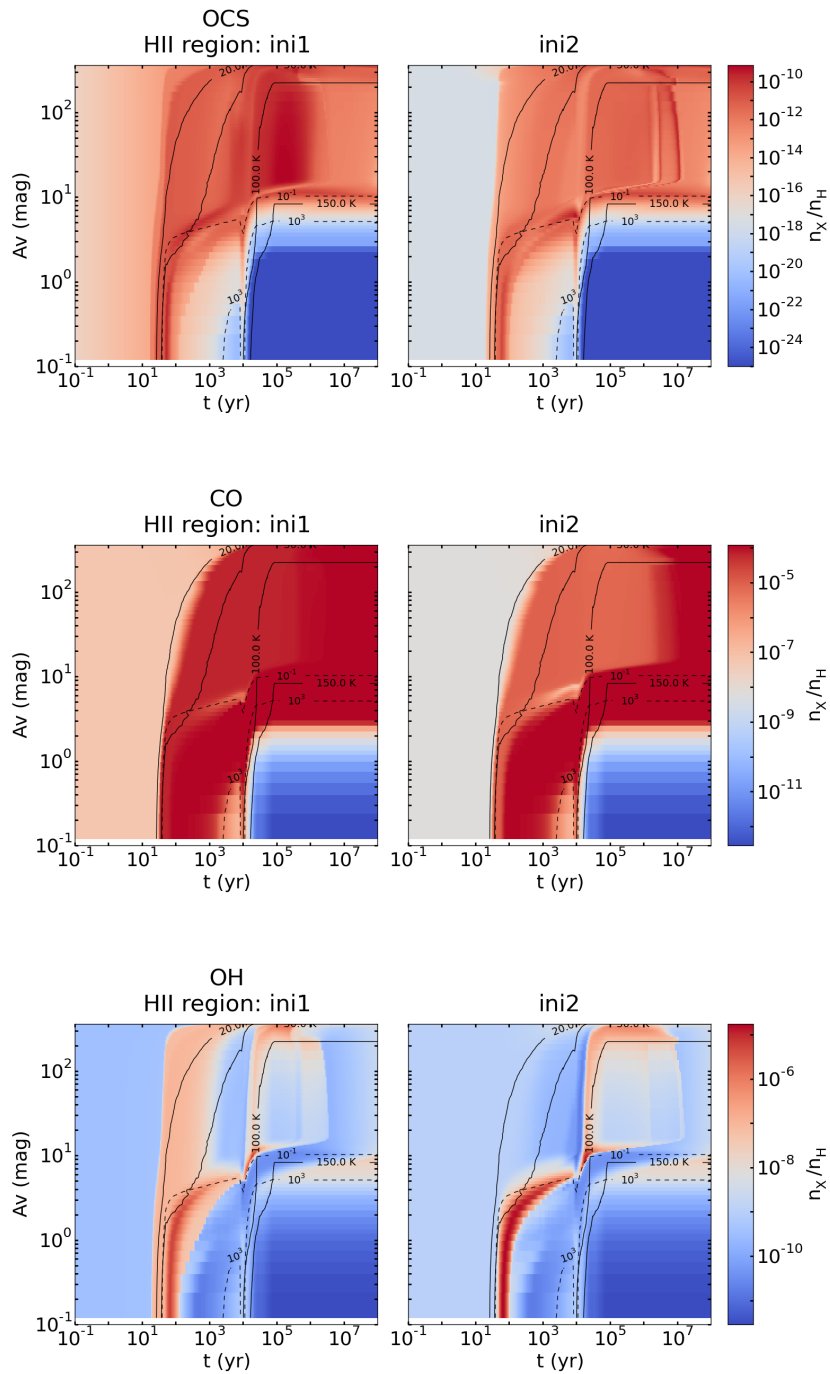
Figure B.23: Abundances of OCS, CO and OH in function of time (x-axis) and visual extinction (y-axis) for HII region with different initial abundances: *ini1* (left panel) and *ini2* (right). The solid black lines appearing on the figures represent the contours for the temperature: 20, 30, 100 and 150 K and the dashed black lines represent some contours for the radiation field intensity: 10^{-1} and 10^3 Draine unit.
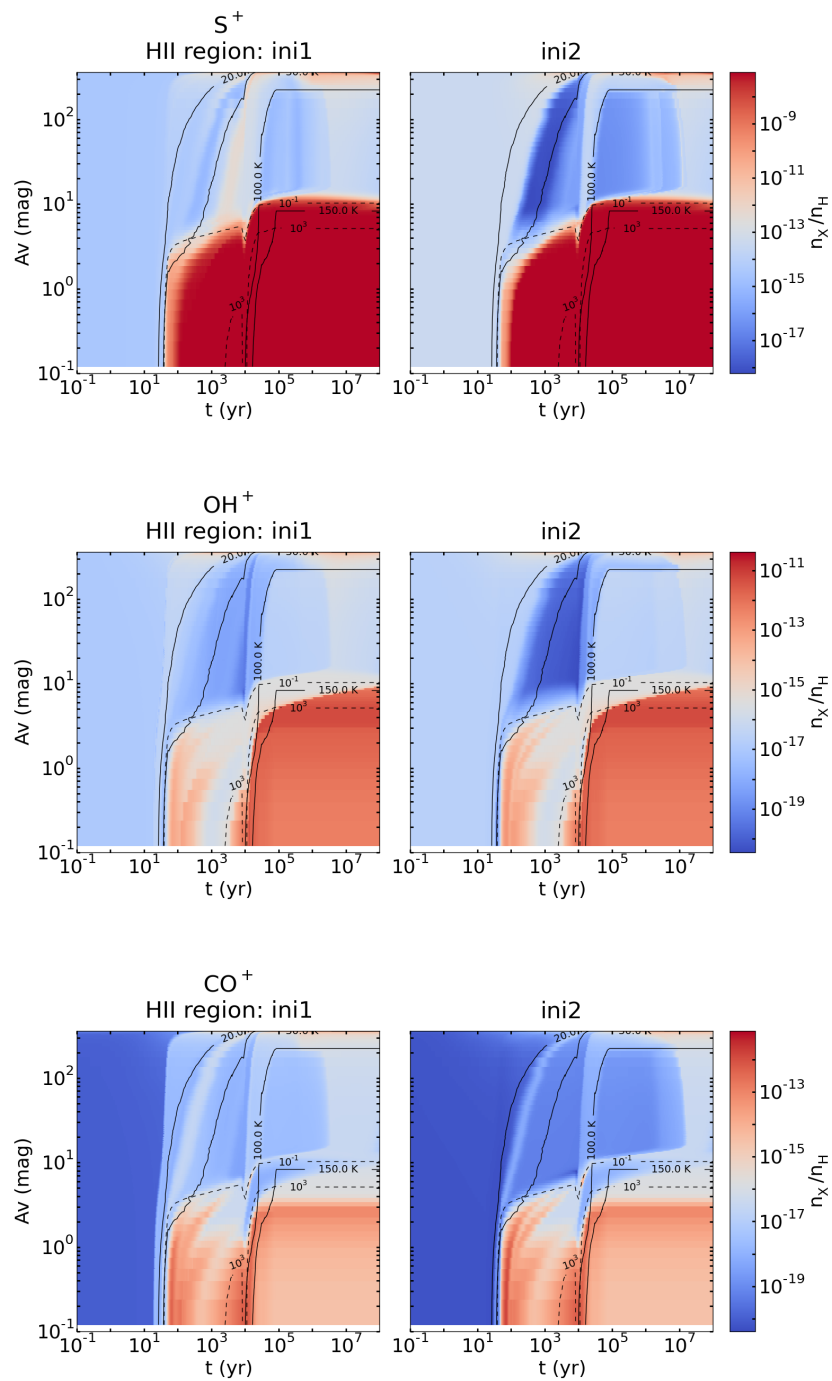
Figure B.24: Abundances of S$^+$, OH$^+$ and CO$^+$ in function of time (x-axis) and visual extinction (y-axis) for HII region with different initial abundances: *ini1* (left panel) and *ini2* (right). The solid black lines appearing on the figures represent the contours for the temperature: 20, 30, 100 and 150 K and the dashed black lines represent some contours for the radiation field intensity: 10^{-1} and 10^3 Draine unit.
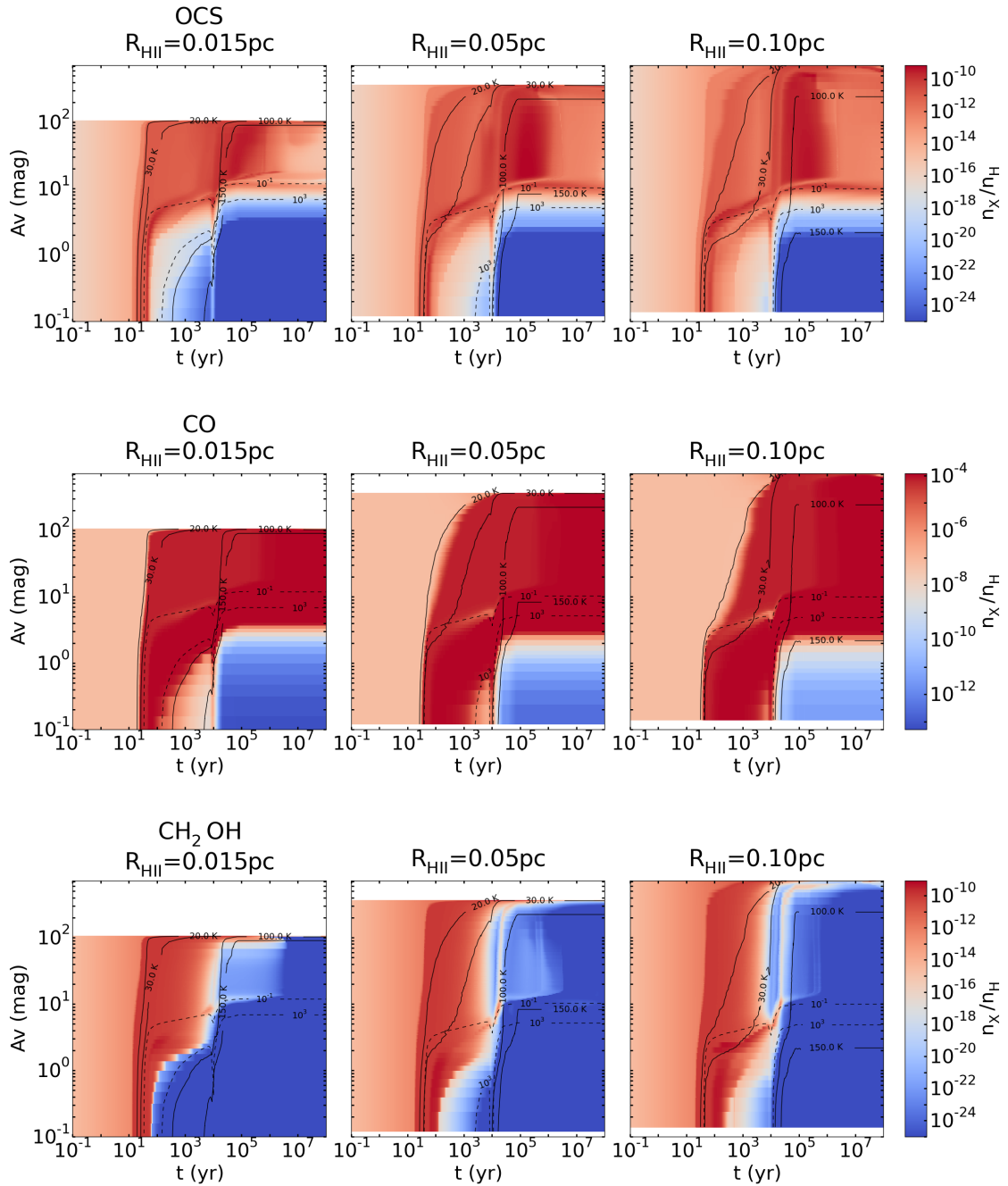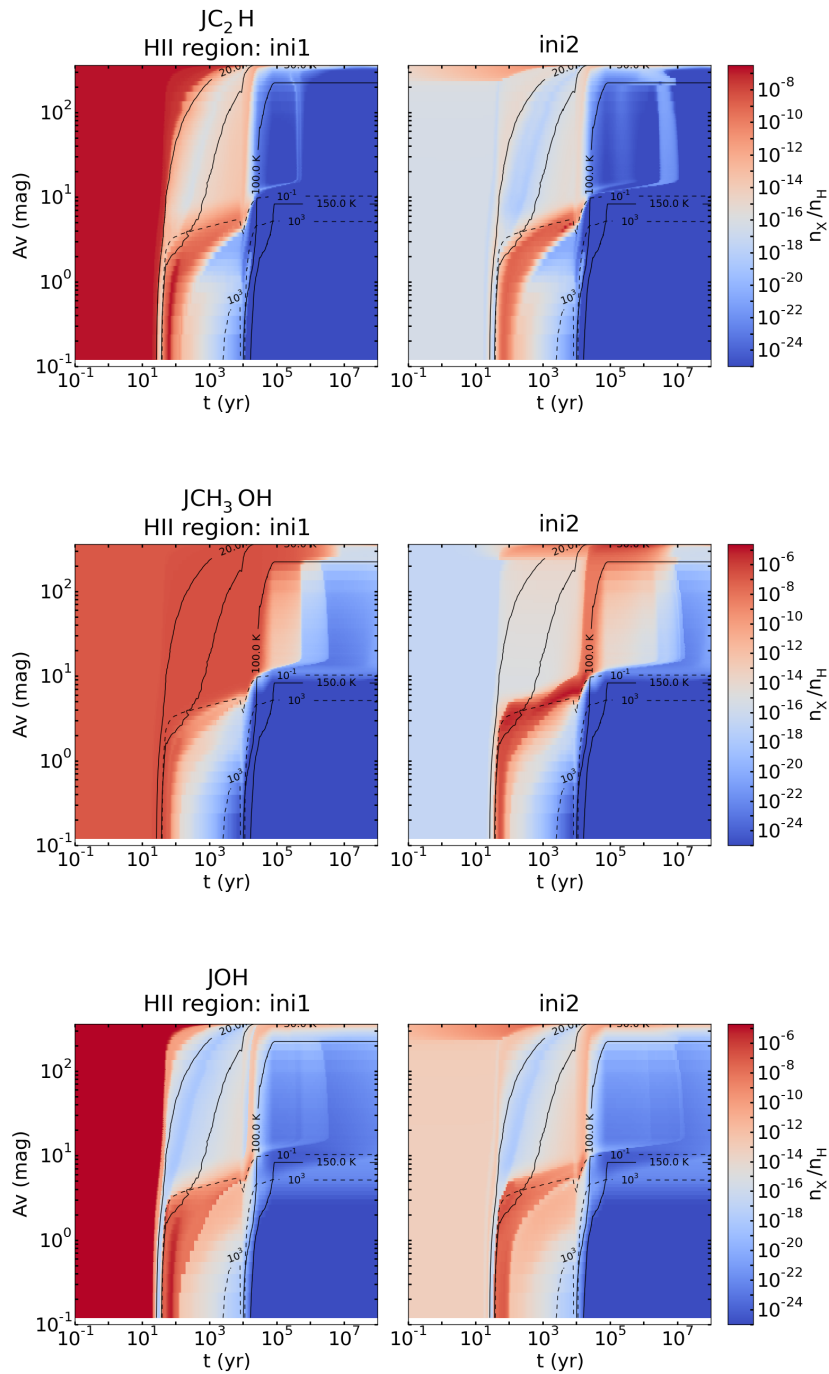
Figure B.25: Abundances of s-C$_2$H, s-CH$_3$OH and s-OH in function of time (x-axis) and visual extinction (y-axis) for HII region with different initial abundances: *ini1* (left panel) and *ini2* (right). The solid black lines appearing on the figures represent the contours for the temperature: 20, 30, 100 and 150 K and the dashed black lines represent some contours for the radiation field 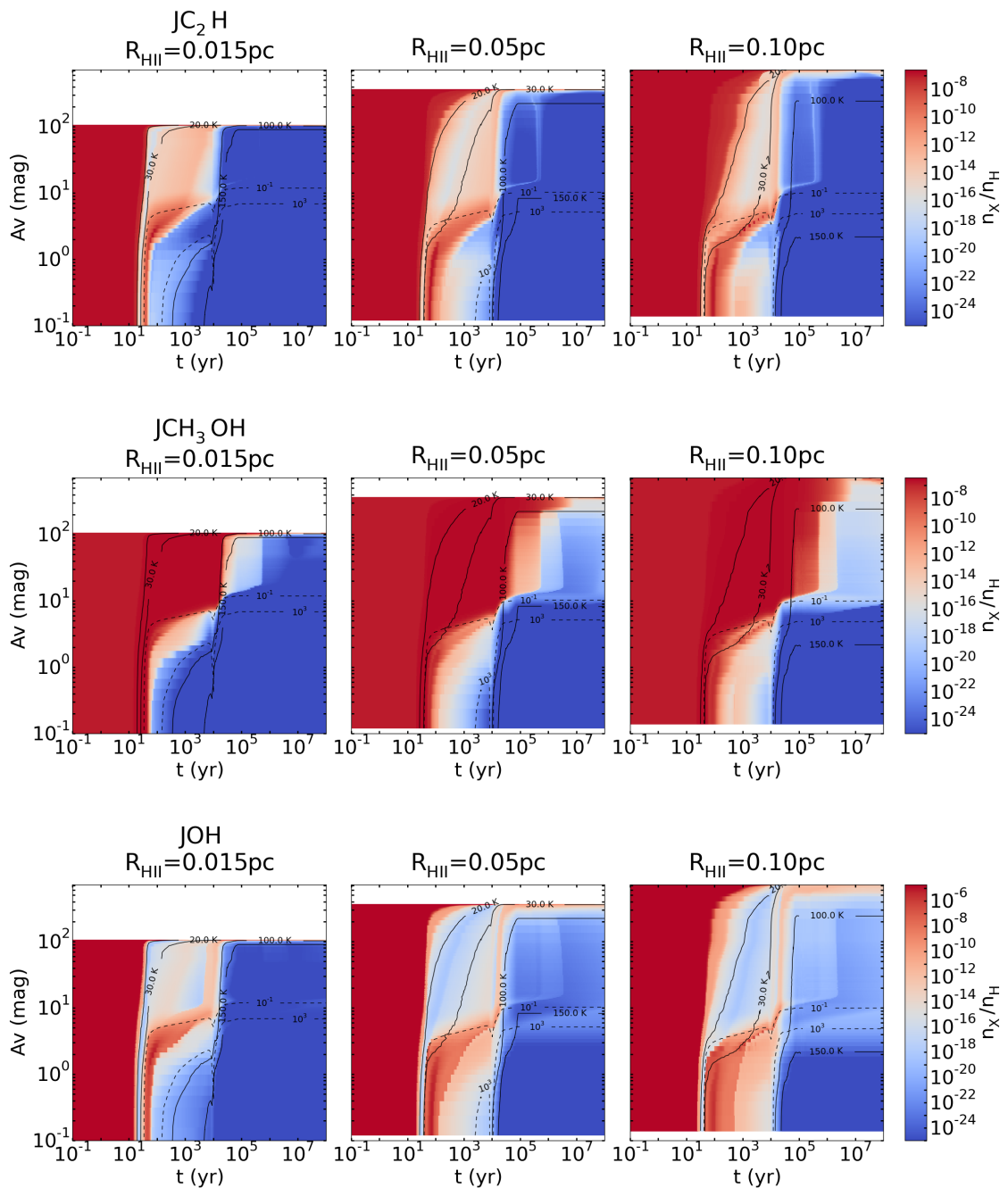intensity: 10^{-1} and 10^3 Draine unit. The letter "J" in the name of the species in the title means it is a grain species.

C

Dust spectral index in Sgr B2(N)

Contents

Beside this main project reported in this thesis, we have worked on another project in collaboration with Prof. Dr. Edwin Bergin and in continuation of the work conducted by Dr. Justin Neill. This appendix presents the big lines of this project consisting on the determination of the dust spectral index in the hot molecular core Sgr B2(N) via the analysis of CH$_3$OH lines with two independent methods. The following text is a part of the article *Stéphan, Bergin, Schilke et al.* in preparation.

C.1 Introduction

Dust emission at millimeter, sub-millimeter and far-infrared wavelengths is widely used as a probe of the physical structure of the dense ISM. Dust plays an important role in the galactic energy re-distribution as stellar photons are attenuated and then re-emitted by grains ($\sim 30\%$ in the IR, see Bernstein et al. 2002). In this regard, observations of

thermal dust emission and its spectral energy distribution (SED) set useful constraints on different properties of the dense ($n > 100$ cm^{-3}) interstellar medium, such as its column density, its mass, and its temperature (Savage & Mathis 1979; Hildebrand 1983; Chini et al. 1986; Lis 2000).

Furthermore, properties of interstellar dust (structure, morphology, composition, size distribution), which are the precursors to solar system solids, can be deduced by both absorption and emission (Draine & Li 2007; Draine 2003). For low frequency ranges (far-IR, sub-mm) the overall dust SED of star-forming molecular gas is often well fit by two modified black bodies, one for the cold outer envelope and another sampling warmer material closer to the star (Adams et al. 1987; Molinari et al. 2008). From these types of analysis the radial (line of sight) physical structure of star forming regions is often reconstructed with critical assumptions regarding dust properties. More specifically, the determination of the dust density and temperature structure relies on its overall wavelength-dependent properties which can be related to a gas physical structure assuming a dust-to-gas mass ratio and thermal coupling (e.g., van der Tak et al. 2000b). These dust-derived physical structures have been an important astrophysical tool and can be compared to models of dense molecular core collapse and star formation (e.g, Larson 1969; Shu 1977; Krumholz 2006, 2008) and also used to explore chemical gradients (Viti & Williams 1999; van der Tak et al. 2000a; Bergin & Tafalla 2007).

To extract this information requires knowledge of key quantities specific to interstellar grains such as the wavelength dependent mass opacity and its spectral index ($\kappa(\lambda) \propto \lambda^{\beta}$). This can be determined in two ways – first models of analog interstellar grains (Draine & Lee 1984; Ossenkopf & Henning 1994; Stognienko et al. 1995) set limits on expected values; as one example, $\kappa^{OH5}_{850}\mu$m $= (0.65 - 0.97)$ and $\beta_{OH5} = 1.85$ obtained from the coagulated ice grains model of Ossenkopf & Henning (1994). Alternately one might attempt to derive these quantities from the dust absorption/emission by comparing, for instance, the dust emission at sub-mm wavelengths to the dust extinction in the IR. These studies find a best fit $\beta \geq 2$ (Kramer et al. 2003; Bianchi et al. 2003; Shirley et al. 2011) The dust spectral emissivity index is also constrained using a modified black body to match the spectral emissions:

$$I_{\nu}(\lambda) \propto \epsilon_0 \left(\frac{\lambda}{\lambda_0}\right)^{-\beta} B_{\nu}(\lambda, T_{\mathrm{d}})$$

where I is the intensity, ϵ_0 the emissivity, B$_{\nu}$ the Planck function at a wavelength λ and a dust temperature T_{d}.

Herschel observations in several wide fields find median value of the spectral index of $\sim$ 2.3 between 100 μm and 500 μm (Paradis et al. 2010), with a range of studies estimating values between 2 and 3 for the dense molecular medium (Goldsmith et al. 1997; Paradis et al. 2009) and near unity for young disk systems implying dust growth and evolution (Beckwith & Sargent 1991; Beckwith et al. 1990; Adams et al. 1990; Andre et al. 1990).

Most estimates of grain properties arise from observations of the dust itself. We provide here an independent method to explore the question of the dust spectral index using the emission of methanol in Sgr B2 cloud and principally in its north region Sgr B2(N). This cloud, situated approximately at a projected distance of 120 pc from the center of our galaxy, is one of the most massive star-forming region in the Milky Way with a mass of about 10^7 M$_\odot$ (Lis & Goldsmith 1989,1990). The Sgr B2(N) region itself inferred to be a forming cluster of massive stars surrounded by a dense heated envelope of molecular gas

which also exhibits the richest chemical inventory seen in the galaxy (Snyder et al. 1994; Mehringer et al. 1997; Neill et al. 2014). The Kuan, Mehringer, & Snyder (1996) study of Sgr B2(N) at 3 mm shows that the region is dominated by thermal dust emission deduced from a very high dust spectral index $\beta = 3.7 \pm 0.7$ which could also be an evidence of ice-coated core-mantle grains.

Methanol has thousands of emission lines spanning from low mm-wave frequencies (tens to hundreds of GHz) to the sub-mm (THz). In Sgr B2, and other galactic hot cores, the methanol emission dominates the emission from the hot molecular gas that resides in close proximity to young embedded protostars (so called hot cores). The hot core CH_3OH emission passes through a massive dust rich envelope resulting in differential absorption from low to high frequency thereby bearing direct information on the dust spectral index. Previous estimates of the spectral index relied on dust emission itself and this new method provides a completely independent measurement of dust properties.

C.2   Data

Sgr B2(N) has been observed with the Herschel Space Observatory as part of the Heterodyne Instrument for the Far Infrared (HIFI[1]) spectral survey (Neill et al. 2014). Observations were centered on the following position $\alpha_{J2000} = 17^h47^m19^s.88$ and $\delta_{J2000} = -28^o22'18''.4$ with an assumed error of $2''$. They were carried out with the two Wide Band Spectrometers (WBSs) with a spectral resolution of 1.1 MHz. Thus both polarizations were used to get the spectra which were collected in dual beam switch mode, with reference beams $3'$ to the east and west of the science target. Each frequency was measured with eight local oscillator (LO) settings for bands 1 to 5 and with four for bands 6 and 7. As HIFI is a double-sideband spectrometer, each channel needs to be measured with multiple LO settings. The seven bands, whose parameters are described in Tab. C.1 covering the full HIFI frequency range, are used in this work. For our analysis we target Q-branch methanol bands and the individual optically thick lines that are spread throughout the HIFI spectral range.

The data reduction was performed with the Herschel Interactive Processing Environment (HIPE, Ott 2010) using the HIPE pipeline Level 2 (for details see Bergin et al. 2010; Crockett et al. 2010; Neill et al. 2014). At the end, two types of spectra were produced: the ones with continuum and those without. The latter were used to model emission lines and the others for absorption lines modeling. The continuum was fit with a low-order polynomial, saved and then removed from the scans, along with strongest lines (to avoid ghost features). The spectra were then deconvolved with and the strong lines and continuum placed back into the spectra.

---

[1]HIFI is the first high spectral resolution instrument (it is a spectrometer) from the far-infrared to sub-millimeter wavelength regimes with no gaps imposed by atmospheric windows. It covers the spectral ranges: $480 - 1250$ and $1410 - 1910$ GHz.

Table C.1: Sgr B2(N) spectral survey: Observed bands, their frequency range and observation parameters.

Band	Frequency range (GHz)	Observation ID	Date	η_A	RMS (T_A, K)	Beamwidth ($''$)
1a	479.5 – 561.1	1342205491	22 Sept 2010	0.68	0.015	41
1b	554.5 – 636.5	1342206364	12 Oct 2010	0.67	0.02	36
2a	626.1 – 726.0	1342204703	15 Sept 2010	0.67	0.025	31
2b	714.1 – 801.2	1342204812	17 Sept 2010	0.67	0.03	28
3a	799.1 – 860.0	1342204731	16 Sept 2010	0.67	0.04	26
3b	858.1 – 961.0	1342204829	17 Sept 2010	0.67	0.05	23
4a	949.1 – 1061.0	1342218198	07 Apr 2011	0.66	0.09	21
4b	1050.3 – 1122.0	1342206370	12 Oct 2010	0.66	0.06	20
5a	1108.2 – 1242.8	1342205855	05 Oct 2010	0.56	0.2	18
5b	1227.2 – 1280.0	1342215934	12 Mar 2011	0.56	0.25	17
6a	1425.9 – 1535.0	1342204692	14 Sept 2010	0.64	0.5	14
6b	1574.0 – 1702.8	1342206498	15 Oct 2010	0.64	0.5	13
7a	1697.3 – 1797.9	1342216701	24 Mar 2011	0.63	0.6	12
7b	1788.4 – 1906.5	1342206643	16 Oct 2010	0.62	0.6	12

C.3   Determination of the dust spectral index

In order to determine the dust spectral emissivity index in Sgr B2(N), two independent methods using methanol lines were pursued. Each of them has advantages and drawbacks. In both cases we have knowledge regarding line blends throughout the full HIFI band fitting of Neill et al. (2014).

1. The first method uses several a-type bands (e.g., Wang et al. 2011), focusing on the ground state, that individually are isolated in frequency tracing a range of energy states within a confined spectra region (see Tab. C.2). The HIFI spectrum has five bands of CH_3OH that collectively span from 482 to 1256 GHz. This method assumes local thermodynamic equilibrium (LTE) to fit the spectrum over a wide span of excitation. Moreover only a small fraction of the total methanol lines are used.

2. The second method relies on individual optically thick lines of methanol and is independent of the LTE model. These lines are scattered throughout the spectrum. Here line-blends are an issue which along with uncertainties in the baseline corrupt individual lines. However the large number of lines used, approximately 600, counteract those disadvantages.

Table C.2: CH$_3$OH a-type transition frequency range and upper energy range.

Band	Central Frequency (GHz)	E$_u$ range (approximate) (K)
1a	483.5	130-610
1a	532.5	150-650
1b	580	180-800
1b	628	210-950
2a	676.7	240-980
2b	724.7	300-1400
2b	772.7	350-1170
3a	821	380-1100
3b	869.5	440-900
3b	918	460-920
4a	966	510-920
4a	1014	560-1020
4b	1062	610-1070
4b	1111	660-1120
5a	1159	720-1180
5a	1208	790-1180
5b	1255	840-1300

C.3.1   First method: CH$_3$OH a-type bands

In this method we fit methanol a-type bands in the HIFI spectrum using *XCLASS*[2] assuming LTE. The lower end of the frequency range suffers from less dust extinction than higher frequencies. Given that the bands cover similar excitation energies and conditions the fit of lower frequency bands predicts how strong the emission would be in higher frequency bands, excluding the effects of dust optical depth; thus providing a direct constraint of the amount of dust extinction required as a function of frequency. Since the CH$_3$OH photons propagate through a common dust column, the main difference in extinction as a function of frequency is due to the dust properties, in particular the spectral index.

XCLASS is a program using *CLASS* with access to spectral catalogs: CDMS (Müller et al. 2001, 2005) and JPL (Pickett et al. 1998). The modeled emission spectra are described by *XCLASS* as follows (Comito et al. 2005; Zernickel et al. 2012; Neill et al. 2014):

$$
\begin{aligned}
\Delta T_\mathrm{A}(\nu) &= T_\mathrm{line}(\nu) - T_\mathrm{cont}(\nu) \\
&= \sum_m \sum_c \eta_\mathrm{bf}(\theta_{m,c}, \nu) J(T_{\mathrm{ex}_{m,c}}) \left(1 - e^{-\tau(\nu)_{m,c}}\right) e^{-\tau_\mathrm{d}(\nu)}
\end{aligned} \qquad \text{(C.1)}
$$

---

[2]https://www.astro.uni-koeln.de/projects/schilke/XCLASS

where $\tau(\nu)$ is the line optical depth:

$$
\begin{aligned}
\tau(\nu)^{m,c} &= \sum \tau(\nu)^l_{m,c} \\
\tau(\nu)^{m,c}_l &= \frac{c^3}{8\pi\nu^3} A_{ul} N^{m,c}_{\text{tot}} \frac{g_l e^{-E_l/kT^{m,c}_{\text{ex}}}}{Q(m, T^{m,c}_{\text{ex}})} \left(1 - e^{-h\nu/kT^{m,c}_{\text{ex}}}\right) \phi(\nu)^{m,c}
\end{aligned}
\tag{C.2}
$$

where $\phi(\nu)^{m,c}$ is the Gaussian line profile:

$$
\phi(\nu)^{m,c} = \frac{2\sqrt{\ln 2}}{\sqrt{\pi}\Delta v_{m,c}} \, exp\left(\frac{\nu_l\left(1 - \frac{v_{\text{LSR}m,c}}{c}\right)^2 - \nu}{(\Delta v_{m,c}\frac{\nu_l}{c})^2/4\ln 2}\right)
\tag{C.3}
$$

and $\eta_{bf}(\theta^{m,c}, \nu)$ is the beam filling factor:

$$
\eta_{\text{bf}}(\theta^{m,c}, \nu) = \frac{(\theta^{m,c})^2}{(\theta^{m,c})^2 + \theta^2_{\text{beam}}(\nu)} \sim \frac{\theta^2_{\text{s}}}{\theta^2_{\text{b}}}.
\tag{C.4}
$$

The beam filling factor η_{bf} can be simplified as the beam size $\theta_{\text{b}} = \frac{21200}{\nu(GHz)}$ for HIFI is bigger than the source size $\theta_{\text{s}} = 3.1''$. The spectrum is summed over the lines l, for each component c of each molecule m. T_{ex} represents the excitation temperature and is assumed to be the same for every transition. τ_{d} is the dust optical depth, N_{tot} is the total column density, Δv is the full-width at half-maximum linewidth assumed to be the same for every line here and v_{LSR} is the source velocity. The line frequencies ν_l, the Einstein A coefficients A_{ul}, the lower level energy E_l, the statistical weights g_l and the partition functions Q, are provided by the spectral catalogs. The source function is defined as follow:

$$
J(T_{\text{ex}}, \nu) = \frac{h\nu}{k} \frac{1}{\exp(\frac{h\nu}{kT_{\text{ex}}}) - 1}.
\tag{C.5}
$$

The factor $e^{-\tau_{\text{d}}}$ takes the dust attenuation into account where the dust mass opacity is taken from Ossenkopf & Henning (1994). We adopt a value of $\kappa_{1.3\text{mm}} = 0.42 \text{ cm}^2\,\text{g}^{-1}$. This value is between the values for non-coagulated dust grains with thin ice mantles, $0.51 \text{ cm}^2\,\text{g}^{-1}$, and without ones, $0.31 \text{ cm}^2\,\text{g}^{-1}$. The component coming from the cosmic microwave background (CMB) is not taken into account here as at HIFI frequencies the CMB source function is negligible.

Each band is first modeled without taking the dust attenuation into account $\beta = 0$ and then we correct for the required absorption needed to match the predicted emission levels to the observed source emission. Both fits are shown for a few bands (part of 1a, 2b and 3b) in Fig. C.1. The non attenuated models (dashed red lines) obtained for each band are multiplied by a single scale factor in order to fit the data (solid red lines). Two LTE components are required to fit the data: a hot component with a temperature of 170 K and a column density of $5\times10^{18} \text{ cm}^{-2}$ that corresponds to the core (size = $3.1''$) and the cold component with $T = 80$ K and $N_{\text{H}} = 1\times10^{16} \text{ cm}^{-2}$ corresponds to the envelope (size $\sim 30''$). We note that the greatest effects of dust absorption is seen in HIFI bands 6 and 7 (~ 1425 to 1907 GHz). However, these are not used because the large dust optical depth extinguishes all lines that originate from the hot central regions of the core, such as methanol.
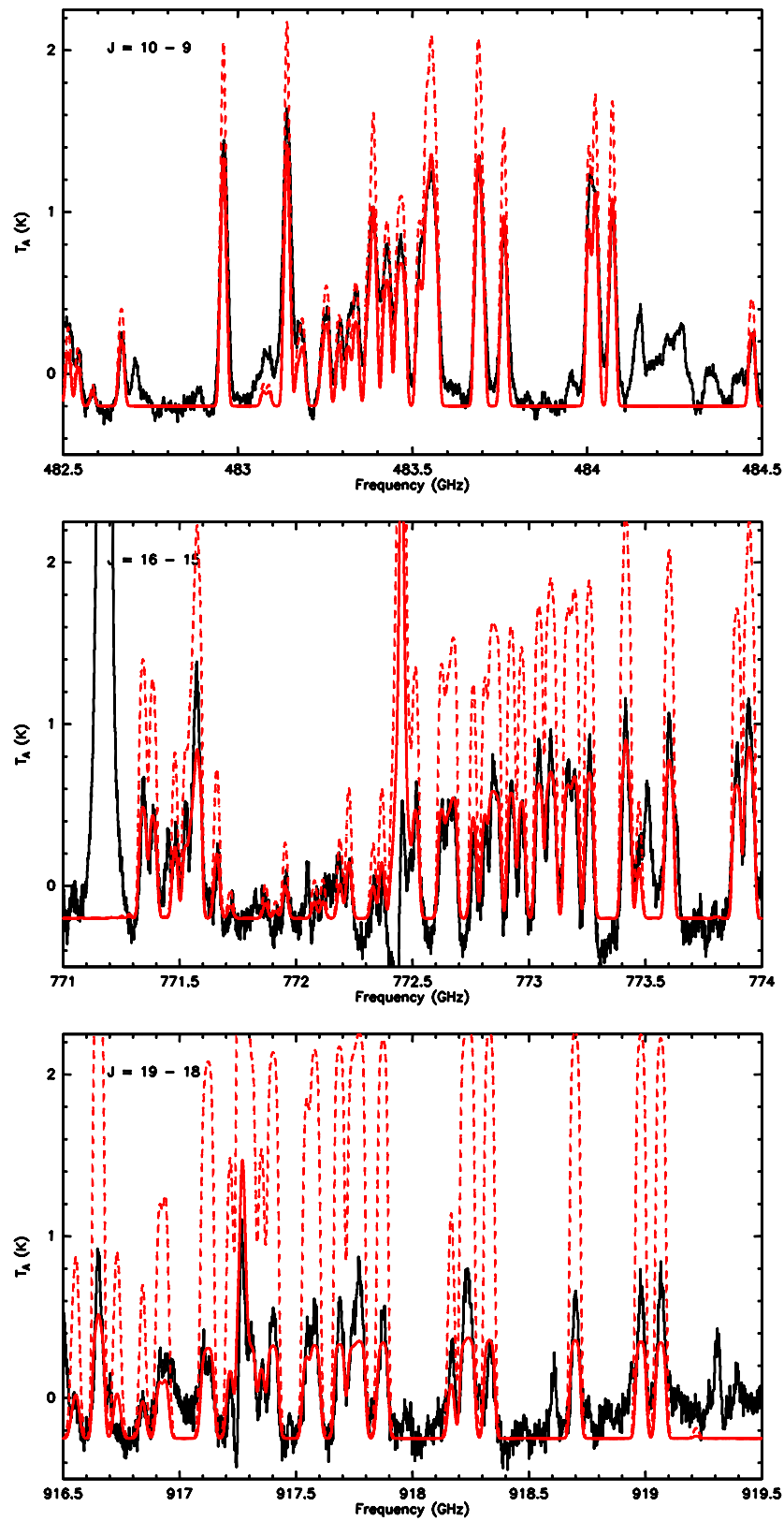
Figure C.1: Bands 1a, 2b and 3b of CH_3OH showing the effects of dust absorption. The CH_3OH LTE model is in solid red line. The dashed red line is the same but without the dust attenuation $\beta = 0$.
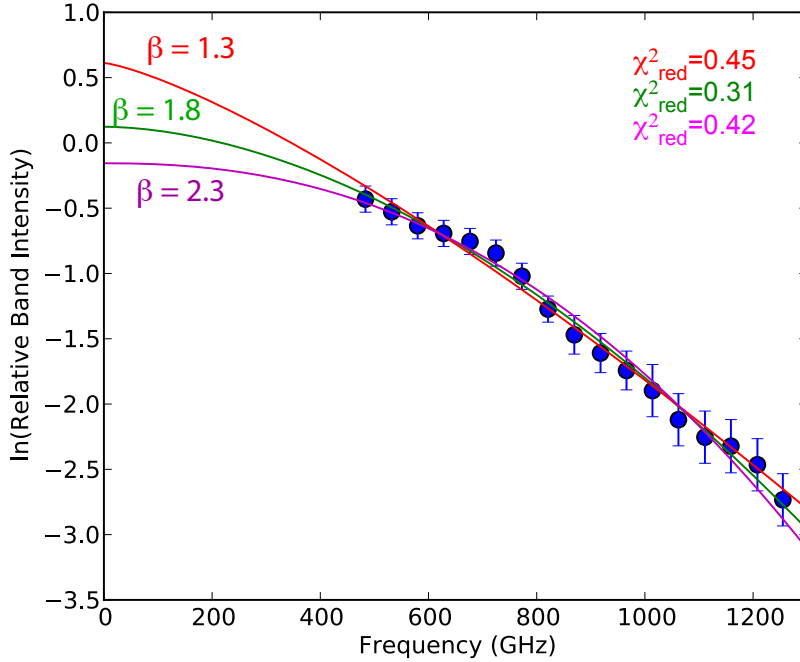
Figure C.2: $\ln(I/I_0)$ for each band (blue points) modeled for three different values of β.

The scale factor corresponds to I/I_0, where I_0 is the intensity of the fit made with *XCLASS* without dust attenuation and I is the intensity of the spectra:

$$\frac{I}{I_0} \;=\; e^{-\tau_d} \tag{C.6}$$

$$\tau_d \;=\; \tau_0 \left(\frac{\nu}{\nu_0}\right)^{\beta} - c_0 \tag{C.7}$$

We normalize at the low end of the spectral range to explore the relative changes in the dust absorption towards higher frequencies. Thus $\nu_0 = 480$ GHz is the critical frequency where we assume that the dust is optically thin. This parameter is fixed but τ_0 the critical optical depth and c_0 a constant are free parameters as well as β. Fig. C.2 shows the resulting scaling factors for each band and the clear effect of dust attenuation as a function of frequency (! Preliminary results !). This observational result is independent of dust emission and we then explore what values of the dust spectral index fit the data. The uncertainties in Fig. C.2 are chosen to be equal to 10% for lower frequency ranges and, from bands 3b, 20% as the data are more noisy for high frequency ranges and thus the determination of the scale factor is less accurate. The best fit has a χ^2 of 0.31 and is obtained for $\beta = 1.82 \pm 0.21$, $\tau_0 = 0.50 \pm 0.12$ and $c_0 = 0.11 \pm 0.15$.

C.3.2   Second method: Optically thick CH$_3$OH lines

The second method uses optically thick CH$_3$OH lines which, similar to the a-type branches, span a wide range of energy and excitation conditions. However, these lines are significantly more numerous allowing for greater statistics. There is some concern that the

higher energy CH_3OH emission could arise from a smaller more compact source with a different dust absorption column than CH_3OH transitions with more moderate excitation energies. With greater statistics we can therefore explore whether this is biasing our results.

The optical depth τ_{ul} of the methanol lines has been computed the same way as in Nummelin et al. (2000).

$$
\begin{aligned}
\tau_{ul} &= \sqrt{\frac{\ln 2}{16\pi^3}} \frac{c^3 A_{ul} g_u N_{\mathrm{tot}}}{\nu_{ul}^3 Q(T_{\mathrm{rot}}) \Delta v} \, e^{-E_u/kT_{\mathrm{rot}}} \left(e^{h\nu_{ul}/kT_{\mathrm{rot}}} - 1\right) \qquad \text{(C.8)} \\
&= 1.178 \times 10^{-13} \frac{S_{ij}\mu^2 N_{\mathrm{tot}}}{Q(T_{\mathrm{rot}})\Delta v} \, e^{-E_u/T_{\mathrm{rot}}} \left(e^{h\nu/kT_{\mathrm{rot}}} - 1\right)
\end{aligned}
$$

with the following relation:

$$
A_{ul} = 1.16397 \times 10^{-20} \frac{S_{ij}\mu^2 \nu^3}{g_u}
$$

The optical depth threshold was limited to lines with $\tau_{\mathrm{line}} \geq 2$. Each line is described as follows:

$$
\begin{aligned}
\Delta T_A(\nu) &= \eta_{bf} \, J(T_{\mathrm{ex}}) \left(1 - e^{-\tau_{\mathrm{line}}}\right) e^{\tau_d} \\
&\sim \eta_{\mathrm{bf}} \, J(T_{\mathrm{ex}}) \, e^{\tau_d} \qquad \text{(C.9)}
\end{aligned}
$$

Then, we get with Eq. C.4, C.7 and C.9:

$$
\begin{aligned}
\ln(\Delta T_A \, \theta_b^2) &= \ln\left(J(T_{\mathrm{ex}}) \, \theta_s^2\right) - \tau_0 \left(\frac{\nu}{\nu_0}\right)^\beta \\
&= I_0 - \tau_0 \left(\frac{\nu}{\nu_0}\right)^\beta \qquad \text{(C.10)}
\end{aligned}
$$

where $J(T_{\mathrm{ex}})$ and θ_s are line independent.

First, all the optically thick lines are binned in range of 50 K in upper state energy E_u (e.g., $150 - 200$ K). This gives a good statistics as there are between $40 - 70$ transitions within each 50 K bin. Each range has a different number of transitions, lower energy bins contain more transitions than the higher energy bins. Lines with an energy of the upper level below 100 K and above 650 K are not included because the lower energy lines originate in the envelope and are seen in absorption, while the higher energy lines are optically thin.

A gaussian fit is used to determine the brightness temperature of each transition in an energy bin. The baselines have been set by eye and are likely to be the key uncertainty in the determination of peak T_b. Thus we set the error on the estimated baseline to be $\pm$ 0.2 K, regardless of the transition and its spectral location. In Fig. C.3 we show the peak intensity (blue scattered points), scaled by θ_b^2, of all the transitions present in the energy range $200 - 250$ K. They present a trend that can be fit using Eq. C.10 (fit in red). We obtain a fitted value of β for each energy bin. The errorbars show the uncertainties on the peak intensity set to 20%.

Not only methanol has been modeled using *XCLASS* but also other molecules in order to determine which individual methanol line is mixed with another molecule line. These lines, as well as the blended lines (i.e. CH_3OH lines blended with CH_3OH lines) and the absorption lines have been avoided for the fit in Fig. C.3. More fits are obtained including the blended lines without modification and with subtraction of the intensity of other molecules from the Gaussian fit.
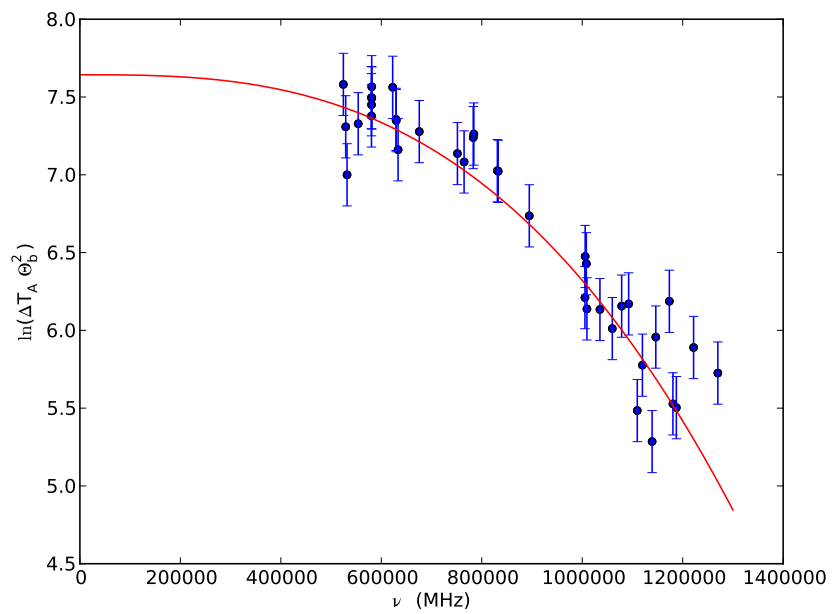
Figure C.3: Values for each line of $\ln(\Delta T_{\mathrm{A}}\,\theta_{\mathrm{b}}^2)$, in the energy range of $200 - 250$ K, with their uncertainties in blue and the fit is in red.

D
Paper

Chemical modeling of HC/UCHii regions and their internal PDR.

G. Stéphan[1,2], P. Schilke[1], J. Le Bourlot[2], et al., R. Choudhury[1,3], B. Godard[2], A. Schmiedeke[1,3], and Á. Sánchez-Monge[1]

[1] I. Physikalisches Institut, Universität zu Köln, Zülpicherstrasse 77, 50937 Köln, Germany
e-mail: stephan@ph1.uni-koeln.de
[2] LERMA, Observatoire de Paris, 5 place Jules Janssen, 92190, Meudon, France

[3] Max-Planck-Institut für extraterrestrische Physik, Giessenstrasse 1, 85748, Garching, Germany

ABSTRACT

Aims. We want to investigate chemistry in HC/UCHii regions and their internal PDRs and determine if there are specific tracers to this evolutionary stage of massive star formation.
Methods. We model HC/UCHii regions by coupling an astrochemical code to a radiative transfer code obtaining a detail abundances profiles as well as synthetic spectra and we compare them to hot molecular cores models. We investigate the evolution of the chemistry in Hii regions with models of different densities, different sizes and different initial abundances.
Results. We obtain the time evolution of synthetic spectra for a dozen of molecules as well as ratios of their integrated intensities.
... We determine that some molecules like C, N_2H^+, CN and HCO seem to not trace the inner core and so are not good tracers to distinguish the Hii regions to the HMCs phase. C^+ and O seem to trace the internal PDRs but are unfortunately not currently observable with the required spatial resolution.

Key words. astrochemistry – stars: formation – stars: massive – ISM: molecules – ISM: lines – ISM: evolution

1. Introduction

The chemical evolution of hot molecular cores (HMCs) has been the focus of many studies (Garrod & Herbst 2006; Vasyunin & Herbst 2013; Garrod 2013) as these objects often present a very rich and complex chemistry. HMCs are compact (≤ 0.10 pc), very dense ($n_H \geq 10^6$ cm^{-3}) and hot (T $\geq$ 100 K). They are a characteristic early stage of massive star formation (Kurtz et al. 2000). They are transient objects with a lifetime, although not well constrained, of about 10^4–10^5 years (Herbst & van Dishoeck 2009). It is still unclear if they are formed before the hyper compact Hii (HCHii) region stage or coexist with it (Gaume et al. 1995; Kurtz 2005; Beuther et al. 2007). HCHii regions eventually evolve into ultracompact Hii (UCHii) regions (Wood & Churchwell 1989; Kurtz et al. 2000; Hoare et al. 2007; Sánchez-Monge et al. 2013) as the embedded proto-star(s) becomes more luminous and gradually ionizes its surrounding, although HII regions may not homogeneously expand but flicker as theoretically proposed by Peters et al. (2010a,b) and observed by De Pree et al. (2014).

Most chemical models do not extend their studies to the evolutionary stages associated with HCHii and UCHii regions. Due to the proximity of the star and the very dense gas, the ultraviolet radiation field is very strong at the edge of the Hii region. Thus, HC/UCHii regions present internal photo-dissociation regions (PDRs) formed at the border between the Hii region and the molecular dense cloud where they are embedded. So far, only few studies have investigated internal PDRs (e.g., Bruderer et al. 2009a,b; Lee et al. 2015) in the case of an outflow cavity around low-mass stars with weak UV fields. These internal PDRs are very dense ($n_H \geq 10^6$ cm^{-3}) and very thin because of the fast

decrease of the radiation field ($r_{PDR} \approx 200$ AU, corresponding to $A_V = 1.6$ mag obtained with the standard Milky-Way values $R_v = 3.1$ and $N_H/E(B-V) = 5.8 \times 10^{21}$ cm^{-2}).

Observationally, HMCs and embedded UCHii regions have comparable spectral energy distributions in the infrared (IR) and sub-mm regime (Churchwell 2002). But during the HMC phase the proto-star is not sufficiently evolved and does not have any detectable free-free emission. Thus, HMCs are weak or even unobservable in the radio-continuum regime (Hoare et al. 2007; Beuther et al. 2007). This is the main observational difference between these two evolutionary stages of massive star formation. Do other observational ways prevail to differentiate these two phases? Can they be characterized by some specific chemical tracers? Can the presence of the internal PDRs be detected and how?

In this work we study the chemistry happening in HC/UCHii regions and the internal PDRs as well as in HMCs, before the hot core is destroyed by UV radiation. We include the spatio-temporal evolution of the radiation field in the Hii region models as well as the evolution of the dust temperature. We compare the effects of physical parameters like the radiation field intensity on the chemistry and on the tracers' emissivity. We produce several models of HMCs with an embedded hot star to study the chemistry when changing the sizes of the ionized cavity, the density and the initial abundances.

The paper is structured as follows: In Sect. 2 we describe our extended HMC model, the physical parameters as well as the chemical code and the different modifications implemented since our previous paper (Choudhury et al. 2015). In Sect. 3 we derive properties of the dissociation front using a semi-analytical code
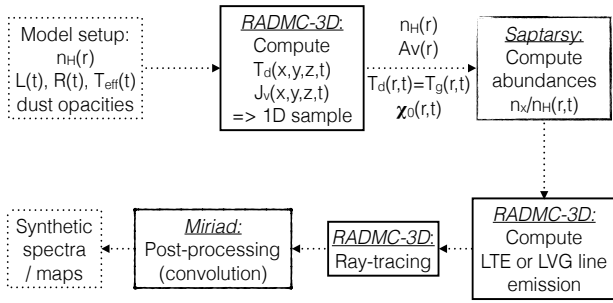
Fig. 1: Flowchart showing the modeling framework *Pandora*.

Fig. 2: Scheme of the HMC (left), HHMC (middle) and HII region (right) models. The spatio-temporal evolution of the radiation field is included in the computation of the relative abundances only for the HII region models.

dealing with H_2 chemistry. We present our results in Sect. 4 and we discuss them in Sect. 5. Finally we present our conclusion in Sect. 6. In Sect. A we detail some more improvements made in the chemical code.

2. Method

The chemical modeling is performed with *Saptarsy* (Choudhury et al. 2015). The code is described in Sec. 2.3. *Saptarsy* works along with *RADMC-3D*[1] through the *Python* based code *Pandora* (Schmiedeke et al. 2016), as shown by the flowchart in Fig. 1, to obtain synthetic spectra using the detailed modeling of the spatio-temporal evolution of the chemical abundances. We can summarize the modeling framework as follows: First, based on a density profile and the evolution of stellar parameters, *RADMC-3D* calculates both the dust temperature and the mean intensity of the radiation field self-consistently. The gas temperature is assumed to be equal to the dust temperature in all models. This approximation will be lifted in a further work since it is known that the gas temperature maybe much higher than the dust temperature at the inner edge of the PDR. The density profile and the spatio-temporal evolution of the dust temperature and radiation field intensity are then used by *Saptarsy* to compute relative abundances. Finally, we use the abundances as inputs for *RADMC-3D* to produce time-dependent synthetic spectra using the LTE approximation. The spectra can then be post-processed (convolved) to be compared to observations. The structure of the models and the chemical code are described in more details below.

2.1. Hollow HMC model

HMCs are modeled as symmetric spherical cores containing a single central protostar. The star is surrounded by gas and dust with a density profile defined as follows:

$$n(r) = 2n_c \left(1 + \left(\frac{r}{r_p}\right)^2\right)^{-\gamma} \tag{1}$$

where r_p is the Plummer-like radius and n_c the half of the central density. The exponent γ defines the steepness of the Plummer function.

To model a HII region from this HMC model we implement a spherical cavity around the proto-star only filled with ionized hydrogen and electrons uniformly distributed, i.e. a Strömgren sphere (see also Schmiedeke et al. 2016). We want to compare
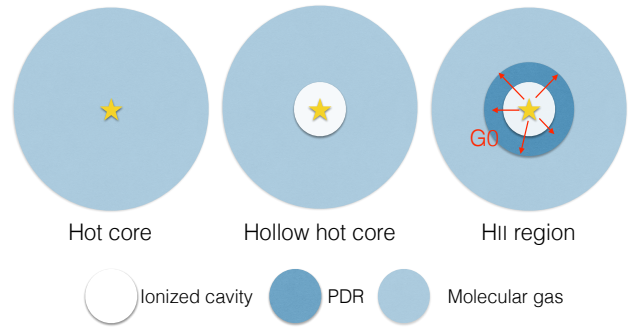
the model with an HII region[2] and the HMC model but the chemical evolution is not easily comparable because the radial profile of the temperature is not exactly the same because the cavity does not contain dust. IR radiation is the main heating source in the HMC model and the attenuation by dust on a larger area results into smaller temperatures at the same radii. We decide to use an artifice and to implement an ionized cavity into the HMC model as well (see Fig. 2). Thus we obtain the extended HMC model, also called hollow HMC (HHMC) model. The HHMC model has the same density structure than the HII region model and consequently the same total column density, and also the same spatio-temporal evolution of the temperature. This obviously changes the lines intensity compared to a HMC model without cavity due to smaller species column densities. The main difference between the HII region and the HHMC models is the emission of UV photons from the proto-star, which is modeled in *Saptarsy* with the implementation of the spatio-temporal evolution of the radiation field in the HII region model. We can then focus on the effect of the radiation field onto the chemistry in the core.

2.2. Physical parameters

The ionized cavity in the HHMC and HII region models is assumed to be filled only with HII and electrons. The temperature is set to the typical HII region temperature of 10^4 K and the electron density is equal to 10^5 cm^{-3}. The cavity is present from the beginning of the time evolution and it does not expand in time as we consider a HII region whose expansion is limited by the high accretion flow (Peters et al. 2010a). We need to define several other parameters in order to compute the dust temperature and the radiation field intensity using *RADMC-3D*: the stellar luminosity, the density, the grid and the grain properties.

Stellar luminosity: Hosokawa & Omukai (2009) model predicts the time evolution of a spherically accreting massive proto-star ($\dot{M} = 10^{-3}$ $M_\odot$ yr^{-1}). The proto-star is the only heating source of the core because no external radiation field is included. The radiation of the proto-star is isotropic. The effective temperature $T_{\text{eff}}(t)$ of the proto-star is no longer a constant parameter (see Fig. 3) as in Choudhury et al. (2015). We use:

$$T_{\text{eff}}(t) = \left(\frac{L_{\text{tot}}(t)}{4\pi R_*^4(t)\sigma}\right)^{1/4}$$ where R_* is the star radius, L_{tot} the to-

[2] Hereafter we will use HII region to refer to this model although the ionized gas is only used as a boundary condition.
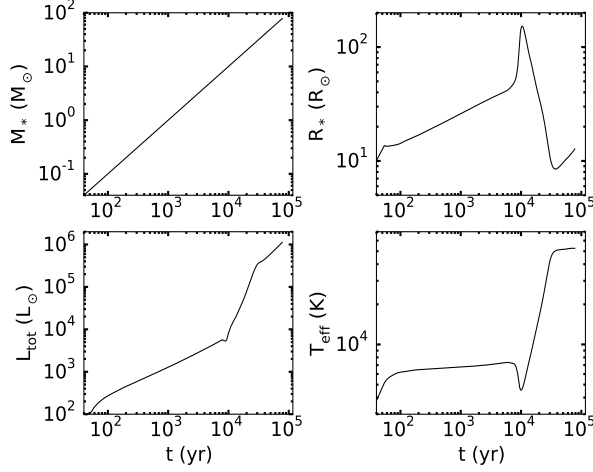
Fig. 3: Time evolution of the parameters for an accreting massive proto-star with an accretion rate of 10^{-3} $M_\odot$ s^{-1} (Hosokawa & Omukai 2009). The different panels show the mass of the star M_* (top left), the star radius R_* (top right), the total luminosity L_{tot} (bottom left) and the effective temperature T_{eff} (bottom right).
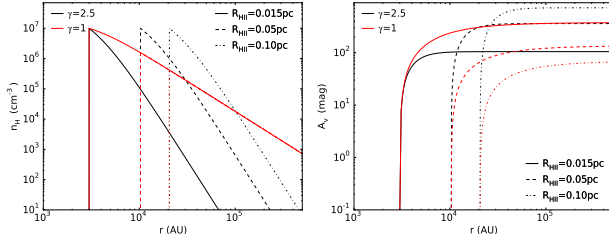
Fig. 4: Top panel: Density distributions in function of radius for a Plummer function with exponent $\gamma = 2.5$ (black) and $\gamma = 1$ (red) for the three sizes of HII regions: 0.015 (solid), 0.05 (dashed), 0.10 pc (dash-dotted). Bottom panel: Visual extinction in function of radius.

tal luminosity provided by T. Hosokawa and σ is the Stefan-Boltzmann constant. The stellar data cover a range going from 54 to 7.8×10^4 years. A linear interpolation is used from 0 to 54 years and at the beginning of the evolution, when there is no radiation field, the dust temperature is set to 10 K. Beyond 10^5 years, the stellar parameters are constant in time resulting in a constant dust temperature and radiation field intensity.

Density distribution: The density distribution is defined in Eq. 1. We distinguish two models with different exponents γ (see Fig. 4). In a first case (black curves), γ is equal to 2.5 like the hot core models in Choudhury et al. (2015). This factor gives an asymptotical decrease in r^{-5} and agrees with Qin et al. (2011) in the case of Sgr B2(N)-SMA1, region close to the UCHII region K2. r_p corresponds to the size of a HII region and n_c is defined so that the density at the ionization front is 10^7 cm^{-3} (or $10^5 - 10^6$ cm^{-3} for models with lower density). In a second case (red curves), γ is equal to 1 which gives asymptotically a decrease as r^{-2}. This is closer to the results of Didelon et al. (2015) in the case of the central UCHII region in Mon R2. However in this case, r_p is fixed and equal to 3.10^3 AU whatever the size of the HII region and n_c is equal to 10^7 cm^{-3}.

Grain properties: We adopt the grains absorption and scattering coefficients from Laor & Draine (1993). The grains are

chosen to be 100% carbonaceous and they all have a size of 0.1 μm. It also assumed that they all are spherical. It is possible to use a size distribution inside *RADMC-3D* for the computation of the dust temperatures but it has not been implemented because *Saptarsy* can only deal with one grain temperature and because we only need the total grain surface for the chemistry as there is no real radiative transfer treatment. For the same reasons we do not include silicate grains.

Modeling grid: *RADMC-3D* computes the dust temperature and the radiation field intensity in the whole modeling cube and for each star luminosity. We use a 3D spherical grid and the edges of the modeling cube are reached when the density has decreased to 10^1 cm^{-3}. The size of the cube influences a lot the lines intensity because the column density varies.

In the end, the HII region and the HHMC models have the same structure (same temperatures, same opacities, a cavity of HII gas and no dust around the star). The difference between these for the spatio-temporal evolution of the UV radiation field which is not accounted for in the HHMC model. In a HMC the density near the star is high enough so that the UV radiation is immediately and totally attenuated. This difference is taken care of during the relative abundances computation performed by the chemical code.

2.3. Chemical code

Saptarsy is a gas-grain code based on the rate equation approach solving both the spatial and temporal evolution of chemical abundances. It uses the Netlib library solver *DVODPK*[3] (Differential Variable-coefficient Ordinary Differential equation solver with the Preconditioned Krylov method GMRES for the solution of linear systems) to solve the ordinary differential equations and the solver of sparse system of linear equations MA28[4] from HSL library (Harwell Mathematical Software Library).

We extend the use of the code to study HC/UCHII regions and the associated internal PDR. We include the spatio-temporal evolution of the radiation field intensity χ_0. It is obtained using the mean intensity of the radiation field J_ν computed by *RADMC-3D*.

$$G(r) = \frac{1}{1.08 \times 10^{-13}} \int_{912\text{Å}}^{2400\text{Å}} \frac{4\pi}{c} J_\lambda(r) \, d\lambda \quad \text{(Draine unit)}$$

We use a reduced OSU network including new reactions for HCN and HNC (Graninger et al. 2014; Loison et al. 2014). We have reduced the OSU network as it considerably decreases the computation time and because many species are not relevant for this work. This includes all molecules bearing Cl, P, Na and Mg, all anions as well as long carbon chains with more than four carbon atoms. For Si and Fe only the neutral, ionized and grain surface atomic form are included in the network. We have also updated desorption energies E_D for some species (see Tab. 1 for the new values). As only few data exist for diffusion barrier, it is related to the desorption energy via the following relation: $E_b/E_D = 0.50$.

Photo-processes and secondary photon processes were not used in the previous version of *Saptarsy*. We add photo-dissociation reactions in the gas phase and on the grain surface as described in Semenov et al. (2010). Photo-desorption is also included as defined in Le Bourlot et al. (2012) in the case of H$_2$ for a dozen of molecules (s-H, s-H$_2$, s-O, s-O$_2$, s-OH, s-H$_2$O, s-CO,

---

[3] http://www.netlib.org/ode
[4] http://www.hsl.rl.ac.uk/

Table 1: Desorption energies: the second column shows the energies used in the current models; the third column shows the energies used in the previous work (Choudhury et al. 2015).

Species	E_D (K)	Old E_D (K)
H_2	430[e]	23
O	1660[a]	800
O_2	930[b]	1000
O_3	1833[b]	1800
SO	1745[c]	2600
NO	2460[c]	1600
HNO	2910[c]	2050
H_2CO	3300[d]	2050
O_2H*	4510	3650
OCN*	3260[c]	2400
HNCO*	3710[c]	2850
N_2O*	3260[c]	2400
NO_2*	4120[c]	2400
SiO_2*	6020[c]	4300
NHNO*	3710[c]	2850
NH_2NO*	4160[c]	3300
CH_3OCH_3*	4010[c]	3150
C_2H_5OH*	6260[e]	6580
$HCOOCH_3$*	5200[e]	6295
CH_2NH_2*	4680[e]	5006

Notes. [a] He et al. (2015) [b] Jing et al. (2012) [c] Derived from E_D(O) [d] Noble et al. (2012) [e] Garrod (2013) [*] Only for a network including COMs, with 334 species.

Table 2: Initial abundances of the principal species. The first and second column values a(b) refers to a×10[b] through the paper. The grain surface species are written with 's-' before the name.

Species	n_X/n_H: ini1	n_X/n_H: ini2
H_2	4.99(-1)	4.99(-1)
He	9(-2)	9(-2)
s-H_2	1.24(-4)	1.24(-4)
s-H_2O	9.87(-5)	2.46(-4)
s-CO	9.19(-5)	9.58(-6)
s-OH	1.91(-5)	7.24(-14)
s-HNO	2.89(-5)	3.12(-7)
s-N_2	1.33(-5)	6.14(-12)
s-O	1.16(-5)	2.74(-16)
s-HCN	6.23(-6)	4.17(-7)
s-CH_4	6.2(-6)	1.1(-4)
s-NH_3	8.03(-6)	7.53(-5)
s-H_2CO	3.20(-7)	7.12(-9)
s-CH_3OH	1.29(-7)	2.67(-17)
s-CO_2	9.83(-8)	5.91(-10)
s-H_2S	3.09(-8)	7.93(-8)
s-Si	8(-9)	8(-9)
s-Fe	3(-9)	3(-9)

s-HCO, s-H_2CO, s-N_2, s-CO_2 – We represent the grain species with s- throughout this paper). In the associated reaction rate the photon flux also takes into account the secondary photon flux. The direct dissociation by cosmic-rays and the secondary photon processes were previously treated the same way. Secondary photon processes are now treated as expressed in Le Petit et al. (2006). Desorption via exothermic surface reactions, also called reactive desorption, with an efficiency of 1% has been added from Garrod et al. (2007). Furthermore, self-shielding is an im-
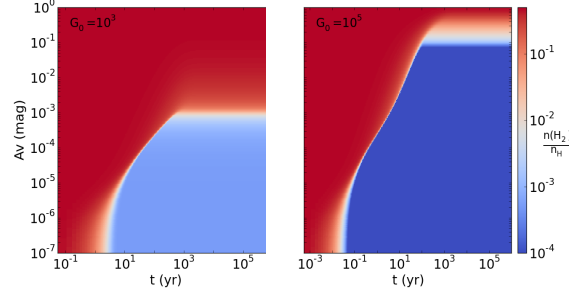
Fig. 5: H_2 abundance in function of time (x-axis) and extinction (y-axis) for different radiation field intensity: 10^3 (left panel) and 10^5 Draine unit (right).

portant process in internal PDRs. We include a simple treatment of the self-shielding for H_2 and CO following Lee et al. (1996), Draine & Bertoldi (1996), Panoglou et al. (2012) and Sternberg et al. (2014). It is used in the code only if the model is a HII region model. More modifications have been made in *Saptarsy* and are quickly described in the appendix A.

The initial abundances are obtained by simulating the collapse of a pre-stellar core in two steps. We start with the elemental abundances from Wakelam & Herbst (2008). The core has a temperature of 10 K, an extinction of 10 mag and no radiation field. In the first step, the core has a density of 10^4 cm^{-3} and we let the chemistry evolve up to 10^5 years. Then we increase the density to 10^7 cm^{-3} and repeat the process using the results of the first step. Thus, for all the models of HII regions, HHMCs and HMCs, we start with a medium where molecules are depleted onto grains. The carbon is mostly found in s-CO, the oxygen is in s-H_2O and the nitrogen is mainly in s-N_2 as seen in the second column of Tab. 2. Otherwise, an important amount of carbon is also found in s-CH_4 and s-HCN, oxygen is also found in s-O and s-OH and nitrogen in s-HNO and s-NH_3. As for the hydrogen it is in the molecular form H_2. To simplify the comparisons, we use the same initial abundances for every model except when changing the size of the network and for models with the second set of initial abundances (see third column of Tab.2).

3. Dissociation front

Before analyzing the results of the full modelization, it is useful to develop a qualitative feeling of the size and time scales involved. To this end, we developed a semi analytic model of pure hydrogen gas, and computed the evolution of the dissociation front. In this 1D time dependent code the formation of H_2 uses a standard constant rate $k_f = R_f\, n_H\, n(H)$ (Jura 1974). The H_2 evolution equation is described in Eq. 2.

$$\frac{dn(H_2)}{dt} = R_f\,(n_H - 2n(H_2)) - (k_d + k_c)\,n(H_2), \qquad (2)$$

where R_f is the formation rate of H_2 on grains is a constant value and equal to 3×10^{-17} s^{-1} (Jura 1975), k_c the cosmic rays destruction rate and k_d the dissociation rate:

$$k_d = k_d^0 I_{UV} \exp\left(-\sigma_g N_H\right) f(N_2). \qquad (3)$$

k_d^0 is the photodissociation rate in free space and is equal to 5.8×10^{-11} s^{-1}, I_{UV} is the radiation field intensity in Draine unit, σ_g is the typical dust extinction coefficient in the FUV and is equal to 1.9×10^{-21} cm^2 H^{-1}, N_H is the total column density, N_2
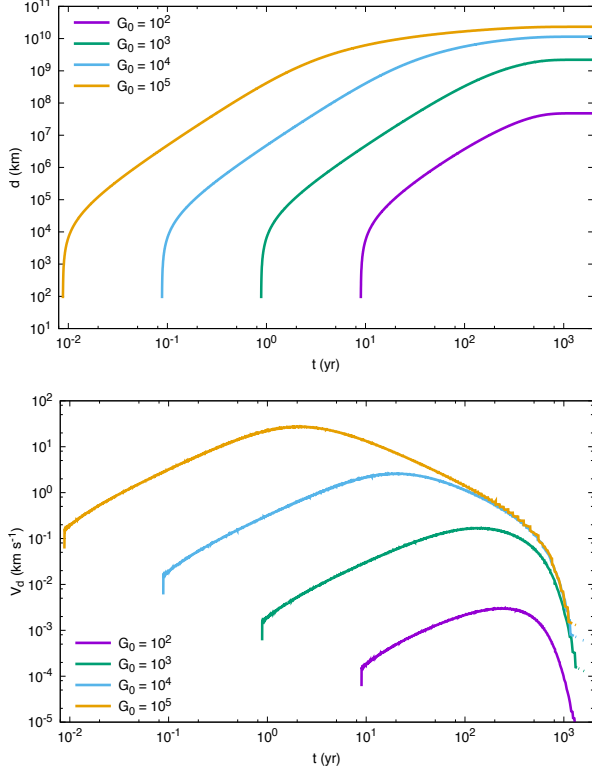
Fig. 6: Distance of the dissociation front for different radiation field intensity (top panel) and velocity of the front for different radiation field intensity (bottom panel). For a gas temperature of 250 K the sound speed is about 1.5 km s^{-1} depending on the mean molecular mass.

is the column density of H_2, and finally $f(N_2)$ is the shielding function described in Draine & Bertoldi (1996).

In this model, the temperatures and radiation field intensity are constant in time and the density is uniform in the core. Several models are obtained using a density of $n_H = 10^6$ cm^{-3} and a radiation field intensity varying from 10^2 to 10^5 Draine unit. The model does not depend on gas temperature. In Fig. 5 we show the H_2 abundance in function of time in years (x-axis) and visual extinction in magnitude (y-axis). The colorbar represents the variations of the H_2 abundance from lower abundances in blue to higher ones in red. All abundance profiles, as well as the temperature and radiation field variations, are represented the same way along the article.

We find that the dissociation time τ at the edge of the cloud is as described in Eq. 4. It only depends on the radiation field as seen also in the top panel of Fig. 6. In this figure we show the distance between the edge of the core and the front. The position of the front has been chosen such as $x = \frac{n(H_2)}{n_H} = 0.1$. This is rather arbitrary but it describes properly the transition between the atomic state and the molecular one.

$$\tau = \frac{1}{2 R_f n_H + k_d^0 I_{UV}}, \qquad (4)$$

where R_f is a constant value equal to 3×10^{-17} s^{-1}, k_d^0 is the photodissociation rate in free space and is equal to 5.8×10^{-11} s^{-1} and I_{UV} is the radiation field intensity in Draine unit.

The size of the atomic region depends only on the radiation field intensity as seen in Eq. 5.

$$A_v = \frac{2 R_v}{C_D} (5 \times 10^{14} cm^{-2}) \frac{k_d^0}{R_f n_H} I_{UV}. \qquad (5)$$

We also derive the dissociation front velocity (Eq. 6).

$$V_d(z) = \frac{\Delta z}{\Delta t} = \left((2 + k_d') x - 1 \right) \left(\frac{\partial x}{\partial s} \right)^{-1} \qquad (6)$$

$$\frac{\partial x}{\partial s} = -\frac{1}{(2 + k_d')^2} \frac{\partial k_d'}{\partial s}$$

where z is the position of the front which is time dependent and with k_d', x and s defined as follows: $k_d' = \frac{k_d + k_c}{R_f n_H}$ and $s = s' \frac{n_H}{5 \times 10^{14}}$. s' is the distance from the edge of the cloud to the position of the front. In the bottom panel of Fig. 6, the velocity of the front is shown for several radiation field intensity. The typical sound speed is about 1.5 km s^{-1} in these regions. Thus, we see that the radiative times are shorter than the dynamic time for high radiation field intensities. The resulting dynamical response of the gas (formation of a shock front) is out of the scope of this analytic approximation.

4. Results

The spatio-temporal evolution of the dust temperature and the radiation field intensity for the reference model *mHII:r0.05n7p2.5s183ini1c1* are presented in Fig. 7. With these two parameters profiles we can constrain some regions in the core evolution. We start with the initial conditions ($T_d = 10$ K and $\chi_0 = 10^{-20}$ Draine unit) up to 50 years and have the grain surface region where all molecules are frozen onto the surface. From 50 years, χ_0 is equal to 10^{-1} and T_d is superior to 50 K. We go to a molecular region as the species are released into the gas phase. Deeper in the cloud the transition from grain surface to gas phase might be delayed because the temperature is still a bit low. From approximately 10^4 years, the radiation field becomes really strong but only for extinctions up to 10 – 20 mag. The temperature is also the highest in this region. Thus we form an atomic-ionized region, i.e. a PDR, although the spatial resolution and the approximate treatment of ionization and thermal balance induce some inaccuracies that disappear further in. The column density involved is too small to have an observational impact. For the latest phase of the evolution (from 10^4 years) and deep in the cloud ($A_V > 20$ mag), the temperature is the parameter influencing the chemistry. It is high enough, around 100 K, to have every molecule in the gas phase.

4.1. Models

The reference model is a Hɪɪ region with a size of 0.05 pc, a density of 10^7 cm^{-3} at the ionization front and a Plummer exponent of 2.5. According to Table 3 in Kurtz (2005) this is a UCHɪɪ at least by its size. Several comparisons between this reference model and others are made. The other models are listed below:

1. The first models' comparison is between Hɪɪ region, HHMC and HMC models.
2. Models with different sizes of Hɪɪ regions are produced. In addition to $R_{HII} = 0.05$ pc (10300 AU) we have $R_{HII} = 0.015$ pc and 0.10 pc (or 3000 and 20600 AU). The model where $R_{HII} = 0.015$ pc is clearly a HCHɪɪ region and the one with a size of 0.10 pc is at the transition from a UC to a Compact Hɪɪ region.

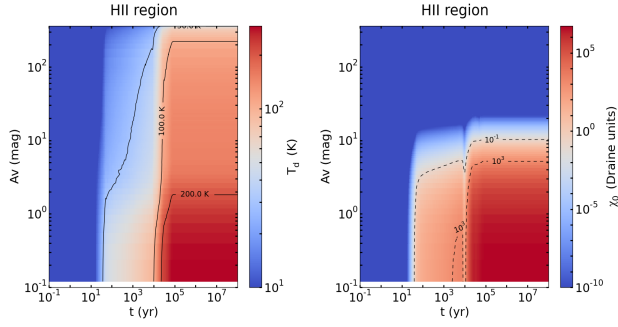Fig. 7: Spatio-temporal evolution of the dust temperature (left) and radiation field intensity (right) in the case of the reference model *mHII:r0.05n7p2.5s183ini1c1*. Contours are plotted: solid line for T_d (30, 100 and 200 K) and dashed lines for χ_0 (10^{-1} and 10^3 Draine unit).

Table 3: Models abbreviations.

	Parameter	Value	Abbreviation
1	UCHII region model		*mHII*
	HHMC model		*mHHC*
	HMC model		*mHC*
2	Size of the HII region (pc)	0.05	*r0.05*
		0.015	*r0.015*
		0.10	*r0.10*
3	Density at the	10^5	*n5*
	ionization front (cm^{-3})	10^6	*n6*
		10^7	*n7*
4	Plummer exponent γ	1	*p1*
		5/2	*p2.5*
5	Number of species	183	*s183*
	in the network	334	*s334*
6	Initial conditions		*ini1*
			ini2
7	Cut-off density (cm^{-3})	10^1	c1
		10^6	c6

3. As the reference model has a density closer to the density of a HCHII region we also compare it to models with lower density at the ionization front to be closer to UCHII regions' densities: 10^6 and 10^5 cm^{-3}.

4. We compare models changing the exponent of the Plummer function: $\gamma = 2.5$ or 1.

5. We use two gas-grain networks: the first one contains 183 species and 2437 reactions and the second one has 334 species and 3684 reactions. They have 50 and 100 grain species, respectively.

6. We also have a second set of initial conditions to compare with the previous one. These initial conditions are shown in the second column of Tab. 2. They are obtained for the steady state of a pre-stellar core model at a density of 10^7 cm^{-3}. In these conditions the species are again frozen on grains but

hydrogen which is molecular. Carbon is found mostly in s-CH$_4$, oxygen in s-H$_2$O and nitrogen in s-NH$_3$.

7. A model with a smaller modeling grid, i.e. we stop the grid at a cut-off density of 10^6 instead of 10^1 cm^{-3}, is also produced to trace the emission coming from the inner core only.

To distinguish the different models we use the abbreviations presented in Tab. 3 and the different comparison points are referred as "Item i" from the list of Sec. 4.1. We annotate the reference model as *mHII:r0.05n7p2.5s183ini1c1*.

4.2. Abundances

Item 1: We obtain with *Saptarsy* the spatio-temporal evolution of the relative abundances of all species present in the network. Fig. 8 shows the abundance profile of HCN and C$^+$ for the reference HII region model *mHII:r0.05n7p2.5s183ini1c1* (left panels) and for the one of the HHMC model *mHHC:r0.05n7p2.5s183ini1c1* (right). We see that C$^+$ is formed in the HII region model, from about 100 years when the UV radiation becomes strong (see dashed contours), while HCN disappears. From these abundance profiles and the ones of other species we can identify the grain surface chemistry region, the molecular gas and the atomic-ionized gas regions defined previously. In addition, a region partly molecular partly atomic can be seen as well as a transition region between this molecular-atomic region and the molecular region. Schemes of the different regions seen in the HII region and the HMC/HHMC models are shown in Fig. 9. The molecular-atomic and atomic-ionized regions form the internal PDR in the HII region models. It is created by the UV radiation field. Thus, photo-desorption is the dominant desorption process in these areas. In the HMC/HHMC models, the grain surface chemistry region is slightly larger close to the edge of the cavity for these models, as seen in the right panel of Fig. 8 and 9. Thermal desorption seems to happen around 10^4 years. This is not the case for species with low desorption energy like CO. For those molecules desorption happens at the same time as in HII region models but it is smoother.

Item 2: It appears that the grain surface chemistry lasts longer deep into the core for models with larger HII regions. It stops at 100 years for the *mHII:r0.015* and lasts until 10^4 years for *mHII:r0.10*. s-H$_2$O seems to stay on the surface even after 10^5 years when the size of the cavity increases because the temperature does not go up as fast into the core due to the distance. In the molecular-atomic region, the abundance of most gas phase species becomes larger as the core evolves for larger size model because of of a smaller radiation field. This is also the case for grain surface species with high desorption energy like methanol. The desorption of more complex molecules like methanol is delayed when we increase the size of the cavity. In addition, the size of the atomic-ionized region seems to not depend on the temperature but only on χ_0. Furthermore, when A$_V$ > 10 mag and around 10^4 years we see a decrease in the abundance of HCN, as well as HNC or CH$_3$OH, before a sudden increase due to thermal desorption (Fig. 8). This decrease, mainly due to an important accretion of the species on the grain, occurs on a larger area when the size of the HII region increases.

Item 3: The abundance of ions and radicals is higher for models with lower density all along the evolution, mainly in the atomic-ionized region. From 100 to 10^4 years and for extinction up to 2 – 3 mag, the abundance of gas phase molecules, such as CH$_3$OH or HCN, as well as grain species is consequently lower.
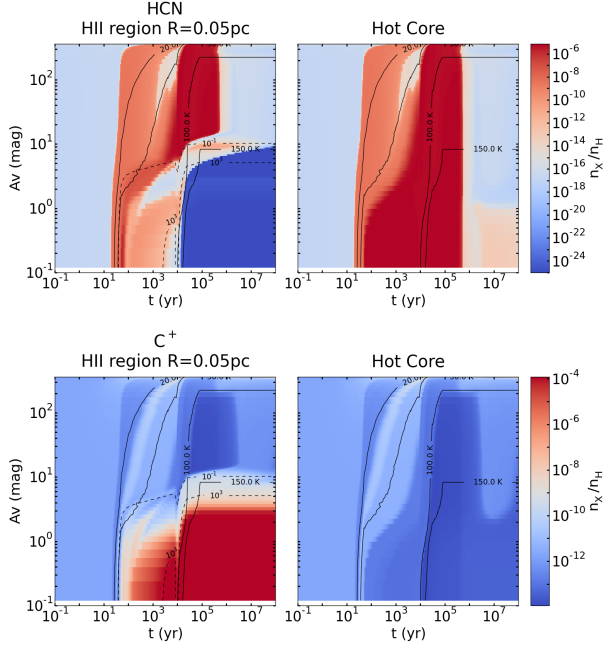
Fig. 8: Spatio-temporal evolution of the abundance of HCN (top panels) and C$^+$ (bottom) for the reference model *mHII* (left panels) and model *mHHC* (right). Contours are plotted: solid line for T_d (20, 30, 100 and 150 K) and dashed lines for χ_0 (10^{-1} and 10^3 Draine unit).
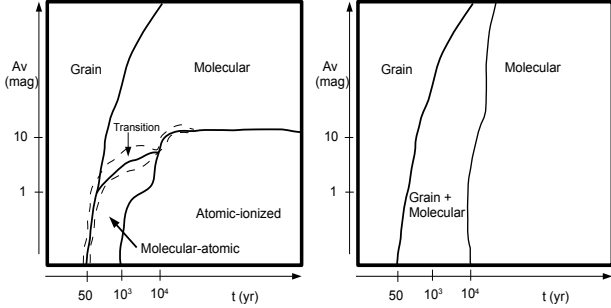
Fig. 9: Schemes showing the different regions in the Hɪɪ region models (left) and in the HMC/HHMC models (right). (symbol 1) Photo-desorption dominates, (symbol2) thermal desorption dominates.

Item 4: For model *mHII:r0.015p1* the density at the ionization front is 10^7 cm^{-3}, for *mHII:r0.05p1* it is 1.56×10^6 cm^{-3}, and 4.15×10^5 cm^{-3} for *mHIIr0.10p1* (instead of 10^7 cm^{-3} in models *mHII:p2.5*). The temperature and radiation field profiles are also slightly different in models *p1* compared to *p2.5*. We retrieve the same conclusions as in the comparison of models with different densities at the ionization front (Item 3).

Item 5: The species abundance changes slightly when using the model *s334*, as we can expect. The main difference appears first between 100 and 10^4 years for extinctions up to 10 mag. Several species have larger abundances in model *s334* like CO$^+$, (s-)CH$_3$OH and (s-)CO$_2$. On the contrary, molecules like O and C$^+$ are less abundant in this region. Secondly, another difference appears around $10^6 - 10^7$ years for higher extinctions. The abundances are lower for model *s334* for H$_2$CO, HCNH$^+$ or C$_2$H$_4$,
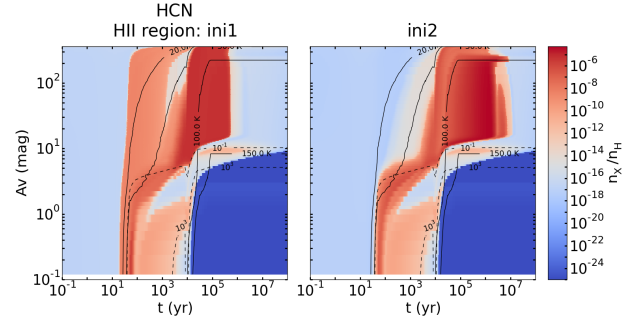
Fig. 10: Spatio-temporal evolution of the abundance of CH$_3$OH for the reference model *mHII* (left panels) and model *mHII:ini2* (right panels). Contours are plotted: solid line for T_d (20, 30, 100 and 150 K) and dashed lines for χ_0 (10^{-1} and 10^3 Draine unit).
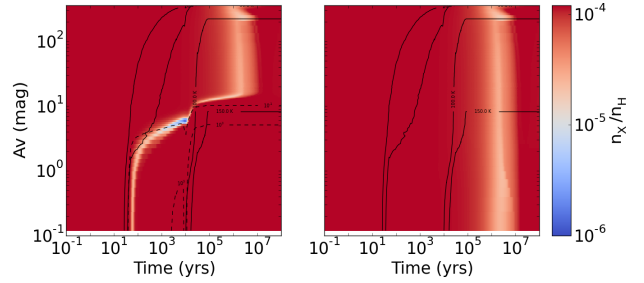
Fig. 11: Spatio-temporal evolution of the C-bearing main species abundances (C$^+$, C, CO, CH$_4$, s-CO, s-CH$_4$) for model *mHII:ini2* (left panel) and model *mHHC:ini2* (right).

and higher for CN, HNC$^+$ for example. First, we have more complex molecules in the *mHHC* model but the abundance of HCOOCH$_3$ decreases around 10^5 years from the edge of the cavity to the core. It is only seen for this complex molecule. Second, we observe a decrease of the abundances in models with bigger Hɪɪ cavity. Finally, more complex molecules are present in models *s334* with lower densities up to 3 mag and from 10^2 to 10^3 years.

Item 6: The dust temperature and radiation field intensity profiles are similar for models with different initial abundances. In model *ini2* we start with about 15 times more s-CH$_4$ and about 10 times less s-CO as seen in Tab. 2. Complex molecules or their precursors are less abundant and we have also less carbon chains in the gas phase and on grain surface. After 30 K carbon chains form on the grain surface until they desorb, before ~ 100 K for most of them, and they begin to form in the gas phase only after 20 K (instead of 15 K for *ini1*). Then, more carbon chains are produced, up to three orders of magnitude, and for a longer period, $2 - 3 \times 10^6$ years longer (see WCCC model in Sakai et al. (2009) for further discussions). In the molecular area from 10^4 to 10^6 years, the abundance of CH$_4$, H$_2$O and NH$_3$ is also higher (15, 5 and 10 times higher respectively). The abundance of radicals leading to these species is also higher but in a lesser extent. On the contrary, CO, O$_2$ and N$_2$ are less abundant (approximatively 10, 7 and 25 times less) until 10^6 years when they become the dominant species.

Table 4: H_2 dissociation front position from the ionization front at 10^5 years for the different models. The dissociation front position is defined at $\frac{n(H_2)}{n_H} = 0.1$. The model with (*) is the reference model.

Models	A_V (mag)	r (AU)	n_H (cm^{-3})
r0.015n7p2.5s183ini1	6.8	88.7	9.26×10^6
r0.05n7p2.5s183ini1 (*)	5.2	64.2	9.82×10^6
r0.10n7p2.5s183ini1	4.8	59.2	9.90×10^6
r0.05n6p2.5s183ini1	5.5	758.3	8.30×10^5
r0.05n5p2.5s183ini1	3.6	54568.4	5.46×10^1
r0.015n7p1s183ini1	6.8	86.4	9.72×10^6
r0.05n7p1s183ini1	5.5	455.3	1.44×10^6
r0.10n7p1s183ini1	4.7	1508.2	3.62×10^5

An interesting result in model *ini2* concerning the C-bearing species is that it exists an area where the main species do not dominate in the medium. It can be seen in Fig. 11 where we sum up the relative abundance of the following species: C, C^+, CO, CH_4, s-CH_4 and s-CO. Some radicals such as CH or CH_3 appear to have larger abundances in the transition area, up to 5 mag, shown in Fig. 9 (left panel). The frontier between different chemical regimes is marked by a dispersion of the elements over a large number of species. But given the short period of time when they pop up it is unlikely to detect them. Between 5 and 10 mag, more complex grain species like s-CO_2, s-C_2H_2, s-C_3H_2 or s-CH_3OH prevail. At higher extinctions few other molecules such as HCN are the dominant species. For $A_V > 300$ mag, as there is no radiation field but the temperature is still higher than 30 K, carbon chains, mostly s-C_4H_2, are formed on the grain surface. Furthermore, when we use the network with 334 species, this decrease of the abundance of the main C-bearing species is less important. In general, the abundance of the transition molecules is higher with a network of 183 species.

Item 7: The abundance profiles are the same for models *c1* and *c6* they just do not extend as much for the last ones.

4.3. Dissociation front

With the abundance profiles we can also define the size of the PDR. In Tab. 4 we present the position of the dissociation front for all our models following the rule detailed in Sec. 3, i.e. the dissociation front is located where $\frac{n(H_2)}{n_H} = 0.1$. For models *mHII:p2.5* the size of the PDR decreases with the size of the HII region and the density at the dissociation front is higher because the radiation field is less strong at the ionization front. On the contrary and as we could expect when the density at the ionization front decreases the size of the PDR increases as the UV radiation penetrate deeper into the core. In the case of model *mHII:r0.05n5p2.5* the PDR covers almost the whole modeling cube. For models *mHII:p1* the distance from the ionization front and the dissociation front increases with the size of the HII region due to a decrease of the density at the ionization front and despite the lower incident radiation field.

4.4. Line emission

We study the line emission for the molecular and atomic transitions presented in Tab. 5. These species are chosen as they might be formed in the internal PDR due the UV radiation like the typical PDR species C^+ and O or on the contrary destroyed or not

Table 5: List of the selected species and one of their transition and its frequency in GHz.

Molecules	Transition	Frequency (GHz)
NH_3	$5(5,1) - 5(5,0)$	24.53
$HC^{15}N$	$1 - 0$	86.06
HCO	$1(0,1) - 0(0,0)$	86.71
$HN^{13}C$	$1 - 0$	87.09
HCO^+	$1 - 0$	89.19
N_2H^+	$1 - 0$	93.17
H_2CO	$2(0,2) - 1(0,1)$	101.33
CN	$1 - 0$	113.12
CH_3OH	$2(2,1) - 3(1,2)$	335.13
$H_2^{18}O$	$4(1,4) - 3(2,1)$	390.61
C	$^3P_1 - {}^3P_0$	492.16
HCN	$7 - 6\ v_2 = 1$	623.36
HNC	$7 - 6\ v_2 = 1$	638.91
C^+	$^2P_{3/2} - {}^2P_{1/2}$	1900.54
O	$^3P_1 - {}^3P_2$	4744.78

formed like $HC^{15}N$ or CH_3OH. We also study HCN (7–6) vibrationally excited states as they trace mainly hot gas found in the inner core. Most of the transitions are chosen because the lines are optically thin and not blended with other lines from the same species. Thus, we use $HC^{15}N$ and $HN^{13}C$ because HCN and HNC are optically thick and self-absorbed after 10^4 years. Even $HC^{15}N$ is optically thick from 10^4 to 3×10^4 years. No isotopologues are included in the chemical network, so to obtain their spectra we use the local ISM isotopologues ratio from Wilson & Rood 1994: $^{12}C/^{13}C = 70$, $^{14}N/^{15}N = 450$ and $^{16}O/^{18}O = 500$.

Assumed detectability threshold: If we consider a rms noise of about 3 mK, all lines with a peak intensity lower than 15 mK or with an integrated intensity below 5×10^{-2} K km s^{-1} can be considered undetectable.

4.4.1. Maps & Integrated intensities

Item 1: With *RADMC-3D* we produce synthetic cubes from which we can extract synthetic maps and spectra. Fig. 12 shows maps of the peak intensity of $HC^{15}N$ (1–0) for model *mHII:r0.05n7p2.5s183ini1c1* (top panels) and model *mHC:r0.05n7p2.5s183ini1c1* (bottom). The maps are shown for different times between 10^3 and 10^5 years and the x-axis represents the distance in parsec from the proto-star. The six top maps are unconvolved and the others are convolved to the beam of the IRAM 30 m telescope. We see that the emission of $HC^{15}N$ increases with time and the HII region emission is weaker than the HMC emission. It also presents a ring structure around the central proto-star. This ring structure is not seen in the convolved spectra[5].

Synthetic spectra obtained for CH_3OH (2(2,1)–3(1,2)) are shown at 1.5×10^4 and 7.5×10^4 years in Fig. 13 for model *mHII* (black), *mHHC* (blue) and *mHC* (green). For the HHMC and HII region models there is no methanol emission around 10^4 years. Later the emission of these two models increased but it remains weaker than in the HMC model by almost one order of magnitude. We can also compute the integrated intensities of the different selected lines. We show the temporal evolution of integrated

---

[5] The free-free continuum was not included, which would result in the lines being seen in absorption.
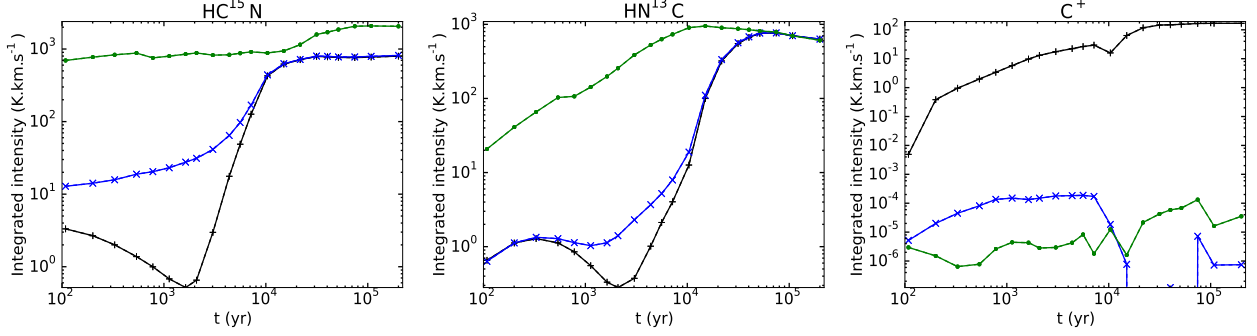
Fig. 14: Time evolution of the integrated intensities of HC^{15}N (1–0) (top left), HN^{13}C (1–0) (top right) and C$^+$ (^{2}P$_{3/2}$–^{2}P$_{1/2}$) (bottom left). Model *mHII* is represented in black, model *mHHC* in blue and model *mHC* in green.
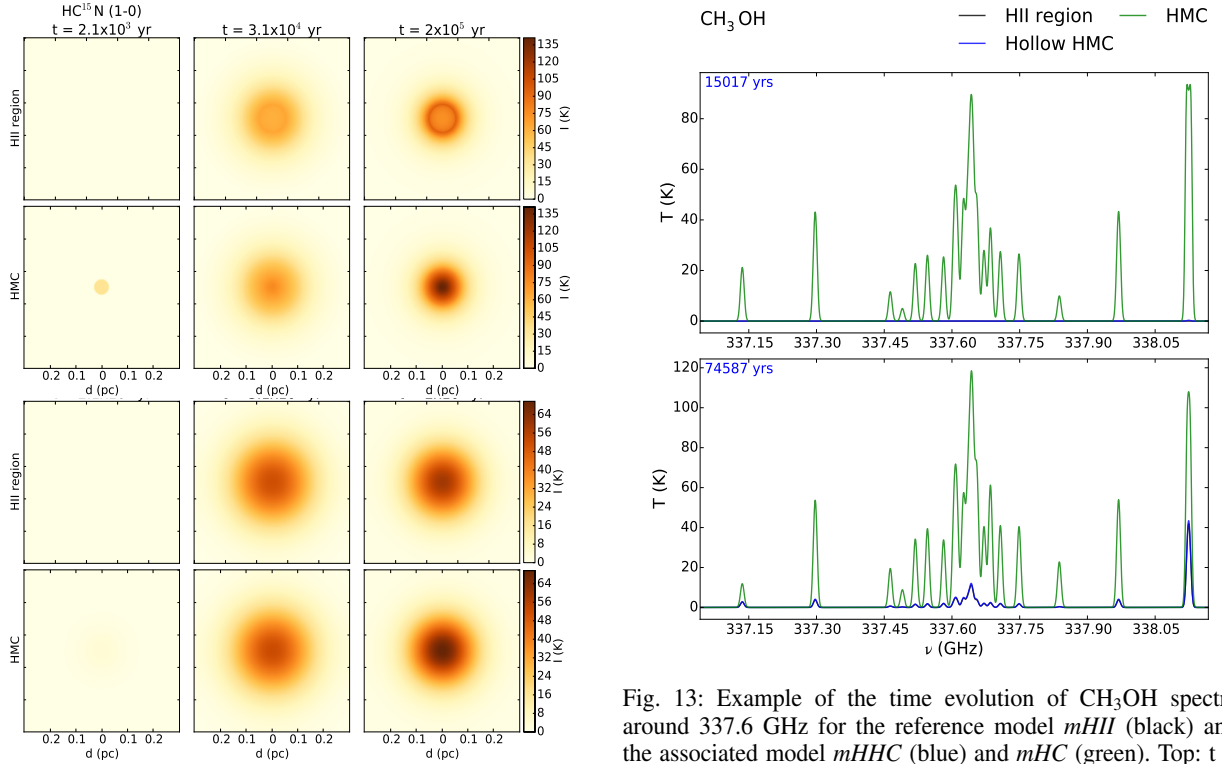
Fig. 12: Time evolution of the HC^{15}N (1–0) maps for the reference model *mHII* (top) and the associated model *mHC* (bottom). The bottom maps represent the same spectra convolved to the beam of the IRAM 30 m telescope. Note that the colorbar scale is different for the raw and convolved spectra. The convolved spectra have a weaker intensity.

Fig. 13: Example of the time evolution of CH$_3$OH spectra around 337.6 GHz for the reference model *mHII* (black) and the associated model *mHHC* (blue) and *mHC* (green). Top: t = 1.5×10^4 years, bottom: t = 7.46×10^4 years.

intensities for HC^{15}N, HN^{13}C and C$^+$ in Fig. 14. The emission of HN^{13}C is similar to the ones of HC^{15}N. Until 10^4 years, the emission of the HHMC model is also stronger than the emission in the HII region model by approximately one order of magnitude for HC^{15}N and a bit less for HC^{15}N. Then they are equal. The emission increases in time for all models and it is stronger for the HMC model. On the contrary the emission for C$^+$ is stronger in the HII region model and appears to be under the detectability of 5×10^{-2} K km s^{-1} for the HMC and HHMC models.

There is no general trend in the evolution of the integrated intensities from one species to another. The emission of O in

the different models behave like for C$^+$. For C, the HII region emission is stronger than the two other models but it becomes equal to the HHMC emission at 10^4 years and the HMC emission is stronger than the HHMC emission until 10^4 years before it decreases to become undetectable. For HCO$^+$ and N$_2$H$^+$ the HHMC and HII region emissions are equal. For H$_2$CO, H$_2^{18}$O and NH$_3$ the HII region emission is stronger than the HHMC emission until 10^4 years. And then it is slightly weaker until 4×10^4 years for H$_2^{18}$O and NH$_3$ before they become equal. For CH$_3$OH, HCO and CN the behavior is the same as HN^{13}C but the HMC emission becomes stronger again after 2×10^4 years in the case of CN. In the case of the vibrationally excited state of the transition 7–6 of HCN and HCN, the HHMC emission is stronger than the HII region but only until 3×10^4 years for HNC.

We also note that the emission of some species is considered as undetectable because it is lower than the threshold of

5×10^{-2} K km s^{-1}. For H$_2^{18}$O and NH$_3$ it happens in the HHMC and Hıı region models before 10^4 years. For HCN and HNC vibrationally excited transitions, it is until about 3×10^3 years for the HHMC model and until 10^4 years for the Hıı region model. CN line can be considered undetectable before 10^3 years for the HMC and HHMC models. The HMC emission for C is lower than the threshold after 2×10^4 years. For CH$_3$OH, it happens for the Hıı region model between 10^4 and 2×10^4 years approximately.

Item 2: Intensities for C$^+$ and O are stronger for the smallest Hıı regions. The opposite happens for N$_2$H$^+$. For the other species the integrated intensity is the strongest for the smallest Hıı region at the beginning of the time evolution and for the biggest Hıı region at the end of the evolution. In the cases of HC^{15}N, HN^{13}C, H$_2$CO and CH$_3$OH the integrated intensity slightly decreases before increasing with a delay when the size of the Hıı region increases. This is due to a delay of the desorption of grain species.

Item 3: For *mHII:n5* models, the integrated intensity of all species, except C$^+$ and O, drops fast from about 10^3 years and after 10^4 years there is no line as we only have atomic-ionized species. Thus at this density the emission for*mHHC* is always stronger except before 500 years. For the other density models *n7* and *n6* the emission is the strongest for the model *n7* except for C$^+$ and O as well as for H$_2$CO until 10^4 years.

Item 4: With this density profile, when we increase the Hıı region size we also decrease the density. The model with the smallest Hıı region size *r0.015* has the highest intensity as its density is higher. This is not the case for the late evolution of C$^+$ and HCO for which the intensities are equal for the different models *mHII:p1*. For CN the intensity is 3 times lower for the model with the biggest Hıı region and it is 2 times lower for N$_2$H$^+$and HCO$^+$. In addition, HCO$^+$ and N$_2$H$^+$ emissions are quite similar for models *mHHC* and *mHII* except for model *r0.10* where the HHMC emission is 10 times lower.

Item 5: For the considered species the results for the models *s183* and *s334* are similar.

Item 6: When we compare models with different initial abundances, we obtain different results except for C$^+$ and O. The integrated intensities are also very similar for molecules like H$_2^{18}$O and HCO$^+$ and C. The strongest difference appears for N$_2$H$^+$ for which model *ini2* gives lower integrated intensities. We also obtain lower intensities for HN^{13}C, HC^{15}N as well as for HCO and CN until about 10^4 years.

Item 7: When we compare the integrated intensities for models with different size of the modeling cube *c1* and *c6*, we observe that C, HCO, HCO$^+$, CN and N$_2$H$^+$ integrated intensities are lower for the small grid, about ten times lower after 10^4 years. The methanol and formaldehyde emission is slightly affected, less than a factor two lower for model *c6*, between 10^3 and 10^4 years approximately for the first molecule and between 10^4 and 3×10^4 years for the second one.

5. Discussion

5.1.

From the abundance profiles of the Hıı region and HMC/HHMC models, we define several regions. The evolution starts with the grain surface chemistry area as molecules are frozen onto the surface in the initial conditions. It ends when the proto-star is evolved enough to emit infrared (IR) as well as UV photons in the Hıı region model. Then, as the proto-star is switched on, the

temperature and radiation field increase. The IR photons penetrate deeper into the cloud and heat up the grains leading to evaporation of some grain surface species between 15 and 30 K for high extinction but it takes more time than close to the Hıı region. Molecules with higher desorption energy thermally desorb later. In reality, they might desorb earlier but photo-desorption reactions are not included in the model for many species. The molecular-atomic and atomic-ionized region, i.e. the internal PDR, is created by the radiation field which dissociates and ionizes the species. This apparition of the PDR is the main difference between the Hıı region and HMC/HHMC models. In addition, we can note that the decrease in the effective temperature of the proto-star (see bottom right panel of Fig. 3) happening at 10^4 years affects the temperature and radiation field intensity. They both decrease at this time and thus affect the abundance and line emission of the species.

We have seen that C$^+$ and O emit only in the Hıı region models and their emission is not affected when we remove the envelope. This indicates that they are possible tracers of the internal PDR. Furthermore, we have seen that the internal PDR is extremely thin with a size ranging between 50 and 1500 AU depending on the models' parameters. Assuming a source at a distance of 1 kpc, we would need an angular resolution of maximum $0.04 - 0.05''$ to be able to resolve the minimal size of the internal PDR. Thus, to trace it and avoid extended emission we need high spatial resolution interferometric observations which are now possible with ALMA. But no instruments currently allow the observations of the THz frequency range necessary to observe C$^+$ and O at the required resolution for internal PDRs. In addition, limitations of the models, such as the absence of an external radiation field, might underestimate the emission of these atoms coming from the envelope. Interferometric observations are thus absolutely mandatory to filter out the extended emission.

The emission from the envelope affects the emission of some species. C could also trace the internal PDR as the emission is stronger in the Hıı region in the early stage of the evolution until 10^4 years. This is harder to observe due to the short time spent by the object in this phase. In addition, C emission is affected by the envelope mostly after that time as the HMC emission is in absorption and the intensity of the line in the Hıı region model decreases when we filter out the extended emission in the late times of the evolution. Since atomic carbon can be observed with ALMA band 8, this is an interesting test to try. Some other species emission is as well strongly affected by the envelope. Those species are N$_2$H$^+$, HCO, HCO$^+$ and CN. Due to the decrease in their emission they might not be good tracers to distinguish between Hıı regions and HMC as they do not trace the inner core. NH$_3$ emission is also affected when removing the extended emission but in a lesser extent.

Molecules like CH$_3$OH, H$_2^{18}$O or NH$_3$ appear to be detectable (I$_{peak} \geq 15$ mK) around 10^4 years for the HHMC models and only around 4×10^4 years for the Hıı region models. The intensities of methanol in theHHMC models yet remain quite low (I$_{peak} \sim 0.1$ K) during the time when the Hıı region emission is still too weak. It seems these molecules are destroyed mainly during the desorption process when the UV radiation field starts to be strong. The few molecules which desorb are photo-dissociated in a short time (~ 50 years). They appear again after 10^4 years due to thermal desorption outside the PDR before being destroyed at 10^6 years. However in the HMC model, model without the ionized cavity around the proto-star, the abundance for these molecules is also high at the center inducing strong intensities from 100 years. These molecules might help to
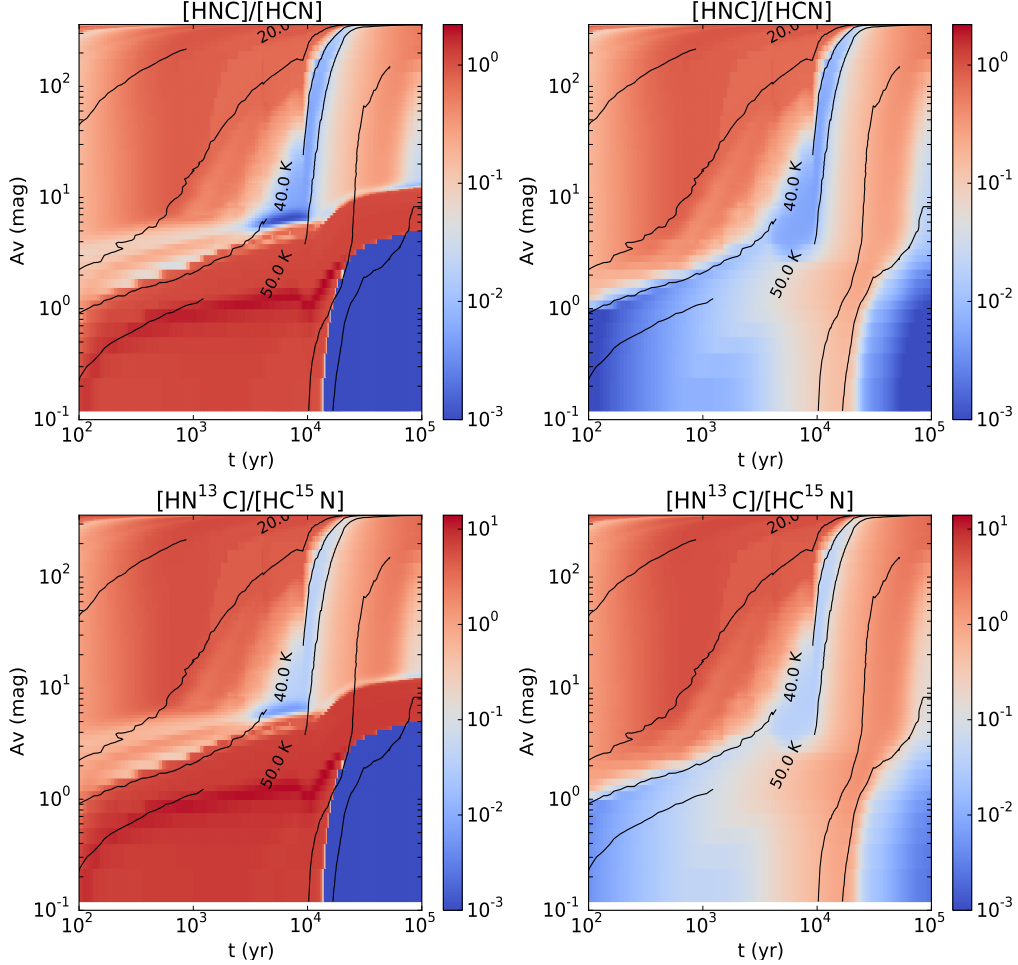
Fig. 15: Spatio-temporal evolution, focused between 100 and 10^5 years, of the abundance ratio [HNC]/[HCN] for the reference model *mHII* (left) and the corresponding *mHHC* model (right). Contours are plotted for T_d (20, 30, 40, 50, 100 and 150 K). The bottom panels show the same results for [HN^{13}C]/[HC^{15}N].

trace the HMC phase as well as H_2CO. It is always detectable for the three models but the emission for the HMC model is much stronger despite that they tend to be equal once it thermally desorbs. In addition, a ring structure seems to appear in the HII region model in the raw synthetic maps. But the convolution to the beam of the IRAM 30 m telescope for example attenuates this effect. The vibrationally excited levels of HCN trace the hot gas and could be used to distinguish the hot core and the HII region as the emission is stronger in the HHMC model. This is not the case for HNC vibrationally excited level. This difference between HCN and HNC could happen because the abundance of HCN is really high near the ionized cavity ($\geq 10^{-6}$) for the HHMC model whereas the HNC abundance is about four magnitudes lower. The region up to an extinction of 5 mag has then more influence on the intensity for HCN.

Our results show that the region where UV radiation influences chemistry is spread in time but remains thin, mainly for high density ($\geq 10^6$ cm^{-3}). Hence, we do not obtain certain molecules which appear to be abundant in observations. HCO$^+$ is usually optically thick in observations of hot cores or HII regions but in the models it is destroyed around 10^4 years. Destruction of HCO$^+$ is mainly due to dissociative recombination forming H and CO and by reactions with HCN and H_2O which are re-

ally abundant because of thermal desorption. In addition, CO$^+$ is an important species in PDRs and its abundance is enhanced when irradiated by strong UV fields. However we do not produce enough CO$^+$ in the models. In model *n5* the low frequency transitions (e.g., 117.69 and 235.79 GHz) are not detectable but it weakly appear, $I_{peak} \approx 30$ mK, for higher frequency transitions (353.74, 471.67 GHz) on a short time around 100 years. CO$^+$ is rapidly destroyed to form C$^+$. For the other models the medium is too dense, the UV field cannot penetrate deep enough into the cloud and thus the PDR remains too thin. This issue has been discussed in Bruderer et al. (2009b). They circumvent it by modeling a proto-star embedded in a cavity produced by a bipolar outflow. It provides a larger surface to UV radiation.

There is also an important dependence of the results on the initial abundances. Obtaining good initial conditions is thus a critical matter. In this work the first set of initial abundances, from the collapsing cold core in two steps, seems to be more realistic than the second set. However, implementing a real collapse of the core by adding the temporal evolution of the density like in Garrod & Herbst (2006) would be the next step.

The spectra are obtained without including the free-free emission which might be an important for transitions at lower frequency in the HII region models. Thus, the continuum level
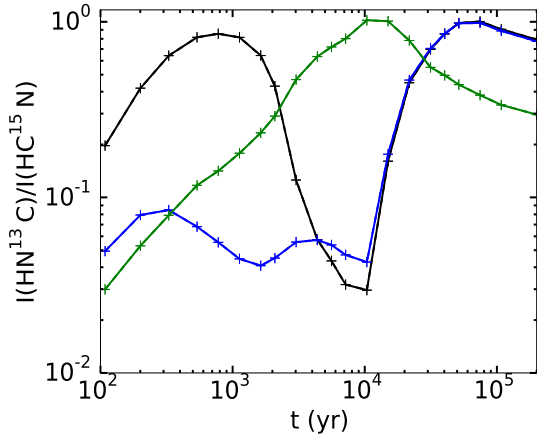
Fig. 16: Time evolution for the reference model *mHII* (black), *mHHC* (blue) and *mHC* (green) of integrated intensity ratio $(HN^{13}C (1–0) / HC^{15}N (1–0))$

for H$_{II}$ region models' spectra is lower, close to zero for the lower frequency transitions.

5.2. [HNC]/[HCN]

In Fig. 15 we present the spatio-temporal variations of the abundance ratio [HN^{13}C]/[HC^{15}N] and [HNC]/[HCN] for the H$_{II}$ region (left) and HHMC (right) models. The colorbar varies from 10^{-3} and 14 because the ratio varies from approximately 10^{-2} to 14, if we do not consider the PDR region from 10^4 years and A_V < 5 mag. The maximum ratio appears in the H$_{II}$ region model. In the HHMC model the maximum is around 6.5. The variations for the ratio [HNC]/[HCN] are from 10^{-3} to 1.07 for *mHHC* and to 2.16 for *mHII*. The variations in the abundance ratio result into temporal variations of the line intensity ratio seen in Fig. 16. The main contribution to the intensity ratio comes from the part of the core where the extinction is higher than 4 mag approximately, whatever the size of the H$_{II}$ region. The ratio is barely affected by the evolution of the radiation field which influences the core only for extinction lower than 5 mag. Different works on the [HNC]/[HCN] ratio show that it depends on the kinetic temperature in the cloud (Goldsmith et al. 1986; Schilke et al. 1992; Wang et al. 2009; Jin et al. 2015). In the model the ratio increases until the temperature is around 20 K, then it decreases. It goes through a minimum when the temperature of the core is between 40 and 50 K. The ratio increases again until the temperature reaches about 150 K. The behavior found for [HN^{13}C]/[HC^{15}N] is the same for [HNC]/[HCN]. This strong decrease around 40 K is due to the thermal desorption of s-HCN which is faster than for s-HNC. The thermal desorption of s-HNC is slowed down due to the decrease of the abundance of s-HNC around 3×10^3 years because it reacted with s-H to form s-HCN or HCN via reactive desorption.

In Schilke et al. (1992) the minimum for a cloud with a density of 10^7 cm^{-3} appears at 30 K and in Graninger et al. (2014) the abundance ratio is found to go through a minimum for a temperature around $30 – 40$ K. This ratio also depends on the density of the core as the integrated intensity ratio is smaller for lower density due to a lower abundance ratio but the minimum is the same.

The intensity ratio of the vibrationally excited line of HNC and HCN decreases from 10^4 to 10^5 years. Before these times the

ratio does not exist because the line emission is extremely low / undetectable. The decrease of the ratio indicates that the major contribution to the line emission for these transitions comes from the inner core where the temperature is high. The abundance ratio decreases close to the ionized cavity for *mHII* and *mHHC* affecting in a similar manner the intensity ratio.

6. Conclusion

6.1. Summary

We investigate the spatio-temporal evolution of the chemistry in HC/UCH$_{II}$ region and hot molecular cores using the spatio-temporal evolution of the dust temperature and the UV radiation field to obtain the detailed modeling of relative abundances and the temporal evolution of line emission of selected species. All the abundance profiles clearly show a difference between these two phases of massive star formation. But the tracers of the HC/UCH$_{II}$ region phases, C$^+$ and O, appear to not be observable due to the capabilities of the current instruments which do not allow to resolve the internal PDR in the THz range. C might be a target for ALMA. The PDR is extremely thin, with a size ranging from about 50 to 1500 AU, and barely affects the emission of the other species. The HMC emission is stronger than the H$_{II}$ region, due to an increased column density, during most of the time evolution for some species: HC^{15}N, HN^{13}C, H$_2$CO, H$_2^{18}$O, NH$_3$ and CH$_3$OH. More species could exhibit this behavior and remain to be investigated.

6.2. Outlook

In addition, the models can be improved in many different ways. Some outlooks for this work are as follows:

1. We assume in the current models a gas temperature equals to the dust temperature. We have seen that this is not the case in the PDR where the gas temperature is about ten times the dust temperature. Improving the treatment of thermal balance is necessary. This could be done by implementing relevant heating and cooling processes in *Saptarsy*.
2. We also would like to investigate HC/UCH$_{II}$ regions in the context of ionized cavities (Peters et al. 2010a) or PDRs on outflow cavities (Visser et al. 2012; Bruderer et al. 2009b) which create large surfaces and thus more easily observable chemistry. Therefore, we would have to increase the complexity of the source structure.
3. We are currently improving the treatment of the grain chemistry by incorporating a multilayer ice mantle.
4. Finally, we plan to implement the treatment of dynamics in the models (e.g., including infall and following the parcels of gas or by post-processing data obtained with a MHD code). It appears essential to obtain dynamical models for the pre-stellar phase in order to fix the initial conditions.

We would like to compare our results with molecular lines found in the main PDR surrounding the UCH$_{II}$ region of Monoceros R2. This UCH$_{II}$ region is the closest with a distance of 830 pc (Herbst & Racine 1976) and is irradiated by the main infrared B0-type star IRS 1. In this region densities are around 10^6–10^7 cm^{-3} and the UV field is superior to 10^5 Habing unit which fits our models parameters. In Treviño-Morales (2015), integrated intensities for all lines observed with IRAM 30 m telescope are tabulated (see also Treviño-Morales et al. (2014)).

References

Beuther, H., Churchwell, E. B., McKee, C. F., & Tan, J. C. 2007, Protostars and Planets V, 165

Bruderer, S., Benz, A. O., Bourke, T. L., & Doty, S. D. 2009a, A&A, 503, L13

Bruderer, S., Benz, A. O., Doty, S. D., van Dishoeck, E. F., & Bourke, T. L. 2009b, ApJ, 700, 872

Choudhury, R., Schilke, P., Stéphan, G., et al. 2015, A&A, 575, A68

Churchwell, E. 2002, ARA&A, 40, 27

De Pree, C. G., Peters, T., Mac Low, M.-M., et al. 2014, ApJ, 781, L36

Didelon, P., Motte, F., Tremblin, P., et al. 2015, A&A, 584, A4

Draine, B. T. & Bertoldi, F. 1996, ApJ, 468, 269

Garrod, R. T. 2013, ApJ, 765, 60

Garrod, R. T. & Herbst, E. 2006, A&A, 457, 927

Garrod, R. T., Wakelam, V., & Herbst, E. 2007, A&A, 467, 1103

Gaume, R. A., Goss, W. M., Dickel, H. R., Wilson, T. L., & Johnston, K. J. 1995, ApJ, 438, 776

Goldsmith, P. F., Irvine, W. M., Hjalmarson, A., & Ellder, J. 1986, ApJ, 310, 383

Graninger, D. M., Herbst, E., Öberg, K. I., & Vasyunin, A. I. 2014, ApJ, 787, 74

He, J., Shi, J., Hopkins, T., Vidali, G., & Kaufman, M. J. 2015, ApJ, 801, 120

Herbst, E. & van Dishoeck, E. F. 2009, ARA&A, 47, 427

Herbst, W. & Racine, R. 1976, AJ, 81, 840

Hoare, M. G., Kurtz, S. E., Lizano, S., Keto, E., & Hofner, P. 2007, Protostars and Planets V, 181

Hosokawa, T. & Omukai, K. 2009, ApJ, 691, 823

Jin, M., Lee, J.-E., & Kim, K.-T. 2015, ApJS, 219, 2

Jing, D., He, J., Brucato, J. R., et al. 2012, ApJ, 756, 98

Jura, M. 1974, ApJ, 191, 375

Jura, M. 1975, ApJ, 197, 575

Kurtz, S. 2005, in IAU Symposium, Vol. 227, Massive Star Birth: A Crossroads of Astrophysics, ed. R. Cesaroni, M. Felli, E. Churchwell, & M. Walmsley, 111–119

Kurtz, S., Cesaroni, R., Churchwell, E., Hofner, P., & Walmsley, C. M. 2000, Protostars and Planets IV, 299

Laor, A. & Draine, B. T. 1993, ApJ, 402, 441

Le Bourlot, J., Le Petit, F., Pinto, C., Roueff, E., & Roy, F. 2012, A&A, 541, A76

Le Petit, F., Nehmé, C., Le Bourlot, J., & Roueff, E. 2006, ApJS, 164, 506

Lee, H.-H., Herbst, E., Pineau des Forets, G., Roueff, E., & Le Bourlot, J. 1996, A&A, 311, 690

Lee, S., Lee, J.-E., & Bergin, E. A. 2015, ApJS, 217, 30

Loison, J.-C., Wakelam, V., & Hickson, K. M. 2014, MNRAS, 443, 398

Noble, J. A., Theule, P., Mispelaer, F., et al. 2012, A&A, 543, A5

Panoglou, D., Cabrit, S., Pineau Des Forêts, G., et al. 2012, A&A, 538, A2

Peters, T., Banerjee, R., Klessen, R. S., et al. 2010a, ApJ, 711, 1017

Peters, T., Mac Low, M.-M., Banerjee, R., Klessen, R. S., & Dullemond, C. P. 2010b, ApJ, 719, 831

Qin, S.-L., Schilke, P., Rolffs, R., et al. 2011, A&A, 530, L9

Sakai, S., Motome, Y., & Imada, M. 2009, Physical Review Letters, 102, 056404

Sánchez-Monge, Á., Kurtz, S., Palau, A., et al. 2013, ApJ, 766, 114

Schilke, P., Walmsley, C. M., Pineau Des Forets, G., et al. 1992, A&A, 256, 595

Schmiedeke, A., Schilke, P., Möller, T., et al. 2016, A&A, 588, A143

Semenov, D., Hersant, F., Wakelam, V., et al. 2010, A&A, 522, A42

Sternberg, A., Le Petit, F., Roueff, E., & Le Bourlot, J. 2014, ApJ, 790, 10

Treviño-Morales, S. P., Pilleri, P., Fuente, A., et al. 2014, A&A, 569, A19

Treviño-Morales, S. 2015, PhD thesis, http://hdl.handle.net/10481/42409

Vasyunin, A. I. & Herbst, E. 2013, ApJ, 762, 86

Visser, R., Kristensen, L. E., Bruderer, S., et al. 2012, A&A, 537, A55

Wakelam, V. & Herbst, E. 2008, ApJ, 680, 371

Wang, M., Chin, Y.-N., Henkel, C., Whiteoak, J. B., & Cunningham, M. 2009, ApJ, 690, 580

Wilson, T. L. & Rood, R. 1994, ARA&A, 32, 191

Wood, D. O. S. & Churchwell, E. 1989, ApJS, 69, 831

Appendix A: *Saptarsy*: further modifications

In addition to use the patio-temporal evolution of the mean intensity into *Saptarsy* we made some other modifications in the code. We choose to give to the solver the natural logarithm of the chemical abundances of each species instead of the abundances in order to improve the stability of the code. The ordinary differential equations as well as the Jacobian matrix are thus computed differently. We compute the chemical abundances of the different species n_x using $\frac{dn_x}{dt}$ and $J_F = \frac{\partial \dot{n}_{x_i}}{\partial n_{x_j}}$. Now we want to compute $ln(n_x)$, so the new differential equations are $\frac{dln(n_x)}{dt} = \frac{1}{n_x}\frac{dn_x}{dt}$ and the Jacobian is now:

$$J_G(i,i) = \frac{\partial ln(\dot{n}_i)}{\partial ln(n_i)} = \frac{\partial \dot{n}_i}{\partial n_i} - \frac{1}{n_i}\frac{dn_i}{dt}$$

$$J_G(i,j) = \frac{\partial ln(\dot{n}_i)}{\partial ln(n_j)} = \frac{n_j}{n_i}\frac{\partial \dot{n}_i}{\partial n_j}$$

The gas and dust temperatures and the radiation field intensity are defined as time-dependent polynomials using the values computed by *RADMC-3D*. A spline interpolation is performed to determine the function parameters and thus the time derivatives and Jacobian parameters for these variables which are then used by the solver. Thanks to the interpolation we are no longer restricted to use the same number of time steps than the ones used in *Pandora* for the computation of T_d and J_ν. Thus, the models can be less time consuming. As a final major change, the reaction rates are now computed for each internal time step of *DVODPK* giving more accurate results for the abundances.

Bibliography

Adams, F. C., Emerson, J. P., & Fuller, G. A. 1990, ApJ, 357, 606

Adams, F. C., Lada, C. J., & Shu, F. H. 1987, ApJ, 312, 788

Andre, P., Montmerle, T., Feigelson, E. D., & Steppe, H. 1990, A&A, 240, 321

Bacmann, A., Taquet, V., Faure, A., Kahane, C., & Ceccarelli, C. 2012, A&A, 541, L12

Balucani, N., Ceccarelli, C., & Taquet, V. 2015, MNRAS, 449, L16

Bates, D. R. & Spitzer, Jr., L. 1951, ApJ, 113, 441

Beckwith, S. V. W. & Sargent, A. I. 1991, ApJ, 381, 250

Beckwith, S. V. W., Sargent, A. I., Chini, R. S., & Guesten, R. 1990, AJ, 99, 924

Bergin, E. A., Phillips, T. G., Comito, C., et al. 2010, A&A, 521, L20

Bergin, E. A. & Tafalla, M. 2007, ARA&A, 45, 339

Bernstein, R. A., Freedman, W. L., & Madore, B. F. 2002, ApJ, 571, 56

Beuther, H., Churchwell, E. B., McKee, C. F., & Tan, J. C. 2007, Protostars and Planets V, 165

Bianchi, S., Gonçalves, J., Albrecht, M., et al. 2003, A&A, 399, L43

Bjorkman, J. E. & Wood, K. 2001, ApJ, 554, 615

Black, J. H. & Dalgarno, A. 1976, ApJ, 203, 132

Blake, G. A., Sutton, E. C., Masson, C. R., & Phillips, T. G. 1987, ApJ, 315, 621

Bohlin, R. C., Savage, B. D., & Drake, J. F. 1978, ApJ, 224, 132

Bonnell, I. A., Bate, M. R., Clarke, C. J., & Pringle, J. E. 1997, MNRAS, 285, 201

Bonnell, I. A., Bate, M. R., & Zinnecker, H. 1998, MNRAS, 298, 93

Boulanger, F., Abergel, A., Bernard, J.-P., et al. 1996, A&A, 312, 256

Brinch, C. & Hogerheijde, M. R. 2010, A&A, 523, A25

Brown, P. N., Byrne, G. D., & Hindmarsh, A. C. 1989, SIAM J. Sci. Stat. Comput., 10, 1038

Brown, P. N. & Hindmarsh, A. C. 1989, in Proceedings of the Conference on Numerical Ordinary Differential Equations (New York, NY, USA: ACM), 40–91

Bruderer, S., Benz, A. O., Bourke, T. L., & Doty, S. D. 2009a, A&A, 503, L13

Bruderer, S., Benz, A. O., Doty, S. D., van Dishoeck, E. F., & Bourke, T. L. 2009b, ApJ, 700, 872

Calcutt, H., Viti, S., Codella, C., et al. 2014, MNRAS, 443, 3157

Cazaux, S. & Tielens, A. G. G. M. 2004, ApJ, 604, 222

Cesaroni, R., Churchwell, E., Hofner, P., Walmsley, C. M., & Kurtz, S. 1994, A&A, 288

Cesaroni, R., Hofner, P., Walmsley, C. M., & Churchwell, E. 1998, A&A, 331, 709

Charnley, S. B. 1998, ApJ, 509, L121

Charnley, S. B. 2001, ApJ, 562, L99

Chini, R., Kruegel, E., & Kreysa, E. 1986, A&A, 167, 315

Choudhury, R., Schilke, P., Stéphan, G., et al. 2015, A&A, 575, A68

Comito, C., Schilke, P., Phillips, T. G., et al. 2005, ApJS, 156, 127

Crockett, N. R., Bergin, E. A., Wang, S., et al. 2010, A&A, 521, L21

Csengeri, T., Bontemps, S., Schneider, N., Motte, F., & Dib, S. 2011, A&A, 527, A135

Dickey, J. M. & Lockman, F. J. 1990, ARA&A, 28, 215

Didelon, P., Motte, F., Tremblin, P., et al. 2015, A&A, 584, A4

Downes, D., Winnberg, A., Goss, W. M., & Johansson, L. E. B. 1975, A&A, 44, 243

Draine, B. T. 1978, ApJS, 36, 595

Draine, B. T. 2003, ARA&A, 41, 241

Draine, B. T. 2011, Physics of the Interstellar and Intergalactic Medium

Draine, B. T. & Bertoldi, F. 1996, ApJ, 468, 269

Draine, B. T. & Lee, H. M. 1984, ApJ, 285, 89

Draine, B. T. & Li, A. 2007, ApJ, 657, 810

Dullemond, C. P. 2012, RADMC-3D: A multi-purpose radiative transfer tool, Astrophysics Source Code Library

Flower, D. R., Pineau des Forets, G., & Hartquist, T. W. 1985, MNRAS, 216, 775

Fuente, A., Rodrıguez-Franco, A., Garcıa-Burillo, S., Martın-Pintado, J., & Black, J. H. 2003, A&A, 406, 899

Garrod, R. T. 2008, A&A, 491, 239

Garrod, R. T. 2013a, ApJ, 765, 60

Garrod, R. T. 2013b, ApJ, 778, 158

Garrod, R. T. & Herbst, E. 2006, A&A, 457, 927

Garrod, R. T., Wakelam, V., & Herbst, E. 2007, A&A, 467, 1103

Gillespie, D. T. 1976, Journal of Computational Physics, 22, 403

Godard, B., Falgarone, E., & Pineau des Forêts, G. 2014, A&A, 570, A27

Goldsmith, P. F., Bergin, E. A., & Lis, D. C. 1997, ApJ, 491, 615

Graninger, D. M., Herbst, E., Öberg, K. I., & Vasyunin, A. I. 2014, ApJ, 787, 74

Green, N. J. B., Toniazzo, T., Pilling, M. J., et al. 2001, A&A, 375, 1111

Habing, H. J. 1968, Bull. Astron. Inst. Netherlands, 19, 421

Hasegawa, T. I. & Herbst, E. 1993a, MNRAS, 261, 83

Hasegawa, T. I. & Herbst, E. 1993b, MNRAS, 263, 589

Hasegawa, T. I., Herbst, E., & Leung, C. M. 1992, ApJS, 82, 167

He, J., Shi, J., Hopkins, T., Vidali, G., & Kaufman, M. J. 2015, ApJ, 801, 120

Heiles, C. & Troland, T. H. 2003, ApJ, 586, 1067

Herbst, E. & van Dishoeck, E. F. 2009, ARA&A, 47, 427

Herbst, W. & Racine, R. 1976, AJ, 81, 840

Hildebrand, R. H. 1983, QJRAS, 24, 267

Hoare, M. G., Kurtz, S. E., Lizano, S., Keto, E., & Hofner, P. 2007, Protostars and Planets V, 181

Hollenbach, D. J. & Tielens, A. G. G. M. 1997, ARA&A, 35, 179

Hoq, S., Jackson, J. M., Foster, J. B., et al. 2013, ApJ, 777, 157

Horn, A., Møllendal, H., Sekiguchi, O., et al. 2004, ApJ, 611, 605

Hosokawa, T. & Omukai, K. 2009, ApJ, 691, 823

Jeans, J. H. 1955, The dynamical theory of gases

Jing, D., He, J., Brucato, J. R., et al. 2012, ApJ, 756, 98

Jones, A. P. 2012, A&A, 540, A2

Jones, A. P., Fanciullo, L., Köhler, M., et al. 2013, A&A, 558, A62

Jura, M. 1974, ApJ, 191, 375

Kramer, C., Richer, J., Mookerjea, B., Alves, J., & Lada, C. 2003, A&A, 399, 1073

Krumholz, M. 2008, in Astronomical Society of the Pacific Conference Series, Vol. 390, Pathways Through an Eclectic Universe, ed. J. H. Knapen, T. J. Mahoney, & A. Vazdekis, 16

Krumholz, M. R. 2006, ArXiv Astrophysics e-prints [astro-ph/0607429]

Kuan, Y.-J., Mehringer, D. M., & Snyder, L. E. 1996, ApJ, 459, 619

Kurtz, S. 2005, in IAU Symposium, Vol. 227, Massive Star Birth: A Crossroads of Astrophysics, ed. R. Cesaroni, M. Felli, E. Churchwell, & M. Walmsley, 111–119

Kurtz, S., Cesaroni, R., Churchwell, E., Hofner, P., & Walmsley, C. M. 2000, Protostars and Planets IV, 299

Kurtz, S. E. 2000, in Revista Mexicana de Astronomia y Astrofisica Conference Series, Vol. 9, Revista Mexicana de Astronomia y Astrofisica Conference Series, ed. S. J. Arthur, N. S. Brickhouse, & J. Franco, 169–176

Laor, A. & Draine, B. T. 1993, ApJ, 402, 441

Larson, R. B. 1969, MNRAS, 145, 271

Le Bourlot, J., Le Petit, F., Pinto, C., Roueff, E., & Roy, F. 2012, A&A, 541, A76

Le Petit, F., Nehmé, C., Le Bourlot, J., & Roueff, E. 2006, ApJS, 164, 506

Lee, H.-H., Herbst, E., Pineau des Forets, G., Roueff, E., & Le Bourlot, J. 1996, A&A, 311, 690

Lee, S., Lee, J.-E., & Bergin, E. A. 2015, ApJS, 217, 30

Leger, A., Jura, M., & Omont, A. 1985, in NATO Advanced Science Institutes (ASI) Series C, Vol. 157, NATO Advanced Science Institutes (ASI) Series C, ed. G. H. F. Diercksen, W. F. Huebner, & P. W. Langhoff, 701

Leurini, S., Wyrowski, F., Wiesemeyer, H., et al. 2015, A&A, 584, A70

Li, C. & White, S. D. M. 2009, MNRAS, 398, 2177

Lis, D. C. 2000, in ESA Special Publication, Vol. 445, Star Formation from the Small to the Large Scale, ed. F. Favata, A. Kaas, & A. Wilson, 187–194

Lis, D. C. & Goldsmith, P. F. 1989, in IAU Symposium, Vol. 135, Interstellar Dust, ed. L. J. Allamandola & A. G. G. M. Tielens, 205P

Lis, D. C. & Goldsmith, P. F. 1990, ApJ, 356, 195

Loison, J.-C., Wakelam, V., & Hickson, K. M. 2014, MNRAS, 443, 398

Mathis, J. S. 1990, ARA&A, 28, 37

Mathis, J. S., Rumpl, W., & Nordsieck, K. H. 1977, ApJ, 217, 425

McKee, C. F. & Ostriker, J. P. 1977, ApJ, 218, 148

McKee, C. F. & Tan, J. C. 2003, ApJ, 585, 850

McMillan, P. J. 2011, MNRAS, 414, 2446

Mehringer, D. M., Snyder, L. E., Miao, Y., & Lovas, F. J. 1997, ApJ, 480, L71

Minissale, M., Dulieu, F., Cazaux, S., & Hocuk, S. 2016, A&A, 585, A24

Miville-Deschênes, M.-A., Salomé, Q., Martin, P. G., et al. 2016, ArXiv e-prints [[arXiv]1602.03340]

Molinari, S., Pezzuto, S., Cesaroni, R., et al. 2008, A&A, 481, 345

Möller, T., Bernst, I., Panoglou, D., et al. 2013, A&A, 549, A21

Müller, H. S. P., Schlöder, F., Stutzki, J., & Winnewisser, G. 2005, Journal of Molecular Structure, 742, 215

Müller, H. S. P., Thorwirth, S., Roth, D. A., & Winnewisser, G. 2001, A&A, 370, L49

Neill, J. L., Bergin, E. A., Lis, D. C., et al. 2014, ApJ, 789, 8

Noble, J. A., Theule, P., Mispelaer, F., et al. 2012, A&A, 543, A5

Nummelin, A., Bergman, P., Hjalmarson, Å., et al. 2000, ApJS, 128, 213

Ossenkopf, V. & Henning, T. 1994, A&A, 291, 943

Panoglou, D., Cabrit, S., Pineau Des Forêts, G., et al. 2012, A&A, 538, A2

Paradis, D., Bernard, J.-P., & Mény, C. 2009, A&A, 506, 745

Paradis, D., Veneziani, M., Noriega-Crespo, A., et al. 2010, A&A, 520, L8

Peñarrubia, J., Ma, Y.-Z., Walker, M. G., & McConnachie, A. 2014, MNRAS, 443, 2204

Peimbert, M. 1967, ApJ, 150, 825

Peretto, N., Fuller, G. A., Duarte-Cabral, A., et al. 2013, A&A, 555, A112

Peretto, N., Hennebelle, P., & André, P. 2007, A&A, 464, 983

Peters, T., Banerjee, R., Klessen, R. S., et al. 2010a, ApJ, 711, 1017

Peters, T., Mac Low, M.-M., Banerjee, R., Klessen, R. S., & Dullemond, C. P. 2010b, ApJ, 719, 831

Pickett, H. M., Poynter, R. L., Cohen, E. A., et al. 1998, J. Quant. Spectr. Rad. Transf., 60, 883

Pilleri, P., Fuente, A., Cernicharo, J., et al. 2012, A&A, 544, A110

Qin, S.-L., Schilke, P., Rolffs, R., et al. 2011, A&A, 530, L9

Rizzo, J. R., Fuente, A., Rodríguez-Franco, A., & García-Burillo, S. 2003, ApJ, 597, L153

Röllig, M., Ossenkopf, V., Jeyakumar, S., Stutzki, J., & Sternberg, A. 2006, A&A, 451, 917

Roy, N., Kanekar, N., Braun, R., & Chengalur, J. N. 2013, MNRAS, 436, 2352

Ruffle, D. P. & Herbst, E. 2000, MNRAS, 319, 837

Saury, E., Miville-Deschênes, M.-A., Hennebelle, P., Audit, E., & Schmidt, W. 2014, A&A, 567, A16

Savage, B. D. & Mathis, J. S. 1979, ARA&A, 17, 73

Savage, B. D. & Wakker, B. P. 2009, ApJ, 702, 1472

Schilke, P., Benford, D. J., Hunter, T. R., Lis, D. C., & Phillips, T. G. 2001, ApJS, 132, 281

Schilke, P., Walmsley, C. M., Pineau Des Forets, G., et al. 1992, A&A, 256, 595

Schmiedeke, A., Schilke, P., Möller, T., et al. 2016, A&A, 588, A143

Seifried, D., Schmidt, W., & Niemeyer, J. C. 2011, A&A, 526, A14

Seifried, D. & Walch, S. 2016, MNRAS, 459, L11

Semenov, D., Hersant, F., Wakelam, V., et al. 2010, A&A, 522, A42

Shirley, Y. L., Huard, T. L., Pontoppidan, K. M., et al. 2011, ApJ, 728, 143

Shu, F. H. 1977, ApJ, 214, 488

Smith, M. D. 2014, MNRAS, 438, 1051

Smith, R. K. & Dwek, E. 1998, ApJ, 503, 831

Snyder, L. E., Kuan, Y.-J., & Miao, Y. 1994, in Lecture Notes in Physics, Berlin Springer Verlag, Vol. 439, The Structure and Content of Molecular Clouds, ed. T. L. Wilson & K. J. Johnston, 187

Sparke, L. S. & Gallagher, III, J. S. 2000, Galaxies in the universe : an introduction, 416

Stecher, T. P. & Williams, D. A. 1967, ApJ, 149, L29

Sternberg, A., Le Petit, F., Roueff, E., & Le Bourlot, J. 2014, ApJ, 790, 10

Stognienko, R., Henning, T., & Ossenkopf, V. 1995, A&A, 296, 797

Sutton, E. C., Peng, R., Danchi, W. C., et al. 1995, ApJS, 97, 455

Taquet, V., Ceccarelli, C., & Kahane, C. 2012a, ApJ, 748, L3

Taquet, V., Ceccarelli, C., & Kahane, C. 2012b, A&A, 538, A42

Taquet, V., Peters, P. S., Kahane, C., et al. 2013, A&A, 550, A127

Tielens, A. G. G. M. 2005, The Physics and Chemistry of the Interstellar Medium

Tielens, A. G. G. M. & Allamandola, L. J. 1987, in Astrophysics and Space Science Library, Vol. 134, Interstellar Processes, ed. D. J. Hollenbach & H. A. Thronson, Jr., 397–469

Treviño-Morales, S. P., Pilleri, P., Fuente, A., et al. 2014, A&A, 569, A19

Trevino-Morales, S. P., Fuente, A., Sanchez-Monge, A., et al. 2016, ArXiv e-prints [[arXiv]1607.06265]

van der Tak, F. F. S., van Dishoeck, E. F., & Caselli, P. 2000a, A&A, 361, 327

van der Tak, F. F. S., van Dishoeck, E. F., Evans, II, N. J., & Blake, G. A. 2000b, ApJ, 537, 283

Vasyunin, A. I. & Herbst, E. 2013, ApJ, 762, 86

Visser, R., Kristensen, L. E., Bruderer, S., et al. 2012, A&A, 537, A55

Viti, S. & Williams, D. A. 1999, MNRAS, 305, 755

Wakelam, V. & Herbst, E. 2008, ApJ, 680, 371

Walmsley, M. 1995, in Revista Mexicana de Astronomia y Astrofisica Conference Series, Vol. 1, Revista Mexicana de Astronomia y Astrofisica Conference Series, ed. S. Lizano & J. M. Torrelles, 137

Wang, S., Bergin, E. A., Crockett, N. R., et al. 2011, A&A, 527, A95

Wienen, M., Wyrowski, F., Schuller, F., et al. 2012, A&A, 544, A146

Wilson, T. L., Bania, T. M., & Balser, D. S. 2015, ApJ, 812, 45

Wilson, T. L. & Rood, R. 1994, ARA&A, 32, 191

Wilson, T. L., Snyder, L. E., Comoretto, G., Jewell, P. R., & Henkel, C. 1996, A&A, 314, 909

Wolfire, M. G. & Cassinelli, J. P. 1987, ApJ, 319, 850

Wood, D. O. S. & Churchwell, E. 1989, ApJS, 69, 831

Wright, M. C. H., Plambeck, R. L., & Wilner, D. J. 1996, ApJ, 469, 216

Zernickel, A., Schilke, P., Schmiedeke, A., et al. 2012, A&A, 546, A87

Erklärung

Ich versichere, dass ich die von mir vorgelegte Dissertation selbstäntik angefertigt, die benutzen Quellen und Hilfsmittel vollständig angegeben und dieStellen der Arbeit – einschliesslich Tabellen, Karten und Abbildungen –, die anderen Werken im Wortlaut oder dem Sinn nach entnommen sind, in jedem Einzelfall als Entlehnung kenntlich gemacht habe; dass diese Dissertation abgesehen von Observatoire de Paris noch keiner anderen Fakultät oder Universität zur Prüfung vorgelegen hat; dass sie – abgesehen von unten angegebenen Teilpublikationen – noch nicht veröffentlich worden ist, sowie, dass ich eine solche Veröffentlichung vor Abschluss des Promotionsverfahrens nicht vornehmen werde. Die Bestimmungen der Promotionsordnung sind mir bekannt. Die von mir vorgelegte Dissertation ist von Prof. Dr. Peter Schilke und Prof. Dr. Jacques Le Bourlot betreut worden.

Gwendoline Stéphan

Köln, 5th September, 2016

Lebenslauf

Personal Data

Name	Gwendoline Stéphan
Address	Brunostrasse 1 50678 Köln
Born in	15 June 1989
Geburtsort	Pont l'Abbé
Nationality	Französich

School & Study

2012 – 2016	PhD student in Physics "Modeling chemistry in massive star forming regions with internal PDRs" in I. Physikalisches Institut der Universität zu Köln
2010 – 2012	Master degree "Astronomie, Astrophysique et Ingénierie Spatiale" in Université Paris XXI, Orsay
2009 – 2010	Bachelor degree (3rd year) in Université Paris XXI, Orsay
2007 – 2009	Bachelor equivalent (Preparatory studies for engineering schools) in Lycée Ste Anne, Brest
2007	High school degree in Lycée Le Likès, Quimper

Köln, 5th September, 2016